Université Claude Bernard - Lyon 1

Mémoire présenté en vue de l'obtention du diplôme
d'habilitation à diriger des recherches

par

Frédéric Deschamps

Enseignant-chercheur associé à l'Institut de Géophysique de
l'École Polytechnique Fédéral de Zürich (Suisse)

Mélodies en sous-sols

*Études sur la structure thermochimique et
la dynamique du manteau terrestre*

Jury

Mr Yanick RICARD	Professeur, ENS Lyon	Rapporteur
Mme Christine THOMAS	Professeur, Univ. Liverpool	Rapporteur
Mme Andréa TOMMASI	Directrice de recherches, Univ. Montpelier	Rapporteur
Mme Isabelle DANIEL	Professeur, Univ. Lyon 1	Examinateur
Mr Stéphane LABROSSE	Professeur, Univ. Lyon 1	Examinateur
Mr Paul TACKLEY	Professeur, ETH Zürich	Examinateur

Table des matières

Frédéric Deschamps

Puncak Merapi

Enseignant-chercheur associé à l'École Polytechnique Fédérale de Zürich

Institut de Géophysique
ETH Zürich, NO H9.1, Sonnegstrasse 5
8092 – Zürich
Suisse

Email: deschamps@erdw.ethz.ch
Tél.: +41 44 6336806

Expérience professionnelle

Sept. 2005- **Enseignant-chercheur associé** (oberassistant) à l'École Polytechnique Fédérale (ETH) de Zürich (Suisse).

1998-2005 **Postdoc** à l'Université d'Utrecht (Pays-Bas).

1997-1998 **ATER** à l'Université de Nantes.

Formation

1994-1997 **Thèse de doctorat**, Universités de Paris XI et de Nantes. Félicitation du jury.

Titre Convection de Rayleigh-Bénard à viscosité variable: applications géophysiques et planétologiques.

Directeur Christophe Sotin

1991-1992 **DEA Géodynamique et physique de la Terre** (Paris XI, Paris VI, ENS Paris). Mention bien. Major.

Encadrement

2007- **Directeur de thèse** de *Lionel Duchoiselle*, 'The role of the post-perovskite phase transition in the mantle dynamics', ETH Zürich (Suisse).

2005 **Co-encadrement du projet de Licence** de *Jürg Hunziker*, ETH Zürich (Suisse).

2003 **Directeur du projet de Master** de *Luuk van Gerven*, Université d'Utrecht (Pays-Bas).

2001-2002 **Co-encadrement de la thèse** de *Stéphanie Godey*, Université d'Utrecht (Pays-Bas).

1998 **Co-encadrement du TER** de *Loïc Mevel*, Université de Nantes.

Enseignement

2005- **École Polytechnique Fédérale (ETH) de Zürich** (Suisse). Introduction à la géophysique (niveau licence), Stage de terrain en gravimétrie (niveau licence).

2000-2005 **Université d'Utrecht** (Pays-Bas). Mathématiques appliquées aux Sciences de la Terre (niveau licence), Sciences de la Terre et société (niveau licence).

1994-1998 **Université de Nantes** (monitorat puis ATER). Astrophysique (DEUG 1ère année), Planétologie comparée (maîtrise), Informatique et programmation (DEUG 2ième année).

Expérience de terrain

1998 **Chine 98**. Maintenance d'un réseau sismologique entre Xining et Yushu (Chine, province de Qinghai).

1997 **GéoFrance 3D**. Maintenance du réseau sismologique GéoFrance 3D-Armor 2.

1995 **Campagne océanographique** à bord de l'Atalante (IFREMER) entre Dakar et Brest.

1993 **Observatoire de géophysique interne de Crozet** (Terres Australes et Antarctiques Françaises). Responsable de station dans le cadre du service national civil.

Projets de recherche financés

2007-2010 **The role of the post-perovskite phase transition in the mantle dynamics**, SNF (Fond National Suisse de la Recherche Scientifique).

2003-2005 **Testing thermochemical convection models against seismological, gravity, and topographic data**, NWO (Organisation Néerlandaise pour la Recherche) et ISES.

Activités scientifiques pour la communauté

2000-2008 **Revues d'articles scientifiques** pour plusieurs périodiques (*Earth and Planetary Science Letters*, *Geophysical Journal International*, *Icarus*, *Monographies de l'American Geophysical Union*, *Tectonophysics*).

2005-2008 **Expertises de projets de recherche** auprès de plusieurs instituts (*SEDIT-CNRS*, *American National Science Foundation*, *Fonds Québequois de Recherche sur la Nature et les Technologies*).

2007-2008 **Organisation de sessions dans des congrès internationaux.** EGU 2007 (Vienne), EGU 2008 (Vienne), IGC 2008 (Oslo), Fall AGU 2008 (San Francisco, en préparation).

2008- **Membre du comité d'organisation** du 11ième workshop international sur la convection du manteau et la dynamique de la lithosphère (Braunwald, 28 Juin-3 Juillet 2009, en préparation).

Membre de jurys de thèse: Axel Röhm (1999, Université d'Utrecht), Stéphanie Godey (2002, Université d'Utrecht), François Couturier (2007, Université de Nantes).

Responsabilités administratives et collectives

2005-2008 **Organisation du séminaire hebdomadaire** de l'Institut de Géophysique de l'École Polytechnique Fédérale de Zürich.

2005-2008 **Webmaster** du site web du laboratoire 'Geophysical Fluid Dynamics' de l'École Polytechnique Fédérale de Zürich (http://www.gfd.ethz.ch).

2005-2008 **Responsable réseau et informatique** du laboratoire 'Geophysical Fluid Dynamics' de l'École Polytechnique Fédérale de Zürich.

Publications

Grasset O., C. Sotin, et F. Deschamps, 2000. On the internal structure and dynamics of Titan, *Planet. Space Sci.*, *48*, 617-636.

Deschamps, F., et C. Sotin, 2000. Inversion of two-dimensional numerical convection experiments for a fluid with a strongly temperature-dependent viscosity, *Geophys. J. Int.*, *143*, 204-218.

Deschamps, F., et C. Sotin, 2001. Thermal convection in the outer shell of large icy satellites, *J. Geophys. Res.*, *106*, 5107-5121.

Deschamps, F., R. Snieder et J. Trampert, 2001. The relative density-to-shear velocity scaling in the uppermost mantle, *Phys. Earth Planet. Inter.*, *124*, 193-211.

Deschamps, F., J. Trampert et R. Snieder, 2002. Anomalies of temperature and iron in the uppermost mantle inferred from gravity data and tomographic models, *Phys. Earth Planet. Inter.*, *129*, 245-264.

Deschamps, F., et J. Trampert, 2003. Mantle tomography and its relation to temperature and composition, *Phys. Earth Planet. Inter.*, *140*, 277-291.

Godey, S., F. Deschamps, J. Trampert et R. Snieder, 2004. Thermal and compositional anomalies beneath the North-American continent, *J. Geophys. Res.*, *109*, B01308, doi 10.1029/2002JB002263.

Deschamps, F., et J. Trampert, 2004. Towards a lower mantle reference temperature and composition, *Earth Planet. Sci. Lett.*, *222*, 161-175.

van Gerven, L., F. Deschamps, et R.D. van der Hilst, 2004. Geophysical evidence for chemical variations in the Australian continental mantle, *Geophys. Res. Lett.*, *31*, L17607, doi 10.1029/2004GL020307.

Trampert, J., F. Deschamps, J. Resovsky, et D.A. Yuen, 2004. Probabilistic tomography maps chemical heterogeneities throughout the lower mantle, *Science*, *306*, 853-856.

Deschamps, F., J. Trampert, et P.J. Tackley, 2007. Thermo-chemical structure of the lower mantle: seismological evidences and consequences for geodynamics, in D.A. Yuen et al. Eds., *Superplumes: beyond plate tectonics*, Springer, pp. 293-320.

Deschamps, F., S. Lebedev, T. Meier, et J. Trampert, 2008a. Azimuthal anisotropy of Rayleigh-wave phase velocities in the east-central United States, *Geopys. J. Int.*, *173*, 827-843.

Deschamps, F., S. Lebedev, T. Meier, et J. Trampert, 2008b. Stratified seismic anisotropy reveals past and present deformation beneath the east-central United States, *Earth Planet. Sci. Lett.*, *274*, 489-498.

Peter, D., L. Boschi, F. Deschamps, B. Fry, G. Ekström, et D. Giardini, 2008. Surface-wave tomography : finite-frequency shear-velocity inversions for the European-Mediterranean region, *Geophys. Res. Lett.*, *35*, L16315, doi: 10.1029/2008GL034769.

Deschamps, F., et P.J. Tackley, 2008a. Searching for models of thermo-chemical convection that explain probabilistic tomography. I. Principles and influence of rheological parameters, *Phys. Earth Planet. Inter.*, *171*, 357-373.

Deschamps, F., et P.J. Tackley, 2008b. Searching for models of thermo-chemical convection that explain probabilistic tomography. II. Influence of physical and compositional parameters parameters, en revision pour *Phys. Earth Planet. Inter.*.

Soldati, G., L. Boschi, F. Deschamps, et D. Giardini, 2008. Inferring radial models of mantle viscosity from gravity (GRACE) data and an evolutionary algorithm, en revision pour *Phys. Earth Planet. Inter.*.

Nakagawa, T., P.J. Tackley, F. Deschamps, et J.A.D. Connolly, 2008. Incorporating self-consistently calculated mineral physics into thermo-chemical mantle convection simulations in a 3D spherical shell and its influence on seismic anomalies in Earth's mantle, en revision pour *Geochem. Geophys. Geosys.*.

Expérience pédagogique

Mon activité d'enseignement s'inscrit successivement dans le cadre de mon monitorat (1994-1997), puis de mes fonctions d'ATER à l'Université de Nantes (1997-1998), de postdoc à l'Université d'Utrecht (2000-2005), et d'enseignant-chercheur associé (oberassistant) à l'École Polytechnique Fédérale (ETH) de Zürich (depuis Septembre 2005). À Nantes, j'ai participé à l'élaboration et à l'encadrement de cours, de travaux dirigés et de travaux pratiques en géophysique, astrophysique et informatique destinés aux étudiants de DEUG, de licence et de maîtrise. À Utrecht, j'ai encadré les travaux dirigés de 'Mathématiques appliquées aux Sciences de la Terre', et de j'ai participé aux enseignements de 'Sciences de la Terre et Société'. À Zürich j'enseigne le cours d'introduction à la géophysique portant sur le champ de gravité terrestre et la géodésie, et j'assure le volet gravimétrie du stage de terrain en géophysique appliquée destiné aux étudiants de troisième année. J'ai également encadré ou co-encadré plusieurs étudiants dans le cadre de leur thèse de doctorat ou de leur projet de maîtrise.

1. Enseignements

• Planétologie comparée (1997-1998 – Maîtrise des Sciences de la Terre, Université de Nantes). Cette série de cours et de travaux dirigés s'articule autour de la structure interne et de la dynamique interne des planètes telluriques telles que Vénus, Mars, et bien sûr la Terre. La différenciation des planètes, le transfert de chaleur dans les manteaux planétaires, l'évolution des satellites des planètes géantes font partis des thèmes abordés, ainsi que l'apport des missions spatiales récentes à ces recherches. Ce cours est l'occasion de souligner quelques notions de physique qui sont à la base des phénomènes rencontrés en géophysique et en planétologie comparée.

• Astrophysique (1994-1998 – DEUG A 1ère année, Université de Nantes). Avec le reste de l'équipe enseignante, j'ai renouvelé, une série de travaux dirigés qui avaient pour but d'illustrer le cours magistral à partir de quelques exemples faisant intervenir des notions de physique fondamentale. Des sujets tels que les systèmes de coordonnées astronomiques,

le refroidissement des planètes telluriques ou encore l'évolution des étoiles sont abordés de manière plus ou moins simplifiée. Lors de mon ATER (1997-1998), j'ai par ailleurs réalisé 1/3 des cours magistraux, et j'ai partagé mon service d'enseignement entre l'Université de Nantes et son antenne de Saint-Nazaire.

• Informatique et programmation (1994-1997 – DEUG B 2ième année, Université de Nantes). Cet enseignement fait parti du module 'Mathématique et Informatique' proposé dans la filière, son but étant d'introduire les méthodes utilisées en programmation numérique, tout en appliquant des notions étudiées pendant le cours de mathématique. Quelques méthodes simples d'analyse numérique sont également abordées.

• Mathématiques appliquées aux Sciences de la Terre (2000-2005 – Licence et Maîtrise de Sciences de la Terre, Université d'Utrecht). Cet enseignement est organisé sous forme de cours-TD intégrés. Il est basé sur le livre de Roel Snieder (*A Guided Tour of Mathematical Methods for the Physical Sciences*, Cambridge University Press), et il aborde des notions fondamentales et centrales en Sciences de la Terre, notamment sur les fonctions de variables complexes, les distributions, la résolution d'équations différentielles, mais aussi l'algèbre linéaire et l'analyse de Fourier. La variété des exercices permettent aux étudiants de retrouver par eux-mêmes certains théorèmes et résultats démontrés en cours.

• Sciences de la Terre et Société (2003-2005 – Maîtrise de Sciences de la Terre, Université d'Utrecht et University College). Les différents modules de cet enseignement ont pour but de souligner les nombreuses interactions entre les Sciences de la Terre et la société civile (urbanisme, vie économique et culturelle, …). Chaque module comporte un cours magistral et des travaux pratiques sur ordinateur. J'ai plus particulièrement enseigné le module consacré à l'aléa sismique.

• Gravimétrie et géodésie (Depuis Septembre 2005 – Licence de Sciences de la Terre, École Polytechnique Fédérale de Zürich). Il s'agit de la première partie d'un cours magistral d'introduction à la géophysique (la seconde partie traite du géomagnétisme) basée sur le manuel de William Lowrie (*Fundamentals of Geophysics*, Cambridge University Press). Deux principaux thèmes sont abordés, le champ de gravité terrestre et la géodésie. Après quelques rappels sur la gravitation universelle, le cours se concentre, entre autre, sur la modélisation du champ de gravité terrestre, la mesure, la modélisation et l'interprétation des anomalies de gravité à différentes échelles, la forme de la Terre et les variations de sa vitesse de rotation. En plus de ce cours, j'assure l'organisation et l'encadrement d'une expérience gravimétrique (détection d'un tunnel ferroviaire) dans le cadre d'un stage de terrain d'introduction aux méthodes géophysiques appliquées.

2. Encadrement d'étudiants

• Co-encadrement du stage de TER de Loïc Mevel, en maîtrise de Sciences de la Terre (Université de Nantes) sur la 'La tectonique d'Europe'. Plus particulièrement, je suis intervenu dans l'estimation des propriétés (épaisseur, viscosité, profil de température) de l'enveloppe superficielle de glace.

• Co-encadrement de la thèse de Stéphanie Godey (Université d'Utrecht). Dans sa thèse, intitulée 'Structure of the uppermost mantle beneath North America: Regional surface wave tomography and thermo-chemical interpretation', Stéphanie Godey a développé un modèle tomographique régional pour l'Amérique du Nord, puis elle a interprété ce modèle en termes de variations de température et de composition. J'ai supervisé la partie de ce travail consacrée à l'interprétation thermochimique du modèle tomographique régional. Celle-ci est détaillée dans un article publié dans *Journal of Geophysical Researches* (Godey et al., 2004).

• Projet de recherche de Luuk van Gerven, dans le cadre de son Master en Sciences de la Terre (Université d'Utrecht) intitulé 'Thermal and compositional contributions to the density of the Australian continental lithosphere'. À partir d'un modèle tomographique récent du manteau supérieur sous l'Australie, Luuk van Gerven a déterminé un profil du facteur d'échelle ($\zeta = \partial \ln \rho / \partial \ln V_S$) pour trois provinces tectoniques distinctes. Ces recherches ont fait l'objet d'un article dans *Geophysical Research Letters* (van Gerven et al., 2004).

• Thèse de Lionel Duchoiselle (École Polytechnique Fédérale de Zürich). Lionel Duchoiselle a débuté sa thèse en Mai 2007. Dans un premier temps, il tente d'établir des relations entre les observables (température interne, flux de chaleur) et les paramètres (nombre de Rayleigh, rayon de courbure) dans le cas de la convection purement thermique en géométrie sphérique. Par la suite, il calculera des modèles de convection thermochimique en géométrie sphérique, qu'il comparera à un ensemble d'observables géophysiques (dont la tomographie probabiliste). Il étudiera en particulier l'influence de la phase post-pérovskite sur la dynamique du manteau.

Expérience de terrain

Parallèlement à mon activité de recherche, et sans liens avec celles-ci, j'ai participé à plusieurs missions de terrain pour l'acquisition de données géophysiques ou la maintenance d'observatoires.

• **Observatoire de géophysique interne de Crozet** (Terres Australes et Antarctiques Françaises). Cet observatoire permanent est situé dans le sud de l'Océan Indien, dans l'archipel des Crozet. Il abrite une station sismologique large-bande appartenant au réseau GEOSCOPE, et un observatoire géomagnétique (mesures absolues et variations lentes) appartenant au réseau INTERMAGNET (Figure ci-dessous). Dans le cadre de mon service national, j'ai occupé les fonctions de responsable de station durant toute l'année 1993, et j'ai participé au traitement des données (à l'EOST de Strasbourg) à l'issu de l'hivernage.

Observatoire de géophysique interne de Crozet (Base Alfred Faure, Terres Australes et Antarctiques Françaises). (a) Shelters géomagnétisme. (b) STS1 vertical de la station GEOSCOPE.

• **Atalante.** 'L'Atalante' est un navire de l'IFREMER. J'ai participé à la mission DABRE (6-17 Avril 1995, chef de mission: Jean-Pierre Rhéault), entre Dakar et Brest. Au cours de ce transit, des profils sismiques ont été acquis le long de la marge de Galice et du banc de Goringe.

• **GéoFrance 3D-Armor2.** Ce programme a pour objectif une meilleure connaissance de la structure profonde du Massif Armoricain, et en particulier de l'extension et de la géométrie des cisaillements armoricains (thèse de Sébastien Judenherc, à l'EOST). De 1997 à 1999, deux expériences de sismologie passive ont été déployées conjointement par l'EOST (Michel Granet) et le LGIT (Georges Poupinet), le long d'une ligne Saint-Malo/Rennes/Nantes. J'ai participé, en 1997 et 1998, à la mise en place et à la maintenance de ce réseau.

• **Chine 98.** En 1998, Gérard Wittlinger (EOST) et Georges Poupinet (LGIT) ont organisé et dirigé une expérience de sismologie passive dans la province chinoise du Qinghai, entre Gonghe et Yushu. J'ai assuré la maintenance de ce réseau pendant un mois. Les données recueillies ont été utilisées pour réaliser une imagerie détaillée de la base de la croûte et du sommet du manteau sous la partie nord-est du plateau Tibétain (thèse de Jérôme Vergne, à l'EOST).

En quelques mots

La Terre est un objet complexe, et son étude nécessite une approche pluridisciplinaire. Ainsi, pour déterminer la structure thermochimique du manteau terrestre, qui se révèle plus complexe qu'on ne le pensait il-y-a une dizaine d'années seulement, il est nécessaire d'intégrer les observables géophysiques disponibles aux modèles géodynamiques, donc de lier des résultats obtenus dans différentes disciplines, notamment en sismologie, en physique des minéraux, et en géodynamique. Il serait toutefois naïf de penser que la simple superposition de résultats donne accès, pour un problème donné, à une solution claire et unique. Au contraire, les incertitudes sur les données, les biais de traitement (en particulier, dans le cas des méthodes inverses, la prescription d'information *a priori*), et l'existence de trade-offs, pour ne citer que ces trois difficultés, assurent la non-unicité des solutions. Une exploration appropriée de l'espace des modèles s'impose pour estimer la validité d'une solution particulière, ou mieux, sa probabilité. Les travaux présentés dans ce mémoire intègrent ces exigences de multidisciplinarité et de validation des solutions, et abordent successivement trois sujets principaux : la distribution de l'anisotropie sismique sous les continents; la stabilité des racines continentales (100–300 km); et la structure thermochimique du manteau inférieur (660–2891 km).

Le premier chapitre de ce mémoire porte un nouveau regard sur la reconstruction de l'histoire de la déformation de la croûte profonde et du sommet du manteau. Lorsque ces régions subissent des déformations d'origine géodynamique, elles enregistrent des fabriques qui sont sans doute responsables de l'anisotropie sismique observée par les sismologues. L'étude des variations azimutales de la vitesse de phase des ondes de Rayleigh sous le centre-est des États-Unis (31°N-41°N et 82°E-92°E) m'a permis de mettre clairement en évidence une distribution verticale de l'anisotropie dans cette région. Des déformations actuelles et passées d'origines géodynamiques différentes (vraisemblablement, et en remontant le temps, l'écoulement asthénosphérique contemporain, la dérive de la plaque Nord-Américaine vers 160-125 Ma, et la fermeture de l'orogène Appalachienne il-y-a 270 Ma) ont donc créé des fabriques, qui sont aujourd'hui distribuées en trois couches superposées, de la plus ancienne (proche de la surface) à la plus récente (profonde).

Le second chapitre tente d'interpréter les modèles tomographiques du manteau peu profond (c'est-à-dire, jusque vers 300 km) en termes de distributions thermochimiques, et d'en tirer les conséquences quant à la stabilité des racines continentales. La plupart des modèles tomographiques s'accordent sur la présence de zones de vitesses sismiques élevées sous les cratons continentaux, jusque vers 200-300 kilomètres de profondeur. En surface, ces racines sont également associées aux provinces les plus anciennes, ce qui suggère que les racines sont plus froides que le manteau moyen. Pour compenser ce refroidissement, on invoque le plus souvent un appauvrissement chimique de ces racines. Afin de tester cette hypothèse, j'ai mené plusieurs études basées sur la calibration des anomalies de densité à partir des anomalies de gravité. L'interprétation thermochimique des modèles tomographiques et des anomalies de gravité prédit effectivement un appauvrissement chimique en fer. De plus, la rhéologie des racines (en particulier les variations de viscosité avec la température) participe sans doute activement à la stabilité des cratons.

La dernière partie de ce mémoire (séparée en deux chapitres) se penche sur la structure thermochimique du manteau inférieur. De nombreux indices convergent en faveur de la présence de fortes variations latérales de composition, notamment à la base du manteau. Dans un premier temps, j'ai déterminé des profils moyens de température et de composition à partir des données de physiques des minéraux disponibles, et du modèle sismologique de référence PREM. Les incertitudes sur ces quantités restent importantes, en particulier à cause des incertitudes sur les dérivées des modules élastiques des minéraux présents dans le manteau, et des corrections appliquées pour la présence de fer. J'ai ensuite calculé des distributions thermochimiques 3D pour le manteau inférieur. Ici encore, il est nécessaire de contraindre la densité pour résoudre le trade-off existant entre la température et la composition. La méthode de tomographie probabiliste permet justement de le faire, et des modèles récents ont apporté des contraintes robustes sur les distributions des anomalies de vitesses sismiques et de densité. À partir de ces distributions, j'ai calculé des distributions de température et de composition (perovskite et fer) qui font apparaître du matériau enrichi en fer et (donc chimiquement plus dense que le manteau moyen) dans les régions habituellement associées aux superplumes. Enfin, j'ai entrepris une exploration exhaustive de l'espace des modèles de convection thermochimique afin d'identifier le ou les paramètres capables de maintenir des réservoirs de matériau dense à la base du manteau. Selon cette recherche, le rapport de viscosité thermique et la pente de Clapeyron de la transition de phase à 660 km jouent des rôles cruciaux pour maintenir de tels réservoirs sur des périodes de temps comparables à l'âge de la Terre.

Remerciements

Les travaux de recherche présentés dans ce mémoire sont le fruit de plusieurs collaborations entreprises après ma thèse, d'abord à l'Université d'Utrecht, puis à l'Ecole Polytechnique Fédérale de Zürich. Je remercie Roel Snieder et Jeannot Trampert, à Utrecht, et Paul Tackley et Domenico Giardini, à Zürich de m'avoir donné l'opportunité et les moyens de réaliser ces travaux.

A Utrecht comme à Zürich, j'ai bénéficié d'un environnement scientifique exceptionnel, et je souhaite remercier toutes les personnes qui y ont participé de près ou de loin, notamment Arie van den Berg (U), Lapo Boschi (Z), Chris Finlay (Z), Bill Fry (Z), Taras Gerya (Z), Rob van der Hilst (U), Jeroen van Hunen (U & Z), Boris Kaus (Z), Amir Khan (Z), Sergei Lebedev (U), Hanneke Paulsen (U), Joe Resovsky (U), Henri Samuel (Z), Jesper Spetzler (U), et Arie van Wettum (U).

Yanick Ricard m'a permis de soutenir cette habilitation à l'Université Claude Bernard de Lyon, et il a accepté de faire partie de mon jury, ce dont je le remercie chaleureusement. Je suis aussi très reconnaissant à Christine Thomas, Andréa Tommasi, Isabelle Daniel, Stéphane Labrosse, et Paul Tackley d'avoir accepter de faire partie de mon jury.

Je remercie également Anne Sornette (Z), qui a relu mon manuscrit et m'a donné de précieux conseils pour la soutenance, et Nicolas Coltice (L), dont l'aide de m'a été très utile pour préparer et organiser la-dite soutenance.

Introduction

Où l'auteur justifie le titre de ce mémoire

Nous savons tout les deux que le Monde sommeille par manque d'imprudence

(Jacques Brel, Jojo)

Le titre de ce mémoire est un clin d'œil au cinéma populaire français des années 60 (Figure I.1). Jean Gabin, un truand chevronné sortant d'un séjour prison, et Alain Delon, un jeune voyou inexpérimenté, s'associent pour entreprendre le casse du casino de Cannes. À défaut d'espèces sonnantes et trébuchantes, les coffres forts que les géophysiciens cherchent à percer protègent des secrets bien gardés sur la structure, la composition, l'évolution, et la dynamique de la Terre. Le géophysicien n'a pas, en principe, à craindre l'irruption de la brigade antigang dans son laboratoire, mais il doit démêler des pistes souvent brouillées par l'œuvre du temps, l'interférence entre plusieurs phénomènes – physiquement reliés ou, au contraire, indépendants –, le manque de données, ou encore l'incapacité de ces dernières à résoudre clairement le problème posé. On le voit, la tâche est compliquée, et il convient de progresser prudemment. C'est presque un oxymore, et de fait, trop de prudence (ou, pour reprendre Brel, de manque d'imprudence) ne conduirait qu'à trop d'immobilité. Une façon de concilier progrès et prudence est de proposer des solutions moins tranchées, idéalement d'attribuer une probabilité à chaque modèle en concurrence, ou à chaque valeur possible pour un paramètre donné. Donner une solution unique n'a de toute façon pas de signification mathématique au sens des distributions.

Le sous-titre est plus explicite et reflète bien le message, relativement simple, que ce mémoire souhaite faire passer : il existe, à différents niveaux du manteau terrestre, de fortes variations latérales de composition. On s'en doutait, mais on manquait de preuves tangibles. La décennie écoulée les a livrées, notamment grâce à des progrès en sismologie (meilleur résolutions radiales et latérales, utilisation des modes propres pour contraindre la densité, développement de méthodes probabilistes pour la tomographie), en physique des

minéraux (calculs des propriétés thermo-élastiques par calculs *ab initio*, et des diagrammes de phase en minimisant l'énergie libre, découverte de la post-pérovskite), et en modélisation géodynamique (convection thermochimique, géométrie sphérique). Lorsqu'ils sont soigneusement assemblés, ces résultats mettent en évidence la présence de variations latérales de composition (dont il à reste préciser la nature) dans le manteau, et en particulier dans sa partie la plus profonde.

Figure I.1 - L'affiche de 'Mélodie en Sous-sol', film d'Henri Verneuil (1963), avec Jean Gabin et Alain Delon dans les rôles principaux.

Non-unicité, incertitudes, et indéterminations

La Terre profonde n'est pas totalement muette. Elle communique, souvent violement (tremblements de Terre, éruptions volcaniques) avec la surface. Les données et observations générées par ces évènements, mais aussi les signaux gravitaires, géomagnétiques et géochimiques, constituent autant d'indices sur la structure thermochimique qu'il nous faut déchiffrer. L'ensemble de ces données devrait, dans le meilleur des mondes, conduire à une mélodie harmonieuse décrivant la structure et la dynamique du manteau terrestre.

Il n'en est rien. Ainsi, si j'ai rajouté un 's' à 'mélodie', ce n'est pas par souci du copyright, mais bien parce que la Terre fredonne plusieurs mélodies. Différents ensembles de données conduisent à des conclusions parfois contradictoires, et il existe plusieurs façons d'interpréter un même ensemble de données, ne serait-ce que parce que différentes écoles de pensée auront tendance à interpréter différemment un même résultat. Par exemple, les zones bleues des modèles tomographiques sont, dans la réalité, froides pour certains et

chimiquement différenciées pour d'autres. Derrière ces désaccords se cachent souvent des ambiguïtés plus fondamentales liées aux données elles-mêmes, ou au traitement que nous en faisons.

Un problème bien connu des scientifiques, et en particulier des géophysiciens, est l'existence de trade-offs entre différentes variables, et que l'on pourrait résumer ainsi : il-y-a plusieurs causes possibles pour un même effet. Les vitesses sismiques n'échappent pas à cette difficulté, et il existe un trade-off très marqué entre la température et la composition. Toute, sinon la plus grande partie, de la difficulté à interpréter les modèles tomographiques résident dans ce trade-off. Ainsi, les variations de vitesses sismiques observées dans le manteau peuvent s'interpréter par des anomalies purement thermiques, purement chimiques, ou par un mélange des deux (Figure I.2a). Sans parler de la fusion partielle et de la présence éventuelle de fluides. Un autre exemple de trade-off nous est fourni par l'inversion de vitesses d'ondes de surfaces pour un modèle de vitesse d'onde de volume autour d'une discontinuité, par exemple le Moho (Figure I.2b). Ici, ce sont les valeurs des vitesses d'onde de volume dans les couches adjacentes à la discontinuité qui entrent en compétition avec la profondeur de cette discontinuité. À moins de disposer d'information complémentaire et indépendante des observables déjà disponibles, il est impossible de privilégier une solution plutôt qu'une autre.

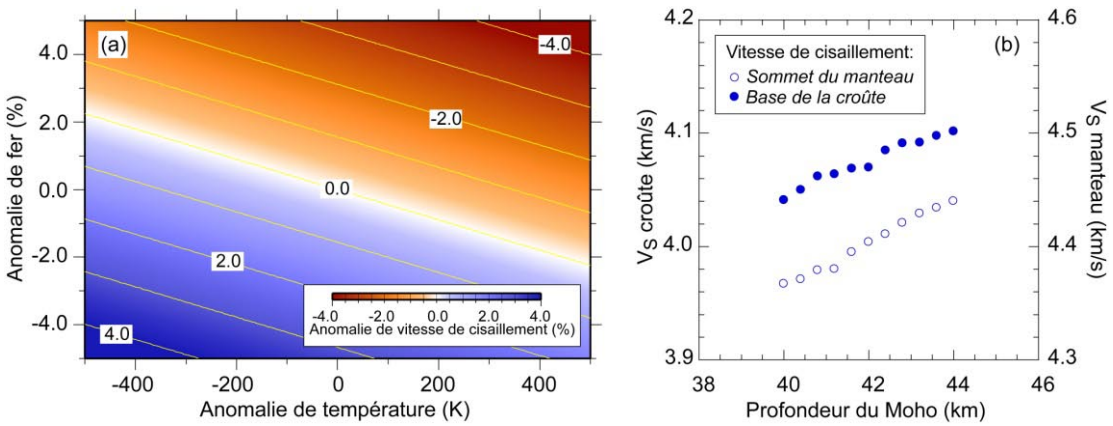

Figure I.2 – Deux exemples de trade-off. (a) Entre les anomalies de température et de fer, pour expliquer les anomalies de vitesses de cisaillement (ici, à 2500 km de profondeur). (b) Entre la profondeur du Moho et les vitesses d'onde de cisaillement dans les couches adjacentes au Moho, pour expliquer les anomalies isotropiques de la vitesse de phase des ondes de Rayleigh (ici, sous le centre-est des État-Unis).

À défaut d'information indépendante, on impose souvent de l'information *a priori* basée sur des intuitions ou des considérations physiques, géologiques, ou géochimiques, mais qui, comme son nom l'indique, est totalement subjective. L'information *a priori* sélectionne un modèle ou une catégorie de modèles parmi les solutions possibles. Par exemple, si l'on pense que la convection dans le manteau terrestre est purement thermique,

on décidera d'interpréter les variations de vitesses sismiques des modèles tomographiques en termes de variations de températures uniquement. Citons aussi un type d'information *a priori* très répandu, qui est d'imposer au modèle d'être suffisamment lisse ou régulier. Les affaires se compliquent un peu plus si une partie de l'espace modèle n'est pas contrainte par les données. Cette région de l'espace modèle, encore appelée 'espace nul', rassemble tous les modèles $\mathbf{m}$ tels que $\mathbf{Am} = 0$, où $\mathbf{A}$ est la matrice décrivant le problème directe. Puisque les modèles appartenant à l'espace nul ne sont pas contraints par les données, la combinaison d'une solution approximative (et contrainte par les données) avec n'importe quel modèle de l'espace nul explique les données aussi bien que la solution approximative seule. Autrement dit, la fonction de coût, qui mesure la capacité des modèles à expliquer les données, possède un minimum d'autant plus plat que l'espace nul est étendu, et le problème s'en trouve d'autant plus indéterminé. À titre d'exemple, la Figure I.3 montre comment faire apparaître clairement un slab sur une image tomographique, sans dégrader l'accord entre cette image tomographique et les données. Répétons-le, l'information *a priori* sélectionne une ou des solutions dans une portion seulement de l'espace modèle en ignorant tout le reste … et tant pis si nos intuitions de départ se révèlent en fin de compte erronées. Soyons fair-play, il arrive parfois que certaines intuitions soient parfaitement justifiées.

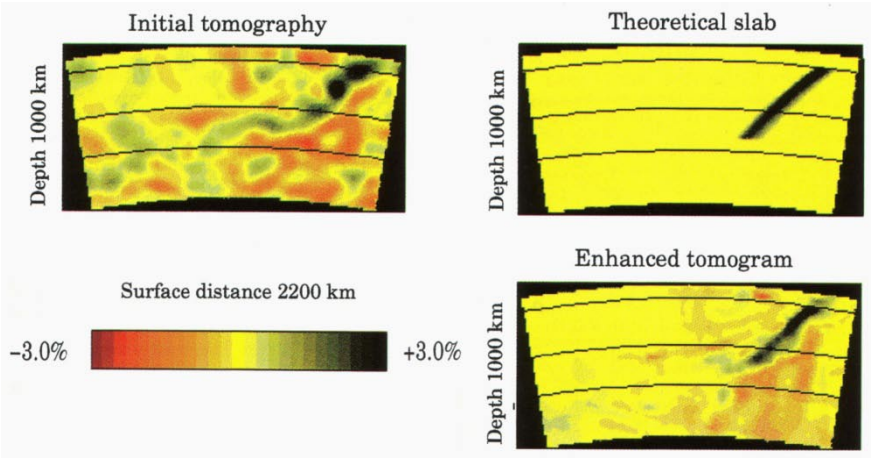

Figure I.3 – Une conséquence de la prescription d'information *a priori* en présence d'un espace nul. L'image de gauche représente une image tomographique prise dans la région des Tonga, et sur laquelle on devine un slab (Deal et al., 1999). Un slab théorique (en haut à droite) est ensuite défini et projeté dans l'espace nul (c'est-à-dire l'ensemble des modèles non-contraints par les données). Cette projection est additionnée à avec l'image tomographique initiale pour produire une image tomographique améliorée (en bas à droite). Bien que très différente, cette nouvelle image explique les données aussi bien que l'image initiale.

Est-il besoin de souligner les difficultés liées aux incertitudes sur les données ? Quelque soit le traitement que l'on fait de ces données, les incertitudes initiales se propagent, ou plutôt s'amplifient, puisque chaque étape du traitement ajoute une incertitude (inversions, choix de valeurs de paramètres, …) ou une perte d'information

(filtrages, moyennes, …). Sans doute l'exemple le plus marquant, dans le cadre de ce mémoire, est l'incertitude sur les paramètres thermo-élastiques des minéraux du manteau terrestre aux pressions et températures du manteau. Celles-ci sont en grande partie responsables des incertitudes actuelles (~ 300 K) sur le modèle radial moyen de température calculé à partir des modèles sismiques de référence (Deschamps et Trampert, 2004). Ici, les sources d'incertitudes sont multiples : les valeurs de surface des paramètres thermo-élastiques et de leurs dérivées (en température et en pression) bien sûr, mais aussi les corrections qu'il faut apporter à ces paramètres en fonction de la composition pétrologique supposée (en particulier, pour les pôles ferreux des minéraux), ainsi que les lois utilisées pour l'extrapolation aux pressions du manteau.

Un autre problème concerne la disponibilité des données. Une distribution non-uniforme ou biaisée de ces données conduit à des problèmes inverses mal posés, où certaines régions du globe sont sur-échantillonnées, tandis que d'autres sont sous-échantillonnées. C'est le cas de l'information sismologique qui, bien qu'essentielle, reste tributaire de la distribution respective des sources (les tremblements de Terre) et des capteurs (les stations sismologiques) sismiques. Les progrès technologiques récents, et en particulier le développement et la mise en place de sismomètres adaptés aux fonds marins (OBS), et le déploiement de réseaux temporaire denses permettent d'améliorer la couverture instrumentale à la surface de la Terre. En revanche, sauf pour des études très locales (pour lesquelles des charges explosives remplacent les tremblements de Terre), il paraît difficile de modifier la cartographie des sources sismiques.

Les problèmes inverses, souvent sollicités en géophysique combinent plusieurs des difficultés précédentes. La prescription de matrices de covariance et un traitement approprié (p.e., Tarantola et Valette, 1982) permettent de propager les erreurs des observables vers les modèles. En revanche, le manque de données, leur répartition inégale ou leur mauvaise qualité conduisent à une formulation maladroite du problème et imposent souvent la prescription d'information *a priori*. Le plus souvent celle-ci consiste à amortir l'amplitude du modèle ou à lisser ce modèle. La quantité d'information *a priori* est choisie de façon à obtenir un bon compromis entre la régularité du modèle (sa capacité à expliquer l'information *a priori*), et son accord avec les données (sa capacité à expliquer les données). Tient, tient, mais … ne serais-ce pas là un trade-off ?

Notons enfin que les modélisateurs, même s'ils n'interviennent pas directement sur les données, sont confrontés à d'autres difficultés d'ordre numérique (développement d'algorithmes stables, précis et rapides) et théorique (choix et pertinence des approximations, identification des paramètres de contrôle). Trop de complexité nuit à la compréhension physique du problème et augmente le risque de commettre des erreurs

numériques (au sens large). D'un autre côté, un modèle trop simple ne parviendra pas à décrire des détails qui peuvent apparaître importants aux yeux de certains. Ici aussi, il faut trouver le bon équilibre entre le réalisme (la complexité) d'un modèle et sa simplicité. Doit-on encore parler de trade-off ?

La liste des difficultés rencontrées par les géophysiciens et les géochimistes est bien sûr loin d'être close. On en trouvera de nombreux exemples supplémentaires dans l'excellent ouvrage de Don Anderson, 'New Theory of the the Earth' (Anderson, 2007).

Où il est question d'une virée sur la toile, d'un célèbre modèle de référence, et d'un noble sentiment

La toile informatique planétaire (World Wide Web) a révolutionné notre façon de collecter de l'information. Le volume des données et des informations disponibles est considérable, ce qui n'est pas forcément un avantage. Il faut en effet opérer un tri, parfois ultra-sélectif, pour éliminer les informations non pertinentes, incomplètes ou erronées, et ne garder que ce qui est utile à notre recherche. Illustrons cette nouvelle source d'ambiguïté par un petit exemple géophysique.

Il-y-a quelques mois, par curiosité, j'ai entré le mot clé (ou googlet) `PREM` dans un célèbre moteur de recherche. Surprise, la première entrée m'apprend que 'prem' est un mot sanskrit signifiant 'amour'. La troisième entrée m'indique que 'prem' est le mot indonésien pour 'prune' (le fruit). Suivent quelques personnalités indiennes prénommées Prem, sans aucun doute en référence à la première entrée. Le géophysiquement célèbre modèle de référence construit par Dziewonski et Anderson (Dziewonski et Anderson, 1981) n'arrive que bien plus loin, vers la dixième position. Mais les choses évoluent rapidement sur la toile. Aujourd'hui (20 Septembre 2008), au moment de terminer ce mémoire, c'est un homme d'affaire indien qui tient le haut du pavé. Le modèle terrestre de référence préliminaire a conquis la troisième entrée, et les traductions sanskrite et indonésienne sont toujours présentent dans le haut du tableau. Pour ajouter à la confusion les différentes versions nationales du fameux moteur de recherche conduisent des résultats sensiblement différents.

Ce petit exercice nous mène à la conclusion (aux accents tautologiques) suivante : avant de lancer une recherche sur le Web il est utile d'avoir dès le départ une petite idée de ce que l'on cherche, et d'entrer le googlet le plus détaillé possible en fonction des informations préalablement disponibles et/ou du contexte de la recherche entreprise. Ainsi, le googlet `Preliminary Reference Earth Model` nous amène droit au but. En attendant le Web 2.0, que l'on nous promet plus intelligent que son prédécesseur.

Enfin, il n'est pas impossible que Dziewonski et Anderson aient nommé leur modèle en connaissance de cause. Pour autant, doit-on en conclure que les ondes de Love ont une influence particulière sur ce modèle, où encore que la Terre a la forme d'une prune, et non celle d'une poire ?

Problèmes, objectifs, méthodes

Un 's' doit aussi être rajouté à 'sous-sol' car le manteau supérieur (1er sous-sol), le manteau inférieur (2ième sous-sol), le noyau externe et la graine (3ième et 4ième sous-sols) doivent être traités séparément, même si, indiscutablement, ils interagissent entre eux. Ainsi la pétrologie du manteau inférieur est considérablement simplifiée par rapport à celle du manteau supérieur. On y compte 2 phases principales (perovskite et magnésio-wüstite), accompagnées de leurs pôles ferreux et magnésiens (ainsi que, pour la perovskite, un pôle alumineux et un pôle calcique). En comparaison, une bonne description du manteau supérieur nécessite la prise en compte de 4 phases principales (olivine, orthopyroxène, clinopyroxène, grenat), de leurs différents pôles, et bien sûr d'un diagramme de phase pression-température adéquate pour tenir compte de la transformation de ces phases lorsqu'elles traversent la zone de transition (410-660 km). Ajoutez-y encore d'autres phases si, de plus, vous souhaitez tenir compte de structures particulières (par exemple, la coesite dans ce cas des slabs). La découverte récente de la phase post-pérovskite complique sensiblement notre vision du manteau profond, mais globalement le manteau inférieur reste pétrologiquement plus facile à modéliser que le manteau inférieur. Par ailleurs des frontières physiques, fortement marquées par des discontinuités sismologiques, existent à chaque interface (660-km, CMB, ICB) et réduisent fortement ou totalement le transfert de matière d'une couche vers l'autre.

La structure radiale du manteau terrestre au premier ordre est bien connue, avec une couche riche en olivine, jusque vers 410 km de profondeur, une zone de transition entre 410 et 660 km, dans laquelle l'olivine se transforme successivement en waldsleyite et en ringwoodite (ses phases hautes pressions), et un manteau inférieur dominé par le couple pérovskite/magnésio-wüstite. Difficile d'en dire plus avec certitude. Des complications surviennent, notamment avec les grenats qui poursuivent leur transformation au delà de 660 km, et, à la base du manteau, la présence de la couche D" dont la nature et la topographie sont encore imprécises. Quant à la structure thermique radiale, même un paramètre aussi important que le profil moyen de température est mal connu. Que dire de la structure 3D du manteau, sinon que nombreuses pièces manquent au puzzle, et que l'image que nous avons du manteau (et en particulier du manteau profond) reste très parcellaire et plutôt floue. L'information la plus détaillée dont nous disposions est, jusqu'à

présent d'origine sismologique. Les modèles tomographiques nous révèlent que la structure sismique du manteau (la distribution des zones de vitesses sismiques lentes et rapide) est plutôt bien corrélée avec la tectonique de surface jusque vers 250 km de profondeur, et que la base du manteau (disons entre 2500 km et la CMB) est très hétérogène. Malheureusement, l'interprétation de ces anomalies en termes de structures thermochimiques n'est pas si simple.

Parmi les questions non résolues, citons l'origine de la stabilité des racines continentales, au sommet du manteau, peut-être liée à la structure thermochimique de ces racines (Jordan, 1975). Également toujours d'actualité, l'origine du volcanisme intra-plaque, les hotspots (Anderson, 2005; Courtillot et al., 2003), et le destin des slabs océaniques (Fukao et al., 2001). D'autres questions nous renvoient très loin dans le passé, dans la jeunesse de notre planète. Plusieurs scénarios de Terre primitives (Boyet et Carlson, 2006; Labrosse et al., 2007) impliquent une différenciation partielle des silicates conduisant à la formation d'un réservoir riche en fer à la base du manteau. Reste à savoir si ce réservoir a survécu à la convection pendant quelques 4 milliard d'années, si oui pourquoi, et quelles sont sa structure et sa distribution actuelles. Notons que toutes ces questions impliquent à des degrés divers d'importantes variations latérales de température et de composition.

Une question clé pour la détermination des structures thermochimiques est la distribution des anomalies de densité (les puristes dirons, avec raison, de masse volumique. La plupart du temps, le terme 'densité' est cependant devenu synonyme de 'masse volumique', et c'est dans ce sens que je l'emploierai dans la suite de ce mémoire, sauf dans certains contextes ou expressions tel que les 'fonctions de densité de probabilité'). L'intérêt principal de la densité est de lever partiellement le trade-off entre la température et la composition. Déterminer la densité n'est cependant pas une mince affaire, en particulier parce que les ondes de surface et de volume y sont peu sensibles. La plupart du temps, on se contente de calibrer la densité à partir des vitesses sismiques. Le champ de gravité permet d'affiner ces calibrations, sans pour autant recouvrir l'intégralité de la distribution en densité. À ce jour, les contraintes les plus fiables sont sans doute celles apportées par les mesures de modes propres (Ishii et Tromp, 1999; Trampert et al., 2004).

Un autre problème est de relier les anomalies de vitesses sismiques et de densité à leurs sources supposées, c'est-à-dire de calculer vitesses sismiques et densité à pression, température et composition minéralogique données. On regroupe généralement cette activité sous le terme de modélisation de l'équation d'état, ce qui implique à la fois le choix d'une paramétrisation adaptée au problème (par exemple, pour l'extrapolation aux pressions du manteau inférieur, l'équation de Birch-Murnaghan au troisième ordre), et la

connaissance des propriétés thermo-élastiques des minéraux en surface. Ce dernier point est central, car des incertitudes, parfois élevées, subsistes sur ces paramètres de surface. Récemment, les méthodes *ab initio*, basées sur la résolution des équations de Schrödinger pour une structure cristalline donnée, ont permis de calculer directement les propriétés thermo-élastiques de certains minéraux aux pressions et températures du manteau (p.e., Oganov et al., 2001). Ces méthodes restent coûteuses en temps de calculs, et ne sont pas exempte d'approximations, mais les résultats qu'elles fournissent sont très utiles pour affiner les extrapolations classiques aux pressions et températures du manteau.

Supposons un instant que l'on connaisse les distributions thermochimiques avec une précision raisonnable. Ce que l'on voudrait maintenant comprendre, c'est comment elles s'intègrent dans les modèles de dynamique mantellaire. Etant donnés un certain nombre d'ingrédients, à quel mode de convection doit-on s'attendre? L'outil numérique est ici indispensable. Les codes disponibles à ce jour incluent de nombreuses complexités (mode de chauffage, rhéologie, compressibilité, convection thermochimique) qui sont autant de paramètres à explorer. Ici, la difficulté est de ne pas inclure trop de complexité, et de déterminer quels sont les paramètres les plus pertinents et les plus influents, par exemple à l'aide d'études systématiques. La puissance de calcul disponible et la parallélisation des algorithmes permettent déjà des recherches systématiques relativement ambitieuses. L'approche qui sera privilégiée dans ce mémoire est une approche directe qui consiste à comparer les distributions thermochimiques prédites par différents modèles de convection avec celles observées par les modèles tomographiques.

L'estimation de barres d'erreur pour chacune de ces étapes est un challenge plus difficile qu'il n'y paraît. Plus généralement on souhaiterait définir une fonction de densité de probabilité pour chaque paramètre d'un modèle. L'idée est de résoudre le problème direct en explorant l'espace des modèles à l'aide de méthodes de Monte-Carlo. En définissant une fonction de coût à partir de comparaisons avec les observables disponibles, on peut estimer quels modèles ou quelles valeurs de paramètres sont les plus probables. De nouveau, l'accroissement de la puissance de calcul et le développement de méthode de Monte-Carlo intelligentes (Metropolis, algorithme de voisinage) permettent aujourd'hui d'explorer convenablement l'espace des modèles pour de nombreux problèmes. Il se pourra que les barres d'erreurs soient élevées (que la fonction densité de probabilité soit étalée) et ne permettent pas de départager les valeurs de paramètres en concurrence. Dans la plupart des cas, cependant, elles permettent d'exclure certaines solutions, ce qui est en soit un résultat.

Les recherches présentées dans ce mémoire ont pour ambition d'assembler les contraintes apportées par la sismologie, la physique des minéraux et la gravimétrie, puis de

les intégrer aux modèles géodynamiques issus de modélisations numériques de la façon la plus judicieuse et la plus robuste possible. En espérant, bien sûr, apporter un début de réponse à quelques unes des questions posées précédemment.

Contenu

Le matériau rassemblé dans ce mémoire est le résultat de recherches menées à l'Université d'Utrecht avec Roel Snieder et Jeannot Trampert, puis à l'Institut Polytechnique de Zürich avec Paul Tackley et Domenico Giardini. Ces travaux ont été publiés ou sont en cours de publication dans des revues scientifiques internationales sous forme d'articles, que le lecteur trouvera à la fin de chaque chapitre. Dans cette version française abrégée, j'ai omis de nombreux détails techniques, que l'on trouvera dans les articles. En revanche, j'ai insisté sur d'autres détails qui me semblaient importants, et j'ai ajouté quelques figures et réflexions qui apportent un éclairage complémentaire, parfois critique, sur mes travaux.

Le fil conducteur de ces travaux est l'interprétation des observables géophysiques (principalement de l'information sismologique) en termes de structures thermochimiques, et leur intégration dans les modèles géodynamiques. Pour cela, on progressera de la croûte profonde (l'entresol), vers le manteau inférieur jusqu'à la limite noyau-manteau. Le noyau externe et la graine ne seront pas abordés dans ce travail. Bien entendu, il reste beaucoup de chemin à parcourir, et j'indiquerai, pour chaque thème abordé, quelques perspectives qui me semble intéressantes et accessibles à court ou moyen terme.

Le premier chapitre concerne la détection et la cartographie de d'anisotropie azimutale des vitesses sismiques (plus précisément de la vitesse de phase des ondes de Rayleigh) dans une région des États-Unis qui a subi plusieurs orogènes successives depuis 1.8 milliard d'années. Ces orogènes, mais aussi les écoulements asthénosphériques passés (160-125 Ma) et contemporains, ont laissé des traces – des fabriques – auxquelles les vitesses des ondes sismiques sont sensibles. Cela se traduit par une distribution verticale de l'anisotropie en trois couches, très clairement détectable à partir de nos mesures.

Avec le chapitre 2, nous passerons définitivement dans le manteau supérieur. L'origine de la stabilité des racines continentales est une question toujours débattue. L'inversion conjointe des anomalies de gravité et de vitesse sismique permet de calibrer les anomalies de densité et semble confirmer, dans ces grandes lignes, le modèle de 'tectosphère' proposé par Jordan (1975). Le refroidissement des racines continentales serait ainsi compensé par un appauvrissement chimique.

Nous traverserons ensuite la zone de transition sans s'y arrêter, pour passer directement dans le manteau inférieur. Notre connaissance de ce dernier a radicalement changée depuis une petite dizaine d'années. Citons simplement, pour le moment, la

détermination de contraintes indépendantes sur la distribution de la densité (Ishii et Tromp, 1999; Trampert et al., 2004) et la découverte de la phase post-perovskite (Murakami et al., 2004; Oganov et Ono, 2004), dont on est finalement pas certain qu'elle soit présente à la base du manteau. Ce changement de point de vu justifie que deux chapitres de ce mémoire soient consacrés au manteau inférieur. Le chapitre 3 retrace l'établissement d'un modèle moyen de température et de composition, et l'interprétation de la tomographie probabiliste (Resovsky et Trampert, 2003; Trampert et al., 2004) en termes de distributions thermochimiques. Ces deux opérations nécessitent une modélisation adéquate des propriétés thermo-élastiques du manteau à hautes pressions et températures. Le chapitre 4 est lui consacré à une recherche relativement exhaustive dans l'espace des modèles de convection thermochimique pour identifier le ou les ingrédient(s) que ces modèles doivent inclure pour expliquer correctement la tomographie probabiliste.

En filigrane, nous verrons que la prise en compte des sources d'incertitudes disponibles, loin de jeter le discrédit sur les résultats, permet de les renforcer. Un moyen simple et élégant de prendre en compte ces sources d'incertitudes est de les traduire en fonctions de densité de probabilité, qui attribuent un poids, une probabilité d'occurrence, à chaque point de l'espace des modèles. L'exploration systématique de l'espace des modèles, pour un problème défini, et sa cartographie en termes de probabilités est transposable à de nombreux problèmes en sciences de la Terre. Et ceci d'autant plus que l'on dispose aujourd'hui de méthodes de Monte-Carlo 'intelligentes' (p.e., Metropolis, ou l'algorithme de voisinage) et de capacités de calculs satisfaisantes. Ce sera aussi la conclusion de ce mémoire.

Bibliographie

Anderson, D.L., 2005. Scoring hotspots : the plume and plate paradigm, in R.G. Foulger et al. Eds., Plates, plumes and paradigms, *Geol. Soc. Am. Spec. Paper*, **388**, 31-54.

Anderson, D.L., 2007. New Theory of the Earth, Cambridge University Press, 384 pp..

Boyet, M., et R.W. Carlson 2006. ^{142}Nd evidence for early (>4.53 Ga) global differentiation of the silicate Earth, *Science*, **309**, 576-581.

Courtillot, V., A. Davaille, J. Besse, et J. Stock, 2003. Three distinct type of hotspot in the Earth's mantle, *Earth Planet. Sci. Lett.*, **205**, 295-308.

Deal, M.M., G. Nolet, et R.D. van der Hilst, 1999. Slab temperature and thickness from seismic tomography. 1.Method and application to Tonga, *J. Geophys. Res.*, **104**, 28789-28802.

Deschamps, F., et J. Trampert, 2004. Towards a lower mantle reference temperature and composition, *Earth Planet. Sci. Lett.*, **222**, 161-175.

Dziewonski, A.M., et D.L. Anderson, 1981. Preliminary Reference Earth Model, *Phys. Earth Planet. Inter.*, **25**, 297-356.

Fukao, Y., S. Widiyantoro, et M. Obayashi, 2001. Stagnant slabs in the upper and lower transition regions, *Rev. Geophys.*, **39**, 291-323.

Ishii, M., et J. Tromp, 1999. Normal-mode and free-air gravity constraints on lateral variations in velocity and density of Earth's mantle. *Science*, **285**, 1231-1236.

Jordan, T.H., 1975. The continental tectosphere, *Rev. Geophys. Space Phys.*, **13**, 1-12.

Labrosse, S., J.W. Hernlund, et N. Coltice, 2007. A crystallizing dense magma ocean et the base of the Earth's mantle, *Nature*, **450**, 866-869.

Murakami, M., K. Hirose, K. Kawamura, N. Sata, et Y. Ohishi, 2004. Post-perovskite phase transition in $MgSiO_3$, *Science*, **304**, 855-858.

Oganov, A.R., J.P. Brodholt, and G.D. Price, 2001b. The elastic constants of $MgSiO_3$ perovskite at pressures and temperatures of the Earth's mantle, *Nature*, **411**, 934-937.

Oganov, A.R., et S. Ono, 2004. Theoretical and experimental evidence for a post-perovskite phase of $MgSiO_3$ in Earth's D" layer, *Nature*, **430**, 445-448.

Resovsky, J.S., et J. Trampert, 2003. Using probabilistic seismic tomography to test mantle velocity-density relationships, *Earth Planet. Sci. Lett.*, **215**, 121-134.

Tarantola, A., et B. Valette, 1982. Generalized nonlinear inverse problems solved using the least square criterion, *Rev. Geophys. Space Phys.*, **20**, 219-232.

Trampert, J., F. Deschamps, J. Resovsky, et D.A. Yuen, 2004. Probabilistic tomography maps chemical heterogenities throughout the mantle, *Science*, **306**, 853-856.

Chapitre 1

Anisotropie stratifiée et déformations actuelles et passées

Avant de plonger plus profondément dans le manteau terrestre, arrêtons-nous un instant autour du Moho. Dans certains milieux, en particulier dans les terrains subissant (ou ayant subi) des déformations importantes, les ondes sismiques se propagent avec des vitesses différentes selon leurs directions de propagation. On parle d'anisotropie sismique. La détection d'anisotropie sismique est aujourd'hui relativement aisée, mais son interprétation reste souvent délicate, l'une des principales difficultés étant de pouvoir localiser précisément la ou les source(s) d'anisotropie le long du trajet des ondes sismiques. Dans ce chapitre, je montre que l'étude des variations azimutales de la vitesse de phase du mode fondamental des ondes de Rayleigh permet, dans le cas d'une région des Etats-Unis ayant subie plusieurs orogènes successives, de résoudre la distribution verticale de l'anisotropie. Ces travaux, menés en collaboration avec Sergei Lebedev, Thomas Meier et Jeannot Trampert, sont décrits plus en détails dans les deux articles qui font suite à ce chapitre (Deschamps et al., 2008a, 2008b).

1.1 Anisotropie et déformation

En réponse aux contraintes régionales qu'ils subissent, certains minéraux de la croûte et du manteau terrestre développent des fabriques particulières. C'est le cas de l'amphibole, présente dans la croûte profonde, et de l'olivine, le minéral le plus abondant du manteau supérieur. Les propriétés élastiques des minéraux et des agrégats qu'ils composent s'en trouvent modifiées, et les ondes sismiques se propagent plus rapidement dans des

directions privilégiées qui sont généralement les directions de déformations maximales (p.e., Christensen, 1984; Nicolas et Christensen, 1987). Le corolaire de ce phénomène est que l'anisotropie sismique, pour peu que l'on puisse la détecter et la cartographier correctement, renferme des renseignements forts utiles au géodynamicien qui chercherait à reconstituer la déformation (actuelle et passée) de la lithosphère.

Le lien entre anisotropie et écoulement asthénosphérique en milieu océanique a été fait assez tôt et semble bien compris (p.e., Forsyth, 1975; Ribe, 1989). Le cas des continents est un peu plus complexe, en partie parce que l'histoire tectonique y est plus complexe. Certaines formations, dont les cratons Précambriens, ont subi peu de déformation, sans doute grâce à (ou à cause de, je laisse au lecteur le choix de la formule) une viscosité élevée et/ou à des variations chimiques (p.e., Sleep, 2005). D'autres structures ont, en revanche, subi plusieurs cycles de déformations successifs. Les collisions continentales, par exemple, sont responsables de déformations crustales à grande échelle. La répartition des déformations induites par ces collisions dans la lithosphère reste âprement discutée. Soit les déformations sont distribuées plus ou moins uniformément dans la lithosphère (Molnar, 1988), soit elles sont concentrées le long de frontières entre différents blocs lithosphériques (Tapponnier et al., 2001). Se pose enfin la question de l'évolution de la lithosphère après l'orogène, en particulier si cette lithosphère a subi un réchauffement important.

On le voit, l'interprétation de l'anisotropie sismique sous les continents nécessite de bien connaître sa distribution verticale. Grâce à une bonne répartition géographique des stations sismologiques, de nombreuses mesures de déphasage d'ondes de volume (en particulier pour les ondes *SKS*) ont pu être effectuée (p.e., Silver, 1996). Ces mesures ont une excellente résolution latérale, mais pas ou peu de résolution verticale. Autrement dit, elles ne parviennent pas à localiser la ou les sources anisotropiques le long du rai sismique. Dans certaines régions, la direction de propagation rapide de ces déphasages est cohérente avec des structures tectoniques locales. La source anisotropique est sans doute située dans la croûte et, éventuellement, au sommet du manteau. Ailleurs, au contraire, elle est parallèle à la vitesse de plaque absolue (VPA, ou en anglais APM, pour 'absolute plate motion'), ce qui semble indiquer une origine asthénosphérique de l'anisotropie.

Les ondes de surface échantillonnent des intervalles de profondeurs différents en fonction de leur période, et à ce titre elles procurent la résolution verticale nécessaire à la localisation de l'anisotropie. À l'échelle continentale, plusieurs études ont observé des structures anisotropiques indépendamment dans la lithosphère profonde et dans l'asthénosphère (Simons et al., 2002 ; Debayle et al., 2005 ; Marone et Romanowicz, 2007). À des échelles plus locales, cependant, ces études n'ont pas la résolution latérale nécessaire pour détecter et interpréter correctement les structures anisotropiques locales. Il faut alors

faire appel à des études locales, basées sur des réseaux denses de stations sismiques large-bande. L'étude des variations azimutales des vitesses de phase des ondes de surface donne alors des images 'en haute résolution' de la lithosphère sub-continentale (p.e., Pedersen et al., 2006; Yang et Forsyth, 2006, Deschamps et al., 2008a).

1.2 Une région test : le centre-est des Etats-Unis (31°N-41°N et 82°E-92°E)

1.2.1 Contexte régional

Le centre-est des Etats-Unis est traversé par deux fronts orogéniques, Grenville et Appalache, approximativement parallèles mais d'âges différents. La direction de ces fronts est globalement NE-SO jusque vers 34°N, latitude à laquelle ils sont défléchis vers l'ouest (Figure 1.1). L'orogène Grenvilliennee est le dernier épisode (1.3-1.0 Ga) d'une série d'accrétions de micro-continents sur la frontière sud de la Laurentia ayant démarée il-y-a 1.8 milliard d'années (p.e., Hoffman, 1988; Dalziel, 1991; Karlstrom et al., 2001). L'orogène

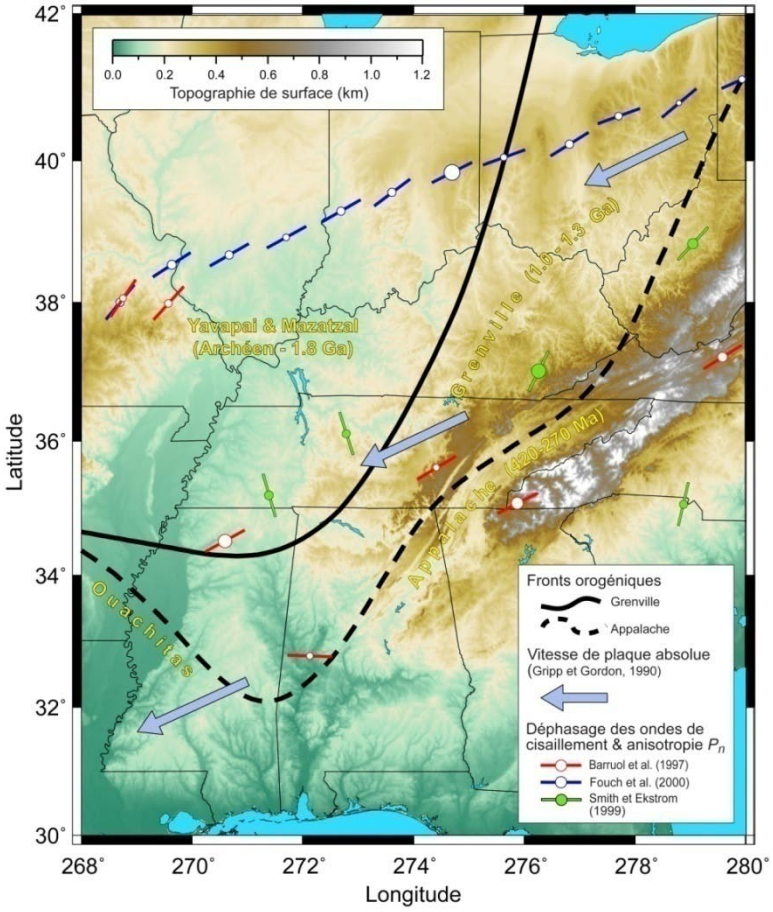

Figure 1.1 – Contexte régional et observations de déphasages d'ondes sismiques. Le fond de carte représente la topographie de surface.

Appalachienne est plus récente (420-270 Ma), et correspond à la collision du Gondwana avec l'Amérique du Nord (Ziegler, 1989). Par ailleurs, durant l'orogène Appalachienne, une partie de la lithosphère Grenvilienne a été remaniée. Les terrains situés au nord et à l'ouest du front de Grenville appartiennent aux provinces tectoniques de Yavapai et Mazatzal et ont été mis en place lors d'orogènes éponymes il-y-a 1.8 à 1.6 milliard d'années. Ils font partie d'une plateforme cratonique stable qui n'a pas ou peu subie d'activité tectonique depuis environs 1.6 Ga.

Un mécanisme de déformation possible conduisant à la formation d'anisotropie est le mouvement relatif de la lithosphère et de l'asthénosphère. Selon NUVEL-1, qui détermine les VPAs par rapport à un système de points chauds supposés fixes (Gripp et Gordon, 1990), la dérive actuelle de la plaque Nord-Américaine est dirigée vers le SE avec un azimuth (par rapport au nord) de 245° et une amplitude de 2.6 cm/an (Figure 1.1). Les vitesses de plaque varient dans le temps, et les données paléomagnétiques permettent de reconstruire le mouvement des plaques dans le passé. Ainsi, il-y-a environs 180 millions d'années, suite à l'ouverture de l'Atlantique Nord, l'Amérique du Nord a amorcé une dérive vers le NNO. Ce mouvement s'est amplifié vers 160 Ma et s'est poursuivi jusque vers 125 Ma (Beck et Housen, 2003). Nous verrons que cet épisode est sans doute à l'origine d'anisotropie fossile observée dans la lithosphère profonde.

1.2.2 Observations sismologiques: déphasage d'onde de cisaillement et anisotropie P_n

Le déphasage des ondes de cisaillement (plus précisément des ondes *SKS*) dans cette région des États-Unis est bien documenté. En s'appuyant sur le réseau sismique temporaire Missouri to Massachusetts (MOMA), Fouch et al. (2000) ont mesuré des temps de déphasage entre 0.5 et 2.2 s (Figures 1.1 et 1.6, symboles bleus). Détail important, la direction dans laquelle les ondes de cisaillement se propagent le plus rapidement (ou axe rapide) est cohérente à l'échelle régionale et parallèle à la direction de la VPA pour l'Amérique du Nord. La compilation de Barruol et al. (1997), qui regroupe des mesures sur une plus grande superficie, met également en évidence des déphasages importants (Figures 1.1 et 1.6, symboles rouges). De nouveau, la direction de l'axe rapide est cohérente à l'échelle régionale, quoique plus dispersée, et s'accorde bien avec la direction de la VPA pour l'Amérique du Nord. Sur la base de ces observations, il est tentant de conclure que le déphasage des ondes *SKS* trouve son origine dans la déformation liée à l'écoulement asthénosphérique, et qu'il est localisé au sommet de l'asthénosphère. Toutefois, il faut garder à l'esprit que les mesures de déphasage d'ondes *SKS* ont une mauvaise résolution verticale, et qu'elles ne permettent pas de localiser la région source de l'anisotropie sans

ambiguïté. Cette ambiguïté peut être levée par l'étude des variations azimutales de la vitesse de phase des ondes de surface.

Les anomalies liées aux ondes P_n, en revanche, sont bien localisées et trouvent leur source au sommet du manteau, immédiatement sous le Moho. Smith et Ekström (1999) ont mesuré l'anisotropie des ondes P_n en de nombreuses stations sismologiques réparties sur l'ensemble du globe. Pour la partie des Etats-Unis qui nous intéresse, ces mesures montrent que l'amplitude de l'anisotropie et la direction de propagation rapide dépendent de la localisation géographique (Figures 1.1 et 1.6a, symboles verts). Dans la partie orogénique (au sud et à l'est du front de Grenville), l'amplitude de l'anisotropie est forte (4.5% et plus), et l'axe de propagation rapide est parallèle aux fronts orogéniques Grenvillien et Appalachien. Dans la partie cratonique, en revanche, l'anisotropie est plus faible (moins de 4.0%), et l'axe rapide est grossièrement perpendiculaire aux fronts orogéniques. Une interprétation possible de ces observations est que les orogènes Grenvillienne et Appalachienne se sont accompagnées de fortes déformations liées à la compression et/ou à l'extrusion latérale de racines lithosphériques (Meissner et Mooney, 1998; Messner et al., 2002) autour du Moho.

1.3 Un modèle régional de la vitesse de phase des ondes de Rayleigh

1.3.1 Données sismologiques et courbes de dispersion

Les réseaux sismiques régionaux sont bien adaptés à l'étude de la croûte profonde et du manteau supérieur sous la région où ils sont déployés. Chaque paire de stations défini un trajet le long duquel on peut mesurer, si les données le permettent, une courbe de dispersion pour la vitesse de phase des ondes de Rayleigh. La méthode dite des 'deux stations', introduite par Sato (1955) a été largement utilisée pour la mesure des courbes de dispersion. Pour cette étude, j'ai utilisé une variante de cette méthode mise au point par Meier et al. (2004). Moyennant une bonne répartition géographique et azimutale des courbes mesurées (c'est le cas ici), il est possible de contraindre les variations régionales (isotropiques et anisotropiques) de vitesse de phase sous ce réseau sismique.

Dans notre cas, la mesure des courbes de dispersion est basée sur une collection d'environ 20000 sismogrammes correspondant à plus de 3000 évènements enregistrés à 17 stations différentes localisées entre 31°N-41°N et 82°E-92°E (Figure 1.2a). La plupart de ces stations font parties de réseaux permanents (USNSN et NM), ce qui garanti une meilleur qualité et un meilleur suivi des données. Quatre stations appartiennent à l'expérience sismologique temporaire 'Florida to Edmonton' (FLED), pendant de l'expérience (MOMA), toutes deux menées dans le cadre du programme PASSCAL.

Bien sûr, le nombre d'évènements disponibles et leur qualité varient beaucoup d'une paire de stations à l'autre, soit à cause de facteurs globaux (principalement, la distribution de zones sismiques le long du grand cercle reliant les deux stations), soit à cause de facteurs locaux (qualité du site, qualité instrumentale, histoire de la station). De plus, le nombre d'évènements exploitables (c'est-à-dire effectivement utilisés pour la construction des courbes de dispersion) est en général beaucoup plus petit que le nombre d'évènements sélectionnés. Ces différences se retrouvent évidemment dans la qualité des courbes de dispersion (Figures 1.2b-e), ces dernières étant obtenues en moyennant toutes les mesures sélectionnés pour un trajet donné. Pour la majorité des paires, de 60 à 120 évènements sont disponibles parmi lesquels de 20 à 50 sont exploitables, ce qui m'a permis de mesurer des courbes de dispersion pour 60 trajets (Figure 1.2a, lignes oranges), avec une bonne couverture (régionale et azimutale) pour les périodes comprises entre 12 et 140 s.

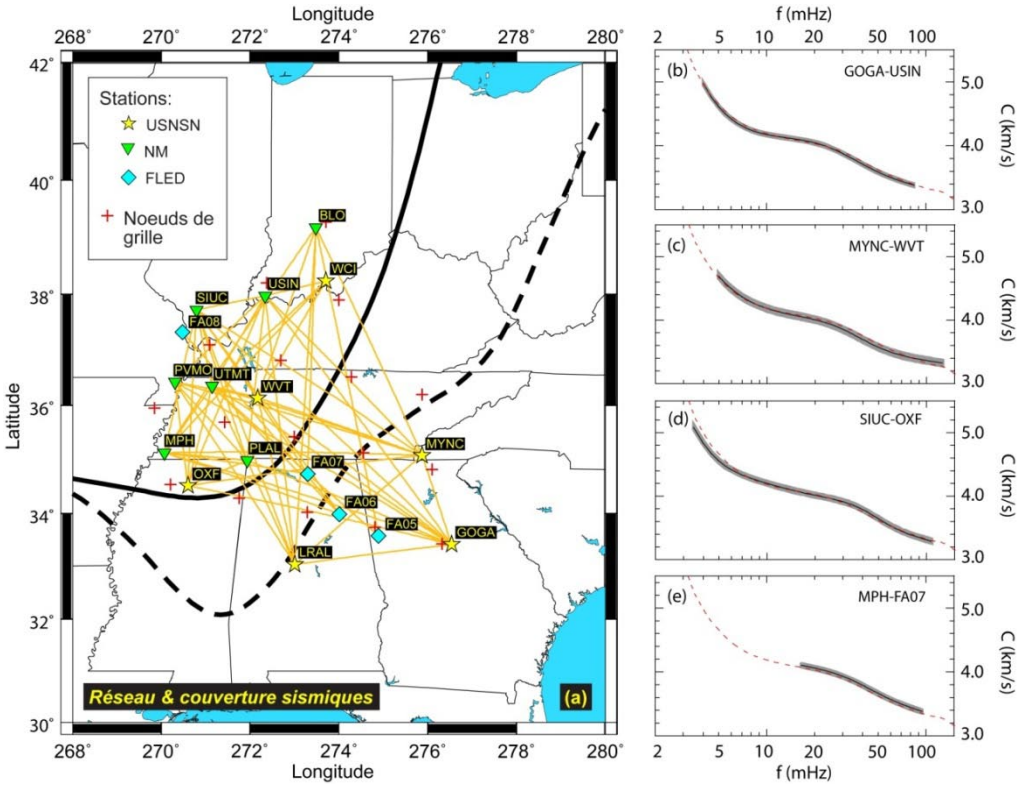

Figure 1.2 – (a) Réseau et couverture sismiques. (b-e) Courbes de dispersions de la vitesse de phase des ondes de Rayleigh. La courbe rouge en pointillée représente la moyenne régionale des courbes de dispersion, et la zone grisée couvre une déviation standard autour de la courbe de dispersion moyenne mesurée pour un trajet donné.

Etant donnée la sensibilité des ondes de Rayleigh à la profondeur, cette collection de courbes de dispersion peut raisonnablement contraindre la structure sismique de la croûte inférieure et du manteau supérieur jusque vers 250 km de profondeur. Une comparaison visuelle entre les courbes de dispersion révèle d'importantes différences d'un trajet à l'autre

(Figure 1.2b-e). La Figure 1.3, qui représente la vitesse mesurée en fonction de l'azimut du trajet pour plusieurs périodes, indique également des variations importantes de la vitesse en fonction de l'azimut, en particulier pour des périodes comprises entre 18 et 32 s, et, plus modestement, autour de 140 s. Ces variations sont un indice précieux, mais pour autant, à ce stade, il est difficile d'affirmer la présence d'anisotropie azimutale à ces périodes, et encore moins de la quantifier. En effet, rien ne nous indique que les variations de vitesse observées résultent uniquement des variations azimutales de la vitesse de phase. La dispersion relativement importante des mesures pour un azimut donné suggère qu'il existe vraisemblablement une contribution isotropique, liée à des variations régionales de structure (température et composition). Pour séparer ces deux contributions, isotropiques et anisotropiques il est nécessaire d'inverser les courbes de dispersion pour un modèle régional d'onde de Rayleigh.

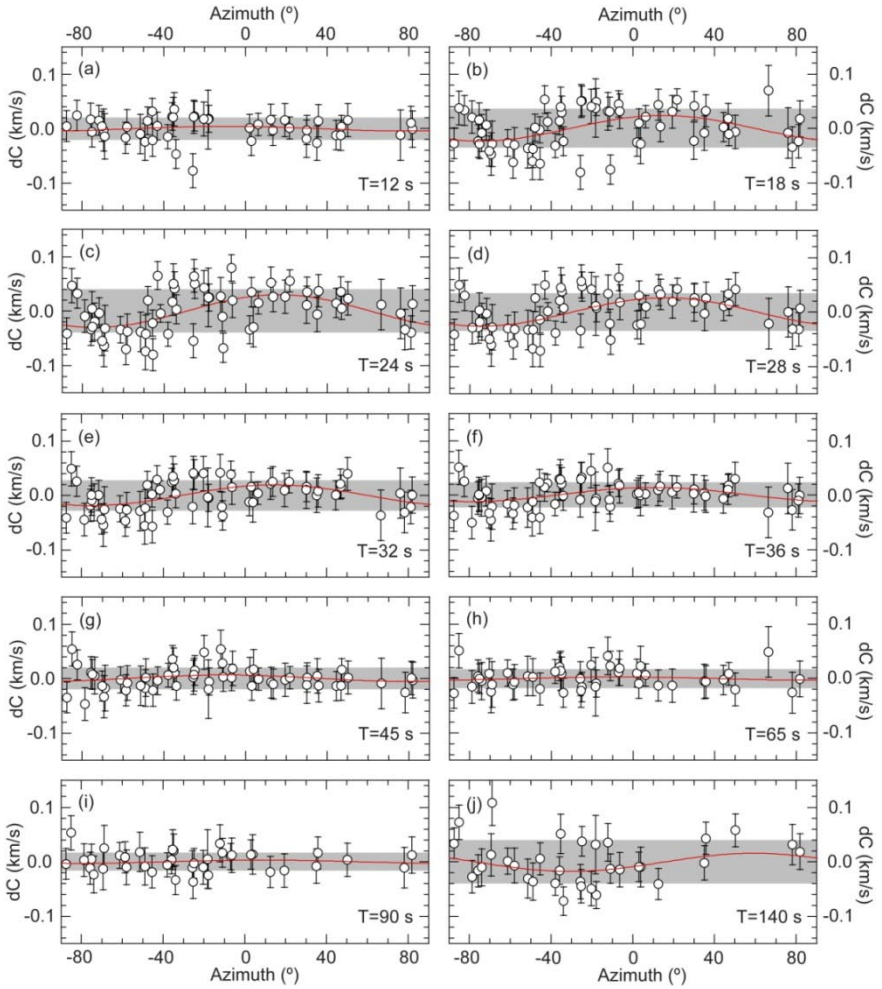

Figure 1.3 – Distribution azimutale des variations de la vitesse de phase des ondes de Rayleigh pour plusieurs périodes. Les bandes grisées couvrent une déviation standard autour de la moyenne régionale de la vitesse de phase. Les courbes rouges représentent la fonction sinusoïdale de la forme $\varsigma(\Psi) = a.\cos(2\Psi) + b.\cos(2\Psi)$, où Ψ est l'azimut, qui explique le mieux les mesures.

1.3.2 Inversion des courbes de dispersion

L'anomalie totale de vitesse d'onde de Rayleigh observée peut s'écrire comme la somme d'une contribution isotropique et d'une contribution anisotropique. Cette dernière est souvent décrite par un terme en 2Ψ et un terme en 4Ψ (Smith et Dahlen, 1973),

$$\delta C(\varphi,\theta) = \delta C_{iso}(\varphi,\theta) + \delta C_{2\Psi}(\varphi,\theta) + \delta C_{4\Psi}(\varphi,\theta), \quad (1.1)$$

où Ψ est l'azimut, et où les contributions 2Ψ et 4Ψ s'écrivent

$$\delta C_{2\Psi}(\varphi,\theta) = A_{2\Psi}\cos(2\Psi) + B_{2\Psi}\sin(2\Psi) \quad (1.2a)$$

et $$\delta C_{4\Psi}(\varphi,\theta) = A_{4\Psi}\cos(4\Psi) + B_{4\Psi}\sin(4\Psi). \quad (1.2b)$$

L'amplitude des anomalies anisotropiques et l'azimut de la direction de propagation rapide sont données par

$$\begin{cases} \Lambda_{2\Psi} = \sqrt{A_{2\Psi}^2 + B_{2\Psi}^2} \\ \Theta_{2\Psi} = \frac{1}{2}\arctan\left(\frac{B_{2\Psi}}{A_{2\Psi}}\right) \end{cases} \quad (1.3a)$$

et $$\begin{cases} \Lambda_{4\Psi} = \sqrt{A_{4\Psi}^2 + B_{4\Psi}^2} \\ \Theta_{4\Psi} = \frac{1}{4}\arctan\left(\frac{B_{4\Psi}}{A_{4\Psi}}\right) \end{cases}. \quad (1.3b)$$

L'interprétation des contributions en 4Ψ (i.e., la vitesse est maximale dans deux directions perpendiculaires, $\Theta_{4\Psi}$ et $\Theta_{4\Psi}+\pi/2$) n'est pas claire, mais plusieurs études globales (Montagner et Tanimoto, 1991 ; Trampert et Woodhouse, 2003) ont montré que cette contribution n'était pas négligeable. Dans notre cas, l'amplitude des anomalies 4Ψ est d'environ 1/3 celle des anomalies 2Ψ, mais un test statistique (F-test, Bevington et Robinson, 1992) montre que ces contributions n'améliorent pas le fit des courbes de dispersions de façon significative, et qu'elles peuvent donc être négligées (ce que je supposerai dans la suite de ce chapitre). Un test similaire indique en revanche que les contributions 2Ψ observées à différentes périodes (cf §1.5) sont nécessaires pour expliquer correctement les courbes de dispersions observées. Par simplicité, dans la suite de ce chapitre j'appellerai 'anisotropie azimutale' la contribution 2Ψ des anomalies anisotropiques de la vitesse de phase des ondes de Rayleigh.

L'inversion utilisée pour séparer les contributions isotropiques des contributions anisotropiques est détaillée dans Deschamps et al. (2008a). Brièvement, il s'agit d'une méthode LSQR (Page et Saunders, 1982) pondérée par de l'information *a priori*, ici une combinaison de lissage latéral et d'amortissement de l'amplitude. Le modèle est paramétrisé sur une grille triangulaire (Wang et Dahlen, 1995) de 17 nœuds (les croix rouges sur la Figure 1.2a) espacés d'environ 140 km. La valeur moyenne de la vitesse de

phase le long d'un trajet i et à la période T (la courbe de dispersion que l'on a mesuré) est la somme des anomalies de vitesse le long de ce trajet (que l'on cherche à déterminer):

$$\langle \delta C_i(T) \rangle = \iint K_i(\varphi,\theta)\delta C(\varphi,\theta,T) d\theta d\varphi \qquad (1.4)$$

où δC(φ,θ) est donné par l'équation 1.1. Les fonctions K_i sont les kernels de sensibilité calculés pour chaque trajet en attribuant un poids à chaque nœud, et sont approximées par des bandes de largeur finie autour du trajet considéré. En écrivant l'équation 1.4 pour chaque trajet, on obtient un système d'équations que l'on peut résoudre indépendamment pour chaque période.

Comme souvent lorsque l'on inverse un ensemble de données, les choix du type et du poids de l'information *a priori* (ou régularisation) sont hautement subjectif. Le lissage appliqué lors de l'inversion minimise les dérivées secondes de la vitesse de phase, ce qui permet de bien contraindre les gradients de vitesse réguliers. Par contre, d'éventuelles anomalies locales de faible amplitude seront diluées dans le signal moyen et n'apparaîtront pas sur le modèle. L'amplitude du lissage est contrôlé par un paramètre d'amortissement, ε, que l'on choisit de façon à obtenir un bon compromis entre la régularité du modèle (forte valeur de ε) et sa capacité à expliquer les courbes de dispersion (faible valeur de ε). Ce compromis est traditionnellement visualisé sur des courbes de trade-off (ou courbes en L), ce que j'ai fait, mais en gardant à l"esprit que ce procédé reste subjectif. Pour compléter ce choix, il convient d'estimer l'influence de la régularisation (et en particulier de ε) sur le modèle de sortie. Dans notre cas, il est intéressant de noter que la direction rapide et l'amplitude de l'anisotropie azimutale varient très peu au delà d'une valeur de ε relativement modeste (2.5, pour être précis). Cela indique que notre modèle 'préféré' est plutôt robuste par rapport à la régularisation.

1.4 Anomalies isotropiques et profondeur du Moho

L'inversion des courbes de dispersion donne accès à une distribution des anomalies isotropiques de la vitesse de phase des ondes de Rayleigh. La distribution et l'amplitude de ces anomalies dépend de la période (Deschamps et al., 2008a). Les amplitudes les plus élevées apparaissent entre 16 et 34 s. Entre 40 et 140 s, en revanche, les anomalies sont peu prononcées. Sans doute le fait le plus marquant est un gradient de vitesse de direction SO-NE pour la plage de période 12-50 s.

En chaque point du modèle, il est possible de reconstruire une courbe de dispersion pour la partie isotropique de la vitesse de phase des ondes de Rayleigh (C), puis d'inverser cette courbe de dispersion pour un profil de la vitesse d'onde de cisaillement (V_S) à la verticale de ce point, les deux vitesses étant reliées par

$$C(\varphi,\theta,T) = \iint K_d(z,T)V_S(\varphi,\theta,z)\mathrm{d}z. \qquad (1.5)$$

Les fonctions (ou kernels) $K_d(z,T)$ décrivent la sensibilité des ondes de Rayleigh à la profondeur, et dépendent du profil de V_S. Autrement dit, l'équation (1.5) n'est pas linéaire et son inversion nécessite l'utilisation de méthodes itératives, ici, une recherche de gradient, qui réactualise le profil de V_S de à chaque itération, calcule (d'après Schwab et Knopoff, 1972) la courbe de dispersion associée à ce profil, et la compare avec la courbe de dispersion observée. En plus du profil V_S, l'inversion détermine la profondeur du Moho. Les détails de l'inversion (dont la paramétrisation et la régularisation) sont discutés dans Deschamps et al. (2008a). Lors de l'inversion, l'incertitude sur les courbes de dispersion locales se propage aux profils V_S, et la régularisation induit une erreur supplémentaire.

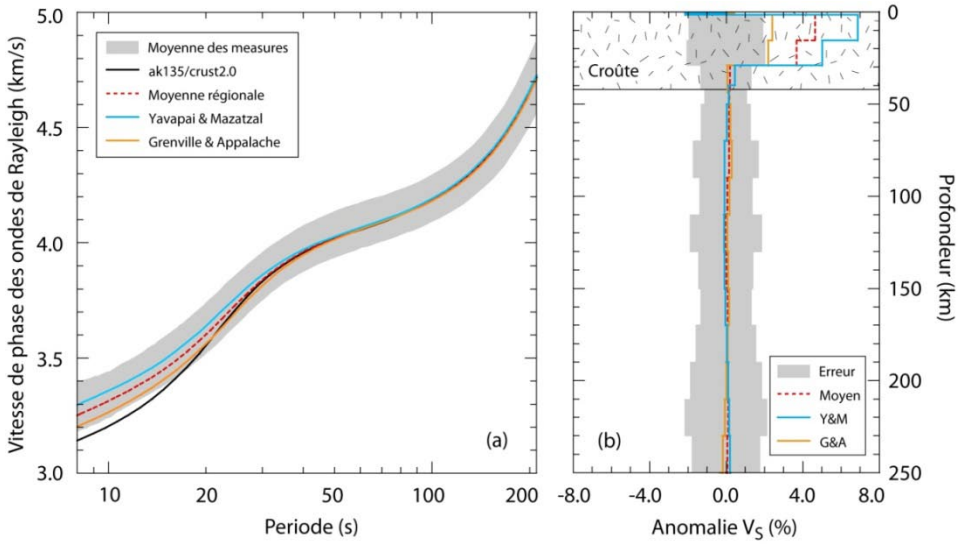

Figure 1.4 – (a) Courbes de dispersion régionales. La surface grisée couvre deux déviations standard autour de la courbe régionale moyenne observée. La courbe noire représente la courbe de dispersion obtenue pour le profil de vitesse de cisaillement de référence construit à partir du modèle ak135 dans le manteau et de la moyenne régionale de crust2.0 dans la croûte. La courbe rouge a été construite à partir de la moyenne régionale des profils de vitesse de cisaillement inversés. Les courbes orange et bleue représentent des moyennes similaires, mais respectivement limitées à la partie orogénique et à la partie cratonique. (b) Profils régionaux d'anomalies de vitesse de cisaillement par rapport au profil de référence ak135/crust2.0. Les courbes rouge, orange et bleue représentent respectivement la moyenne régionale, la moyenne obtenue dans la partie orogénique (Grenville et Appalache), et la moyenne obtenue dans la partie cratonique (Yavapai et Mazatzal). La bande grisée couvre deux fois les barres d'erreur (estimées à partir des incertitudes sur les courbes de dispersion) autour de la valeur de référence.

À cela, il faut ajouter un trade-off important entre la profondeur du Moho et les vitesses de cisaillement dans les couches adjacentes au Moho. L'erreur cumulée varie de 2 à 3% selon la profondeur, et le résultat est sans appel (Figure 1.4b). A l'intérieur des barres d'erreur, il est impossible de distinguer le profil régional moyen de V_S du modèle V_S de référence ak135 (Kennett et al., 1995). Toujours à l'intérieur des barres d'erreur, on n'observe pas de différences significatives entre les profils moyens pour la partie cratonique (Yavapai et Mazatzal) et pour la partie orogénique (Grenville et Appalache). Idem pour les profils

moyens dans la croûte profonde (z > 30 km) : ils restent proches du modèle crust2.0 (http://mahi.ucsd.edu/Gabi/rem.html). Dans la croûte supérieure et intermédiaire, par contre, nos profils se démarquent clairement de crust2.0, et les vitesses de cisaillement sont nettement plus élevée sous la partie cratonique que sous la partie orogénique.

Pour les mêmes raisons que précédemment, l'incertitude sur la profondeur du Moho est également élevée, de l'ordre de 4 km en moyenne. Toutefois, même en tenant compte de ces incertitudes, la profondeur du Moho prédite par notre modèle (Figure 1.5b) est notablement différente de celle prédite par crust2.0 dans cette région (Figure 1.5a). La profondeur moyenne du Moho est de 41.7 km, soit environ 3 km plus profonde que celle de crust2.0, et la différence maximum entre les deux modèles atteint 10 km dans le sud-est de la zone étudiée. Le Moho déduit de notre modèle est plus profond sous les provinces orogéniques (43.4 km) que sous la partie cratonique (39.7 km). On notera enfin qu'il est bien corrélé à la topographie de surface, comme l'on s'y attend dans l'hypothèse d'une compensation isostatique du relief.

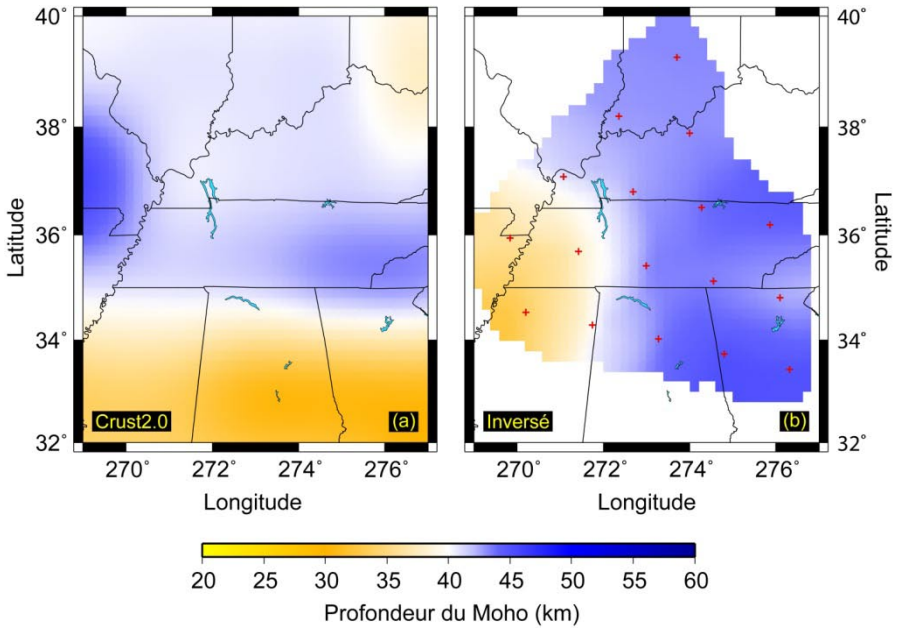

Figure 1.5 – Profondeur du Moho. (a) Modèle crust2.0 ; (b) modèle obtenu en inversant la partie isotrope du modèle d'onde de Rayleigh présenté dans ce chapitre (Deschamps et al., 2008a).

1.5 Anisotropie azimutale de la vitesse de phase des ondes de Rayleigh

Quid de l'anisotropie azimutale (en fait, de la contribution 2Ψ des anomalies anisotropiques) de la vitesse de phase des ondes de Rayleigh ? Cela dépend de la période (Figure 1.6). Entre 20 et 34 s, d'importantes disparités régionales sont visibles. Sous les provinces orogéniques (Grenville et Appalache), l'anisotropie est forte en amplitude (1% et

plus, par rapport à la vitesse isotropique moyenne), et la direction de propagation rapide est régionalement cohérente, avec un azimuth Θ ~ 32°. A l'ouest du front de Grenville, par contre, l'anisotropie est plus faible (en moyenne, 0.5 %), et la direction de propagation rapide est très dispersée. Entre 45 et 60 s, le signal est également plus faible en amplitude (~ 0.5%), mais la direction de propagation rapide est cohérente à l'échelle régionale, avec un azimuth Θ ~ 165° (c'est-à-dire approximativement perpendiculaire à la direction de propagation rapide observée sous les provinces orogéniques entre 20 et 34 s). Enfin, autour de 140 s, l'anisotropie est de nouveau forte en amplitude (> 1%) et la direction de propagation rapide est uniforme, avec Θ ~ 54°. Dans les autres intervalles de périodes, notamment entre 65 et 100 s, il n'y a pas d'indices clairs laissant supposer la présence d'anisotropie.

Ce résultat est particulièrement intéressant. Puisque les ondes de Rayleigh sont sensibles à différents intervalles de profondeurs en fonction de leur période, il signifie que l'anisotropie est distribuée dans deux ou trois couches indépendantes. Mieux, il existe des corrélations entre les directions de propagation rapides que nous observons, les observations de déphasage *SKS* et d'anisotropie P_n disponibles pour cette région, et certaines caractéristiques tectoniques régionales (Figure 1.6).

Entre 20 et 34 s (Figure 1.6a), les ondes de Rayleigh échantillonnent la croûte profonde et le sommet du manteau. Le bon accord (amplitude et direction) entre notre modèle et l'anisotropie P_n (Smith et Ekström, 1999) confirme que l'anisotropie que nous observons est distribuée autour du Moho. L'anisotropie est forte et cohérente dans la partie orogénique (Grenville et Appalache), mais pas dans la partie cratonique (Yavapai et Mazatzal). De cela, on déduit que l'anisotropie est sans doute liée à des fabriques acquises lors des orogènes Grenvillienne et/ou Appalachienne et gelées depuis. Un processus de déformation possible est l'extrusion latérale de la racine lithosphérique comme semble indiquer le fait que la direction de propagation rapide est parallèle aux fronts orogéniques (p.e. Meissner et Mooney, 1998; Messner et al., 2002). Dans la partie cratonique, en revanche, l'anisotropie est peu marquée et la lithosphère n'a sans doute pas ou peu subie de déformation.

Entre 45 et 60 s (Figure 1.6b), les ondes de Rayleigh échantillonnent principalement la lithosphère moyenne et inférieure. L'anisotropie, bien que faible, est présente à la fois dans la partie orogénique et dans la partie cratonique avec la même direction de propagation rapide. L'anisotropie n'est probablement pas liée à l'un des épisodes orogéniques ayant affectés cette région. Par contre, la direction de propagation rapide est parallèle à la direction du mouvement de la plaque Nord-Américaine il-y-a 160-125 Ma, déduite de reconstructions paléo-tectoniques (Beck et Housen, 2003). L'anisoprie que nous

observons est sans doute le résultat de fabriques acquises lors de cet épisode de dérive continentale, et gelées depuis lors.

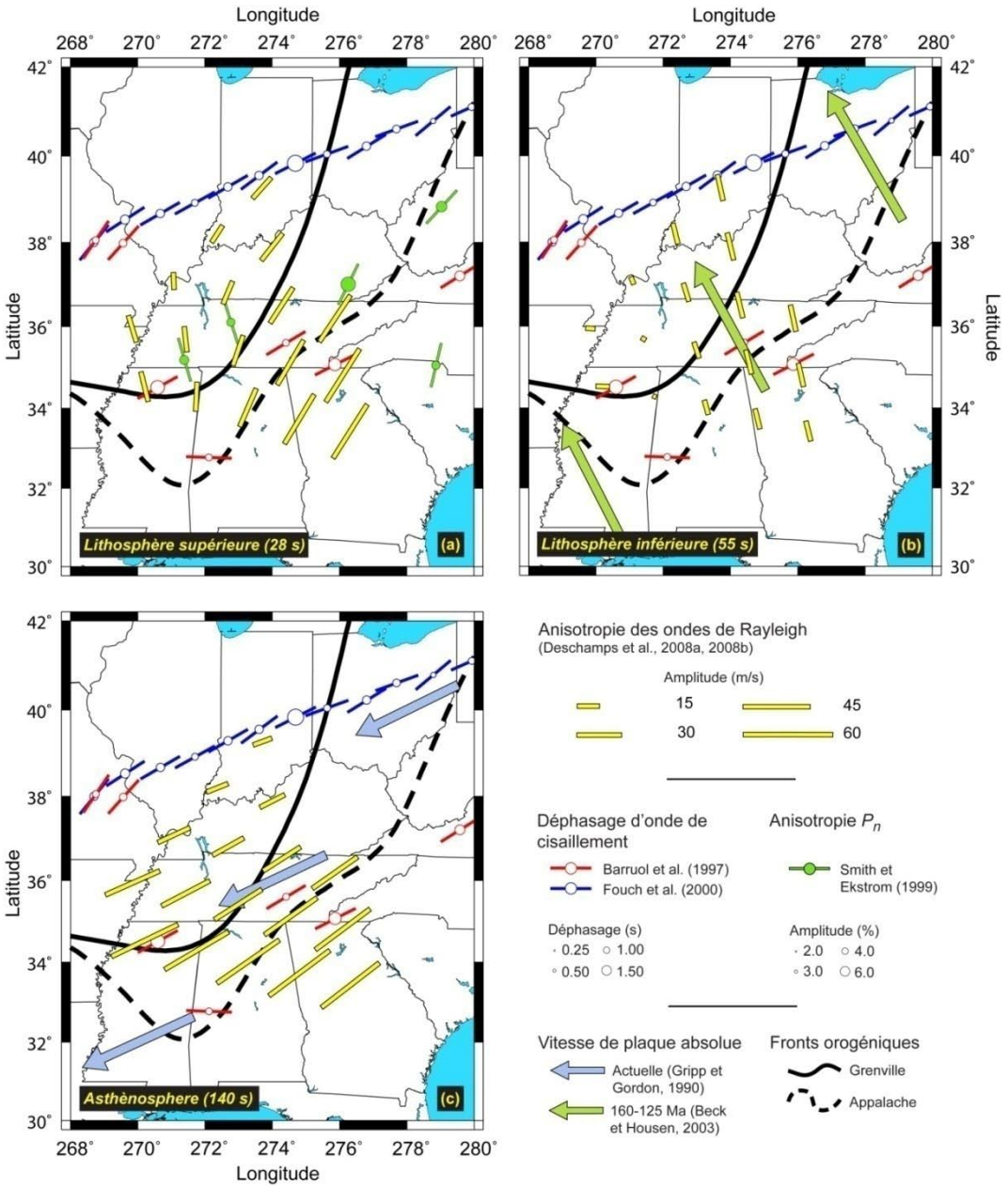

Figure 1.6 – Anisotropie azimutale des ondes de Rayleigh (barres jaunes) à 28, 55, et 140 s. L'orientation et la longueur des barres indiquent respectivement la direction de propagation rapide, et l'amplitude de l'anisotropie. Les vitesses isotropiques régionales à 28, 55, et 140 valent respectivement 3,816, 4,053, et 4.336 km/s. (a) A 28 s, dans la partie orogénique, direction de propagation rapide est parallèle aux fronts orogéniques et s'accorde bien avec les mesures d'anisotropie P_n. (b) A 55 s, la direction de propagation rapide est parallèle à la direction de la dérive de la plaque Nord-Américaine durant la période Mésozoique. (c) A 140 s, la direction de propagation rapide est parallèle à la direction de la vitesse de plaque absolue actuelle et s'accorde bien avec les déphasages *SKS* observés dans cette région.

Enfin, autour de 140 s (Figure 1.6c), les ondes de Rayleigh échantillonnent le manteau à partir de 150 km de profondeur environ. Notons en passant que l'amplitude de l'anisotropie est plus forte sous la partie orogénique que sous la partie cratonique. La direction de propagation rapide est uniforme et parallèle au mouvement actuel de la plaque Nord-Américaine (Gripp et Gordon, 1991). Ces éléments suggèrent que la forte anisotropie observée à ces périodes résulte de la déformation induite par l'écoulement asthénosphérique actuel (ou contemporain). C'est aussi l'interprétation que Barruol et al. (1997) et Fouch et al. (2000) donnent de leurs mesures de déphasages *SKS*, dont les directions rapides sont également en excellent accord avec le mouvement de la plaque Nord-Américaine, sans toutefois pouvoir localiser précisément la source de ces déphasages. Nos résultats semblent indiquer que ces déphasages sont effectivement d'origine asthénosphérique. J'y reviendrai.

1.6 Vitesse de cisaillement et anisotropie stratifiée

1.6.1 Profils anisotropiques régionaux

L'anisotropie azimutale des ondes de surface et ses variations en fonction de la période donne une première idée de à la distribution verticale de l'anisotropie. Cela reste cependant très qualitatif, et l'on aimerait bien localiser les différentes sources d'anisotropie plus précisément, par exemple à l'aide d'un modèle radial d'anisotropie de vitesse de cisaillement. L'équation 1.5 ne peut pas être utilisée pour inverser directement les anomalies anisotropiques de vitesse de phase pour des anomalies anisotropiques de vitesse de cisaillement. Par contre, rien ne nous empêche de construire, en chaque point du modèle de vitesse de phase, une courbe de dispersion pour la vitesse de phase dans la direction de propagation rapide, $C_{rapide} = C_{iso} + A_{2\psi}\cos(2\Theta) + B_{2\psi}\sin(2\Theta)$, une seconde courbe de dispersion dans la direction perpendiculaire (c'est-à-dire, dans la direction de propagation lente), $C_{lente} = C_{iso} + A_{2\psi}\cos(2\Theta+\pi) + B_{2\psi}\sin(2\Theta+\pi)$, puis de calculer (en utilisant l'équation 1.5 et le même type d'inversion que dans le paragraphe 1.4) les profils de vitesses de cisaillement V_{rapide} et V_{lente} correspondants à ces courbes de dispersion, et enfin d'en déduire les profils isotropiques, $V_{iso} = \frac{1}{2}(V_{rapide} + V_{lent})$, et anisotropiques, $V_{aniso} = \frac{1}{2}(V_{rapide} - V_{lent})$, de vitesse de cisaillement.

Bien sûr, il faut définir une direction rapide. Dans notre cas, ce choix est simplifié par le fait que les directions de propagation rapide observées entre 20 et 34 s et autour de 140 s sont approximativement parallèles ($\Theta \sim 32°$ et $\Theta \sim 54°$, respectivement), et perpendiculaires à la direction de propagation rapide observée entre 45 et 60 s ($\Theta \sim 165°$). Il est donc judicieux de choisir $\Theta_{rapide} = 45°$ comme direction rapide. Une conséquence de ce

choix est que dans les couches supérieure et inférieure, l'anisotropie apparaîtra en positif, tandis que dans la couche intermédiaire elle apparaîtra en négatif. Notons également que l'amplitude de la couche intermédiaire sera légèrement sous-estimée, puisque la direction lente (Θ_{lente} ~ 135°) ne pointe pas tout-à-fait dans la direction de propagation rapide de l'anisotropie observée entre 45 et 60 s.

La Figure 1.7 représente les profils isotropiques et anisotropiques moyen pour la partie orogénique (courbes oranges) et pour la partie cratonique (courbes bleues) de notre étude. Trois couches anisotropiques, 30-70 km, 70-150 km, et 150-250 km, sont clairement présentes sous les provinces orogéniques. La couche la plus profonde semble se prolonger jusque vers 350 km, mais la perte de sensibilité au delà de 250 km (liée au fait que nos courbes de dispersions s'étendent, au mieux jusqu'à 200 s) ne permet pas de contraindre cette propriété avec certitude. Sous les provinces cratoniques, l'anisotropie est globalement plus faible, quelque soit la profondeur. Aux profondeurs inférieures à 70 km, elle ne semble pas significative. Aux profondeurs plus importantes, on reconnait la distribution observée sous les provinces orogéniques, mais avec des amplitudes plus modestes.

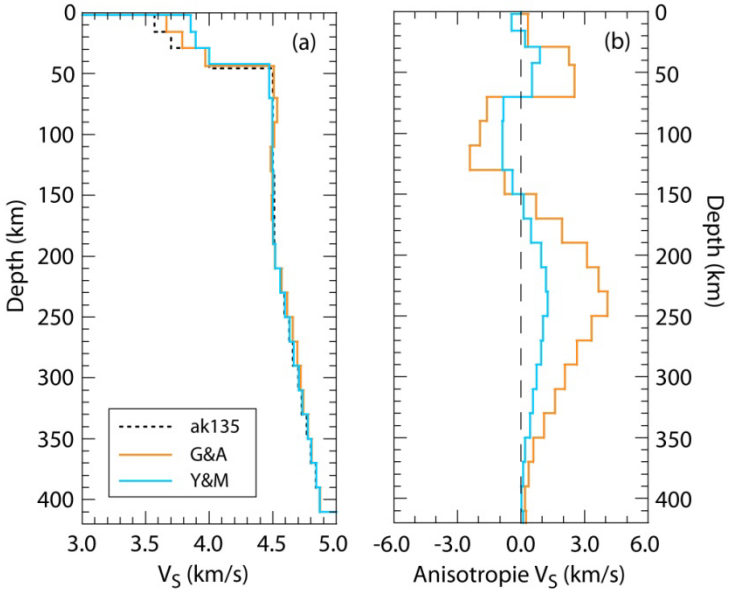

Figure 1.7 – (a) Profils de vitesse isotrope moyen pour la partie orogénique (courbe orange) et la partie cratonique (courbe bleue). (b) Profils d'anomalies anisotropiques moyens pour la partie orogénique (courbe orange) et la partie cratonique (courbe bleue).

1.6.2 Un petit test

Les profils d'anisotropie *Vs* confirment ce que l'anisotropie des vitesses d'ondes de Rayleigh pressentait, et précisent les frontières des différentes couches anisotropiques. Le lecteur est cependant en droit de ce demander si ce résultat n'est pas biaisé par l'inversion des courbes

de dispersions mesurées (entre les paires de stations sismiques) pour le modèle de vitesse de phase (§1.3). Pour éliminer ce doute et étayer nos conclusions, un petit test basé sur une inversion directe des courbes de dispersions mesurées s'impose. Prenons deux courbes dispersion de bonne qualité entièrement (ou presque) contenues dans les provinces orogéniques, l'une ayant un azimut d'environ 45° (LRAL-MYNC fera l'affaire), l'autre un azimut perpendiculaire (disons GOGA-WVT), inversons-les séparément pour un profil V_S, et calculons la différence de ces deux profils. Pour parfaire le test, utilisons pour l'inversion une méthode de Monte-Carlo, ce qui élimine les incertitudes induites par la régularisation.

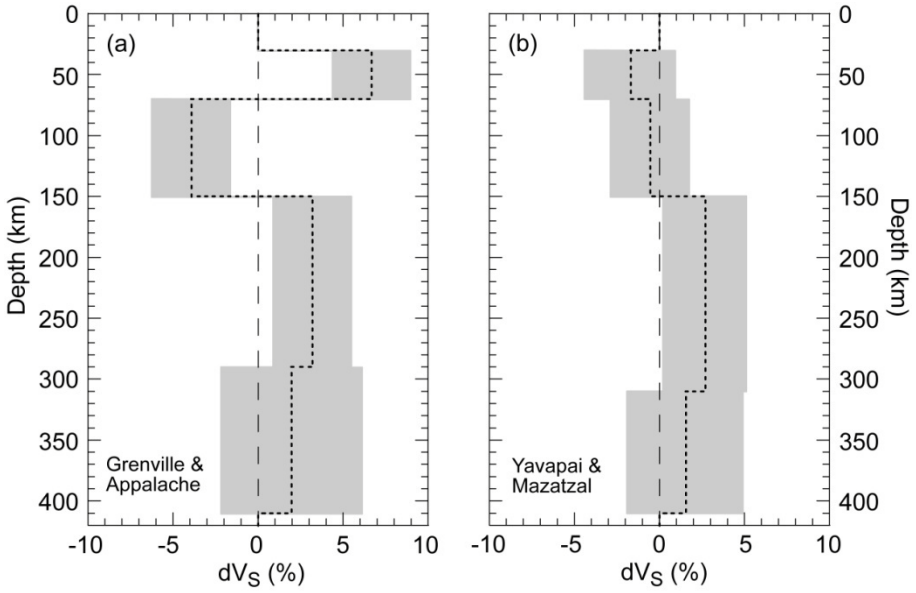

Figure 1.8 – Profils anisotropiques calculés directement à partir des courbes de dispersions mesurées. (a) Provinces orogéniques Grenville et Appalache. (b) Provinces cratoniques Yavapai et Mazatzal. Chaque courbe de dispersion est inversée selon une méthode de Monte-Carlo, en échantillonnant l'espace modèle avec 10^7 profils V_S.

On limitera la résolution verticale à 4 couches (30-70 km, 70-150 km, 150-310 km, et 310-400 km), ce qui permettra une exploration exhaustive de l'espace modèle. Chaque modèle V_S, prédit une courbe de dispersion que l'on calculera selon Schwab et Knopoff (1972), et que l'on comparera à la courbe mesurée en lui attribuant une probabilité

$$p(V_S) = k\exp\left(-\frac{\chi^2}{2}\right), \tag{1.6}$$

où $$\chi^2 = \sum_j \frac{\Delta C_j}{\sigma_j}, \tag{1.7}$$

k est une constante de normalisation, ΔC_j la différence entre les vitesses de phase mesurée et calculée pour la période T_j, et σ_j l'incertitude sur la vitesse de phase mesurée pour cette période. La fonction de densité de probabilité ainsi obtenue nous permettra de calculer le

profil V_S moyen (1er moment) et sa déviation standard (2ième moment). Enfin, on fera le même exercice pour deux courbes de dispersion contenues dans les provinces cratoniques (MPH-UTMT pour la direction rapide et PVMO-OXF pour la direction lente). Le résultat de ces opérations (Figure 1.8) confirme les résultats obtenus à l'échelle régionale (Figure 1.7).

1.6.3 Retour sur les déphasages d'onde de cisaillement

En ouvrant ce chapitre, j'ai soulevé la question de la localisation de la région source des déphasages *SKS*. À partir des profils régionaux de l'anisotropie V_S (Figure 1.7), j'ai estimé la contribution de chaque couche anisotropique au déphasage observé en surface (Table 1.1) en suivant une méthode développée par Montagner et al. (2000) et Simons et al. (2002).

Profondeur (km)	Grenville & Appalache		Yavapai & Mazatzal	
	$\langle \delta t \rangle$	$\sigma_{\delta t}$	$\langle \delta t \rangle$	$\sigma_{\delta t}$
30-70	0.18	0.09	0.03	0.08
70-150	-0.20	0.08	-0.09	0.09
150-400	1.10	0.20	0.37	0.20

Table 1.1 – Déphasages d'onde *S* intégrés dans chaque couche anisotropique pour les régions orogéniques (Grenville et Appalache) et les régions cratoniques (Yavapai et Mazatzal). $\langle \delta t \rangle$ et $\sigma_{\delta t}$ sont respectivement la moyenne et la variance régionale.

Dans la partie orogénique, le délai induit par le passage de l'onde dans la couche supérieure (30-70 km) est de l'ordre de 0.2 s, mais ce déphasage est entièrement compensé par le délai acquis lors du passage dans la couche intermédiaire (70-150 km). Il est donc fort probable que les mesures de déphasage *SKS* ne distinguent pas ces deux contributions. En revanche, le déphasage intégré lors du passage dans la couche inférieure (150-400 km) est important, supérieur à 1 s, ce qui est en bon accord avec les déphasages observés (Barruol et al., 1997; Fouch et al., 2000). Enfin, dans la partie cratonique, les déphasages intégrés sont petits, même dans la couche inférieure où l'on s'attend pourtant à observer de forts déphasages liés à l'écoulement asthénosphérique. Un épaississement de la lithosphère et/ou la topographie locale de l'asthénosphère pourrait contribuer à la faiblesse de l'anisotropie observée autour de 150-300 km sous la partie cratonique.

1.7 Une machine à remonter le temps sismologique - Perspectives

Les modèles tomographiques donnent une image instantanée du manteau et de la croûte. Les structures, lentes ou rapides, que l'on y observe reflètent l'état thermochimique contemporain de la région imagée. Toutefois, l'anisotropie sismique, si l'on admet qu'elle est effectivement liée à des fabriques acquises lors de différents épisodes de déformation et

gelées par la suite, ouvre une fenêtre sur le passé. Plusieurs épisodes peuvent se succéder, et l'anisotropie de se stratifier. À partir de la structure verticale de l'anisotropie observée sous le centre-est des Etats-Unis, on peut ainsi construire un scénario pour l'histoire de la déformation de la lithosphère continentale de cette région (Figure 1.9).

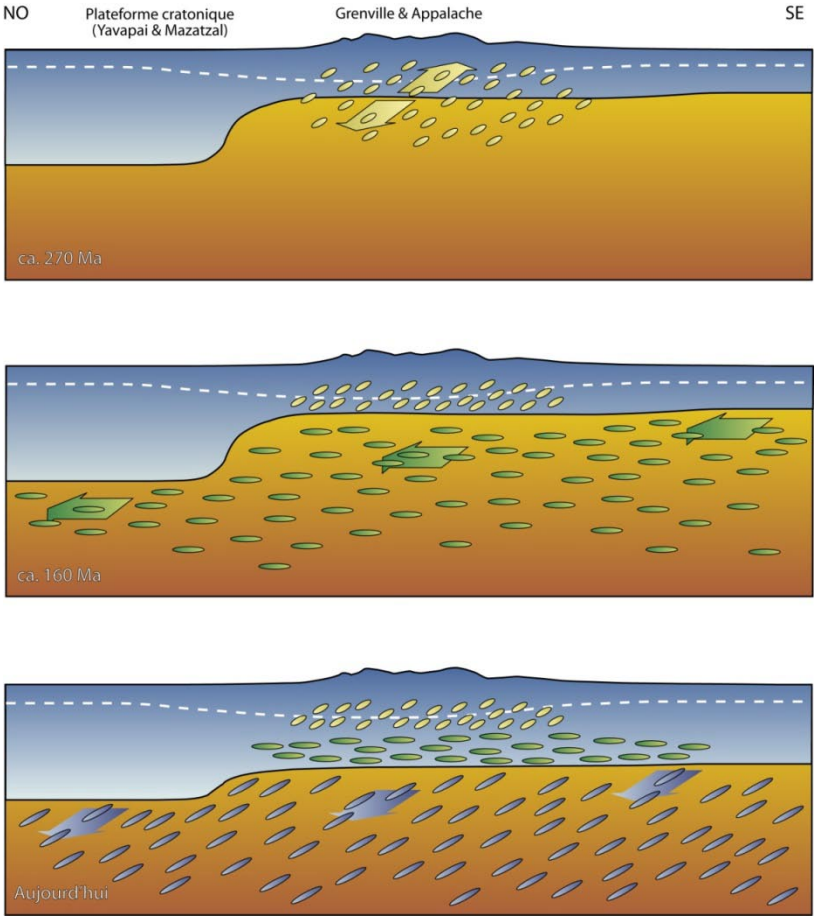

Figure 1.9 – Un scénario possible pour l'origine de l'anisotropie stratifiée observée dans la centre-est des Etats-Unis (Deschamps et al., 2008b). (a) Déformation (extrusion latérale?) liée à l'orogène Appalachienne jusque vers 270 Ma. (b) Suite à cet épisode orogénique, la lithosphère est plus chaude et malléable, et elle enregistre le mouvement vers le NNO de la plaque Nord-Américaine (160-125 Ma). Progressivement, la lithosphère se refroidit et se renforce. (c) De nos jours, l'écoulement asthénosphèrique induit de fortes déformations au sommet de la lithosphère, à partir de 150 km de profondeur environ. Les fabriques liées aux déformations passées restent gelées, ce qui induit une structure verticale de l'anisotropie en trois couches distinctes.

Lors de l'orogène Appalachienne (jusque vers 270 Ma), la croûte et le somment de la lithosphère subissent d'importante déformations, dont, sans doute vers la fin de l'orogène, l'extrusion latérale (d'une partie) de la racine lithosphérique (p.e., Meissner et Mooney, 1998). À la fin de cet épisode, la lithosphère est épaisse d'environ 70 km. Sa température est élevée, et donc elle est facilement déformable. Elle a pu acquérir des fabriques lors de la dérive de la plaque Nord-Américaine vers le nord-ouest (160-125 Ma), tout en se refroidissant progressivement, ce qui limite l'amplitude de la déformation (et donc de

l'anisotropie que l'on observe aujourd'hui). De nos jours, le mouvement de la plaque Nord-Américaine (vers le sud-ouest) induit de fortes déformations au somment de l'asthénosphère, à partir de 150 km de profondeur. Aujourd'hui, encore, les ondes de surface qui se propagent dans la croûte et le manteau supérieur sous le centre-est des Etats-Unis sont, selon leur période, sensibles aux différentes fabriques présentes à différentes profondeurs.

Refermons ce chapitre par quelques perspectives. Le but initial de cette étude était de détecter la présence éventuelle d'anisotropie sismique dans la croûte profonde et le manteau supérieur, et ses possibles variations en fonction de la période. Mission accomplie. De plus, il nous a été possible de déterminer la distribution verticale d'anisotropie et de relier ce profil à l'histoire de la déformation lithosphérique dans cette partie des États-Unis. Voilà qui ouvre la porte à d'autres études, pour d'autres régions. À commencer par d'autres segments le long des orogènes Grenvillienne et Appalachienne (il suffit, pour s'enconvaincre, de jeter un coup d'œil vers le nord-est ou vers l'ouest de la carte de la Figure 1.1). Plus au nord, le craton Canadien est une cible privilégiée, et il sera intéressant de voir à quelle profondeur apparaît l'anisotropie liée à l'écoulement asthénosphérique (pour autant qu'elle soit présente). On s'attend bien sûr à ce que la lithosphère y soit plus épaisse, ce qui, difficulté supplémentaire, implique de pouvoir mesurer des courbes de dispersion jusqu'à des périodes élevées (disons 300 s). Petit problème, il existe pour le moment très peu de stations sismologiques permanentes dans cette région. Changeons de continent. l'Australie est globalement divisée en trois grandes provinces dont l'âge diminue d'ouest en est, et il n'est pas inconcevable que d'importantes variations régionales d'anisotropie y soient présentent. Simons et al. (2002) notent d'ailleurs, sans pouvoir la résoudre suffisamment, que la structure anisotropique est relativement complexe jusque vers 150 km. Au delà, l'anisotropie semble être relié au mouvement de la plaque Australie, point sur lequel l'étude de Debayle et al. (2005) est beaucoup plus affirmative que celle de Simons et al. (2002).

Des améliorations méthodologiques sont aussi envisageables (souhaitables), notamment pour détecter la présence éventuelle d'anisotropie radiale, et cartographier ses variations géographiques. Dans l'hypothèse où l'écoulement asthénosphérique est compliqué par la topographie de la frontière lithosphère/asthénosphère, on s'attend à ce qu'une composante radiale de l'anisotropie soit effectivement présente à l'aplomb des fronts orogéniques. La méthode que nous avons utilisée pour les ondes de Rayleigh est en tout point transposable aux ondes de Love. Cependant, au moins dans notre cas, les courbes de dispersion mesurées par la méthode des deux stations sont globalement de moins bonne qualité et couvrent des plages de fréquence beaucoup plus réduites. D'autres méthodes

devront sans doute être employées, par exemple inversant les différences de temps d'arrivée entre deux stations et à différentes périodes (Pedersen et al., 2006). Autre direction possible, utiliser le bruit de fond sismique. L'idée est d'appliquer la méthode des deux stations aux traces obtenues en cumulant le bruit enregistré en deux stations différentes sur une longue période de temps.

Enfin, bien que le modèle schématisé sur la Figure 1.9 rende compte de la structure verticale de l'anisotropie observée sous le centre-est des États-Unis, il reste qualitatif. Le temps caractéristique de refroidissement (par diffusion) d'une couche de 150 km est compatible avec notre scénario (Deschamps et al., 2008b), mais une recherche plus exhaustive dans l'espace des paramètres du modèle de refroidissement doit être menée. Plus généralement, il serait intéressant de conduire des modélisations numériques pour différent cas de figure, par exemple pour l'extrusion latérale d'une racine lithosphérique. Ces modèles devront bien sûr résoudre l'équation de conservation de l'énergie pour modéliser l'évolution thermique du système. Le lien avec l'anisotropie pourrait ensuite être envisagé en utilisant des méthodes existantes (p.e., D-Rex, Kaminski et al., 2004).

Bibliographie

Barruol, G., P.G. Silver, et A. Vauchez, 1997. Seismic anisotropy in the eastern United States: deep structure of a complex continental plate, *J. Geophys. Res.*, **102**, 8329-8348.

Beck, M.E., et B.A. Housen, 2003. Absolute velocity of North America during the Mesozoic from paleomagnetic data, *Tectonophysics*, **377**, 33-54.

Bevington, P.R., et D.K. Robinson, 1992. Data reduction and error analyses for the physical sciences, McGraw-Hill, New-York.

Christensen, N.I., 1984. The magnitude, symmetry and origin of upper mantle anisotropy based on fabric analyses of ultramafic tectonics, *Geophys. J. R. Astron. Soc.*, **76**, 89-112.

Dalziel, I.W.D., 1991. Pacific margins of Laurentia and East Antarctica-Australia as a conjugate rift pair: evidences and implications for an Eocambrian supercontinent, *Geology*, **19**, 598-601.

Debayle, E., B.L.N. Kennett, et K. Priestley, 2005. Global anisotropy and the thickness of continents, *Nature*, **433**, 509-512.

Deschamps, F., S. Lebedev, T. Meier, et J. Trampert, 2008a. Azimuthal anisotropy of Rayleigh-wave phase velocities in the east-central United States, *Geopys. J. Int.*, **173**, 827-843.

Deschamps, F., S. Lebedev, T. Meier, et J. Trampert, 2008b. Stratified seismic anisotropy reveals past and present deformation beneath the east-central United States, *Earth Planet. Sci. Lett.*, **274**, 489-498.

Forsyth, D.W., 1975. The early structural evolution and anisotropy of the oceanic upper mantle, *Geophys. J. R. Astron. Soc.*, **43**, 103-162.

Fouch, M.J., K. Fisher, E.M. Parmentier, M.E. Wysession, et T.J. Clarke, 2000. Shear-wave splitting, continental keels, and pattern of mantle flow, *J. Geophys. Res.*, **105**, 6255-6275.

Gripp, A.E., et R.G. Gordon, 1990. Current plate velocities relative to hotspots incorporating the NUVEL-1 global plate motion model, *Geophys. Res. Lett.*, **17**, 1109-1112.

Hoffman, P.F., 1988. United Plates of America, the birth of a craton. Early Proterozoic assembly and growth of Laurentia, *Ann. Rev. Earth Planet. Sci.*, **16**, 543-603.

Kaminski, E, N.M. Ribe, J.T. Browaeys, 2004. D-Rex, a program for calculation of seismic anisotropy due to crystal lattice preferred orientation in the convective upper mantle, *Geophys. J. Int.*, **157**, 1-9.

Karlstrom, K.E., K.-I. Åhäll, S.S. Harlan, M.L. Williams, J. McLelland, et J.W. Geissman, 2001. Long-lived (1.8-1.0 Ga) convergent orogen in southern Laurentia, its extension to Australia and Baltica, and implications for refining Rodinia, *Precambrian Res.*, **111**, 5-30.

Kennett, B.L.N., E.R. Engdahl, et R. Buland, 1995. Constraints on seismic velocities in the Earth from traveltimes, *Geophys. J. Int.*, **122**, 108-124.

Marone, F., and B. Romanowicz, 2007. The depth distribution of azimuthal anisotropy in the continental upper mantle, *Nature*, **477**, 198-203.

Meier, T., K. Dietrich, B. Stöckhert, and H.-P. Harjes, 2004. One-dimensional model of shear wave velocity for the eastern Mediterranean obtained from the inversion of Rayleigh-wave phase velocities and tectonic implications, *Geophys. J. Int.*, **156**, 45-58.

Meissner, R., et W. Mooney, 1998. Weakness of the lower continental crust : a condition for delamination, uplift, and escape, *Tectonophysics*, **296**, 47-60.

Meissner, R., W. Mooney, et I. Artemeva, 2002. Seismic anisotropy and mantle creep in young orogens, *Geophys. J. Int.*, **149**, 1-14.

Molnar, P., 1988. Continental tectonics in the aftermath of plate tectonics, *Nature*, **335**, 131-137.

Montagner, J.-P., et T. Tanimoto, 1991. Global upper mantle tomography of seismic velocities and anisotropies, *J. Geophys. Res.*, **96**, 20337-20351.

Montagner, J.-P., D.A. Griot-Pommera, et J. Lavé, 2000. How to relate body wave and surface wave velocity ?, *J. Geophys. Res.*, **105**, 19015-19027.

Nicolas, A., et N.I. Christensen, 1987. Formation of anisotropy in upper mantle peridotites – a review, in: K. Fuchs and C. Froidevaux (Ed.), *Composition, structure and dynamics of the Lithosphere-Asthenosphere system*, pp. 111-123.

Paige, C.C., et M.A. Saunders, 1982. LSQR : analgorithm for sparse linear equations and sparse least squares, *ACM Trans. Math. Softw.*, **8**, 43-71.

Pedersen, H.A., M. Bruneton, V. Maupin, and the SVEKALAPKO Seismic Tomography Working group, 2006. Lithospheric and sublithospheric anisotropy beneath the Baltic shield from surface-wave array analysis, *Earth Planet. Sci. Lett.*, **244**, 590-605.

Ribe, N., 1989. Seismic anisotropy and mantle flow, *J. Geophys. Res.*, **94**, 4213-4223.

Sato, Y., 1955. Analysis of dispersed surface waves by mean of Fourier transform: Part. 1, *Bull. Earthquake Res. Tokyo*, **33**, 33-47.

Schwab, F., et L. Knopoff, 1972. Fast surface wave and free mode computations, in B.A. Bolt (Ed.), *Method in Computational Physics*, **11**, Academic Press, New-York.

Silver, P.G., 1996. Seismic anisotropy beneath the continents: probing the depths of geology, *Annu. Rev. Earth Planet. Sci.*, **24**, 385-432.

Simons, F.J., R.D. van der Hilst, J.-P. Montagner, et A. Zielhuis, 2002. Multimode Rayleigh-wave inversion for heterogeneity and azimuthal anisotropy of the Australian upper mantle, *Geophys. J. Int.*, **151**, 738-754.

Sleep, N.H., 2005. Evolution of the continental lithosphere, *Annu. Rev. Earth Planet. Sci.*, **33**, 369-393.

Smith, M.L., et F.A. Dahlen, 1973. Azimuthal dependence of Love and Rayleigh wave propagation in a slightly anisotropic medium, *J. Geophys. Res.*, **78**, 3321-3333.

Smith, G.P., and G. Ekström, 1999. A global study of P_n-anisotropy beneath continents, *J. Geophys. Res.*, **104**, 963-980.

Tapponnier, P., Z.Q. Xu, F. Roger, B. Meyer, N. Arnaud, G. Wittlinger, J.S. Yang, 2001. Oblique stepwise rise and growth of the Tibet Plateau, *Science*, **294**, 1671-1677.

Trampert, J., et J.H. Woodhouse, 2003. Global anisotropic phase velocity maps for fundamental modes surface waves between 40 and 150 seconds, *Geophys. J. Int.*, **154**, 154-165.

Wang, Z., et F.A. Dahlen, 1995. Spherical-spline parameterization of 3-dimensional Earth models, *Geophys. Res. Lett.*, **22**, 3099-3102.

Yang, Y., et D.W. Forsyth, 2006. Rayleigh-wave ohase velocities, small-scale convection, and azimuthal anisotropy beneath southern California, *J. Geophys. Res.*, **111**, doi: 10.1029/2005JB004180.

Ziegler, P.A., 1989. Evolution of Laurussia: a study in late Paleozoic plate tectonics, 102 pp., Kluwer Academic Publishers, Dordrecht.

Geophys. J. Int. (2008) **173,** 827–843 doi: 10.1111/j.1365-246X.2008.03751.x

Azimuthal anisotropy of Rayleigh-wave phase velocities in the east-central United States

Frédéric Deschamps,[1,2] Sergei Lebedev,[2] Thomas Meier[3] and Jeannot Trampert[2]

[1]*Institut für Geophysik, Swiss Federal Institute of Technology, ETH Hönggerberg HPP* L8.1, 8093 *Zürich, Switzerland. E-mail: frederic.deschamps@erdw.ethz.ch*

[2]*Department of Earth Sciences, Utrecht University, Budapestlaan* 4, PO Box 80021, 3508 *TA Utrecht, The Netherlands*

[3]*Ruhr University Bochum, Universitätsstrasse* 150, NA3/165, 44780 *Bochum, Germany*

Accepted 2008 February 4. Received 2008 February 4; in original form 2006 November 6

SUMMARY

We explore the Rayleigh-wave phase velocity structure of the east-central US in a broad period range (10–200 s). Using a recent implementation of the two-stations method, we first measure interstation dispersion curves of Rayleigh-wave phase velocities along 60 paths. We then invert our collection of dispersion curves for isotropic and azimuthally anisotropic (2Ψ and 4Ψ) phase–velocity maps. The inversion is performed by a damped, smoothed LSQR, and the output model is parametrized on a triangular grid of knots with a 140 km grid spacing. Using the isotropic component of the phase velocity maps to constrain regional variations in shear velocity and Moho-depth, we observe that over the upper-middle crust depth range ($z < 30$ km) shear wave velocities are lower beneath the Grenville and Appalachian orogenic provinces than beneath the Central Plains to the west. The amplitude of (2Ψ) anisotropy and the azimuth of the fast-propagation direction at periods between 20 and 34 s vary laterally. Beneath the Grenville and Appalachian provinces, the amplitude of anisotropy reaches 1 per cent of the average phase velocity, and the azimuth of the fast-propagation direction is uniform and equal to 32°. West of the Grenville front, the average amplitude falls to 0.5 per cent, and the azimuth of the fast-propagation direction is less uniform. In the period range 45–60 s, anisotropy is smaller in amplitude (∼0.5 per cent) and with a regionally uniform azimuth of the fast-propagation direction of around 165°. Around 140 s, the amplitude of 2Ψ anisotropy is larger again (>1 per cent), and the azimuth of the fast-propagation direction is uniform over the entire region and equal to 54°. Our results suggest that azimuthal anisotropy beneath the east-central US is vertically distributed in three distinct layers, with a different geodynamic origin for each of them.

Key words: Surface waves and free oscillations; Seismic anisotropy; North America.

1 INTRODUCTION

Azimuthal anisotropy is of great interest to infer past and present deformation in the lithosphere and asthenosphere, and can be retrieved by studying either the polarization of seismic waves speeds (mainly SKS and S), or the azimuthal dependence of body or surface wave speeds. In one given region, lithospheric and asthenospheric deformations are often discussed as alternative origin for azimuthal anisotropy. Stratification of anisotropy, however, has increasingly been revealed by recent surface wave observations, sometimes combined with shear wave splitting data (e.g. Simmons *et al.* 2002; Smith *et al.* 2004; Sebai *et al.* 2006; Marone & Romanowicz 2007). In this paper, we build an anisotropic model of Rayleigh-wave phase velocity in the east-central US (31°N–41°N, and 82°E–92°E), and observe different azimuthal anisotropy patterns in three distinct period ranges, suggesting that in this region azimuthal anisotropy is vertically distributed in at least three layers.

The tectonics of the east-central US is dominated by the southern part of the Grenville and Appalachian orogenic belts. During the Grenville orogeny, which was active between 1.3 and 1.0 Gyr, small continents accreted to the Laurentia supercontinent (see Hoffman 1988 for a review; and Karlstrom *et al.* 2001, for a recent study). The southern portion of the Grenville front (thick curve in Fig. 1) runs southwestwards down to 34°N latitude, and bends westwards. The Appalachian front (thick dashed curve in Fig. 1) is associated with a more recent orogeny (350–300 Ma), during which Gondwana and North America collided (e.g. Ziegler 1989). It also runs southwestwards down to 32°N latitude, where it bends westwards (Ouachitas mountains). West of the Grenville front are the stable cratonic Central Plains. These terrains are believed to have experienced little or no tectonic activity during the past 1.6 Gyr (Hoffman 1988).

Strong shear wave splitting has been reported in the east-central US (Barruol *et al.* 1997; Fouch *et al.* 2000). Fouch *et al.* (2000) measured shear wave splitting at each station of the MOMA

© 2008 The Authors
Journal compilation © 2008 RAS

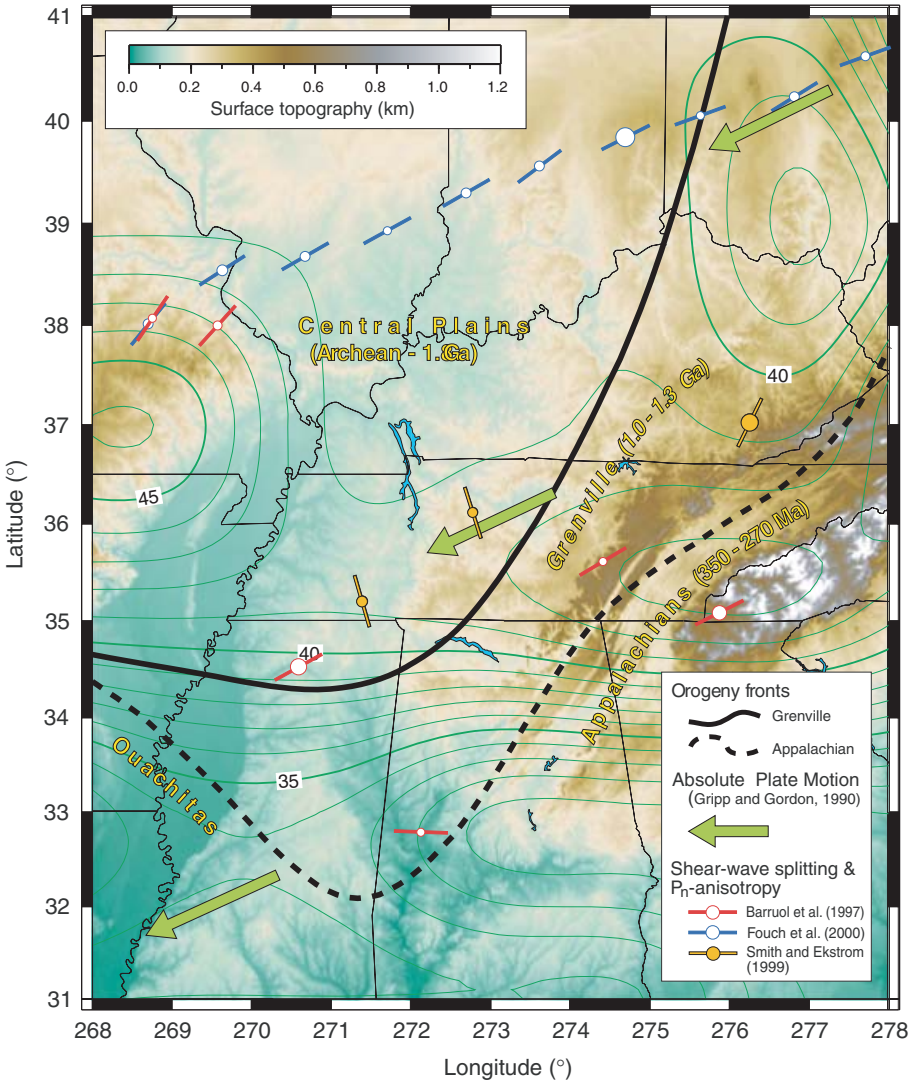

Figure 1. Tectonic setup. The background map shows surface topography from GTOPO30, and the dark green contour lines represent the Moho depth from crust2.0 (http://mahi.ucsd.edu/Gabi/rem.html) interpolated on a 0.2° × 0.2° grid mesh. The thick plain and dashed black curves denote the Grenville and Appalachian fronts, respectively. Also shown are the regional absolute plate motion (Gripp & Gordon 1990), shear wave splitting from Fouch *et al.* (2000) and Barruol *et al.* (1997), and P_n-anisotropy from Smith & Ekström (1999). Circle sizes are proportional to the amount of splitting.

network, and found splitting times between 0.5 and 2.2 s, depending on the station (Fig. 1, blue symbols). Barruol *et al.* (1997) compiled measurements in a wider region, and found similar directions of fast propagation, with more scatter (Fig. 1, red symbols). The directions of fast propagation fit well the regional absolute plate motion (Gripp *et al.* 1990) (Fig. 1, green arrows), supporting the hypothesis that shear wave splitting in this region results primarily from asthenospheric deformation due to the relative motion of the lithosphere and asthenosphere. However, due to the tectonic context, it is reasonable to assume that frozen fabric due to past deformation is also present in the lithosphere beneath the Appalachian and Grenville provinces, producing seismic anisotropy. This hypothesis is supported by P_n-anisotropy measurements (Smith & Ekström 1999), which shows different directions of fast propagation beneath the Central Plains and beneath the Grenville and Appalchian provinces (Fig. 1, orange symbols). Interestingly, the direction of fast propagation beneath the Grenville and Appalachian provinces is compatible with that inferred from shear wave splitting in this region.

Shear wave splitting measurements have an excellent lateral resolution, but poor radial resolutions and therefore cannot locate the anisotropy unambiguously. On the contrary, surface waves are sensitive to different depths depending on their period, and can thus constrain azimuthal anisotropy with a better radial resolution than shear wave splitting. Arrays are well suited to retrieve isotropic and anisotropic regional structures sampled by surface waves, but methodology and data availability often limit the explored period range (e.g. Friederich & Huang 1996; Freybourger *et al*. 2001; Li *et al*. 2003). Recently, dense arrays allowed the construction of high-resolution models of Rayleigh-wave phase velocity in various regions. For instance, Yang & Forsyth (2006) built a Rayleigh-wave phase velocity model for southern California in the period range 25–143 s, and retrieved regional average azimuthal anisotropy, which they attributed to both lithospheric deformation and asthenospheric flow, the latter locally disrupted by small-scale convection. Pedersen *et al.* (2006) measured Rayleigh wave dispersion curves for the Baltic Schield in a broad (15–190 s) period range, and

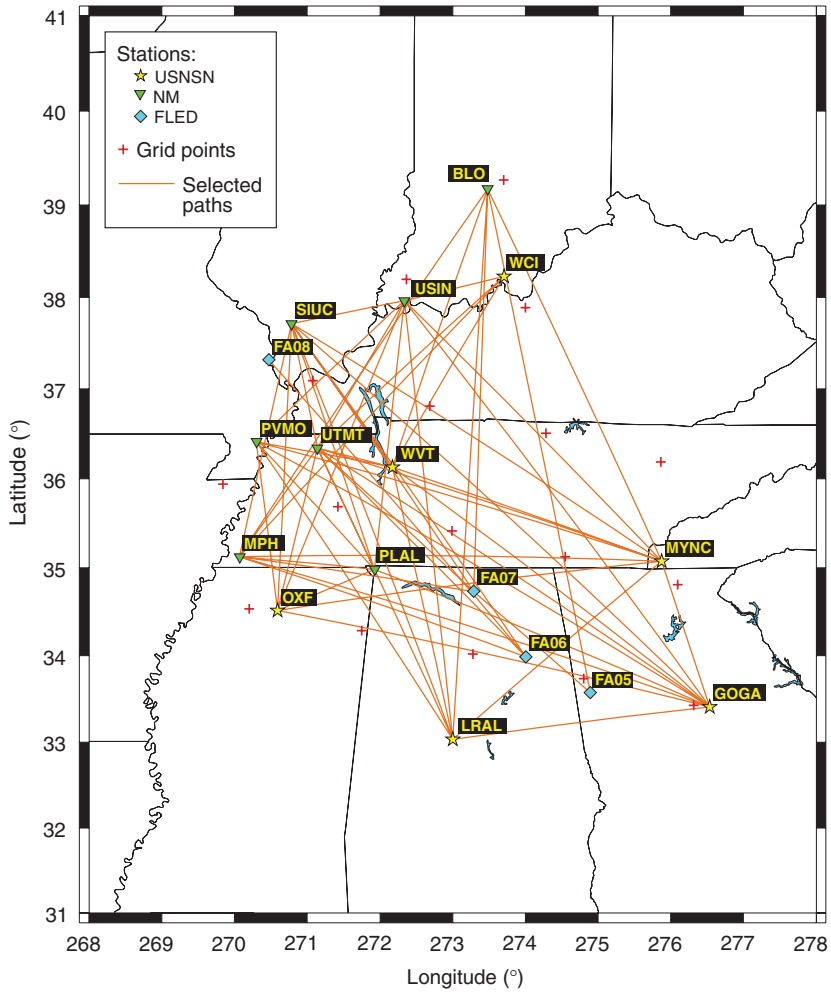

Figure 2. Data setup. Seismic stations are represented by different symbols, depending on the network they belong to. Selected paths used to compute the anisotropic model are shown in orange. The red crosses indicate the knots of the triangular grid on which the phase velocity model is calculated.

inferred azimuthal anisotropy in this region between 20 and 100 s. The amplitude of azimuthal anisotropy they observed was small between 20 and 60 s (sampling the lower crust and uppermost lithospheric mantle), but strongly increased in the period range 70–100 s (sampling the deep lithospheric mantle). Here, we measured dispersion curves of Rayleigh-wave phase velocity using a new implementation of the two-station method (Meier *et al.* 2004). Application of this technique to high-quality broad-band data enables measurements of interstations dispersion curves in a period range (10–200 s) that is broad enough to sample the Earth from the middle crust down to the subcratonic asthenosphere.

2 DATA AND REGIONAL SETTING

To investigate the Rayleigh-wave phase velocity structure of the east-central US (31°N–41°N, and 82°E–92°E), we used seismograms recorded at 17 seismic stations located in this area (Fig. 2). Most of these stations belong to permanent seismic networks (USNSN and NM), but we also used data from the Florida to Edmonton (FLED) temporary PASSCAL experiment (http://epsc.wustl.edu/seismology/FLED/proposal.html). Each pair of stations defines a path along which we can measure, data permitting, a phase–velocity dispersion curve for the fundamental Rayleigh mode.

The two-station method requires that the angles between the great circle connecting a pair of stations and the great circles connecting the stations and the event are not too large. In this study, we put this limit to 10°. Epicentral distances are between 10 and 170°, and all distances between pairs of seismic stations are smaller than 800 km. From the IRIS database, we extracted more than 20 000 records satisfying these criteria, from more than 3000 events. Events and source regions are different for each pair of stations. As an example, Fig. 3 shows event locations and great circles connecting events to the seismic stations for the pairs BLO-LRAL and MPH-MYNC. Due to global (distribution of source regions along the path azimuth) and local (site and instrumental qualities, station history) factors, the number of selected events greatly varies from one pair to another (Table 1). The interstation dispersion curve for a path connecting a pair of stations is averaged from all measurements for this pair of stations. Data availability and selection procedures resulted in the construction of average phase–velocity curves for 60 different paths (Fig. 2).

3 DISPERSION CURVES OF THE FUNDAMENTAL RAYLEIGH MODE

A collection of dispersion curves, one for each path connecting a pair of seismic stations of an array, can be used to constrain regional

© 2008 The Authors, *GJI*, **173,** 827–843
Journal compilation © 2008 RAS

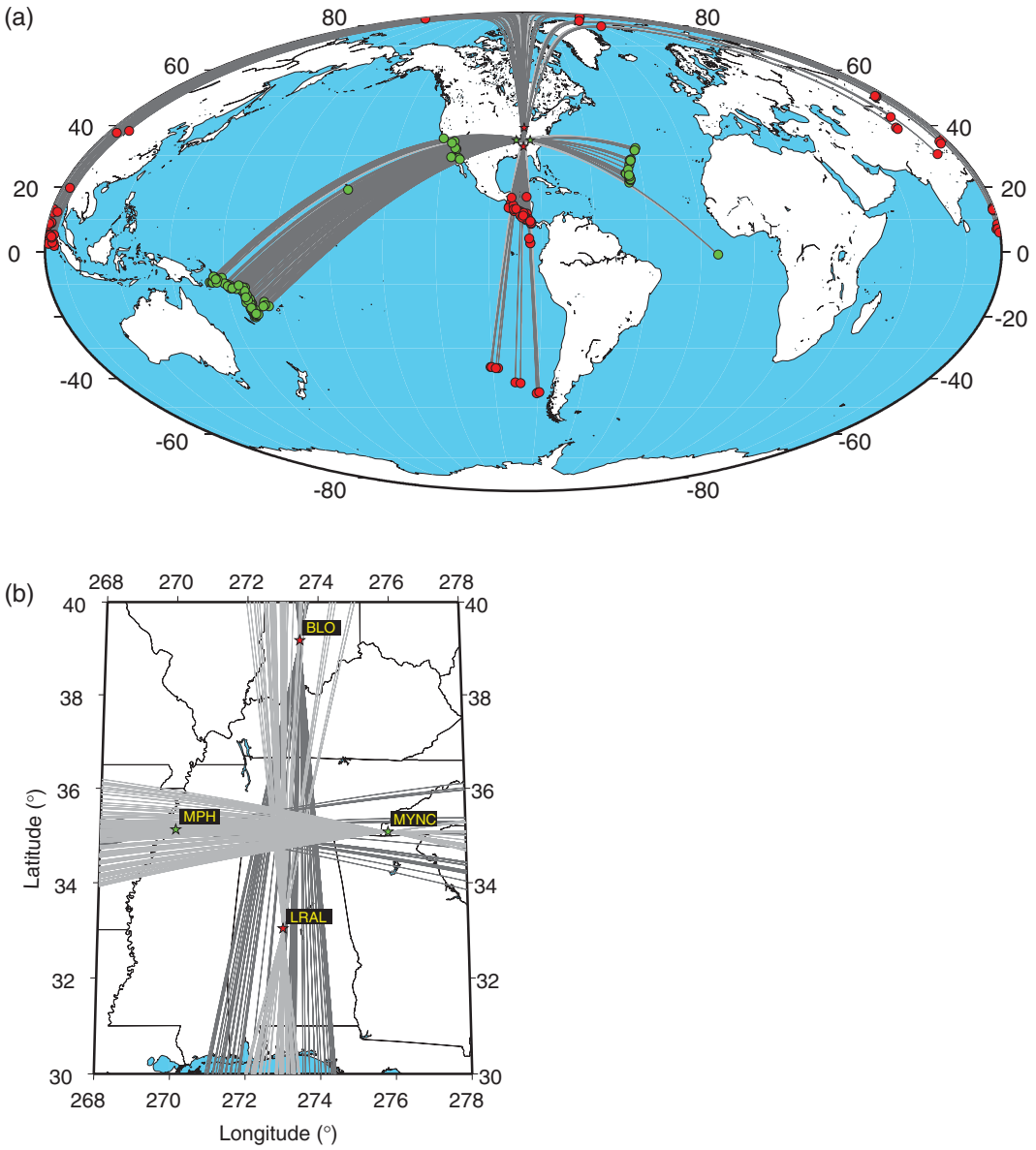

Figure 3. Events and great circles from events to stations for the pairs BLO-LRAL and MPH-MYNC. Red and green dots indicate the selected events for the pair BLO-LRAL and MPH-MYNC, respectively.

2-D variations in phase velocity beneath the array. The two-station method, first introduced by Sato (1955), has been extensively used to measure dispersion curves of surface waves (for a review of early works, see Knopoff 1972). In this study, we use a recent implementation of the cross-correlation approach (Meier *et al.* 2004). As shown below, this implementation allows measurements of dispersion curves in a broad period range (10–200 s).

For each selected event, the vertical components of the displacement recorded at the two stations of a pair are cross-correlated. To minimize the effects of noise and interferences, the cross-correlation function is first filtered with a frequency-dependent Gaussian band-pass filter. Side lobes caused by correlations of the fundamental mode with scattered waves or higher modes are then down weighted by applying in the time domain a frequency-dependent Gaussian window to the filtered cross-correlation function. This approach to filtering and windowing is effective as long as the fundamental mode has the largest amplitude on the seismogram and, consequently, on the cross-correlation function. The cross-correlation is then transferred in the frequency domain, and its complex phase $\Phi(\omega)$ is used to calculate the phase velocity $c(\omega)$ following

$$c(\omega) = \frac{\omega\,(\Delta_1 - \Delta_2)}{\zeta(\omega)}, \quad \zeta(\omega) = \arctan\left\{\frac{\mathrm{Im}\,[\Phi(\omega)]}{\mathrm{Re}\,[\Phi(\omega)]}\right\} + 2n\pi, \quad (1)$$

where Δ_1 and Δ_2 are the epicentral distances to each of the two stations. Because of the 2π ambiguity of the *arctan* function, the solution of eq. (1) is non-unique and is represented by an array of curves (one for each $n \in N$). Phase velocity is measured within a frequency range that is chosen interactively. Several non-overlapping frequency ranges can be selected for one single event. Seismic-wave diffraction and interference of Rayleigh- and Love-wave, fundamental and higher modes can bias the measurements. These effects, however, have a strong frequency dependence, which manifests itself in irregularities and roughness of measured curves. Selection of only smooth portions of the curves, removal of outliers

Table 1. Selected pairs.

Pair	D (km)	Az (°)	N_{eve}	N_t	f (mHz)	σ_C (m s^{-1})
BLO-FA05	634.1	−11.1	77	51	7.0–79.5	26.8
BLO-FA07	493.1	1.9	31	18	12.0–89.0	25.5
BLO-LRAL	682.3	3.5	67	43	4.5–77.5	36.5
BLO-MPH	541.8	33.0	153	85	5.0–100.0	31.6
BLO-MYNC	285.5	−24.4	123	43	4.0–110.4	31.2
BLO-WVT	356.8	18.5	72	33	7.5–129.4	30.5
FA05-FA07	195.7	−48.5	50	13	17.5–132.9	33.5
FA06-FA08	489.0	−39.9	16	10	24.5–79.5	16.1
GOGA-LRAL	331.8	81.8	65	37	4.0–101.5	33.1
GOGA-MYNC	194.2	−18.1	171	50	5.0–119.4	25.0
GOGA-OXF	562.6	−75.8	110	48	4.5–94.0	29.6
GOGA-WVT	500.4	−51.7	110	34	3.5–110.4	36.1
LRAL-MYNC	348.3	48.7	32	32	7.0–122.4	30.4
LRAL-WVT	351.7	−12.3	73	58	3.0–79.5	34.4
MPH-FA06	383.0	−69.6	22	14	25.5–89.0	27.5
MPH-FA07	297.5	−80.7	31	20	16.5–94.0	27.6
MPH-GOGA	624.8	−70.5	117	80	3.0–81.5	33.9
MPH-MYNC	529.2	88.9	39	24	4.5–96.5	28.3
MPH-PLAL	170.1	−84.2	130	113	5.0–81.5	31.5
MPH-SIUC	294.6	12.4	145	86	5.5–126.0	28.5
MPH-UTMT	166.2	35.2	103	65	6.5–129.4	29.6
MPH-WCI	473.8	42.3	47	40	14.5–110.4	26.9
MYNC-OXF	487.3	81.2	91	32	16.5–96.5	30.5
MYNC-WVT	355.3	−69.7	68	30	5.0–126.0	38.9
PLAL-GOGA	459.1	−66.4	98	63	5.0–110.4	41.8
PLAL-OXF	132.8	66.5	89	13	15.0–69.5	46.5
PLAL-PVMO	216.4	−42.3	101	31	21.5–116.4	25.6
PLAL-SIUC	320.1	−18.3	203	41	3.0–91.5	53.8
PLAL-USIN	333.0	6.2	24	27	15.0–107.4	20.6
PLAL-UTMT	166.9	−25.1	172	22	5.0–96.5	27.2
PVMO-GOGA	659.6	−57.9	36	22	7.0–79.5	24.0
PVMO-LRAL	449.1	−32.7	127	68	6.0–119.4	26.4
PVMO-MYNC	525.4	−72.0	34	12	9.0–89.0	27.2
PVMO-OXF	212.7	−7.0	81	17	7.5–67.5	24.3
PVMO-USIN	249.5	45.8	44	37	14.0–132.9	20.9
PVMO-WVT	170.9	−78.8	45	18	7.0–77.5	29.9
SIUC-FA06	506.0	−34.2	37	29	5.5–104.5	25.3
SIUC-FA07	400.5	−33.5	48	31	8.5–77.5	30.2
SIUC-GOGA	706.7	−45.9	157	73	3.5–77.5	34.3
SIUC-LRAL	557.0	−20.6	92	43	4.0–96.5	31.3
SIUC-MYNC	542.4	−55.8	69	26	8.0–94.0	28.6
SIUC-OXF	355.8	2.7	98	25	3.5–107.4	26.8
SIUC-USIN	139.4	78.0	108	30	6.5–58.5	37.2
SIUC-UTMT	155.5	−11.6	235	15	19.5–63.5	26.5
SIUC-WVT	215.0	−34.7	171	61	5.0–143.4	36.3
USIN-GOGA	632.1	−35.8	98	45	4.0–84.0	21.9
USIN-LRAL	550.3	−6.1	94	49	4.5–75.5	31.7
USIN-MYNC	450.9	−43.6	89	32	7.0–119.4	29.6
USIN-OXF	414.0	21.7	43	16	20.0–107.4	20.3
USIN-UTMT	209.2	30.2	55	22	18.5–99.0	26.8
USIN-WCI	123.8	75.9	91	44	24.5–163.4	46.3
UTMT-FA06	369.9	−44.2	29	15	27.5–89.0	23.8
UTMT-FA07	264.7	−46.9	36	15	28.5–84.0	25.1
UTMT-GOGA	590.8	−55.1	98	40	5.0–94.0	31.8
UTMT-LRAL	404.8	−24.5	94	31	5.0–96.5	30.4
UTMT-MYNC	451.1	−70.5	65	31	15.0–96.5	27.6
UTMT-OXF	209.0	13.5	75	10	20.0–126.0	27.6
UTMT-WCI	309.5	47.6	53	37	17.5–155.4	27.5
WCI-WVT	269.9	29.9	81	24	18.0–126.0	34.1
WVT-UTMT	95.9	−75.5	68	23	22.5–75.5	31.3

Note: For each pair, we list the distance between the two stations (D), the azimuth of the path (Az), the number of event downloaded from the IRIS database (N_{eve}), the number of events used to build the phase velocity dispersion curve (N_t), the frequency range of the dispersion curve (f), and the estimated average standard deviation in phase velocity (σ_C).

(unrealistically far from the reference), and subsequent averaging over many measurements strongly minimize these effects and turn out to be sufficient to warrant the accuracy of the measured dispersion in almost all cases (Meier *et al.* 2004; Lebedev *et al.* 2006; Pedersen 2006). Remaining biases are substantial only in areas of exceptionally strong lateral heterogeneity. Even in these cases, however, the biases are usually easy to identify by inconsistency from measurements on waves arriving from different source regions, especially from the opposite directions.

The selection of the frequency ranges is thus based on the smoothness of the dispersion curves and on the consistency between these curves and an initial *a priori* dispersion curve. Further information for the selection of frequency range(s) is given by time–frequency plots of the two seismograms and of the cross-correlation function, illustrating the properties of the waveforms of the fundamental Rayleigh mode (Meier *et al.* 2004). Scattering and noise are easily detected on these plots. The operations described are performed on the records of all selected events, leading to a collection of phase velocity measurements in various frequency ranges (Figs 4a–d). Selected measurements for a given pair of stations are then assembled to compute averages and standard deviations of the phase velocity along the path that connects the two stations. This averaging reduces biases due to seismic-wave diffraction and interferences between the fundamental and higher modes.

We constructed dispersion curves for 60 different paths (Fig. 2, orange lines). Depending on the number and characteristics of available seismograms, the accuracy of the dispersion curves and the frequency range in which they were measured vary from path to path. For instance, the dispersion curve for path MPH-FA07 (Figs 4d and h) was constructed with 20 events, but poor quality of the data did not allow estimates of the velocity outside the frequency range 16.5–94 mHz (period range 11–60 s). For most paths, however, data allowed the determination of phase velocity between 10 and 80 mHz (100 and 12 s) with a standard deviation around 30 m s^{-1} (Table 1). All 60 paths cover the frequency range 30–55 mHz (period range 18–34 s). For many paths (33) the dispersion curve extends down to a frequency of 7 mHz (up to a period of 140 s), and for about 1/3 of the paths (e.g. GOGA-USIN, Figs 4a and e, and OXF-SIUC, Figs 4c and g), we could measure the dispersion curve down to a frequency of 5 mHz (up to a period of 200 s). The regional coverage also varies with period (Fig. 5). The path density is slightly higher in the western half than in the eastern half at all periods, but on the whole the selected paths fully cover the explored area, even at $T = 10$ s where only 27 paths are available. The azimuthal repartition of paths (histograms in Fig. 5) shows a slight excess of paths with azimuth between $-90°$ and $0°$ (in particular around $\Psi = -40°$).

Our collection of dispersion curves thus covers a broad period range and yields a dense coverage of the explored area for periods between 12 and 140 s. Given the sensitivities of Rayleigh waves (Fig. 6), we can expect our dispersion curves to constrain the seismic structure of both the lower crust and the upper half of the upper mantle. A qualitative comparison between the phase velocity curves for each path and the regionally averaged phase velocity curve (dashed red curves in Figs 4e–h) reveal substantial variations in the phase velocity. These anomalies may be both isotropic and anisotropic in origin.

Although our dispersion curves are each averaged from many measurements and are overall smooth, a certain roughness of small scale and small amplitude is still present. To test whether this small-scale roughness has some effect on the phase velocity maps, we computed the maps both using the original curves and using the curves that were smoothed further. This additional smoothing was

© 2008 The Authors, *GJI*, **173,** 827–843
Journal compilation © 2008 RAS

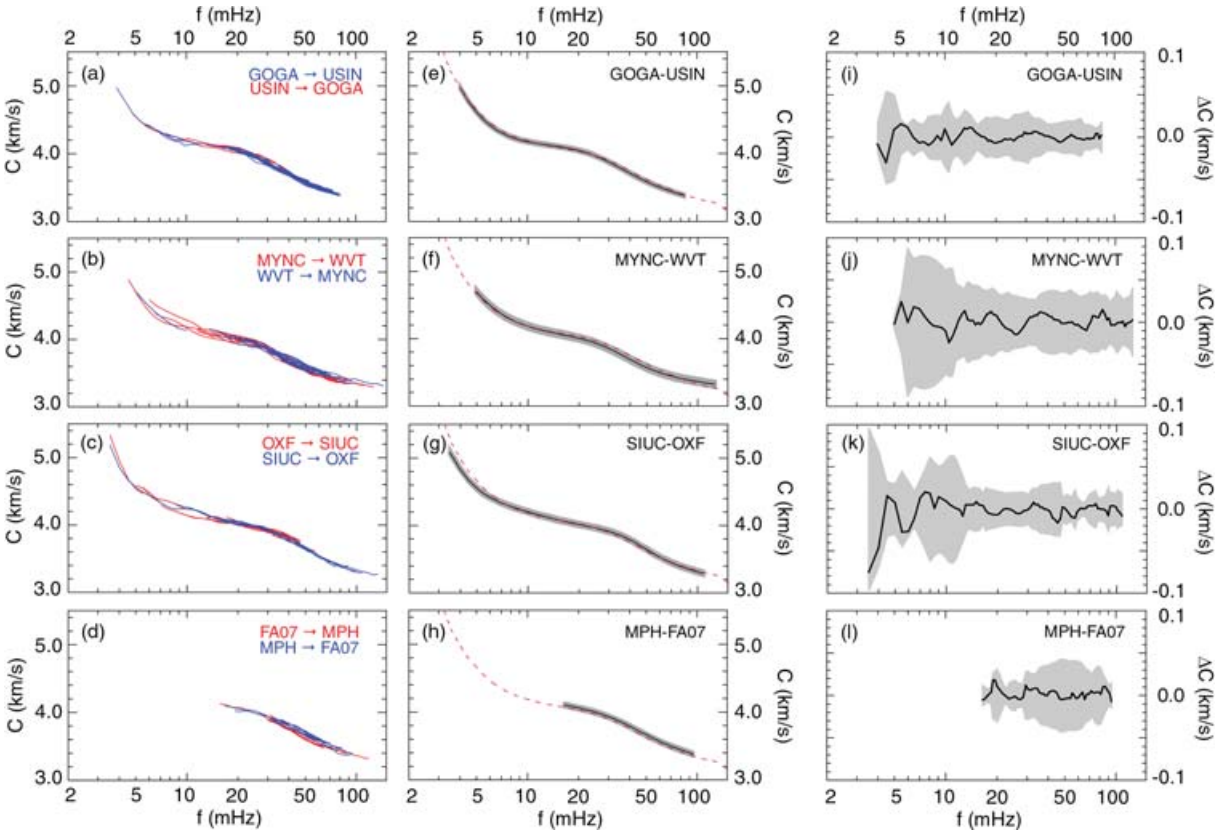

Figure 4. Phase velocity dispersion curves for four different paths. Panels (a–d) plot measurements used to construct the average curves. The direction of propagation is indicated by the colour code (red or blue). In panels (e–h), the bold black lines represent the average smoothed dispersion curves, and the shaded areas cover one standard deviation around this average. The red dashed curve in each plot shows the phase velocity curve averaged over all the 60 paths. Panels (i–l) show the differences between the original and smoothed average dispersion curve.

performed by means of inverting each dispersion curve for a radial model of shear wave velocity (as in Section 5). The inversion is regularized very weakly. It produces a (not necessarily realistic) radial model from which we calculate a theoretical phase velocity curve that is taken as the smoothed version of the original curve. It is important to note that the smoothed dispersion curves fit well within the observed standard deviations and are very similar to the observed average dispersion curve (Figs 4i–l). This approach is in line with the realization that a path-average V_S profile can be seen as a summary of the dispersion properties of the medium along a path for one ore more surface wave modes (Yoshizawa & Kennett 2002; Visser *et al.* 2007). When we inverted the phase–velocity curves with and without the additional smoothing, we found that the differences in the resulting phase–velocity maps were minimal. In the following we use the smoothed curves but acknowledge that the smoothing has not produced any appreciable effect. This could be expected given that the differences between the smoothed and original curves are small and well within the error bars.

The standard deviation in the measured phase velocity at each period is a good estimate of the error in the dispersion curve. The error generally increases with period. In this study, we compute phase–velocity maps by inversions of dispersion curves at different periods that are set up independently from each other (Section 4), rather than by inverting single-path dispersion curves for path-averaged V_S profiles. The phase velocity maps will be thus affected by variations in the errors from one path to another, rather than by the frequency dependence of the errors. For this reason, we chose to use a frequency-independent estimated error for every dispersion curve and fixed the value of this error to the rms of the observed error over the frequency range of the curve.

4 REGIONAL ANISOTROPIC PHASE VELOCITY MAPS

To separate isotropic and anisotropic contributions to the Rayleigh-wave phase velocity anomalies, we performed simultaneous inversions for regional variations in these contributions at each period. The anisotropic part is described by a 2Ψ and a 4Ψ contribution (Smith & Dahlen 1973). Previous studies (Montagner & Tanimoto 1991; Trampert & Woodhouse 2003) showed that 4Ψ-anisotropy is not negligible and should be accounted for in the inversion. The total phase velocity anomaly at longitude φ and latitude θ is given by

$$\delta C(\varphi,\theta) = \delta C_{iso}(\varphi,\theta) + \delta C_{2\Psi}(\varphi,\theta) + \delta C_{4\Psi}(\varphi,\theta), \quad (2)$$

where $\delta C_{\rm iso}$ is the isotropic anomaly, and $\delta C_{2\Psi}$ and $\delta C_{4\Psi}$ are the 2Ψ- and 4Ψ-anisotropic anomalies defined by

$$\delta C_{2\Psi}(\varphi,\theta) = A_{2\Psi}\cos(2\Psi) + B_{2\Psi}\sin(2\Psi), \quad (3a)$$

$$\delta C_{4\Psi}(\varphi,\theta) = A_{4\Psi}\cos(4\Psi) + B_{4\Psi}\sin(4\Psi), \quad (3b)$$

respectively, where Ψ is the local azimuth of the ray, and $A_{2\Psi}$, $B_{2\Psi}$, $A_{4\Psi}$ and $B_{4\Psi}$ are four anisotropic coefficients defined for each longitude φ and latitude θ. The amplitudes of anisotropic anomalies,

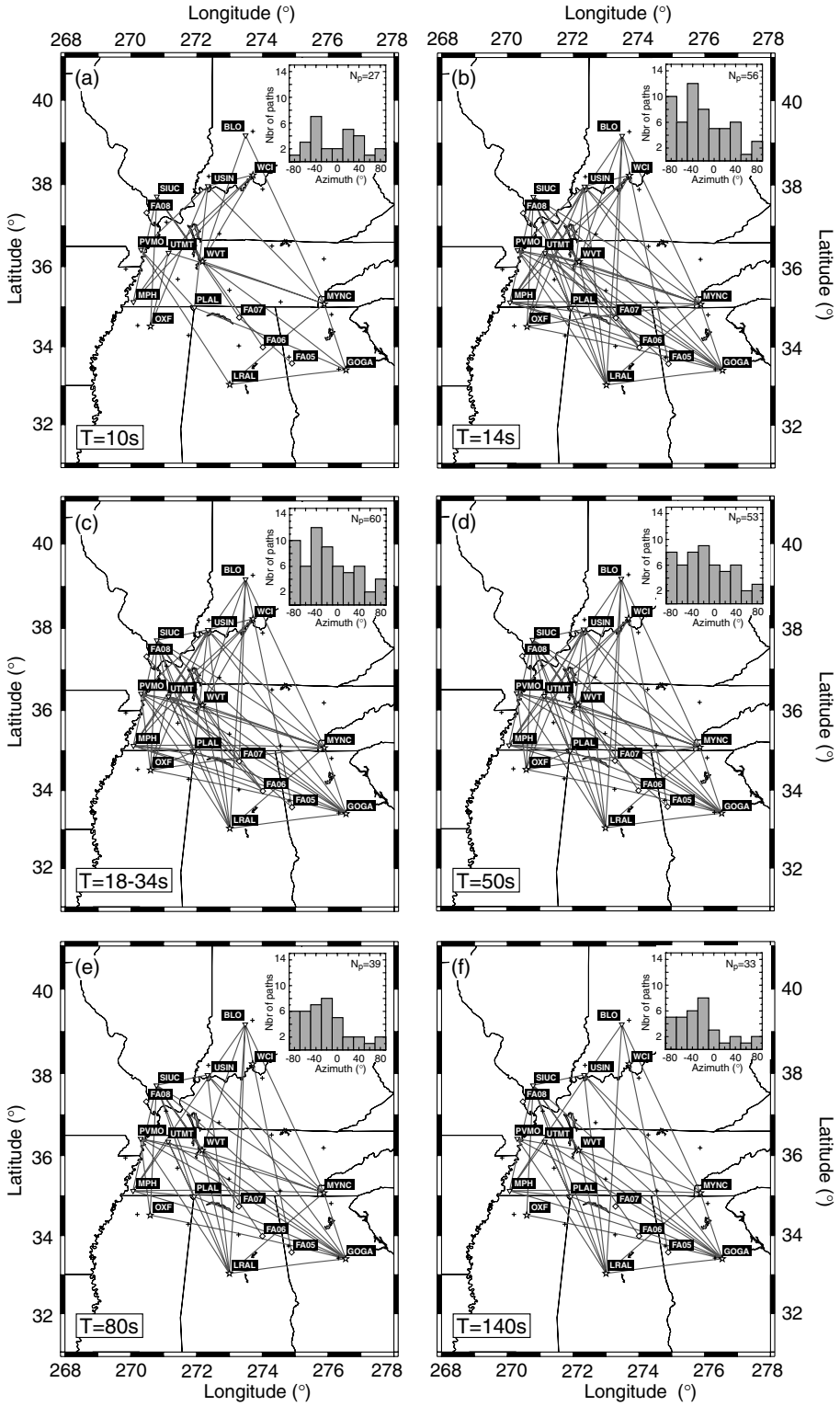

Figure 5. Path coverage at six periods. For each period (or period range) the N_p selected paths are shown in dark grey, and the azimuthal distribution of the selected paths is plotted in a histogram.

Λ, and the directions of fast propagation, Θ, are given by

$$\begin{cases} \Lambda_{2\Psi} = \sqrt{A_{2\Psi}^2 + B_{2\Psi}^2} \\ \Theta_{2\Psi} = \frac{1}{2}\arctan\left(\frac{B_{2\Psi}}{A_{2\Psi}}\right) \end{cases} \quad \text{and} \quad \begin{cases} \Lambda_{4\Psi} = \sqrt{A_{4\Psi}^2 + B_{4\Psi}^2} \\ \Theta_{4\Psi} = \frac{1}{4}\arctan\left(\frac{B_{4\Psi}}{A_{4\Psi}}\right) \end{cases}. \quad (4)$$

We thus invert our collection of phase velocity dispersion curves for five parameters, $\delta C_{\rm iso}$ and the four anisotropic coefficients.

The model is parametrized on a triangular grid (Wang & Dahlen 1995) of 32 knots with a grid spacing of 140 km. In post-processing (inversion for radial models of V_S), we did not account for the

© 2008 The Authors, *GJI*, **173,** 827–843
Journal compilation © 2008 RAS

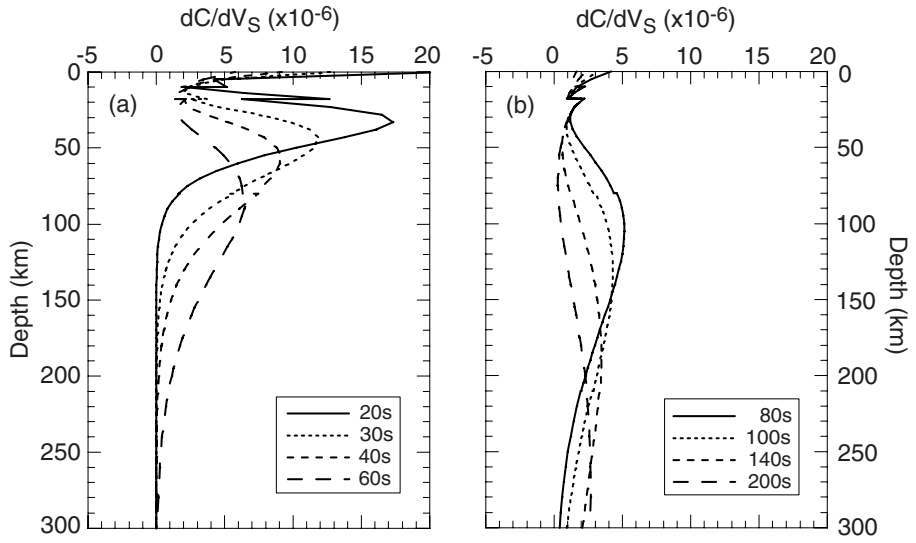

Figure 6. Depth sensitivity kernels of Rayleigh waves for periods between 20 and 200 s. The Frechet derivatives are for isotropic terms, but they can also give an idea of the radial distribution of the azimuthal anisotropy (Montagner & Nataf 1986).

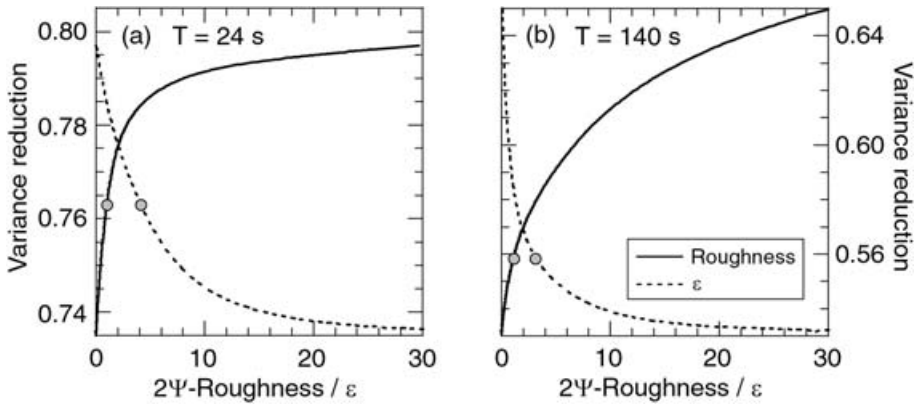

Figure 7. Trade-off curves. The variance reduction is plotted and as a function of the smoothness coefficient ε (dotted curves) and of the roughness in the distribution of 2Ψ-anisotropy anomalies (plain curves). Smoothness coefficients for isotropic anomalies and 4Ψ-anisotropic terms are kept constant. The circles indicate our preferred model. (a) $T = 24$ s; preferred model is for $\varepsilon = 4.2$. (b) $T = 140$ s; preferred model is for $\varepsilon = 3.1$.

peripheral knots, where resolution is poorer, and kept only 17 knots (red crosses in Fig. 2). At each period, the average phase–velocity anomaly along the path i is

$$\overline{\delta C_i} = \int_\varphi \int_\theta K_i(\varphi, \theta)\, \delta C(\varphi, \theta)\, \mathrm{d}\theta\, \mathrm{d}\varphi, \tag{5}$$

where the local anomalies $\delta C(\varphi,\theta)$ are given by eqs (2) and (3). The sensitivity kernels $K_i(\varphi,\theta)$ contain the weight of each knot for that particular path (Lebedev & van der Hilst 2006), and were approximated by paths of finite width. In the calculations, we fixed the path width to 20 km. We varied the path width between 10 and 300 km, but did not find significant differences in the results. The rms of the discrepancies between solutions obtained with different values of the path width is about 2 m s^{-1}, that is, much less than the rms of the estimated error bar on isotropic and anisotropic parameters, which is around 8–12 m s^{-1}. This result suggests that the effect of the assumption of the width of the sensitivity area is limited. For each period, we build a system of linear equations (one equation for each available path at the period, i.e. maximum 60) based on a discrete version of eq. (5) (see Appendix). We then solve this system using the LSQR method (Paige & Saunders 1982) with lateral smoothing and slight norm damping. Isotropic and anisotropic terms are smoothed and damped independently. Choosing the amount of smoothing and damping is always subjective. We defined our preferred model as a compromise between model smoothness and ability to explain observed data (variance reduction). Compromise can be visualized on trade-off curves, as those plotted in Fig. 7. The smoothing we imposed penalizes the second spatial derivatives of each term. Strong smoothing will therefore result in a constant gradient in the inferred distribution.

Estimates of uncertainties due to measurement errors

LSQR does not provide covariances matrices. In order to estimate error bars in the model parameters due to measurement errors, we perform a Monte Carlo search. At each period, we randomly perturb the dispersion curves within their uncertainties. The random noise is generated from a Gaussian probability distribution with a zero mean and standard deviations equal to the curve uncertainties. We then invert this set of perturbed dispersion curves for a perturbed regional model of phase velocity (including isotropic and anisotropic anomalies). By repeating these operations a large number of times

(100 000), we obtain a set of phase velocity models, from which we compute the average anomalies (isotropic and anisotropic) and their standard deviations. These standard deviations are good estimates of the uncertainties in dispersion measurements. The regional rms of these uncertainties vary between 8 and 12 m s^{-1}, depending on the period and the parameter considered.

Importance of anisotropy

To test the significance of anisotropy in explaining our data, we first performed an inversion in which anisotropic terms are neglected. Damping and smoothing are similar to those of the preferred model. Because the number of inverted parameters is not the same, comparing the variance reductions obtained in each inversion is meaningless. Instead, we computed the reduced χ^2 defined as (Trampert & Woodhouse 2003)

$$\chi^2 = \frac{1}{(N_p - T)}(\mathbf{d} - \mathbf{Gm})^{\mathbf{T}}\mathbf{C}_{\mathbf{d}}^{-1}(\mathbf{d} - \mathbf{Gm}), \quad (6)$$

where N_p is the number of data, T the trace of the resolution matrix, **d** and **m** the data and model vectors, **G** the kernel matrix (eq. A3) and $\mathbf{C_d}$ the covariance matrix. Fig. 8 plots the resulting χ^2 as a function of period. Models with lower reduced χ^2 explain the data better. To decide whether differences in reduced χ^2 are significant, we performed F-tests (Bevington & Robinson 1992). For all periods, the reduced χ^2 is smaller when anisotropy is accounted for (Fig. 8). This difference is the largest in the period ranges 16–34 s and 120–160 s, and F-tests show that these differences are 99 per cent significant. Between 36 and 80 s, the decrease in χ^2 is modest, and F-tests indicate that it is only 36 per cent significant. Note that at periods greater than 160 s, the reduced χ^2 is large even when anisotropy is accounted for. In this period range, our results may be less reliable due to poorer data and azimuthal coverage. The reduced χ^2 decrease further when 4Ψ terms are accounted for, but compared to the model with isotropic and 2Ψ terms only, differences are very small and F-tests show that they are not significant. These tests demonstrate that azimuthal 2Ψ-anisotropy is needed to explain the data in period ranges 16–34 s, 120–160 s.

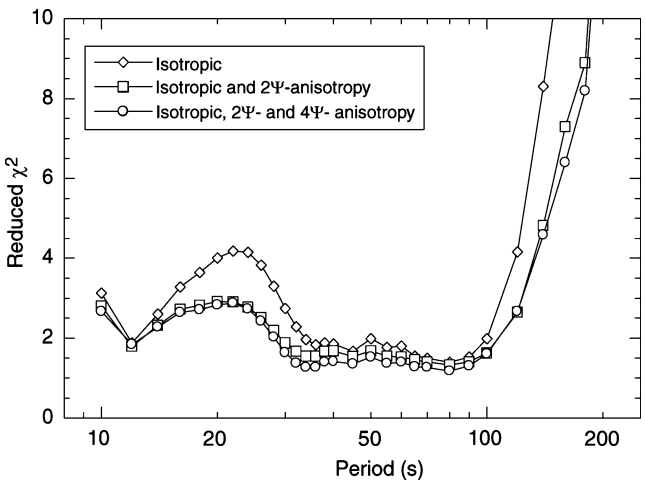

Figure 8. Reduced χ^2 as a function of period. Inversion is performed for isotropic anomalies only (diamonds), isotropic and 2Ψ-anisotropy anomalies (squares), and isotropic and full anisotropy (2Ψ and 4Ψ) (circles). The damping and smoothing factor are those of the preferred model.

Preferred model

The isotropic and anisotropic anomalies of our preferred model are displayed in Fig. 9 for various periods. Throughout this paper, isotropic and anisotropic anomalies are relative to a reference model that is defined as the regional average of the isotropic dispersion curve (Fig. 10c). The regional rms amplitudes of the relative isotropic, and 2Ψ-anisotropic anomalies are shown in Fig. 10. The 4Ψ-anisotropic terms are not needed to explain the data (see previous subsection), and in the remainder of the paper we will focus on isotropic and 2Ψ-term (hereafter simply referred to as anisotropy) anomalies.

Isotropic phase–velocity anomalies

The distribution and average amplitude of isotropic anomalies strongly depends on the period. Largest anomalies are found in the period range 16–34 s. At 20 s, for instance, the average amplitude is ∼0.8 per cent of the reference velocity, but the maximum amplitude is close to 1.7 per cent. Between 40 and 140 s, deviations from the regional average are small, 0.3 per cent on average. At longer periods (160 s and above), amplitudes of anomalies increase again, and are comparable to those observed between 16 and 32 s.

The dominant feature in the distribution of isotropic anomalies is a negative velocity gradient from SW to NE in the period range 12–50 s. This gradient is strongest between 16 and 32 s. There are some indications for the persistence of the SW–NE gradient up to 60 s, but on the whole, between 55 and 100 s, fast anomalies are confined to the SW portion. Finally, at periods larger than 120 s, we observe a pocket of fast anomalies that increases in amplitude with increasing period.

Anisotropic phase–velocity anomalies

We observe strong anisotropy between 20 and 34 s, with significant regional variations in the amplitude and azimuth of the fast-propagation direction. Beneath the orogenic terrains (Grenville and Appalachian), the average amplitude reaches 1 per cent of the reference velocity, and the azimuth of the fast-propagation direction is regionally uniform. West of the Grenville front, the average amplitude is smaller (∼0.5 per cent), and the fast-propagation directions are less uniform. Between 45 and 60 s, in contrast, azimuthal anisotropy is weaker, reaching only ∼0.5 per cent in amplitude. The direction of fast propagation is laterally uniform and equal to 165°, that is, nearly perpendicular to the fast-propagation direction observed in the range 20–34 s. We do not see indications for strong azimuthal anisotropy in the period range 65–100 s. The average amplitude is small (<0.4 per cent), and the azimuth of fast-propagation direction is not regionally uniform. Around 140 s, we observe substantial anisotropy again. The amplitude of anisotropy is large, >1 per cent on average, and the azimuth of fast-propagation direction is regionally uniform around 54°. At 160 s, the average amplitude and the azimuth of fast-propagation direction are comparable to those at 140 s, but there is more variability in the azimuths. Finally, at 180 s and longer periods (not shown), the amplitude of anisotropy is large, but the azimuth of the fast-propagation direction is not regionally coherent. Only 23 paths could be used at these long periods (compared to 60 for periods between 20 and 34 s, and 33 around 140 s), and most of them have an azimuth between −90° and 0°, which probably biases the model.

© 2008 The Authors, *GJI*, **173,** 827–843
Journal compilation © 2008 RAS

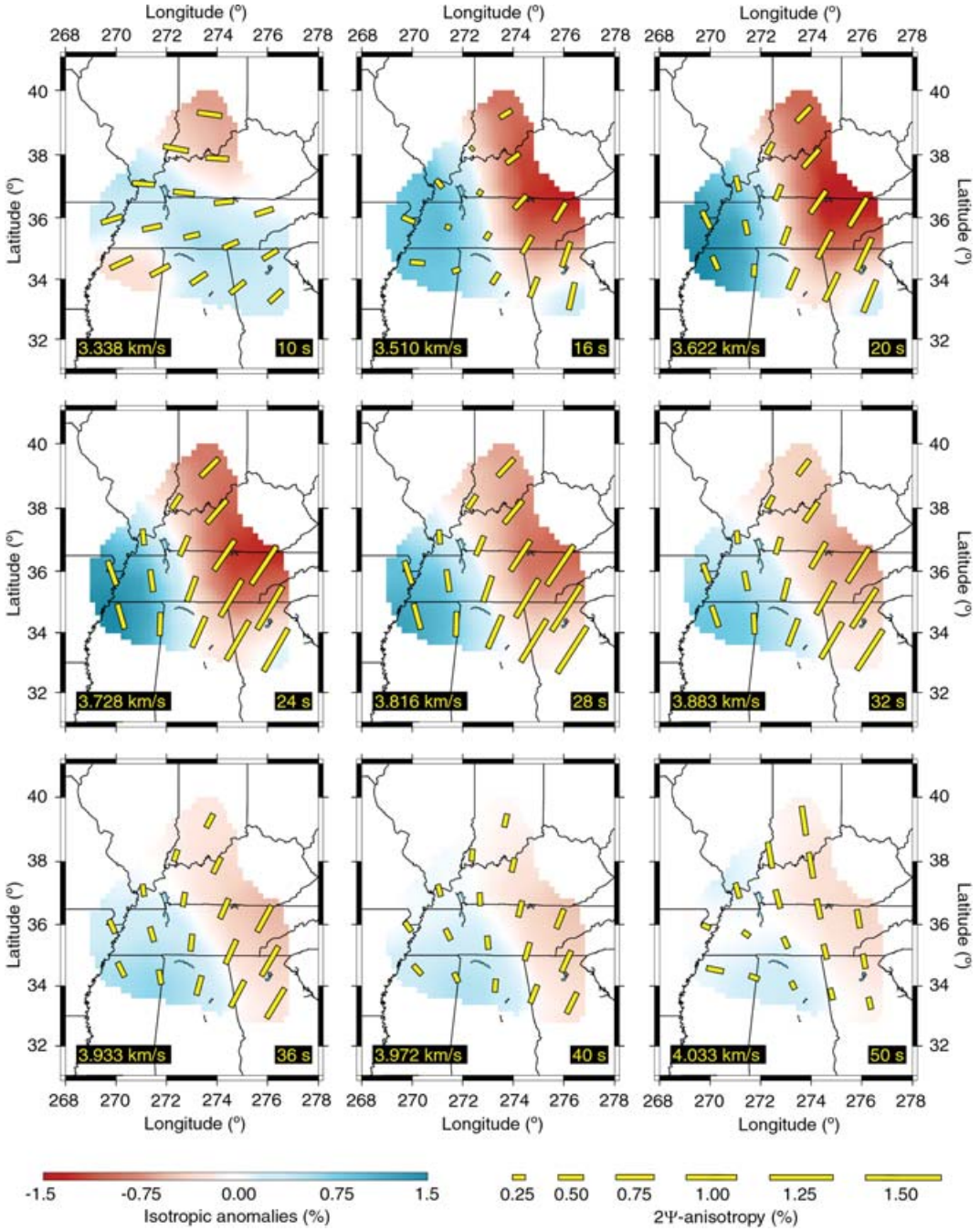

Figure 9. Relative isotropic and anisotropic anomalies of our preferred model at various periods. The length and the direction of the bars denote the amplitude and the fast-propagation direction of anisotropy, respectively. All anomalies are relative to the regional average dispersion curve (Fig. 10c). The value of the reference velocity at each frequency is indicated on each plot.

Influence of regularization

The type and strength of smoothing influence the results of the inversions. The smoothing we imposed penalizes the second lateral derivatives of the phase velocity distribution, and is therefore well suited to retrieve regular gradients in seismic anomalies. Large-scale gradients in phase velocity anomalies will be recovered by our inversions, whereas small local anomalies, if present, will be averaged out by smoothing and will not appear in our models.

The choice of the amount of smoothing is subjective. To estimate the influence of the smoothing coefficient ε on the models, we both plotted trade-off curves (Fig. 7) and examined the results of inversions with different values of the smoothing coefficients. Fig. 11 shows the influence of the smoothing of anisotropy at 24 s. There are large discrepancies between the anisotropic patterns obtained with small smoothing coefficients ($\varepsilon = 2.5$ and less), but interestingly, the azimuths of fast-propagation direction obtained with values of ε larger than 3.0 are not very sensitive to ε. The influence of smoothing

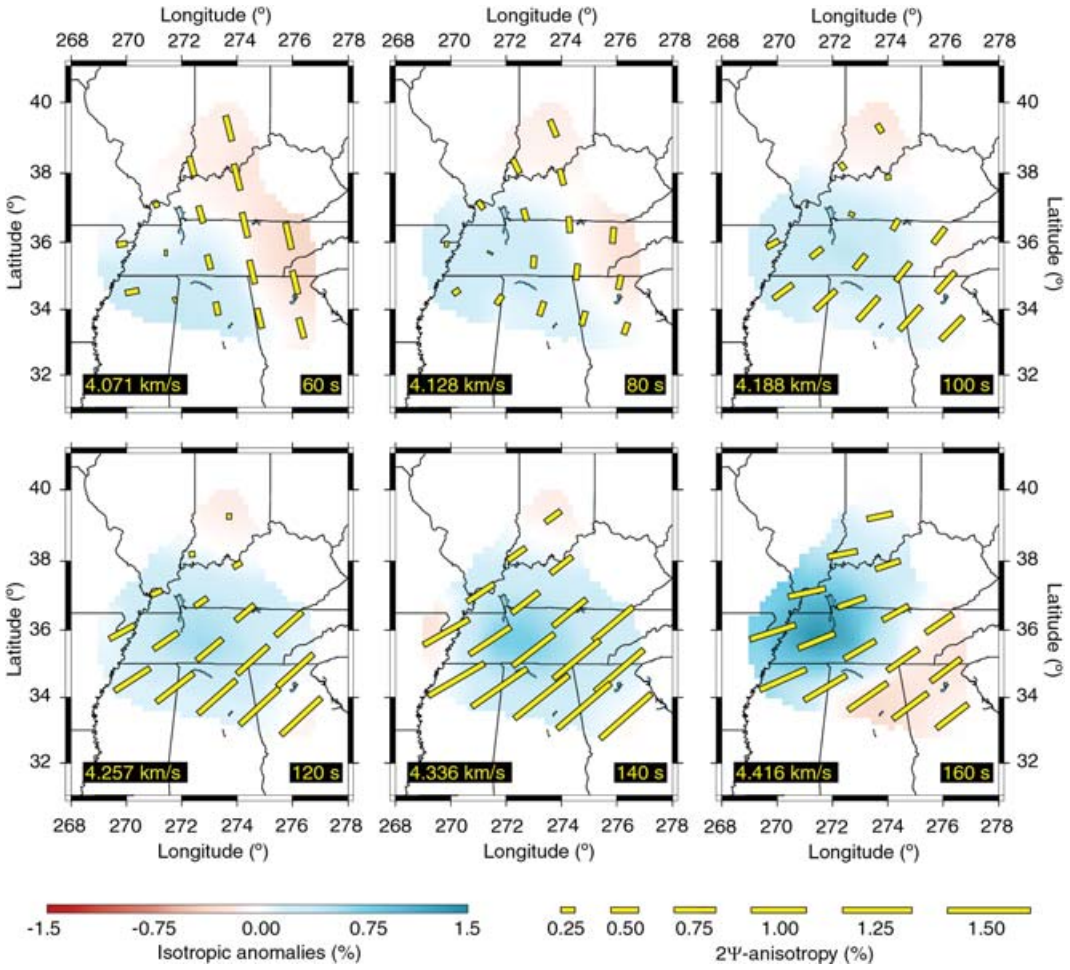

Figure 9. (*Continued.*)

on the amplitude of anisotropy is stronger. The rms of the amplitude of anisotropy at 24 s with $\varepsilon = 3$ and 10 are equal to 0.8 and 0.5 per cent, respectively.

Data sampling varies with the period. All 60 paths sample the period range 18–34 s, but periods outside this range are more sparsely sampled (for instance, only 20 paths sample periods up to 200 s). If we use the same damping coefficients with our damping scheme at all periods, the maps at period with weak sampling will be oversmoothed. To avoid such oversmoothing, we have adjusted the damping coefficient with period.

Trade-off and resolution matrices

To estimate the trade-off between isotropic and anisotropic terms, we defined test models m^{test} in which the isotropic anomalies are equal to those of the preferred model, and the anisotropic anomalies have been set to zero. We then compute test data

$$d^{\text{test}} = Gm^{\text{test}}, \tag{7}$$

and invert them for phase velocity anomalies (Fig. 12). Damping and smoothing coefficients are similar to those used for the preferred model. Clearly, the isotropic anomalies are very close to those of our preferred model. Between 20 and 40 s, there are small discrepancies in the structure (for instance, the southeast corner at 24 s is now slower than average), but the regionally average amplitudes are 80 per cent of that observed in our preferred model. At longer periods, the amplitude discrepancy slightly increases. More importantly, the amplitudes of artificial 2Ψ-term anisotropy are very small, about 2 m s^{-1} on average, at all periods. This series of inversions suggest that trade-off between isotropic and anisotropic terms do exist, but are small.

The LSQR method does not directly provide resolution matrices. It is possible, however, to reconstruct the resolution matrix **R** by 'inverting' each column j of the kernel matrix **G** (Trampert & Lévêque 1990). Given the LSQR operator, **L**, we have

$$R = LG \tag{8}$$

and, therefore, for each column j,

$$R_j = LG_j. \tag{9}$$

Fig. 13 shows resolution matrices at 24 and 140 s. If the inverted parameters are perfectly resolved, the resolution matrix is equal to the identity matrix, whereas smearing indicates linear dependencies between inverted parameters. Fig. 13 confirms that trade-offs between isotropic and anisotropic terms are present, but limited. In the diagonal submatrices, stronger lateral (or geographical) trade-offs in the distribution of each of the isotropic and anisotropic terms are apparent. These geographical trade-offs are mostly due to the imposed smoothness.

The effect of smoothing is to spread out local anomalies. As a consequence, narrow anomalies of the same sign can be distinguished

© 2008 The Authors, *GJI*, **173,** 827–843
Journal compilation © 2008 RAS

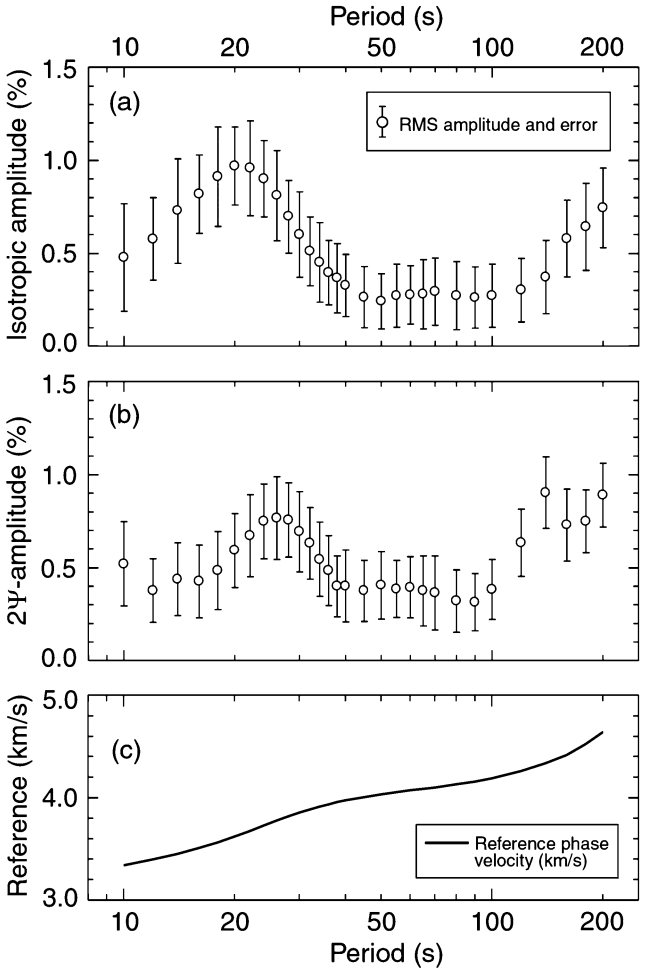

Figure 10. The rms amplitude and error of relative isotropic anomalies (a) and 2Ψ-anisotropy anomalies (b) as a function of period. Errors are due to the uncertainties in the dispersion curves. (c) Regional average isotropic dispersion curve.

only if they are distant enough. The shortest distance at which they can be resolved is the resolution length, also equal to the half width of the image of a δ-function anomaly as it would appears in the model (Lebedev & Nolet 2003). Note that anomalies wider than the resolution length and sharp transitions with anomaly sign change are correctly retrieved. To measure the resolution length for our preferred model, we defined a series of test models in which we set the isotropic and anisotropic parameters (eqs 2 and 3) to zero except at two selected gridpoints, where we set them to the same arbitrary values. We then computed test data (eq. 7) and inverted it for phase velocity anomalies. Smoothing and damping are as for our preferred model. By varying the distance between the two selected spots and their location on the grid, we estimated the resolution length and its geographical variations. We found resolution lengths of ∼200 km for isotropic anomalies, and ∼300 km for anisotropy anomalies.

5 ISOTROPIC DISPERSION CURVES AND SHEAR WAVE VELOCITY

We inverted the isotropic phase velocity maps locally for radial models of shear wave velocity (V_S). The inversion is a Gauss–Newton gradient search. The V_S-profiles are parametrized with boxcar and triangular basis functions. Given a reference background radial model, the gradient search iteratively updates the model parameters, calculates a synthetic phase velocity curve from the new V_S-profiles, and compares it to the observed dispersion curve. Synthetic phase velocities are calculated following the method of Schwab & Knopoff (1972). The inversion is stopped when the synthetic phase velocity curve fits the observed one with a prescribed precision. Norm damping penalizes deviations from the reference profile. Parameters corresponding to all of the basis functions are damped independently. The depth of the Moho is also a parameter of the inversion. The difference between its inverted and reference (here, crust2.0, http://mahi.ucsd.edu/Gabi/rem.html) values is penalized using an independent damping factor.

We have inverted the isotropic dispersion curve at each gridpoint (red crosses in Fig. 2) for a local radial V_S profile, and assembled these profiles in order to constrain the shear speed structure in this region. At periods larger than 30 s (Fig. 14) our measured dispersion curves are similar to a reference curve computed for an ak135 mantle profile and a region average crustal model accounting for crust2.0. At shorter periods, the measured Rayleigh wave phase velocity are larger than the reference. The difference between the measurement-average and reference phase velocities reaches 150 m s^{-1} at 10 s. Inverted shear wave velocities are higher than those in crust2.0 down to the middle crust, but are indistinguishable from ak135 in the mantle.

In Fig. 15, we plotted the variations in Moho depth and shear wave velocity anomalies (relative to the regional average) that result from our inversions. The distributions in Fig. 15 are affected by three main sources of uncertainties. First, the uncertainties in measured dispersion curves propagate to the V_S-profiles. Second, inversion of the dispersion curve for V_S profiles is sensitive to the applied regularization, and various damping values will result in different profiles. Finally, V_S anomalies in the lower crust and uppermost mantle adjacent to the Moho can trade-off with variations in the Moho depth. Rough estimates of the total uncertainties are ∼3 per cent in V_S anomalies and ∼4 km in the Moho depth. Even accounting for uncertainties of a few kilometres, however, the Moho-depths we inferred are substantially different from those in crust2.0 in this region. The average Moho depth is 41.7 km, that is, more than 3.0 km deeper than in crust2.0. The biggest differences are found in the southeastern part, where the Moho we observe is deeper than that in crust2.0 by about 10 km. The Moho is deeper beneath the orogenic regions (43.4 km) than beneath the central plains (39.7 km). It is shallowest in the southwestern part, in agreement with crust2.0 but with shallower (up to 5 km) values. It is interesting to note that the Moho correlates with surface topography, as expected for Airy isostasy, deepest Moho being found beneath the Appalachian mountain range. The shear wave velocity structure is more uncertain, with amplitude of V_S anomalies comparable or smaller than the estimated uncertainties, except in the upper and middle crust (Fig. 14b).

Comparing radial profiles of the average isotropic anomalies (Fig. 14b) beneath the orogenic terrains (including the Grenville and Appalachian provinces, light blue curve), and beneath the Central Plains (west of the Grenville front, orange curve), we observe that the upper-middle crust is faster than crust2.0 beneath both regions, whereas crustal shear wave velocities are higher beneath Central Plains than beneath the orogenic terrains. This is consistent with the pattern seen in the phase velocity maps at short periods (Fig. 9). In the lower crust, shear wave velocities are close to those in crust2.0 beneath both the Central Plains and the orogenic terrains. Finally, shear velocities beneath the Central Plains and the orogenic terrains are very close to those in ak135 in the lithospheric upper mantle.

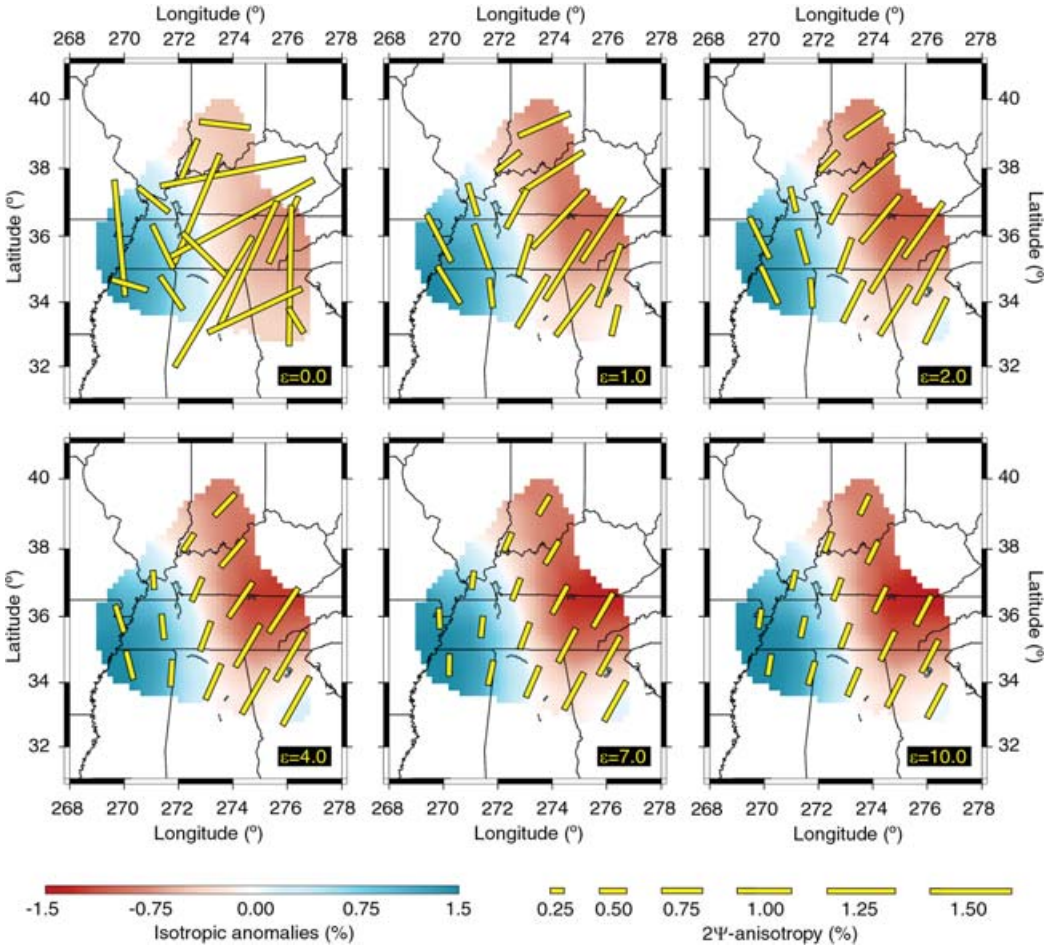

Figure 11. Influence of the 2Ψ-anisotropy smoothing coefficient (ε) on the output model. The smoothing coefficients for isotropic and 4Ψ-anisotropic anomalies are kept constant. The period is $T = 24$ s. At each point, the direction and the size of the bar indicate the direction of the fast axis and the amplitude of the 2Ψ-anisotropic relative anomalies, respectively. The relative isotropic anomalies are also displayed, as indicated by the colour scale.

The grey shaded area in Fig. 14(b) covers twice the estimated uncertainties due to errors in the data. These uncertainties are smaller than the actual uncertainties in V_S because we did not account for the effect of trade-offs between parameters at different depths. Even with these underestimated uncertainties, it is clear that the data do not require that the V_S-profiles in the mantle deviate from ak135.

6 CONCLUDING REMARKS

The main result of this study is the observation of strong anisotropy below east-central US in three distinct period ranges: 20–34, 45–60 and 140–160 s. The amplitude of 2Ψ-term anisotropic anomalies is slightly larger around 140 s than between 20 and 34 s, and the azimuths of the fast-propagation directions in the two period ranges are slightly different from one another. Between 45 and 60 s, anisotropy is smaller in amplitude. Although anisotropy is not required to explain phase–velocity data in this period range, the mapped direction of fast propagation is regionally uniform and perpendicular to that in the period ranges 20–34 and 120–160 s. The anisotropic properties of the mantle layer sampled by Rayleigh wave at 45–60 s are thus distinct from those in the layers above and beneath. In terms of radial structure, our results strongly suggest that azimuthal anisotropy beneath the east-central US is stratified in at least three separate layers. This is in good agreement with recent observations for North America (Marone & Romanowicz 2007).

The azimuths of the fast-propagation directions we inferred in the period range 20–34 s agree very well with those of P_n-anisotropy reported by Smith & Ekström (1999). Smith & Ekström (1999) also observe that azimuthal anisotropy west of the Grenville front is weaker and has a different fast-propagation direction compared to that beneath the Grenville and Appalachian provinces (see their Fig. 11a). The agreement with P_n anisotropy suggests that the anisotropic layer responsible for the phase–velocity anisotropy we observe at 20–34 s includes the uppermost mantle immediately below the Moho. Depth-sensitivity kernels (Fig. 6) predict that this layer may extend from about 25 to 70 km (lowermost crust and uppermost mantle). Interestingly, the azimuth of fast-propagation direction in the Grenville and Appalachian provinces is parallel to the orogenic sutures. Thus, the azimuthal anisotropy we observe in this region is likely the result of deformation during these orogenies, with the anisotropic fabric frozen since then. Both compression and lateral extrusion of the lithospheric roots (Meissner & Mooney 1998; Meissner *et al.* 2002) provide possible mechanisms of deformation. West of the Grenville front, the cratonic Central Plains are likely to have experienced much less deformation during the orogenies, which explains the weaker and less uniform azimuthal anisotropy.

The azimuth of fast-propagation direction we observe at 140 s agrees very well with previously measured direction of shear wave splitting (Barruol *et al.* 1997; Fouch *et al.* 2000), and is also parallel

© 2008 The Authors, *GJI*, **173,** 827–843
Journal compilation © 2008 RAS

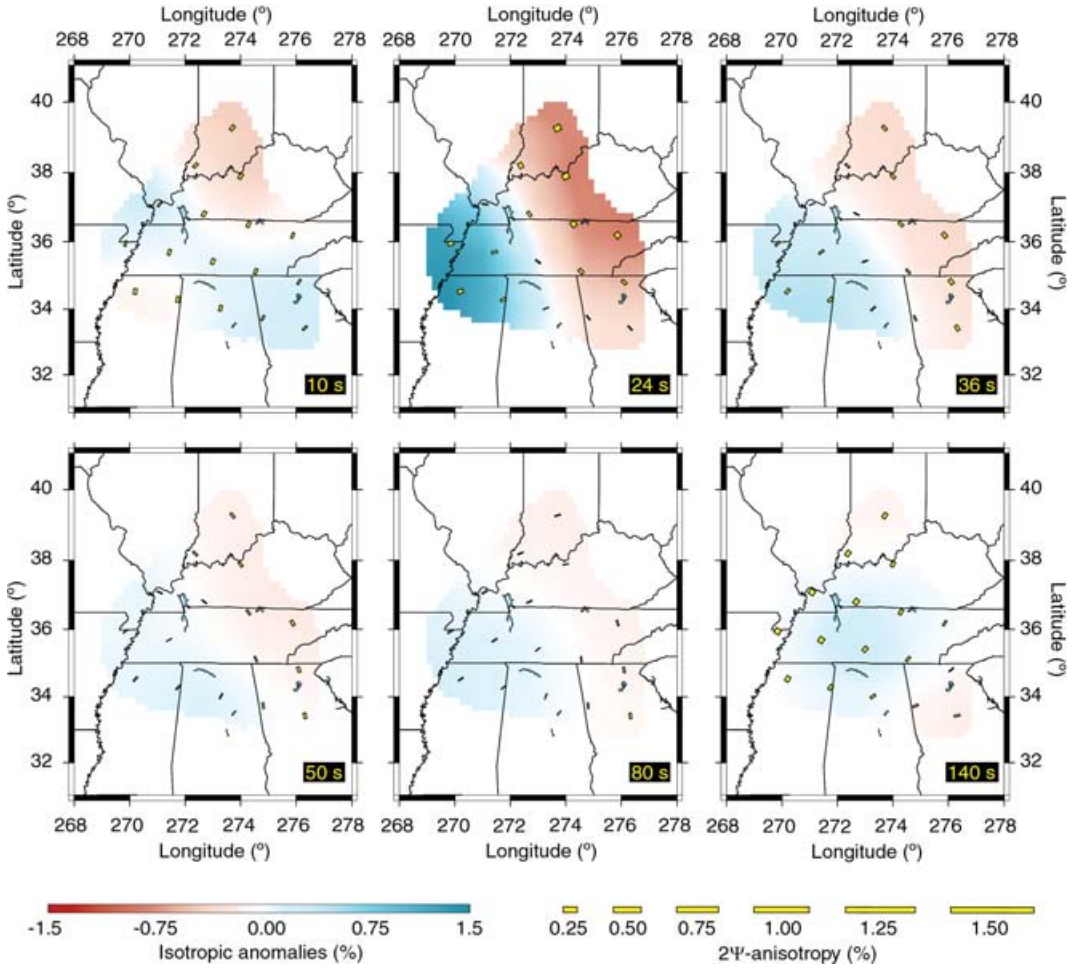

Figure 12. Trade-off between isotropic and anisotropic terms. Input isotropic distributions are those of the preferred model (Fig. 9), and input anisotropic distributions are set to zero. Smoothness coefficients are those of the preferred model.

to the direction of the absolute plate motion predicted by HS2-NUVEL1 (Gripp & Gordon 1990) for the east-central US. The anisotropy observed around 140 s is therefore likely due to current and recent deformation linked to asthenospheric flow. Rayleigh wave sensitivity kernels at these periods indicate that this flow is likely to be located around 150–250 km depth.

Precise estimates of the contribution of each anisotropic layer to the observed shear wave splitting are beyond the scope of this paper. However, we would like to point out that 1–2 per cent of shear velocity anisotropy at 25–70 km (corresponding to the maximum sensitivity range of phase velocity at 20–34 s) would produce shear wave splitting of only 0.1–0.2 s. Phase velocity at 120–160 s sample a thicker layer (say, 150 to 300–350 km depth) and show stronger stronger (1.5 per cent), indicating that shear velocity anisotropy is this layer probably exceeds 2 per cent. This is sufficient to account for the ∼1 s shear wave splitting observed in this region. We thus conclude that most of shear wave splitting observed in the east-central US originates in the asthenosphere.

ACKNOWLEDGMENTS

We are grateful to Gabi Laske, Don Forsyth and an anonymous colleague for their very constructive comments and reviews, which greatly helped to improve the first version of this paper. We also appreciated discussions with Bill Fry and Edi Kissling. This research was partly funded by Utrecht University.

REFERENCES

Barruol, G., Silver, P.G. & Vauchez, A., 1997. Seismic anisotropy in the eastern United States: deep structure of a complex continental plate, *J. geophys. Res.,* **102,** 8329–8348.

Bevington, P.R. & Robinson, D.K., 1992. *Data Reduction and Error Analyses for the Physical Sciences,* McGraw-Hill, New-York.

Fouch, M.J., Fischer, K., Parmentier, E.M., Wysession, M.E. & Clarke, T.J., 2000. Shear-wave splitting, continental keels, and patterns of mantle flow, *J. geophys. Res.,* **105,** 6255–6275.

Freybourger, M., Gaherty, J.B., Jordan, T.H. & the Kaapvaal Seismic Group, 2001. Structure of the Kaapvaal craton from surface waves, *Geophys. Res. Lett.,* **28,** 1109–1112.

Friederich, W. & Huang, Z.-X., 1996. Evidence for upper mantle anisotropy beneath southern Germany from Love and Rayleigh wave dispersion, *Geophys. Res. Lett.,* **23,** 1135–1138.

Gripp, A.E. & Gordon, R.G., 1990. Current plate velocities relative to the hotspots incorporating the NUVEL-1 global plate motion model, *Geophys. Res. Lett.,* **17,** 1109–1112.

Hoffman, P.F., 1988. United Plates of America, the birth of a craton: early Proterozoic assembly and growth of Laurentia, *Ann. Rev. Earth Planet. Sci.,* **16,** 543–603.

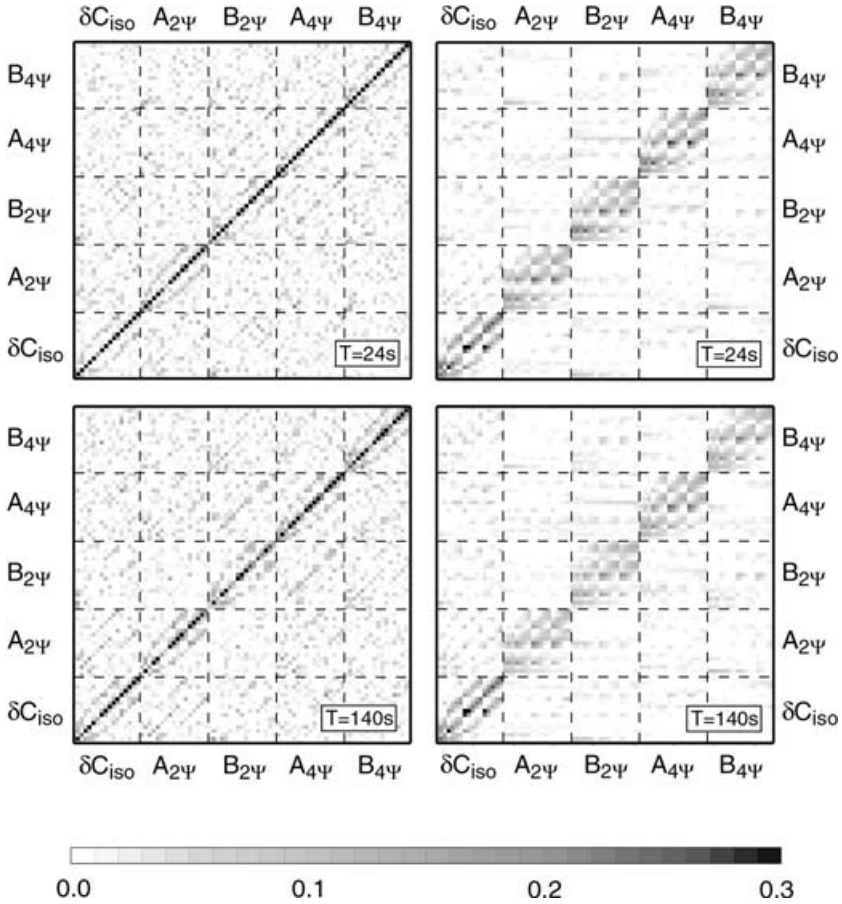

Figure 13. Resolution matrices at 24 s and 140 s without damping and smoothing (left-hand side) and with damping and smoothing similar to those of the preferred model (right-hand side). Each line (column) of the matrix represents a parameter (here, 5 terms at 17 geographical locations, i.e. a total of 85 parameters). For presentation, we separate each matrix in submatrices (dashed lines) of size 17 × 17, that is, that the lines (columns) of the submatrices represent the geographical knots of our model. The diagonal submatrices indicate lateral trade-offs, that is, trade-offs between parameters representing a given term (isotropic anomalies, 2Ψ-anisotropy, or 4Ψ-anisotropy) at different geographical locations. These trade-offs are in large part due to smoothing. The off-diagonal matrices indicate trade-offs between model parameters of different types (isotropic anomalies, and 2Ψ- and 4Ψ-anisotropy terms).

Karlstrom, K.E., Åhäll, K.-I., Harlan, S.S., Williams, M.L., McLelland, J. & Geissman, J.W., 2001. Long-lived (1.8–1.0 Ga) convergent orogen in southern Laurentia, its extension to Australia and Baltica, and implications for refining Rodinia, *Precambrian Res.,* **111,** 5–30.

Kennett, B.L.N., Engdahl, E.R. & Buland, R., 1995. Constraints on seismic velocities in the Earth from traveltimes, *Geophys. J. Int.,* **122,** 108–124.

Knopoff, L., 1972. Observation and inversion of surface-wave dispersion, *Tectonophysics,* **13,** 497–519.

Lebedev, S. & Nolet, G., 2003. Upper mantle beneath southeast Asia from S velocity tomography, *J. geophys. Res.,* **108,** 2048, doi:10.1029/2000JB000073.

Lebedev, S. & Van Der Hilst, R.D. 2008. Global upper-mantle tomography with automated multimode inversion of surface and S wave forms, *Geophys. J. Int.,* in press.

Lebedev, S., Meier, T. & Van Der Hilst, R.D., 2006. Asthenospheric flow and origin of volcanism in the Baikal Rift area, *Earth planet. Sci. Lett.,* **249,** 415–424.

Li, A., Forsyth, D.W. & Fischer, K.M., 2003. Shear velocity structure and azimuthal anisotropy beneath North America from Rayleigh wave inversion, *J. geophys. Res.,* **108,** 2362, doi:10.1029/2002JB002259.

Marone, F. & Romanowicz, B., 2007. The depth distribution of azimuthal anisotropy in the continental upper mantle, *Nature,* **447,** 198–203.

Meier, T., Dietrich, K., Stöckhert, B. & Harjes, H.-P., 2004. One-dimensional model of shear wave velocity for the eastern Mediterranean obtained from the inversion of Rayleigh-wave phase velocities and tectonic implications, *Geophys. J. Int.,* **156,** 45–58.

Meissner, R. & Mooney, W., 1998. Weakness of the lower continental crust: a condition for delamination, uplift and escape, *Tectonophysics,* **296,** 47–60.

Meissner, R., Mooney, W. & Artemevia, I., 2002. Seismic anisotropy and mantle creep in young orogens, *Geophys. J. Int.,* **149,** 1–14.

Montagner, J.-P. & Nataf, H.-C., 1986. A simple method for inverting the azimuthal anisotropy of surface waves, *J. geophys. Res.,* **91,** 511–520.

Montagner, J.-P. & Tanimoto, T., 1991. Global upper mantle tomography of seismic velocities and anisotropies, *J. geophys. Res.,* **96,** 20 337–20 351.

Paige, C.C. & Saunders, M.A., 1982. LSQR: an algorithm for sparse linear equations and sparse least squares, *ACM Trans. Math. Softw.,* **8,** 43–71.

Pedersen, H.A., 2006. Impacts of non-plane waves on two-station measurements of phase velocities, *Geophys. J. Int.,* **165,** 279–287.

Pedersen, H.A., Bruneton, M., Maupin, V. & the SVEKALAPKO Seismic Tomography Working group, 2006. Lithospheric and sublithospheric anisotropy beneath the Baltic shield from surface-wave array analysis, *Earth planet. Sci. Lett.,* **244,** 590–605.

Sato, Y., 1955. Analysis of dispersed surface waves by mean of of Fourier transform: Part. 1, *Bull. Earthquake Res. Tokyo Univ.,* **33,** 33–47.

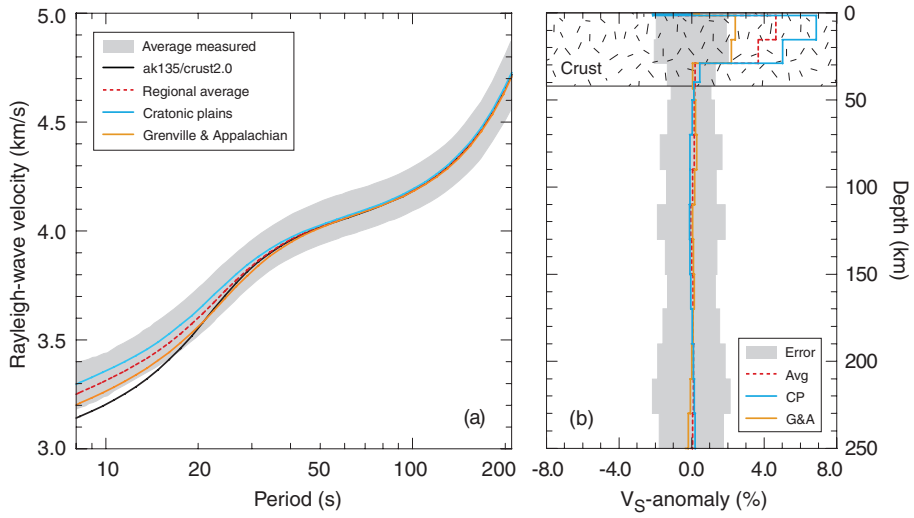

Figure 14. Regional average dispersion curves and shear wave velocity profiles. (a) Dispersion curves. The grey shaded area covers two standard deviations around the regional average over the measured dispersion curves. The black curve is constructed from ak135 (in the mantle) and the regional average of crust2.0 (in the crust). The red dashed curve is constructed from the average of inverted V_S profiles. The orange and blue curves are constructed from the average of inverted V_S profiles beneath the orogenic and cratonic regions, respectively. (b) Profiles of shear wave velocity anomalies relative to ak135/crust2.0. The three profiles represented are the regional average (Avg, red dashed curve), the average profile beneath the Grenville and Appalachian provinces (G&A, orange curve), and the average profile beneath the Central Plains west of Grenville front (CP, blue curve). The grey shaded area covers twice the error bar (defined as the rms of the error due to uncertainties in dispersion curves) around the zero value.

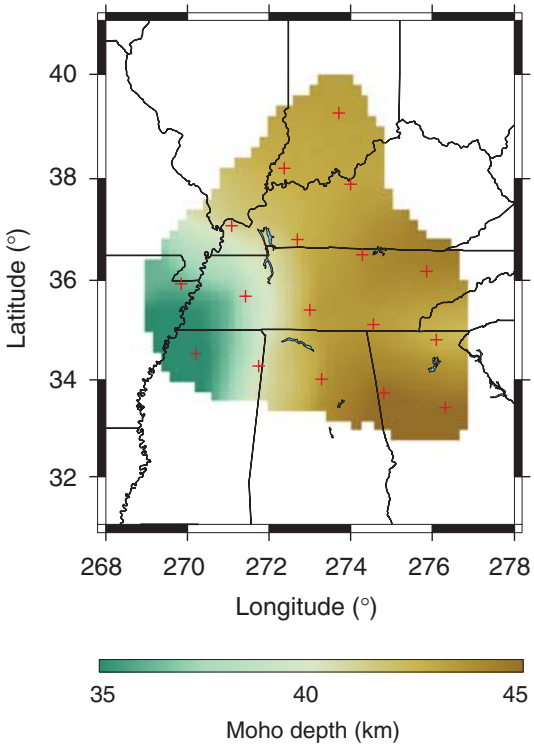

Figure 15. Inverted Moho depth. Red crosses indicate location at which the model is inverted for.

Schwab, F. & Knopoff, L., 1972. Fast surface wave and free mode computations, in *Method in Compotational Physics,* **Vol. 11**, ed. B.A. Bolt, Academic Press, New York.

Sebai, A., Stutzmann, E., Montagner, J.P., Sicilia, D. & Beucler, E., 2006. Anisotropic structure of the African upper mantle from Rayleigh and Love wave tomography, *Phys. Earth planet. Inter.,* **155,** 48–62.

Simons, F.J., Van Der Hilst, R.D., Montagner, J.-P. & Zielhuis, A., 2002. Multimode Rayleigh wave inversion for heterogeneity and azimuthal anisotropy of the Australian upper mantle, *Geophys. J. Int.,* **151,** 738–754.

Smith, M.L. & Dahlen, F.A., 1973. Azimuthal dependence of Love and Rayleigh wave propagation in a slightly anisotropic medium, *J. geophys. Res.,* **78,** 3321–3333.

Smith, G.P. & Ekström, G., 1999. A global study of Pn-anisotropy beneath continents, *J. geophys. Res.,* **104,** 963–980.

Smith, D.B., Ritzwoller, M.H. & Shapiro, N.M., 2004. Stratification of anisotropy in the Pacific upper mantle, *J. geophys. Res.,* **109,** B11309, doi:10.1029/2004JB003200.

Trampert, J. & Lévêque, J.-J., 1990. Simultaneous iterative reconstruction technique: physical interpretation based on the generalized least square solution, *J. geophys. Res.,* **95,** 12 553–12 559.

Trampert, J. & Woodhouse, J.H., 2003. Global anisotropic phase velocity maps for fundamental modes surface waves between 40 and 150 seconds, *Geophys. J. Int.,* **154,** 154–165.

Visser, K., Lebedev, S., Trampert, J. & Kennett, B.L.N., 2007. Global Love wave overtone measurements, *Geophys. Res. Lett.,* **34,** L03302, doi:10.1029/2006GL028671.

Wang, Z. & Dahlen, F.A., 1995. Spherical-spline parameterization of 3-dimensional Earth models, *Geophys. Res. Lett.,* **22,** 3099–3102.

Yang, Y. & Forsyth, D.W., 2006. Rayleigh-wave phase velocities, small-scale convection, and azimuthal anisotropy beneath southern California, *J. geophys. Res.,* **111,** B07306, doi: 10.1029/2005JB004180.

Yoshizawa, K. & Kennett, B.L.N., 2002. Non-linear waveform inversion for surface waves with a neighbourhood algorithm—application to multimode dispersion measurements, *Geophys. J. Int.,* **149,** 118–133.

Ziegler, P.A., 1989. *Evolution of Laurussia: A Study in Late Paleozoic Plate Tectonics,* 102 pp., Kluwer Academic Publishers, Dordrecht.

APPENDIX: GENERALIZED MATRIX

The system of linear equations that we solved to determine the lateral isotropic and anisotropic anomalies assembles a discrete version of eq. (5) for each path, and can be noted

$$\mathbf{d} = G\mathbf{m} \tag{A1}$$

The data vector **d** contains the path-average Rayleigh-wave phase velocity anomaly measured on the dispersion curve at the selected period (see Section 3). The model vector **m** includes five terms (one for isotropic anomalies, 2 for 2Ψ anisotropy, and 2 for 4Ψ anisotropy) for each knot of the grid (eqs 2 and 3). If N is the number of paths available at a given period, and M the number of knots, the transposed data and model vectors are

$$\mathbf{d^T} = (\overline{\delta C}_1 \cdots \overline{\delta C}_N) \tag{A2a}$$

and

$$\mathbf{m^T} = \left(\delta C_{iso,1} \cdots \delta C_{iso,M}\ A_{2\Psi,1} \cdots A_{2\Psi,M}\ B_{2\Psi,1} \cdots B_{2\Psi,M} \qquad A_{4\Psi,1} \cdots A_{4\Psi,M}\ B_{4\Psi,1} \cdots B_{4\Psi,M}\ ,\right) \tag{A2b}$$

respectively. The generalized matrix is composed of five submatrices:

$$\mathbf{G} = \left(\mathbf{G_{iso}} \quad \mathbf{G_{C2\Psi}} \quad \mathbf{G_{S2\Psi}} \quad \mathbf{G_{C4\Psi}} \quad \mathbf{G_{S4\Psi}}\right) \tag{A3}$$

with

$$\mathbf{G_{iso}} = \begin{pmatrix} K_{11} & \cdots & K_{1M} \\ \cdots & \cdots & \cdots \\ K_{N1} & \cdots & K_{NM} \end{pmatrix},$$

$$\mathbf{G_{C2\Psi}} = \begin{pmatrix} a_1K_{11} & \cdots & a_1K_{1M} \\ \cdots & \cdots & \cdots \\ a_NK_{N1} & \cdots & a_NK_{NM} \end{pmatrix}, \quad \mathbf{G_{S2\Psi}} = \begin{pmatrix} b_1K_{11} & \cdots & b_1K_{1M} \\ \cdots & \cdots & \cdots \\ b_NK_{N1} & \cdots & b_NK_{NM} \end{pmatrix},$$

$$\mathbf{G_{C4\Psi}} = \begin{pmatrix} c_1K_{11} & \cdots & c_1K_{1M} \\ \cdots & \cdots & \cdots \\ c_NK_{N1} & \cdots & c_NK_{NM} \end{pmatrix}, \quad \mathbf{G_{S4\Psi}} = \begin{pmatrix} d_1K_{11} & \cdots & d_1K_{1M} \\ \cdots & \cdots & \cdots \\ d_NK_{N1} & \cdots & d_NK_{NM} \end{pmatrix}.$$

In these matrices, the K_{ij} are the weights of path i for knot j (or sensitivity areas), and the azimuthal dependence is accounted for by the constants $a_i = \cos(2\Psi_i)$, $b_i = \sin(2\Psi_i)$, $c_i = \cos(4\Psi_i)$ and $d_i = \sin(4\Psi_i)$, where Ψ_i is the azimuth of the path i.

© 2008 The Authors, *GJI*, **173,** 827–843
Journal compilation © 2008 RAS

Earth and Planetary Science Letters 274 (2008) 489–498

Contents lists available at ScienceDirect

Earth and Planetary Science Letters

journal homepage: www.elsevier.com/locate/epsl

Stratified seismic anisotropy reveals past and present deformation beneath the East-central United States

Frédéric Deschamps [a,*], Sergei Lebedev [b,c], Thomas Meier [d], Jeannot Trampert [c]

[a] Institute of Geophysics, Swiss Federal Institute of Technology, ETH Hönggerberg HPP L8.1, 8093 Zürich, Switzerland
[b] Dublin Institute for Advanced Studies, Geophysics Section, 5 Merrion Square, Dublin 2, Ireland
[c] Department of Earth Sciences, Utrecht University, PO Box 80021, 3508 TA Utrecht, The Netherlands
[d] Ruhr University Bochum, Universitätsstrasse 150, NA3/165, 44780 Bochum, Germany

ARTICLE INFO

Article history:
Received 28 April 2008
Received in revised form 29 July 2008
Accepted 31 July 2008
Available online 18 September 2008

Editor: R.D. van der Hilst

Keywords:
seismic anisotropy
surface wave
stratified anisotropy
shear-wave anisotropy
lithospheric deformation

ABSTRACT

Evolution of continental lithosphere during orogenies and the following periods of relative stability is poorly understood, largely because of the lack of relevant observational constraints. Measurements of seismic anisotropy provide such constraints, but due to limitations in the resolving power of available data sets and, more generally, of various data types, detailed mapping of lithospheric anisotropy has remained elusive. Here we apply surface-wave array analysis to data from the East-central U.S. and determine the layering of azimuthal anisotropy beneath the Grenville–Appalachian orogen in the entire lithosphere–asthenosphere depth range. Combined measurements of Rayleigh-wave phase velocities along 60 interstation paths constrain phase-velocity maps with statistically significant anisotropy. Distinct anisotropy patterns in three different period ranges point to the existence of three distinct layers beneath the orogen, with different anisotropic fabric within each. We invert phase-velocity maps and, alternatively, pairs of selected measured dispersion curves for anisotropic shear-velocity structure. The results confirm that three anisotropic layers with different fabric within each are present, two in the lithosphere (30–70 km; 70–150 km depths) and another in the asthenosphere beneath (>150 km). Directions of fast wave propagation in the upper lithosphere are parallel to the Grenville and Appalachian fronts, suggesting that the region-scale anisotropy pattern reflects the pervasive deformation of the lower crust and uppermost mantle during the continental collisions. The fast-propagation azimuth within the lower lithosphere is different, parallel to the NNW direction of North America's motion after the orogeny (~160–125 Ma). This suggests that the lithosphere, 70-km thick by the end of the Appalachian orogeny, gradually thickened to the present 150-km while inheriting the fabric from the sheared asthenosphere below, as the plate moved NNW. Below 150 km, the fast-propagation direction is parallel to the present plate motion, indicating fabric due to recent asthenospheric flow. Anisotropy in narrower depth ranges beneath the region has been sampled previously. Published results (from observations of P_n and *SKS* and waveform tomography) can be accounted for and reconciled by the three-layered model of anisotropy for the lithosphere–asthenosphere depth range constrained in this study. In particular, the anisotropy we detect in the asthenosphere can account for the magnitude of *SKS*-wave splitting, with the fast wave-propagation directions inferred from *SKS* and surface-wave data also consistent, both parallel to the current plate motion.

© 2008 Elsevier B.V. All rights reserved.

1. Introduction

In the course of the evolution of continental lithosphere, long periods of relative stability are interrupted by episodes of intense deformation. Many Precambrian cratons appear to have deformed little since their stabilization in the Archean or Proterozoic, thanks to the high viscosity, yield strength and compositional buoyancy of the cratonic lithosphere (e.g. Sleep, 2005). Other continental units, however, have been deformed, reworked and reshaped repeatedly in the Phanerozoic.

Our understanding of the history of such deformation and the dynamics of deforming continental lithosphere is still very incomplete. Current motions of the Earth's surface in regions undergoing active deformation are now mapped in increasing detail using Global Positioning System measurements (e.g. McClusky et al., 2000; Zhang et al., 2004), and past tectonic activity can be inferred from the geological record (e.g. Dickinson, 1971). Deformation in the deep lithosphere, however, is poorly known, largely due to the insufficiency of relevant observational constraints.

Continental collisions produce broad zones of crustal deformation (Zhang et al., 2004). Whether deformation in the mantle lithosphere is

* Corresponding author.
E-mail addresses: frederic.deschamps@erdw.ethz.ch (F. Deschamps), sergei@cp.dias.ie (S. Lebedev), meier@geophysik.ruhr-uni-bochum.de (T. Meier), jeannot@geo.uu.nl (J. Trampert).

0012-821X/$ – see front matter © 2008 Elsevier B.V. All rights reserved.
doi:10.1016/j.epsl.2008.07.058

also distributed over broad areas or, instead, occurs primarily at narrow faults has been a matter of a controversy. According to one view, continuous distributed deformation does occur in the mantle lithosphere and acts to accommodate the convergence of continental blocks (Molnar, 1988; Molnar et al., 1999). According to another view, the strong mantle lithosphere is decoupled from the deforming upper crust, and convergence in orogens is accommodated by the relative motions of nearly rigid mantle-lithospheric blocks (Tapponnier et al., 2001).

Even though much of the debate is focussed on active collisions and processes that disrupt the lithosphere, an equally important issue is the post-orogenic lithospheric evolution and the dynamics of deep lithosphere at times when the crust is relatively stable and undisturbed. One important question, in particular, is whether and how the lithosphere heals after undergoing deformation in an orogeny.

Measurements of seismic anisotropy can offer the much needed information regarding the past and present deformation in the lithosphere and mantle below. Finite strain within the crust and mantle gives rise to the lattice preferred orientation (LPO) of anisotropic major minerals, in particular amphibole and olivine in the lower crust and the upper mantle, respectively. The LPO results in the directional dependence of seismic wavespeeds, or seismic anisotropy (Christensen, 1984; Nicolas and Christensen, 1987; Becker et al., 2006; Meissner et al., 2006; Tatham et al., 2008). Azimuthal anisotropy of up to a few percent (relative to the isotropic average shear or compressional speed value) has been detected beneath both continents and oceans and appears to be a common property of both the lithosphere and asthenosphere. Beneath oceans, large-scale patterns of coherent azimuthal anisotropy have been inferred from surface-wave observations, with directions of the fastest *S*-wave propagation usually parallel to the paleo-spreading direction within the lithosphere and to the current plate motion within the asthenosphere. These patterns are consistent with basic models of mantle deformation during the development of the lithosphere near a mid-ocean ridge (in the remote past) and the shearing in the asthenosphere beneath the base of the moving oceanic plate (in the near past and at present) (Forsyth, 1975; Nishimura and Forsyth, 1989; Smith et al., 2004).

On continents, higher density of seismic stations has enabled the mapping of variations in azimuthal anisotropy with high lateral resolution using teleseismic body waves, the most common approach being with measurements of *SKS*-wave splitting (Vinnik et al., 1984; Silver, 1996). Distributions of the splitting times and fast-propagation azimuths measured at stations across continents display both large- and small-scale variations (Becker et al., 2007). In some regions, the *SKS*-inferred fast-propagation azimuths vary at small scales and appear to follow tectonic trends, whereas in other regions, including eastern North America, coherent patterns extend over broad areas, characterized by fast-propagation azimuths parallel to those of the absolute plate motion (APM) (e.g. Silver, 1996; Becker et al., 2007; Fouch and Rondenay, 2006; Savage, 1999). Because of their poor vertical resolution, however, *SKS* measurements are difficult to use for constraining the depth distribution of anisotropy. Arguments have been put forward for *SKS*-sampled anisotropy to occur predominantly within the lithosphere or predominantly within the asthenosphere (Silver, 1996; Becker et al., 2007; Fouch and Rondenay, 2006; Savage, 1999; Vinnik et al., 1992; Fischer and Wiens, 1996).

Surface waves can provide the necessary vertical resolution. Continental-scale tomographic models constrained with surface-wave observations have revealed distinctly different patterns of azimuthal anisotropy within the continental lithosphere and asthenosphere (e.g., Marone and Romanowicz, 2007; Simons et al., 2002; Debayle et al., 2005; Sebai et al., 2006). The lower lateral resolution of the large-scale imaging, however, makes it difficult to map anisotropic layering at the relatively small scale of tectonic units, so that the relationship of the inferred lithospheric anisotropy to tectonic history and history of deep lithospheric deformation is often unclear and open to debate. There is no consensus, as well, regarding the occurrence of anisotropy in subcontinental asthenosphere (e.g. (Marone and Romanowicz, 2007; Debayle et al., 2005; Gaherty and Jordan, 1995; Gung et al., 2003).

Recently, data sets from dense arrays of broad-band seismic stations have been growing in both their number and size. Applications of surface-wave analysis to array data have been producing increasingly high imaging resolution, both lateral and radial (Li et al., 2003; Pedersen et al., 2006; Yang and Forsyth, 2006; Yao et al., 2006; Zhang et al., 2007; Deschamps et al., 2008). Array data enable the mapping of anisotropic layering in the lithosphere and asthenosphere at the scale of tectonic units, thus providing essential constraints on the history of continental deformation.

In this paper, we use measurements of interstation surface-wave dispersion in the East-Central U.S. and constrain the layering of azimuthal anisotropy beneath the Grenville–Appalachian orogenic region. We show that anisotropy beneath this Proterozoic–Phanerozoic orogen is different from that beneath the neighbouring cratonic platform of an older age. Three layers with different anisotropic fabric within each occur beneath the orogen and characterize successive stages of the evolution of its lithosphere.

2. East-central US: tectonic history and observations of anisotropy

The Grenville and Appalachian orogenic deformation fronts (Hoffman, 1988) cross the region sampled by our data (33°–40°N, 83°–91°E) at an approximately NE–SW azimuth (Fig. 1). The Grenville orogeny is thought to be the last episode (1.3–1.0 Ga) of a major continental accretion sequence along the southern edge of Laurentia that started about 1.8 Ga ago (Hoffman, 1988; Dalziel, 1991; Karlstrom et al., 2001). The Appalachian orogen is associated with more recent collisions at 0.42–0.27 Ga (Ziegler, 1989). Parts of the Grenville lithosphere have been reworked at that time. The plains to the west and north of the Grenville front are largely within a Proterozoic cratonic platform, in the Yavapai and Mazatzal provinces. These units were accreted during the Yavapai and Mazatzal orogenies (1.8–1.6 Ga) and have experienced little tectonic activity since then (Hoffman, 1988) (one exception is the Reelfoot Rift zone, a failed rift that was active 0.60–0.45 Ga ago (Ervin and McGinnis, 1975)).

The Appalachian region remained in the interior of the supercontinent Pangea until about 180 Ma, at which time rifting started to the East and the Atlantic Ocean began to open (Kazmin and Natapov, 1998; Beck and Housen, 2003). North America then began drifting NNW, a motion that continued until ~125 Ma (Kazmin and Natapov, 1998; Beck and Housen, 2003). At present, the absolute plate motion (APM) of North America is in the SE direction (azimuth 245°) at a rate of 2.6 cm/yr in the hotspot reference frame (Gripp and Gordon, 1990).

Seismic anisotropy has been detected throughout the area (e.g. Barruol et al., 1997; Fouch et al., 2000). The knowledge of the distribution of anisotropy at depth can help us constrain the history of deformation within the lithosphere and asthenosphere. The studies to date, however, have each mapped anisotropy in parts of but not the entire lithosphere–asthenosphere depth range, with results from different studies and different types of measurements complementary to one another in some instances but seemingly inconsistent with one another in other instances.

Shear-wave splitting observations in the eastern U.S. display a coherent large-scale pattern with the azimuth of fast wave propagation parallel to that of the APM (Fig. 2) (Barruol et al., 1997; Fouch et al., 2000). This can be interpreted as evidence for anisotropy in the asthenosphere due to the flow associated with the motion of the North American plate (Barruol et al., 1997; Fouch et al., 2000). The nearly uniform distribution of *SKS*-inferred fast-propagation azimuths thus may not, by itself, offer any information on lateral variations of anisotropy in the lithosphere.

Marone and Romanowicz (2007) combined surface-wave data and shear-wave splitting to constrain azimuthal anisotropy in the upper mantle beneath North America, and found two distinct anisotropic

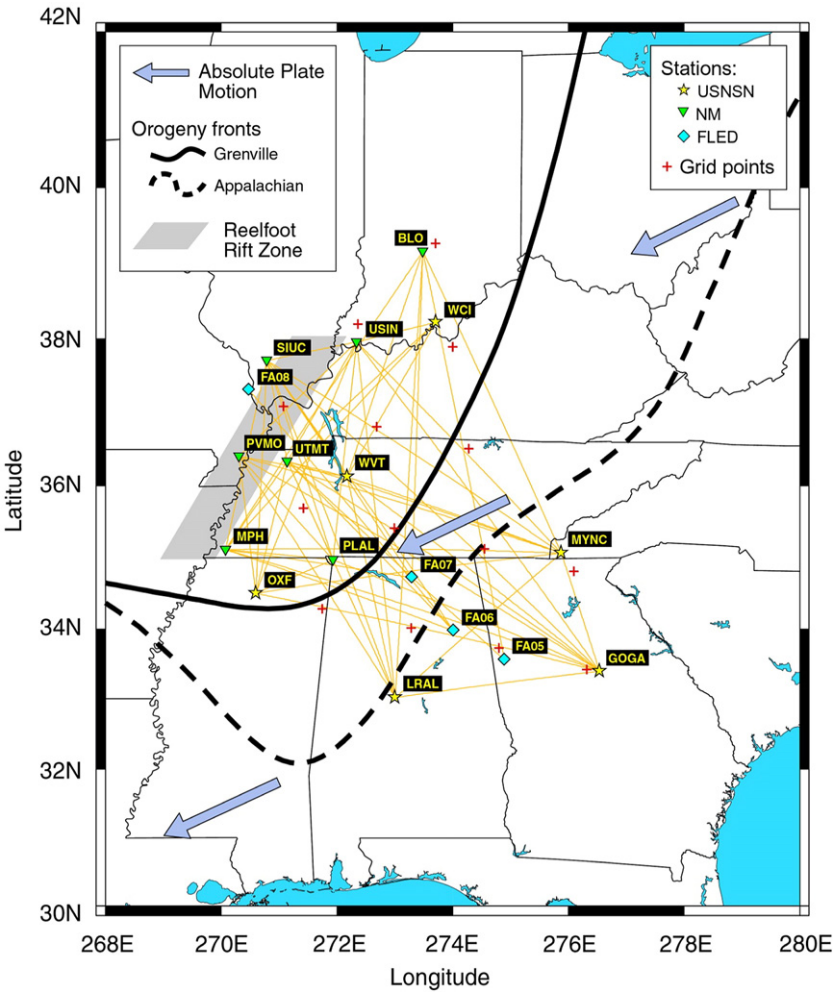

Fig. 1. The region of study and the interstation path coverage. The seismic stations used for the analysis are from both permanent and temporary networks (Deschamps et al., 2008). Red crosses show the grid knots at which we plot azimuthal anisotropy in Fig. 2; they belong to the grid used to parameterize the inversion for phase-velocity maps (Fig. 2). Grenville and Appalachian orogenic fronts are shown with a thick plain curve and a thick dashed curve, respectively. The Reelfoot Rift Zone is shown near the western boundary of the model area. Blue arrows indicate the absolute plate motion (APM) in the hotspot reference frame predicted by HS2-NUVEL1 (Gripp and Gordon, 1990). (For interpretation of the references to colour in this figure legend, the reader is referred to the web version of this article.)

layers, one in the lithospheric mantle, and another in the asthenosphere. Fast-propagation directions in the asthenosphere are parallel to the APM, in agreement with the inferences from *SKS* observations. Debayle et al. (2005), however, map only weak anisotropy in the asthenosphere beneath the eastern U.S. in their global model and argue that the rate of motion of North America and other continents, with the exception of Australia, is not sufficient to produce substantial anisotropy in the asthenosphere.

Smith and Ekström (1999) mapped azimuthal anisotropy of P_n waves which sample the uppermost mantle and found fast-propagation directions in the East-central U.S. that were roughly parallel to the Appalachian front (Fig. 2). This observation is consistent with pervasive deformation of the upper lithosphere (crust and uppermost mantle) to have occurred at the time of the Grenville and Appalachian orogenies. Marone and Romanowicz (2007) did not see this layer in their model because of the lack of surface-wave measurements at sufficiently short periods in their data set. Instead, they observed an anisotropic layer in the East-central U.S. lithosphere with a NNW-oriented fast-propagation azimuth, parallel neither to the APM nor to the Grenville and Appalachian fronts.

In this study we use broad-band, interstation measurements of Rayleigh-wave dispersion (Deschamps et al., 2008) and constrain the stratification of azimuthal anisotropy beneath the East-central U.S. in the entire lithosphere–asthenosphere depth range. Surface waves at different frequencies sample Earth structure at different depths. The frequency band of the measurements we use here is sufficiently broad (periods as short as 10 s to as long as 200 s) to resolve the layering of seismic structure and anisotropy from the crust down to the asthenosphere.

3. Layering of anisotropy

In a previous study (Deschamps et al., 2008), we have measured interstation phase-velocity curves for 60 pairs of stations in the East-central U.S. (Fig. 1) and constructed and validated anisotropic phase-velocity maps for the region. A robust phase-velocity curve was derived for each station pair by averaging over tens (up to over a hundred) of dispersion curves, each measured using the same station pair and signals from different earthquakes, normally in a number of different source regions (Meier et al., 2006). For all 60 paths, the period range includes the interval 18–34 s. For 33 paths the dispersion curve extends up to a period of 140 s, and for about 20 paths we could measure the dispersion curve up to a period of 200 s. In the phase-velocity maps, statistically significant azimuthal anisotropy with a π-periodic ("2Ψ") dependence of phase velocity on azimuth was detected (Smith and Dahlen, 1973). The resolution (averaging) lengths of the phase-velocity maps were estimated (Lebedev and Nolet, 2003) at ~210 km for isotropic anomalies and ~280 km for anisotropic

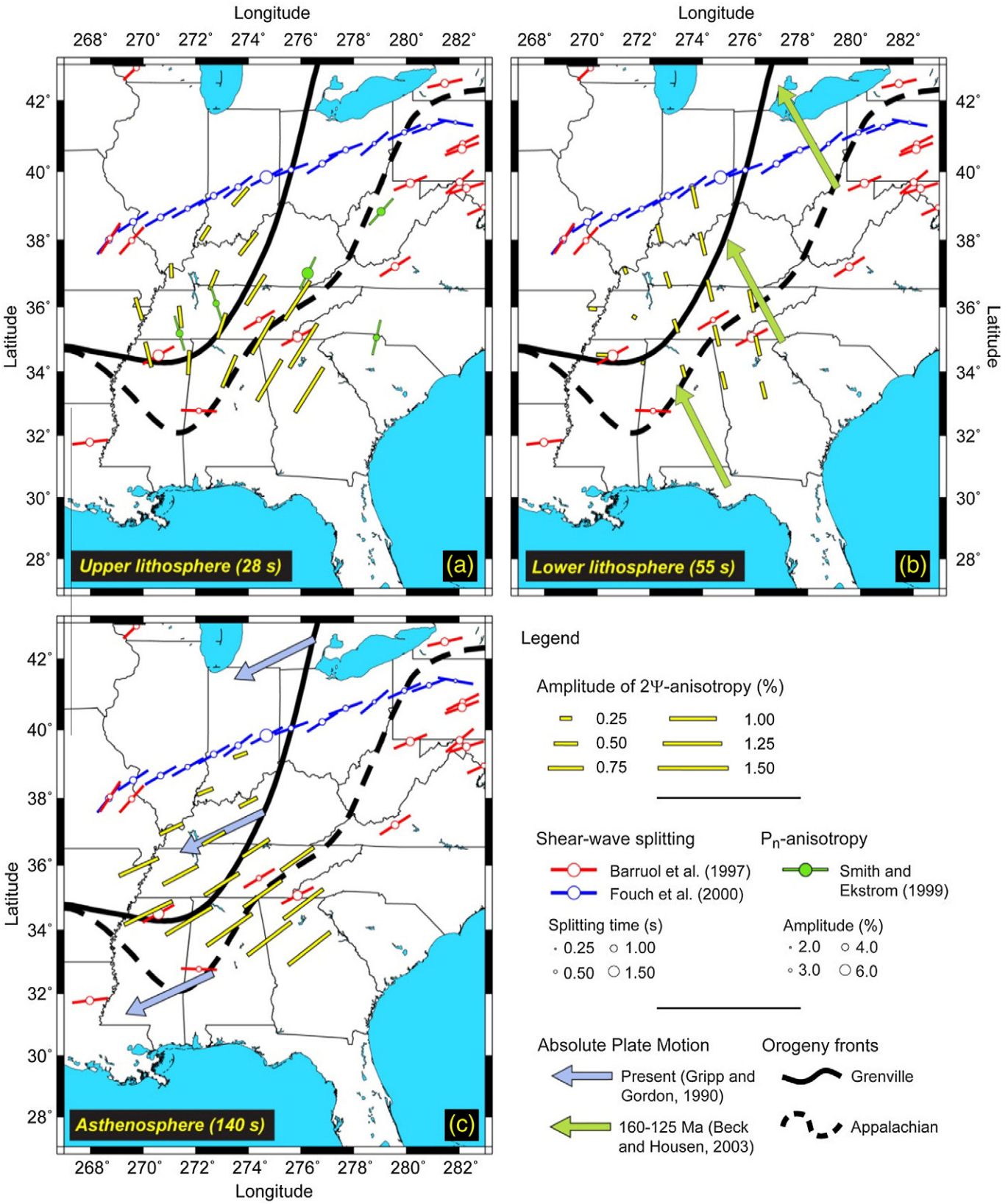

Fig. 2. Rayleigh wave azimuthal anisotropy (yellow bars) at 28, 55, and 140 s. The orientation and size of the bar show the direction of fastest propagation of Rayleigh waves at the period and the amplitude of the anisotropy, respectively. The isotropic average Rayleigh-wave velocities at 28, 55, and 140 s are 3.816, 4.053, and 4.337 km/s, respectively. Also plotted are main tectonic boundaries, past and present absolute plate motion, and previous anisotropy measurements. (a) At 28 s, the Rayleigh-wave fast-propagation direction beneath orogenic provinces is roughly parallel to the Grenville and Appalachian fronts, as well as to P_n fast-propagation direction (Smith and Ekström, 1999). (b) At 55 s, the fast-propagation azimuth is close to the direction of the NNW drift of the North American plate during the Mesozoic (Beck and Housen, 2003). (c) At 140 s, the fast-propagation direction is parallel to the current absolute plate motion (Gripp and Gordon, 1990), as well as to most fast-propagation directions inferred from shear-wave splitting observations in the area (Barruol et al., 1997; Fouch et al., 2000).

anomalies. Using Monte-Carlo sampling, errors in the amplitude of anisotropy and the fast-propagation azimuth were estimated at 8–10 m/s (i.e., 0.2–0.3% of the average isotropic velocity), and 15–20°, respectively, depending on the period (Deschamps et al., 2008).

Comparisons of dispersion curves for station-station pairs oriented at different azimuths strongly hinted at the occurrence of azimuthal anisotropy (Deschamps et al., 2008). The curve variability, however, also reflected isotropic heterogeneity. Inversions for phase-velocity maps have enabled us to separate anisotropic and isotropic signal; the presence of anisotropy in the models has been shown to be statistically significant (Deschamps et al., 2008). In this study we investigate further the depth distributions of *S*-velocity anisotropy and invert phase-velocity data for anisotropic point profiles as well as for region-average and path-average profiles. The results of these targeted inversions, together with the results of the phase-velocity analysis, allow us to derive robust conclusions regarding the layering of anisotropy and the evolution of the lithosphere–asthenosphere system.

3.1. Phase-velocity maps

Distributions of azimuthal anisotropy across the Rayleigh-wave phase-velocity maps (Deschamps et al., 2008) change gradually with the wave period. Within the period range 18–160 s they display distinctly different patterns in three period sub-ranges: 20–35 s, 50–60 s, and 100–160 s (between these sub-ranges patterns of anisotropy distributions gradually reshape one into the other). In Fig. 2 we plot azimuthal anisotropy at three representative periods (28, 55, 140 s), one within each of the three sub-ranges.

In the period range 20–35 s, phase-velocity azimuthal anisotropy is relatively strong (~1% of the isotropic average velocity) beneath the Grenville and Appalachian orogenic provinces, with the fast-propagation direction roughly parallel to the fronts (average azimuth is $\Psi_{\text{fast}}=32°$). Beneath the cratonic part of the region (eastern Yavapai and Mazatzal provinces) anisotropy is weaker (~0.6%) and has different and less coherent fast directions. Rayleigh waves at the 20–35 s periods sample primarily the lower crust and uppermost mantle. We infer that the anisotropy we observe indicates the fabric created in the upper lithosphere during the Grenville and Appalachian orogenies and frozen into the lower crustal and upper mantle rock ever since. According to Smith and Ekström (Smith and Ekström, 1999), the fast-propagation azimuth of P_n waves in the region is also parallel to the fronts, just as the Rayleigh-wave fast propagation azimuths mapped here (Fig. 2). The agreement between the patterns of anisotropy of Rayleigh waves (primarily sensitive to *S* velocities) around 28 s and P_n waves — both sample the uppermost mantle — reinforces the evidence for the occurrence of fabric oriented parallel to the orogeny fronts in the Grenville–Appalachian uppermost mantle.

In the period range 50–60 s, phase-velocity anisotropy is smaller (~0.5%), but the direction of fast propagation is laterally coherent. It is clearly different ($\Psi_{\text{fast}}=165°$) from that at shorter periods. Rayleigh waves at 50–60 s sample primarily mid-lower lithosphere, and we infer that no fabric created during the Grenville–Appalachian orogenies is apparent in this part of the lithosphere. Instead, the fast propagation direction is close to that of the paleo-APM, the direction of plate motion at 160–125 Ma according to plate-tectonic reconstructions (Beck and Housen, 2003). The anisotropy may thus indicate the fabric frozen into the lower lithosphere at those times, 160–125 Ma.

Around 140 s, phase-velocity azimuthal anisotropy is, again, stronger (>1%), and the direction of fast propagation is laterally uniform ($\Psi_{\text{fast}}=54°$) and parallel to the present APM direction (Gripp and Gordon, 1990). The anisotropy thus appears to be due to the strain associated with current and recent asthenospheric flow. Anisotropy is weaker beneath parts of the cratonic area (eastern Yavapai and Mazatzal provinces) in the North of our study region but is still present, with the same direction of fast propagation. The fast-propagation direction we mapped also matches the fast azimuths inferred from shear-wave splitting observations (Barruol et al., 1997; Fouch et al., 2000) (Fig. 2). This is consistent with an asthenospheric origin of most of the shear-wave splitting signal.

The anisotropic phase-velocity maps (Fig. 2) indicate that azimuthal anisotropy beneath the East-central U.S. is stratified into three layers. Anisotropic fabric within each layer appears to be of a different age, the age decreasing with increasing depth.

3.2. Inversion for shear-wave anisotropy

In order to investigate the stratification of shear-wave anisotropy more quantitatively, we now perform a series of inversions of phase-velocity data for anisotropic shear-velocity profiles. Using specific properties of anisotropic layering in the East-central U.S., we avoid complicated inversions for shear-velocity distributions with arbitrary depth-dependent azimuthal anisotropy and, instead, set up simple inversions for models that are approximate but sufficiently accurate for our purposes.

We observe that the fast-propagation direction at long periods (140 s) (Fig. 2) is nearly perpendicular to that at intermediate periods (55 s) and nearly parallel to that at short periods (28 s, Appalachian sub-region). We define a “fast” direction at an azimuth of 45°, close to the fast propagation azimuth at the long and short periods, and a “slow” direction perpendicular to it (135°, slow propagation at the long and short periods). Rayleigh waves at intermediate periods (50–60 s) will, in contrast to those at the long and short periods, travel faster at azimuth 135°, and slower at 45°. For any point, we can extract from the anisotropic phase-velocity maps a pair of “directional” dispersion curves containing phase velocities of Rayleigh waves propagating in the “fast” (45°) and the “slow” (135°) directions. At short and long periods, phase velocities will be higher in the “fast” direction, and at intermediate periods, higher in the “slow” direction.

A pair of such phase-velocity curves (the “fast” one and the “slow” one) can be inverted for a pair of shear-velocity profiles. We parameterize the inversion so as to solve simultaneously for an isotropic average profile and a profile of the amount of anisotropy, defined here as the difference in the speed of the shear waves that propagate in the “fast” and the “slow” directions. This inversion for the amount of anisotropy is approximate because our “slow” direction (135°) is not quite the same as the actual direction of fast Rayleigh-wave propagation at intermediate periods (165°). Even though the cosine function changes slowly near its maxima and minima, this difference will have an effect of reducing somewhat the difference between the fastest and slowest phase velocities at intermediate periods that go into the inversion, and, thus, will result in an underestimation of the amount of shear-wave anisotropy.

The inversion is non-linear and consists in a Gauss–Newton gradient search (from MATLAB optimization toolbox) parameterized with 15 boxcar and triangular functions that span a depth range from the upper crust down to a depth of 650 km. At each iteration, synthetic phase velocities are recomputed directly from shear-wave velocity profiles (Schwab and Knopoff, 1972) and compared to the ones according to our regional maps (Deschamps et al., 2008). The inversion minimizes the difference between the synthetic phase velocities and those from our maps. Compressional- and shear-velocity perturbations are coupled (δV_P (m/s)=δV_S (m/s)). Norm damping factor is applied independently to the isotropic and anisotropic terms. The Moho depth is also a free parameter of the inversion, and its damping is controlled by an independent parameter.

3.3. Anisotropic shear-wave profile at a point within the orogen

Fig. 3 illustrates the inversion and shows an anisotropic profile obtained for a point located in the orogenic part of the region (35.1°N, 274.5°E). The inversion was for the isotropic average profile (dashed black line, Fig. 3a) and for the profile of the amount of anisotropy,

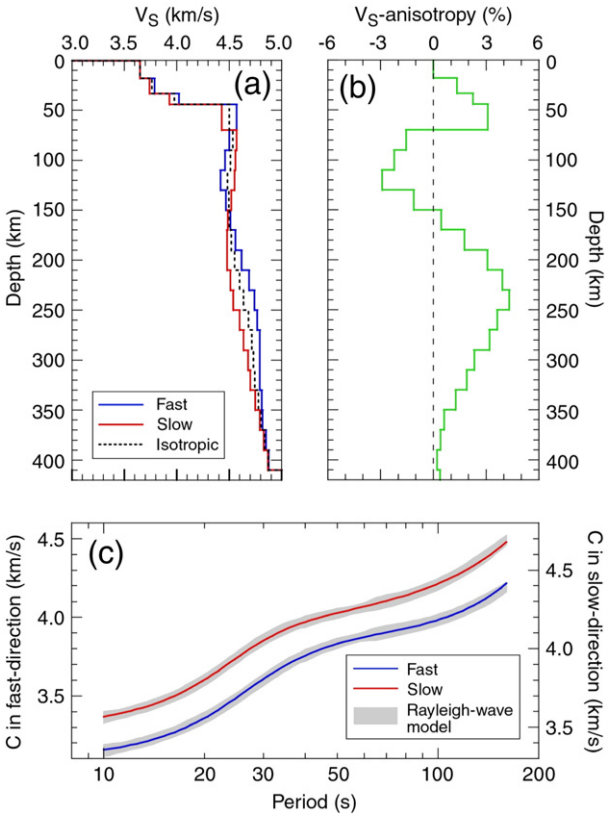

Fig. 3. Inversion for an anisotropic shear-wave velocity profile at a location within the orogenic part of the region (35.1°N, 274.5°E). (a) The dashed black curve shows the isotropic average V_S profile, the blue and red curves the speeds of the shear wave propagation in the "fast" and "slow" direction, respectively. (b) Anisotropic anomalies (difference between shear-wave propagation speeds at azimuths 45° and 135°) projected on the 45° azimuth. (c) Synthetic dispersion curves computed for the "fast" (blue) and "slow" (red) profiles (a). The gray shaded areas show the directional dispersion curves (extracted from the anisotropic phase-velocity maps and indicating phase velocities of Rayleigh waves at azimuths 45° and 135°) plus/minus the estimated error. (Note that the two dispersion curves are plotted using vertical axes shifted with respect to one another, each plotted on one side of the frame). (For interpretation of the references to colour in this figure legend, the reader is referred to the web version of this article.)

defined as the difference between shear speeds at the two azimuths, 45° and 135° (Fig. 3b). The blue and red profiles in Fig. 3a show the resulting shear-wave velocities in the "fast" and "slow" directions, respectively. Synthetic dispersion curves (Fig. 3c) computed for the best-fitting anisotropic shear-wave profile fit the dispersion curves extracted from the phase-velocity maps well within error bars (note that for clarity the fast and slow dispersion curves are plotted using vertical axes shifted with respect to one another, each plotted on one side of the frame).

If shear waves propagate faster at the azimuth 45° than at 135°, such anisotropy appears as positive on the profile in Fig 3b, if slower at 45° than at 135°, as negative. Three layers with distinctly different anisotropy are present at depths of about 15–70 km, 70–150 km, and below 150 km (beneath 250 km, the sensitivity of the phase-velocity data decreases, and the magnitude of decrease in anisotropy below this depth is not well constrained). The difference between the highest and lowest *S*-wave propagation speeds reach 2–3% within each of the three layers.

3.4. Region-average anisotropic shear-wave profiles

Taking $\Psi_{fast}=45°$ and $\Psi_{slow}=135°$, we have inverted pairs of the directional (at azimuths 45° and 135°) Rayleigh-wave phase-velocity curves simultaneously for isotropic average V_S profiles and profiles of anisotropy at each point of the model. We used phase-velocity maps in the period range 10–160 s (Deschamps et al., 2008). Fig. 4 shows the sub-region average profiles of the isotropic V_S (a) and of anisotropy (b) beneath the orogenic and cratonic areas.

Three anisotropic layers, associated with the Rayleigh-wave anisotropy observed at 20–35 s, 50–60 s and 140 s and higher, are clearly present beneath the orogenic part. In the upper lithosphere between the 30 km and 70 km depths, V_S anisotropy reaches 2.5% relative to isotropic V_S. In the 70–150 km depth range, anisotropy is with a direction of fastest V_S propagation nearly perpendicular to that in the layer above; the anisotropy reaches 2–2.5% and may be somewhat underestimated (see Section 3.2). Below ~150 km, anisotropy is, once more, with a faster wave propagation at the 45° azimuth, reaching 3–4% at 200–250 km. The pattern of anisotropy appears to change from a "frozen", lower-lithospheric one to an asthenospheric one near 150 km, indicating that the lithosphere–asthenosphere boundary (LAB), if it is identified to the mechanical boundary separating the rigid lithosphere from the deforming asthenosphere (Gung et al., 2003; Regan and Anderson, 1984), is currently located around this depth. The vertical resolution of our model does not allow us to estimate the sharpness of the LAB. A recent study using converted waves (Rychert et al., 2007), has indicated that the LAB beneath the Northeastern United States (NE of our study region) may be as sharp as 10 km in thickness.

V_S anisotropy averaged over the cratonic (Yavapai and Mazatzal) part of the region appears to be weaker than that beneath the orogen. In part, this is because of the greater variability in its fast-propagation directions, especially in the upper lithosphere (Fig. 2). Due to the smaller amplitude of anisotropy, it is difficult to estimate the depth of the LAB beneath the cratonic part of the region, although the profile (Fig. 4b) suggests that it may be somewhat deeper than beneath the orogen.

3.5. Anisotropic shear-wave profiles constrained with measured dispersion curves

The anisotropic phase-velocity maps (Section 3.1) are a result of regularized inversions of measured interstation dispersion curves (Deschamps et al., 2008). They are non-unique solutions of inverse problems, and this translates into an additional uncertainty on the shear-velocity profiles obtained in the following inversions (Section 3.2) in which we assume the maps to be data. In order to validate further our

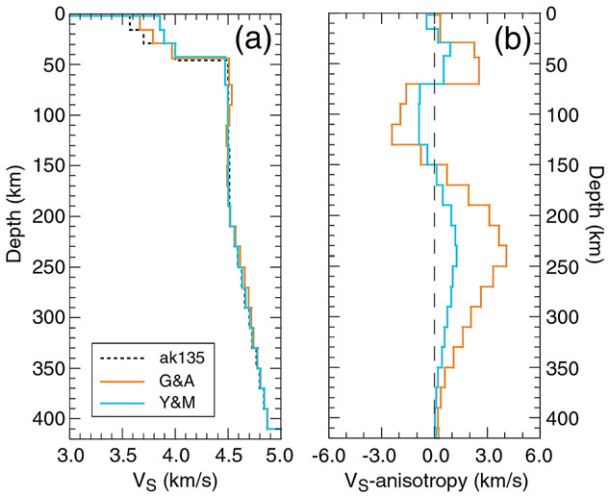

Fig. 4. (a) Average profiles of isotropic shear-wave velocity beneath the orogenic (orange curve) and cratonic (eastern Yavapai and Mazatzal provinces; blue curve) parts of the region. The black dashed curve is ak135 (Kennett et al., 1995). (b) Average V_S anisotropy beneath the orogenic (orange) and cratonic (blue) provinces (the difference between shear-wave propagation speeds at azimuths 45° and 135°). (For interpretation of the references to colour in this figure legend, the reader is referred to the web version of this article.)

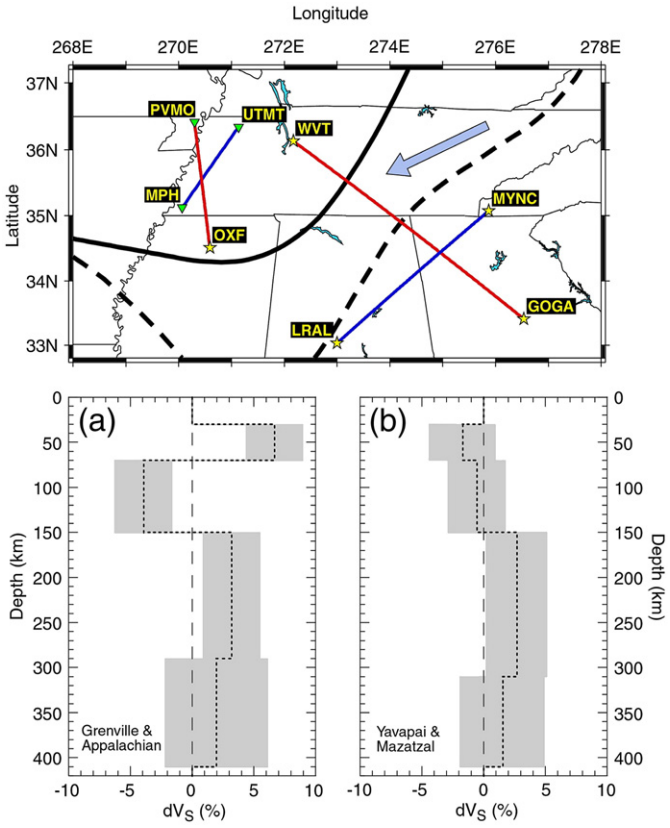

Fig. 5. Azimuthal anisotropy in the orogenic (a) and cratonic (eastern Yavapai and Mazatzal provinces) (b) parts of the region inferred from the inversion of selected pairs of measured dispersion curves. Monte-Carlo sampling was applied to radial V_S models that fit measured dispersion curves along 4 specially chosen paths (top map; see Fig. 1 for legend). The gray bands in plots a and b show probable anisotropy in the orogenic and cratonic regions and were defined by two standard deviations around the difference between a model obtained for a path striking near 45° and a model for a path striking near 135°. (a) Orogen: the paths are LRAL-MYNC (fast direction) and GOGA-WVT (slow direction). (b) Craton: the paths are MPH-UTMT (fast direction) and PVMO-OXF (slow direction).

conclusions regarding the layering of anisotropy, we now also invert selected measured dispersion curves directly for V_S profiles. Adopting a Monte-Carlo approach, we also aim to estimate the uncertainty of the anisotropic layering detected.

We choose one pair of station-station paths sampling primarily the orogenic part of the region (LRAL-MYNC and GOGA-WVT), and another pair of paths located in the cratonic part (MPH-UTMT and PVMO-OXF). The two paths in the orogenic part are nearly perpendicular to each other, one striking close to the direction of fast wave propagation at short and long periods, and the other close to the direction of slow propagation at short and long periods (but fast propagation at intermediate periods). The paths in the cratonic part (which, similarly to those within the orogen, were chosen both for their location and for the bandwidth of the corresponding dispersion curves) are also at a steep angle to one another, although not quite perpendicular. Of the four interstation paths, LRAL-MYNC and MPH-UTMT are thus at azimuths close the direction of fast wave propagation in the upper and lower anisotropic layers, and GOGA-WVT and PVMO-OXF are at azimuths nearly perpendicular to this direction.

In order to compute the average and standard deviation of the V_S profiles that fit the dispersion curves, we perform a Monte-Carlo search, generating a large (10^7) number of random V_S profiles. Each profile is constructed by an addition of random perturbations (up to 10%) in four layers (30–70 km, 70–150 km, 150–310 km, and 310–410 km) to the regional average profile. Computing a synthetic dispersion curve for each of these profiles, we compare it to the measured one and obtain the profile's probability p:

$$p(V_S) = ke^{-\frac{\chi^2}{2}}, \tag{1}$$

where

$$\chi^2 = \sum_j \frac{\Delta C_j^2}{\sigma_j^2} \tag{2}$$

and k is a normalization constant. ΔC_j is the difference between the calculated and measured phase velocity at period T_j, and σ_j is the uncertainty of the measurement at this period. Using these probabilities as weights, we then compute the weighted average and standard deviation of V_S, using the profiles that fit the data within twice the error bars.

The differences between the profiles obtained for LRAL-MYNC and GOGA-WVT and the profiles obtained for MPH-UTMT and PVMO-OXF are shown in Fig. 5a and b, respectively. Beneath the orogen (Fig. 5a), a three-layered profile of anisotropy with the direction of fast propagation in the intermediate layer nearly perpendicular to those in the upper and lower layers, is required in order to fit the measured dispersion curves. Beneath the cratonic part, anisotropy appears to be required only in the asthenospheric layer (150–310 km).

3.6. Agreement with shear-wave splitting observations

The fast shear-wave propagation direction in the asthenosphere derived from Rayleigh-wave data matches the fast-propagation directions inferred from *SKS*-splitting observations (Barruol et al., 1997; Fouch et al., 2000) (Fig. 2). This suggests that most if not all of the splitting may originate in the asthenosphere. Anisotropy in the upper lithosphere, where the fast-propagation directions in the orogenic part of the region are similar to those in the asthenosphere, may also contribute to the observed *SKS*-splitting signal.

In order to estimate the contribution of each anisotropic layer to the observed *SKS* splitting, we computed the times of the shear-wave splitting that would originate within each layer of our anisotropic models following Montagner et al. (2000) and Simons et al. (2002). In Table 1, we list the integrated splitting times (regional average and variance) for the three layers beneath both the orogenic and cratonic parts of the region. Beneath the orogen, the integrated shear-wave splitting time in the layer 30–70 km is about 0.2 s. This signal, however, may well be largely absent in the *SKS* waveforms due to anisotropy in the layer 70–150 km. The fast-propagation directions within the two layers are nearly perpendicular to one another, with similar amplitudes of their integrated splitting. Their contributions to the observed *SKS* splitting may thus balance one another. In the depth range 150–400 km, the integrated shear-wave splitting time reaches 1.1 s, in the range of the observed *SKS*-splitting values (Barruol et al., 1997; Fouch et al., 2000). Shear-wave splitting in this region can thus be accounted for by azimuthal anisotropy in the asthenosphere, the frozen fabrics in the upper layers contributing to the splitting only slightly. Thus, the conclusion that *SKS* splitting originates primarily in the asthenosphere does not preclude the presence of anisotropy in the lithosphere.

Table 1
Integrated shear-wave splitting that will originate in different layers beneath the orogenic (Grenville–Appalachian) and cratonic (Yavapai–Mazatzal) parts of the study region, according to the layering of anisotropy we have mapped $\langle \delta t \rangle$ and σ_{reg} are the regional average and variance, respectively

Layer	Orogenic terrains		Central plains	
	$\langle \delta t \rangle$ (s)	σ_{reg} (s)	$\langle \delta t \rangle$; (s)	σ_{reg} (s)
30–70 km	0.18	0.09	0.03	0.08
70–150 km	−0.20	0.08	−0.09	0.09
150–400 km	1.10	0.20	0.37	0.20

Beneath the cratonic part, the integrated splitting time estimates are smaller in all layers. Regarding the asthenospheric layer in particular, this apparent reduction in the magnitude of anisotropy in the northernmost part of our region may be surprising, given the fact that the shear beneath the moving North American plate should occur there as well as beneath the orogenic part, and the fact that the observed shear-wave splitting just north of the region sampled by our data is as strong as that in the east-central part of the region (Fig. 2). Whether the weakness of anisotropy we resolve may be due to a greater lithospheric thickness beneath the craton in the north of our study region, or due to complexities of asthenospheric flow caused by topography on the LAB, or simply due to the reduction in the resolving power of our data set in the northernmost part of the region will become clear in the future, when denser station coverage makes possible additional measurements of both surface-wave dispersion and *SKS* splitting.

4. Lithospheric evolution

The layered anisotropy beneath the Grenville–Appalachian orogen reflects the history of deformation of its lithosphere over the last few hundred million years. Anisotropic fabric in the upper lithosphere (~25–70 km) with a direction of fast wave propagation parallel to the Grenville and Appalachian fronts, as indicated both by S-wave azimuthal anisotropy mapped in this study and by P_n-wave azimuthal anisotropy (Smith and Ekström, 1999). This represents evidence for pervasive deformation of the upper lithosphere, including lithospheric mantle, during the continental collisions, with front-parallel extension (Silver, 1996; Meissner et al., 2002). After the end of the Appalachian orogeny (~270 Ma), the region has not experienced major tectonic activity, and the anisotropic fabric has remained frozen in the upper lithosphere.

By the end of the Appalachian orogeny, the lithosphere is likely to have been at least 70 km thick. The fabric within the 70-km thick upper lithosphere is preserved to this day, whereas in the deeper lithosphere the fabric is different, probably unrelated to the orogeny. One may contemplate a scenario in which the lithosphere was thicker than 70 km but was easily deformable and unable to preserve the fabric below 70 km. Such behavior, however, would make this deep deformable layer essentially asthenospheric, at least from a rheological point of view.

The direction of fast wave propagation in the 70–150 km depth range is parallel neither to the orogenic fronts, nor to the direction of the present absolute plate motion (APM). Instead, it is parallel to the direction of paleo-APM, the NNW motion of the North American plate at ~160–125 Ma. The fabric in the 70–150 km depth range may thus be of that age, 160–125 Ma.

In the recent times, the lower lithosphere beneath the Grenville–Appalachian orogen in the East-central US must not have experienced substantial deformation in the depth interval 70–150 km. It preserves anisotropic fabric that is distinctly different from that found in the asthenosphere below ~150 km depth. It thus appears likely that the

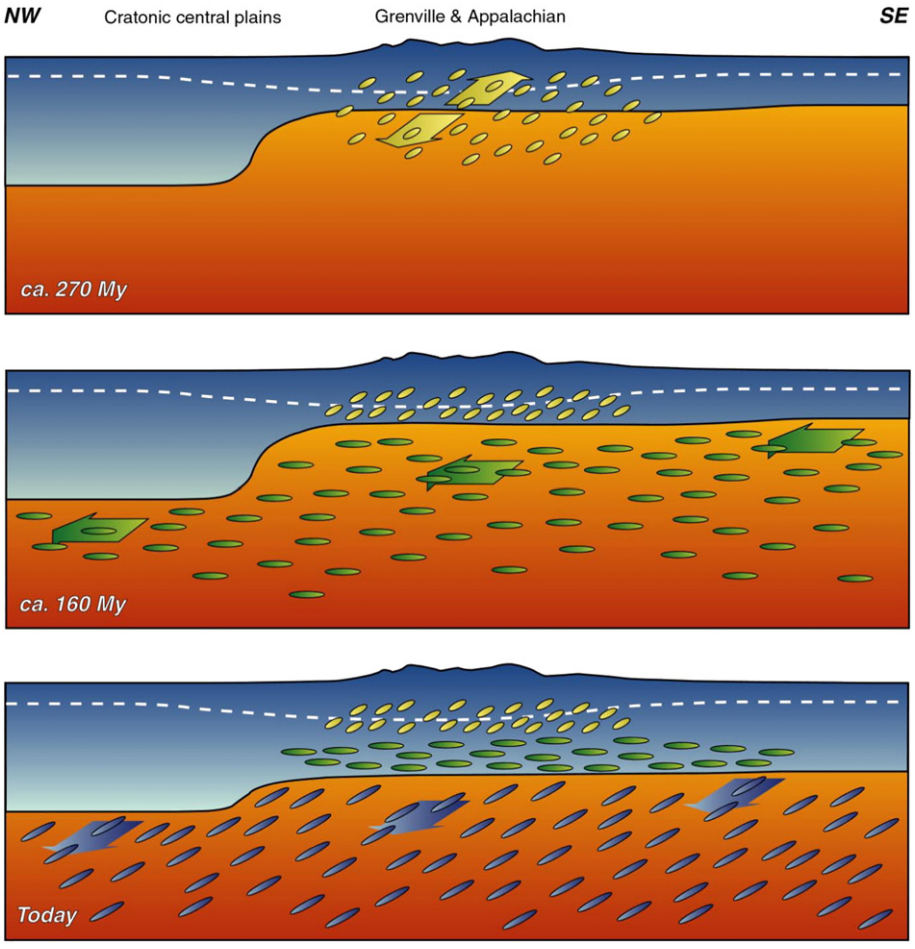

Fig. 6. A possible scenario for the origin of anisotropic layering beneath the East-central United States. During the Appalachian orogeny (up to 270 My), pervasive deformation occurred in the lower crust and lithospheric mantle. By the end of the orogeny, the lithosphere was 70 km thick. The warm, deformable material below 70 km then cooled down. Between 160 and 125 Ma, the lithosphere thickened. The lower lithosphere inherited the fabric from the asthenosphere below (of which it was forming); the fabric trended NNW, parallel to the direction of then plate motion. The two episodes of deformation resulted in two layers of frozen seismic anisotropy beneath the orogen. Today, the motion of the North American plate induces deformation giving rise to seismic anisotropy in the asthenosphere.

lithosphere has grown in thickness, from 70 km thick immediately after the Appalachian orogeny to 150 km thick at present. As it was thickening, the lower lithosphere has inherited the fabric of the sheared asthenosphere below (Fig. 6). This would explain why the fabric frozen into the lower lithosphere is characterized by a fast wave-propagation direction parallel to the azimuth of the plate motion at 160–125 Ma.

To investigate this scenario further, we modelled the diffusive cooling of a thickening lithosphere (Fig. 7). We solved the equation of diffusion in one dimension with a constant thermal diffusivity ($\kappa = 10^{-6}$ m^2/s) using an implicit finite-differences scheme. At time $t=0$, we imposed a temperature $T_m = 1300$ °C everywhere between $z=70$ and $z=220$ km. Between the surface and $z=70$ km, the initial geotherm is computed following Chapman (1986) and a surface heat flux equal to 60 mW/m^2. The whole layer is then cooled down by imposing the surface and bottom temperatures, $T_{surf}=0$ and $T_{220}=T_m=1300$ °C, respectively. We have then computed the differential stress (strength envelop) following the approach of Kohlstedt et al. (1995). We assumed a non-Newtonian relationship between strain rate and differential stress with stress exponent $n=3.6$, and activation energy $Q=535$ kJ/mol. We neglected the effects of grain size and water. According to this model, a 150 km thick layer that is initially at mantle temperature will thermally relax in about 150 Ma. Interestingly, the observed fast-propagation direction in the lower lithosphere is roughly parallel to the reconstructed plate motion at 160–125 Ma, i.e. up to 150 Ma after the end of the Appalachian orogeny. By the end of this episode the material would have already cooled down substantially, which may have limited the amount of any subsequent deformation and preserved then existing anisotropic fabric frozen in this layer. This scenario provides a coherent explanation for the presence of two layers of frozen anisotropy, but is mainly qualitative. In addition, it refers to the thermal lithosphere, which is only a good proxy for the mechanical lithosphere if the root is not affected by chemical depletion. Chemical differentiation may, however, have played a key role in the lithospheric growth. Recent analogue experiments and stability analysis (Jaupart et al., 2007) suggest that continental lithosphere is close to the instability of thermochemical convection, and may have grown by successive episodes of oscillatory convection. Further geodynamical modeling of root removal (or extrusion) and lithospheric growth, including thermochemical convection and an extensive exploration of the lithospheric-cooling model space (initial geotherm, radiogenic heating, thermal diffusity) would be needed to built a more quantitative scenario.

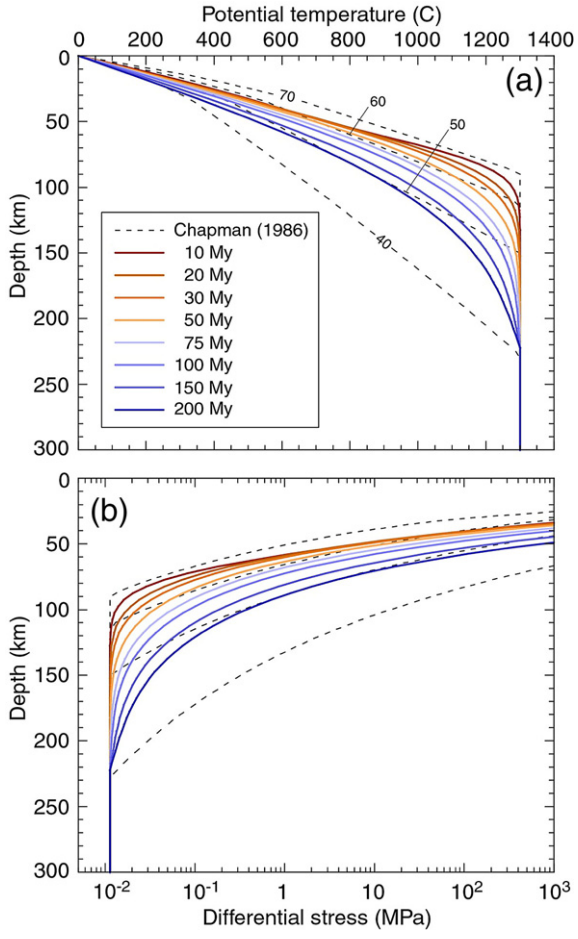

Fig. 7. (a) Diffusive cooling of a 150 km layer initially at mantle temperature. The thermal diffusivity is constant and equal to 10^{-6} m^2/s. For comparison, the dotted profiles show Chapman's geotherms for surface heat flux equal to 40, 50, 60 and 70 mW/m^2 (Chapman, 1986). The initial temperature profile is computed according to Chapman with a surface heat flux equal to 60 mW/m^2. At $t=0$, a temperature $T_m=1300$ °C is imposed between $z=70$ km and $z=220$ km. The system then starts to cool down, as shown by the series of temperature profiles. At $t=150$ My, the temperature profile is close to the Chapman's geotherm for $q_s=50$ mW/m^2, which is typical of stable platforms (Rohm et al., 2000). (b) Lithospheric strength envelopes (differential stress) computed for each of the temperature profile in plot (a). Following Kohlstedt et al. (1995), we assumed a non-Newtonian relationship between the strain rate and the differential stress, with a stress exponent $n=3.6$, and an activation energy $Q=535$ kJ/mol. Lithosphere gets stronger as it cools down.

Anisotropy in the deepest anisotropic layer we detect, below 150 km, appears to be due to current and recent asthenospheric flow. The direction of fast wave propagation is parallel to the current and recent APM. Simple shear in the asthenosphere due to the relative lithosphere–asthenosphere motion deforms mantle minerals. Given sufficient finite strain, olivine, the most abundant mineral in the upper mantle, develops preferred orientation in the direction of the flow, which results in seismic anisotropy (e.g. Karato, 1998). We have shown that the anisotropy we detect can account for published shear-wave splitting observations, both the fast-propagation directions and the splitting times. With continent-scale tomography, Marone and Romanowicz (2007) have also recently mapped asthenospheric anisotropy beneath eastern North America with fast-propagation directions parallel to the APM, and also pointed out that surface-wave and *SKS*-splitting observations are compatible. This consistency is further evidence for the plate-motion related anisotropy in the asthenosphere.

5. Conclusions

We have constrained the stratification of azimuthal anisotropy in the entire lithosphere–asthenosphere depth range beneath the Grenville–Appalachian orogen in the East-central U.S. Anisotropic patterns in parts of this depth range have been detected in the region previously, displaying different directions of fast wave propagation: parallel to tectonic trends, parallel to the current plate-motion direction, or not parallel to either (Marone and Romanowicz, 2007; Barruol et al., 1997; Fouch et al., 2000; Smith and Ekström, 1999).

Here we show that three distinct layers with different anisotropic fabric within each are present. The upper lithosphere (30–70 km depth range) is characterized by fast-propagation directions parallel to the Grenville and Appalachian fronts. We interpret this anisotropy as an indication of fabric frozen within the lower crust and uppermost mantle since the time of the Appalachian orogeny (>270 Ma). The lower lithosphere (70–150 km) displays fabric with a NNW fast-propagation direction. This is parallel to the direction of the North America plate motion at 160–125 Ma, and we infer that that is the age of the lower-lithospheric fabric. The asthenosphere (>150 km) shows anisotropic fabric with the direction of fast wave propagation parallel to the direction of the current plate motion; this fabric, apparently, is due to current and recent strain in the asthenosphere.

The layering of seismic anisotropy yields important new information regarding the history of deformation and evolution of the lithosphere. The front-parallel pattern of anisotropy in the uppermost

mantle and its occurrence at a scale of hundreds of kilometers (as shown by both surface-wave and P_n analyses) are evidence for pervasive, distributed deformation of the entire lithosphere at the time of the orogenies. The lithosphere appears to have been 70 km thick by the completion of the Appalachian suturing, because the fabric that is, apparently, associated with the orogeny is found above but not below 70 km. At present, the lithosphere is likely to be ~150 km thick, because below 150 km the fabric trends parallel to the present plate-motion direction, probably an expression of current and recent deformation in the asthenosphere, and above 150 km the fabric is oriented differently and appears to be fossil.

Post-orogenic evolution of the lithosphere has thus included substantial thickening, likely to have occurred by "freezing" of asthenospheric material onto the bottom of moving lithosphere. Because the fabric found in the lower lithosphere trends parallel to the plate motion at 160–125 Ma, much of the thickening of the lithosphere must have occurred at that time, with the new lithosphere inheriting the fabric from the sheared asthenosphere below, from which it was forming.

Acknowledgments

We are grateful to Thorsten Becker and Barbara Romanowicz for their insightful, constructive reviews.

References

Barruol, G., Silver, P.G., Vauchez, A., 1997. Seismic anisotropy in the eastern United States: deep structure of a complex continental plate. J. Geophys. Res. 102, 8329–8348.
Beck, M.E., Housen, B.A., 2003. Absolute velocity of North America during the Mesozoic from paleomagnetic data. Tectonophysics 377, 33–54.
Becker, T.W., Chevrot, S., Schulte-Pelkum, V., Blackman, D.K., 2006. Statistical properties of seismic anisotropy predicted by upper mantle geodynamic model. J. Geophys. Res. 111. doi:10.1029/2005JB004095.
Becker, T.W., Browaeys, J.T., Jordan, T.H., 2007. Stochastic analysis of shear-wave splitting length scales. Earth Planet. Sci. Lett. 259, 526–540.
Chapman, D.S., 1986. Thermal gradients in the continental crust. In: Dawson, J.B., Carswell, D.A., Hall, J., Wedepohl, K.H. (Eds.), The nature of the continental crust. Spec. Publ. Geol. Soc. London, vol. 24, pp. 63–70.
Christensen, N.I., 1984. The magnitude, symmetry and origin of upper mantle anisotropy based on fabric analyses of ultramafic tectonics. Geophys. J. R. Astron. Soc. 76, 89–112.
Dalziel, I.W.D., 1991. Pacific margins of Laurentia and East Antarctica–Australia as a conjugate rift pair: evidences and implications for an Eocambrian supercontinent. Geology 19, 598–601.
Debayle, E., Kennett, B.L.N., Priestley, K., 2005. Global anisotropy and the thickness of continents. Nature 433, 509–512.
Deschamps, F., Lebedev, S., Meier, T., Trampert, J., 2008. Azimuthal anisotropy of Rayleigh-wave phase velocities in the east-central United States. Geophys. J. Int. 173, 827–843.
Dickinson, W.R., 1971. Plate tectonics in geologic history. Science 174, 108–113.
Ervin, C.P., McGinnis, L.D., 1975. Reelfoot rift: reactivated precursor to the Mississippi embrayement. Geol. Soc. Am. Bull. 86, 1287–1295.
Fischer, K.M., Wiens, D.A., 1996. The depth distribution of mantle anisotropy beneath the Tonga subduction zone. Earth Planet. Sci. Lett. 142, 253–260.
Forsyth, D.W., 1975. The early structural evolution and anisotropy of the oceanic upper mantle. Geophys.J. R. Astron. Soc. 43, 103–162.
Fouch, M.J., Rondenay, S., 2006. Seismic anisotropy beneath stable continental interiors. Phys. Earth Planet. Inter. 158, 292–320.
Fouch, M.J., Fischer, K., Parmentier, E.M., Wysession, M.E., Clarke, T.J., 2000. Shear-wave splitting, continental keels, and patterns of mantle flow. J. Geophys. Res. 105, 6255–6275.
Gaherty, J.B., Jordan, T.H., 1995. Lehmann discontinuity as the base of an anisotropic layer beneath continents. Science 268, 1468–1471.
Gripp, A.E., Gordon, R.G., 1990. Current plate velocities relative to the hotspots incorporating the NUVEL-1 global plate motion model. Geophys. Res. Lett. 17, 1109–1112.
Gung, Y., Panning, M., Romanowicz, B., 2003. Global anisotropy and the thickness of continents. Nature 422, 707–711.
Hoffman, P.F., 1988. United Plates of America, the birth of a craton. Early Proterozoic assembly and growth of Laurentia. Ann. Rev. Earth Planet. Sci. 16, 543–603.
Jaupart, C., Molnar, P., Cottrell, E., 2007. Instability of a chemically dense layer heated from below and overlain by a deep less viscous fluid. J. Fluid Mech. 572, 433–469.
Karato, S., 1998. Seismic anisotropy in the deep mantle, boundary layers, and the geometry of mantle convection. Pageoph 151, 565–587.
Karlstrom, K.E., Åhäll, K.I., Harlan, S.S., Williams, M.L., McLelland, J., Geissman, J.W., 2001. Long-lived (1.8–1.0 Ga) convergent orogen in southern Laurentia, its extension to Australia and Baltica, and implications for refining Rodinia. Precambrian Res. 111, 5–30.
Kazmin, V.G., Natapov, L.M. (Eds.), 1998. Paleogeographic Atlas of Northern Eurasia. Institute of Tectonics of Lithospheric Plates, Moscow. CD-ROM.
Kennett, B.L.N., Engdahl, E.R., Buland, R., 1995. Constraints on seismic velocities in the Earth from traveltimes. Geophys. J. Int. 122, 108–124.
Kohlstedt, D.L., Evans, B., Mackwell, S.J., 1995. Strength of the lithosphere: constraints imposed by laboratory experiments. J. Geophys. Res. 100, 17587–17602.
Lebedev, S., Nolet, G., 2003. Upper mantle beneath southeast Asia from S velocity tomography. J. Geophys. Res. 108. doi:10.1029/2000JB000073.
Li, A., Forsyth, D.W., Fischer, K.M., 2003. Shear velocity structure and azimuthal anisotropy beneath North America from Rayleigh-wave inversion. J. Geophys. Res. 108. doi:10.1029/2002JB002259.
Marone, F., Romanowicz, B., 2007. The depth distribution of azimuthal anisotropy in the continental upper mantle. Nature 447, 198–203.
McClusky, A., Blassanian, S., Barka, A., et al., 2000. Global positioning system constrains on plate kinematics and dynamics in the eastern Mediterranean and Caucasus. J. Geophys. Res. 105, 5695–5719.
Meier, T., Dietrich, K., Stöckhert, B., Harjes, H.P., 2006. One-dimensional model of shear wave velocity for the eastern Mediterranean obtained from the inversion of Rayleigh-wave phase velocities and tectonic implications. Geophys. J. Int. 156, 45–58.
Meissner, R., Mooney, W., Artemevia, I., 2002. Seismic anisotropy and mantle creep in young orogens. Geophys. J. Int. 149, 1–14.
Meissner, R., Rabbel, W., Kern, H., 2006. Seismic lamination and anisotropy of the Lower Continental Crust. Tectonophysics 416, 81–99.
Molnar, P., 1988. Continental tectonics in the aftermath of plate tectonics. Nature 335, 131–137.
Molnar, P., Anderson, H., Audoine, E., Eberhart-Phillips, D., Gledhill, K., Klosko, E., McEvilly, T., Okaya, D., Savage, M., Stern, T., Wu, F., 1999. Continuous deformation versus faulting through continental lithosphere: tests using New Zealand as a laboratory for the study of continental dynamics. Science 286, 516–519.
Montagner, J.P., Griot-Pommera, D.A., Lave, J., 2000. How to relate body wave and surface wave anisotropy? J. Geophys. Res. 105, 19,015–19,027.
Nicolas, A., Christensen, N.I., 1987. Formation of anisotropy in upper mantle peridotites — a review. In: Fuchs, K., Froidevaux, C. (Eds.), Composition, structure and dynamics of the Lithosphere–Asthenosphere system, pp. 111–123.
Nishimura, C.E., Forsyth, D.W., 1989. The anisotropic structure of the upper mantle in the Pacific. Geophys. J. Int. 96, 203–229.
Pedersen, H.A., Bruneton, M., Maupin, V., SVEKALAPKO Seismic Tomography Working group, 2006. Lithospheric and sublithospheric anisotropy beneath the Baltic shield from surface-wave array analysis. Earth Planet. Sci. Lett. 244, 590–605.
Regan, J., Anderson, D.L., 1984. Anisotropic models of the upper mantle. Phys. Earth Planet. Inter. 35, 227–263.
Rohm, A., Snieder, R., Goes, S., Trampert, J., 2000. Thermal structure of continental upper mantle inferred from S-wave velocity and surface heat flow. Earth Planet. Sci. Lett. 181, 395–407.
Rychert, C.A., Rondenay, S., Fischer, K.M., 2007. P-to-S and S-to-P imaging of a sharp lithosphere–asthenosphere boundary beneath eastern North America. J. Geophys. Res. 112. doi:10.1029/2006JB004619.
Savage, M.K., 1999. Seismic anisotropy and mantle deformation: what we have learned from shear-wave splitting. Rev. Geophys. 37, 65–106.
Schwab, F., Knopoff, L., 1972. Fast surface wave and free mode computations. In: Bolt, B.A. (Ed.), Method in Compotational Physics, vol. 11. Academic Press, New-York.
Sebai, A., Stutzmann, E., Montagner, J.P., Sicilia, D., Beucler, E., 2006. Anisotropic structure of the African upper mantle from Rayleigh and Love wave tomography. Phys. Earth Planet. Inter. 155, 48–62.
Silver, P.G., 1996. Seismic anisotropy beneath the continents: probing the depths of geology. Annu. Rev. Earth Planet. Sci. 24, 385–432.
Simons, F.J., van der Hilst, R.D., Montagner, J.P., Zielhuis, A., 2002. Multimode Rayleigh-wave inversion for heterogeneity and azimuthal anisotropy of the Australian upper mantle. Geophys. J. Int. 151, 738–754.
Sleep, N.H., 2005. Evolution of the continental lithosphere. Annu. Rev. Earth Planet. Sci. 33, 369–393.
Smith, G.P., Ekström, G., 1999. A global study of *Pn*-anisotropy beneath continents. J. Geophys. Res. 104, 963–980.
Smith, M.L., Dahlen, F.A., 1973. The azimuthal dependence of Love- and Rayleigh-wave propagation in a slightly anisotropic medium. J. Geophys. Res. 78, 3321–3333.
Smith, D.B., Ritzwoller, M.H., Shapiro, N.M., 2004. Stratification of anisotropy in the Pacific upper mantle. J. Geophys. Res. 109. doi:10.1029/2004JB003200.
Tapponnier, P., Xu, Z.Q., Roger, F., Meyer, B., Arnaud, N., Wittlinger, G., Yang, J.S., 2001. Oblique stepwise rise and growth of the Tibet Plateau. Science 294, 1671–1677.
Tatham, D.J., Lloyd, G.E., Butler, R.W.H., Casey, M., 2008. Amphibole and lower crustal seismic properties. Earth Planet. Sci. Lett. 267, 118–128.
Vinnik, L.P., Kosarev, G.L., Makeyeva, L.I., 1984. Anisotropy of the lithosphere from the observations of SKS and SKKS. Proc. Acad. Sci. USSR Geol. Sci. Sect., Engl. Transl.
Vinnik, L.P., Makeyeva, L.I., Milev, A., Usenko, A., 1992. Global patterns of azimuthal anisotropy and deformations in the continental mantle. Geophys. J. Int. 111, 433–447.
Yang, Y., Forsyth, D.W., 2006. Rayleigh-wave phase velocities, small-scale convection, and azimuthal anisotropy beneath southern California. J. Geophys. Res. 111. doi:10.1029/2005JB004180.
Yao, H., van der Hilst, R.D., de Hoop, M.V., 2006. . Surface-wave array tomography in SE Tibet from ambient seismic noise and two-station analysis — I. Phase velocity maps. Geophys. J. Int. 166, 732–744.
Zhang, P.Z., Shen, Z.K., Wang, M., Gan, W.J., Bürgmann, R., Molnar, P., Wang, Q., Niu, Z.J., Sun, J.Z., Wu, J.C., Hanrong, S., Xinzhao, Y., 2004. Continuous deformation of the Tibetan Plateau from global positioning system data. Geology 32, 809–812.
Zhang, X., Paulssen, H., Lebedev, S., Meier, T., 2007. Surface wave tomography of the Gulf of California. Geophys. Res. Lett. 34. doi:10.1029/2007GL030631.
Ziegler, P.A., 1989. Evolution of Laurussia: A Study in Late Paleozoic Plate Tectonics. Kluwer Academic Publishers, Dordrecht. 102 pp.

Chapitre 2

L'origine de la stabilité des racines continentales

Une propriété sismologique du manteau sous-continental est la présence de zones de vitesse sismiques élevées, plus connues sous le terme de racines continentales, et qui, selon les modèles et les endroits, peuvent s'étendre jusque vers 200 à 250 km de profondeur. La distribution de ces racines est bien corrélée avec celle des terrains Précambriens, donc âgés (Polet et Anderson, 1995). L'idée qui vient immédiatement à l'esprit est que les racines continentales sont plus froides que le manteau moyen. Question : pourquoi ce matériau froid n'a pas été déstabilisé puis recyclé dans le manteau plus profond ? Plusieurs pistes ont été avancées pour expliquer ce paradoxe, notamment chimiques (y compris le rôle des fluides) et rhéologiques. Comme souvent en science, la réponse à cette question est sans doute une combinaison de ces différentes hypothèses. Ce chapitre et les articles qui lui sont associés abordent ce sujet à l'échelle globale (Deschamps et al., 2001, 2002) et à l'échelle régionale (Godey et al., 2004; van Gerven et al. (2004), en cherchant à contraindre les anomalies de densité à partir des anomalies de gravité.

2.1 L'apport des anomalies de gravité

2.1.1 Modélisation des anomalies de gravité et kernels du géoïde

Les anomalies de gravité sont bien sûr sensibles aux anomalies de densité localisées en profondeur, mais il s'agit là d'un signal est intégré dont il faut séparer les contributions en fonction de la profondeur. La première étape est donc de modéliser le champ de gravité, c'est-à-dire de calculer le signal observé en surface pour une distribution de densité donnée.

La principale difficulté liée à cette modélisation est de décrire et d'estimer correctement les contributions dynamiques (l'écoulement du manteau) aux anomalies de gravité (p.e., Ricard et al., 1984; Forte et Peltier, 1987; Hager et Richards, 1989). La topographie dynamique aux interfaces (surface et CMB) induite par l'écoulement, par exemple, contribue significativement aux anomalies de gravité. En pratique, ces effets peuvent être pris en compte en modulant les distributions de densité par des fonctions noyau, ou kernels de géoïde.

Kernels radiaux

En un point donné, l'anomalie de gravité peut être calculée en intégrant les anomalies de densité à la verticale de ce point. Plus précisément, il faut écrire une intégrale pour chaque degré d'harmonique sphérique ℓ,

$$\mathrm{d}g_\ell(\theta,\varphi) = \frac{3g_0}{\rho_m R}\frac{(\ell-1)}{(2\ell+1)}\int_{r_{CMB}}^{R} G_\ell(r)\delta\rho_\ell(r,\theta,\varphi)\mathrm{d}r \ , \qquad (2.1)$$

où ρ_m est la densité moyenne de la Terre, g_0 l'accélération de gravité en surface, R le rayon de la Terre, et r_{CMB} le rayon de la CMB. On passe facilement des anomalies de gravité (δg) aux anomalies de géoïde (δN) par

$$\mathrm{d}N_\ell(\theta,\varphi) = \frac{R}{g_0}\frac{1}{(\ell-1)}\mathrm{d}g_\ell(\theta,\varphi) \ . \qquad (2.2)$$

Dans l'équation (2.1), les anomalies de densités sont modulées par les fonctions radiales $G_\ell(r)$, les kernels de géoïde. Ces fonctions décrivent la réponse du géoïde (ou des anomalies de gravité) à une anomalie ponctuelle de densité, en tenant compte des contributions dynamiques liées à l'écoulement du manteau. Un courant ascendant (descendant) se traduit par une bosse (un creux) du géoïde. L'écoulement est modélisé en développant puis en résolvant les équations de conservation de la masse et de la quantité de mouvement et la relation contrainte/déformation sur une base d'harmoniques sphériques généralisés. On trouvera les détails de la méthode utilisée pour résoudre ces équations dans Forte et Peltier (1991). Notons simplement que cette méthode est valable pour un fluide compressible, et qu'elle tient compte des variations radiales de la viscosité. Les variations latérales de viscosité ne sont en revanche pas prises en compte, c'est-à-dire que la composante toroïdale de l'écoulement est absente de nos modèles, approximation qu'il faudra garder à l'esprit par la suite.

Les kernels de géoïde dépendent fortement du profil radial de viscosité (Figure 2.1). Ces différences sont très marquées pour les degrés d'harmonique sphérique les plus faibles, qui échantillonnent le manteau dans son ensemble. Elles s'atténuent lorsque le degré d'harmonique sphérique augmente. Pour $\ell \geq 10$, la caractéristique principale des kernels de

géoïde est un maximum prononcé dans le manteau peu profond (au dessus de la zone de transition), et une valeur proche de zéro dans le manteau moyen et le manteau profond ($z \geq$ 1000 km). La localisation précise du maximum dépend à fois du profil de viscosité et du degré d'harmonique sphérique. Les anomalies de gravités à moyennes et petites longueurs d'ondes sont donc principalement sensibles au manteau peu profond, qui nous intéresse dans ce chapitre. En revanche, les grandes et très grandes longueurs d'ondes échantillonnent principalement la zone de transition et le manteau inférieur (leurs contributions aux profondeurs plus faibles sont petites par rapport à celles des degrés d'harmonique sphérique supérieur), et risquent d'en biaiser l'interprétation. Pour contraindre les anomalies de densité dans le manteau peu profond, il sera préférable de filtrer les anomalies de gravité (et de vitesse d'onde de cisaillement), pour des degrés d'harmoniques sphériques suffisamment élevés, disons pour $\ell \geq 10$.

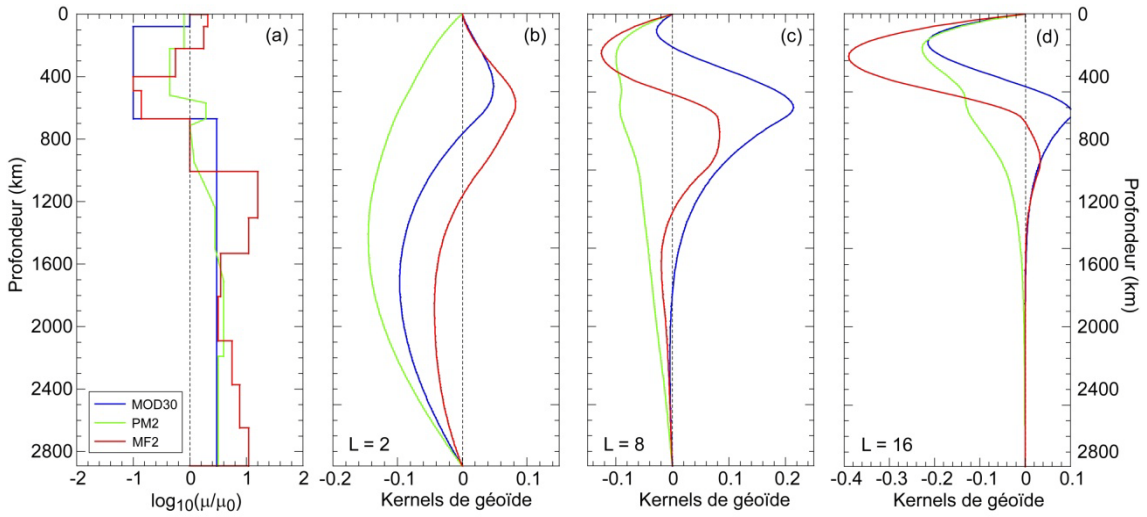

Figure 2.1 – Kernels de géoïde pour plusieurs degrés d'harmoniques sphériques (b-d) calculés avec différents profils de viscosité (a), dont celui de Mitrovica et Forte (1997) (en rouge).

Kernels régionaux

Les kernels représentés sur la Figure 2.1 ne tiennent compte que des anomalies de densité à la verticale du point considéré. Cela suffit tant que l'on utilise les modèles tomographiques globaux, mais pour l'interprétation de modèles régionaux il est nécessaire de tenir compte des contributions latérales des anomalies de densité, en étendant l'intégration de ces anomalies à la longitude et à la latitude. Difficulté supplémentaire, à l'inverse des anomalies globales de gravité, les modèles tomographiques régionaux ne sont en général pas développés en harmoniques sphériques. Pour utiliser ces modèles régionaux, il faut sommer les anomalies de gravité dans une gamme de longueur d'onde que l'opérateur doit définir. L'équation 2.1 devient

$$dg(\theta,\varphi) = \frac{3g_0}{4\pi\rho_m R}\int_{r_{CMB}}^{R}\int_0^{\pi}\int_{-\pi/2}^{\pi/2} K_g(\Delta,r)\delta\rho(r,\theta',\varphi')\sin\theta' d\theta' d\varphi' dr \ , \qquad (2.3)$$

où les kernels régionaux (ou locaux) $K_g(\Delta,r)$ sont déduits des kernels radiaux et des polynômes de Legendre selon

$$K_g(\Delta,r) = \sum_{\ell=\ell_1}^{\ell_2}(\ell-1)G_\ell(r)P_\ell^0(\cos\Delta) \ , \qquad (2.4)$$

et où l'on a utilisé le théorème de complétude,

$$P_\ell^0(\cos\Delta) = \frac{4\pi}{(2\ell+1)}\sum_{m=-\ell}^{\ell} Y_\ell^m(\varphi,\theta)\, Y_\ell^{m*}(\varphi',\theta') \ . \qquad (2.5)$$

Dans les équations précédentes, Δ est la distance angulaire entre les positions (φ,θ), où l'anomalie de gravité est estimée, et (φ',θ'), où se trouve l'anomalie de densité. Les kernels diminuent rapidement avec la distance angulaire (Figure 2.2), ce qui justifie l'approximation faite à l'échelle globale. De plus, pour limiter le temps de calcul dans le cas des études régionales, on pourra tronquer ces kernels au delà d'un angle limite Δ_c sans modifier notablement les résultats.

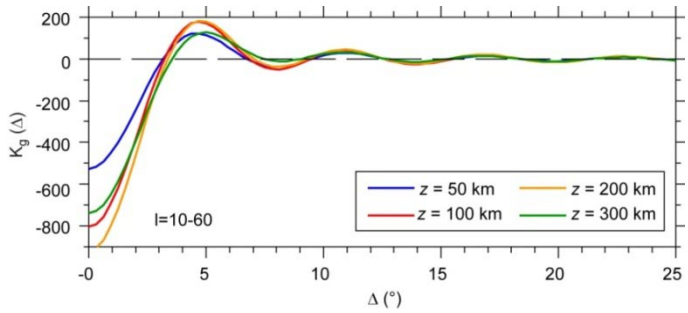

Figure 2.2 – Kernels de géoïde locaux construits à partir du modèle de viscosité de Mitrovica et Forte (1997). Les géoïdes radiaux (en rouge sur la Figure 2.1) sont sommés entre les degrés d'harmoniques sphériques $\ell_1 = 10$ et $\ell_2 = 60$.

Autres contraintes, autres kernels

Des intégrales similaires à l'équation 2.1 peuvent être écrites pour la topographie dynamique en surface et à la CMB, ainsi que pour la composante horizontale de la vitesse de l'écoulement en surface. Bien sûr, les kernels de géoïde doivent être remplacées par des kernels propres à chacune de ces quantités (Forte et Peltier, 1991). L'utilisation de ces contraintes supplémentaires et le bénéfice qu'elles apportent ne sont toutefois pas évidents. Par exemple, pour relier la topographie dynamique à la topographie observée, il faut faire des hypothèses supplémentaires concernant la compensation isostatique (ou non) de la croûte. La topographie de la CMB, quant à elle, n'est pas très bien contrainte. Plusieurs études pour le manteau supérieur (Perry et al., 2003) et pour le manteau global (Forte et Mitovica, 2001) ont néanmoins inclus ces contraintes supplémentaires dans leurs analyses.

2.1.2 Anomalies de densité calibrées

L'étape suivante est de calibrer les anomalies relatives de densité à partir des anomalies relatives de vitesse de cisaillement à l'aide du rapport entre ces anomalies,

$$\zeta(r) = \frac{\partial \ln \rho(r,\theta,\varphi)}{\partial \ln V_S(r,\theta,\varphi)} . \qquad (2.6)$$

Si l'on écrit les anomalies de densité en fonction de ce rapport, l'équation (2.1) devient

$$\mathrm{d}g_\ell(\theta,\varphi) = \int_{r_{CMB}}^{R} \mathrm{K}_\ell(r)\zeta(r)\delta V_{S_\ell}(r,\theta,\varphi)\mathrm{d}r , \qquad (2.7a)$$

avec $$\mathrm{K}_\ell(\theta,\varphi) = \frac{3g_0}{\rho_m R}\frac{(\ell-1)}{(2\ell+1)}\frac{\langle\rho(r)\rangle}{\langle V_S(r)\rangle}\mathrm{G}_\ell(\theta,\varphi) , \qquad (2.7b)$$

où $\langle\rho(r)\rangle$ et $\langle V_S(r)\rangle$ sont les profils moyens de densité et de vitesse de cisaillement. En se donnant un modèle de vitesse d'onde de cisaillement, on peut inverser les anomalies de gravité observées pour un modèle radial de ζ, et utiliser ce modèle pour calibrer les anomalies de densité. On trouvera plus de détails concernant l'inversion des anomalies de gravité pour les profils de ζ et l'influence des différents paramètres de cette inversion (profil de viscosité, filtrage, régularisation) dans Deschamps et al. (2001). Un point important concerne l'estimation de barres d'erreurs pour ζ. L'idée est de générer un grand nombre de modèles de vitesse de cisaillement en perturbant le modèle moyen à l'intérieur de ses barres d'erreurs (supposées ou modélisées), puis d'inverser chacun de ces modèles perturbés individuellement pour un profil de ζ. La moyenne et la déviation standard de cette collection de profils sont une bonne estimation du profil de ζ et de son incertitude.

Autant le dire tout de suite, la méthode que l'on vient de décrire comporte un inconvénient majeur. Ce que l'on contraint, en fait, c'est la partie des anomalies de densité qui est corrélée aux anomalies de vitesse de cisaillement. Nous verrons dans les prochains chapitres que dans le manteau inférieur ces deux quantités, lorsqu'elles sont déterminées indépendamment, ne sont absolument pas corrélées. Une partie du signal en densité reste ainsi inaccessible, ce qui pourrait biaiser l'interprétation de ces anomalies calibrées en termes de structures thermochimiques.

2.2 Variations thermochimiques latérales et stabilité des racines

2.2.1 Variations de température et de composition

Avec ces deux distributions, les anomalies de vitesse de cisaillement et de densité, on peut tenter de contraindre les variations latérales de température et de composition dans le manteau peu profond. Un premier problème est de paramétriser la composition. Plusieurs choix sont possibles. On peut, par exemple, considérer les variations de la fraction

volumique d'olivine, le minéral le plus important du manteau supérieur, et répartir les excès ou les défauts d'olivine entre les autres minéraux (grenats, clinopyroxènes et orthopyroxènes). Un choix plus judicieux, cependant est de paramétriser les anomalies de composition en terme de variation de la fraction volumique globale de fer x_{Fe}, en particulier parce que les anomalies de vitesses sismiques et de densité induites par les variations de x_{Fe} sont beaucoup plus fortes que celles induites par variations de la fraction volumique d'olivine. Par exemple une anomalie de fer de ±4% induit une anomalie de vitesse de cisaillement de ±1%, tandis qu'une anomalie en olivine de ±20% n'induit qu'une anomalie de vitesse de ±0.4%. Les anomalies de vitesse de cisaillement et de densité s'écrivent alors

$$\begin{cases} \mathrm{d}\ln V_S = \frac{\partial \ln V_S}{\partial T}\mathrm{d}T + \frac{\partial \ln V_S}{\partial x_{Fe}}\mathrm{d}x_{Fe} \\ \mathrm{d}\ln\rho = \frac{\partial \ln \rho}{\partial T}\mathrm{d}T + \frac{\partial \ln \rho}{\partial x_{Fe}}\mathrm{d}x_{Fe} \end{cases} . \qquad (2.8)$$

Le calcul des sensibilités (ou dérivées partielles) à la température et au fer ressemble à celui que l'on développera pour le manteau inférieur (Chapitre 3). Il s'agit de modéliser l'équation d'état du manteau, c'est-à-dire de déterminer les propriétés thermo-élastiques du manteau pour une température, une pression, et une pétrologie donnée.

On trouvera plus de détails concernant cette modélisation, ainsi que les paramètres thermo-élastiques de surface dans Deschamps et al. (2002). D'un certain point de vue, l'extrapolation aux pressions du manteau supérieur est plus simple dans le manteau supérieur que dans le manteau inférieur, car elle se limite à l'ordre 2 du développement de Birch-Murnaghan. En revanche, la diversité minéralogique est plus grande dans le manteau supérieur, et le calcul des propriétés moyennes de l'agrégat y est sensiblement plus compliqué. Une autre différence par rapport au cas du manteau inférieur est la prise en compte de l'anélasticité, selon le modèle de Minster et Anderson (1981). Les roches du manteau ne sont pas parfaitement élastiques, et les ondes de cisaillement s'y propagent un peu moins rapidement que dans un milieu parfaitement élastique, l'atténuation étant contrôlée par le facteur de qualité. Ces différences ne sont pas visibles en laboratoire, où la fréquence de la déformation est très élevée (autour de 1 MHz). À la fréquence des ondes sismiques (0.01-1.0 Hz), par contre, elles ne peuvent pas être négligées.

2.2.2 Stabilité des racines

Un dernier exercice consiste à estimer la flottaison locale en chaque point du modèle, et de comparer sa moyenne radiale à la flottaison critique prédite par une analyse de stabilité. La flottaison locale est le rapport entre l'anomalie locale de densité chimique, $\mathrm{d}\rho_c$, et la variation locale de densité thermique (en fait, son opposé). Sa moyenne radiale pour une racine d'épaisseur d_r est

$$\langle B \rangle = \frac{1}{d_r} \int_{R-d_r}^{R} \frac{d\rho_c}{\alpha \rho_0 dT} dr \,, \qquad (2.9)$$

où est α l'expansion thermique, ρ_0 la densité de référence, et dT l'anomalie locale de température. La variation de pression par rapport à l'équilibre hydrostatique liée à la superposition d'une anomalie de température dT et d'une anomalie de densité chimique $d\rho_c$ permet de définir la flottaison critique en fonction des dimensions de la racine (sa longueur l_r, et son épaisseur d_r) et de l'épaisseur de la couche limite thermique δ (Lenardic et Moresi, 1999),

$$B_c = \frac{\delta_r'}{l_r' d_r'} \,, \qquad (2.10)$$

où les primes indiquent que l'on a utilisé les quantités adimensionnées. Par ailleurs, il est utile de définir le rapport entre l'épaisseur thermique et l'épaisseur chimique de la racine, $r = \delta/d_r$. Dans le cas où les anomalies de température sont négatives (c'est *a priori* le cas des racines continentales), la racine reste stable si la flottaison locale est supérieure à B_c.

Une petite modification doit être apportée à l'équation 2.10 pour tenir compte des forces de friction, qui stabilisent la racine et sont proportionnelles à la viscosité μ du fluide,

$$f = A \frac{\mu \kappa}{d_r^2} \,. \qquad (2.11)$$

A est une constante adimensionnée qui caractérise la stabilité de la couche limite thermique (elle joue le rôle de nombre de Rayleigh critique pour cette couche limite) et qui dépend du mode de convection. Un intérêt de cette modification est de tenir compte implicitement du rôle joué par la rhéologie de la racine dans la stabilisation de celle-ci. Ainsi, pour le régime de couvercle conductif, on s'attend à une valeur élevée de A (Deschamps et Sotin, 2000), ce qui accroît la stabilité de la racine pour une distribution thermochimique donnée. Bien sûr, cette analyse n'est pas tout à fait correcte, car les valeurs de A que nous allons utiliser sont inspirées de modèles de convection purement thermiques. Depuis la publication de ces travaux, une analyse de stabilité plus appropriée et des expériences de laboratoire ont permis de mieux décrire la stabilité d'une couche limite thermochimique (Jaupart et al., 2007). On notera toutefois que cette étude ne tient pas compte des variations de viscosité avec la température, ce qui pourrait avoir des effets non-négligeables sur la stabilité système. Quoiqu'il en soit, dans notre analyse simplifiée, la flottaison critique s'écrit maintenant

$$B_c = \frac{\delta_r'}{l_r' d_r'} + \frac{A}{dT' d_r'^3 l_r' Ra} \,, \qquad (2.12)$$

où Ra est le nombre de Rayleigh du manteau.

Pour une anomalie de température négative le terme de friction diminue la valeur de B_c, ce qui implique bien un accroissement de la stabilité de la racine. Toujours selon

l'équation 2.12, la stabilité de la racine augmente (B_c diminue) avec sa longueur et avec le rapport $r = \delta/d_r$ (A étant proportionnel à δ^3). L'analyse de stabilité linéaire menée par Jaupart et al. (2007) contredit ce dernier point, et suggère que l'épaisseur de la racine a peu d'influence sur sa stabilité. De plus, le fait que B_c diminue de façon monotone lorsque la longueur de la racine augmente est contre intuitif. Comme dans le cas purement thermique, on s'attend à ce qu'il existe une valeur optimale de la longueur d'onde des perturbations thermochimiques pour laquelle le nombre de Rayleigh critique est le plus faible (ce que montre aussi l'analyse de Jaupart et al., 2007). Cette contradiction est sans doute liée au fait que la définition de B_c repose sur l'équilibre de la pression hydrostatique seulement, et pas sur une analyse de stabilité linéaire (donc dynamique).

Le terme de friction est contrôlé par le rapport entre A/Ra et la variation locale (adimensionnée) de température. Des valeurs élevées de A associées à de petites ou modestes variations de température stabilisent la racine. Comme je l'ai souligné un peu plus haut, des valeurs élevées de A sont obtenues, entre autre, pour un fluide dont la viscosité dépend fortement de la température. Dans ce cas, une couche rigide et visqueuse, parfois appelée couvercle conductif, se forme au sommet du fluide (p.e., Davaille et Jaupart, 1993; Moresi et Solomatov, 1995; Deschamps et Sotin, 2000). Et la rhéologie de la racine d'entrer en scène. À ce stade, on notera cependant une légère incohérence. Rappelons en effet que les kernels de géoïde (§ 2.1.1) sont calculés pour un fluide dont la viscosité ne dépend que de la profondeur.

2.3 Modèles globaux et modèles régionaux

2.3.1 Echelle globale

La méthode esquissée dans les paragraphes précédents peut être appliquée à l'échelle globale en utilisant le modèle de vitesse d'onde de cisaillement S16RLBM (Woodhouse et Trampert, 1995), les anomalies de gravité EGM96 (Lemoine et al., 1998), et PREM (Dziewonski et Anderson, 1981) comme modèle de référence (équation 2.7b). À partir de ces modèles filtrés pour les degrés d'harmoniques sphériques $11 \leq \ell \leq 16$, il est possible de calculer un profil moyen du facteur de calibration ζ séparément pour les continents et pour les océans (Figure 2.3), la fonction océan/continent étant celle définie par 3SMAC (Nataf et Ricard, 1996). Par contre, la résolution de S16RLBM (limité à au degré d'harmonique sphérique $\ell = 16$) ne permet pas de contraindre ζ pour des régions intra-continentales (notamment les cratons). Résultat intéressant, l'amplitude de ζ est faible, de l'ordre de 0.05 au maximum, aussi bien pour le manteau sous-continental que pour le manteau sous-océanique. Si le manteau peu profond était chimiquement homogène et parfaitement

élastique, on s'attendrait à des valeurs supérieures d'un ordre de grandeur environs. Selon Isaac (1992), ce rapport serait de l'ordre de 0.45 dans le cas de l'olivine. La faible amplitude de ζ ne s'explique que par une forte atténuation (Karato, 1993) et/ou la présence d'anomalies latérales de composition (Deschamps et al., 2001). Les valeurs négatives, elles, nécessitent des variations latérales de composition. À ce stade, il est cependant difficile de proposer une interprétation plus fine de ces valeurs. Autre fait marquant, la dichotomie entre les deux profils, le profil sous-océanique s'annulant moins profondément (~ 140 km) que son pendant sous-continental (~ 220 km), observation que l'on peut relier à la présence des racines continentales. Au delà de 250 km de profondeur cette différence disparaît, et la structure du manteau ne semble plus être influencée par la tectonique de surface.

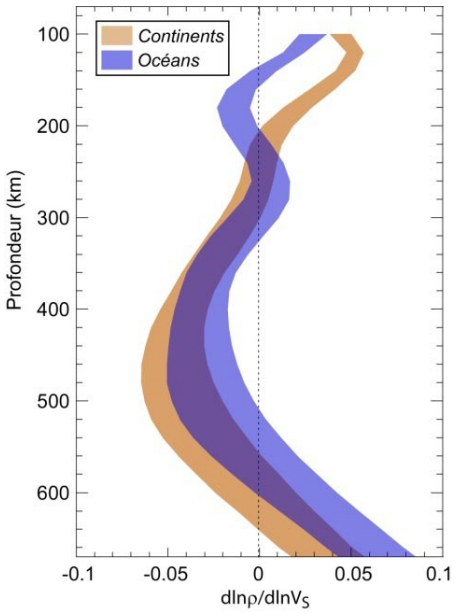

Figure 2.3 – Profil du facteur de calibration de la densité, ζ, pour le manteau sous-continental (en brun) et le manteau sous-océanique (bleu).

L'étape suivante est d'inverser S16RLBM et les modèles de ζ représentés sur la Figure 2.3 pour des anomalies de température et de composition suivant le système (2.8). Soulignons de nouveau que seules les anomalies de densités corrélées aux anomalies de vitesse de cisaillement sont contraintes, ce qui implique que les anomalies de température et de fraction volumique de fer sont elles aussi parfaitement corrélées. La distribution thermochimique que l'on obtient (Figure 2.4a-d, pour les anomalies de fer) est donc incomplète. Néanmoins elle permet déjà quelques conclusions intéressantes. Lorsque l'on détermine les valeurs moyennes des anomalies de température et de fer pour chacune des 4 principales provinces tectoniques définies par 3SMAC (Nataf et Ricard, 1996), il apparaît clairement que sous les cratons et, dans une moindre mesure, sous les boucliers continentaux, le manteau est simultanément appauvri en fer (Figure 2.4e-h) et plus froid

que le manteau moyen jusque vers 200 km de profondeur. Sous les océans et les zones tectoniquement actives, par contre, le manteau est thermochimiquement proche du manteau moyen, avec des anomalies de température et de fer distribuées autour de zéro. Vers 250 km et au delà, c'est l'ensemble du manteau qui paraît homogène, indépendamment de la tectonique de surface. Ce résultat est cohérent avec d'autres études similaires (p.e., Forte et Perry, 2000), et il confirme le modèle de tectosphère, avec une lithosphère continentale archéenne plus froide, mais chimiquement appauvrie en éléments denses.

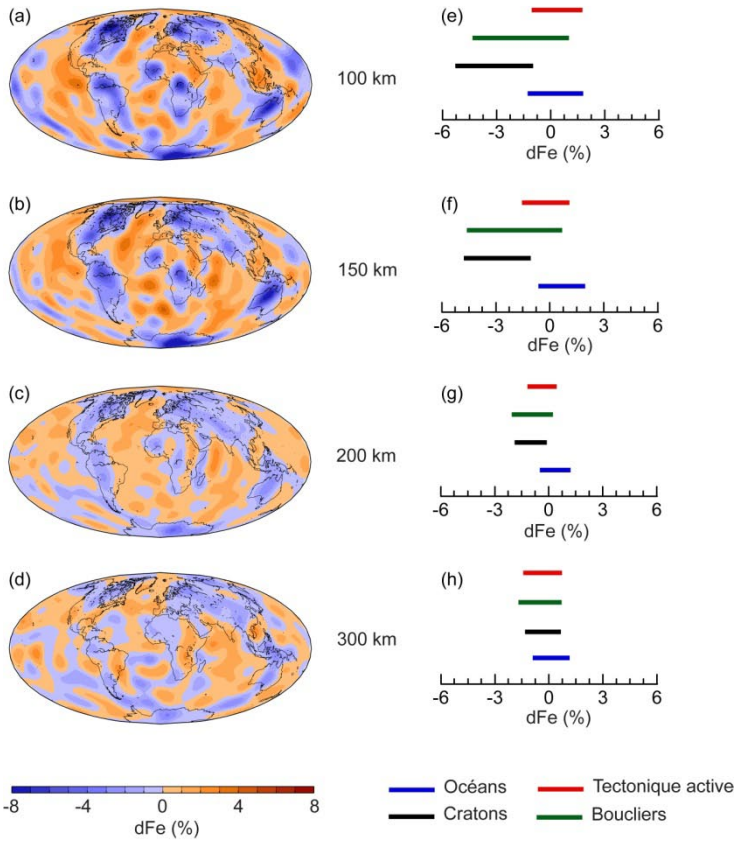

Figure 2.4 – Distribution globale des anomalies de fer dans le manteau supérieur (Deschamps et al., 2002). (a-d) Distributions latérales. (e-h) Moyennes et déviations standards pour les 4 principales provinces tectoniques définies par 3SMAC (Nataf et Ricard, 1996).

Dernière étape, calculer la flottaison locale intégrée (equation 2.9) des racines continentales, et la comparer à la flottaison critique (equation 2.12). L'anomalie de densité chimique est facilement déduite des anomalies de la fraction volumique de fer calculées précédemment (Figure 2.4). Pour les zones cratoniques, et en supposant une épaisseur de racine de 200 km, la flottaison locale intégrée est en moyenne de 0.84, avec une déviation standard de 0.07. Dans ces conditions, notre analyse de stabilité indique que les racines de grande dimension ($l_r > 0.75$), ou dont l'épaisseur est grande devant celle de la couche limite thermique ($r < 0.5$) sont stables, et ceci indépendamment des propriétés rhéologiques de la

racine rhéologie (Figure 2.5). En revanche, la stabilité de racines aux dimensions plus modestes dépend fortement de sa rhéologie. Pour de petites valeurs de A ($A/Ra \sim 10^{-7}$, correspondant à un écoulement isovisqueux) la racine est instable. Des valeurs plus élevées (obtenues, par exemple, pour un fluide dont la viscosité dépend fortement de la température) parviennent à stabiliser la racine, pourvu que les anomalies de température ne soient pas trop fortes. Répétons-le, ces conclusions sont à prendre en gardant à l'esprit les limites de la méthode utilisée, notamment pour la calibration des anomalies de densité (§ 2.2.2) et pour le calcul de la flottaison critique (§ 2.3.2).

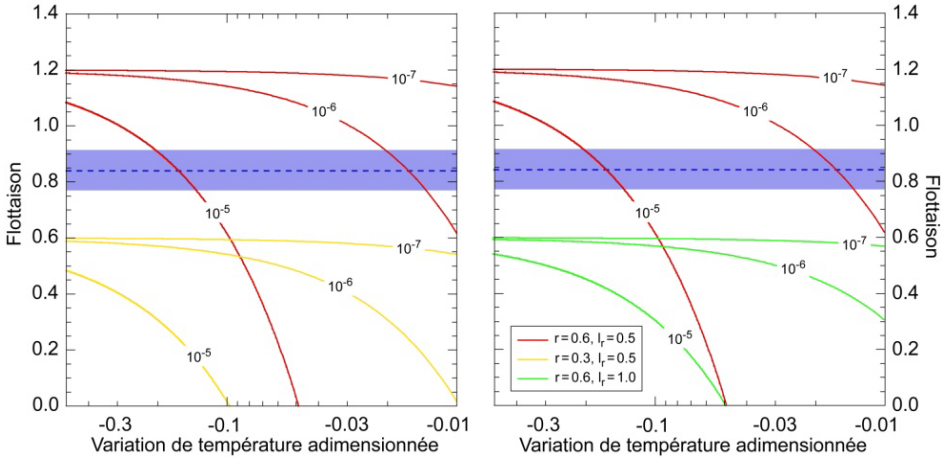

Figure 2.5 – Flottaison critique B_c en fonction de l'anomalie de température adimensionnée et pour plusieurs valeurs de $C = A/\mathrm{Ra}$ (Deschamps et al., 2002). Deux valeurs différentes de r (rapport entre l'épaisseur thermique et l'épaisseur chimique de la racine) et de la longueur l_r de la racine sont considérées. L'échelle de température est ΔT = 2500 K, l'échelle de longueur verticale D = 3000 km, et l'échelle de longueur horizontale L = 2000 km. B_c est donné par l'équation 2.12. La bande bleue couvre une déviation standard autour de la moyenne régionale calculée pour les cratons et pour une racine d'épaisseur d_r = 200 km.

2.3.2 Un petit tour en Amérique du Nord …

Une étude similaire peu être menée à l'échelle continentale, pour l'Amérique du Nord. Le modèle de vitesse de cisaillement (Godey et al., 2004) est basé sur l'inversion d'un jeu de courbes de dispersion pour la vitesse de phase des ondes de Rayleigh, et sa résolution est au mieux de 400 km. Pour simplifier, le profil de ζ utilisé pour calibrer les anomalies de densité est le profil continental que nous venons de calculer à l'échelle globale (Figure 2.3).

Comme à l'échelle globale, les distributions d'anomalies de température et de fer dépendent de la tectonique de surface (Figure 2.6). Jusque vers 220 km de profondeur, le manteau sous le craton Canadien apparaît plus froid que le manteau moyen (au maximum de 400 K, vers 120 km) et appauvri en fer, tandis que sous les zones tectoniquement actives (principalement, l'ouest des Etats-Unis) le manteau est proche du manteau moyen. De nouveau, ces observations semblent accréditer le modèle de tectosphère.

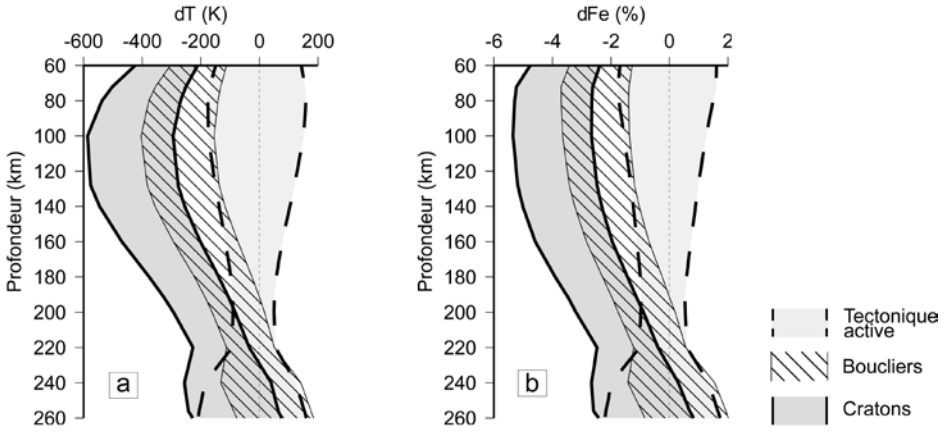

Figure 2.6 – Profil moyen d'anomalies de température et de fer sous l'Amérique du Nord (Godey et al., 2004).

2.3.3 … et en Australie

Dernier exemple, le cas de l'Australie. Ce continent est globalement divisé entre trois grandes provinces dont l'âge diminue d'ouest en est. Les terrains situés les plus à l'ouest sont Archéens et datés à plus de 2500 Ma, tandis que les terrains les plus à l'est sont datés à moins de 500 Ma. Si l'hypothèse d'une tectosphère est applicable à ce continent, on s'attend à des différences majeures entre les profils de ζ pour chacune de ces provinces. Pour vérifier cela, prenons un modèle régional de vitesse de cisaillement, AUS04-Vs (Simons et al., 2002), filtrons les anomalies de gravité EGM96 entre les degrés d'harmoniques sphériques $\ell = 10$ et $\ell = 60$, et utilisons la formulation locale des kernels de géoïde (§ 2.1.1). L'inversion (on en trouvera les détails dans van Gerven et al. (2004)) révèle effectivement des différences importantes entre les différents profils de ζ (Figure 2.7).

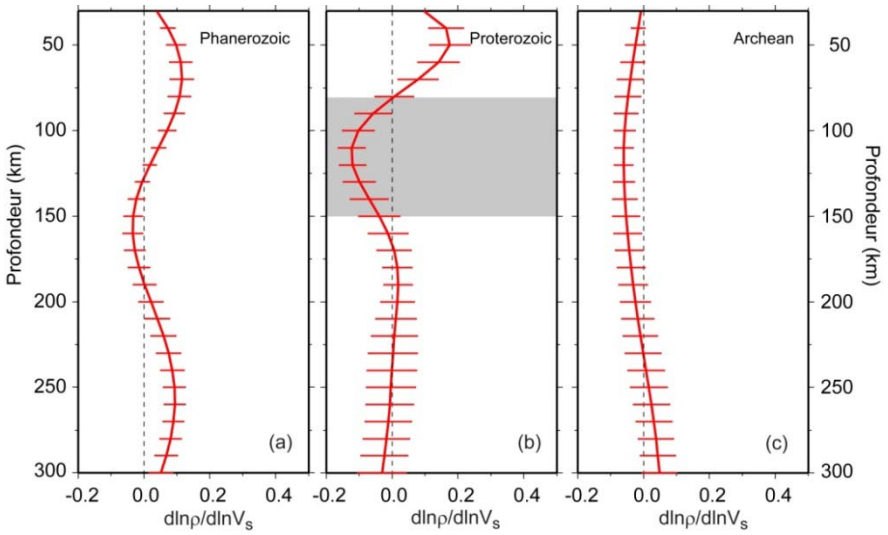

Figure 2.7 – Profil du facteur d'échelle $d\ln\rho/d\ln V_S$ pour chacune des trois principales provinces tectoniques australienne (van Gerven et al., 2004).

Sous les terrains phanérozoïques (les plus jeunes), ζ et positif et s'annule vers 120 km de profondeur (Figure 2.7a), ce qui correspond à la base de la lithosphère continentale vue par les ondes de surfaces (Simons et al. (2002)). Sous les terrains Archéens (les plus anciens), on s'attend à des valeurs négatives de ζ sur un large intervalle de profondeurs, liées à de fortes anomalies chimiques. C'est effectivement le cas (Figure 2.7c), mais l'amplitude de ζ est relativement faible, de l'ordre de grandeur des barres d'erreurs. De plus, dans cette région, AUS04-Vs est mal résolu. Difficile donc, d'être affirmatif. Par contre, sous les terrains protérozoïque (d'âge intermédiaire), ζ est clairement négatif entre 90 et 150 km de profondeur (Figure 2.7b). Notons que dans cette région, la lithosphère continentale est localisée un peu plus profondément, vers $z = 200$ km.

2.4 La tectosphère et la stabilité des racines continentales

Globalement, les études qui constituent ce chapitre apportent de l'eau au moulin de la tectosphère. Pour compenser le refroidissement des racines continentales, et éviter qu'elles ne sombrent dans le manteau, les racines continentales doivent être appauvries en matériau dense. Les éléments tels que le fer, l'aluminium et le calcium ont tendance à se concentrer dans le mélange fondu, qui forme ensuite la croûte, et se retrouvent donc en moindre quantité la lithosphère continentale. Cette hypothèse n'est pas nouvelle, puisqu'elle a été formulée il-y-a plus de trente ans (Jordan, 1975, 1978). Elle comporte toutefois une faiblesse, car elle n'explique pas vraiment pourquoi les racines continentales n'ont pas ou peu subi de déformation pendant les 3 milliard d'années écoulés.

Il faut donc bien admettre que les racines continentales sont aussi plus rigides que la lithosphère qui les entoure. C'est ce que suggèrent les modèles numériques incluant des racines différenciées (p.e., Doin et al., 1997; deSmet et al., 1999). Comment renforcer les racines continentales ? L'hypothèse la plus séduisante est que les racines continentales sont appauvries en eau (Pollack, 1986), hypothèse également avancée pour expliquer l'absence de tectonique des plaques sur une autre planète du système solaire, Vénus. L'eau est extraite des roches du manteau lors leur fusion partielle, en restant préférentiellement dans le mélange fondu, puis en remontant en surface. Bien qu'il y ait fusion partielle, le résultat net est une augmentation de la viscosité du manteau résiduel, puisqu'il est appauvri en eau (Karato, 1986; Hirth et Kohlstedt, 1996). À l'Archéen, le manteau, plus riche en eau et plus chaud que le manteau actuel, aurait fondu (partiellement) plus profondément, laissant place à une lithosphère plus rigide et moins dense.

Le contraste de viscosité avec ces racines et la lithosphère 'régulière' est sans doute important pour expliquer le peu de déformation qu'elles ont subie, mais n'est pas nécessaire

à leur stabilité (Jaupart et al. 2007). En absence de variations latérales de viscosité (p.e. liées aux variations de température), la stabilité des racines continentales est principalement contrôlée par leur flottaison et leur nombre de Rayleigh. Ce dernier est à son tour contrôlé par l'épaisseur de la racine. Une hypothèse intéressante, basée sur une analyse de stabilité linéaire et des expériences analogiques de convection thermochimique, est que les racines continentales seraient proches de leur seuil d'instabilité (Cottrell et al., 2004; Jaupart et al., 2007). Dans ce cas de figure, elles pourraient être animées par des oscillations verticales successives sur des échelles de temps de quelques centaines de million d'années, évènements qui contribueraient à la croissance des continents. Un paramètre supplémentaire à prendre en compte est la production de chaleur interne dans la racine, car il y modifie le profil de température (Michaut et Jaupart, 2007). Les racines continentales pourraient ainsi ajuster naturellement leur épaisseur et leur production de chaleur de façon à rester dans leur domaine de stabilité.

Reste à estimer l'influence des variations de viscosité avec la température, qui dans le cas de la convection purement thermique est d'accroitre la stabilité de la couche limite thermique. Dans le cas de la convection thermochimique, on s'attend donc à ce que l'appauvrissement en éléments denses nécessaire pour stabiliser la racine soit moins élevé, ce que semble indiquer notre analyse simplifiée (§ 2.2.2, équation 2.12). Une étude plus détaillée doit cependant être menée pour reproduire numériquement les expériences de Jaupart et al. (2007), et pour les étendre au cas d'un fluide dont la viscosité dépend fortement de la température.

2.5 Limites et perspectives

La principale difficulté rencontrée par la méthode développée dans ce chapitre est qu'elle ne contraint qu'une partie seulement des anomalies de densité, plus précisément celle qui est corrélée aux anomalies de vitesse sismiques de cisaillement. Cela résulte de ce que l'on impose un même modèle radial du facteur de calibration ζ pour toute une région (p.e., les continents dans leur ensemble, ou les cratons, ou encore les océans), que l'on peut comprendre comme une moyenne régionale de ζ. Idéalement, il faudrait calculer un profil de ζ en chaque point du modèle, ce qui est difficilement réalisable car le problème devient alors totalement sous-déterminé. En imposant un même profil de ζ à toute une région, on suppose implicitement que l'origine des anomalies de vitesse et de densité est de même nature partout à l'intérieur de cette région. La proportion entre les contributions d'origine thermique et les contributions d'origine chimique y est partout identique, et les anomalies de température et de composition sont parfaitement corrélées. Il n'y a, bien sûr, pas de

raison physique à ce qu'il en soit ainsi. Sauf si les anomalies de vitesse sismiques sont d'origine purement thermique, ce qui ne semble pas être le cas.

La définition d'une valeur moyenne de ζ pour une région donnée n'est cependant pas complètement dénuée de signification, si cette région thermochimiquement homogène. C'est probablement le cas de la lithosphère continentale formée à l'Archéen (la tectosphère), qui résulte sans doute de l'extraction massive d'éléments denses et d'eau. La lithosphère océanique résulte de processus d'extraction qui varient peu d'un point à l'autre des rides océaniques, et constitue donc aussi un ensemble cohérent. Le profil global obtenu pour les continents (Figure 2.3, en brun) est plus contestable, car il inclut des portions de lithosphère continentale formées plus récemment, au Protérozoïque puis au Phanérozïque, probablement moins marquées par l'appauvrissement en éléments lourds. Si la résolution des modèles tomographiques le permet, on lui préférera des profils intra-continentaux pour chacune de ces grandes provinces tectoniques, comme ce qui a été tenté pour l'Australie (van Gerven et al., 2004).

Dans le chapitre suivant, nous verrons l'ambiguïté qu'il y a à utiliser les rapports sismiques (dont ζ fait parti). Une partie de cette ambiguïté est liée, on vient de le voir, à ce que l'on utilise des valeurs moyennes régionales ou globales. Une autre difficulté est liée à la définition même de ces quantités : elles sont indéfinies ou très mal contrainte lorsque le dénominateur (ici, les anomalies relatives de vitesses de cisaillement) est nul ou proche de zéro. Néanmoins, les faibles valeurs de ζ (par rapport aux valeurs attendues dans le cas d'une origine purement thermique des vitesses sismiques), permettent de diagnostiquer avec une certaine assurance, la présence de fortes variations de composition dans la lithosphère continentale.

Etant donné ce qui vient d'être dit, on peut se demander si les études basées sur la calibration des anomalies de densité à partir des anomalies de gravité ont encore de l'avenir. Tout dépend de ce que l'on veut leur faire dire. Souhaite-t-on simplement déterminer un ou des profils de ζ pour une région donnée, ou avoir une idée approximative des anomalies de température et de composition dans cette région ? La méthode développée dans ce chapitre est sans doute utilisable, moyennant quelques améliorations, notamment l'apport de contraintes supplémentaires sur la densité (par exemple, les anomalies de vitesse d'onde de compression, qui, comme les anomalies de vitesse d'onde de cisaillement, peuvent se décomposer en une contribution thermique et une contribution chimique, ou la topographie dynamique, qui, moyennant l'hypothèse d'une compensation isostatique de la croûte, peut être reliée à la topographie observée (p.e., Forte et al., 1993), pour laquelle on dispose d'une excellente couverture), et sur la température (à l'aide du flux de chaleur en surface, p.e., Artemevia et Mooney (2001); Perry et al. (2006)). Il sera aussi souhaitable de

définir une paramétrisation plus convenable des anomalies de composition, par exemple en termes de variations en grenat, dont les effets sont proches de ceux des variations en fer. Souhaite-t-on cartographier précisément les anomalies de température et de composition dans une région donnée ? Il est alors indispensable de contraindre les anomalies de densité avec des informations indépendantes des anomalies de vitesses sismiques. La combinaison de modes propres et d'ondes de surface semble être une voie prometteuse (p.e., Resovsky et Trampert, 2003), mais la résolution latérale et verticale des modèles existant interdit pour le moment une étude détaillée de la lithosphère continentale.

Bibliographie

Artemevia, I.M., et W.D. Mooney, 2001. Thermal thickness and evolution of Precambrian lithosphere: a global study, *J. Geophys. Res.*, **106**, 16387-16414.

Cottrell, E., C. Jaupart, et P. Molnar, 2004. Marginal stability of thick continental lithosphere, *Geophys. Res. Lett.*, **31**, L18612, doi 10.1029/2004GL020332.

Davaille, A., et C. Jaupart, 1993. Transient high-Rayleigh number thermal convection with large viscosity variations, *J. Fluid Mech.*, **253**, 141-166.

Deschamps, F., et C. Sotin, 2000. Inversion of two-dimensional numerical experiments for a fluid with strongly temperature-dependent viscosity, *Geophys. J. Int.*, **143**, 204-218.

Deschamps, F., R. Snieder, et J. Trampert, 2001. The relative density-to-shear velocity scaling in the uppermost mantle, *Phys. Earth Planet. Int.*, **124**, 193-211.

Deschamps F., J. Trampert et R. Snieder, 2002. Anomalies of temperature and iron in the uppermost mantle inferred from gravity data and tomographic models, *Phys. Earth Planet. Int.*, **129**, 245-264.

deSmet, J., A.P. van den Berg, et N.J. Vlaar, 1999. The evolution of continental roots in numerical thermo-chemical mantle convection models including differentiation by partial melting, *Lithos*, **48**, 153-170.

Doin, M.-P., L. Fleitout, et U.R. Christensen, 1997. Mantle convection and stability of depleted and undepleted continental lithosphere, *J. Geophys. Res.*, **102**, 2771-2787.

Dziewonski, A.M., et D.L. Anderson, 1981. Preliminary Reference Earth Model, *Phys. Earth Planet. Inter.*, **25**, 297-356.

Forte, A.M., et W.R. Peltier, 1987. Plate tectonics and aspherical Earth's structure : the importance of poloidal -toroidal coupling, *J. Geophys. Res.*, **92**, 3645-3679.

Forte, A.M., et W.R. Peltier, 1991. Viscous flow models of global geophysical observables. I. Forward problems, *J. Geophys. Res.*, **96**, 20131-20159.

Forte, A.M., W.R. Peltier, A.M. Dziewonski et R.L. Woodward, 1993. Dynamic surface topography: a new interpretation based upon mantle flow models derived from seismic tomography, *Geophys. Res. Lett.*, **20**, 225-228.

Forte, A.M., et A.C. Perry, 2000. Seismic-geodynamic evidence for a chemically depleted continental tectosphere, *Science*, **290**, 1940-1944.

Forte, A.M., et J.X. Mitrovica, 2001. Deep-mantle high-viscosity flow and thermochemical structure inferred from seismic and geodynamic data, *Nature*, **410**, 1049-1056.

Godey, S., Deschamps F., J. Trampert et R. Snieder, 2004. Thermal and compositional anomalies beneath the North American continent, *J. Geophys. Res.*, **109**, B01308, doi: 10.1029/2002JB002263.

Hager, B.H., et M.A. Richards, 1989. Long wavelength variations in Earth's geoid: physical models and dynamical implications, *Philos. Trans. R. Soc. Lon. A*, **328**, 309-327.

Hirth, G., et D.L. Kohlstedt, 1996. Water in the oceanic upper mantle: implication for rheology, melt extraction and the evolution of the lithosphere, *Earth Planet. Sci. Lett.*, **144**, 93-108.

Isaac, D.G., 1992. High-temperature elasticity of iron-bearing olivines, *J. Geophys. Res.*, **97**, 1871-1885.

Jaupart, C., P. Molnar, et E. Cottrell, 2007. Instability of a chemically dense layer heated from below and overlain by a deep less viscous fluid, *J. Fluid Mech.*, **572**, 433-469.

Jordan, T.H., 1975. The continental tectosphere, *Rev. Geophys. Space Phys.*, **13**, 1-12.

Jordan, T.H., 1978. Composition and development of the continental tectosphere, *Nature*, **274**, 544-548.

Karato, S.-I., 1986. Does partial melting reduce the creep strength of the upper mantle?, *Nature*, **319**, 309-310.

Karato, S.-I., 1993. Importance of anelasticity in the interpretation of seismic tomography, *Geophys. Res. Lett.*, **20**, 1623-1629.

Lemoine, F.G., S.C. Kenyon, J.K. Factor, et al., 1998. The development of the joint NASA GSFC and National Imagery Mapping Agency (NIMA) geopotential model EGM96, NASA/TP-1998-206861, NASA, GSFC, Greenbelt, Maryland 20771.

Lenardic, A. et L.-N. Moresi, 1999. Some thoughts on the stability of cratonic lithosphere: effects of buoyancy and viscosity, *J. Geophys. Res.*, **104**, 12747-12748.

Michaut, C., et C. Jaupart, 2007. Secular cooling and thermal structure of continental lithosphere, *Earth Planet. Sci. Lett.*, **257**, 83-93.

Minster, J.B., et D.L. Anderson, 1981. A model of dislocation-controlled rheology for the mantle, *Philos. Trans. R. Soc. London*, **299**, 319-356.

Mitrovica, J.X., et A.M. Forte, 1997. Radial profile of the mantle viscosity: results from the joint inversion of convection and postglacial observables, *J. Geophys. Res.*, **102**, 2751-2769.

Moresi, L.-N., et V.S. Solomatov, 1995. Numerical investigation of 2D convection with extremely large viscosity variations, *Phys. Fluids*, **7**, 2154-2162.

Nataf, H.-C., et Y. Ricard, 1996. 3SMAC: an a-priori tomographic model for upper mantle based on geophysical modeling, *Phys. Earth Planet. Inter.*, **95**, 101-122.

Perry, A.C., A.M. Forte, et D.W.S. Eaton, 2003. Upper-mantle thermochemical structure beneath North America from seismic-geodynamic flow models, *Geophys. J. Int.*, **154**, 279-299.

Perry, H.K.C., C. Jaupart, J.-C. Mareschal, et N.M. Shapiro, 2006. Upper-mantle velocity-temperature conversion and composition determined from seismic refraction and heat flow, *J. Geophys. Res.*, **111**, doi: 10.1029/2005JB003921.

Polet, J., et D.L. Anderson, 1995. Depth extent of cratons as inferred from tomographic studies, *Geology*, **23**, 205-208.

Pollack, H.N., 1986. Cratonization and thermal evolution of the mantle, *Earth Planet. Sci. Lett.*, **80**, 175-182.

Resovsky, J.S., et J. Trampert, 2003. Using probabilistic seismic tomography to test mantle velocity-density relationships, *Earth Planet. Sci. Lett.*, **215**, 121-134.

Ricard, Y., L. Fleitout, et C. Froideveaux, 1984. Geoid heights and lithospheric stresses for a dynamic Earth, *Ann. Geophys.*, **2**, 267-286.

Simons, F.J., R.D. van der Hilst, J.-P. Montagner, et A. Zielhuis, 2002. Multimode Rayleigh-wave inversion for heterogeneity and azimuthal anisotropy of the Australian upper mantle, *Geophys. J. Int.*, **151**, 738-754.

van Gerven L., F. Deschamps, et R.D. van der Hilst, 2004. Geophysical evidence for chemical variations in the Australian continental mantle, *Geophys. Res. Lett.*, **31**, L17607, doi: 10.1029/2004GL020307.

Woodhouse, J.H. et J. Trampert, 1995. Global upper mantle structure inferred from surface wave and body wave data, *EOS Trans AGU*, p. F422.

ELSEVIER

Physics of the Earth and Planetary Interiors 124 (2001) 193–211

PHYSICS OF THE EARTH AND PLANETARY INTERIORS

www.elsevier.com/locate/pepi

The relative density-to-shear velocity scaling in the uppermost mantle

Frédéric Deschamps*, Roel Snieder[1], Jeannot Trampert

Department of Geophysics, Utrecht University, Budapestlaan 4, P.O. Box 80021, 3508 TA Utrecht, The Netherlands

Received 25 October 2000; received in revised form 12 March 2001; accepted 15 March 2001

Abstract

We perform inversions of gravity data (geopotential model EGM96) and seismic tomography model (S16RLBM) for the scaling factor (ζ), which relates relative density anomalies to relative S-wave velocity anomalies. The gravity data and tomographic model are anti-correlated below continents down to a depth of $z = 200$ km. This anti-correlation is not present below oceans. Except for smoothness, which is controlled by a damping factor, no a priori information is added to the inversion. Data are filtered between degrees $\ell = 11$ and $\ell = 16$ of the spherical harmonic expansion. This spectral window is well suited for the study of intermediate-size (2000–4000 km) anomalies in the uppermost mantle. Calculations are made separately for sub-continental and sub-oceanic mantle. The sub-continental and sub-oceanic scaling factors are significantly different at depths shallower than 260 km. In both cases, the magnitude of ζ is around 0.05. The sub-continental scaling factor has a positive root down to $z = 220$ km, whereas the sub-oceanic scaling factor yields positive values down to $z = 140$ km only. At depth shallower than 350 km, models of ζ do not depend on the damping factor or the viscosity model. At depths greater than 350 km, the resolution of $\zeta(z)$ decreases significantly and low degrees ($\ell = 2$–4) add information from large-scale anomalies and from the lower mantle. As a result, the shape and values of ζ for $\ell = 2$–16 and $\ell = 11$–16 are significantly different at depths greater than 350 km. A possible explanation of the discrepancies between the sub-continental and sub-oceanic scaling factor is that intermediate-scale anomalies are more important in the continental uppermost mantle than in the oceanic uppermost mantle. © 2001 Elsevier Science B.V. All rights reserved.

Keywords: S-wave velocity anomalies; Density anomalies; Mantle structure

1. Introduction

The density (ρ) and the S-wave velocity (V_S) of the Earth's mantle are both related to temperature, composition and pressure. Therefore, the inference of the density structure from V_S-anomalies is not straightforward. To make a crude diagnostic of the origin of the anomalies, one can use a scaling factor (ζ) defined as the ratio of the relative density variations to the relative V_S-anomalies.

$$\zeta(r,\theta,\varphi) = \frac{\partial \ln \rho(r,\theta,\varphi)}{\partial \ln V_S(r,\theta,\varphi)} \tag{1}$$

Purely thermal anomalies result in positive values of ζ, because an increase (decrease) of temperature lowers (raises) both the density and the shear velocity. Extrapolations of experimental data for olivine yield values of ζ between 0.35 and 0.45, depending on temperature (Isaac et al., 1989; Isaac, 1992). Karato (1993) accounted for anelasticity and found

* Corresponding author.
E-mail address: deschamp@geo.uu.nl (F. Deschamps).
[1] Present address: Department of Geophysics, Colorado School of Mines, Golden, CO 80401, USA.

0031-9201/01/$ – see front matter © 2001 Elsevier Science B.V. All rights reserved.
PII: S0031-9201(01)00199-6

smaller values: $0.2 \leq \zeta \leq 0.3$ in the upper mantle. Vacher et al. (1996) have computed values of ζ using a simplified mineralogical model of the upper mantle and temperature distributions predicted by isoviscous convection. They found values of ζ ranging between 0.42 at the surface, and 0.37 at $z = 660$ km depth. To determine ζ in the mantle, one needs two independent data sets, which constrain seismic velocity and density, respectively. Here, we used a global S-wave velocity model and geodetic data.

Seismic tomography of the upper mantle yields high-velocity roots below continents, but not below oceans (for recent S-wave models see Woodhouse and Trampert, 1995; Li and Romanowicz, 1996; Su and Dziewonski, 1997; Ritsema et al., 1999). This difference was first pointed out by Jordan (1975), who proposed that material in the sub-continental mantle is colder than in the sub-oceanic mantle. The increase of density induced by the relatively low temperature is balanced by differences in the respective chemical composition of the sub-continental and sub-oceanic mantle. Forte et al. (1994a) computed a radial model of ζ related to the continent–ocean anomalies of seismic velocities, and arrived at similar conclusions.

Inversions of gravity data and tomographic models have been performed (e.g. King and Masters, 1992; Kogan and McNutt, 1993; Forte et al., 1994a,b) to investigate chemical differences in the mantle. These studies are based on flow models driven by density anomalies, and they use Eq. (1) to convert velocity anomalies into density anomalies. However, King and Masters (1992) and Kogan and McNutt (1993) have assumed a constant value of ζ throughout the mantle. Forte et al. (1994a,b) have imposed the shape of the function $\zeta(r)$, and inverted gravity data for the parameters describing this curve. Moreover, the spatial resolution of these studies is limited to the spherical harmonic degrees less or equal to $\ell = 8$ (Forte et al., 1994a,b) or $\ell = 12$ (Kogan and McNutt, 1993). Low degrees of the gravity anomalies depend strongly on the structure of the deep mantle, and are weakly influenced by medium-size ($L \sim 2000$–4000 km) anomalies in uppermost mantle ($z < 400$ km).

In the present study, we invert V_S-anomalies and gravity anomalies for a radial model of ζ without assuming a priori values or shape. We have used the global S-wave model S16RLBM (Woodhouse and Trampert, 1995), which is expressed in a spherical harmonic expansion up to degree and order 16, and the geoid model EGM96 (Lemoine et al., 1998). Calculations are made separately for oceanic and continental regions. It turns out that ζ has positive values down to $z = 220$ km below continents, and down to $z = 140$ km below oceans. At depths greater than 350 km, ζ is not well constrained. A variety of tests suggest that these results are robust.

2. Method and data

Inversions presented in this paper are carried out using a relationship between the gravity anomalies (δg), the V_S-anomalies (δV_S) and the scaling factor (ζ). For each degree ℓ of the spherical harmonic expansion, the gravity anomaly (δg_ℓ) is related to the integrated density anomaly ($\delta \rho_\ell$) weighted by the geoid kernels (G_ℓ) (e.g. Forte and Peltier, 1987).

$$\delta g_\ell(\theta, \varphi) = \frac{3 g_0}{\bar{\rho} R} \frac{\ell - 1}{2\ell + 1} \int_{r_{\mathrm{CMB}}}^{R} G_\ell(r) \delta \rho_\ell(r, \theta, \varphi)\, \mathrm{d}r \quad (2)$$

where R and $\bar{\rho}$ are the Earth's radius and mean density, r_{CMB} the radius of the core, and g_0 the acceleration of gravity at the surface.

The geoid kernels (G_ℓ) describe the geoid response to a given density anomaly located at a given depth, and they depend on mantle dynamics. In the present study, we have computed these kernels following the method proposed by Forte and Peltier (1991). The conservation of mass, momentum, and the stress–strain relationship are expanded in terms of generalized spherical harmonics and solved for the poloidal flow in a compressible mantle. This method accounts for radial viscosity variations, and therefore it is possible to test different dynamical models of the Earth's mantle. However, the effects due to the toroidal flow, which imply lateral viscosity variations, are not considered here. Fig. 1 represents geoid kernels for the viscosity profile MF2 developed by Mitrovica and Forte (1997). For degrees up to $\ell = 8$ (Fig. 1b), the geoid kernels have non-negligible values throughout the mantle. On the other hand, at higher degrees ($\ell > 10$) (Fig. 1c), the geoid kernels yield small values in the deep ($z > 1000$ km) mantle. Therefore, the lowest degrees of the gravity anomalies integrate density anomalies over the whole mantle, whereas degrees higher than

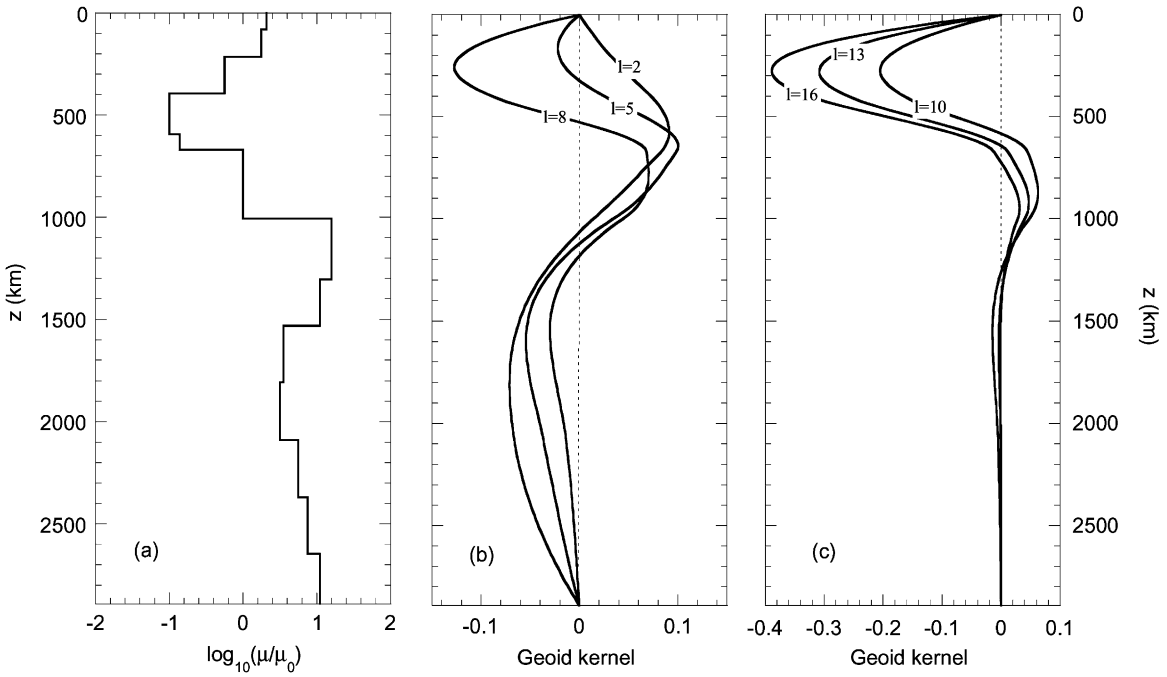

Fig. 1. Geoid kernels computed for the viscosity model MF2 (Mitrovica and Forte, 1997), and for degrees 2, 5 and 8 (left) and 10, 13 and 16 (right) of the spherical harmonic expansion. The computational method is fully described in Forte and Peltier (1991).

$\ell = 10$ are mostly sensitive to density anomalies in the upper mantle ($z < 700$ km). Similar conclusions can be drawn for other viscosity models, although the shape of the kernel changes. For a constant viscosity, kernels have negligible values in the deep mantle ($z > 1000$ km) only for degrees higher than $\ell = 20$.

Inserting Eq. (1) into Eq. (2), one can relate the density variations to the V_S-anomalies. If one assumes that the scaling factor does not vary laterally within a given region, Eq. (2) becomes

$$\delta g_\ell(\theta,\varphi) = \frac{3g_0}{\bar{\rho}R}\frac{\ell-1}{2\ell+1}\int_{r_{CMB}}^{R} G_\ell(r)\rho_0(r)\zeta(r) \times \frac{(\delta V_S)_\ell(r,\theta,\varphi)}{V_0(r)}\,dr \quad (3)$$

where $\rho_0(r)$ and $V_0(r)$ are the reference profiles for density and S-wave velocity, respectively. Note that one could have used geoid heights (δN) rather than gravity anomalies, since

$$\delta N_\ell(\theta,\varphi) = \frac{1}{\ell-1}\frac{R}{g_0}\,\delta g_\ell(\theta,\varphi) \quad (4)$$

The geoid is dominated by degrees $\ell = 2$ and $\ell = 3$. The root-mean-square (rms) amplitude of the geoid decreases sharply as the spherical harmonic degree increases: for $\ell = 10$ and $\ell = 20$, the rms amplitude is, respectively, 6.8 and 1.8% of that for $\ell = 2$. In comparison, the spectrum of the rms amplitude of gravity anomalies is much flatter: for $\ell = 10$ and $\ell = 20$, the rms amplitude is, respectively, 61.5 and 34.6% of that for $\ell = 2$. As a consequence, to sample structures smaller than ~4000 km, gravity anomalies carry more information than geoid heights.

Gravity and V_S-anomalies are then summed up for spherical harmonic degrees between ℓ_1 and ℓ_2.

$$\delta g(\theta,\varphi) = \sum_{\ell=\ell_1}^{\ell_2}\delta g_\ell(\theta,\varphi) \quad (5)$$

$$K(r,\theta,\varphi) = \frac{3\rho_0(r)g_0}{\bar{\rho}R}\sum_{\ell=\ell_1}^{\ell_2}\frac{\ell-1}{2\ell+1}\,G_\ell(r) \times \frac{(\delta V_S)_\ell(r,\theta,\varphi)}{V_0(r)} \quad (6)$$

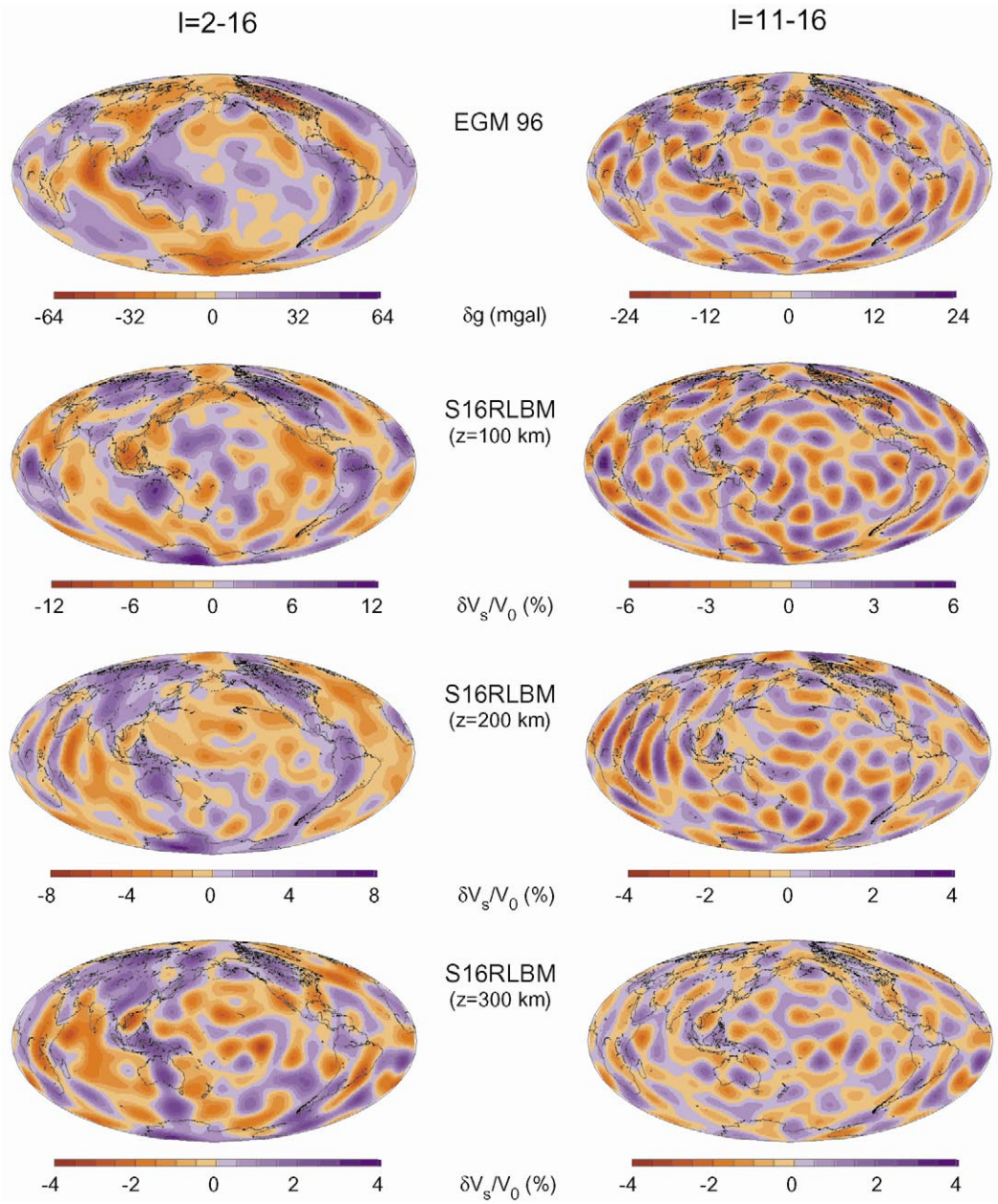

Fig. 2. Gravity anomalies from EGM96 (Lemoine et al., 1998) (top row) and S-wave velocity anomalies S16RLBM (Woodhouse and Trampert, 1995) at $z = 100$, 200 and 300 km depth. Models are filtered for degrees $\ell = 2$–16 (left column) and $\ell = 11$–16 (right column) of the spherical harmonics expansion.

Eq. (3) becomes

$$\delta g(\theta, \varphi) = \int_{r_{\mathrm{CMB}}}^{R} K(r, \theta, \varphi)\zeta(r)\,\mathrm{d}r \tag{7}$$

We have solved Eq. (7) for a radial model of scaling factor using a generalized inversion method (e.g. Snieder and Trampert, 1999). This method is outlined in Appendix A. Gravity anomalies constitute the data vector, while V_S-anomalies and geoid kernels are used to define the generalized inverse matrix. The inversion is regularized using a smoothness constraint with a damping factor ε. No other a priori information is introduced.

In the following calculations gravity anomalies and V_S-anomalies are sampled with an interval of $\mathrm{d}\theta$ in colatitude and $\mathrm{d}\varphi$ in longitude. To avoid over-sampling at high latitudes, the longitude interval ($\mathrm{d}\varphi$) increases from the equator to the poles, such that the surface element ($\mathrm{d}\Omega = \sin\theta \times \mathrm{d}\theta \times \mathrm{d}\varphi$) is constant. For instance, if $\mathrm{d}\varphi = 5^\circ$ on the equator, then $\mathrm{d}\Omega = 7.6 \times 10^{-3}$ steradian and $\mathrm{d}\varphi = 28.8^\circ$ at $\theta = 20^\circ$.

Inversions can be made for a selected geographical area. Here, we have computed radial models of ζ for oceans and continents separately. To define oceanic areas and continental areas, we have constructed a continent–ocean function derived from the 3SMAC tectonic regionalization (Nataf and Ricard, 1996). This data set has a resolution of $2^\circ \times 2^\circ$. The zero-mean continent–ocean function computed with the 3SMAC repartition is equal to 0.631 for continental areas and -0.369 for oceanic areas. The spherical harmonic expansion of this continent–ocean function is dominated by degrees 4 and 5. Hence, the continental and oceanic contributions to degrees 11 to 16 of gravity data and tomographic models are distinct.

The gravity data (δg) are tide-free, non-hydrostatic free-air gravity anomalies derived from the model EGM96 (Haagmans et al., 1998; Lemoine et al., 1998). EGM96 represents the Earth's gravitational potential up to spherical harmonic degree $\ell = 360$, and includes recent satellite tracking data and terrestrial gravity data. To remove the hydrostatic rotational flattening, we used the model of Nakiboglu (1982). The V_S-anomalies (δV_S) are provided by the global tomographic model S16RLBM (Woodhouse and Trampert, 1995), and the reference models of density ($\rho_0(r)$) and velocity ($V_0(r)$) are given by PREM (Dziewonski and Anderson, 1981). In S16RLBM, the three-dimensional V_S-anomalies structure is obtained from the inversion of Love and Rayleigh phases velocities (Trampert and Woodhouse, 1995) together with body waveform data. The model is expanded laterally in spherical harmonics up to degree $\ell = 16$ and vertically on a spline basis, leading to a vertical resolution of about 75 km in the top 400 km of the mantle. Fig. 2 shows EGM96 and S16RLBM at different depths for $\ell = 2$–16 and $\ell = 11$–16.

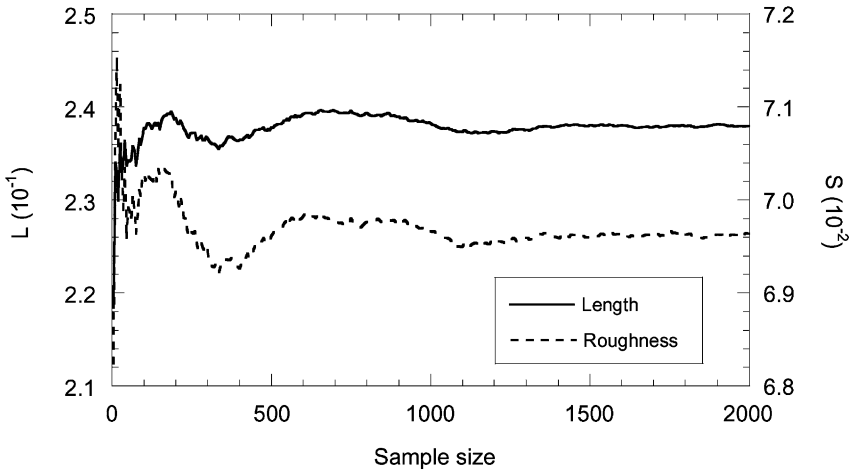

Fig. 3. Length ($\bar{L}$) and roughness ($\bar{S}$) of the mean model, as a function of the sample size. To reach stable values of $\bar{L}$ and $\bar{S}$, one must consider a large enough collection of perturbated models. This example corresponds to the sub-continental scaling factor represented in Fig. 6a.

The model S16RLBM does not provide error estimates on the V_S-anomalies. These errors would propagate to the values of ζ. To account for likely uncertainties, we have introduced a priori errors in the original tomographic model, which leads to an estimate of the variance in $\zeta(\sigma_\zeta)$. We have generated random errors with a Gaussian probability distribution (e.g. Press et al., 1989, pp. 191–203) and added them to the local values of the relative V_S-anomalies ($\delta V_S/V_0$). The distribution of these errors has a zero mean and a variance σ_{err}. In other words, 95% of the simulated errors have values within $\pm 2\sigma_{\text{err}}$. We thus obtain an ensemble of perturbed tomographic models, and invert each of these models for a perturbed radial model of the scaling factor (ζ_{per}). Finally, at each depth, we compute the mean value ($\bar{\zeta}$) and the variance (σ_ζ) over the collection of the estimated models ζ_{per}. To get statistically relevant values of the scaling factor, one must consider a large enough collection of perturbed models (sample size). A good test is provided by the length ($\bar{L}$) and the roughness (i.e. the norm of the derivative, $\bar{S}$) of the mean model (Appendix A). A satisfactory solution is reached when the values of $\bar{L}$ and $\bar{S}$ are independent of the sample size (Fig. 3).

3. Correlation between gravity and V_S-anomalies

At shallow depths, S16RLBM correlates with surface tectonics and yields strong continent–ocean differences down to $z = 250$ km depth (Woodhouse and Trampert, 1995). In the sub-continental mantle, between 60 and 180 km depth, S16RLBM is strongly anti-correlated with surface heat flow (Röhm et al., 2000). Röhm et al. (2000) used the depth consistency of S16RLBM to define a seismic lithosphere in the sub-continental mantle: the correlation of the V_S-anomalies with respect to the V_S-anomalies at a reference depth of 100 km falls off rapidly below 180 km. Here, we computed the correlation (C) between S16RLBM and the gravity anomalies derived from EGM96.

$$C(z) = \frac{1}{\sigma_{\delta g}\sigma_{\delta V_S}(z)\Omega}\int_\Omega \delta V_S(z,\theta,\varphi)\delta g(\theta,\varphi)\,\mathrm{d}\Omega \quad (8)$$

where the correlation is computed over the spatial domain Ω, $\sigma_{\delta V_S}(z)$ is the variance in the V_S-anomalies at depth $z = R - r$ and $\sigma_{\delta g}$ the variance in the gravity anomalies.

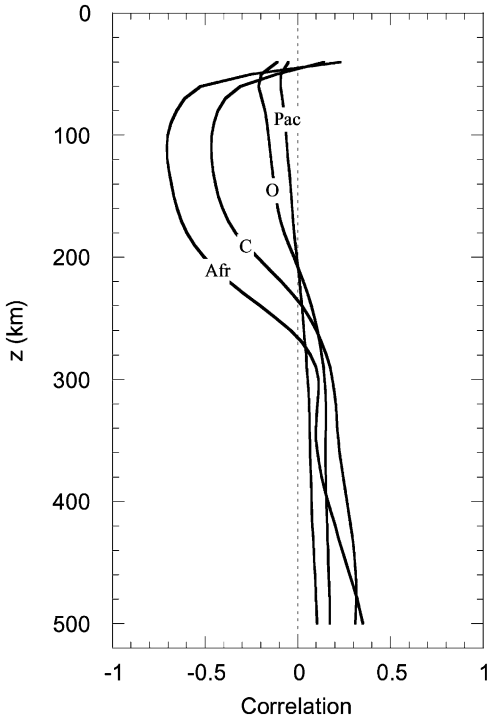

Fig. 4. Coefficient of correlation between S16RLBM V_S-anomalies and EGMG96 gravity anomalies as a function of depth, and for different regions. Data are filtered for the degrees $\ell = 11$–16 of the spherical harmonic expansion. C: all continental regions, O: all oceanic regions, Afr: Africa and Pac: Pacific. The resolution $\mathrm{d}\theta \times \mathrm{d}\varphi$ of the calculation is $2^\circ \times 2^\circ$ for regional areas, and $5^\circ \times 5^\circ$ for continents and oceans.

Fig. 4 shows the correlation as a function of depth for some regions. In the shallow sub-continental mantle, S16RLBM and EGM96 are anti-correlated (i.e. high δV_S correspond to low δg). For instance, the sub-African mantle yields a root between the depths $z = 70$ and $z = 180$ km, in which the value of C lies between -0.6 and -0.7 (Fig. 4). A similar root is observed in the whole-sub-continental mantle, although the anti-correlation is weaker (around -0.5). On the other hand, in the sub-oceanic mantle, we do not find a significant correlation between gravity and V_S-anomalies. In the sub-Pacific mantle, the correlation is between -0.1 and 0.1 at least down to $z = 500$ km. Higher correlation is seen in the shallow sub-Atlantic mantle (not shown in Fig. 4), but

in the whole sub-oceanic mantle, correlation remains small, between −0.2 and 0.2. We have also computed correlation between V_S-anomalies and geoid anomalies, and found results similar to those in Fig. 4.

The root observed in the sub-continental mantle is very similar in shape to that reported by Röhm et al. (2000). Thus, the seismic lithosphere is associated with negative gravity anomalies. Moreover, S-wave velocity profiles yield strong positive anomalies in the sub-continental mantle (Woodhouse and Trampert, 1995; Röhm et al., 2000). The strong anti-correlation between tomographic models and geodetic data suggests that the positive V_S-anomalies in the sub-continental mantle may be related to an excess of mass (positive density anomalies). However, it does not provide information about the origin of such an excess of mass. The pronounced anti-correlation between the surface heat flux and the tomographic model S16RLBM (Röhm et al., 2000) favors a thermal origin, but one cannot exclude compositional origin and other effects. For instance, accounting for anelasticity may reduce the amplitude of temperature anomalies associated with velocity anomalies (Karato, 1993).

4. Scaling factor in the uppermost mantle

4.1. Preferred model

We performed a series of 2000 inversions including simulated errors in the relative V_S-anomalies. This sample size is big enough to provide relevant values of the mean scaling factor (Fig. 3). We assumed a variance of the distribution of the errors (σ_{err}) equal to 2% for continental areas and 1% for oceanic areas. For $\ell = 2$–16, the mean value of the relative V_S-anomalies below continents (oceans) in the uppermost mantle varies between $\overline{\delta V_S/V_0} \sim 2\%$ (−1%) and $\overline{\delta V_S/V_0} \sim 0.5\%$ (−0.5%). For $\ell = 11$–16, these mean relative anomalies are about one order of magnitude smaller (solid curves in Fig. 6). Therefore, taking $\sigma_{err} = 2\%$ for continents and $\sigma_{err} = 1\%$ for oceans will simulate errors as large as 100% of the original tomographic model for $\ell = 2$–16, and even more if one considers $\ell = 11$–16. Such large simulated errors should cover most sources of possible real errors.

Geoid kernels were computed according to the viscosity model MF2 (Mitrovica and Forte, 1997), which results from joint inversion of gravity anomalies and relative sea level variations. For degrees higher than $\ell = 11$, the geoid kernels peak around $z = 250$ km depth (Fig. 1c), and have small values in the lower mantle. The lowest degrees ($\ell = 2$–8), on the other hand, have non-negligible values throughout the mantle. Moreover, for degrees lower than $\ell = 11$ the horizontal wavelength of the anomalies is larger than 4000 km. To get a good sampling of the shallow mantle ($z = 50$–400 km), we removed low degrees of gravity and V_S-anomalies. Here, data are summed up for the spherical harmonic degrees $\ell = 11$–16. Since geoid kernels for $\ell = 11$–16 have low values in the lower mantle, Eq. (7) is integrated from a depth of 1000 km up to the surface.

The damping factor (ε) controls the relative importance of a priori information (here, the smoothness) and data. To choose its value, we have performed a set of experiments in which the original (i.e. non-perturbed) V_S-anomalies are inverted for $\zeta(z)$ as a function of ε. The results are displayed on a trade-off curve (Fig. 5), by plotting the misfit of the reconstructed to observed gravity anomalies as a function of roughness of the estimated model. Usually, one defines the preferred model as the best compromise between the smoothness and the variance reduction. The trade-off curves in Fig. 5 have a hyperbolic shape, and therefore the preferred model is located on the respective elbow of these curves. According to this criterion, the variance reduction of the preferred continental model is equal to 30%, which corresponds to a damping factor around 400. The correlation between the observed and reconstructed gravity anomalies reaches 56%. For oceans, the variance reduction and the correlation are poorer (10 and 31%, respectively), and the preferred value of the damping is around 250. We did similar experiments for other spatial resolutions, and noted that for a given value of the variance reduction, ε is roughly multiplied by 2 as the spatial resolution is divided by 2.

The mean value ($\bar{\zeta}$) and the variance (σ_ζ) of the estimated model are shown in Fig. 6 for continents (left) and oceans (right). The sub-continental scaling factor (Fig. 6a) is positive down to $z = 220$ km, and has a local maximum around $z = 120$ km. It reaches a minimum at $z = 500$ km, and remains negative down to $z = 600$ km. However, the variance of the model increases with depth. The resolution matrix (Fig. 7)

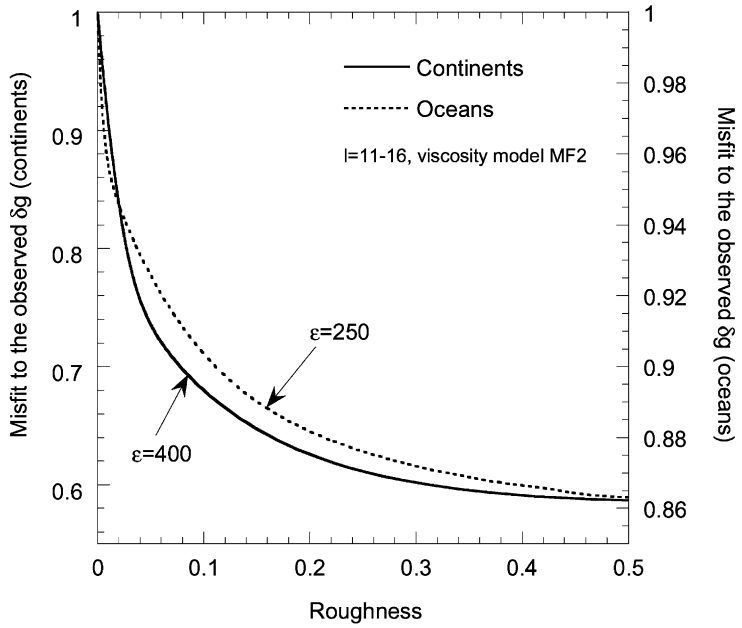

Fig. 5. Trade-off curve for the choice of the damping factor (ε), for continents (plain curve) and oceans (dashed curve). Inversions of gravity anomalies and original V_S-anomalies are carried out with different values of ε. The misfit to the observed gravity anomalies ($1-X$) is plotted as a function of the model roughness (S). Rough models yield a good variance reduction, whereas very smooth models have a poor variance reduction. A relevant value of ε should lie on the elbow of the curve in between these two end-members, as indicated by the arrows. Data were filtered out in the range $\ell = 11$–16, and the surface element was kept constant, with $d\theta = 5^\circ$ and $d\varphi = 5^\circ$ on the equator.

yields substantial smearing between 300 and 450 km depth. At depths greater than 450 km, the scaling factor is poorly resolved. This poor resolution has two origins. First, the geoid kernels for $\ell = 11$–16 peak in the layer $z = 100$–400 km, and have small values in the deeper mantle. In particular, the geoid kernels are close to zero around $z = 650$ km, and the resolution is poor around this depth. Second, the amplitude of the S16RLBM anomalies decreases rapidly at depths greater than about 400 km (Woodhouse and Trampert, 1995). Therefore, any interpretation concerning the transition zone ($z = 420$–670 km) and the lower mantle is difficult. We have also reconstructed gravity data from $\bar{\zeta}$ and the original V_S-anomalies. The variance reduction of this synthetic data set to the observed gravity anomalies is equal to 29.3%, which is close to the variance reduction obtained by inverting the original V_S-anomalies. The sub-oceanic scaling factor (Fig. 6b) decreases down to $z = 180$ km and is positive down to $z = 140$ km. In the layer $220 \leq z \leq 280$ km, it remains close to zero. The variance reduction to the observed gravity data is equal to 8.9%, which is significantly poorer than for continental areas. At depths greater than 260 km, the sub-continental and sub-oceanic scaling factors are close to each other.

One may note that the variance reduction of the observed to reconstructed gravity anomalies is quite poor. First, it must be noted that the damping imposes a low variance reduction. Second, most of the gravity signal is in low degrees. For $\ell = 11$–16 gravity anomalies have small absolute values, and therefore small absolute errors can lead to high relative errors. Moreover, the variance reduction compares reconstructed gravity anomalies to observed gravity anomalies, but it does not account for errors on the observed gravity anomalies ($\sigma_{\delta g}$), on the tomographic model ($\sigma_{\delta V_S}$), and on the inverted model of ζ (σ_ζ). To account for these errors, we performed a χ^2-test. For the whole Earth, and assuming $\sigma_{\delta g} = 0.15$ mgal, $\sigma_{\delta V_S}/\delta V_S = 10\%$ and the σ_ζ plotted in Fig. 6a, we find $\chi^2 = 4.3$. Therefore, the gravity anomalies predicted by our inverted model of scaling factor yield within $\pm 2\sigma_{\delta g}$ of the observed gravity anomalies. Note that because the correlation

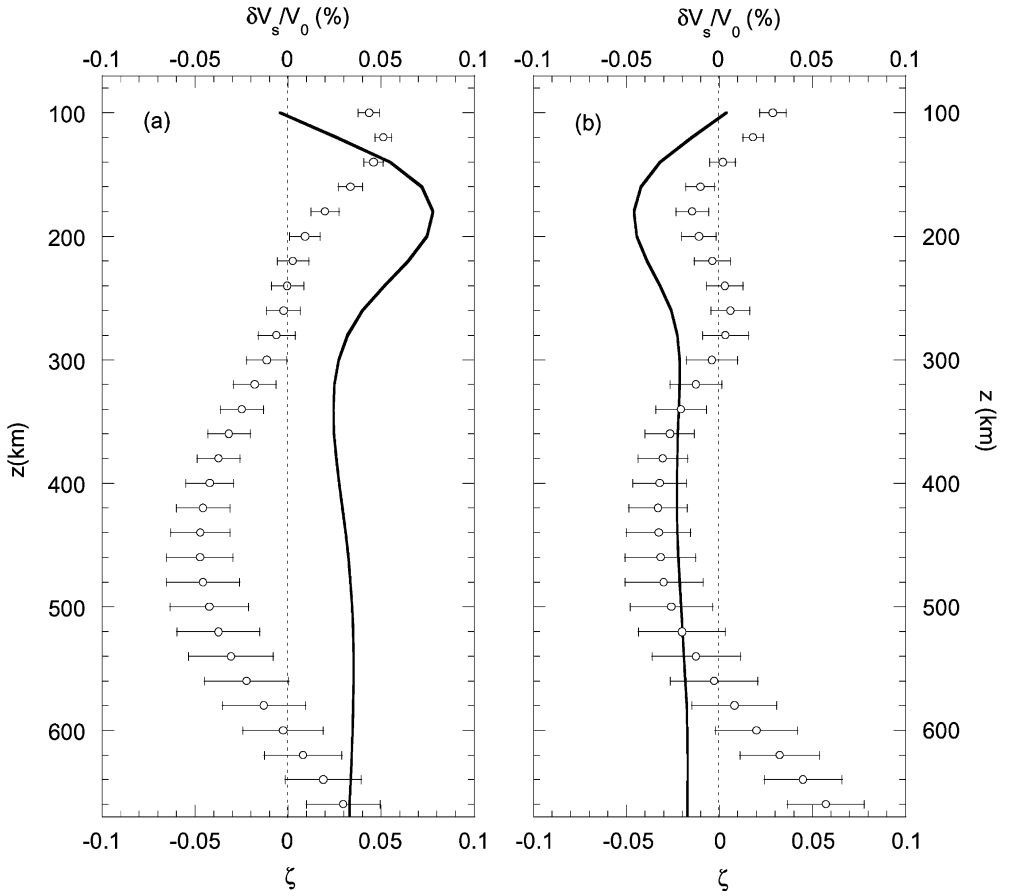

Fig. 6. Inverted scaling factor (ζ) in the sub-continental (a) and sub-oceanic (b) upper mantle. Open circles indicate the mean value of ζ, and the error bars represent the variance in ζ. The damping factor is equal to 400 and 250 for continents and oceans, respectively. Data are filtered for degrees $\ell = 11$–16, integration (7) is performed from $z = 1000$ km depth up to the surface, and the viscosity model is MF2. The bold curve represents the mean relative V_S-anomalies for degrees $\ell = 11$–16 as a function of depth below continents (a) and oceans (b). Note that these mean relative anomalies are roughly one order of magnitude smaller that of the total tomographic model.

between observed and reconstructed gravity anomalies is only about 50%, our model of $\zeta(z)$ cannot explain the observed gravity anomalies completely.

The bold plain curves in Fig. 6 represent the mean value of relative V_S-anomalies (for degrees $\ell = 11$–16) as a function of depth, in the sub-continental (left) and sub-oceanic (right) mantle. Clearly, these curves have very different shapes than those of the scaling factor. Therefore, the results of joint inversions do not yield simply the variations of V_S-anomalies with depth. Chemical, thermal and/or physical processes may be responsible for the change in the sign of ζ in the uppermost mantle, as well as for the difference between the sub-continental and sub-oceanic scaling factor.

Results in Fig. 6 were obtained for given values of some input parameters that may be unsuitable for the uppermost mantle. Therefore, to test the robustness of these results, it is important to evaluate the influence of parameters such as the smoothness and the radial viscosity model.

4.2. Damping factor (ε)

To evaluate the influence of a priori information on the estimated model of ζ, we performed other series

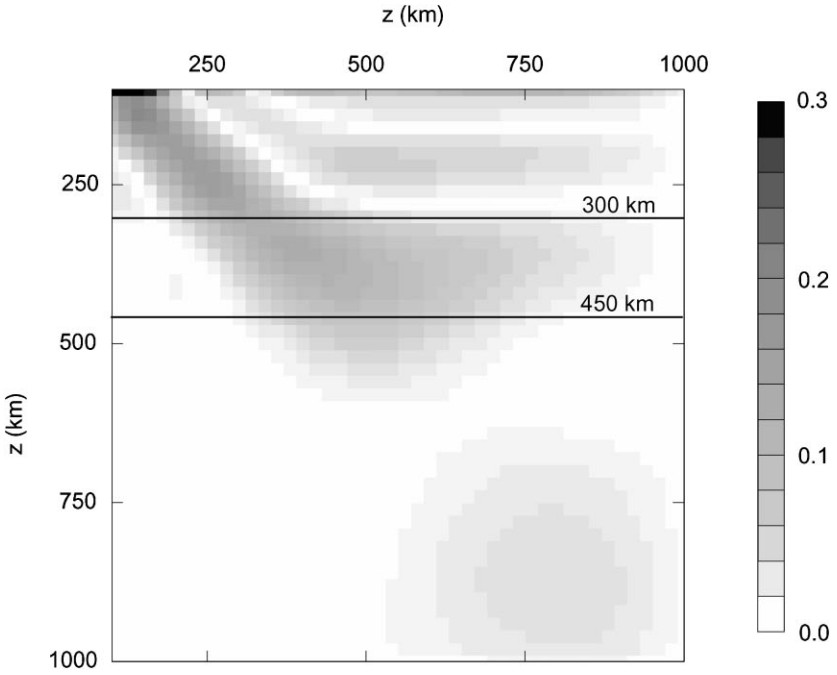

Fig. 7. Model resolution matrix for the preferred sub-continental scaling factor. Some smearing is present since $z = 300$ km depth (shallower horizontal line), and below $z = 450$ km the resolution is poor. In this example, original data are inverted for the sub-continental scaling factor in the window $\ell = 11$–16, and integration (7) is performed from $z = 1000$ km depth up to the surface. The damping factor is equal to 400. The viscosity model is MF2 and the element of surface is constant with $\mathrm{d}\varphi = 5^\circ$ on the equator.

of inversions with different values of the damping. For values of ε smaller than those of our preferred model (and therefore, for rougher estimated model), ζ becomes negative at shallower depths (Fig. 8). Similarly, for higher values of ε (not shown here), ζ changes sign deeper in the mantle. However, the shape of the function $\zeta(z)$ does not change dramatically. Rougher models result in slightly stronger radial variations in the layer 200–300 km, and significantly higher variances throughout the upper mantle. Variances are higher because a weaker damping allows bigger radial derivatives, and therefore wider ranges of values, for ζ. Note that the preferred models (dashed curves in Fig. 8) remain within these error bars. In other words, weaker a priori information does not induce dramatic changes in the shape and amplitude of ζ. Moreover, the difference between the sub-continental and sub-oceanic scaling factor is still present. Therefore, the damping factor is not a sensitive parameter. This result is important, since the determination of the best value of ε is subjective.

4.3. Viscosity model

We made additional calculations to estimate the influence of the viscosity profile. The viscosity model does not appear explicitly in Eq. (3), but it is required to compute the geoid kernels $G_\ell(r)$. The model MF2 (Mitrovica and Forte, 1997) was built to provide a good fit of both the long-wavelength gravity anomalies and the relaxation times estimated from postglacial uplift. The first alternative model we have considered (FDW, Fig. 9a) has been constructed by Forte et al. (1993) to provide good fit of the degree 2 of the geoid. We have then used the model M2 of Peltier (1996) (PM2 in Fig. 9a). This model results from inversion of relative sea level variations induced by the postglacial uplift only. In PM2, the viscosity in the mid-lower mantle is about 10 times that in the mid-upper mantle. Finally, we have considered a model predicted by numerical experiments of thermal convection (cv2D, Fig. 9a). This model consists of two layers representing the upper and lower mantle. The reference

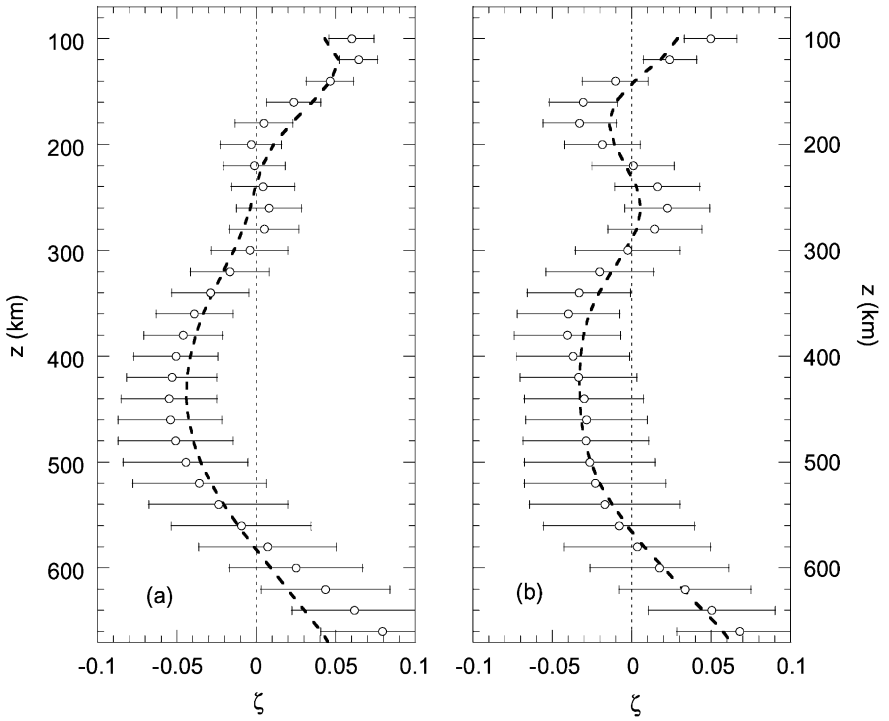

Fig. 8. Inverted scaling factor in the sub-continental (a) and sub-oceanic (b) upper mantle, for $\varepsilon = 200$ and $\varepsilon = 125$, respectively. The other parameters are the same as those in Fig. 4. The dotted curves represent the preferred sub-continental (a) and sub-oceanic (b) scaling factors.

viscosity of the lower layer is 10 times that of the upper layer, and the ratio of the top to the bottom viscosity of the upper and lower layer are 10^4 and 10^3, respectively. The viscosity is an exponential law of temperature, and temperature profiles are given by 2D-numerical experiments of convection (Deschamps and Sotin, 2000).

At depths shallower than 350–400 km, the scaling factors obtained for $\ell = 11$–16 and the viscosity models discussed above are very similar, for both sub-oceanic and sub-continental mantle (Fig. 9b and c). In particular, the depth at which the scaling factor becomes negative does not depend on the viscosity model. In each case, the sub-continental scaling factor has a local maximum around $z = 120$–140 km depth. In addition, if we consider the scaling factor obtained by inversion of the original V_S-anomalies, the variance reduction of the reconstructed to the observed gravity (or geoid) anomalies is nearly the same, whatever the viscosity model. At depths greater than 400 km, significant differences appear, depending on the viscosity model. To account for an eventual viscous layer at the top of the mantle, we modified the model MF2. Down to $z = 300$ km depth, we imposed $\mu/\mu_0 = 10^3$ (instead of $\mu/\mu_0 \sim 2$ in the original model) covering thus three orders of magnitude. Below 300 km, we let MF2 unchanged. However, inversions performed with this modified version of MF2 do not lead to significant differences in the model of scaling factor. Finally, we did an inversion in the (unlikely) case of a viscosity that decreases with depth (namely, the model symmetric to MF2 in respect with the $\log(\mu/\mu_0) = 0$ axis), and still found no significant differences down to $z = 400$ km depth. Thus, the nature of the scaling factor calculated in the uppermost mantle results from information in the data. Moreover, uncertainties on the radial model of viscosity do not broaden the variance in ζ.

The geoid kernels for degrees higher than $\ell = 10$ peak in the uppermost mantle and have small values at depth greater than 1000 km. This feature is

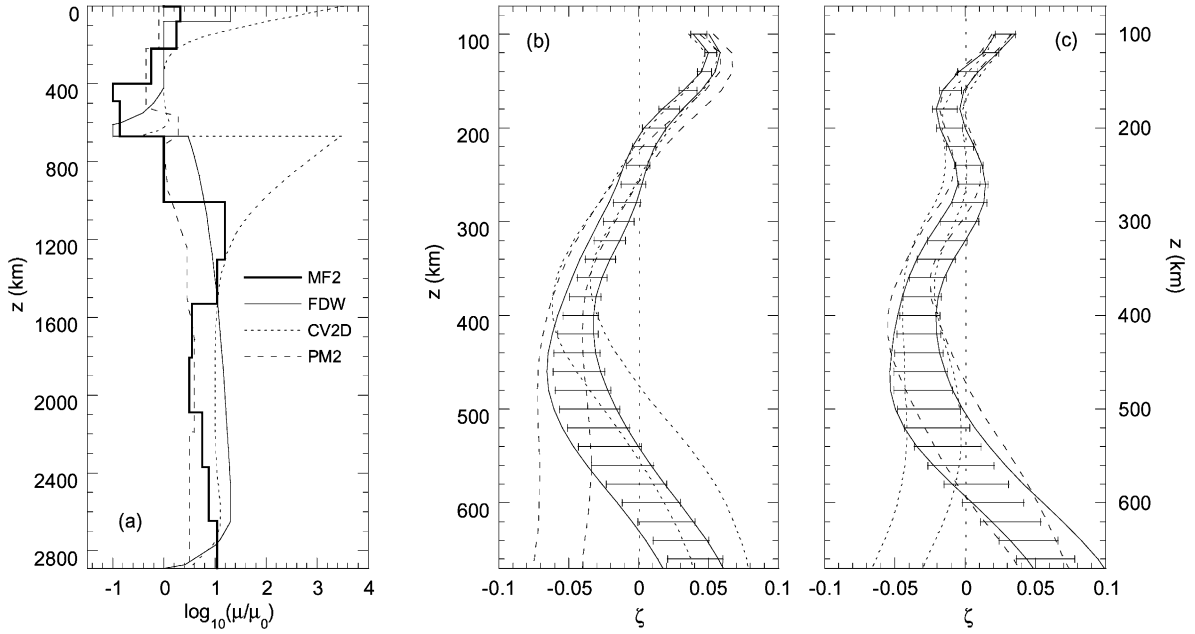

Fig. 9. Various possible viscosity profiles in the mantle (see text for references) (a); their corresponding inverted scaling factor in the sub-continental (b); and sub-oceanic (c) mantle. For each case, two curves are drawn, representing the minimal ($\bar{\zeta} - \sigma_\zeta$) and maximal ($\bar{\zeta} + \sigma_\zeta$) values of the scaling factor. Our preferred model (viscosity MF2) is indicated by the error bars. Data are filtered out for degrees $\ell = 11$–16, and Eq. (7) is integrated from $z = 1000$ km depth up to the surface. The damping factor is equal to 400 for continents, and 250 for oceans.

independent of the viscosity profile and may explain why, in the uppermost mantle, the model of scaling factor for $\ell = 11$–16 does not depend on this parameter. Indeed, by considering degrees $\ell = 2$–8 only we find that models of scaling factor for different viscosity profiles are slightly different even above $z = 400$ km. Some smaller differences are also present if one considers $\ell = 2$–16, but we do not observe dramatic changes in the shape and amplitude of ζ.

Previous inversions of tomographic models and geodetic data have focused on the determination of a suitable viscosity model for the mantle (King and Masters, 1992; Forte et al., 1993, 1994b). Such studies have imposed a priori values of the scaling factor based on laboratory measurement. However the present results suggest that at depths smaller than 400 km, the scaling factor is not sensitive to realistic variations in the viscosity model. Therefore, in the uppermost mantle, it is more relevant to impose a viscosity profile and to invert for the scaling factor than to do the opposite.

4.4. Wavelength of the heterogeneities

In Eq. (3), we have assumed that the scaling factor does not depend on the spherical harmonic degree. To test this assumption, we did additional inversions for different windows of the spherical harmonics expansion, including degrees lower than $\ell = 11$ (Fig. 10). Calculations were made for the viscosity model MF2, and appropriate values of the damping factor. Because low-degree kernels have non-negligible values throughout the mantle, the integration (7) was performed from the core-mantle boundary up to the surface. Obviously, for $\ell = 11$–16, modification of the integral bounds does not change the results of the inversion at all. Down to $z = 350$ km depth, the models of scaling factor for $\ell = 2$–16 and $\ell = 11$–16 are similar. At greater depths, on the other hand, they differ significantly. The model of ζ for degrees $\ell = 2$–8 only is different from the others even in the uppermost mantle. Finally, by removing the lowest degrees ($\ell = 2$–4), the scaling factor is in good agreement

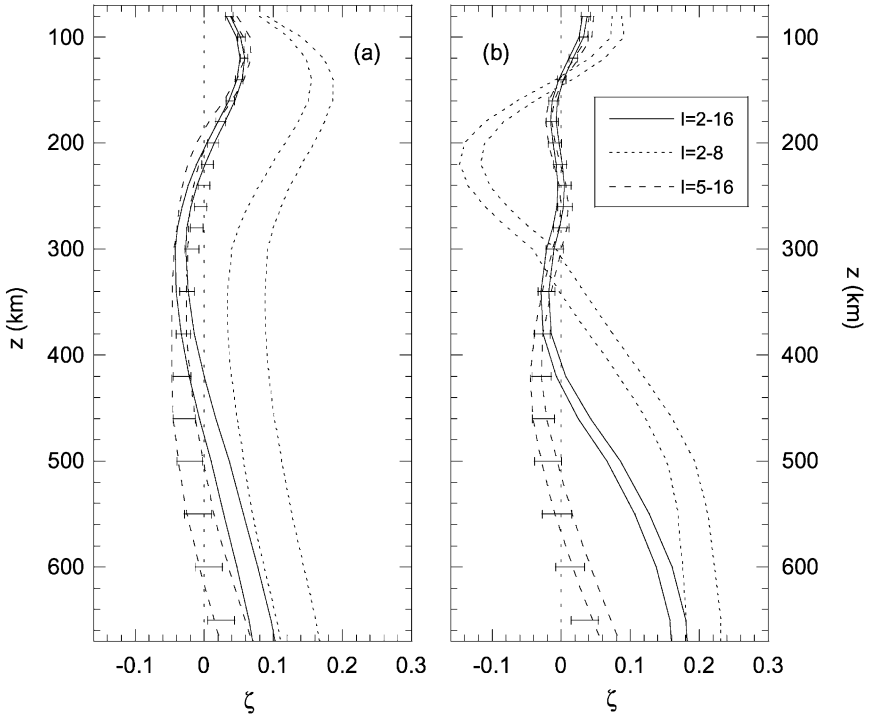

Fig. 10. Inverted scaling factor in the sub-continental (a) and sub-oceanic (b) mantle, for different windows of the data spectrum: $\ell = 2$–16, $\ell = 2$–8 and $\ell = 5$–16. For each case, two curves are drawn, representing the minimal $(\bar{\zeta} - \sigma_\zeta)$ and maximal $(\bar{\zeta} + \sigma_\zeta)$ values of the scaling factor. Our preferred model ($\ell = 11$–16) is indicated by the error bars. Eq. (7) is integrated from the core-mantle boundary up to the surface. For each calculation, the viscosity model is MF2. For continents (oceans) and $\ell = 2$–16, $\ell = 2$–8, $\ell = 5$–16 and $\ell = 11$–16, the damping factor is equal to 900, 450, 600 and 400 (500, 250, 450 and 250), respectively.

with the case $\ell = 11$–16 down to $z = 600$ km depth. In the deep mantle ($z \geq 350$ km), low degrees ($\ell = 2$–4) have therefore a strong influence on the scaling factor, but one can safely remove them to compute values of ζ in the uppermost mantle ($z \leq 350$ km).

A possible explanation is related to the shape of the geoid kernels and to the power spectrum of S16RLBM (Fig. 11). Down to $z = 300$ km depth, the low degrees ($\ell = 2$–4) do not dominate V_S-anomalies (Fig. 11a–c). In addition, the geoid kernels have small absolute values, compared to the higher degrees ($\ell = 8$–16) (Fig. 1b and c). For instance, in the layer $100 \leq z \leq 300$ km, $G_{\ell=2}$ increases from 0.1 to 0.05, whereas $G_{\ell=11}$ ranges between -0.16 and -0.26. At depths greater than 400 km, the dominant degree of V_S-anomalies is $\ell = 2$ (Fig. 11d and e). Moreover, at these depths, low degree geoid kernels have values comparable to or larger than those of the higher degrees. For low degrees, the absolute values of the quantity $K(r, \theta, \varphi)$ (Eq. (6)) at shallow depths are small, compared to those at depths greater than 400 km. As a result, the contribution of shallow depths to the gravity anomalies (Eq. (7)) is small, and ζ is not very well constrained. A similar effect happens for high degrees at depths greater than 350 km. The degree $\ell = 5$ dominates V_S-anomalies down to $z = 150$ km depth (Fig. 11a). However, the geoid kernel for $\ell = 5$ yields low values down to $z = 300$ km, and peaks around $z = 600$ km (Fig. 1b). For $\ell = 5$, the low geoid sensitivity balances the high V_S-signal, and the scaling factor for $\ell = 11$–16 is close to that for $\ell = 5$–16 (Fig. 10). This result emphasizes the robustness of the inversion.

The inversion is not very sensitive to parameters such as the viscosity profile and a priori information (smoothness in the present study). If one considers

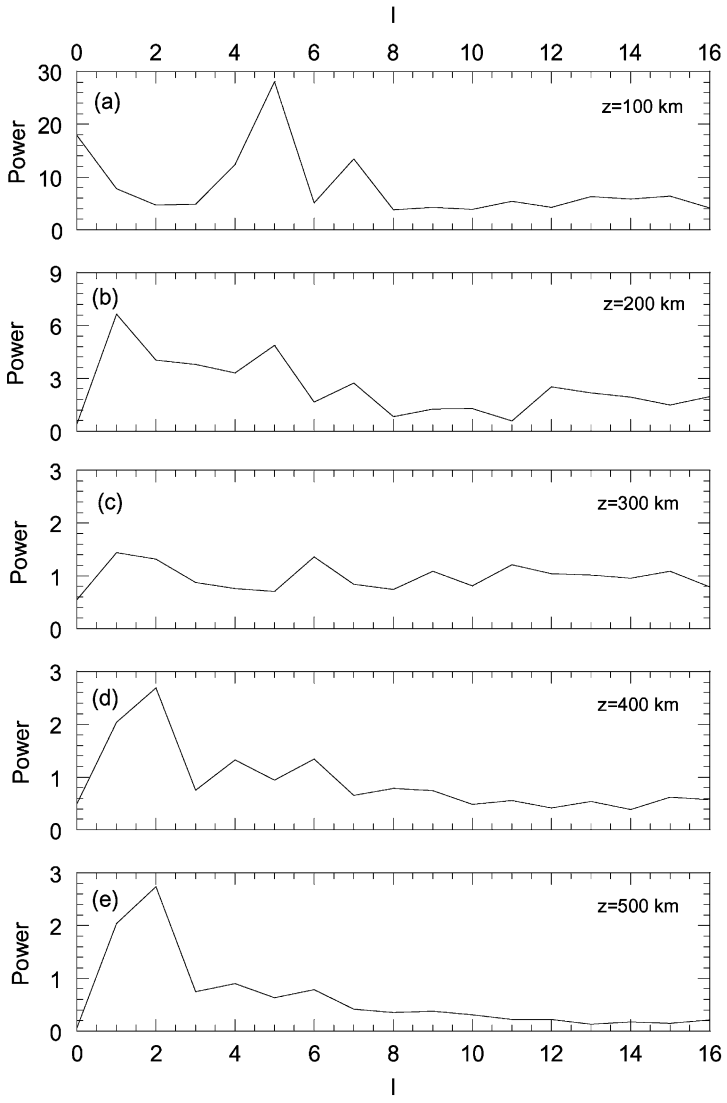

Fig. 11. Power spectrum of the global model S16RLBM at $z = 100$ km (a); $z = 200$ km (b); $z = 300$ km (c); $z = 400$ km (d); and $z = 500$ km (e). The dominant degrees are $\ell = 5$ down to $z = 150$ km, and $\ell = 2$ at depths greater than $z = 350$–400 km. In between these depths, the spectrum is flat.

different viscosity models and values of the damping factor, the shape and the amplitude of the function $\zeta(z)$ at depths shallower than 400 km does not change dramatically, and the continent–ocean difference is still present. Finally, we did calculations with the global S-wave model S20RTS (Ritsema et al., 1999), and found results very close to those obtained with S16RLBM in the uppermost mantle (small differences appeared in the amplitude of the scaling factor, but not in its shape). Therefore, we believe that the features reported in this section are quite robust.

5. Discussion

King and Masters (1992) assumed $\zeta = 0.4$ throughout the mantle, and inverted degrees $\ell = 2$–8 for the radial viscosity profile. By inverting S16RLBM and

EGM96 with their model MODLSHC, we have found a scaling factor and variance reduction similar to those obtained with the model MF2, for both $\ell = 2$–16 and $\ell = 11$–16. As shown in Section 4, in the uppermost mantle, inversions are more relevant for the scaling factor than for the radial viscosity model. Note that we do not account for lateral viscosity variations. Since in the uppermost mantle ζ does not depend strongly on the viscosity model, such lateral variations should only have limited consequences. The method used to compute geoid kernels (expansion of conservative equations in terms on generalized spherical harmonics) do not allow lateral variations of viscosity. However, an approximate and suitable way to account for lateral viscosity variations would be to consider regional studies with adapted viscosity models for each region.

Using gravity data up to $\ell = 12$, Kogan and McNutt (1993) performed joint inversions for Eurasia. They have tested different viscosity models depending on the region considered. Assuming a constant value for the scaling factor throughout the mantle, they found $\partial V_S/\partial\rho = 12$, or, using PREM as a reference model, $\zeta \sim 0.11$. For the sub-continental upper mantle, and using degrees $\ell = 2$–12 and the viscosity model MF2, the values of ζ predicted by the present method are close to but smaller than this value (ζ becomes negative at $z = 220$ km, and lies between 0.05 at $z = 80$ km and 0.1 at $z = 120$ km).

Forte et al. (1994b) performed joint inversions for the whole mantle, and proposed different models for the scaling factor, based on different possible parameterizations. In another study, Forte et al. (1994a) have inverted data separately for the scaling factors correlated (ζ_{co}) and not correlated (ζ_{th}) to the continent–ocean difference, using degrees $\ell = 2$–8 and a given model of viscosity. They assumed a general shape for the curve $\zeta(z)$ and found that in the upper mantle, ζ_{co} ranges between -0.3 and 0.3 and changes sign at $z \sim 300$ km depth. They interpreted this sign reversal as a signature of the stabilization of the continent–ocean heterogeneity. Once again, the values reported in the previous section are smaller, even for the case $\ell = 2$–16.

The major improvement of the present study is that it does not assume any a priori value or shape for the scaling factor. The model $\zeta(z)$ is determined only by the smoothed linear inversion of a tomographic model and gravity data, and thus it contains information brought by these data sets only.

Our preferred model is built with $\ell = 11$–16, which constitutes a second improvement. Low degree ($\ell = 2$–4) geoid kernels are mostly representative of the deep mantle, and they do not sample depths shallower than 350 km very well. On the contrary, geoid kernels for degrees higher than $\ell = 11$ do not sample the mantle below $z = 1000$ km depth, and have large absolute values in the shallow mantle. As pointed out in Section 4.4, this difference of sensitivity together with the power spectrum of S16RLBM result in significantly different values of the scaling factor below $z = 350$ km depth, whether one accounts for the low degrees or not. Degrees $\ell = 11$–16 are well-suited to study the uppermost mantle, and allow the resolution of the continent–ocean difference, which is present down to $z \sim 260$ km. However, by filtering V_S-anomalies between $\ell = 11$ and $\ell = 16$, one removes most of the seismic signal available at depths greater than $z = 400$ km (Fig. 11d and e). At depths, our preferred model is probably not relevant. To compute relevant values of the scaling factor in the transition zone and in the lower mantle, one must include low degrees. On the other hand, to detect compositional changes within the shallow sub-continental mantle one needs degrees higher than $\ell = 16$. This last task also requires regional tomographic models rather than a global model.

A final improvement is to perform inversions separately for the sub-continental and sub-oceanic mantle. This distinction is not equivalent to the inversions performed by Forte et al. (1994a). The differences between the sub-continental and sub-oceanic scaling factor can be used to interpret the continent–ocean difference. But in addition, separate models provide information about compositional changes within the sub-continental and sub-oceanic mantles: using Eq. (1), one can interpret the scaling factor models in terms of thermal and/or compositional lateral variations.

The difference in shape of the sub-oceanic and sub-continental scaling factors is related to the source of anti-correlation between gravity and V_S-anomalies, which is present below continents between 80 and 180 km. At these depths the sub-continental scaling factor is clearly positive, reaching a local maximum around $z = 120$ km. On the other hand, there is no significant correlation between gravity and V_S-anomalies

below oceans. Another important difference appears in the variance reduction of the reconstructed to the observed gravity anomalies. For $\ell = 11$–16, this variance reduction is significantly poorer for the sub-oceanic scaling factor (∼10%) than for the sub-continental scaling factor (∼30%). On the other hand, if one accounts for low degrees only ($\ell = 2$–8) the variance reduction to the observed gravity anomalies is higher for the sub-oceanic scaling factor (∼50%) than for the sub-continental scaling factor (∼30%). These observations suggest that intermediate-scale heterogeneities might play a more important role in the continental uppermost mantle than in the oceanic uppermost mantle. The oceanic regions seem to be well-explained by low degree anomalies only, and therefore may be dominated by large-scale structures, while the continental uppermost mantle may include more complexities, which are better accounted for by intermediate degrees anomalies.

A full interpretation of our results in term of chemical and/or thermal anomalies is beyond the scope of this paper. However, we now give some elements of comparison between available experimental data and the results of the present inversion.

Experimental values of ζ are usually deduced from the measurements of elastic properties of olivine (Isaac et al., 1989; Isaac, 1992), which is the dominant mineral of the mantle. Such values of ζ are based on the temperature derivative of V_S and ρ, and therefore they account only for temperature variations. For olivine, the typical value of ζ at ambient pressure and $T = 1000$ K is equal to 0.45 (Isaac, 1992). Elastic properties of the other minerals of the upper mantle are less well documented. For a given mineralogical composition, numerical models can provide synthetic values of S-wave velocity and density based on the experimental values of the elastic and thermal parameters of each minerals (e.g. Davies and Dziewonski, 1975; Duffy and Anderson, 1989; Vacher et al., 1996). Following the model of Vacher et al. (1998), we have computed V_S-anomalies and density anomalies associated with pure temperature variations. The reference temperature and pressure are $T = 1280$°C and $p = 4$ GPa, respectively, and the mineralogical model is pyrolite (i.e. the volumic fraction of olivine is equal to 62%). The scaling factor resulting from these anomalies yields values around 0.37–0.38 (Fig. 12, dotted curve). The inverted values

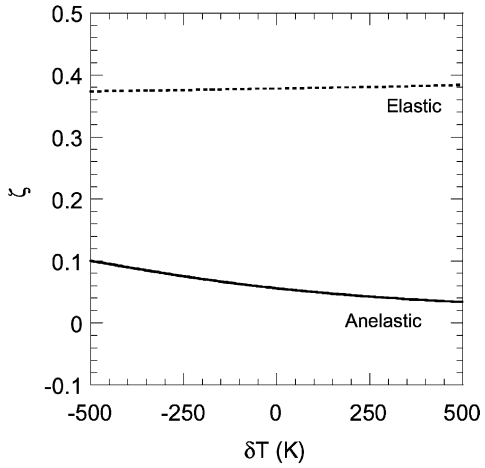

Fig. 12. Scaling factor for pure temperature variations (δT) predicted by experimental mineralogy. Anomalies of density and S-wave velocity are computed following the method of Vacher et al. (1998). The reference temperature is $T = 1280$°C, and the pressure is $p = 4$ GPa. The mineralogical model is pyrolite, as defined by Vacher et al. (1998). The dotted curve is based on laboratory measurement of elastic data performed at very high frequency. The plain curve accounts for anelasticity effects, using the model of quality factor Q1 of Goes et al. (2000) for a frequency $f = 0.1$ Hz.

of ζ reported in this study are significantly smaller, even if one considers only degrees $\ell = 2$–8 of the data. However, in the mantle, one must also account for chemical variations and possible additional effects such as anelasticity (see below). Moreover, elastic moduli depend on the pressure, and the scaling factor may also vary as a function of depth. Finally, extrapolation of laboratory measurements (elastic moduli and their temperature and pressure derivatives) to mantle pressures may induce additional errors.

In the Earth's mantle, anelasticity is responsible for attenuation of seismic waves (e.g. Anderson, 1989, pp. 279–302). Laboratory measurements of elastic data are usually performed at high frequencies (1 MHz and more). Such frequencies are much higher than the upper cut-off frequency of the absorption band. Therefore, laboratory measurements should be corrected before being used to compute velocities in the seismic band. Karato (1993) accounted for anelasticity to compute values of $\partial \ln V_S/\partial T$ and ζ. To compute the anharmonic part of $\partial \ln V_S/\partial T$, he used the model of Duffy and Anderson (1989), which accounts for

pressure dependence of elastic parameters. He found that ζ increases from 0.2 to 0.3 in the upper mantle, and concluded that anelasticity damps the effects of thermal anomalies on seismic velocities. We have also introduced anelasticity effects in the model of Vacher et al. (1998) following the method proposed by Goes et al. (2000). For their model of quality factor Q1 and a frequency equal to 0.1 Hz, we obtained values of ζ around 0.05 (Fig. 12, plain curve). These values are in good agreement with our inverted values.

Unlike temperature variations, compositional changes do not have a well-defined influence on the scaling factor. For instance, the scaling factor can be either positive or negative, depending on the mineralogical variations considered. Using the method of Vacher et al. (1998), we have computed S-wave velocities and densities for mixes with two end-members (Olivine–Garnet and Olivine–Diopside). Increasing the volume fraction of diopside leads to higher densities and velocities, whereas increasing the volume fraction of garnet leads to higher densities, but smaller velocities. Therefore, the scaling factor is positive in the first case, and negative in the second one. Of course, the mineralogy of the mantle is much more complicated, and simultaneous variations in the volume fractions of different minerals could balance each others. Goes et al. (2000) have recently suggested that compositional variations may not induce strong V_S-anomalies. Therefore, chemical variations could explain partially, but maybe not completely, the differences in shape and amplitude between the model of Karato (1993), and that obtained by inversion of gravity and V_S-anomalies. Variations in the iron-content could also play a significant role. Since the model S16RLBM yields a good anti-correlation with the surface heat flux (Röhm et al., 2000), thermal processes in the uppermost mantle probably play an important role to explain the origin of the continental seismic lithosphere. Röhm et al. (2000) have proposed two possible thermal origins: (1) variations in the thickness of the thermal boundary layer; and (2) variations in the shallow radiogenic heat production. Positive values of the scaling factor, as those we observe above 200 km depth, are consistent with thermal origins. The decrease of the scaling factor with depth and its sign change could indicate that thermal (compositional) anomalies are progressively less (more) important, as depth is increasing. However, a systematic study is required to clear up the actual influence of temperature and compositional variations on the scaling factor.

6. Conclusions

The scaling factor relates relative density anomalies to relative V_S-anomalies and is therefore of great interest for the interpretation of seismological models. To invert for this scaling factor in the uppermost mantle, we have used spherical harmonic degrees $\ell = 11$–16 of gravity and S-wave velocity anomalies. This spatial window is well-adapted to the inference of intermediate size anomalies in the uppermost mantle. In the sub-continental mantle, the scaling factor has positive values down to $z \sim 220$ km depth. In the sub-oceanic mantle, the scaling factor is significantly different, and reaches zero-value at shallower depth. At depths greater than 260 km, the sub-continental and sub-oceanic models are close one to each other. These results are quite robust, but they hold in the uppermost mantle only, i.e. at depth shallower than 350 km. At greater depths, low degrees of the spherical harmonic expansion ($\ell = 2$–4) cannot be removed and the model of scaling factor depends on the radial model of viscosity. The observed differences between the sub-continental and sub-oceanic scaling factors suggest that intermediate-scale anomalies are more important below continents than below oceans. Finally, a rapid comparison between our results and experimental mineralogy yields significant discrepancies in the value of the scaling factor. Most of these discrepancies are explained if one accounts for anelasticity. The calculations presented in this paper may be refined to selected geographical areas using regional tomographic models. Regional models of the scaling factor would be a way to account for lateral viscosity variations and could be useful to explain the relative stability of major tectonic units, such as old cratons.

Acknowledgements

John Woodhouse first pointed out the correlation between S16RLBM and gravity anomalies, which led us to carry out the present research. Gravity anomalies were computed using software developed at DEOS, Delft University of Technology. Roger

Haagmans and Arnoud de Bruijne kindly provided us this software and gave us some of their time for useful discussions about the geoid properties. Ernst Schrama and Nikolaos Pavlis provided us variances in EGM96 gravity anomalies. We thank two anonymous reviewers for constructing comments. This research was partly funded by The Netherlands Organization for Scientific Research (NWO, Grant 750.297.02).

Appendix A. Generalized linear inversion

To solve Eq. (7), we used a generalized linear inversion, which minimize a linear combination of estimated errors and a priori information.

$$\boldsymbol{m}^{\mathrm{est}} = \boldsymbol{G}^{-\mathrm{g}}\boldsymbol{d} \tag{A.1}$$

where $\boldsymbol{d}$ is the data vector (here, the gravity anomalies), $\boldsymbol{m}^{\mathrm{est}}$ the estimated model (the scaling factor in our problem), and $\boldsymbol{G}^{-\mathrm{g}}$ the generalized inverse matrix.

$$\boldsymbol{G}^{-\mathrm{g}} = [\boldsymbol{G}^{\mathrm{T}}\boldsymbol{G} + \varepsilon^2\boldsymbol{W}]^{-1}\boldsymbol{G}^{\mathrm{T}} \tag{A.2}$$

where the superscript T denotes the transpose matrix. The matrix $\boldsymbol{G}$ is the kernel matrix. In our example (Eq. (7)), it contains the product K of the relative S-wave velocity anomalies with the geoid kernels (Eq. (6)). The matrix $\boldsymbol{W}$ contains a priori information, and it is weighted by the damping factor ε. Here, we impose our model to vary smoothly as a function of depth. Therefore, $\boldsymbol{W}$ is defined by the product of the flatness matrix $\boldsymbol{F}$ with its transpose.

$$\boldsymbol{W} = FF^{\mathrm{T}}, \quad \text{where}$$
$$\boldsymbol{F} = \begin{pmatrix} -1 & 1 & & & & \\ & -1 & 1 & & & \\ & & \cdots & \cdots & & \\ & & & \cdots & \cdots & \\ & & & & -1 & 1 \end{pmatrix} \tag{A.3}$$

Note that the dimension of $\boldsymbol{F}$ is $M \times (M+1)$, where M is the dimension of the model. To invert the matrix in the brackets in Eq. (A.2), we have used a LU decomposition method.

The resolution matrix $\boldsymbol{R}$ provides information about the resolution of the model.

$$\boldsymbol{R} = \boldsymbol{G}^{-\mathrm{g}}\boldsymbol{G} \tag{A.4}$$

If the estimated model is perfectly resolved, $\boldsymbol{R}$ is equal to the identity matrix. To estimate the quality of the model, one might also consider its norm L, its roughness S (that is to say the norm of the model derivative), and the variance reduction of the reconstructed data to the observed data (X).

$$L = (\boldsymbol{m}^{\mathrm{est}^{\mathrm{T}}}\boldsymbol{m}^{\mathrm{est}})^{1/2} \tag{A.5}$$

$$S = (\boldsymbol{m}^{\mathrm{est}^{\mathrm{T}}}W m^{\mathrm{est}})^{1/2} \tag{A.6}$$

$$X = 1 - \frac{\sum_{i=1}^{N}(d_i - d_i^{\mathrm{est}})^2}{\sum_{i=1}^{N} d_i^2} \tag{A.7}$$

where N is the dimension of the data vector, and $\boldsymbol{d}^{\mathrm{est}} = Gm^{\mathrm{est}}$ the reconstructed data vector. S and X decrease as the damping factor (ε) increases. Usually, one defines the preferred model as being the best compromise between the data information and a priori information (here the roughness). The damping factor ε is therefore chosen on the trade-off curve, which plot the misfit ($1 - X$) as a function of the roughness (e.g. Fig. 5).

To account for the uncertainties of the elements of $\boldsymbol{G}$, we added random simulated errors to these elements, and performed an inversion with each perturbed matrix. This lead to a collection of Z perturbed models ($\boldsymbol{m}^{\mathrm{per}}$). The mean model over this collection ($\bar{\boldsymbol{m}}$) and its variance ($\boldsymbol{\sigma_m}$) are given by

$$\bar{\boldsymbol{m}} = \frac{1}{Z}\sum_{j=1}^{Z}\boldsymbol{m}_j^{\mathrm{per}} \tag{A.8}$$

$$\boldsymbol{\sigma}_{\boldsymbol{m}}^2 = \frac{1}{Z}\sum_{j=1}^{Z}(\boldsymbol{m}_j^{\mathrm{per}} - \bar{\boldsymbol{m}})^2 \tag{A.9}$$

The length ($\bar{L}$), the smoothness ($\bar{S}$) and the variance reduction ($\bar{X}$) of the mean model are given by Eqs. (A.5)–(A.7), where $\boldsymbol{m}^{\mathrm{est}}$ must be replaced by $\bar{\boldsymbol{m}}$. To be relevant, the mean model and its variance must be computed with a large enough collection of perturbed models. To test this condition, one can plot $\bar{L}$ and $\bar{S}$ as a function of Z. The model $\bar{\boldsymbol{m}}$ is statistically relevant when $\bar{L}$ and $\bar{S}$ oscillate around stationary values (Fig. 3).

References

Anderson, D.L., 1989. Theory of the Earth, Blackwell, Boston.

Davies, G.F., Dziewonski, A.M., 1975. Homogeneity and constitution of the Earth's lower mantle and outer core. Phys. Earth Planet. Inter. 10, 336–343.

Deschamps, F., Sotin, C., 2000. Inversion of 2D numerical convection experiments for a strongly temperature-dependent viscosity fluid. Geophys. J. Int. 143, 204–218.

Duffy, T.S., Anderson, D.L., 1989. Seismic wave speeds in mantle minerals and the mineralogy of the upper mantle. J. Geophys. Res. 94, 1895–1912.

Dziewonski, A.M., Anderson, D.L., 1981. Preliminary reference Earth model. Phys. Earth Planet. Inter. 25, 297–356.

Forte, A.M., Peltier, W.R., 1987. Plate tectonics and aspherical Earth's structure: the importance of poloidal–toroidal coupling. J. Geophys. Res. 92, 3645–3679.

Forte, A.M., Peltier, W.R., 1991. Viscous flow models of global geophysical observables. 1. Forward problems. J. Geophys. Res. 96, 20131–20159.

Forte, A.M., Dziewonski, A.M., Woodward, R.L., 1993. Aspherical structure of the mantle, tectonic plate motions, non-hydrostatic geoid, and topography of the core-mantle boundary. In: LeMouël, J.-L., Smylie, D.E., Herring, T., Dynamics of the Earth's Deep Interior and Earth Rotation, Vol. 72. Geophysics Monographic Series, Washington, DC, pp. 135–166.

Forte, A.M., Dziewonski, A.M., O'Connell, R.J., 1994a. Thermal and chemical heterogeneity in the mantle: a seismic and geodynamic study of continental roots. Phys. Earth Planet. Inter. 92, 45–55.

Forte, A.M., Woodward, R.L., Dziewonski, A.M., 1994b. Joint inversions of seismic and geodynamic data for models of three-dimensional mantle heterogeneity. J. Geophys. Res. 99, 21857–21877.

Goes, S., Govers, R., Vacher, P., 2000. Shallow mantle temperatures under Europe from P and S wave tomography. J. Geophys. Res. 105, 11153–11169.

Haagmans, R., de Bruijne, A., de Min, E., 1998. A procedure for combining gravimetric geoid models and independent geoid data, with an example in the north sea region. DEOS Progress Letters, 98.1, Delft University Press, http://www.geo.tudelft.nl/fmr/deosletter.

Isaac, D.G., 1992. High-temperature elasticity of iron-bearing olivines. J. Geophys. Res. 97, 1871–1885.

Isaac, D.G., Anderson, O.L., Goto, T., Suzuki, I., 1989. Elasticity of single-crystal forsterite measured to 1700 K. J. Geophys. Res. 94, 5895–5906.

Jordan, T.H., 1975. The continental tectosphere. Rev. Geophys. Space Phys. 13, 1–12.

Karato, S.I., 1993. Importance of anelasticity in the interpretation of seismic tomography. Geophys. Res. Lett. 20, 1623–1626.

King, S.D., Masters, G., 1992. An inversion for radial viscosity structure using seismic tomography. Geophys. Res. Lett. 19, 1551–1554.

Kogan, M.K., McNutt, M.K., 1993. Gravity field over northern Eurasia and variations in the strength of the upper mantle. Science 259, 473–479.

Lemoine, F.G., Kenyon, S.C., Factor, J.K., Trimmer, R.G., Pavlis, N.K., Chinn, D.S., Cox, C.M., Klosko, S.M., Luthcke, S.B., Torrence, M.H., Wang, Y.M., Williamson, R.G., Pavlis, E.C., Rapp, R.H., Olson, T.R., 1998. The development of the joint NASA GSFC and National Imagery Mapping Agency (NIMA). Geopotential Model EGM96, NASA/TP-1998-206861, NASA, GSFC, Greenbelt, MD 20771.

Li, X.-D., Romanowicz, B., 1996. Global mantle shear velocity model developed using nonlinear asymptotic coupling theory. J. Geophys. Res. 101, 22245–22272.

Mitrovica, J.X., Forte, A.M., 1997. Radial profile of mantle viscosity: results from the joint inversion of convection and postglacial rebound observables. J. Geophys. Res. 102, 2751–2769.

Nakiboglu, S.M., 1982. Hydrostatic theory of the Earth and its mechanical implications. Phys. Earth Planet. Inter. 28, 302–311.

Nataf, H.-C., Ricard, Y., 1996. 3SMAC: an a priori tomographic model for upper mantle based on geophysical modeling. Phys. Earth Planet. Inter. 95, 101–122.

Peltier, W.R., 1996. Mantle viscosity and ice-age ice sheet topography. Science 273, 1359–1364.

Press, W.H., Flannery, B.P., Teukolsky, S.A., Vetterling, W.T., 1989. Numerical Recipes. Cambridge University Press, Cambridge, 702 pp.

Ritsema, J., van Heijst, H.J., Woodhouse, J.H., 1999. Complex shear velocity structure imaged beneath Africa and Iceland. Science 286, 1925–1928.

Röhm, A., Snieder, R.K., Goes, S., Trampert, J., 2000. Thermal structure of continental upper mantle inferred from S-wave velocity and surface heat flow. Earth Planet. Sci. Lett. 181, 395–407.

Snieder, R.K., Trampert, J., 1999. Inverse problems in geophysics. In: Wirgin, A. (Ed.), Wavefield Inversion. Springer, New York, pp. 119–190, http://samizdat.mines.edu.

Su, W.J., Dziewonski, A.M., 1997. Simultaneous inversions for 3-D variations in shear and bulk velocity in the mantle. Phys. Earth Planet. Inter. 100, 135–156.

Trampert, J., Woodhouse, J.H., 1995. Global phase velocity maps of Love and Rayleigh waves between 40 and 150 s. Geophys. J. Int. 122, 675–690.

Vacher, P., Mocquet, A., Sotin, C., 1996. Comparison between tomographic structures and models of convection in the upper mantle. Geophys. J. Int. 124, 45–56.

Vacher, P., Mocquet, A., Sotin, C., 1998. Computation of seismic profiles from mineral physics: the importance of non-olivine components for explaining the 660 km depth discontinuity. Phys. Earth Planet. Inter. 106, 275–298.

Woodhouse, J.H., Trampert, J., 1995. Global upper mantle structure inferred from surface wave and body wave data. EOS Trans. AGU F422.

ELSEVIER

Physics of the Earth and Planetary Interiors 129 (2002) 245–264

PHYSICS OF THE EARTH AND PLANETARY INTERIORS

www.elsevier.com/locate/pepi

Anomalies of temperature and iron in the uppermost mantle inferred from gravity data and tomographic models

Frédéric Deschamps [a,*], Jeannot Trampert [a], Roel Snieder [b]

[a] *Department of Geophysics, Utrecht University, Budapestlaan 4, P.O. Box 80021, 3508 TA Utrecht, The Netherlands*
[b] *Department of Geophysics, Colorado School of Mines, Golden, CO 80401, USA*

Received 29 May 2001; received in revised form 9 October 2001; accepted 9 October 2001

Abstract

We propose a method to interpret seismic tomography in terms of thermal and compositional anomalies. In addition to the tomographic model, we use gravity data, which provide information on the density expressed as a relative density-to-shear wave velocity scaling factor ($\zeta = \partial \ln \rho / \partial \ln V_s$). The inferred values of ζ are not consistent with the presence of thermal anomalies alone. However, simultaneous anomalies of temperature and composition explain the observations. Compositional anomalies can have several origins, but we find the most relevant parameter to be the global volumic fraction of iron (xFe=Fe/(Fe+Mg)). We invert the tomographic model S16RLBM (Woodhouse and Trampert, 1995) and the density anomalies correlated to V_s-anomalies ($\delta\rho/\rho_0 = \zeta \delta V_s/V_0$) for anomalies of temperature (δT) and iron (δFe). The partial derivatives are provided by a numerical method that reconstructs density and seismic velocity for given temperatures and petrologic models (Vacher et al., 1998). Down to $z = 300$ km depth, the distribution of temperature and iron anomalies strongly depends on the surface tectonics. The continental mantle below old cratons and stable platforms is colder than average and depleted in iron, whereas the oceanic mantle is mostly homogeneous. Due to uncertainties on the reference state of the mantle, error bars on δT and δFe reach 10% of the inverted values. Finally, we apply these results to the stability of continental roots and test the hypothesis that the negative buoyancy induced by lower than average temperatures is balanced by the positive buoyancy induced by the depletion in iron. We find that continental roots are stable only if the viscosity of the mantle is strongly temperature-dependent. However, some uncertainties remain on the real effects and importance of rheology. © 2002 Elsevier Science B.V. All rights reserved.

1. Introduction

The continent–ocean distribution is a major feature of the Earth's surface and it extends down to the Earth's shallow interior. Global and regional models of seismic tomography, including recent ones (e.g. Woodhouse and Trampert, 1995; Alsina et al., 1996; Su and Dziewonski, 1997; Mégnin and Romanowicz, 2000; Ritsema and van Heijst, 2000; Villaseñor et al., 2001), report high-velocity roots below continents down to 200–400 km depth. These continental roots were first noted by Jordan (1975), and their origin is still a matter of debate. According to Jordan (1975), the uppermost mantle below continental shields is colder than the oceanic mantle and chemically less dense. Therefore, horizontal temperature gradients are stabilized by horizontal compositional gradients, and the mantle below continental shields is prevented from flowing. This stable layer is usually referred as the tectosphere. An alternative model involves a phase transition (Anderson, 1987): horizontal temperature variations induce variations in the depth at which phase transitions take place. For instance, if the mantle

* Corresponding author.
E-mail address: deschamp@geo.uu.nl (F. Deschamps).

0031-9201/02/$ – see front matter © 2002 Elsevier Science B.V. All rights reserved.
PII: S0031-9201(01)00294-1

is colder than average (e.g. in the slabs), the olivine → β-spinel transition should occur at lower pressure, i.e. at depths shallower than in the rest of the mantle. However, further studies presented arguments for the presence of a stable and chemically distinct layer below cratons. Jordan (1988) reviewed geophysical arguments, including gravimetric and geothermic data, that agree with this hypothesis. Polet and Anderson (1995) pointed out that high-velocity anomaly roots could be explained by a depletion in iron and/or an enrichment in olivine. Doin et al. (1996) showed that a depleted peridotitic layer at the base of the continental lithosphere is consistent with the geoid at intermediate wavelengths (spherical harmonic degrees 6–30).

The difficulties raised by the interpretation of seismic data results from the fact that density and seismic velocities depend simultaneously on temperature, composition and pressure. The recent study by Goes et al. (2000) suggests that in the upper mantle seismic velocity are mostly sensitive to temperature. Numerical models that reconstruct seismic velocities (e.g. Davies and Dziewonski, 1975; Duffy and Anderson, 1989; Vacher et al., 1998) support this conclusion. Temperature variations induce strong relative V_s-anomalies, whereas variations in the volumic fraction of olivine and in the iron content do not (see Fig. 2 in Section 3). In other words, V_s-anomalies may be useful to constrain the temperature distribution, but they are not sufficient to determine the chemical variations, as suggested by Forte and Perry (2000). To infer chemical variations, one needs an additional set of data, such as density anomalies. Relative V_s-anomalies are converted in density anomalies using a scaling factor ζ:

$$\zeta(r,\theta,\varphi) \equiv \frac{\partial \ln \rho(r,\theta,\varphi)}{\partial \ln V_s(r,\theta,\varphi)} \tag{1}$$

Radial models of this scaling factor can be deduced from inversions of tomographic models and gravity data. Previous models (e.g. Kogan and McNutt, 1993; Forte et al., 1995) included strong a priori information about the shape and the amplitude of the function $\zeta(z)$. Forte et al. (1995) used gravity data up to the spherical harmonic degree $\ell = 8$ and concluded to the presence of internally stabilized continent–ocean chemical differences.

Using several geodynamic data sets and tomographic models, Forte and Perry (2000) have recently mapped anomalies of temperature (δT) and iron (δFe) in the uppermost mantle. They showed that the tectosphere is depleted in iron. In this paper, we infer distributions of δT and δFe in the uppermost mantle ($z \leq 300$ km) following a similar method but using different gravity data set, tomographic model and radial model of scaling factor. We also use a refined numerical model to invert V_s-anomalies and density anomalies for δT and δFe. Our results are in good agreement with Forte and Perry (2000), and we use them to study the stability of continental roots.

2. Scaling factor in the uppermost mantle

Fig. 1 represents the sub-continental and sub-oceanic scaling factor deduced from inversions of gravity data and tomographic model (Deschamps et al., 2001). Linear inversions were performed separately for continental and oceanic areas, according to the equation

$$\delta g(\theta,\varphi) = \int_{r_{\mathrm{CMB}}}^{R} K(r,\theta,\varphi)\,\zeta(r)\,\mathrm{d}r, \tag{2}$$

where the gravity anomalies (δg) and the S-wave velocity anomalies (δV_s) are filtered out between spherical harmonic degrees ℓ_1 to ℓ_2:

$$\delta g(\theta,\varphi) = \sum_{\ell=\ell_1}^{\ell_2} \delta g_\ell(\theta,\varphi), \tag{3}$$

$$K(r,\theta,\varphi) = \frac{3\rho_0(r)g_0}{\overline{\rho}R} \times \sum_{\ell=\ell_1}^{\ell_2} \left[\frac{(\ell-1)}{2\ell+1} G_\ell(r) \frac{(\delta V_s)_\ell(r,\theta,\varphi)}{V_0(r)}\right]. \tag{4}$$

In these equations R is the Earth's radius, $\overline{\rho}$ is the mean density, g_0 is the surface acceleration of gravity, and $\rho_0(r)$ and $V_0(r)$ the reference density and S-wave velocity models. In Fig. 1 the reference model is PREM (Dziewonski and Anderson, 1981), the gravity anomalies are the non-hydrostatic gravity anomalies derived from the geoid model EGM96 (Lemoine et al., 1998), and the S-wave anomalies are provided by the global tomographic model S16RLBM (Woodhouse and Trampert, 1995), which is expanded up to the spherical harmonic degree $\ell = 16$. Each degree of the

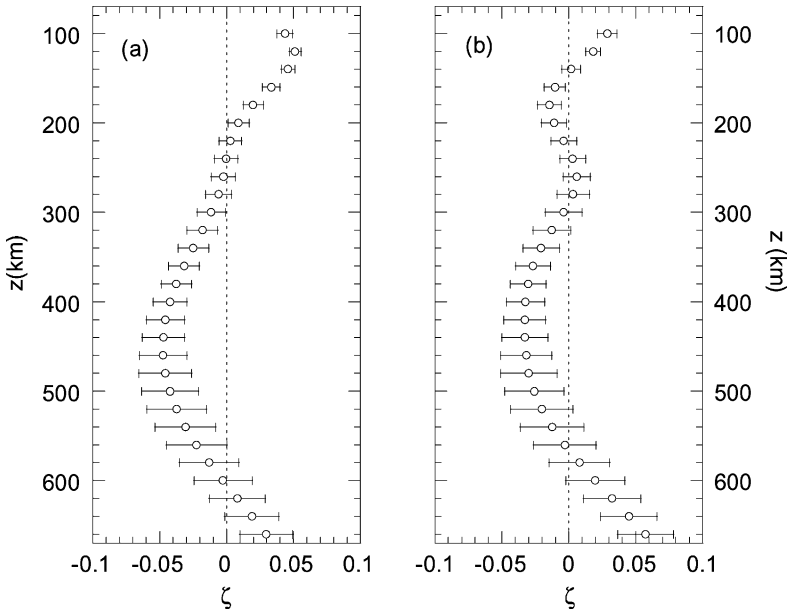

Fig. 1. Inverted scaling factor (ζ) in the sub-continental (a) and sub-oceanic (b) upper mantle. Open circles indicate the mean value of ζ, and the error bars represent the variance in ζ. The variance was estimated by introducing randomly generated errors in the seismological model S16RLBM. Data are filtered for degrees $\ell = 11$–16, integration (2) is performed from $z = 1000$ km depth up to the surface, and the viscosity model is MF2 (Mitrovica and Forte, 1997).

V_s-anomalies expansion is weighted by a geoid kernel $G_\ell(r)$, that is to say the geoid response to an anomaly of density located at radius r. These functions account for mantle dynamics, and therefore, they depend on the radial viscosity model (Forte and Peltier, 1991). To obtain the models of ζ presented in Fig. 1, we used a recent viscosity model proposed by Mitrovica and Forte (1997), which was built to fit both the long-wavelength gravity anomalies and the relaxation time due to postglacial uplift. One may point out that this choice is arbitrary. However, others viscosity models lead to similar results, suggesting that down to $z = 400$ km $\zeta(z)$ does not depend on the viscosity profile (Deschamps et al., 2001). For degrees $\ell \geq 11$ the geoid kernels peak around $z = 200$–300 km and have negligible values from $z = 1000$ km down to the core–mantle boundary. Removing low degrees does not have a dramatic effect on the scaling factor in the uppermost mantle. The models of ζ obtained for degrees $\ell_1 = 2$ to $\ell_2 = 16$ are similar to those presented in Fig. 1, which were obtained by filtering the data between degrees $\ell_1 = 11$ and $\ell_2 = 16$. The spectral window $11 \leq \ell \leq 16$ is, therefore, well suited to sample the shallow mantle ($100 \leq z \leq 400$ km). On the other hand, canceling the lowest degrees ($\ell = 2$–4) removes most of the seismic signal at depths greater than 400 km, and the scaling factors for $\ell = 2$–16 and $\ell = 11$–16 are significantly different. In addition, our model is poorly constrained at depths greater than 350 km. For these reasons, we have voluntarily limited the present study to depths shallower than 300 km. Sub-continental and sub-oceanic scaling factors are clearly different. Below continents (oceans), the scaling factor has positive values down to $z = 220$ km (140 km) depth. The order of magnitude is 0.04, which is small in comparison to the usual experimental mineralogy estimates. Compared to previous models (e.g. Kogan and McNutt, 1993; Forte et al., 1995), our results are significantly different in shape and amplitude. These studies have imposed strong a priori information to constrain the value of ζ. On the other hand, we did not assume any a priori information, except smoothness. Finally, if one accounts for anelasticity, our inverted model of ζ is in good agreement with

experimental mineralogy estimates. However, negative and low values of ζ cannot be explained by pure variations of temperature. Additional variations of composition are the most obvious choice to explain such values.

3. Synthetic anomalies of density and S-wave velocity

Previous studies have constructed numerical approaches to explain seismological models in terms of temperature and mineralogical composition (e.g. Davies and Dziewonski, 1975; Duffy and Anderson, 1989; Vacher et al., 1996). Such techniques reconstruct seismic velocities and densities using laboratory measurements of elastic and thermal properties of the main minerals present in the mantle rocks. Comparison with a globally averaged seismic model (e.g. PREM or ak135) provides good constraints on the value of the mantle adiabat (Vacher et al., 1996). On the other hand, the mineralogical composition, particularly the volume fraction of olivine (X_{ol}), have a limited influence on the seismic velocities. Duffy and Anderson (1989) preferred a piclogitic composition ($X_{\mathrm{ol}} = 40\%$) for the transition zone. Using a more recent compilation of experimental data, Vacher et al. (1998) do not find significant differences between the pyrolitic ($X_{\mathrm{ol}} = 61.7\%$) and piclogitic compositions down to 660 km. At 660 km depth, the presence of ilmenite could explain the observed discontinuity, but it does not matter whether ilmenite is present in pyrolite or in piclogite. Recently, Goes et al. (2000) have computed temperature variations from V_{p}- and V_{s}-anomalies beneath Europe down to 200 km depth. A conclusion is that compositional effects induce velocity anomalies smaller than 1% and would, therefore, be difficult to resolve.

Laboratory measurements of elastic data are usually performed at very high frequencies (around 1 MHz). Recently, Jackson (2000) measured the shear modulus for olivine at frequencies close to those of the seismic waves. At temperatures higher than 900 °C, the values of the shear modulus at 0.01 and 0.3 Hz differ significantly from those at 1 MHz. This discrepancy is attributed to anelasticy, which is also responsible for attenuation in the Earth's mantle. Karato (1993) showed that if one does not account for anelasticity, the temperature anomalies deduced from V_{s}-anomalies are overestimated. Therefore, synthetic seismic velocities computed from elastic data at 1 MHz should incorporate anelastic effects. Velocities that account for anelasticity are usually expressed in terms of the quality factor Q (Minster and Anderson, 1981):

$$V_{\mathrm{anel}} = V_{\mathrm{elast}}\left[1 - \frac{1}{2Q(\omega, p, T)\tan(\pi a/2)}\right] \quad (5)$$

where a is a constant, ω the frequency of the seismic wave, p the pressure and T is the temperature. Anderson and Given (1982) proposed that attenuation results from thermally and volumetrically activated process, and that the quality factor can be expressed by

$$Q(\omega, p, T) = A\omega^{\mathrm{a}} \exp\left[\frac{a(H + pV_{\mathrm{a}})}{RT}\right] \quad (6)$$

where A is a constant, H the activation enthalpy, p the pressure, V_{a} the volume of activation and R is the gas constant. Goes et al. (2000) used this formulation and proposed two possible models for Q. Their model Q_1, based on data by Sobolev et al. (1996) fits well the absorption band model of Anderson and Given (1982). In this paper, we computed relative anomalies of density and S-wave velocity, as a function of temperature and compositional anomalies. Anomalies are calculated with respect to the reference density and velocity obtained for a reference temperature, mineralogical composition, and iron content. Velocities and densities are computed along adiabatic profiles of temperature following the method of Vacher et al. (1998) (this method is outlined in the Appendix A). We accounted for anelastic effects using Eqs. (5) and (6), and the model Q_1 of Goes et al. (2000) that is to say $A = 1.48 \times 10^{-1}$, $a = 0.15$, $H = 500$ kJ/mol and $V_{\mathrm{a}} = 20\,\mathrm{cm}^3$/mol. Most of the following calculations were performed for a frequency $f = 0.1$ Hz. Before turning to the inverse problem, we first consider two illustrations of the direct problem.

First, we have computed relative V_{s}-anomalies ($\delta V_{\mathrm{s}}/V_0$, plain line in Fig. 2) and density anomalies ($\delta\rho/\rho_0$, dashed line in Fig. 2) as a function of variations of temperature (δT), global volumic fraction of iron (δFe) and volumic fraction of olivine (δX_{ol}) with respect to a reference model. The global volumic fraction of iron (or iron ratio) is defined by the ratio $x\mathrm{Fe} = \mathrm{Fe}/(\mathrm{Fe} + \mathrm{Mg})$ of the bulk rock. In Fig. 2, the reference temperature and global iron ratio are equal

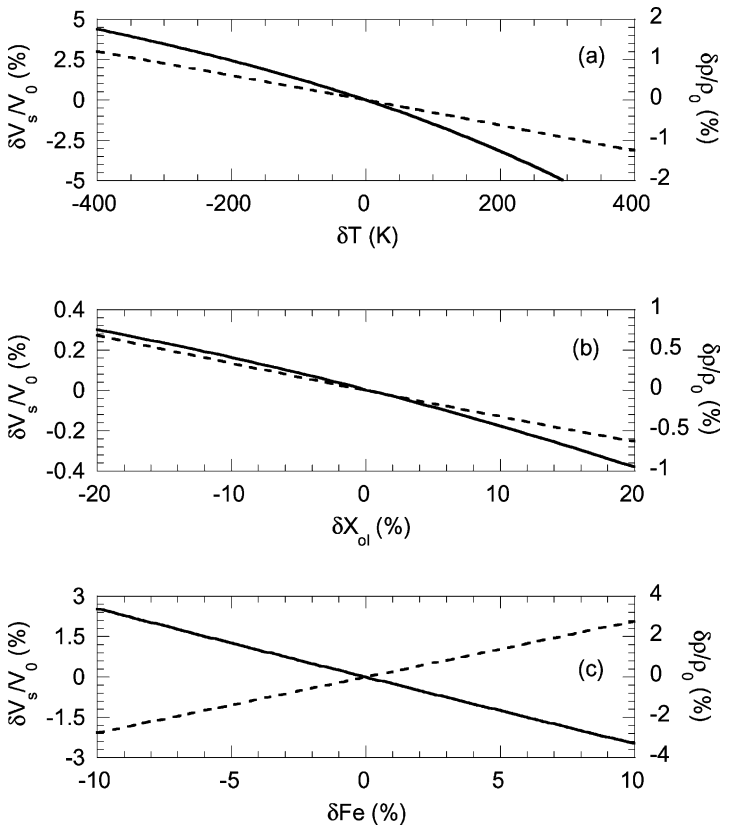

Fig. 2. Relative anomalies of S-wave velocity ($\delta V_s/V_0$, solid curve) and density ($d\rho/\rho_0$, dashed curve) as a function of anomalies of temperature (a), anomalies of the volumic fraction of olivine (b), and anomalies of the global volumic fraction of iron (c). The reference temperature, olivine fraction and iron ratio are $T_{\mathrm{ref}} = 1250\,^{\circ}\mathrm{C}$, $X_{\mathrm{ol,ref}} = 61.7\%$ (pyrolite) and $x_{\mathrm{Fe,ref}} = 11\%$. Anelasticity is accounted for according to the model Q_1 of Goes et al. (2000), and assuming $f = 0.1\,\mathrm{Hz}$.

to 1250 °C and 11%, respectively and the reference mineralogical composition is pyrolite. In pyrolite the volumic fraction of olivine is $X_{\mathrm{ol}} = 61.7\%$, and the non-olivine components (with their volumic fraction) are clinopyroxene (13.3%), orthopyroxene (5.2%), garnet (15.3%) and jadeite (4.5%). The deficit/excess of olivine is shared between the non-olivine minerals as a function of their volumic fraction in the reference composition. For instance, if the rock is depleted in olivine by 10%, the composition of the rock is as follows: olivine 51.7%, clinopyroxene 16.8%, orthopyroxene 6.5%, garnet 19.3% and jadeite 5.7%. It is clear that $\delta V_s/V_0$ is much more sensitive to temperature variations than to mineralogical variations (Fig. 2a and b). If all the deficit/excess in olivine is put in garnet, variations of velocity are more important. However, garnet is richer in iron than the other minerals, and most of the variations are due to the global enrichment/depletion in iron associated with the enrichment/depletion in garnet. The influence of the global iron ratio is stronger than that of the olivine fraction, but it remains weak compared to that of temperature. A velocity anomaly equal to 1% requires an iron anomaly of −4%. The same anomaly can be obtained with a temperature anomaly of −50 K only. The distribution of V_s-anomalies should, therefore, impose relatively strong constraints on the distribution of temperature. Compositional changes, on the other hand, cannot be inferred from V_s-anomalies alone. One needs an additional data set, such as density anomalies. Indeed, the sensitivity of density anomalies to temperature and chemical variations are comparable

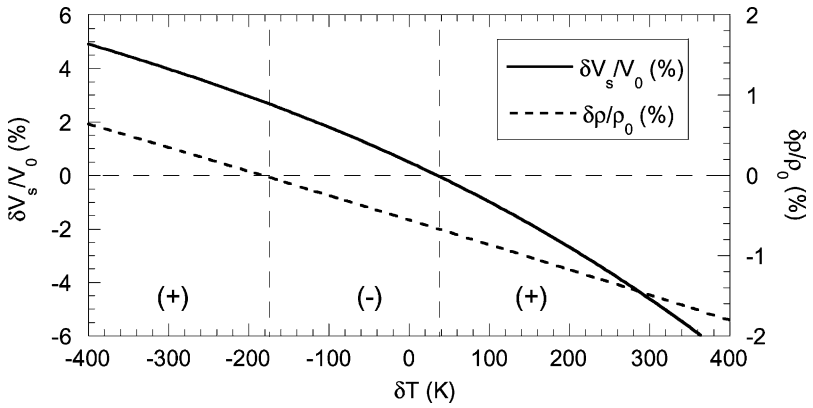

Fig. 3. Relative density anomalies (dashed line) and V_s-anomalies (solid line) as a function of temperature anomalies and for a depletion in iron equal to −2%. The reference temperature, olivine fraction and iron ratio are $T_{ref} = 1250\,^{\circ}C$, $X_{ol,ref} = 61.7\%$ (pyrolite) and $x_{Fe,ref} = 11\%$. The scaling factor is negative for temperature between −180 and +20 K, and positive elsewhere. The correction for anelasticity is the same than in Fig. 2.

(dashed curves in Fig. 2). Note that the iron content has a strong influence on density anomalies. For instance, a depletion in iron of 2% induces the same density anomaly than an increase of temperature of 180 K or than an enrichment in olivine of 17%.

The second example gives a key to interpret the negative and low values of the scaling factor. The density and the seismic velocity are both decreasing (increasing) as the temperature is increasing (decreasing). In the case of purely thermal anomalies the scaling factor is, therefore, always positive, and its typical value (if one accounts for anelasticity) is around 0.2. On the other hand, if the rock is enriched (depleted) in iron, V_s decreases (increases) whereas ρ increases (decreases). For pure anomalies of iron, the scaling factor is always negative, and it has values around −1.1. If one considers simultaneous variations of temperature and iron, it is, therefore, possible that the scaling factor attains values smaller than 0.1 and even that it even is negative. Fig. 3 shows relative anomalies of density ($\delta\rho/\rho_0$, dashed curve) and S-wave velocity ($\delta V_s/V_0$, plain curve) as a function of temperature variations, assuming an iron depletion of 2% (that is to say the global volumic fraction of iron is equal to 9% instead of 11%). Relative anomalies of ρ and V_s cancel for $\delta T \sim 20$ K and $\delta T \sim -180$ K, respectively. As a result, there is a wide range of temperature anomalies for which the scaling factor yields negative values. To interpret our estimated scaling factor (and, therefore, the gravity data and the tomographic model) one must account for simultaneous variations of temperature and composition.

4. Inverse problem

4.1. Method

We have used the method outlined in the previous section as a basis to invert the relative V_s-anomalies and the density anomalies correlated to these V_s-anomalies ($\delta\rho/\rho_0 = \zeta\,\delta V_s/V_0$) for variations of temperature and composition. First, we write the variations of the quantity Y_i relatively to a reference value $Y_{i,ref}$ as a function of the variations in the parameters X_j relatively to a reference value $X_{j,ref}$:

$$\frac{\delta Y_i}{Y_{i,ref}} = \sum_j a_{ij}\delta X_j; \quad a_{ij} = \frac{\delta Y_i}{Y_{i,ref}\delta X_j} \tag{7}$$

To compute the coefficients a_{ij}, we used the approach of Vacher et al. (1998) (Appendix A). Since these coefficients depend on the δX_j, we linearized the system. The process is initiated by imposing a priori starting values of δX_j. At iteration n, the δX_j^n determined at the previous iteration are used to compute the coefficients a_{ij}. Eq. (7) can easily be inverted for estimated values of δX_j^n. These estimated values provide in turn

estimated values of δY_i (δX_j^n). The residues $R_i^n = \delta_i - \delta Y_i^n$ are then used to compute updated values of δX_j (δX_j^{n+1}), following a Newton–Raphson method. This process is stopped when the residues are small enough.

Since we have two sets of parameters ($\delta V_s/V_0$ and ζ), we have access to the variations of two parameters only. In this paper, we focus on anomalies of temperature (δT) and global iron molar fraction (δFe). In that case, one must solve the system:

$$\begin{cases} \dfrac{\delta V_s}{V_0} = A\,\delta T + \delta\mathrm{Fe} \\ \dfrac{\delta V_s}{V_0} = C\,\delta T + D\,\delta\mathrm{Fe} \end{cases} \tag{8}$$

where $A = \delta V_s/(V_0\delta T)$, $B = \delta V_s/(V_0\delta\mathrm{Fe})$, $C = \delta\rho/(\rho_0\delta T)$ and $D = \delta\rho/(\rho_0\delta\mathrm{Fe})$. The choice to invert for anomalies of iron rather than for anomalies of olivine is driven by the observation that densities and seismic velocities are more sensitive to global iron content than to olivine fraction (Fig. 2b and c). Usual values of the velocity anomalies require large anomalies of olivine. For instance, if $\delta V_s/V_0 = 2\%$ the rock is enriched in olivine by 7–14%, depending on the value of ζ. Such anomalies may not be relevant to the case of the Earth's uppermost mantle. In addition, pure anomalies of olivine induce a positive scaling factor (density and velocity are both decreasing as X_{ol} is increasing, Fig. 2c), and may not explain the negative values of the observed ζ.

Forte and Perry (2000) parameterized the chemical variations in terms of a garnet depleted basalt. This choice was driven by the observation that variations in alumina (Al_2O_3), which is preferentially stored in garnet, strongly influence the density and seismic velocities (e.g. Jordan, 1979). We did calculations that confirm this point: for instance, a depletion in garnet equal to 10% induce a V_s-anomaly of -1.2% and a density anomaly of -0.8%. Such anomalies are larger than those induced by variations in olivine, but they remain 3–4 times smaller than those induced by variations in iron. Note that the seismic velocity and the density both decrease as the volumic fraction of garnet decreases, i.e. the scaling factor associated with pure variations of garnet is positive. Accounting for depletion in garnet leads to larger temperature variations and smaller variations in iron. For instance, if one imposes a depletion of garnet of 5%, the anomalies of iron are only 70% of those for a rock undepleted in garnet. To infer garnet and iron variations simultaneously one needs an additional constraint, such as P-wave velocity anomalies. Taking $\partial \ln V_s/\partial \ln V_p = 1.6$ (Robertson and Woodhouse, 1997), and for $\delta V_s/V_0 = 4\%$, the depletion in garnet is close to 2%, and the anomalies of iron are about 90% of those obtained for pyrolite. Since pure variations in garnet fail to explain large velocity anomalies and a negative scaling factor, we chose to consider variations in the iron content only. This is, we believe, the most important effect, keeping in mind that the variations in iron we infer may be slightly overestimated.

4.2. Estimation of error bars

An important issue is to estimate error bars for δT and δFe. Of course, errors in $\delta V_s/V_0$ and in ζ propagate to δT and δFe. The errors on δT ($\sigma\delta T$) and δFe ($\sigma\delta$Fe) can be estimated by the quadratic sum of the errors on δV_s ($\sigma\delta_{Vs}$) and ζ(σ_ζ). After inverting the system (8), one obtains

$$\begin{cases} \sigma_{\delta T}^2 = \dfrac{(D - B\zeta)^2\sigma_{\delta V_s}^2 + (B\,\delta V_s)^2\sigma_\zeta^2}{(AD - BC)^2} \\ \sigma_{\delta\mathrm{Fe}}^2 = \dfrac{(A\zeta - C)^2\sigma_{\delta V_s}^2 + (A\,\delta V_s\,\sigma_\zeta^2)}{(AD - BC)^2} \end{cases} \tag{9}$$

For the shake of simplicity, we assumed that A, B, C and D do not depend on $\delta V_s/V_0$ and ζ. If one provides values for $\sigma_{\delta V_s}$ and σ_ζ, then $\sigma_{\delta T}$ and $\sigma_{\delta\mathrm{Fe}}$ can be calculated during the inversion process (Section 4.1). We performed calculations for many different cases (with $-10\% \le \delta V_s \le 10\%$ and $-0.1 \le \zeta \le 0.1$), and found the relative errors on δV_s and ζ. For instance, if $\sigma_{\delta T}/\delta T = 10\%$ and $\sigma_\zeta/\zeta = 10\%$, Eq. (9) predict values of $\sigma_{\delta T}/\delta T$ and $\sigma_{\delta\mathrm{Fe}}/\delta$Fe close to 10%. The inversion propagates the errors, but does not amplify them. It is interesting to note that most of these errors (about 90%) are due to the error in δV_s. Unfortunately, tomographic models usually do not provide this uncertainty.

An additional source of error results from the choice of the model of reference, i.e. the temperature (T_{ref}), olivine fraction ($X_{ol,ref}$) and iron ratio ($x_{Fe,ref}$) used to compute the reference velocity and density. The inverted values of δT and δFe depend on these parameters. The thermodynamic reference model for

the Earth's mantle is, however, poorly constrained, which leads to uncertainties in δT and δFe. The most sensitive parameter is the reference temperature. The reference temperature can be seen as the potential temperature (i.e. temperature at zero pressure) of the mantle adiabat, and it should fit the average seismic models (such as PREM) reasonably well. The values of δT and δFe for $T_{\mathrm{ref}} = 1000\,^{\circ}\mathrm{C}$ and $1500\,^{\circ}\mathrm{C}$ differ by about 140 K and 1.4%, respectively. The reference olivine fraction is less sensitive than the reference temperature, but variations of δT and δFe with $X_{\mathrm{ol,ref}}$ cannot be neglected. Variations in $x_{\mathrm{Fe,ref}}$, on the other hand, do not induce significant differences in the values of δT and δFe. For instance, the values of δT and δFe for $x_{\mathrm{Fe,ref}} = 5\%$ and $x_{\mathrm{Fe,ref}} = 20\%$ differ by only 2 K and 0.02%, respectively. For these reasons, we have computed values of δT and δFe for all the values of T_{ref} and $X_{\mathrm{ol,ref}}$ that provide values of V_{s} yielding within $\pm 2.5\%$ of the PREM value. As a result, we obtained mean distributions of δT and δFe as a function of $\delta V_{\mathrm{s}}/V_0$ and ζ, together with their variances $\sigma_{\delta T}$ and $\sigma_{\delta \mathrm{Fe}}$. These variances give an estimation of the error bars on δT and δFe. For depths between $z = 100$ and 300 km, error bars on δT (δFe) are equal to about 7% (10%) of the inverted values.

The distributions of δT and δFe presented hereafter (Sections 4.3 and 4.4) are the mean of a collection of distributions obtained for different values of T_{ref} and $X_{\mathrm{ol,ref}}$, as explained above. Since variations in the reference iron ratio induce only small errors, we kept the value of $x_{\mathrm{Fe,ref}}$ constant and equal to 11%. A reasonable estimate of the error due to the uncertainty on T_{ref} and $X_{\mathrm{ol,ref}}$ is about 7–10% of the inverted values. This mean error may increase slightly if one also considers errors due to uncertainties on δV_{s} and ζ (Eq. (9)).

4.3. Simultaneous variations of temperature and iron

To illustrate the method presented in Section 4.1, we first consider simultaneous variations of temperature and global iron content as a function of $\delta V_{\mathrm{s}}/V_0$ and ζ (Fig. 4). Positive (negative) anomalies of V_{s} are associated with negative (positive) anomalies of temperature and iron depletion (enrichment). Anelasticity effects, and therefore, the sensitivity of V_{s} to temperature variations, are increasing with temperature (Eqs. (5) and (6)). As a result, temperature anomalies are getting stronger (in absolute value) as $\delta V_{\mathrm{s}}/V_0$ is increasing (Fig. 4a). For instance, if $\zeta = 0.05$ the anomalies of temperature predicted by relative V_{s}-anomalies of -4 and 4% are equal to 175 and -230 K, respectively. Anomalies of iron, and to a lesser extent, anomalies of temperature, are sensitive to the scaling factor. For a given value of $\delta V_{\mathrm{s}}/V_0$, the anomaly of iron is getting stronger as ζ is decreasing (Fig. 4b).

The inverted anomalies of temperature and iron are both correlated to the V_{s}-anomalies, and are, therefore, correlated one another. This is a consequence of the definition of the scaling factor Eq. (1), which implies that density anomalies are correlated to the V_{s}-anomalies. Eq. (8), however, are independent (the determinant $AD - BC$ is not equal to 0), and the inverted δT and δFe are two different results. The role of the scaling factor is to get correct amplitudes of density anomalies through gravity anomalies, keeping the spatial variations correlated to the V_{s}-anomalies.

The method presented in this study provides the anomalies of temperature and iron that are correlated to the V_{s}-anomalies. Indeed, our model of $\zeta(z)$ does not explain the observed gravity anomalies (δg) completely (Deschamps et al., 2001), and some additional anomalies of temperature and iron, which are not correlated to the velocity, must be present. Presently, we do not have access to these anomalies. However, the gravity anomalies predicted by our model of $\zeta(z)$ yield within $\pm 2 s_{\delta g}$ of the observed gravity anomalies (Deschamps et al., 2001), suggesting that most of the density anomalies are correlated to the velocity anomalies. The distributions of δT and δFe for the Earth's mantle proposed in the next section are, therefore, robust features.

4.4. Application to the uppermost mantle

We now invert relative V_{s}-anomalies and the density anomalies correlated to V_{s}-anomalies for three-dimensional distributions of temperature and iron anomalies in the uppermost mantle. The input data are the spherical harmonic degrees $\ell = 2$–16 of the global S-wave model S16RLBM (Woodhouse and Trampert, 1995), and the radial model of scaling factor proposed by Deschamps et al. (2001). We have computed a collection of distributions of δT and δFe

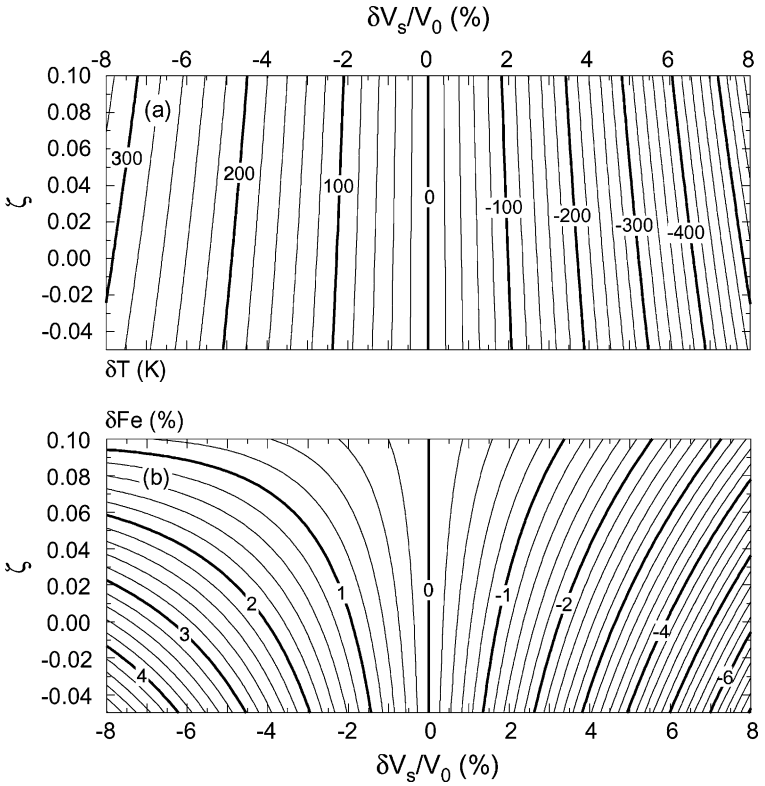

Fig. 4. Inversions of relative V_s-anomalies ($\delta V_s/V_0$) and scaling factor (ζ) for temperature anomalies of temperature (a) and iron ratio (b). The anomalies plotted here are the mean of the anomalies obtained for reference temperatures (T_{ref}) and olivine fraction ($X_{ol,ref}$) that predict reference velocity within ±2.5% of PREM (see text). The reference iron ratio is fixed and equal to 11%. Calculation were conducted for $z = 200$ km-depth.

using coefficients *A*, *B*, *C* and *D* Eq. (8) obtained for several reference temperatures (T_{ref}) and olivine fractions ($X_{ol,ref}$). The reference iron ratio is fixed and equal to 11%. We only kept the cases corresponding to the thermal and compositional reference models (T_{ref} and $X_{ol,ref}$) that could predict PREM within ±2.5%. This results in mean distributions of δT and δFe with error bars of about 10% around the mean values.

As discussed in the Section 4.2, the distributions of δT and δFe are correlated to the distribution of the relative V_s-anomalies. Down to $z = 150$ km, continental cratons and platforms are colder than average and depleted in iron. Tectonically active areas and oceans are slightly hotter than average and enriched in iron. The correlation with surface tectonics holds down to 200 km, although the amplitudes of δT and δFe are smaller. At $z = 250$ km and $z = 300$ km, the correlation with surface tectonics is much weaker and the amplitudes are smaller again. However, negative anomalies of temperature and depletion in iron are still present below cratons and stable platforms.

To quantify the correlation with surface tectonics, we have computed the mean of and the variance in the anomalies of temperature and iron for several regions (oceans, old cratons, stable platforms and tectonic continents as delimited by 3SMAC (Nataf and Ricard, 1996)) and depths. We first checked that, for the whole Earth, the mean anomalies of temperature and iron are close to zero, whatever the depth. For instance, the mean anomalies of iron (temperature) is $\overline{\delta\text{Fe}} = -0.1\%$ ($\overline{\delta T} = -20$ K) at $z = 150$ km, and $\overline{\delta\text{Fe}} = -0.04\%$ ($\overline{\delta T} = -3$ K) at $z = 300$ km. The mean of and variance in temperature anomalies for different provinces and depths are displayed in Fig. 5,

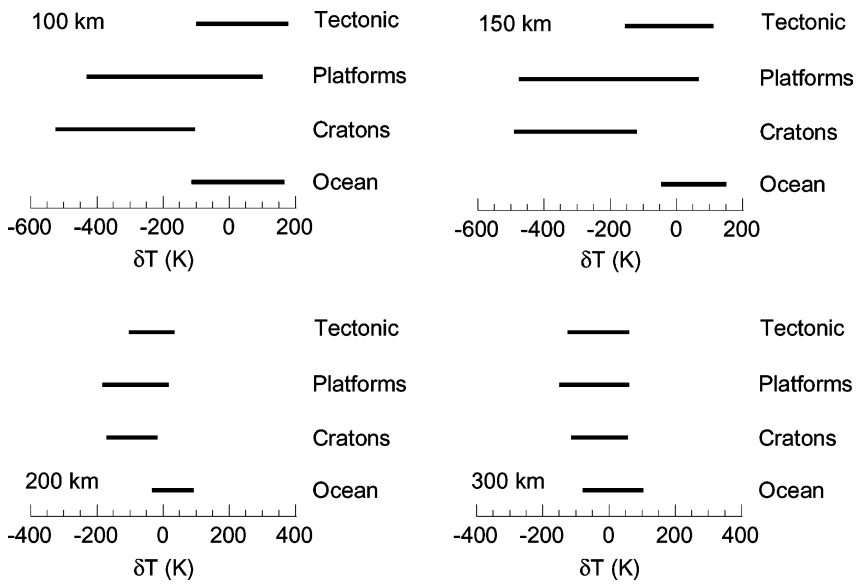

Fig. 5. Statistics on the distribution of temperature anomalies for several regions and depths (indicated on each plot). The tectonic regions are delimited following the model 3SMAC (Nataf and Ricard, 1996).

where each horizontal bar covers the interval $\delta\overline{T}+\sigma_{\delta T}$ Iron anomalies (Fig. 6) reveal a similar pattern. At shallow depths ($z < 200$ km), the distribution of temperature anomalies strongly depends on the observed surface tectonics. Old cratons yield low mean anomalies of temperature and iron ($\overline{\delta T} \sim -310$ K and $\overline{\delta \mathrm{Fe}} \sim -3.0\%$) with variances close to $\sigma_{\delta T} = 200$ K and $\sigma_{\delta \mathrm{Fe}} = 2.0\%$, respectively. Compared to the

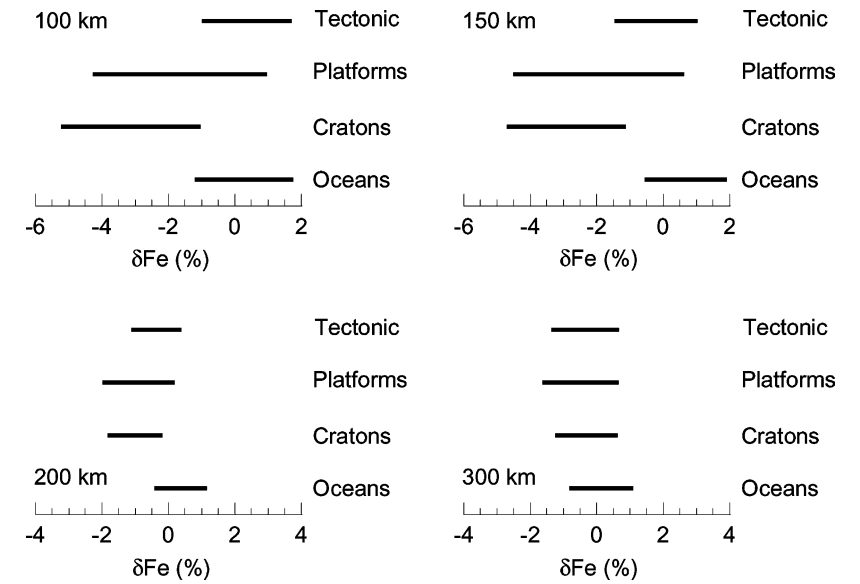

Fig. 6. Statistics on the distribution of iron anomalies for several regions and depths (indicated on each plot). The tectonic regions are delimited following the model 3SMAC (Nataf and Ricard, 1996).

average mantle, old cratons are, therefore, significantly colder and depleted in iron. This feature holds to a lesser extent for stable platforms, which yield higher mean anomalies ($\overline{\delta T} \sim -160$ K and $\overline{\delta \mathrm{Fe}} \sim -1.7\%$) and variances ($\sigma_{\delta T} \sim 260$ K and $\sigma_{\delta \mathrm{Fe}} \sim 2.6\%$) than old cratons. Oceans and tectonic continents, on the other hand, are more homogeneous. For these regions, the mean temperature and iron anomalies are close to zero and the variances are smaller ($\sigma_{\delta T} \sim 130$ K and $\sigma_{\delta \mathrm{Fe}} \sim 1.4\%$), and therefore, there is no significant increase of temperature and/or enrichment in iron. At $z = 150$ km, oceans seem slightly warmer than the average mantle ($\overline{\delta T} \sim 50$ K), but the variance ($\sigma_{\delta T} \sim 90$ K) still suggests that it is not significant. At $z = 200$ km, the differences between tectonic regions is strongly damped. Old cratons remain slightly colder than the average mantle ($\overline{\delta T} \sim -90$ K and $\sigma_{\delta T} \sim 70$ K) and depleted in iron ($\overline{\delta \mathrm{Fe}} \sim -1.0\%$ and $\sigma_{\delta \mathrm{Fe}} \sim 0.8\%$). Anomalies of temperature and iron in stable platforms are now very similar to those observed in old cratons. Tectonic continents are slightly colder and depleted in iron than average, whereas oceans are slightly warmer and enriched in iron. Finally, at $z = 300$ km the distributions of temperature and iron anomalies are homogeneous and do not depend on the surface tectonics. Whatever the region, iron (temperature) anomalies are centered on $\overline{\delta \mathrm{Fe}} = 0$ ($\overline{\delta T} = 0$) with a variance close to $\sigma_{\delta \mathrm{Fe}} = 0.9\%$ ($\sigma_{\delta T} = 90$ K).

The results presented in this paper agree with the recent study of Forte and Perry (2000), who found anomalies of temperature and iron of $\delta T = -400$ K and $\delta \mathrm{Fe} = -2\%$ in continental roots. Forte and Perry (2000) used a method similar to that presented in this paper. A major difference is that they used several geodynamic data sets, including surface dynamic topography, to constrain the density and to compute the scaling factor. In this study, we constrained density with gravity anomalies only. Although dynamic topography is important to constrain the density structure of the upper mantle, the conversion from observed to dynamic topography is very delicate, and we decided to omit it. Another difference is that we used a refined numerical model to invert relative V_s-anomalies and ζ for δT and $\delta \mathrm{Fe}$ (Section 4.1 and Appendix A).

The important conclusion of Figs. 5 and 6 is that seismic and gravity data are explained by simultaneous anomalies of temperature and iron content. The regions where the material is colder than average are also depleted in iron. In other words, the increase of density due to temperature drop is lowered by a lack of iron. Depending on their respective amplitudes, the depletion in iron may balance the cooling of the continents and play an important role in the stability of continental platforms and cratons. We discuss this point is in details in Section 5.

4.5. An additional test

The scaling factor was constructed from gravity and S-wave velocity anomalies. We then determine anomalies of temperature and iron by inverting the V_s-correlated density anomalies and the V_s-anomalies. We omitted the density information uncorrelated to V_s, which may leads to small biases. For instance, our inferred anomalies of temperature and iron remain perfectly correlated to V_s-anomalies, as mentioned in Section 4.3. It would be more appropriate to introduce another independent data set, such as P-wave velocity anomalies. However, few studies provide V_p-anomalies in the upper mantle. In replacement, one can use S and P travel time residuals (δt_s and δt_p). The ratio $a = \delta t_\mathrm{s}/\delta t_p$ is related to the ratio χ of the relative variations of V_p to the relative variations of V_s:

$$\chi = \frac{\partial \ln V_\mathrm{p}}{\partial \ln V_\mathrm{s}} = \frac{1}{a}\frac{V_\mathrm{p,ref}}{V_\mathrm{s,ref}} \tag{10}$$

where $V_\mathrm{p,ref}$ and $V_\mathrm{s,ref}$ are the reference P- and S-waves velocities. For the upper mantle Robertson and Woodhouse (1997) have found $a = 2.85 \pm 0.19$, independently of the tectonic region. For North America, Vinnik et al. (1999) proposed values of a between 3.49 and 3.97. We used this additional constraint to test our results. Following the method of Vacher et al. (1998), we computed the relative anomalies of P-wave predicted by our distributions of δT and $\delta \mathrm{Fe}$. We then obtained values of χ according to Eq. (10), and convert χ into a using PREM (Dziewonski and Anderson, 1981). For the whole Earth, we find $a = 2.78 \pm 0.4$ at $z = 100$ km, and $a = 3.14 \pm 0.2$ at $z = 200$ km depth. For North America, $a = 2.70 \pm 0.4$ at $z = 100$ km, and $a = 3.10 \pm 0.2$ at $z = 200$ km depth. These values are in good agreement with Robertson and Woodhouse (1997) and, to a lesser extent, with Vinnik et al. (1999).

5. Dynamic implications

5.1. Stability analysis

We now perform a stability analysis in the case of a layer submitted to chemical and thermal buoyancy. Chemical buoyancy is driven by anomalies of density $\delta\rho_c$ that result from compositional anomalies located in a root of thickness d_r and length l_r. Thermal buoyancy is driven by anomalies of density resulting from temperature anomalies $\delta\rho_{th} = -\alpha\rho_0\delta T$ (where α is thermal expansion), located in a thermal boundary layer (TBL) of mean thickness δ and length L (this length is also the length of the convective cell). As proposed by Lenardic and Moresi (1999), the characteristic lengths of the problem, which will be used to non-dimensionalize the equations, are the depth of the mantle D and the length of a convective cell L. The parameter $B = -\delta\rho_c/\delta\rho_{th}$ is known as the buoyancy ratio. The deviation from hydrostatic equilibrium induced by the density anomalies $\delta\rho_{th}$ and $\delta\rho_c$ is given by the pressure P:

$$P = (d_r l_r \delta\rho_c - \delta L\, \alpha\rho_0\, \delta T)\frac{g}{L} \tag{11}$$

where g is the acceleration of gravity.

If the term in parenthesis in Eq. (11) is negative, the root is buoyant and does not sink. This corresponds to the third regime defined by Lenardic and Moresi (1999).

Introducing the buoyancy ratio B, and using non-dimensional variables ($l'_r = l_r/L$, $d'_r = d_r/D$ and $\delta' = \delta/D$), one gets a condition for this regime:

$$B > \frac{\delta'}{d'_r l'_r} \tag{12}$$

This condition is the same as Eq. (7) of Lenardic and Moresi (1999) and is valid for negative anomalies of temperature (i.e. $\delta\rho_{th} > 0$) only. Typical values for d_r and l_r are 300 and 1000 km, respectively. Assuming $D \sim 3000$ km (in case of whole mantle convection) and $L \sim 2000$ km, the condition (12) implies that $B > 20\delta'$. For instance, if $B = 1$ the negative buoyancy induced by a 150 km ($\delta' = 0.05$, if one considers whole mantle convection) thick TBL is balanced. If the term in parenthesis in Eq. (11) is positive, the material will sink, with a velocity u_z. However, friction forces inhibit this motion and favor buoyancy. The frictional force per unit of surface (f) is approximated by

$$f \sim A u_z \frac{\mu}{d_r} \tag{13}$$

where A is a constant, and μ the viscosity of the material. The velocity u_z can be scaled according to the physical properties of the system. Usually, velocity is scaled by the ratio of the thermal diffusivity (κ) to the depth of the system (here the depth of the root), and

$$f \sim A' \frac{\mu\kappa}{d_r^2} \tag{14}$$

where A' is a dimensionless constant. Motion occurs when P is greater than f (in absolute value). At the onset, the buoyancy ratio is such that

$$B_c = \frac{\delta'}{d'_r 1'_r} + \frac{C}{\delta T' d'^3_r 1'_r}, \quad C = \frac{A'}{Ra},$$
$$Ra = \frac{\alpha\rho_0 g\, \Delta T\, D^3}{\mu\kappa}. \tag{15}$$

In this equation Ra is the Rayleigh number, ΔT the non-adiabatic temperature difference across the mantle, and $\delta T' = \delta T/\Delta T$. If the buoyancy ratio is greater (smaller) than B_c, the root is stable (sinks). The conditions to create a buoyant root are easier to satisfy as the value of B_c is smaller. A difficulty is to estimate the value of A'. Friction increases with the value of A' (Eq. (14)), which may depend on the rheology of the fluid and/or on the type of boundary condition at the surface. For instance, one expects that A' increases with the strength of the rock (i.e. for harder rheologies). Stability analysis for purely thermal convection (e.g. Sotin and Labrosse, 1999), defines A' as the TBL Rayleigh number (Ra_δ). In the case of an isoviscous fluid with free slip boundaries, studies showed that Ra_δ is roughly constant and equal to 6 for both top and bottom TBLs (Sotin and Labrosse, 1999). If one considers variable viscosity convection, or rigid boundary condition at the surface, the top TBL gets less unstable, and its Rayleigh number yields values around 100 (Deschamps and Sotin, 2000). Considering values of A' between 1 and 100, and Rayleigh numbers between 5×10^5 and 10^7, one gets values of C between 10^{-7} and 5×10^{-3}. Fig. 7 represents B_c as a function of the absolute value of $\delta T'$ and for several values of $r' = \delta'/d'_r$, l'_r and C. For a

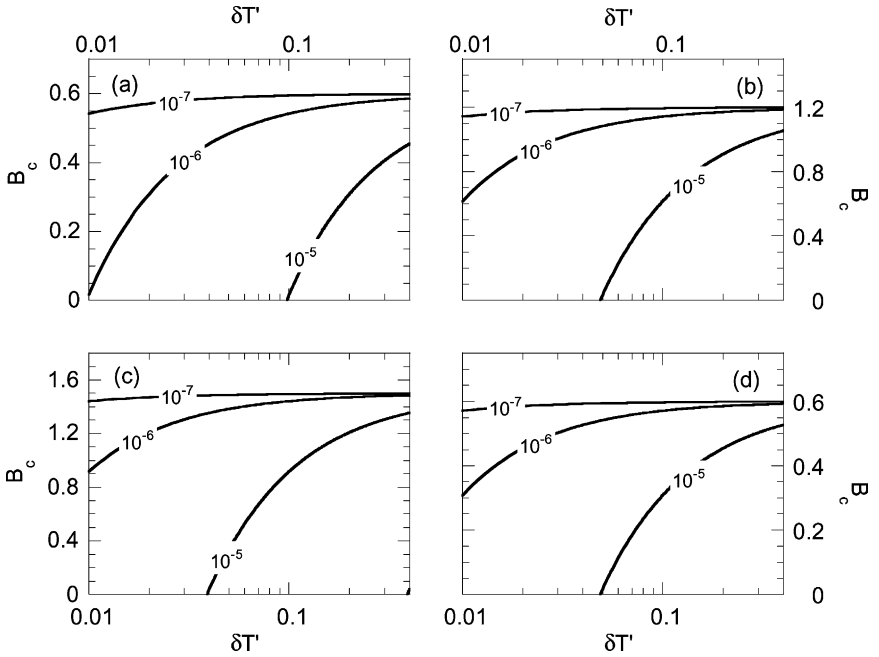

Fig. 7. Buoyancy ratio at the onset of instability (B_c) as a function of the absolute value of non-dimensional temperature anomalies ($\delta T'$) and for several values of $C = A'/Ra$. The ratio of the TBL thickness to the root thickness is $r' = 0.3$ (a), $r' = 0.6$ (b and d) and $r' = 0.75$ (c). The length of the root is $l'_r = 0.5$ (plots a to c) and $l'_r = 1.0$ (plot d).

given value of C, B_c decreases as r' increases (Fig. 7a and c). The stability of the root increases as the root is thicker and/or the TBL is thinner. In addition, the stability of the root increases with the length of the root (compare Fig. 7b and d). Finally, the parameter C has a strong influence on B_c. For given temperature anomaly and Rayleigh number, B_c gets significantly smaller as A' increases. As expected, rheology may play an important role in the stability of the layer.

5.2. Continental roots

A possible origin for the high-velocity anomalies observed in continental roots is that the constitutive material of these roots is simultaneously colder than the average mantle and depleted in iron (Section 4.4). This result has important consequences, since negative anomalies of density induced by low temperature would be balanced by positive anomalies of density induced by the depletion in iron. In other words, depletion in iron would prevent lateral and vertical flow due to the low temperatures of the root and explain the stability of old cratons. To test this hypothesis, we have computed buoyancy ratios associated with the observed continental roots.

First, at a given depth we compute the anomalies of density, respectively induced by the inverted anomalies of temperature and iron. These anomalies of density are then integrated over depth, resulting in mean thermal ($\overline{\delta\rho_{th}}$) and compositional ($\overline{\delta\rho_c}$) density anomalies. At each location, the buoyancy ratio is finally given by $B = -\overline{\delta\rho_c}/\overline{\delta\rho_{th}}$. The error on B due to the uncertainties on the reference temperature is around 10%. Histograms in Fig. 8 represent the frequency of B (i.e. the ratio of the surface having a given value of B to the total surface) for old cratons (Fig. 8a and c) and stable platforms (Fig. 8b and d). Two thicknesses of the root (h_r) are considered: $h_r = 100$ km (Fig. 8a and b) and $h_r = 200$ km (Fig. 8c and d). The buoyancy ratio is centered on $B \sim 0.82$ for $h_r = 100$ km, and $B \sim 0.85$ for $h_r = 200$ km. In every case the dispersion is very small: the buoyancy ratio yields within 0.7 and 0.9 for more than 90% of the total surface of the root. These estimates are in good agreement

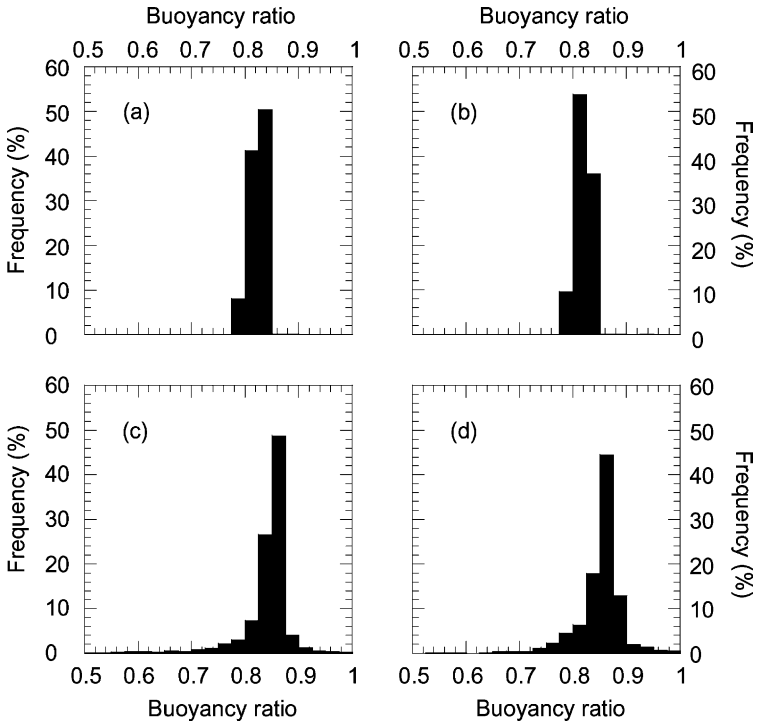

Fig. 8. Buoyancy ratio (B) in old cratons (a and c) stable platforms (b and d). The y-axis represent the percentage of the total surface of the root (or frequency) having a buoyancy ratio equal to a given value of B. The thickness of the root is equal to 100 km (a and b) or 200 km (c and d).

with those of Forte and Perry (2000), who found a buoyancy ratio close to 0.8. Note that the dispersion is higher in stable platforms than in old cratons, and that it increases slightly with the thickness of the root.

To compare these results with those of the stability analysis, one must chose values for ΔT, D and Ra. Different values may be considered, depending on the mode of mantle convection. The temperature at the 660 km discontinuity is relatively well constrained from mineral physics experiments. In the case of layered mantle convection, one may, therefore, chose the value of ΔT around 1600 K. In addition, $D = 660$ km and a typical value of the Rayleigh number is $Ra = 5.0 \times 10^5$. In the case of whole mantle convection $D = 2890$ km and the Rayleigh number is close to 10^7. The temperature at the core–mantle boundary, on the other hand, is poorly constrained. A median value is $T_{\mathrm{CMB}} = 3500$ K (including the adiabatic contribution) (e.g. Williams, 1998). Assuming that the adiabatic increase of temperature across the whole mantle is about 1000 K this estimate leads to $\Delta T \sim 2500$ K. Typical values for the anomalies of temperature below cratons are $\delta T = -330 \pm 200$ K (see Section 4.4). For whole mantle (layered) convection values of $\delta T'$ in old cratons yield between -0.05 and -0.2 (-0.08 and -0.3). To estimate the non-dimensional parameter C, we assumed that A' varies between 1 (for soft rheology) and 100 (for hard rheology). Therefore, $10^{-7} \leq C \leq 10^{-5}$ for whole mantle convection, and $2 \times 10^{-6} \leq C \leq 2 \times 10^{-4}$ for layered convection. Other scaling are reported in Table 1 for whole mantle and layered convection.

TBLs transfer heat by conduction. An estimate of the thickness of the TBL at the top of the mantle is, therefore,

$$\delta = k \frac{\Delta T_{\mathrm{e}}}{q_{\mathrm{m}}} \tag{16}$$

where k is the thermal conductivity of the rock, ΔT_{e} the temperature difference across the TBL, and q_{m}

Table 1
Scaling of the parameters used in stability analysis

Parameter	Typical values (dimensional)	Symbol	Whole mantle convection	Layered convection
Temperature anomaly[a]	100–500 K	$\delta T'$	0.04–0.2	0.06–0.3
TBL thickness	75–270 km[b]	δ'	0.03–0.09	0.1–0.4
–	10–60 km[c]	–	3×10^{-3}–0.02	0.02–0.09
Root thickness	100–300 km	d'	0.04–0.1	0.15–0.45
Root length	1000–2000 km	l'	0.5–1.0	0.5–1.0
A'/Ra[d]		C	10^{-7} to 10^{-5}	2×10^{-6} to 2×10^{-4}

[a] Absolute values.
[b] Case of an isoviscous mantle (see text).
[c] Case of a strongly temperature-dependent mantle viscosity (see text).
[d] A' is a parameter that depends on the rheology and Ra is the Rayleigh number. Higher values of A' (and, therefore, of C) are obtained for harder rheologies (e.g. strongly temperature-dependent mantle viscosity).

the heat flux at the top of the TBL. This heat flow can be estimated by removing the crustal heat production from the surface heat flow. For cratonic areas, Jaupart and Mareschal (1999) estimated q_m around 10–15 mW/m^2 (Canadian shield) and 17 mW/m^2 (South Africa). Studies of experimental and numerical convection have shown that the thickness of the TBL (and, therefore, the temperature difference across this layer) depends on the fluid rheology, and particularly on the properties of the fluid viscosity (e.g. Richter et al., 1983; Davaille and Jaupart, 1993; Moresi and Solomatov, 1995). If the viscosity does not depend on temperature, all the fluid participates in the flow and the top TBL can be safely approximated by the conductive layer that lies at the top of the fluid. Assuming that the temperature at the top of the mantle (around $z = 50$ km depth) is close to 700 K and that the mantle adiabat yields between 1200 and 1600 K, one gets $500 \leq \Delta T_e \leq 800$ K. For $k = 3$ W/m/K and $10 \leq q_m \leq 20$ mW/m^2, the thickness of TBL is between 75 and 270 km (see Table 1 for non-dimensional values). These values constitute an upper bound. Indeed, if the fluid viscosity is strongly temperature-dependent, a viscous lid develops at the top of the fluid. This layer is stable and it does not participate to convection. It transfers heat by conduction with a heat flux equal to that of the TBL. To estimate the thickness of the TBL, one must remove the stable layer from the top conductive layer. Davaille and Jaupart (1993) proposed that ΔT_e is proportional to a "viscous temperature scale" ΔT_v. Following this result and assuming an Arrhenius type of law for the viscosity of the rock, one gets

$$\Delta T_e = 2.24 \frac{R T_m^2}{Q} \quad (17)$$

where R is the gas constant, Q the activation energy of the rock, and T_m is the mean adiabatic temperat ure of the mantle. Taking $2.4 \times 10^5 \leq Q \leq 4.3 \times 10^5$ kJ/mol (e.g. Karato and Wu, 1993) and $1200\,\text{K} \leq T_m \leq 1600\,\text{K}$, one finds $60\,\text{K} \leq \Delta T_e \leq 200\,\text{K}$. If $k = 3$ W/m/K and $10 \leq q_m \leq 20$ mW/m^2, the thickness of the TBL yields between 10 and 60 km (see Table 1 for non-dimensional values). These estimates are significantly lower than those for constant viscosity.

According to Fig. 7, the continental root is more stable if viscosity is strongly temperature-dependent. In that case, the value of C is higher (i.e. the frictions are larger), and the TBL is thinner than in the case of a constant viscosity. For cratons and stable platforms (Fig. 8), the buoyancy ratio is close to $B = 0.8 \pm 0.2$ (this error bar includes dispersion on B and uncertainty due to possible errors on the reference temperature and on the V_s-anomalies). In the case of temperature-dependent viscosity, $\delta \leq 50$ km and if the thickness (d) of the root is equal to 200 km, the ratio $r' = \delta/d$ is lower than 0.3. The value of B for cratons and platforms is clearly higher than the critical buoyancy ratio for $r' = 0.3$, even for low values of C (Fig. 7a). In other words, the negative buoyancy induced by low temperature is completely balanced and the root is stable. If the thickness of the root and of the TBL are equal to 100 and 60 km, respectively, $r' = 0.6$ and one needs values of C around 2×10^{-5} to keep the

root stable (Fig. 7b). This condition is easier to satisfy in the case of layered convection ($A' \sim 10$) than in the case of whole mantle convection ($A' \sim 200$). The case $\delta = 100$ and 60 km is, however, a limit case. First continental roots are present down to 250–300 km. And second, $\delta = 60$ km is an upper bound if one considers a strongly temperature-dependent viscosity. In the case of constant (or slightly temperature-dependent) viscosity, the TBL is likely thicker than 75 km and A' less than 10. For a 200 km-root and small values of the TBL thickness ($75 \leq \delta \leq 100$), $0.375 \leq r' \leq 0.5$ and there is no clear conclusions. In the case of whole mantle convection, on the other hand, C has values higher than 10^{-6} and the root is likely unstable. Note that the opposite conclusion cannot be excluded if one considers large roots ($l'_r = 1.0$) (Fig. 7d). Finally, if the TBL is thicker than $\delta = 100$ km, or if the root is thinner than $d = 200$ km, it is reasonable to think that the root is not stable, whatever the mode of mantle convection (Fig. 7c).

6. Discussion and conclusions

Regions of high positive V_s-anomalies extend down to 250–300 km below old cratons and stable platforms, and are interpreted as chemically distinct mantle, or tectosphere. Previous studies based on seismological observations proposed that the tectosphere is indeed depleted in iron (e.g. Jordan, 1988; Anderson, 1990; Polet and Anderson, 1995). However, because seismic velocities are also sensitive to temperatures, no clear cut conclusions can be made from seismic data only. An alternative is to invert geodynamic data sets (e.g. gravity anomalies) for anomalies of temperature and composition (Forte and Perry, 2000; this study). Such studies support the hypothesis that continental roots are strongly depleted in iron. An important conclusion of the present study is that the relative density-to-shear wave velocity ratio (ζ) is such that temperature anomalies alone cannot be responsible for the observed V_s-anomalies and ζ. Simultaneous variations of iron and temperature are required to explain gravity and seismic velocity anomalies. Regions that are colder (warmer) than the average mantle are also depleted (enriched in iron). For instance, below cratons the mean anomalies of temperature and iron are close to -330 K and -3.2%, respectively. Polet and Anderson (1995) found that the extent of continental roots is strongly correlated to the age of cratons, the Archean cratons having the deepest roots. A current hypothesis is that present day cratonic roots result from an intense volcanic activity at the Archean (e.g. Herzberg, 1993; Polet and Anderson, 1995; and references therein). The melts extracted from a pyrolite source are enriched in CaO, Al_2O_3 and FeO, resulting in a depleted continental uppermost mantle.

It has been proposed that the negative buoyancy induced by temperatures lower than average are balanced by positive buoyancy due to depletion in iron (e.g. Jordan, 1975, 1988; Forte et al., 1995). However, rheology also plays an important role in the stability of roots. Numerical models including both temperature-dependent viscosity and chemical differentiation due to partial melting (deSmet et al., 1999) have shown that the layered structure resulting from differentiation remains stable over a long period of time ($\geq$1.0 Gyr). Using simple physical laws, Lenardic and Moresi (1999) concluded that buoyancy alone cannot stabilize the continental roots. In addition to buoyancy, the mantle viscosity must be strongly temperature-dependent. Our stability analysis is in good agreement with this conclusion, although the value of A' as a function of the rheology is not well constrained. There is, however, a serious restriction in invoking temperature-dependent viscosity: to be consistent, one must assume a temperature-dependent viscosity throughout the whole uppermost mantle (and not only below cratons), which would inhibit plate tectonics (Lenardic and Moresi, 1999). This difficulty can be solved assuming that the cratonic mantle is poor in volatiles. Indeed, Polet and Anderson (1995) noted that cratonic Archean mantle could have been dried out by high-temperature melt extraction. Creep flow laws are significantly different whether the environment is wet or dry, and drier materials have higher strengths (e.g. Karato and Wu, 1993; Mackwell et al., 1998). Therefore, if volatiles have been massively extracted from the continental uppermost mantle during the Archean, old cratons would be difficult to deform, and they would remain stable over long periods of time.

A major concern of this study was to estimate the error bars on the temperature and iron anomalies. These error bars reach 10%, excluding errors induced by the uncertainties on V_s-anomalies. Refined models

of seismic tomography models, including error bars, and a better knowledge of the mantle adiabat would reduce uncertainties on inverted temperature and iron anomalies. Another improvement would be to account for the rheology more accurately, including the role and influence of volatiles. Stability analysis suggests that roots are stable only if the mantle viscosity is strongly temperature-dependent. However, the stability of the top TBL for a fluid including temperature-dependent viscosity and chemical roots is not well understood. Systematic studies of numerical or experimental convection should be conducted to determine criteria of stability as a function of rheology and chemical differentiation.

Acknowledgements

We thank Pierre Vacher who provided us the original version of the software computing synthetic densities and seismic velocities from temperature and mineralogical composition. We are also grateful to two anonymous reviewers for their useful comments. This research was partly funded by the Netherlands Organization for Scientific Research (NWO, grant 750.297.02).

Appendix A. Computation of density and seismic velocities

Numerical models can predict densities and seismic velocities in the mantle, for a given thermodynamic state (temperature and pressure) and a given petrology. In this study, we have used a numerical method based on Grüneisen's and adiabatic finite strain theories (e.g. Duffy and Anderson, 1989; Vacher et al., 1996). Densities and elastic moduli of individual minerals at ambient temperature and pressure are first projected at temperature T and pressure p. The density and elastic moduli of the rock are then obtained by averaging the individual densities and elastic moduli as a function of the petrologic model.

The density and the elastic parameter of each mineral at temperature T are obtained from Grüneisen's theory:

$$\rho(T, p=0) = \rho_0 \exp\left[-\int_{T_0}^{T} \alpha(T')\,\mathrm{d}T'\right], \qquad (A.1)$$

$$M(T, p=0) = M_0 \left[\frac{\rho(T)}{\rho_0}\right]^{\beta_M},$$

$$\beta_M = -\frac{1}{\alpha_0 M_0}\left(\frac{\partial M}{\partial T}\right)_p, \qquad (A.2)$$

where M stands for the bulk (K) or shear (G) modulus and the subscript "0" indicates values of the parameter at ambient temperature (T_0) and pressure ($p = 0$). The temperature dependence of the thermal expansion α is well described by

$$\alpha(T) = a_1 + a_2 T - \frac{a_3}{T_2} + \frac{a_4}{T}, \qquad (A.3)$$

where the coefficient a_i are deduced from laboratory experiments (Table 2).

The density and elastic moduli are then projected at depth following a Birch–Murnaghan adiabatic compression to the third order:

$$p = -3K_{T,0}(1-2\varepsilon)^{5/2}(\varepsilon + \tfrac{1}{2}B\varepsilon^2),$$

$$B = 3K\left[4 - \left(\frac{\partial K}{\partial p}\right)_T\right], \qquad (A.4)$$

where ε is the strain of the mineral. For a given pressure, Eq. (A.4) is solved for the strain. The density, bulk and shear moduli at temperature T and pressure p are then, respectively given by

$$\rho(T, p) = \rho_{T,0}(1-2\varepsilon)^{3/2} \qquad (A.5)$$

$$K(T, p) = (1-2\varepsilon)^{5/2}(K_{T,0} + C_K\varepsilon),$$

$$C_K = 5K_{T,0} - 3K_{T,0}\left(\frac{\partial K}{\partial p}\right)_T, \qquad (A.6)$$

Table 2
Thermal expansion of some minerals[a]

Mineral	a_1 (10^{-5} K^{-1})	a_2 (10^{-8} K^{-2})	a_3 (K)	a_4 (10^{-2})
Olivine	2.832	0.758	0	0
Diopside	3.206	0.811	1.8167	0.1347
Enstatite	2.860	0.720	0	0
Garnet	2.810	0.316	0.4587	0
Jadeite	2.560	0.260	0	0

[a] Thermal expansion is computed following Eq. (A.3). Compilation is after Vacher et al. (1998). See references of experimental studies therein.

Table 3
Densities and elastic properties of some minerals[a]

Mineral	X^b (%)	ρ_0 (g/cm^3)	K_0 (GPa)	$\partial K/\partial p$	$\partial K/\partial T$ (GPa/K)	G_0 (GPa)	$\partial G/\partial p$	$\partial G/\partial T$ (GPa/K)
Olivine	61.7	3.222 + 1.182xFe	128	4.3	−0.016	81 − 30xFe	1.4	−0.014
Diopside	13.3	3.277 + 0.38xFe	105 + 13xFe	6.2 − 1.9xFe	−0.013	67 − 6xFe	1.7	−0.010
Enstatite	5.2	3.215 + 0.799xFe	124	5.6	−0.012	78 − 24xFe	1.4	−0.011
Garnet	15.3	3.565 + 0.76xFe	173 + 7xFe	5.3	−0.021	92 + 7xFe	2.0	−0.010
Jadeite	4.5	3.320	126	5.0	−0.016	84	1.7	−0.013

[a] Compilation is after Vacher et al. (1998). See references of experimental studies therein.
[b] Volumic fraction in pyrolite.

$$G(T, p) = (1 - 2\varepsilon)^{5/2}(G_{T,0} + C_G\varepsilon),$$
$$C_G = 5G_{T,0} - 3K_{T,0}\left(\frac{\partial G}{\partial p}\right)_T. \quad \text{(A.7)}$$

The subscript "T,0" denotes the values of the parameter at temperature T and zero pressure. Values of the elastic moduli at ambient condition, and their derivatives with respect to pressure and temperature are reported in Table 3.

The temperature at the foot of the adiabat must also be projected at depth. The increment of temperature due to the increase of pressure is controlled by the adiabatic gradient of temperature γ_S, and the end (or real temperature) is given by

$$T_f = T + \gamma_s(p - p_0),$$
$$\gamma_s = \left(\frac{\partial T}{\partial p}\right)_S = \left(\frac{\alpha T}{\rho C_p}\right)_{p,T}\left(\frac{\rho_0}{\rho}\right)^{6.5} \quad \text{(A.8)}$$

Knowing the end-temperature, one can estimate the sensitivity of density and seismic velocities to temperature.

Densities and elastic moduli of individual minerals depend on the volumic fraction of iron, i.e. the ratio $x\mathrm{Fe} = \mathrm{Fe}/(\mathrm{Fe} + \mathrm{Mg})$. The method used in this paper accounts for this dependence. For each mineral, and prior to projection at temperature T and pressure p, the density and elastic moduli at ambient temperature and pressure are corrected as indicated in Table 3. One can, therefore, estimate the sensitivity of density and seismic velocities to the iron content. The properties of the rock assemblage are computed from the properties of individual minerals according a petrologic model. Considering different petrologic models, one can estimate the sensitivity of density and seismic velocities to compositional variations (e.g. variations in the volumic fraction of olivine). In this study, we only considered the minerals present in the uppermost mantle (Table 3). The density of the rock ($\overline{\rho}$) is simply the volumetric average of the densities of the minerals composing the rock. The bulk and shear modulus ($\overline{K}$ and $\overline{G}$) are computed following the Hashin–Shtrickman averaging, which is well suited for the upper mantle (Vacher et al., 1996). Finally, the P-wave and S-wave velocity of the rock are given by

$$V_p = \sqrt{\frac{\overline{K} + (4/3)\overline{G}}{\overline{\rho}}} \quad \text{and } V_s = \sqrt{\frac{\overline{G}}{\overline{\rho}}}. \quad \text{(A.9)}$$

References

Alsina, D., Woodward, R.L., Snieder, R.K., 1996. Shear wave velocity structure in North America from large-scale waveform inversions of surface waves. J. Geophys. Res. 101, 15969–15986.

Anderson, D.L., 1987. Thermally induced phase changes, lateral heterogeneity of the mantle, continental roots, and deep slab anomalies. J. Geophys. Res. 92, 13968–13980.

Anderson, D.L., 1990. Geophysics of the continental mantle: an historical perspective. In: M. Menzies (Ed.) Continental Mantle. Clarendon Press, Oxford, pp. 1–30.

Anderson, D.L., Given, J.W., 1982. Absorption band Q model for the Earth. J. Geophys. Res. 87, 3893–3904.

Davaille, A., Jaupart, C., 1993. Transient high Rayleigh number thermal convection with large viscosity variations. J. Fluid Mech. 253, 141–166.

Davies, G.F., Dziewonski, A.M., 1975. Homogeneity and constitution of the Earth's lower mantle and outer core. Phys. Earth Planet Inter. 10, 336–343.

Deschamps, F., Sotin, C., 2000. Inversion of two-dimensional numerical convection experiments for a fluid with a strongly temperature-dependent viscosity. Geophys. J. Int. 143, 204–218.

Deschamps, F., Snieder, R., Trampert, J., 2001. The relative density-to-shear velocity scaling in the uppermost mantle. Phys. Earth Planet Inter. 124, 193–211.

deSmet, J.H., van den Berg, A.P., Vlaar, N.J., 1999. The evolution of continental roots in numerical thermo-chemical mantle convection models including differentiation by partial melting. Lithos 48, 153–170.

Doin, M.-P., Fleitout, L., McKenzie, D., 1996. Geoid anomalies and the structure of continental and oceanic lithospheres. J. Geophys. Res. 101, 16119–16135.

Duffy, T.S., Anderson, D.L., 1989. Seismic wave speeds in mantle minerals and the mineralogy of the upper mantle. J. Geophys. Res. 94, 1895–1912.

Dziewonski, A.M., Anderson, D.L., 1981. Preliminary reference earth model. Phys. Earth Planet. Inter. 25, 297–356.

Forte, A.M., Peltier, W.R., 1991. Viscous flow models of global geophysical observables. I. Forward problems. J. Geophys. Res. 96, 20131–20159.

Forte, A.M., Perry, A.C., 2000. Seismic-geodynamic evidence for a chemically depleted continental tectosphere. Science 290, 1940–1944.

Forte, A.M., Dziewonski, A.M., O'Connell, R.J., 1995. Thermal and chemical heterogeneity in the mantle: a seismic and geodynamic study of continental roots. Phys. Earth Planet Inter. 92, 45–55.

Goes, S., Govers, R., Vacher, P., 2000. Shallow mantle temperatures under Europe from P- and S-wave, tomography. J. Geophys. Res. 105, 11153–11169.

Herzberg, C.T., 1993. Lithosphere peridotites of the Kaapvaal craton. Earth Planet. Sci. Lett. 120, 13–29.

Jackson, A., 2000. Laboratory measurement of seismic wave dispersion and attenuation: recent progress. In: Karato, S.I., Forte, A.M., Lieberman, R.C., Masters, G., Stixrude, L. (Eds.), Earth's Deep Interior: Mineral Physics and Tomography from the Atomic to the Global Scale, Geophys. Monogr. Ser., Vol. 117., American Geophysical Union, Washington, DC, pp. 3–36.

Jaupart, C., Mareschal, J.C., 1999. The thermal structure and thickness of continental roots. Lithos 48, 93–114.

Jordan, T.H., 1975. The continental tectosphere. Rev. Geophys. Space Phys. 13, 1–12.

Jordan, T.H., 1979. Mineralogies, densities and seismic velocities of garnet lherzolites and their geophysical implications. In: Boyd, F.R., Meyer, H.O.A. (Eds.), The Mantle Sample: Inclusions in Kimberlites and Other Volcanics. American Geophysical Union, Washington, DC, pp. 1–14.

Jordan, T.H., 1988. Structure and formation of the continental tectosphere. J. Petrol. (Special Lihosphere Issue), 11–37.

Karato, S.-I., 1993. Importance of anelasticity in the interpretation of seismic tomography. Geophys. Res. Lett. 20, 1623–1626.

Karato, S.-I., Wu, P., 1993. Rheology of the upper mantle: a synthesis. Science 260, 771–778.

Kogan, M.K., McNutt, M.K., 1993. Gravity field over northern Eurasia and variations in the strength of the upper mantle. Science 259, 473–479.

Lemoine, F.G., Kenyon, S.C., Factor, J.K., Trimmer, R.G., Pavlis, N.K., Chinn, D.S., Cox, C.M., Klosko, S.M., Luthcke, S.B., Torrence, M.H., Wang, Y.M., Williamson, R.G., Pavlis, E.C., Rapp, R.H., Olson, T.R., 1998. The Development of the Joint NASA GSFC and National Imagery Mapping Agency (NIMA) Geopotential Model EGM96. NASA/TP-1998-206861, NASA, GSFC, Greenbelt, MD, 20771.

Lenardic, A., Moresi, L.-N., 1999. Some thoughts on the stability of cratonic lithosphere: effects of buoyancy and viscosity. J. Geophys. Res. 104, 12747–12758.

Mackwell, S.J., Zimmerman, M.E., Kohlstedt, D.L., 1998. High-temperature deformation of dry diabase with applications to tectonics on Venus. J. Geophys. Res. 103, 975–984.

Mégnin, C., Romanowicz, B., 2000. The three-dimensional shear velocity structure of the mantle from the inversion of body, surface and higher-mode waveforms. Geophys. J. Int. 143, 708–728.

Minster, J.B., Anderson, D.L., 1981. A model of dislocation-controlled rheology for the mantle. Philos. Trans. R. Soc. London 299, 319–356.

Mitrovica, J.X., Forte, A.M., 1997. Radial profile of mantle viscosity: results from the joint inversion of convection and post-glacial rebound observables. J. Geophys. Res. 102, 2751–2769.

Moresi, L.-N., Solomatov, V.S., 1995. Numerical investigation of two-dimensional convection with extremely large viscosity variations. Phys. Fluids 7, 2154–2162.

Nataf, H.-C., Ricard, Y., 1996. 3SMAC: an a priori tomographic model for upper mantle based on geophysical modeling. Phys. Earth Planet. Inter. 95, 101–122.

Polet, J., Anderson, D.L., 1995. Depth extent of cratons as inferred from tomographic studies. Geology 23, 205–208.

Richter, F.M., Nataf, H.C., Daly, S.F., 1983. Heat transfer and horizontally averaged temperature of convection with large viscosity variations. J. Fluid Mech. 129, 173–192.

Ritsema, J., van Heijst, H., 2000. New seismic model of the upper mantle beneath Africa. Geology 28, 63–66.

Robertson, G.S., Woodhouse, J.H., 1997. Comparison of P- and S-station corrections and their relationship to upper mantle structure. J. Geophys. Res. 102, 27355–27366.

Sobolev, S.V., Zeyen, H., Stoll, G., Werling, F., Altherr, R., Fuchs, K., 1996. Upper mantle temperatures from teleseismic tomography of French Massif Central including effects of composition, mineral reaction, anharmonicity, anelasticity and partial melting. Earth Planet. Sci. Lett. 139, 147–163.

Sotin, C., Labrosse, S., 1999. Three-dimensional thermal convection in an isoviscous, infinite Prandtl number fluid heated from within and from below: applications to the transfer of heat through planetary mantles. Phys. Earth Planet. Inter. 112, 171–190.

Su, W.-J., Dziewonski, A.M., 1997. Simultaneous inversions for three-dimensional variations in shear and bulk velocity in the mantle. Phys. Earth Planet. Inter. 100, 135–156.

Vacher, P., Mocquet, A., Sotin, C., 1996. Comparison between tomographic structures and models of convection in the upper mantle. Geophys. J. Int. 124, 45–56.

Vacher, P., Mocquet, A., Sotin, C., 1998. Computation of seismic profiles from mineral physics: the importance of non-olivine components for explaining the 660 km depth discontinuity. Phys. Earth Planet. Inter. 106, 275–298.

Villaseñor, A., Ritzwoller, M.H., Levshin, A.L., Barmin, M.P., Engdahl, E.R., Spakman, W., Trampert, J., 2001. Shear velocity

structure of central Eurasia from inversion of surface wave velocities. Phys. Earth Planet. Inter. 123, 169–184.

Vinnik, L., Chevrot, S., Montagner, J.P., Guyot, F., 1999. Teleseismic travel time residuals in North America and anelasticity of the asthenosphere. Phys. Earth Planet. Inter. 116, 93–103.

Williams, Q., 1998. The temperature contrast across the D''. In: Gurnis, M., Wysession, M.E., Knittle, E., Buffet, B.A. (Eds.), The Core–Mantle Boundary Region, Geodynamics Series, Vol. 28. American Geophysical Union, Washington, DC, pp. 73–81.

Woodhouse, J.H., Trampert, J., 1995. Global upper mantle structure inferred from surface wave and body wave data. EOS Trans, American Geophysical Union, p. F422.

Thermal and compositional anomalies beneath the North American continent

S. Godey,[1] F. Deschamps, and J. Trampert
Faculty of Earth Sciences, Utrecht University, Utrecht, Netherlands

R. Snieder
Department of Geophysics, Colorado School of Mines, Golden, Colorado, USA

Received 23 October 2002; revised 1 May 2003; accepted 24 September 2003; published 24 January 2004.

[1] The thermal and compositional structure of the upper mantle beneath the North American continent is investigated using a joint inversion of seismic velocities and density perturbations. The velocity data consist of a new regional shear wave velocity model of North America and the Caribbean region obtained by surface wave tomography. The density data are estimated using a relative density-to-shear velocity scaling factor computed for continents by combining regionally filtered seismic and gravity data. We express the mineralogical variations in the mantle in terms of the global volumic fraction of iron, the parameter which has the strongest influence on density and velocity. The inferred thermal and iron content anomalies are well constrained by the data and show an age dependence down to a depth of 230 ± 50 km. Below the North American craton, the mantle is colder than average and depleted in iron. Maximum values are found at 100 km with $\overline{\delta T} = -440$ K and $\overline{\delta \mathrm{Fe}} = -4\%$, relative to the average mantle. These chemical and thermal characteristics induce opposite buoyancy forces which could explain the longevity of cratonic lithosphere. In stable continental areas, the signal is of lower amplitudes ($\overline{\delta T} = -280$ K and $\overline{\delta \mathrm{Fe}} = -2.5\%$ at 100 km). Beneath the western Cordillera, a tectonically active region, we see no significant thermal or chemical anomaly. *INDEX TERMS:* 7218 Seismology: Lithosphere and upper mantle; 7260 Seismology: Theory and modeling; 8124 Tectonophysics: Earth's interior—composition and state (1212); 9350 Information Related to Geographic Region: North America

Citation: Godey, S., F. Deschamps, J. Trampert, and R. Snieder (2004), Thermal and compositional anomalies beneath the North American continent, *J. Geophys. Res.*, *109*, B01308, doi:10.1029/2002JB002263.

1. Introduction

[2] Recent global and regional tomographic models display a high correlation between surface tectonic features and seismic velocities down to moderate depths. In addition, velocity anomalies correlate well with the age of surface materials [e.g., *Polet and Anderson*, 1995; *Ekstrom*, 2000]. A challenge is still to infer the exact thermal and chemical variations that are responsible for the observed seismic velocity anomalies. Important questions, such as the extent of continental roots and their origin are still debated. *Jordan* [1975] first associated high seismic velocity beneath cratons with low temperature and a specific petrology. The analysis of surface xenoliths [e.g., *Rudnick and Nyblade*, 1999], which are direct samples of the Earth's mantle, suggest large compositional variations in the cratonic lithosphere, which would allow the longevity of cratons [*Jordan*, 1979; *Anderson*, 1979]. If high velocities are manifestations of purely thermal variations, the density would increase and subsidence would occur as a consequence of negative buoyancy forces. As the topography does not show signs of such a subsidence, compositional variations are needed to balance the thermal effect.

[3] *Jordan* [1979] suggested that cratons extent down to a depth of 400 km. More recent studies report smaller thicknesses, up to 250 km [*Röhm et al.*, 2000; *Rudnick and Nyblade*, 1999; *Forte and Perry*, 2000; *Artemieva and Mooney*, 2001; *Griffin et al.*, 1999]. Seismic velocities are primarily sensitive to temperature variations [*Duffy and Anderson*, 1989; *Goes et al.*, 2000], and as a consequence, investigation of the continental thermal structure using seismic tomography alone could not isolate compositional variations [e.g., *Yan et al.*, 1989]. Combining heat flow data and seismic tomography, *Röhm et al.* [2000] estimated the thickness of the thermal lithosphere but speculated that compositional variations could influence their results. Beneath cratonic areas, chemical depletion could further explain some inconsistencies observed in seismic data [*Goes and van der Lee*, 2002; *Humphreys and Dueker*, 1994]. *Forte et al.* [1995] showed that the ocean-continent difference in seismic tomography is not purely thermal in origin, but to infer the mineralogical perturbations, addi-

[1] Now at European Mediterranean Seismological Centre, Bruyères-le-Châtel, France.

Copyright 2004 by the American Geophysical Union.
0148-0227/04/2002JB002263$09.00

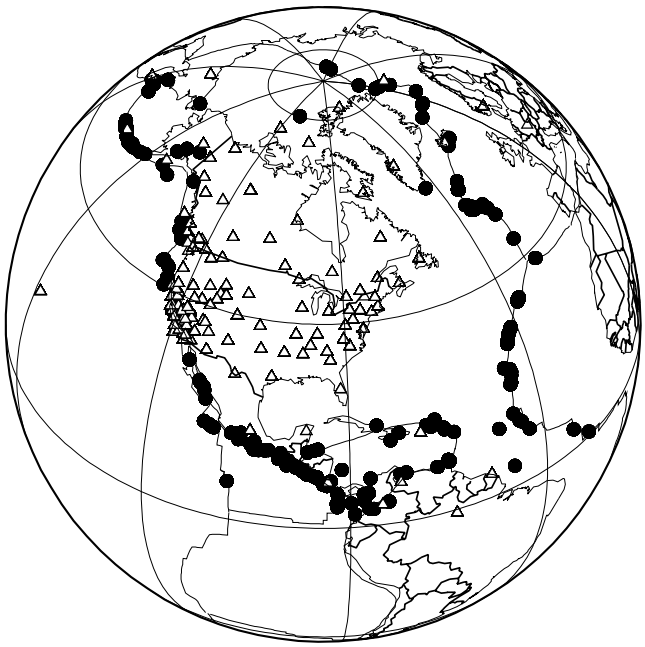

Figure 1. Distribution of earthquakes (circles) and stations (triangles).

tional data are needed. Using gravity anomalies to constrain density, recent studies [*Forte and Perry*, 2000; *Deschamps et al.*, 2002] could invert shear velocity and density for anomalies of temperature and composition. In this paper, we construct a regional tomographic model of *S* wave velocity anomalies for North America. We then use this model and the method of *Deschamps et al.* [2002] to infer distributions of temperature and composition below the North American continent.

2. Shear Wave Velocity Model

[4] Many tomographic models beneath the north American continent have been proposed. They focus on different length scales (local to regional), and the type of data varies from body waves and surface waves to full waveforms. A recent overview of most of these results is given by *Goes and van der Lee* [2002]. Guided by the fact that surface waves provide the best depth resolution, and that the step via classical phase velocity maps allows to incorporate the greatest amount of waveforms, we propose a new shear wave velocity model. Our focus is to achieve the most homogeneous resolution needed to make an interpretation in terms of temperature and composition, rather than the best possible local resolution given our data set.

2.1. Data

[5] We measured phase velocities of fundamental mode Rayleigh waves from 207 events recorded by 142 global (GSN) and regional (CNSN, USNSN, BDSN, Terrascope and Geoscope) stations between 1995 and 1999. The phase velocity measurements are obtained automatically, using the nonlinear waveform inversion of *Trampert and Woodhouse* [1995]. The phase and amplitude as a function of frequency of each seismogram are expanded in terms of B splines. A smoothing constraint is applied to solve the 2π phase ambiguity, particularly at short periods. The necessary starting model is a global phase velocity model of *Trampert and Woodhouse* [1995]. The automatic selection resulted in 7700 phase velocity measurements. The period range extends from 40 s to 150 s, and the same data coverage is obtained for all periods. Focal mechanisms are taken from the Harvard centroid moment tensor solutions. Earthquake depths are limited to 100 km, and the magnitudes vary from 4.9 to 7.0. The area mapped in the present work is bounded by the Arctic region in the north, the Caribbean basin in the south, the Aleutian islands in the east, and the Mid-Atlantic Ridge in the west. The station and source geometry is displayed in Figure 1, and the resulting ray density is shown in Figure 2. We use the method of *Barmin et al.* [2001] to construct phase velocity maps and define a grid of $2^\circ \times 2^\circ$ spacing, which is not to be confused with the achieved lateral resolution (see below), leading to 2569 grid points. Over the inversion region, the cell area, defined by four neighboring points, does not vary by more than 10%. Bilinear interpolation is used to evaluate velocities between the three nearest nodes of the grid.

[6] PREM [*Dziewonski and Anderson*, 1981], used as a reference model in the present study, has a constant crustal thickness, but short-period surface waves are very sensitive to crustal variations. To get an unbiased view of the underlying mantle, a crustal correction is necessary. Correcting the path averaged measurements is less dependent on the local crustal details than correcting the phase velocity maps, and thus more robust. Given the resolution we can achieve with our data coverage (see below), we used CRUST5.1 [*Mooney et al.*, 1998], together with topography and bathymetry to make an exact calculation of the path averaged crustal contribution, which we subtracted from each measurement at each period.

2.2. Phase Velocity Map and Resolution

[7] To obtain equal resolution in all phase velocity maps, we applied the same Laplacian regularization at all periods.

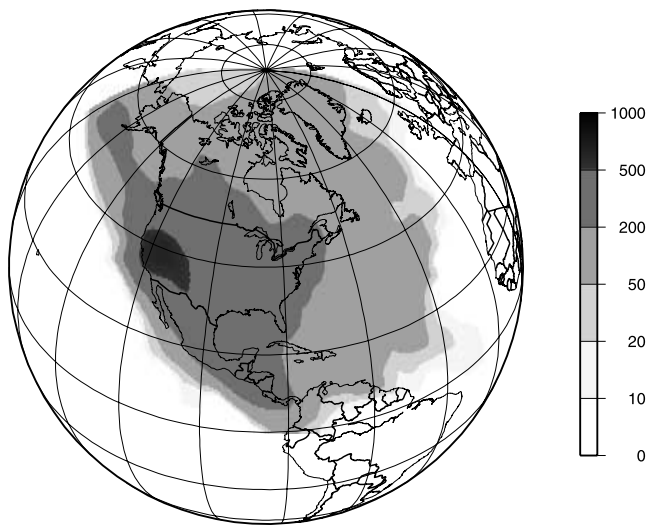

Figure 2. Ray path density, defined as the number of rays intersecting a $2^\circ \times 2^\circ$ cell.

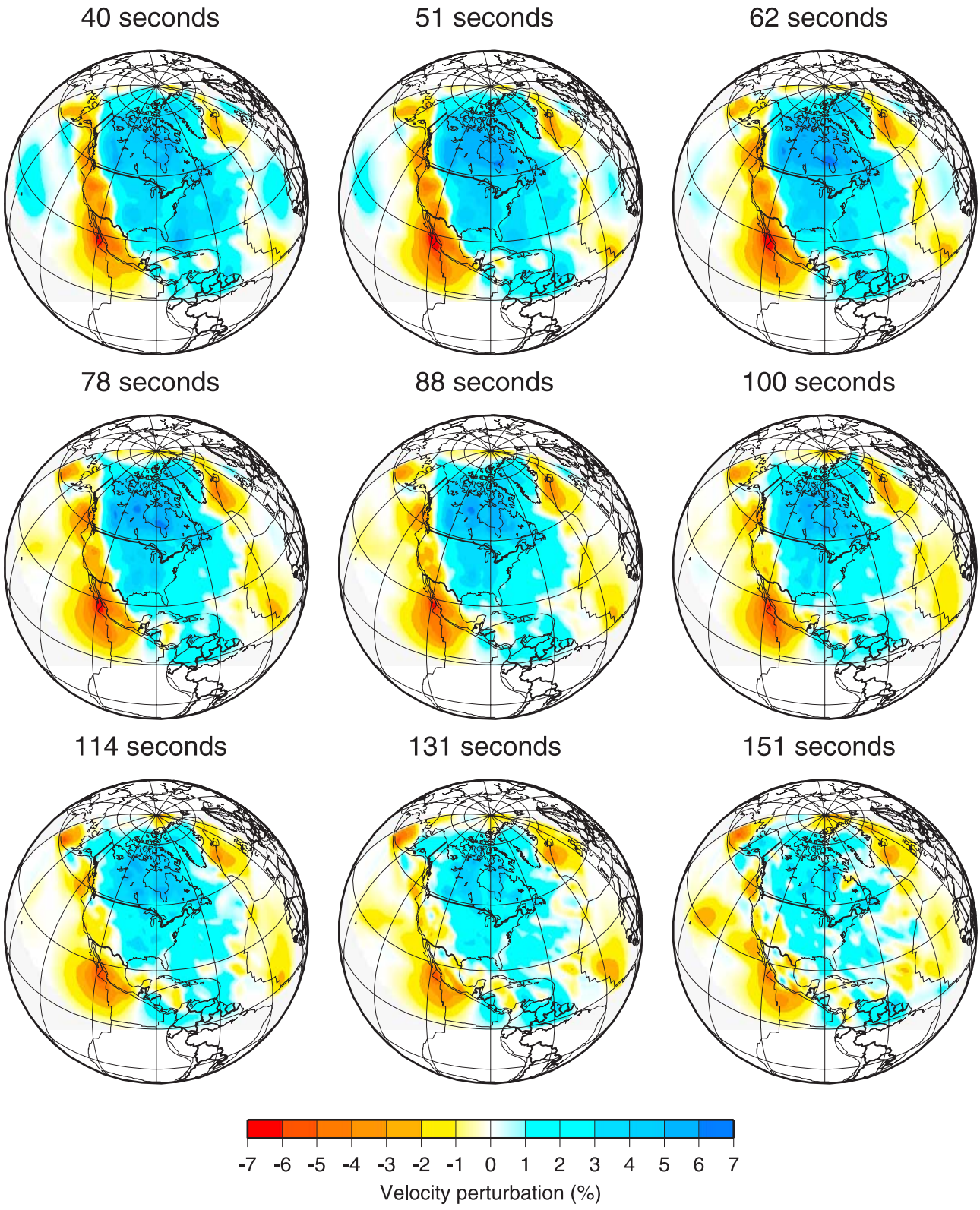

Figure 3. Phase velocity maps for North America and the Caribbean used as input data in the inversion for *S* wave velocities. The velocities are given in percent relative to PREM.

We therefore avoid artifacts in the depth inversion. The estimated phase velocity model is given by

$$\hat{m} = \left(G^T G + \alpha^2 W\right)^{-1} G^T d, \quad (1)$$

where W is a Laplacian regularization operator.

[8] We chose to slightly overdamp the inversion so that robust features are imaged (Figure 3). The spatial resolution is quantified by the resolution spreading function [*Backus and Gilbert*, 1967] and the diagonal elements of the resolution matrix (Figure 4).

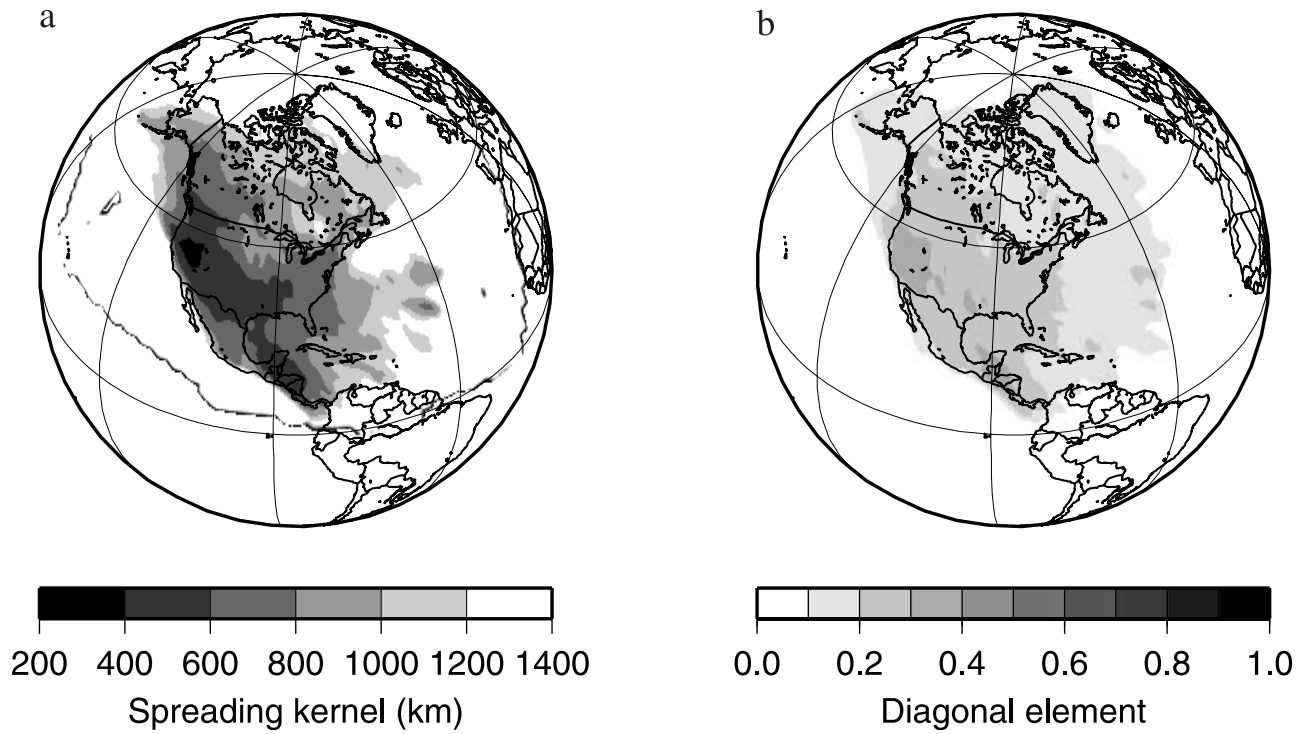

Figure 4. Distribution of (a) the resolution spreading function and (b) the value of the diagonal elements of the resolution matrix for the phase velocity map of 100 s.

$$K_i = \frac{24}{dr} \frac{\sum_{k=1}^{N} D_{ki}^2 R_{ki}^2}{\sum_{k=1}^{N} R_{ki}^2}, \tag{2}$$

with

$$R = \left(G^T G + \alpha^2 W\right)^{-1} G^T G, \tag{3}$$

where R_{ki} is the resolution matrix element (k, i), D_{ki} the distance in kilometers between the parameter node i and the nodes k and dr is the grid spacing 220 km.

[9] The parameter K reflects how far the off-diagonal elements of the resolution matrix spread around each model point. For poorly constrained parameters, the spreading function has large values, whereas for a perfectly defined parameter ($R = I$) the K_i are equal to zero. The damping parameter we have chosen allows an average lateral resolution of 800 km, the best resolution (400 km) being obtained in the western United States. Of course, for regions with lower ray path coverage, the spreading function displays higher values, i.e., lower resolution. The resulting phase velocity maps explain the data with variance reductions of about 90% at short periods and 50% at long periods.

2.3. *S* Wave Velocity Modeling

[10] The Earth's shear velocity structure as a function of depth is derived by combining the phase velocity maps computed for different periods with the same lateral resolution. At each point of the grid, the inverse problem is specified by the data, the local phase velocities ($\delta c/c$), and the model corresponding to a local depth profile for S wave velocity ($\delta v_s/v_s$) relative to PREM. Strictly speaking, the local phase velocities are sensitive to radial and azimuthal anisotropy. *Trampert and Woodhouse* [2003] have clearly shown that neglecting azimuthal anisotropy has only an effect on the shortest wavelength structure, which we are not mapping here. Neglecting transverse anisotropy and given currently known values for its deviation from PREM in the region will bias $\delta \ln v_s$ by 0.3% but may reach locally

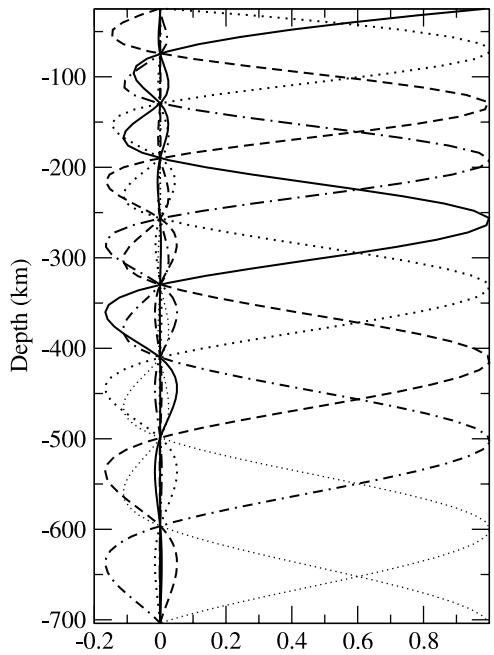

Figure 5. Spline functions used to parameterize the S wave velocity as a function of depth.

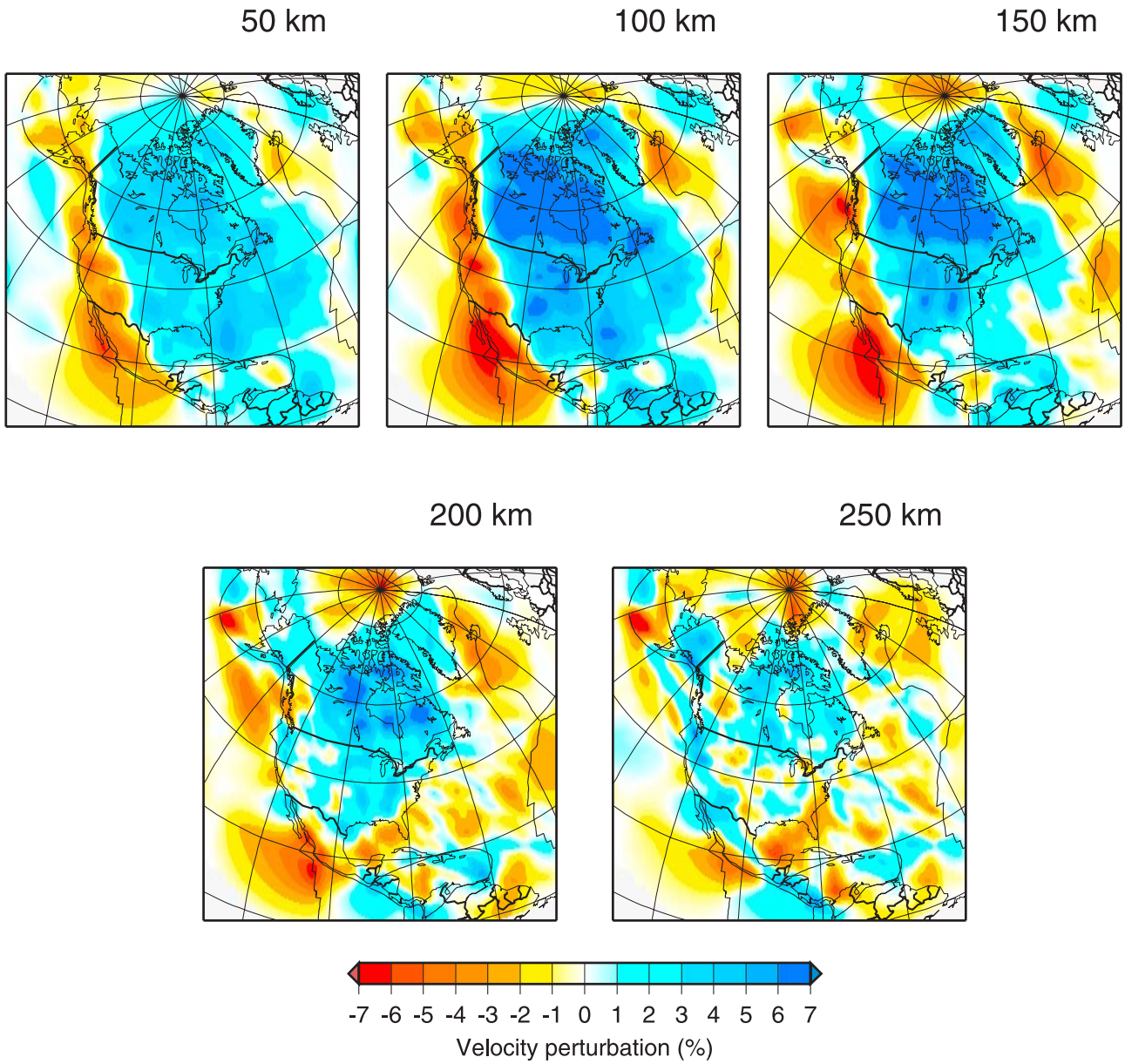

Figure 6. Relative *S* wave velocity perturbation model for depths of 50–250 km.

1.5%. Given the overall strength of the models and errors associated with the thermochemical interpretation, neglecting anisotropy has a minor effect on our conclusions. The relation between data and model assuming isotropy is then

$$\frac{\delta c}{c}(\theta,\phi) = \int_0^R K_s(r)\frac{\delta v_s}{v_s}(r,\theta,\phi)dr + \int_0^R K_p(r)\frac{\delta v_p}{v_p}(r,\theta,\phi)dr + \int_0^R K_\rho(r)\frac{\delta \rho}{\rho}(r,\theta,\phi)dr, \quad (4)$$

where K_s, K_p, K_ρ are the sensitivities of surface waves to *S* wave velocity (v_s), *P* wave velocity (v_p) and density (ρ), respectively. R is the radius of the Earth, θ and ϕ are the latitude and longitude of the grid point considered. As Rayleigh waves are primarily sensitive to *S* and *P* wave velocity, we further neglect the sensitivity to density (third term of equation (4)). We assumed a constant ratio between *S* and *P* wave velocities and used the value proposed by *Robertson and Woodhouse* [1997], $\delta \ln v_s / \delta \ln v_p = 1.6$, which was inferred from travel time data. Because Rayleigh waves are not very sensitive to v_p and ρ, the exact scaling parameter hardly matters for the resulting v_s model. Relation (4) is thus reduced to a term containing $\delta \ln v_s$ only. For our North American data set, which consists of phase velocities between 40 and 150 s, *S* wave velocity perturbations between 60 and 260 km can be retrieved. We expand our model as a function of depth in terms of spline functions. For a given grid point, the *S* wave velocity is

$$m(r,\theta,\phi) = \frac{\delta v_s}{v_s}(r,\theta,\phi) = \sum_{i=1}^{N} b_i(\theta,\phi)B_i(r), \quad (5)$$

where the functions $B_i(r)$ are the cubic splines as a function of depth, and b_i the coefficients we invert for. We used 10 equally spaced splines (Figure 5).

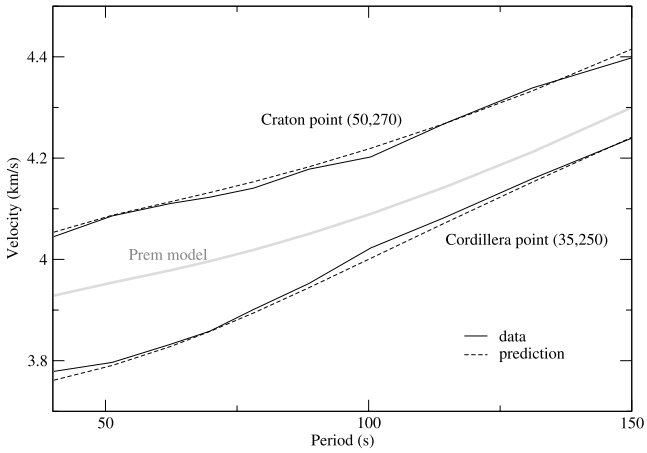

Figure 7. Phase velocity dispersion curves observed (solid line) and predicted (dashed line) by our shear velocity model for two characteristic points. Velocities are given as absolute values and are compared with PREM (grey line).

[11] A regularization term is added, which controls the smoothness of the model. The regularization operator is computed for each model point by integrating the second derivatives of the spline functions:

$$W_{ij} = \int_0^R \frac{d^2B_i(r)}{dr^2}\frac{d^2B_j(r)}{dr^2}dr. \quad (6)$$

The estimated model is obtained using a standard least squares inversion technique, which minimizes simultaneously data fit and model smoothness:

$$(Gm - d)^T(Gm - d) + \alpha^2 m^T W m. \quad (7)$$

The value of α we have chosen is such that the trace of resolution is approximately 3, or that three equivalent spline coefficients are independently resolved.

2.4. *S* Wave Velocity Model

[12] Figure 6 shows our shear wave velocity model expressed as relative perturbations from PREM. Maximum amplitudes are of the order of ±9.5% at 100 km. Interestingly, they do not decrease significantly at larger depths as observed in other studies [e.g., *Van der Lee and Nolet*, 1997; *Grand*, 1994]. The difference is most likely due to different regularization schemes, rather than data constraints. The *S* wave velocity model explains the data with a variance reduction varying between 74 and 85%, depending on the period. Two representative points, one located in the tectonically active western margin (35°N, 110°W) and one in the cratonic area (50°N, 120°W), are chosen to illustrate the data fit. For both locations, we obtain a very good fit over the complete period range, with deviations less than 0.5% from the absolute velocity (Figure 7). We repeated this exercise to all our grid points and found good agreement in amplitude and location of the original phase velocity maps over the entire region, with a maximum difference locally of 1% at 100 s.

[13] Our model agrees well with observed surface tectonics. The two prominent features imaged in our model are the high velocities beneath the North American craton and the lower velocities associated with the western active Cordillera. These structures extend down to depths of 200 km and 150 km, respectively. The boundary separating the two anomalies is sharp, as seen in cross sections of Figure 8, and aligns well with the topography along the Mackenzie mountain range, in Canada, and along the Rocky mountains front, in the United States and Mexico. These anomalies are well reported in the literature and are associated with the different surface tectonic provinces. Using various methods and data sets, previous studies display however different lateral and vertical extensions of the tectonic and cratonic regions [e.g., *Bassin et al.*, 2000; *Grand*, 1994; *Van der Lee and Nolet*, 1997]. A tectonic interpretation of the main features is given by *Goes and van der Lee* [2002, and references therein].

2.5. Seismic Velocities and Surface Heat Flow

[14] Surface heat flow measurements provide additional and independent information on the thermal structure of the crust and the lithosphere. It is interesting to compare tomographic models to surface heat flow data. We used the compilation of global heat flow data by G. Masters and G. Laske (personal communication, 2002). This data set is available on http://mahi.ucsd.edu/Gabi/rem.dir/crust/heatflow.html and consists of 38,000 measurements including the earlier data of *Pollack et al.* [1993]. Figure 9 shows the correlation between our shear velocity model and the surface heat flow on a $2° \times 2°$ grid. A strong anticorrelation of the heat flow with the *S* wave velocity is observed from 60 km (average crustal thickness) to 180 km. *Röhm et al.* [2000] reported a similar result and explained it by a combination of radiogenic heat production in the crust and the thickness of the thermal lithosphere. This result suggests that thermal processes are sufficient to explain *S* wave tomography and heat flow data. It is well established that in the upper mantle, seismic velocities are mostly sensitive to temperature [*Goes and van der Lee*, 2002; *Deschamps et al.*, 2002]. This should not be understood that chemical variations are absent, but rather that other data, such as density variations, are required to detect them.

3. Thermal and Compositional Structure

[15] To infer thermal and compositional variations from our v_s model, we propose to add density variations as an additional constraint. It is currently very difficult to obtain independent density variations from seismology or other data. We therefore follow a classical approach, which constrains density anomalies from observed gravity anomalies using an appropriate scaling to velocity. We can then invert the correlated density anomalies and the velocity anomalies for anomalies of temperature and composition. This requires a careful equation of state modeling and the most recent results of mineral physics.

3.1. Constraining the Density

[16] To constrain density anomalies, we have inverted the global *S* wave velocity anomalies S16RLBM [*Woodhouse and Trampert*, 1995] and the nonhydrostatic gravity anomalies derived from EGM96 [*Lemoine et al.*, 1998] for a radial profile of the relative density-to-shear velocity ratio,

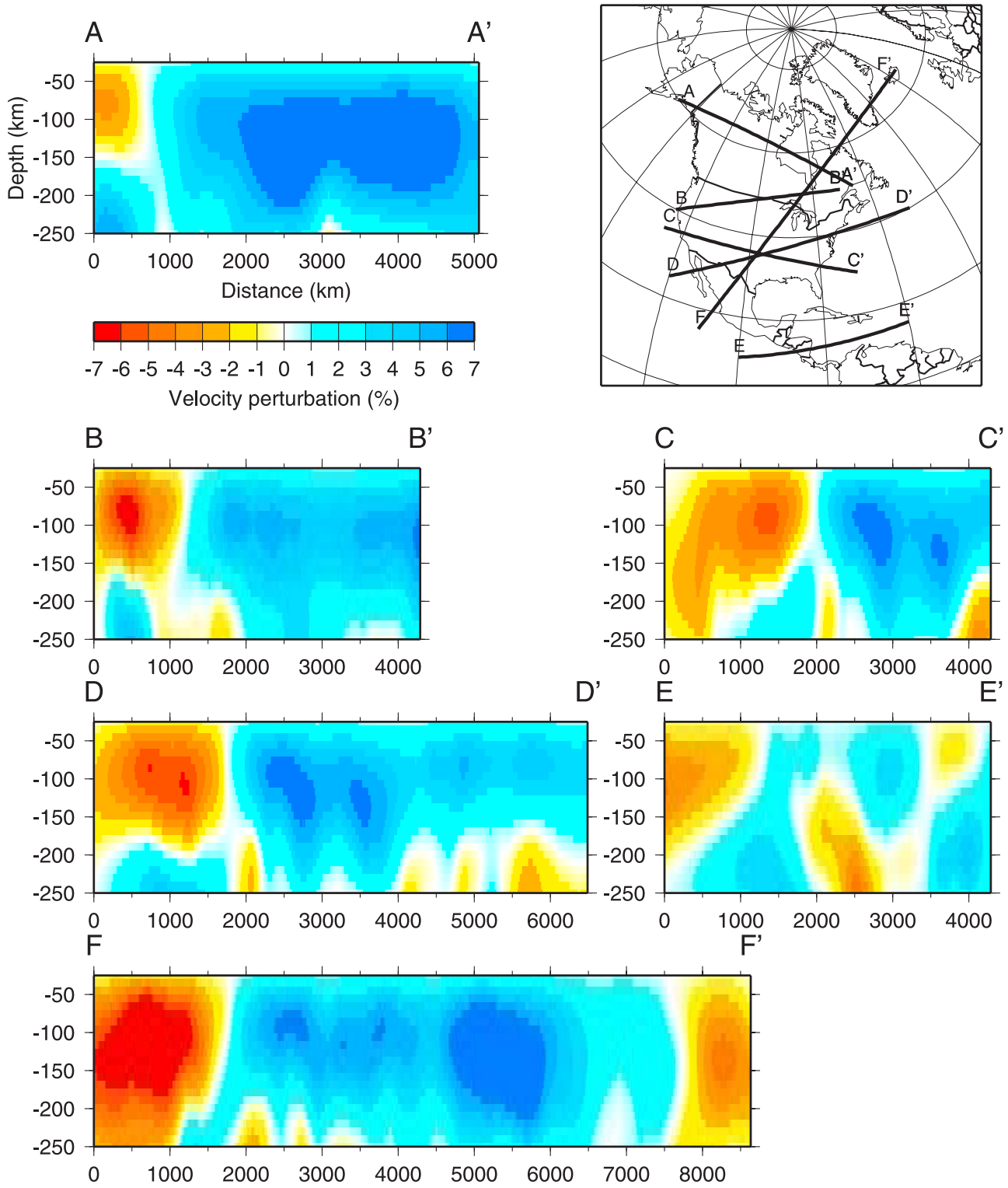

Figure 8. Cross sections through the *S* wave velocity model of Figure 6. The location of the cross sections are shown on the map (top right).

$$\zeta(r,\theta,\phi) \equiv \frac{\delta \ln \rho(r,\theta,\phi)}{\delta \ln v_s(r,\theta,\phi)}. \quad (8)$$

Regionally dependent ratios can be computed from existing data, and the scaling factor used in the present study (Figure 10) is for subcontinental mantle [*Deschamps et al.*, 2001].

[17] Observed gravity anomalies integrate the density anomalies over depth. For each degree ℓ of the spherical harmonic expansion, the gravity anomalies can be written

$$\delta g_\ell(\theta,\phi) = \int_{r_{CMB}}^{R} K_\ell(r)\delta\rho_\ell(r,\theta,\phi)dr \quad (9)$$

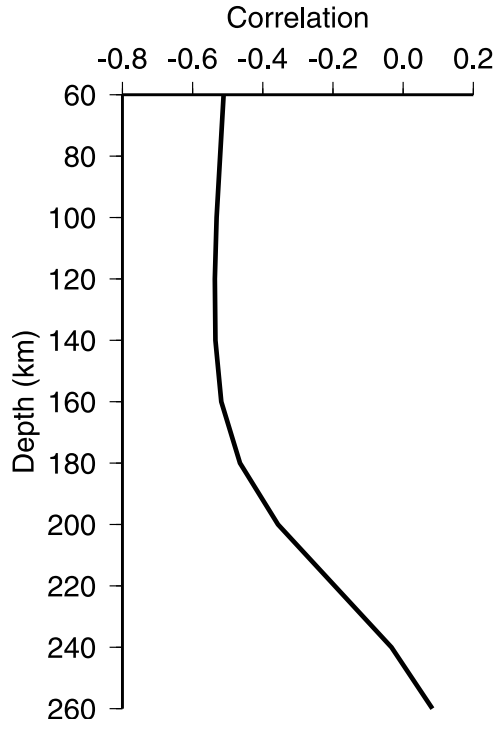

Figure 9. Correlation between *S* wave velocity at a given depth and surface heat flow for North America.

$$K_\ell(r) = \frac{3g_0}{\bar{\rho}R}\frac{(\ell-1)}{(2\ell+1)}G_\ell(r), \tag{10}$$

where R and $\bar{\rho}$ are the Earth's radius and average density, r_{CMB} is the radius of the core, and g_0 is the surface gravity acceleration. The functions G_ℓ(r) are the geoid kernels, i.e., the geoid response to density anomalies located at depth, computed following the method of *Forte and Peltier* [1991]. Introducing equation (8) into equation (9) and filtering each member of equation (9) between spherical harmonic degrees ℓ_1 and ℓ_2, one obtains a linear relation between gravity anomalies, velocity anomalies, and the scaling factor ζ. We solve this equation for radial profiles of ζ in the suboceanic and subcontinental mantle, assuming that ζ does not vary laterally within each of these two regions. Inversions are regularized with a smoothness constraint, the amount of smoothness being controlled by a damping factor. Results depend on a number of parameters that it is important to choose correctly.

[18] First, we filtered S16RLBM and EGM96 to remove the long-wavelength gravity anomalies, which originate from deep mantle structure. Because geoid kernels for degrees 2 to 10 have nonnegligible values throughout the mantle, we only kept degrees 11 to 16 to compute the scaling factor in Figure 10. Interestingly, tests suggested that low degrees do not significantly influence the scaling factor in the upper 400 km [*Deschamps et al.*, 2001]. In the lower mantle, filtering strongly influences the obtained ratio.

[19] Second, geoid kernels depend strongly on the viscosity profile of the mantle. The later is still a mater of debate, and any choice could appear arbitrary. However, for degrees $\ell \geq 10$, geoid kernels peak in the uppermost mantle ($z \leq 200-300$ km) whatever the viscosity profile used, and have negligible values from z = 1000 km depth down to the bottom of the mantle. As a result, down to z = 400 km depth, the scaling factor is not sensitive to the viscosity profile [*Deschamps et al.*, 2001]. At greater depths, of course, major differences appear, depending on the viscosity profile, which prevents us from constraining deep Earth density with our scaling factor. In the present study, we built the geoid kernels using a viscosity profile that fit both the long-wavelength gravity anomalies and the postglacial uplift [*Mitrovica and Forte*, 1997].

[20] The scaling factor thus depends on the viscosity profile and spectral filtering, but most of the differences concern the deep mantle. At shallower depths ($z \leq 400$ km), differences are small. We also checked that the regularization of the inversion, which is always subjective, does not significantly change the shape and amplitude of $\zeta(r)$ [*Deschamps et al.*, 2001]. The main source of uncertainty stems from the uncertainty in the tomographic model. We assumed reasonable errors on δlnv_s [*Deschamps et al.*, 2001] and calculated the corresponding range of ratios shown in Figure 10.

[21] The density anomalies inferred from the scaling factor are, by definition, correlated to the velocity anomalies. Additional density anomalies, and therefore additional temperature and compositional anomalies, which are not correlated to the velocity could well be present. Currently, we cannot map these contributions. We believe, however, that most of the density anomalies are correlated to the velocity anomalies, because the gravity anomalies reconstructed from equation (9) and the correlated density

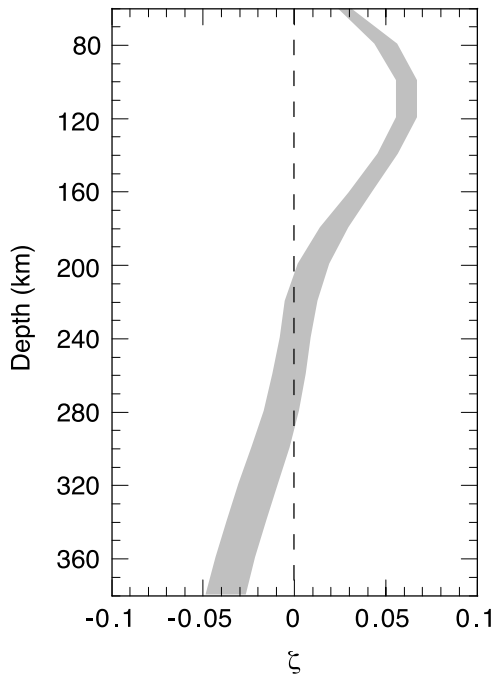

Figure 10. Radial profile of the scaling factor (ζ) for the subcontinental upper mantle. The shaded area represents a range of possible values for ζ and covers one standard deviation around the average value. The standard deviation is estimated at each depth by simulating random errors in the global *S* wave velocity model S16RLBM.

Table 1. Volumic Fraction of Minerals in the Reference Petrological Model (Pyrolite)

Mineral	Volumic Fraction, %
Olivine	61.7
Clinopyroxene	13.3
Orthopyroxene	5.2
Garnet	15.3
Jadeite	4.5

anomalies fit the observed gravity anomalies within two standard deviations.

3.2. Modeling Approach

[22] Numerical methods to compute upper mantle density and seismic velocities from mineral physics data, given temperature, pressure and petrology, are now well established [e.g., *Duffy and Anderson*, 1989]. Such methods allow to calculate relative derivatives (or sensitivities) of seismic velocity and density to temperature and composition. The method we used here is fully described by *Deschamps et al.* [2002]. The density and elastic moduli of a given mineral at ambient temperature and pressure are first extrapolated to foot temperature T_f, following Grüneisen theory. In a second step, they are adiabatically projected at pressure P, following a Birch-Munaghan equation of state to third order. The density and elastic moduli of the aggregate are then obtained by averaging over all individual minerals according to their abundance in the petrological reference model. Before extrapolations to high temperature and pressure, and if data are available, we have corrected the density and elastic parameters of individual minerals for their iron dependence. In the upper mantle, anelasticity significantly influences the reconstruction of seismic velocities [*Karato*, 1993; *Jackson*, 2000]. We accounted for this effect using a quality factor model as described by *Goes et al.* [2000] (model Q1). The presence of partial melt or fluids in the mantle may also influence the reconstruction of seismic velocities. However, the consequences of these effects are difficult to estimate, because they depend on the geometry and interconnection of the melt inclusions [*Hammond and Humphreys*, 2000]. In addition, partial melt is occurring locally. The strong anomalies of temperature and composition that partial melt may require would have a negligible effect on our regional mean values of temperature and compositional variations. In this study, we have therefore neglected the contribution of partial melt. Water effects, which modify primarily anelasticity are also neglected. The average mineralogical composition of the mantle is an important parameter in the computation of sensitivities for velocity and density, but it is still not accurately known. To account for this uncertainty, we have considered a large number of average compositions by varying the volumic fraction of olivine between 57% and 67%. The other mineralogical elements are distributed in the proportion of a pyrolitic model (Table 1).

[23] From the density and S wave velocity variations, we can independently infer the perturbations of temperature and one compositional parameter. Parameterization of composition is not straightforward, as variations in several components of the rock can change density and velocity anomalies in a complicated way. To decide of the most relevant parameter, we have computed the velocity and density perturbations for temperature and three different compositional parameters: iron, garnet, and olivine content. The global volumic fraction of iron is defined by x_{Fe} = Fe/(Fe + Mg). Garnet is richer in iron than other minerals, and its variation may be redundant with those of iron. To estimate the influence of garnet, we have arbitrarily fixed the global volumic fraction of iron to 11% in all the minerals containing iron. This corresponds then to investigate the influence of the aluminium (Al_2O_4), the second most abundant element in garnet. The relative anomalies of density and velocity obtained from thermal and compositional anomalies (iron, garnet and olivine) at 100 km depth are displayed in Figure 11. From Figure 11a, we see that the relative velocities are mainly sensitives to thermal anomalies and to a lesser extent to variations in iron. An increase of 2% in velocity can be explained either by a 120 K decrease in temperature, by a 7.5% depletion in iron, or by a 15% depletion in aluminium. Seismic velocities are much less sensitive to the fraction of olivine. A perturbation of 1% in velocity is produced by more than 50% depletion in olivine. Figure 11b shows the influence of temperature and composition on density. An enrichment of 3.5% in iron induces a 1% increase in density. The same density variation is obtained with a decrease of 400 K in temperature, or

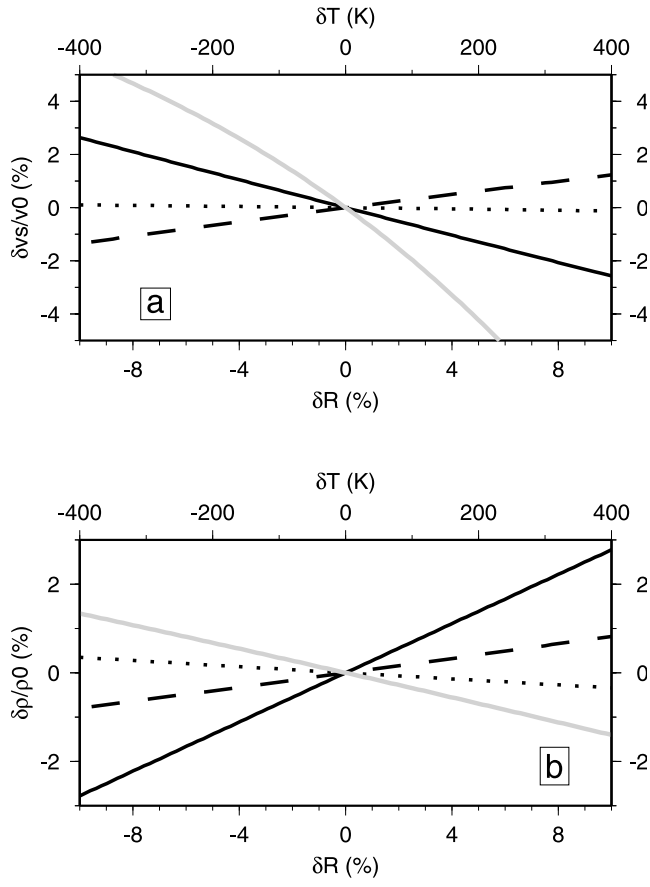

Figure 11. Relative variations of (a) velocity and (b) density as a function of variations of temperature (grey line), global volumic fraction of iron (solid line), volumic fraction of garnet (dashed line), and volumic fraction of olivine (dotted line).

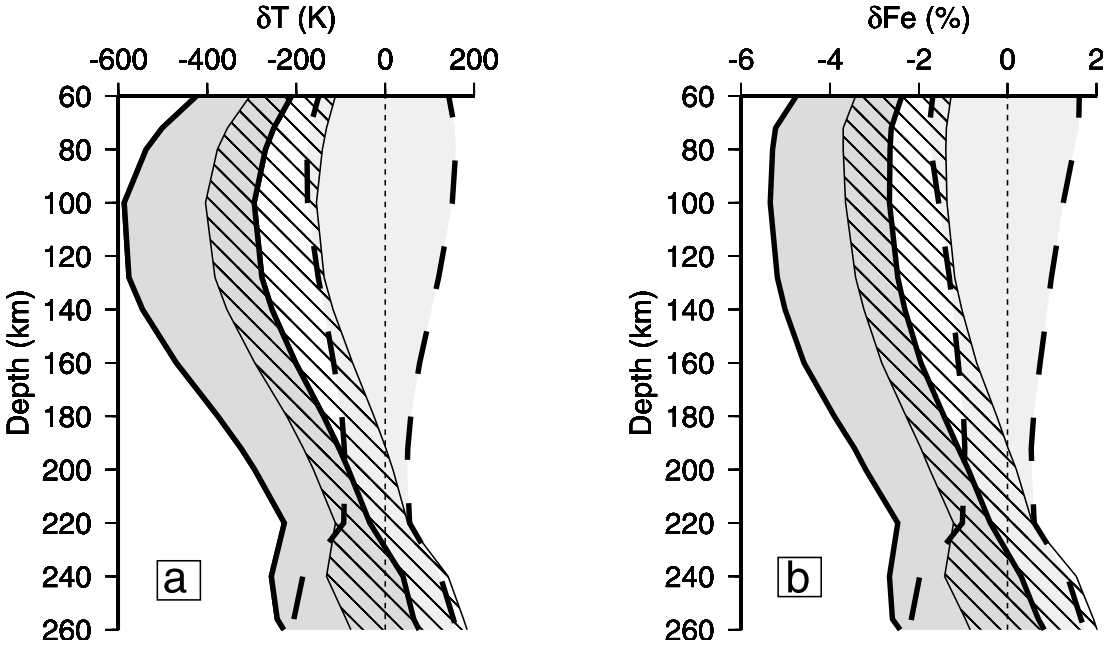

Figure 12. Profiles of (a) temperature and (b) iron anomalies for three different tectonic regions: Archean craton (dark grey), stable platform (hatched), and tectonic continent (light grey).

a 10% increase of aluminium. Among the compositional parameters, iron shows therefore the largest influence on density and velocity. Furthermore, a depletion in aluminium induces simultaneously a decrease in density and velocity. Xenolith analysis report refractory mantle composition (depleted basalts) for cratonic regions [*Schmidberger and Francis*, 1999], which are associated with high seismic velocities. This suggests that for garnet the influence of iron content is stronger than the influence of aluminium content.

[24] We finally decided to invert velocity and density anomalies for variations of temperature and iron alone, reflecting the most relevant parameters. The system to solve is defined by

$$\delta \ln v_s = A\delta T + B\delta \mathrm{Fe} \tag{11}$$

$$\delta \ln \rho = C\delta T + D\delta \mathrm{Fe} \tag{12}$$

with

$$\delta \ln \rho = \zeta \delta \ln v_s. \tag{13}$$

The coefficients A, B, C, D are the sensitivity of velocity and density to temperature (δT) and iron (δFe):

$$A = \frac{\delta \ln v_s}{\delta T}, \quad B = \frac{\delta \ln v_s}{\delta \mathrm{Fe}}, \quad C = \frac{\delta \ln \rho}{\delta T}, \quad D = \frac{\delta \ln \rho}{\delta \mathrm{Fe}} \tag{14}$$

Although $\delta \ln \rho$ is proportional to $\delta \ln v_s$, the matrix defined by A, B, C and D in equations (11) and (12) is not singular and can be inverted. Uncertainties on the tomographic model and scaling factor can propagate into the retrieved temperature and compositional structure. A bigger source of error, however, comes from uncertainties on the temperature and petrological reference models used to compute velocities and densities. We evaluated these errors by

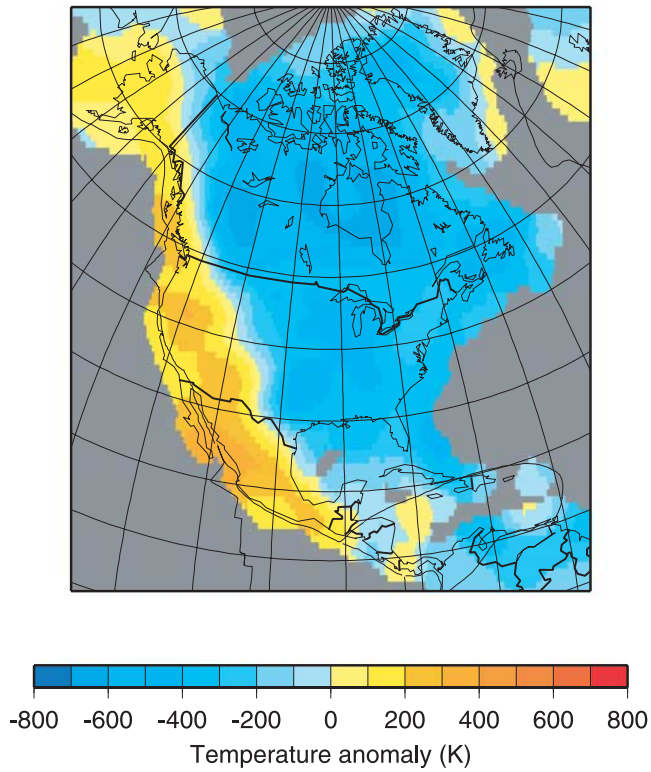

Figure 13. Map of mean temperature anomalies at 100 km depth.

sampling a reasonable range of temperature and petrological reference models. A collection of models is computed by varying the average mantle foot temperature between 800 K and 1400 K, and the olivine fraction between 36.7% and 66.7%. The global iron fraction is set to 11%. For each reference model, we calculate the velocity and density at a given depth and reject models which do not satisfy PREM within 2.5%.

[25] By exploring the mineralogical model space, we compute all possible temperature and compositional sensitivities compatible with PREM, accounting for uncertainties in the reference model. We then invert for temperature and compositional variations using this family of sensitivities. We display the results as mean temperature and compositional anomalies, together with their standard deviation.

3.3. Compositional and Thermal Profiles of the Uppermost Mantle

[26] Figure 12 displays the mean anomaly of temperature and iron and their variance (shaded area) as a function of depth and surface tectonics. We have computed profiles of δT and δFe for cratons, stable platforms and tectonically active continent, as defined by 3SMAC [*Nataf and Ricard*, 1996]. The distributions of temperature and iron anomalies are clearly related to tectonic provinces for depth shallower than 200 km. For larger depths, the difference between tectonic provinces decreases rapidly. This is partly due to the fact that the scaling factor goes to zero at these depths, hence increasing the variances in δT and δFe. An accurate determination of the depth at which the differences between tectonic provinces are cancelling requires to define profiles of the scaling factor independently for each province.

[27] Beneath tectonic continents, no significant temperature and compositional anomalies are seen. The mean values of temperature ($\overline{\delta T}$) and iron content ($\overline{\delta \mathrm{Fe}}$) are close to zero. The ranges of variation (defined as standard deviation) are small ($\sigma_{\delta T}$ = 150 K and $\sigma_{\delta \mathrm{Fe}}$ = 1%, on average). Therefore, for these regions, the mantle is close to the average, with no significant temperature or chemical differentiation. On the contrary, cratonic areas are significantly colder ($\overline{\delta T}$ varies between -200 K and -450 K for $z \leq 200$ km) and depleted in iron ($\overline{\delta \mathrm{Fe}}$ varies from -2% to -4% for $z \leq 200$ km), in comparison with an average mantle. From 60 to 200 km, the average variations are close to $\sigma_{\delta T}$ = 120 K and $\sigma_{\delta \mathrm{Fe}}$ = 1.3%. The maximum iron depletion and temperature anomaly is observed at 100 km depth with $\overline{\delta T} = -440$ K and $\overline{\delta \mathrm{Fe}} = -4\%$. Below 230 km depth, positive values of temperature and iron anomalies cannot be excluded. Defining the depth extent of cratons by the layer in which temperature and iron anomalies are negative within one standard deviation, the North American craton would be 230 ± 50 km thick. The uncertainty is given by the vertical resolution of tomographic models. The profile obtained below continental platforms (hatched curves) is similar to the cratonic profile but with smaller amplitudes ($\overline{\delta T} = -280$ K and $\overline{\delta \mathrm{Fe}} = -2.5\%$ at 100 km depth). Using the same definition as above, the lithosphere would be 190 ± 50 km thick. The bottom parts of our profiles show that at these depths, temperature and iron anomalies are not significant and independent of the surface tectonics.

[28] The temperature and iron perturbations obtained in our study are comparable to those of *Deschamps et al.* [2002], who used a global velocity model. However, our results suggest a cooler and more depleted mantle below the North American craton than the global average values observed in their study ($\delta T = -300$ K and δFe = -3.0% at 100 km depth). Furthermore, we find smaller ranges for temperature and iron variations. The use of a regional tomographic model therefore gives better constraints on these anomalies. Our results also agree well with the study of *Forte and Perry* [2000], who computed thermal and chemical anomalies using different gravity data and global seismic velocity model.

4. Discussion

[29] The distribution of temperature anomalies we obtained (Figure 13) agrees well in general with the work of *Goes and van der Lee* [2002], which is based on inversion of seismic velocities for pure thermal anomalies, and with the work of *Artemieva and Mooney* [2001], which is based on heat flow data. The anomalies of iron (not shown here) are perfectly correlated to the temperature anomalies. This is a consequence of constraining density anomalies with a scaling factor. Of course, additional anomalies of temperature or iron could be present, but we cannot address them, as we do not have full independent information on density. However, the gravity anomalies reconstructed with the correlated part of the density fit the observed gravity anomalies within two standard deviations [*Deschamps et al.*, 2001], suggesting that most of the density anomalies are indeed correlated to the velocity anomalies.

[30] Beneath the Canadian shield and the northern part of the United States, the mantle is significantly colder than average. At z = 100 km, temperature anomalies vary between $\overline{\delta T} = -800$ K and $\overline{\delta T} = -200$ K (Figure 13). The maximum values are observed beneath the Canadian shield and Hudson bay, which were formed during the Precambrian age. The interior platform displays a relatively warmer mantle (~ -300 K). Such lateral variations may be related to geological age and to variations in the lithosphere thickness [*Artemieva and Mooney*, 2001]. Archean and early Proterozoic orogenies modified the shape of the lithosphere, and it is still visible at present day through the action of buoyancy. Another example of age dependence is the feature imaged beneath Greenland, where the cratonic portion (western part) displays a cooler mantle than the platform section (to the east), which correlates well with surface tectonic. *Goes and van der Lee* [2002] suggested that chemical depletion is present in areas where temperatures inferred from P and S wave velocity do not match, such as the North American craton, but they do not give numerical estimates of this depletion. It is worth noting that in our model, these regions show strong iron depletion. As we already mentioned, iron depletion and negative temperature anomalies are correlated. This has some important dynamical consequences. The positive buoyancy induced by chemical depletion may balance the negative buoyancy due to the cooling of the continental root. This may explain the longevity of the Archean craton, by preventing the lithosphere from sinking into the asthenosphere. This hypothesis was formulated quite early [*Jordan*, 1979], but strong observational or numerical evidence is recent [*Forte*

and Perry, 2000; *de Smet et al.*, 2000; *Deschamps et al.*, 2002].

[31] The tectonic Cordillera is underlain by low S velocities following well the tectonic regionalization. It is consistent with an average mantle, and with slightly positive thermal anomalies (δT = 200 K), which are due to the ongoing extension processes occurring in the region.

[32] Using our distribution of temperature and compositional anomalies, we have computed relative v_s and v_p anomalies, and find $\delta lnv_s/\delta lnv_p \simeq 1.7$. Although we used a priori the scaling $\delta lnv_s/\delta lnv_p = 1.6$ to obtain our v_s model, it is reassuring to see that the gravity constraint, via ζ, does not change this ratio very much. More interestingly, most seismological determinations of $\delta lnv_s/\delta lnv_p$ fall within 1.5 ± 0.5 in the uppermost mantle [*Masters et al.*, 2000], and are generally explained by a purely thermal effect with the aid of attenuation [*Karato*, 1993; *Vinnik et al.*, 1999]. We explain the same ratio with a significant contribution from compositional effects, suggesting that $\delta lnv_s/\delta lnv_p$ might not allow to determine the cause of the anomalies unambiguously. The velocities are mainly sensitive to temperature, which does not mean that no significant compositional variations are present.

5. Conclusions

[33] We have inferred variations of temperature and iron in the uppermost mantle beneath North America, using density and S wave velocity perturbations. Density anomalies were estimated from global S wave tomography and gravity anomalies. The regional S wave model is obtained by surface wave tomography and resolves, on the average, lateral structures of 800 km and vertical structures of about 50 km. Our results are in good agreement with previous studies performed at a global scale [*Forte and Perry*, 2000; *Deschamps et al.*, 2002]. In particular, we find that down to a depth of 230 km (±50 km), cratonic roots are significantly colder and depleted in iron, compared to the average mantle. The use of our regional tomographic model improves our image of the thermal and chemical structure of the uppermost mantle, in the sense that ranges of temperature and compositional variations within each major tectonic region are smaller than those observed at a global scale. Next steps will include to refine the distribution of the scaling factor by estimating finer lateral variations of this ratio. In particular, we expect that the depth at which the scaling factor goes to zero vary with the tectonic province. The use of different scaling factors, one for each province, will therefore determine more accurately the depth at which the regional differences in terms of temperature and composition are cancelling.

[34] **Acknowledgments.** This research was founded by the Dutch National Science Foundation (NWO) under grant 750.297.02. We thank E. Humphreys, A. Lenardic, and an anonymous reviewer, whose comments greatly improved the manuscript.

References

Anderson, D. L. (1979), Geophysics of the continental mantle: An historical perspective, in *Continental Mantle*, edited by M. Menzies, pp. 1–30, Clarendon, Oxford, UK.

Artemieva, I. M., and W. D. Mooney (2001), Thermal thickness and evolution of Precambrian lithosphere: A global study, *J. Geophys. Res.*, *106*, 16,387–16,414.

Backus, G. E., and F. Gilbert (1967), The resolving power of gross Earth data, *J. Geophys. Res.*, *16*, 169–205.

Barmin, M. P., M. H. Ritzwoller, and A. L. Levshin (2001), A fast and reliable method for surface wave tomography, *Pure Appl. Geophys.*, *158*, 1351–1375.

Bassin, C., G. Laske, and G. Masters (2000), The current limits of resolution for surface wave tomography in North America, *Eos Trans. AGU*, *81*(48), Abstract S12A-03.

Deschamps, F., R. Snieder, and J. Trampert (2001), The relative density to shear velocity scaling in the uppermost mantle, *Phys. Earth Planet. Inter.*, *124*, 193–211.

Deschamps, F., J. Trampert, and R. Snieder (2002), Anomalies of temperature and iron in the uppermost mantle inferred from gravity data and tomographic models, *Phys. Earth Planet. Inter.*, *129*, 245–264.

de Smet, J. H., A. P. van den Berg, and N. J. Vlaar (2000), Early formation and long-term stability of continents resulting from decompression melting in a convecting mantle, *Tectonophysics*, *322*, 19–33.

Duffy, T. S., and D. L. Anderson (1989), Seismic wave speeds in mantle minerals and the mineralogy of the upper mantle, *J. Geophys. Res.*, *94*, 1895–1912.

Dziewonski, A. M., and D. L. Anderson (1981), Preliminary reference Earth model, *Phys. Earth Planet. Inter.*, *25*, 25,297–25,356.

Ekstrom, G. (2000), Mapping the lithosphere and asthenosphere with surface waves: Lateral structure and anisotropy, in *The History and Dynamics of Global Plate Motions*, *Geophys. Monogr. Ser.*, vol. 121, edited by M. A. Richards, R. G. Gordon, and R. van der Hilst, pp. 239–255, AGU, Washington, D. C.

Forte, A. M., and W. R. Peltier (1991), Viscous flow models of global geophysical observables: 1. Forwards problems, *J. Geophys. Res.*, *96*, 20,131–20,159.

Forte, A. M., and A. C. Perry (2000), Geodynamic evidence for a chemically depleted continental tectosphere, *Science*, *290*, 1940–1944.

Forte, A. M., A. M. Dziewonski, and R. J. O'Connell (1995), Thermal and chemical heterogeneity in the mantle: A seismic and geodynamic study of continental roots, *Phys. Earth Planet. Inter.*, *92*, 45–55.

Goes, S., and S. van der Lee (2002), Thermal structure of the North American uppermost mantle inferred from seismic tomography, *J. Geophys. Res.*, *107*(B3), 2050, doi:10.1029/2000JB000049.

Goes, S., R. Govers, and P. Vacher (2000), Shallow mantle temperatures under Europe from P and S wave tomography, *J. Geophys. Res.*, *105*, 11,153–11,169.

Grand, S. P. (1994), Mantle shear structure beneath the Americas and surrounding oceans, *J. Geophys. Res.*, *99*, 11,591–11,621.

Griffin, W. L., S. Y. O'Reilly, and C. G. Ryan (1999), The composition and origin of sub-continental lithospheric mantle, in *Mantle Petrology: Fields Observations and High-Pressure Experimentation*, edited by Y. Fei, C. M. Bertka, and B. O. Mysen, *Spec. Publ. Geochem. Soc.*, *6*, 13–45.

Hammond, W. C., and E. D. Humphreys (2000), Upper mantle seismic wave velocity: Effects of realistic partial mel geometries, *J. Geophys. Res.*, *105*, 10,975–10,986.

Humphreys, E. D., and K. G. Dueker (1994), Physical state of the western U.S. upper mantle, *J. Geophys. Res.*, *99*, 9635–9650.

Jackson, A. (2000), Laboratory measurement of seismic wave dispersion and attenuation: Recent progress, in *Earth's Deep Interior: Mineral Physics and Tomography from the Atomic to the Global Scale*, *Geophys. Monogr. Ser.*, vol. 117, edited by S. I. Karato et al., pp. 3–26, AGU, Washington, D. C.

Jordan, T. H. (1975), The continental tectosphere: Geophysics and space physics, *Rev. Geophys.*, *13*, 1–12.

Jordan, T. H. (1979), Mineralogies, densities and seismic velocities of garnet lherzolites and their geophysical implications, in *The Mantle Sample: Inclusions in Kimberlites and Other Volcanics*, edited by F. R. Boyd and H. O. A. Myer, pp. 1–14, AGU, Washington, D. C.

Karato, S.-I. (1993), Importance of anelasticity in the interpretation of seismic tomography, *Geophys. Res. Let.*, 1623–1626.

Lemoine, F. G., et al. (1998), The development of the joint NASA/GSFC and National Imagery Mapping Agency (NIMA) geopotential model EGM96, *NASA Tech. Pap., TP-1998-206861*, July.

Masters, G., G. Laske, H. Bolton, and A. Dziewonski (2000), The relative behavior of shear velocity, bulk sound speed, and compressional velocity in the mantle: Implications for chemical and thermal structure, in *Earth's Deep Interior: Mineral Physics and Tomography from the Atomic to the Global Scale*, *Geophys. Monogr. Ser.*, vol. 117, edited by S. I. Karato et al., pp. 63–87, AGU, Washington, D. C.

Mitrovica, J. X., and A. M. Forte (1997), Radial profile of mantle viscosity: Results from the joint inversion of convection and post-glacial rebond observable, *J. Geophys. Res.*, *102*, 2751–2769.

Mooney, W. D., G. Laske, and T. G. Masters (1998), CRUST5.1: A global crustal model at 5° × 5°, *J. Geophys. Res.*, *103*, 727–747.

Nataf, H.-C., and Y. Ricard (1996), 3SMAC: An a priori tomographic model for upper mantle based on geophysical modeling, *Phys. Earth Planet. Inter.*, *95*, 101–122.

Polet, J., and D. L. Anderson (1995), Depth extent of cratons as inferred from tomographic studies, *Geology*, *23*, 205–208.

Pollack, H. N., S. J. Hurter, and J. R. Johnson (1993), Heat flow from the Earth's interior: Analysis of the global data set, *Rev. Geophys.*, 267–280.

Robertson, G. S., and J. H. Woodhouse (1997), Comparison of *P* and *S* station corrections and their relationship to upper mantle structure, *J. Geophys. Res.*, *102*, 27,355–27,366.

Röhm, A., R. Snieder, S. Goes, and J. Trampert (2000), Thermal structure of continental upper mantle inferred from s-wave velocity and surface heat flow, *Earth Planet. Sci. Lett.*, *181*, 396–407.

Rudnick, R., and A. A. Nyblade (1999), The thickness and heat production of Archean lithosphere: Constraints from xenolith thermobarometry and surface heat flow, in *Mantle Petrology: Fields Observations and High-Pressure Experimentation*, edited by Y. Fei, C. M. Bertka, and B. O. Mysen, *Spec. Publ. Geochem. Soc.*, *6*, 3–12.

Schmidberger, S. S., and D. Francis (1999), Nature of the mantle roots beneath the North American craton: Mantle xenolith evidence from Somerset Island kimberlites, *Lithos.*, *48*, 195–216.

Trampert, J., and J. H. Woodhouse (1995), Global phase velocity maps of Love and Rayleigh waves between 40 and 150 seconds, *Geophys. J. Int.*, *122*, 675–690.

Trampert, J., and J. H. Woodhouse (2003), Global anisotropic phase velocity maps for fundamental mode surface waves between 40 and 150 seconds, *Geophys. J. Int.*, *154*, 154–165.

Van der Lee, S., and G. Nolet (1997), Upper mantle *S* velocity structure of North America, *J. Geophys. Res.*, *102*, 22,815–22,838.

Vinnik, L., S. Chevrot, J.-P. Montagner, and F. Guyot (1999), Teleseismic travel time residuals in North America and anelasticity of the asthenosphere, *Phys. Earth Planet. Inter.*, *116*, 93–103.

Woodhouse, J. H., and J. Trampert (1995), Global upper mantle structure inferred from surface wave and body data wave, *Eos Trans. AGU*, *76*(46), Fall Meet. Suppl., F422.

Yan, B., E. K. Graham, and K. P. Furlong (1989), Lateral variations in upper mantle thermal structure inferred from three-dimensional seismic inversion models, *Geophys. Res. Let.*, *16*, 449–452.

F. Deschamps and J. Trampert, Faculty of Earth Sciences, Utrecht University, P.O. Box 80021, 508 TA Utrecht, Netherlands. (deschamp@geo.uu.nl; jeannot@geo.uu.nl)

S. Godey, EMSC, c/o LDG, BP 12, F-91680, Bruyères-le-Châtel, France. (godey@emsc-csem.org)

R. Snieder, Department of Geophysics, Colorado School of Mines, Golden, CO 80401-1887, USA. (rsnieder@mines.edu)

Geophysical evidence for chemical variations in the Australian Continental Mantle

Luuk van Gerven,[1] Frédéric Deschamps,[1] and Robert D. van der Hilst[1,2]

Received 20 April 2004; revised 28 June 2004; accepted 17 August 2004; published 14 September 2004.

[1] The relative density-to-shear velocity scaling (ζ) provides a diagnostic for the presence of compositional variations in the mantle. We invert shear-wave velocity from a recent 3-D model and gravity anomalies for radial profiles of ζ of the uppermost mantle beneath Australia. We performed calculations for the three major tectonic provinces that constitute the continent, and found significant differences between them. The ζ profile for the Phanerozoic region can be explained by thermal variations alone. In contrast, negative values of ζ suggest that variations in composition are important between $\sim$75 and $\sim$150 km depth in the Proterozoic continental lithosphere (central Australia). It is likely that chemical variations are also required to explain the inferences for the Archean craton (west Australia), but poor tomographic resolution precludes a definitive conclusion. The scaling factors found are consistent with chemical depletion of deep Precambrian lithosphere, which supports a tectosphere model for the Australian continental roots. *INDEX TERMS:* 1212 Geodesy and Gravity: Earth's interior—composition and state (8105, 8124); 8124 Tectonophysics: Earth's interior—composition and state (1212); 8120 Tectonophysics: Dynamics of lithosphere and mantle—general; 7218 Seismology: Lithosphere and upper mantle. **Citation:** van Gerven, L., F. Deschamps, and R. D. van der Hilst (2004), Geophysical evidence for chemical variations in the Australian Continental Mantle, *Geophys. Res. Lett.*, *31*, L17607, doi:10.1029/2004GL020307.

1. Introduction

[2] Precambrian cratons are postulated to be underlain by thick continental roots [e.g., *Jordan*, 1978; *Polet and Anderson*, 1995] which stabilized shortly after their formation and have remained coupled to the crust ever since [*Griffin et al.*, 1998]. The nature of these roots and the cause of their long-term stability are still debated [see, e.g., *Shapiro et al.*, 1999a; *Lenardic and Moresi*, 1999]. Ancient continental roots are thought to be colder than oceanic or younger continental lithosphere [*Forte and Perry*, 2000; *Artemieva and Mooney*, 2001] but gravity anomalies and the geoid do not correlate with craton locations [*Jordan*, 1978; *Shapiro et al.*, 1999b]. *Jordan* [1978, 1988] thus postulated that the density increase due to the cooling of the root is balanced by chemical depletion in basaltic components with respect to the average mantle. This iso-pycnic equilibrium is an essential part of the so called "tectosphere" hypothesis, but the need for compositional differentiation has been questioned [e.g., *Pari and Peltier*, 1996]. In addition, the rheology of the continental lithosphere (CL) could play an important role in its formation and stabilization over geological time [*Jordan*, 1988; *Shapiro et al.*, 1999a; *Lenardic and Moresi*, 1999].

[3] To determine if a tectosphere is present beneath Australia we investigate the ratio of relative changes in density and shear speed (ζ), a diagnostic for variations in composition:

$$\zeta(r,\theta,\varphi) \equiv \frac{\partial \ln \rho(r,\theta,\varphi)}{\partial \ln V_S(r,\theta,\varphi)}. \quad (1)$$

Predominance of thermal effects produces positive values of ζ. The precise effect of changes in bulk chemistry on ζ is not well-defined, but depletion in dense elements (e.g., iron or basaltic components) would decrease the amplitude of density anomalies. Small and negative values of ζ therefore indicate that effects of composition are significant. Global scale investigations have determined depth profiles of ζ for continental and oceanic regions [e.g., *Forte et al.*, 1994; *Deschamps et al.*, 2001], and presented evidence for chemical depletion in the tectosphere [*Forte and Perry*, 2000; *Deschamps et al.*, 2002]. More recently, *Perry et al.* [2003] proposed a detailed regional study for North America.

[4] The *SKIPPY* seismometry project [*van der Hilst et al.*, 1994] has enabled the construction of detailed wavespeed models of the continental upper mantle beneath Australia [e.g., *Zielhuis and van der Hilst*, 1996; *Debayle and Kennett*, 2000, 2003; *Simons et al.*, 1999, 2002; *Yoshizawa and Kennett*, 2004]. Here we will use an update, hereinafter referred to as *AUS04-Vs*, of the isotropic part of the model by *Simons et al.* [2002]. We use gravity anomalies according to *EGM96* [*Lemoine et al.*, 1998].

[5] The Australian continent can be divided in three main tectonic provinces (Figure 1a) with a westward age progression from Phanerozoic (<500 Ma), to Proterozoic (500–2500 Ma), and Archean (>2500 Ma). If parts of the Australian continent are underlain by a tectosphere one would expect lateral variations in the depth profiles $\zeta(r)$. Indeed, research presented here suggests that depth profiles for these domains differ from one another and that they can be used to constrain the depth range of chemical depletion.

2. Methodology

[6] We invert gravity (δg) and shear-wave velocity anomalies (δV_S) for radial changes in the scaling factor

[1]Department of Geophysics, Utrecht University, Utrecht, Netherlands.
[2]Now at Department of Earth, Atmospheric, and Planetary Sciences, Massachusetts Institute of Technology, Cambridge, Massachusetts, USA.

Copyright 2004 by the American Geophysical Union.
0094-8276/04/2004GL020307$05.00

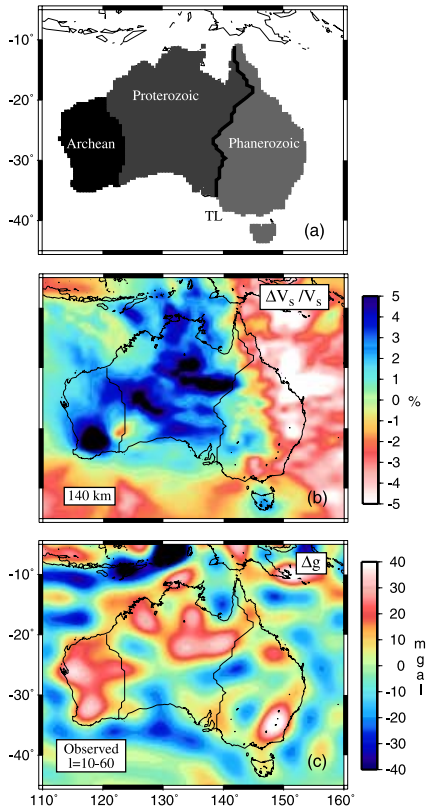

Figure 1. (a) Age-regionalization of the Australia continent. We considered three major regions: Archean, Proterozoic, and Phanerozoic. Across the continent, the age of the crust increases from East to West. *TL* denotes the Tasman Line. (b) Relative shear-velocity anomalies at z = 140 km according to model *AUS04-V_S*. The reference model is *ak135*. (c) Observed gravity anomalies derived from *EGM96* and crustal correction according to *CRUST2.0*. Data are filtered for spherical harmonic degrees $\ell = 10 - 60$.

$\zeta(r,\theta,\varphi)$. To model gravity anomalies we integrate density anomalies $\delta\rho$ vertically and laterally following

$$\delta g(\theta,\varphi) = \frac{3g_0}{4\pi\bar{\rho}R}\int_{r_{CMB}}^{R}\int_{0}^{\pi}\int_{-\pi/2}^{\pi/2} K_g(\Delta,r)\cdot\delta\rho(r,\theta',\varphi') \cdot \sin\theta' d\theta' d\varphi' dr, \quad (2)$$

where R and $\bar{\rho}$ are the Earth's radius and mean density, respectively, r_{CMB} the radius of the core-mantle boundary, g_0 the surface acceleration of gravity, $K_g(\Delta, r)$ the local gravity kernels, and Δ the angular distance between the locations (θ, ϕ) and (θ', ϕ'). This equation is similar to that used by *Kogan and McNutt* [1993].

[7] We perform the analysis in the part of the spectral domain that is sensitive to the uppermost mantle. Spherical harmonic degrees lower than $\ell = 10$ sample the whole mantle and are removed to avoid smearing effects. To focus the study on the depth interval 50–300 km and reduce the influence of the crust we also removed degrees higher than $\ell = 60$. For the band-pass filtering, $\ell_1 \le \ell \le \ell_2$, the local gravity kernels are given by

$$K_g(\Delta,r) = \sum_{\ell=\ell_1}^{\ell_2}(\ell-1)\cdot G_\ell(r)\cdot P_\ell^0(\cos\Delta), \quad (3)$$

where $P_\ell^0(\cos\Delta)$ are Legendre polynomials and $G_\ell(r)$ the radial geoid kernels. The latter depend strongly on the radial viscosity profile and boundary topography and are computed using the method proposed by *Forte and Peltier* [1991] and viscosity profile MF2 due to *Mitrovica and Forte* [1997]. Interestingly, geoid kernels for degrees higher than $\ell = 10$ depend only slightly on the viscosity profile. An important consequence is that within error bars, the scaling factor for the uppermost mantle (z < 400 km) is not sensitive to viscosity [*Deschamps et al.*, 2001].

[8] Radial geoid kernels (and therefore local gravity kernels) for degrees $\ell = 10$ to 60 are sensitive to the upper mantle but have negligible values throughout the lower mantle. The depth integration in equation (2) can then be reduced to the layer $35 \le z \le 670$ km. For different depths, Figure 2 shows the local gravity kernels for $\ell = 10 - 60$. The amplitude of local gravity kernels decreases rapidly with increasing angular distance. This justifies the use of truncated local kernels, which are equal to the local kernels for angular distances smaller than a cut-off angular distance (Δ_c) and zero elsewhere. Here we present results for $\Delta_c = 12°$.

[9] Substitution of equation (1) into equation (2) gives a linear relation between δg, δV_S, and ζ. We use a generalized inversion to estimate ζ from δg and δV_S. We performed simultaneous inversions for each age-region represented in Figure 1a. The regularization is controlled by a damping factor ε. Increasing ε enhances the smoothness of $\zeta(r)$ but leads to higher misfit of the reconstructed data with respect to the observed data. We inferred the optimal value of ε from the trade-off curves shown in Figure 3 and investigated the sensitivity of the solution to the choice of ε.

[10] The (isotropic) shear-wave velocity model *AUS04-Vs* is defined on a $1° \times 0.5°$ lateral grid and for 10 depth layers [see, e.g., *Zielhuis and Van der Hilst*, 1996]. The lateral resolution is ~300 km in eastern and central Australia but degrades toward the Archean west owing to reduced wave path coverage. Figure 1b shows *AUS04-Vs* at 140 km depth. Figure 1c depicts the tide-free, non-hydrostatic free-air gravity anomalies from *EGM96*, filtered for the spectral window $\ell = 10 - 60$. We assumed that the crust is in hydrostatic equilibrium and we used *CRUST2.0* [*Bassin et al.*, 2000] to remove its contribution to gravity anomalies.

[11] The main sources of uncertainty are the errors in the tomographic and crustal models. In absence of formal estimates of error in wavespeed, we studied the effect of random noise generated from a Gaussian probability distribution with zero mean and a standard deviation (σ_{err}) equal to 50% of the RMS of the *AUS04-Vs* values at the depth considered. For each layer of CRUST2.0, the σ_{err} of the

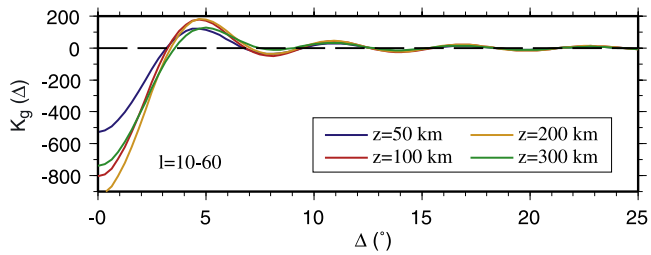

Figure 2. For four different depths, the local gravity kernels (K_g) are shown as a function of angular distance Δ. The spectral window is $\ell = 10 - 60$.

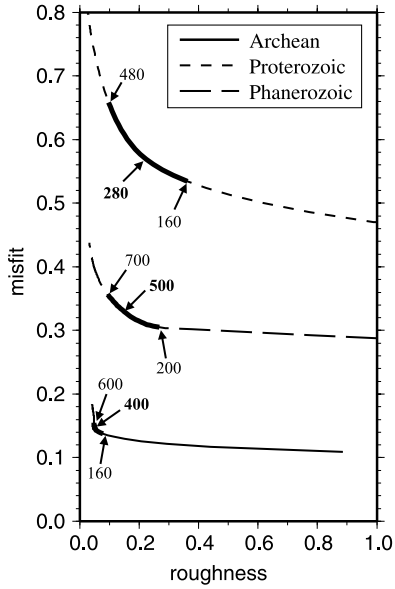

Figure 3. Trade-off between data misfit and model roughness for the three age regions. The bold segments of the trade-off curves indicate the ranges of acceptable values for damping factor ε. The preferred values are indicated in bold. Data filtered for degrees $\ell = 10 - 60$.

error distribution used is 1% of the layer density, but near layer boundaries we use 5% to mitigate effects of incorrect interface depths. We then produced 1000 perturbed V_S and crust models, and we inverted each of them for ζ as a function of depth. At each depth, the mean and standard deviation of the 1000 perturbed profiles thus produced are used as estimates of the scaling factor $\zeta(r)$ and its uncertainty, σ_ζ.

3. Results

[12] The solid curves in Figures 4a–4c represent the average scaling factor $\zeta(r)$ for each region, and the error bars represent one standard deviation uncertainty, σ_ζ. Fortunately, even the generous a priori errors described above do not lead to very large uncertainty in ζ. For reference, we depict with grey shading the thickness of the Phanerozoic and Proterozoic CL as estimated from the high wavespeed lid in *AUS04-Vs*; the Archean CL is poorly resolved by the seismic data used [*Simons et al.*, 2002]. The average scaling factor for Phanerozoic is positive throughout the CL (Figure 4a). It is perhaps slightly negative between 130 and 190 km depth, coincident with the seismic low velocity zone [*Zielhuis and van der Hilst*, 1996], but the large error bars may render this insignificant. The scaling factor profile for the Proterozoic is more complicated. Within error, ζ is positive to a depth of 75 km, negative between 75 and 150 km depth, and statistically zero below. Finally, the average scaling factor for Archean is smaller in amplitude than both others and is negative to a depth of ~200 km (Figure 4c). The negative values appear statistically significant, but we recall that resolution of wavespeed anomalies is poor in this part of the model [e.g., *Simons et al.*, 2002].

[13] It is important to assess the robustness of our results. First, the resolution matrices (Figures 4d–4f) demonstrate that the scaling factors for the Phanerozoic and Proterozoic are well resolved down to ~300 km. Below that depth (not shown here) substantial smearing occurs due to decreasing values of the gravity and surface wave sensitivity kernels. The scaling factor for Archean is poorly resolved even for depths less than 300 km. Second, we computed profiles of scaling factors for several values of the damping factor ε. For low values of ε, profiles are less smooth and uncertainties are larger. However, the shapes of the profiles and, in particular, the negative values between 75 and 150 km depth for the Proterozoic, are fairly robust. Finally, to investigate the influence of the spectral window, we performed calculations for $\ell = 10 - 40$, $\ell = 20 - 60$, and $\ell = 10 - 80$, but we did not find significant changes. We thus conclude that the $\zeta(r)$ inferred for the Phanerozoic and Proterozoic are robust down to 300 km depth.

4. Discussion and Concluding Remarks

[14] The Phanerozoic CL extends down to at most 120 km depth [e.g., *Zielhuis and van der Hilst*, 1996], and the positive scaling factor across this top layer can be explained

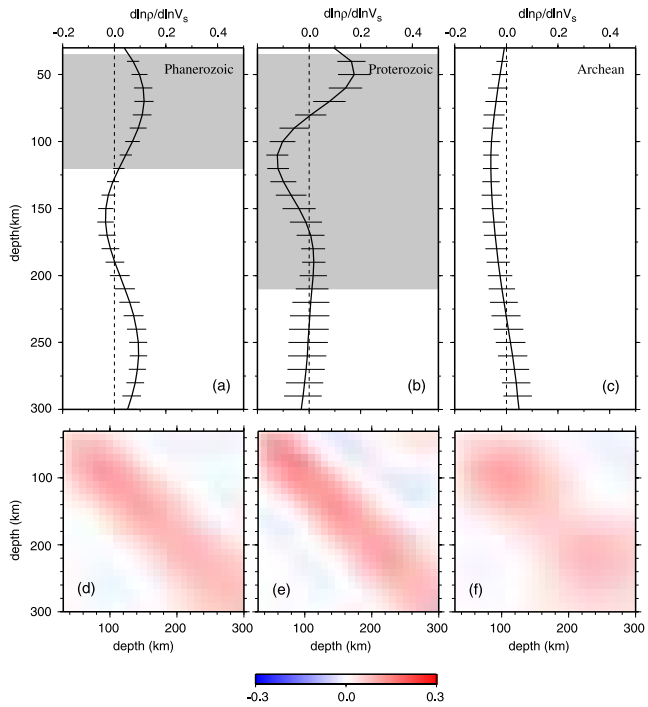

Figure 4. Radial model of scaling factor (equation (1)) for the three age-regions defined in Figure 1a. (a) Phanerozoic; (b) Proterozoic; and (c) Archean. The solid curves represent the average value of ζ at a given depth, and the error bars depict one standard deviation around this average. Error bars are estimated by generating random errors in the tomographic model and the crustal models, assuming Gaussian probability distributions (see text). Data are filtered for degrees $\ell = 10 - 60$, and the damping factor is 400, 280, and 500 for the Archean, Proterozoic, and Phanerozoic regions, respectively. The shaded areas denote the CL inferred from surface wave tomography. The corresponding resolution matrices are displayed in panels d–f.

with thermal effects alone. Small values of ζ might signal compositional changes at larger depth, perhaps associated with the ocean-continent difference. Indeed, *AUS04-Vs* suggests very slow shear wave velocities between 100 and 200 km depth beneath the easternmost part of Australia, which appear continuous to the slow velocities observed beneath the oceanic domain at the east of Australia (Figure 1b). In contrast, variations in composition within the CL are required to explain the inferred scaling factors beneath the Proterozoic shield of central Australia. Purely thermal anomalies can explain $\zeta(r)$ for $z \leq 50$ km, but the sharp decrease of ζ below this depth suggests that chemical depletion is present between 90 and 140 km depth. Similarly, chemical depletion seems to have occurred beneath the Archean province. We cannot propose a robust conclusion, however, because the tomographic model is poorly resolved and shows significant smearing in this region. An outstanding question is the nature and strength of chemical depletion. The scaling factor alone cannot resolve the trade-off between thermal and compositional effects. The amplitude of thermal and compositional variations can be inferred from appropriate statistical analysis of V_S and density distributions [*Deschamps and Trampert*, 2003], but independent information would be needed to constrain density better (e.g., the surface topography, provided it is correctly converted into dynamic topography) and the temperature (e.g., compressional-wave velocity model and heat flow data).

[15] The radial scaling factors that we infer are generally consistent with the tectosphere model due to *Jordan* [1988]. Beneath Precambrian terrains (here, restricted to the Proterozoic) the continental roots appear chemically distinct, whereas data for the Phanerozoic regions can be explained without significant compositional variations in the lithosphere. It is likely that the chemical depletion of the Proterozoic continental lithosphere contributes to the long term stability of the Australian continental roots, but from the work described in this paper it is yet not clear if chemical depletion by itself would be sufficient to prevent gravitational instability due to cooling. Rheology probably plays an important role [*Shapiro et al.*, 1999a; *Lenardic and Moresi*, 1999], but more systematic studies are necessary to understand the stability of a thermal boundary layer in a chemically depleted fluid.

[16] **Acknowledgments.** We are grateful to Eric Debayle and Alessandro Forte for constructive reviews. This research was funded by ISES (grant 627) (FD) and the Nederlands Organization for Scientific Research (NWO, grant VICI 86503001) (RvdH).

References

Artemieva, I. M., and W. D. Mooney (2001), Thermal thickness and evolution of Precambrian lithosphere: A global study, *J. Geophys. Res.*, *106*, 16,387–16,414.

Bassin, C., G. Laske, and G. Masters (2000), The current limits of resolution for surface wave tomography in North America, *Eos Trans. AGU*, *81*(48), Fall Meet. Suppl., S12A-03.

Debayle, E., and B. L. N. Kennett (2000), The Australian continental upper mantle: Structure and deformation inferred from surface waves, *J. Geophys. Res.*, *105*, 25,423–25,450.

Debayle, E., and B. L. N. Kennett (2003), Surface-waves studies of the Australian region, *Spec. Publ. Geol. Soc. Aust.*, *22*, 25–45.

Deschamps, F., and J. Trampert (2003), Mantle tomography and its relation to temperature and composition, *Phys. Earth Planet. Inter.*, *140*, 277–291.

Deschamps, F., R. Snieder, and J. Trampert (2001), The relative density-to-shear velocity scaling in the uppermost mantle, *Phys. Earth Planet. Inter.*, *124*, 193–211.

Deschamps, F., J. Trampert, and R. Snieder (2002), Anomalies of temperature and iron in the uppermost mantle iferred from gravity data and tomographic models, *Phys. Earth Planet. Inter.*, *129*, 245–264.

Forte, A. M., and W. R. Peltier (1991), Viscous flow models of global geophysical observables: 1. Forward problems, *J. Geophys. Res.*, *96*, 20,131–20,159.

Forte, A. M., and H. C. Perry (2000), Geodynamic evidence for a chemically depleted continental tectosphere, *Science*, *290*, 1940–1944.

Forte, A. M., A. M. Dziewonsky, and R. J. O'Connell (1994), Thermal and chemical heterogeneity in the mantle: A seismic and geodynamic study of continental roots, *Phys. Earth Planet. Inter.*, *92*, 45–55.

Griffin, W. L., S. Y. O'Reilly, O. Gaul, and D. A. Ionov (1998), Secular variation in the composition of sub-continental lithospheric mantle: Geophysical and geodynamic implications, in *Structure and Evolution of the Australian Continent*, *Geodyn. Ser.*, vol. 26, edited by J. Braun et al., pp. 1–26, AGU, Washington, D. C.

Jordan, T. H. (1978), Composition and development of the continental tectosphere, *Nature*, *274*, 544–548.

Jordan, T. H. (1988), Structure and formation of the continental tectosphere, *J. Petrol.*, Special Lithosphere Issue, 11–37.

Kogan, M. G., and M. K. McNutt (1993), Gravity field over northern Eurasia and variations in the strength of the upper mantle, *Science*, *259*, 473–479.

Lemoine, F. G., S. C. Kenyon, and J. K. Factor (1998), The Development of the Joint NASA GSFC and NIMA Geopotential Model EGM96, *NASA Tech. Pap., NASA/TP-1998–206861*, 575 pp.

Lenardic, A., and L.-N. Moresi (1999), Some thoughts on the stability of cratonic lithosphere: Effects of buoyancy and viscosity, *J. Geophys. Res.*, *104*, 12,747–12,758.

Mitrovica, J. X., and A. M. Forte (1997), Radial profile of the mantle viscosity: Results from the joint inversion of convection and postglacial rebound observables, *J. Geophys. Res.*, *102*, 2751–2769.

Pari, G., and W. R. Peltier (1996), The free-air gravity constraint on sub-continental mantle dynamics, *J. Geophys. Res.*, *101*, 28,105–28,132.

Perry, H. K. C., A. M. Forte, and D. W. S. Eaton (2003), Upper-mantle thermochemical structure below North America from seismic-geodynamic flow model, *Geophys. J. Int.*, *154*, 279–299.

Polet, J., and D. L. Anderson (1995), Depth extent of cratons as inferred from tomographic studies, *Geology*, *23*, 205–208.

Shapiro, S. S., B. H. Hager, and T. H. Jordan (1999a), Stability and dynamics of the continental tectosphere, *Lithos*, *48*, 115–133.

Shapiro, S. S., B. H. Hager, and T. H. Jordan (1999b), The continental tectosphere and Earth's long-wavelength gravity field, *Lithos*, *48*, 135–152.

Simons, F. J., A. Zielhuis, and R. D. van der Hilst (1999), The deep structure of the Australian continent from surface wave tomography, *Lithos*, *48*, 17–43.

Simons, F. J., R. D. van der Hilst, J.-P. Montagner, and A. Zielhuis (2002), Multimode Rayleigh wave inversion for heterogeneity and azimuthal anisotropy of the Australian upper mantle, *Geophys. J. Int.*, *151*, 738–754.

van der Hilst, R. D., B. L. N. Kennett, D. Christie, and J. Grant (1994), SKIPPY: Mobile broad-arrays to study the seismic structure of the lithosphere and mantle beneath Australia, *Eos Trans. AGU*, *75*, 177 and 180, 181.

Yoshizawa, K., and B. L. N. Kennett (2004), Multimode surface wave tomography for the Australian region using a three-stage approach incorporating finite frequency effects, *J. Geophys. Res.*, *109*, B02310, doi:10.1029/2002JB002254.

Zielhuis, A., and R. D. van der Hilst (1996), Upper-mantle shear velocity beneath eastern Australia from inversion of waveforms from SKIPPY portable arrays, *Geophys. J. Int.*, *127*, 1–16.

F. Deschamps and L. van Gerven, Department of Geophysics, Utrecht University, Budapestlaan 4, PO Box 80021, NL-3508 TA Utrecht, Netherlands. (deschamp@geo.uu.nl)

R. D. van der Hilst, Department of Earth, Atmospheric, and Planetary Sciences, Massachusetts Institute of Technology, Cambridge, MA 02139, USA.

Chapitre 3

Sur la structure du manteau inférieur

L'arrivée dans le manteau inférieur, vers 660 km de profondeur, s'accompagne d'une transition chimique (certains dirons une transition de phase), dont la signature sismologique est très marquée. Selon PREM (Dziewonski et Anderson, 1981), la densité moyenne augmente brutalement de 380 kg/m^3, la vitesse de cisaillement de 380 m/s, et la vitesse de compression de 480 m/s. La transition en question est la transformation de ringwoodite, la phase γ de $(Mg,Fe)_2SiO_4$, en pérovskite, $(Mg,Fe)SiO_3$, et magnésio-wüstite, (Mg,Fe)O. La situation n'est pas aussi simple puisque d'autres phases (généralement rassemblées sous le terme générique de grenats) se transforment aussi en pérovskite et magnésio-wüstite, mais avec un diagramme de phase différent (les grenats restent stables jusque vers 740 km). La structure thermochimique du manteau inférieur est mal connue, jusqu'aux profiles moyens de température et de composition qui sont mal contraints. Depuis une vingtaine d'année, les modèles tomographiques globaux voient des variations latérales de vitesse sismiques, en particulier à la base et au sommet du manteau inférieur, sans en donner d'interprétation thermochimique claire. Ces distributions sont pourtant essentielles pour mieux comprendre la dynamique du manteau. Les obstacles qui se dressent sont principalement un trade-off très marqué entre la température et la composition, et les incertitudes sur les propriétés thermo-élastiques des minéraux aux pressions et températures du manteau inférieur. Ce chapitre rassemble trois études sur la structure thermochimique du manteau inférieur, dont un modèle thermochimique moyen tenant compte des propriétés thermo-élastiques – et de leur incertitudes – disponibles en 2004

(Deschamps et Trampert, 2004), une analyse de la distribution des rapports sismiques en termes de variations thermochimiques latérales (Deschamps et Trampert, 2003), et un modèle quantitatif de distributions latérales de température et de composition déduites de la tomographie probabiliste (Trampert et al., 2004).

3.1 Profiles moyens de température et de composition

Les géophysiciens buttent depuis de nombreuses années sur la détermination d'un profile de température moyen pour le manteau profond. On ne possède pas de mesures directes de la température aux grandes profondeurs, et les seules contraintes dont nous disposions sont deux points d'ancrage, l'un aux environs de 660 km, et l'autre à la limite noyau/manteau (soit environ 2900 km). Le premier de ces points de référence est déduit de la transformation de la ringwoodite en perovskite et magnesio-wüstite, $Mg_2SiO_4 \rightarrow MgSiO_3 + MgO$, qui se produit autour de 660 km. À ces pressions, la température requise pour la transformation de Mg_2SiO_4 est de 1873 K (Ito et Katsura, 1989). Le second point de référence, $T_{CMB} = 3573 \pm 500$ K, est basé sur la température de fusion du fer à la pression de la limite noyau interne/noyau externe, projetée le long d'un profil adiabatique jusqu'à la limite noyau/manteau (Brown et McQueen, 1986). Bien sûr, ces deux valeurs ne suffisent pas à déterminer un profil de température précis. D'où l'idée de faire appel aux profiles moyens de vitesse sismiques (V_S et V_P) et de densité. Ceux-ci sont relativement bien connus (p.e., PREM ou ak135), mais leur interprétation n'est pas sans ambigüités. La vitesse dépend simultanément de la température et de la composition, et le trade-off qui existe entre ces deux paramètres est difficile à lever. À cela s'ajoutent les incertitudes sur la détermination des propriétés thermo-élastiques (principalement, les modules élastiques et leurs dérivées), y compris dans le choix de l'équation d'état.

3.1.1 Modéliser les propriétés thermo-élastiques des minéraux aux conditions du manteau

Depuis quelques années il est possible de calculer directement les propriétés thermo-élastiques des minéraux du manteau terrestre à hautes pressions et hautes températures à partir de méthodes *ab initio*, c'est-à-dire de la résolution (moyennant, bien entendu, quelques approximations sur l'Hamiltonien et l'énergie totale du système) de l'équation de Schrödinger pour un cristal donné (pour une discussion récente sur ce sujet, on pourra se référer à Bukowinski et Akber-Knutson (2005)). Pour une composition (en oxydes) donnée, il est aussi possible de déterminer un diagramme de phase en fonction de la température et de la pression en minimisant l'énergie libre de Gibbs (p.e., Connolly, 2005; Ricard et al., 2005), puis d'en déduire les propriétés thermo-élastiques de l'agrégat (on notera que la détermination du module de cisaillement nécessite toujours d'imposer une équation d'état).

Une méthode plus classique est de porter individuellement chaque minéral à haute température et à haute pression en utilisant des équations d'état appropriées entre la température, la pression, la déformation et les modules élastiques. Cette approche s'apparente à une approche paramétrée, bien que les équations d'état aient une base physique. En plus des équations d'état, il faut se donner les valeurs de surface des paramètres thermo-élastiques (les conditions au limites, dirons les modélisateurs), notamment des modules élastiques et de leurs dérivées en température et en pression. Deux principales stratégies sont employées. Soit on applique une compression isotherme puis on modélise l'effet de la température en calculant une pression thermique (équation de Mie-Debye-Grüneisen) à volume constant. Soit on applique, pour chaque minéral, un chauffage à pression nulle jusqu'à une température potentielle (ou pied de l'adiabat) suivi d'une compression adiabatique (Figure 3.1). Dans ce cas une opération supplémentaire doit être effectuée. La compression adiabatique induit une élévation de la température (on parle parfois de contribution adiabatique) que l'on peut calculer à partir du module d'incompressibilité (à la pression et à la température considérées).

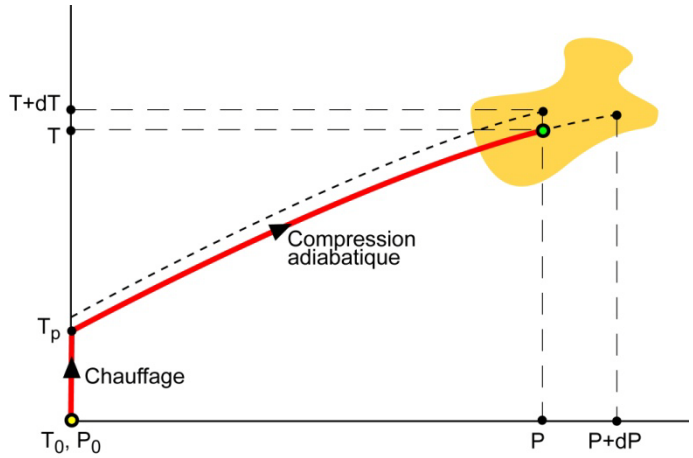

Figure 3.1 – L'approche adiabatique de la modélisation de l'équation d'état, utilisée dans ce mémoire pour extrapoler les propriétés des matériaux du manteau terrestre aux conditions de température et de pression de ce manteau. Les minéraux sont d'abord portés à une température potentielle (le pied de l'abdiabat), puis comprimés adiabatiquement à la pression désirée. Il est de plus tenu compte des incertitudes sur les valeurs des paramètres thermo-élastiques en surface (représentées par la surface orangée).

Jackson (1998) a montré que ces deux approches étaient parfaitement compatibles. Dans les deux cas, on peut de plus calculer les incertitudes sur les propriétés thermo-élastiques à hautes pressions et températures à partir d'une méthode de Monte-Carlo et en variant les paramètres de départ dans leurs barres d'erreurs. Par ailleurs, une phase donnée (p.e., la pérovskite) peut comporter plusieurs pôles (Mg, Fe, Ca, Al), avec des densités et des modules élastiques différents. Pour tenir compte de ces effets, et lorsque des données sont disponibles, on corrige la densité et les modules élastiques (et leurs

dérivées) à pression et température ambiantes et en fonction de la fraction volumique de chaque pôle. Enfin, les propriétés thermo-élastiques de l'assemblage minéralogique sont déduites en moyennant les propriétés individuelles des minéraux à la pression et à la température considérées. Les travaux présentés dans ce chapitre suivent l'approche 'adiabatique', sur laquelle on trouvera plus de détails (notamment pour l'extrapolation à haute température) dans Deschamps et Trampert (2004).

3.1.2 Choix de l'équation d'état pour la compression

L'équation d'état la plus utilisée pour modéliser la compression des minéraux du manteau terrestre est l'équation de Birch-Murnaghan, qui s'obtient en développant l'énergie libre en une série de puissances de la déformation finie, puis en dérivant cette expansion par rapport à la pression (p.e., Poirier, 1991, pp. 58-65). La déformation finie s'écrit

$$\varepsilon = \frac{1}{2}\left[1 - \left(\frac{\rho}{\rho_0}\right)^{2/3}\right], \tag{3.1}$$

où ρ et ρ_0 sont la densité aux pressions P et $P_0 = 0$. Au troisième ordre, l'équation de Birch-Murnaghan relie la pression à la déformation selon

$$P = -3K_{S0}(1-2\varepsilon)^{5/2}\left[\varepsilon + \frac{3}{2}(4 - K'_{S0})\varepsilon^2\right]. \tag{3.2}$$

Une dérivation supplémentaire par rapport à la pression nous donne le module d'incompressibilité,

$$K_S = K_{S0}(1-2\varepsilon)^{5/2}\left[1 + (5 - 3K'_{S0})\varepsilon - \frac{27}{2}(4 - K'_{S0})\varepsilon^2\right]. \tag{3.3}$$

Le raisonnement qui conduit à l'équation 3.3 n'est *a priori* pas transposable au module de cisaillement, G. Par analogie, on utilise pourtant une équation identique à l'équation 3.3 pour extrapoler G à de hautes pressions. Une alternative proposé par Stacey (1995) est de définir une relation linéaire entre le module de cisaillement et le module d'incompressibilité à la pression P,

$$G = aK_S - bP \tag{3.4}$$

où a et b sont deux constantes calculées à pression nulle et à la température potentielle (on suppose donc que ces constantes sont indépendantes de la pression).

D'autres équations que l'équation de Birch-Murnaghan au troisième ordre (BM3) ont été proposées pour extrapoler les propriétés thermo-élastiques aux pressions du manteau. Vinet et al. (1987) ont défini une équation d'état dite universelle (car elle explique les données expérimentales pour un grand nombre de cristaux) à partir de l'énergie de cohésion d'un solide en compression. La pression et le module d'incompressibilité s'écrivent

$$P = 3K_{S0}x^2(x-1)\exp\left[\frac{3}{2}\,(K'_{S0}-1)\frac{(x-1)}{x}\right], \qquad (3.5)$$

et $$K_S = 2K_{S0}\left[x^2 + \frac{x}{4}(3K'_{S0}-5) - \frac{3}{4}(K'_{S0}-1)\right]\exp\left[\frac{3}{2}\,(K'_{S0}-1)\frac{(x-1)}{x}\right], \qquad (3.6)$$

où x = ρ/ρ0. L'équation d'état logarithmique proposée par Poirier et Tarantola (1998) est basée sur la déformation logarithmique (ou déformation de Hencky),

$$\varepsilon_L = -\frac{1}{3}\ln\left(\frac{\rho}{\rho_0}\right), \qquad (3.7)$$

et au troisième ordre en déformation, la pression et le module d'incompressibilité s'écrivent

$$P = -3K_{S0}e^{-3\varepsilon_L}\left[\varepsilon_L + \frac{3}{2}\,(2-K'_{S0})\varepsilon_L^2\right], \qquad (3.8)$$

et $$K_S = K_{S0}e^{-3\varepsilon_L}\left[1 - 3(K'_{S0}-1)\varepsilon_L + \frac{9}{2}\,(K'_{S0}-2)\varepsilon_L^2\right]. \qquad (3.9)$$

Selon Poirier et Tarantola (1998), l'équation d'état logarithmique est équivalente à BM3 pour des pressions modérées (i.e., jusque dans le manteau moyen), et donne de meilleurs résultats pour les pressions régnant à la base du manteau. Enfin, Stacey (2000) a proposé une relation empirique entre le module d'incompressibilité et la pression basée sur la limite asymptotique (i.e., pour des pressions infinies) de sa dérivée en pression, K'_∞, et sur la valeur de surface de sa dérivée seconde en pression, K''_{S0},

$$K_S = K_{S0}\left(1 - K'_\infty\frac{P}{K_S}\right), \qquad (3.10)$$

avec $$K'_\infty = K'_{S0} + \frac{K_{S0}K''_{S0}}{K'_{S0}}. \qquad (3.11)$$

La densité est donnée par

$$\ln\left(\frac{\rho}{\rho_0}\right) = \left(1 - \frac{K'_{S0}}{K'_\infty}\right)\frac{P}{K_S} - \frac{K'_{S0}}{K'^2_\infty}\ln\left(1 - K'_\infty\frac{P}{K_S}\right) \qquad (3.12)$$

Un problème de cette approche est le choix de la dérivée seconde du module d'incompressibilité. Une façon de procéder est de développer l'équation d'état de Birch-Murnaghan pour le module d'incompressibilité au 4ième ordre en déformation et d'écrire que le coefficient du 4ième ordre (qui est fonction de K_{S0}, K_{S0}', et K_{S0}") s'annule, afin de revenir à une expansion au 3ième ordre. On a ainsi

$$K''_{S0} = \frac{1}{K_{S0}}\left[K'_{S0}(7-K'_{S0}) - \frac{143}{9}\right]. \qquad (3.13)$$

Quelle équation d'état choisir pour le manteau inférieur ? Un premier test est de comparer les profiles de modules élastiques et de densité prédits par chacune de ces équations d'état et pour une composition fixée, pyrolitique par exemple, avec une fraction volumique de pérovskite x_{pv} = 0.8 et une fraction volumique de fer (i.e., la fraction globale

de FeO) $x_{Fe} = 0.11$. Au passage, il faut définir un paramètre supplémentaire, le coefficient de partage du fer χ_{Fe} entre la pérovskite et la magnésio-wüstite,

$$\chi_{Fe} = \frac{X_{Fe}^{pv}/(1-X_{Fe}^{pv})}{X_{Fe}^{mw}/(1-X_{Fe}^{mw})}, \qquad (3.14)$$

où X_{Fe}^{pv} et X_{Fe}^{mw} sont les fractions volumiques de fer dans la pérovskite et dans la magnésio-wüstite, et satisfont

$$x_{Fe} = x_{pv} X_{Fe}^{pv} + (1 - x_{pv}) X_{Fe}^{mw} . \qquad (3.15)$$

L'extrapolation à haute température (jusqu'à la température potentielle $T_p = 2000$ K) est la même dans chaque cas. Les valeurs de surface des paramètres thermo-élastiques sont rassemblées dans la Table 3.1. À partir des incertitudes (ou des plages de valeurs expérimentales), lorsqu'elles sont disponibles, et d'une recherche de Monte-Carlo on peut estimer une barre d'erreur pour les propriétés à hautes pressions et températures. Les valeurs de surface des modules de cisaillement (et de leurs dérivées) sont moins bien connues que celles des modules d'incompressibilité, ce qui se traduit par des incertitudes

Pamarètre	Perovskite			Magnesio-wüstite	
	Experimental	*Ab initio*[a]	C_{Fe}[b]		C_{Fe}[b]
ρ (g/cm^3)	4.109	4.107	+1.03[c]	3.584	2.28
K_{S0} (GPa)	264.0	268.9	+20[c]	162.5	+11.5[d] +18.0[e]
K_{S0}'	3.97/3.95/3.77/3.75[d]	4.07	+0.16[c]	4.0 / 4.15	-0.53[e]
$\dot{K}_{S0}$ (10^{-2} GPa/K)	-1.1/-1.5/-1.0/-1.5[d]	-1.2	-	-1.55 / -1.4	-
G_0 (Gpa)	175.0	180.0	-40	130.8	-75.6[d] -108[e]
G_0'	1.8 (0.4)	-	-0.52[c]	2.4 / 2.5	-3.29[e]
$\dot{G}_0$ (10^{-2} GPa/K)	-2.9 (0.3)	-	-	-2.4 / -2.2	-
γ_0	1.31/1.39/1.33/1.41[d]	1.51	-	1.41	-
q	1.0/2.0/1.0/2.0[d]	1.27	-	1.3	-
a_1 (10^{-5} K^{-1})	1.19 (0.17)	2.066	-	3.681	-
a_2 (10^{-8} K^{-2})	1.20 (0.10)	0.909	-	0.9283	-
a_3 (K)	0.0	0.418	-	0.7445	-

Table 3.1. Propriétés thermo-élastiques de la pérovskite $MgSiO_3$ et de la magnésio-wüstite MgO à conditions ambiantes de température et de pression (P = 0 et T = 298 K). On trouvera toutes les références concernant ces données dans Deschamps et Trampert (2004). Les barres d'erreurs, lorsqu'elles sont disponibles, sont indiquées entre parenthèses. ρ est la densité, K_{S0} le module d'incompressibilité adiabatique, G_0 le module de cisaillement, γ_0 le paramètre de Grüneisen, et q une constante. Les primes et les points indiquent les dérivées par rapport à la pression et à la température, respectivement. L'expansion thermique est calculée selon $\alpha = a_1 + a_2 T - a_3 T^{-2}$, où T est la température.

[a] Propriétés de $MgSiO_3$ déduites des calculs *ab initio* d'Oganov et al. (2001a).

[b] Corrections pour la fraction volumique de fer, X_{Fe}^{min}. La valeur corrigée de chaque paramètre M est donnée par $M_{Mg,Fe}^{min} = M_{Mg}^{min} + C_{Fe}^{min} X_{Fe}^{min}$. Les fractions volumiques de fer dans la pérovskite et dans la magnésio-wüstite sont déduites du coefficient de partage du fer (équation 3.14), χ_{Fe}, que l'on a varié entre 0.2 et 0.5.

[c] Kiefer et al. (2002).

[d] Jackson (1998). Pour K_{S0}', $\dot{K}_{S0}$, et γ_0 quatre combinaisons sont considérées, en fonction de K_{T0}' et de q.

[e] Kung et al. (2002).

plus élevées dans le manteau profond (de l'ordre de 20 GPa vers 2000 km de profondeur). À l'intérieur de ces barres d'erreur, il n'est pas possible de distinguer les modules de cisaillement prédits par les différentes équations d'état (Figure 3.2a). En revanche des différences importantes apparaissent dès 1200 km de profondeur (~50 GPa) entre les modules d'incompressibilité (Figure 3.2a) et vers 2200 km (~100 GPa) entre les densités (Figure 3.2b). L'équation logarithmique sous-estime (surestime) les modules élastique (la densité). Pour l'équation de Stacey, c'est l'inverse. Les valeurs calculées par BM3 et l'équation universelle de Vinet restent raisonnablement proches les unes des autres.

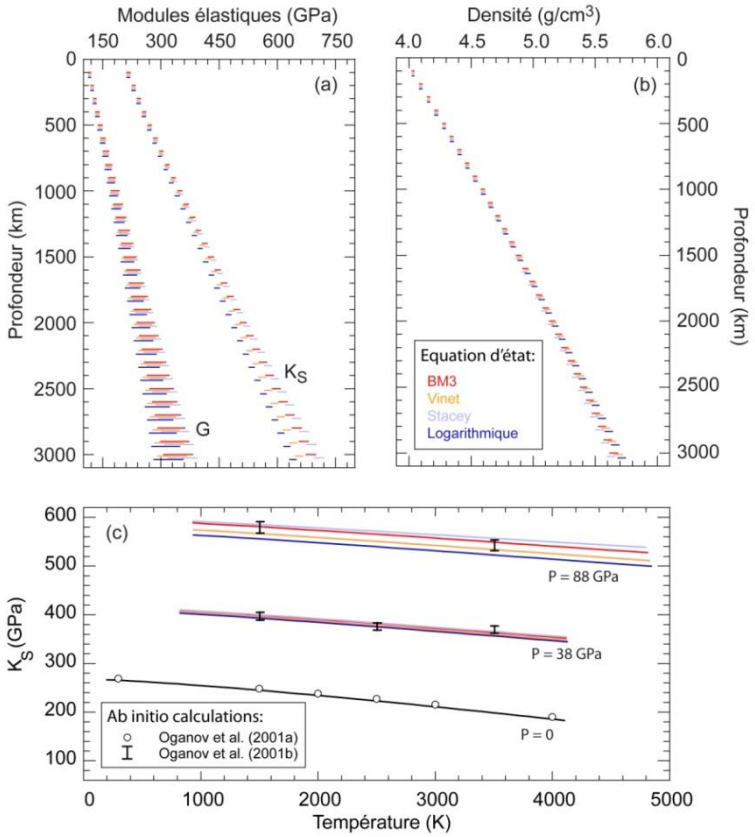

Figure 3.2 – Comparaison entre les modules de cisaillement et d'incompressibilité (a) et la densité (b) obtenus à partir de différentes équation d'état pour la compression adiabatique et pour une composition pyrolitique. (c) Comparaison entre les modules d'incompressibilité à hautes pressions et températures prédits par des calculs *ab initio* (Oganov et al., 2001a, 2001b) et par différentes équations d'état pour $MgSiO_3$. La courbe noire représente l'extrapolation à haute température et P_0=0 obtenu avec notre modèle.

Deuxième test, comparer les modules d'incompressibilité de la pérovskite $MgSiO_3$ prédits pour chaque équation d'état avec des calculs *ab initio* (Oganov et al. (2001b)) (Figure 3.2c). Pour cela, on utilisera les valeurs de surface des paramètres thermo-élastiques déduites des calculs d'Oganov et al. (2001a) (Table 3.1, 3ième colonne). Remarquons que notre extrapolation à haute température explique parfaitement les calculs *ab initio* à hautes température et pression nulle d'Oganov et al. (2001a). À 38 GPa (~1000

km), les quatre équations d'état donnent des résultats très similaires qui s'accordent bien avec les calculs d'Oganov et al. (2001b). Les différences sont nettement plus marquées à 88 GPa (~2000 km), et à l'intérieur des barres d'erreurs fournies par Oganov et al. (2001b), seules BM3 et l'équation universelle de Vinet expliquent correctement les calculs *ab initio*. De ce point de vue, BM3 constitue un choix raisonnable pour la modélisation des propriétés thermo-élastiques aux pressions du manteau profond.

3.1.3 Profiles moyens et incertitudes

Sur la lancée des tests précédents, déterminons (en utilisant BM3 pour extrapoler les propriétés thermo-élastiques aux hautes pressions) un profile moyen de température et de composition (x_{pv} et x_{Fe}) pour le manteau inférieur. L'idée est simple. Il s'agit de définir, pour chaque profondeur, une température et une composition, de calculer la densité et les modules élastiques associés à ces valeurs, et de les comparer à des observables fiables, ici la densité et les vitesses de compression et de cisaillement de PREM (Dziewonski et Anderson, 1981). De plus, on utilisera comme fonction de coût

$$F(z,T,x_{pv},x_{Fe}) = k\exp\left[-\frac{(V_S^{mod}-V_S^{obs})}{2\sigma_{V_S}^{obs}} - \frac{(V_P^{mod}-V_P^{obs})}{2\sigma_{V_P}^{obs}} - \frac{(\rho^{mod}-\rho^{obs})}{2\sigma_{\rho}^{obs}}\right], \qquad (3.16)$$

où σ^{obs} est l'incertitude sur PREM (fixée à 1%) et k une constante de normalisation. La définition de la fonction de coût est légèrement différente dans Deschamps et Trampert (2004), sans que cela ne change fondamentalement les résultats. Les valeurs moyennes et les déviations standards (que l'on utilisera comme estimations des barres d'erreur) de la température et de la composition sont ensuite déterminées à partir du premier et du second moment. Par exemple, en désignant l'espace des modèles par Ω, on a pour la température

$$\langle T\rangle_z = \int_\Omega F(z,T,x_{pv},x_{Fe})T\,d\Omega\,, \qquad (3.17a)$$

$$\langle T^2\rangle_z = \int_\Omega F(z,T,x_{pv},x_{Fe})T^2\,d\Omega\,, \qquad (3.17b)$$

et

$$\sigma_T = \sqrt{\langle T^2\rangle_z - \langle T\rangle_z^2}\,. \qquad (3.17c)$$

Les dérivées du module de cisaillement de la pérovskite

Il n'est pas inintéressant d'estimer l'influence des différents paramètres thermo-élastiques sur la détermination de la température, en variant indépendamment chaque paramètre autour d'une valeur de référence (les autres paramètres restant fixés à leur valeur de référence). Le paramètre le plus influent est la dérivée en pression du module de cisaillement de la pérovskite. La température varie de 1800 K pour sa valeur basse (1.4) à 3400 K pour sa valeur haute (2.2). Pour $G_0' \geq 2.0$, très peu de modèles expliquent PREM. De

plus, les valeurs qui reproduisent le mieux les calculs *ab initio* d'Oganov et al. (2001b) vérifient $G_0' = 1.5 \pm 0.05$ (Deschamps et Trampert, 2004). On notera avec intérêt qu'une étude récente basée sur l'inversion des profiles sismiques pour la température et les propriétés thermo-élastiques d'un assemblage MgO-FeO-CaO-Al_2O_3-SiO_2 (Matas et al., 2007) arrive à des conclusions similaires, et que de nouvelles expériences de laboratoire pour la pérovskite (Murakami et al., 2007) suggèrent $G_0' = 1.56 \pm 0.04$.

La dérivée en pression du module de cisaillement de la pérovskite induit des incertitudes plus faibles. Elle reste cependant mal contrainte, et un problème supplémentaire apparaît lorsque l'on essaye d'expliquer les calculs *ab initio* d'Oganov et al. (2001b) et de Marton et Cohen (2002). Quelque soit la valeur de $\dot{G}_0$ entre -0.032 et -0.012 GPa/K, on ne parvient pas à reproduire simultanément les calculs *ab initio* à 38 et 88 GPa. Ceci suggère qu'une dérivée croisée à pression nulle, $(\partial^2 G/\partial P \partial T)$, est nécessaire pour expliquer ces calculs. Une recherche systématique conduit à une relation linéaire pour cette dérivée croisée,

$$\partial^2 G/\partial P \partial T = c\dot{G}_0 + b \ , \qquad (3.17)$$

où $c = -1.2\times10^{-2}$ GPa^{-1} et $b = -3.3\times10^{-4}$ K^{-1}. Cette prédiction reste à vérifier en laboratoire, faute de quoi il faudra conclure soit que les données expérimentales ne s'accordent pas avec les calculs *ab initio*, soit que BM3 ne décrit pas correctement le module de cisaillement de $MgSiO_3$ aux pressions du manteau inférieur.

Une remarque sur le calcium et deux familles de profiles

Pour la détermination des profiles moyens de température et de composition (Figure 3.3), faisons varier aléatoirement la température potentielle entre 1500 et 5000 K, la fraction volumique de pérovskite entre 0.5 et 1.0, et la fraction volumique de fer entre 0.05 et 0.20. Tenons compte également de la présence possible de Ca-pérovskite en variant sa fraction volumique entre 0.0 et 0.12. Fait intéressant, les propriétés thermo-élastiques de $CaSiO_3$ sont très proches des propriétés de $MgSiO_3$ (Wang et al., 1996; Karki et Crain, 1998), ce qui implique que et les profiles sismologiques ne contraignent pas le profile radial de $CaSiO_3$.

Ce qui ressort le plus de la Figure 3.3, c'est l'influence des corrections sur le fer. Les profiles oranges utilisent les corrections compilées par Jackson (1998), et sont clairement différents des profiles rouges, qui utilisent les données plus récentes de Kiefer et al. (2002) pour la pérovskite et de Kung et al. (2002) pour la magnésio-wüstite. Un examen plus détaillé indique que les différences entre les deux familles de profiles sont majoritairement dues au données de Kung et al. (2002) pour la magnésio-wüstite. Les profiles utilisant les corrections de Kiefer et al. (2002) et de Kung et al. (2002) sont globalement plus froids,

moins riches en pérovskite, et moins riches en fer. La température moyenne est inférieure de 200 à 600 K selon la profondeur, et à partir de $z = 1200$ km les différences entre les deux estimations dépassent les barres d'erreurs. Les différences entre les profiles de composition sont moins marquées (de 2 à 10% sur la valeur moyenne de x_{pv}, et environ 2 à 3% sur la valeur moyenne de x_{Fe}), et à l'intérieur des barres d'erreurs il est possible de trouver des modèles commun aux deux estimations quelque soit la profondeur.

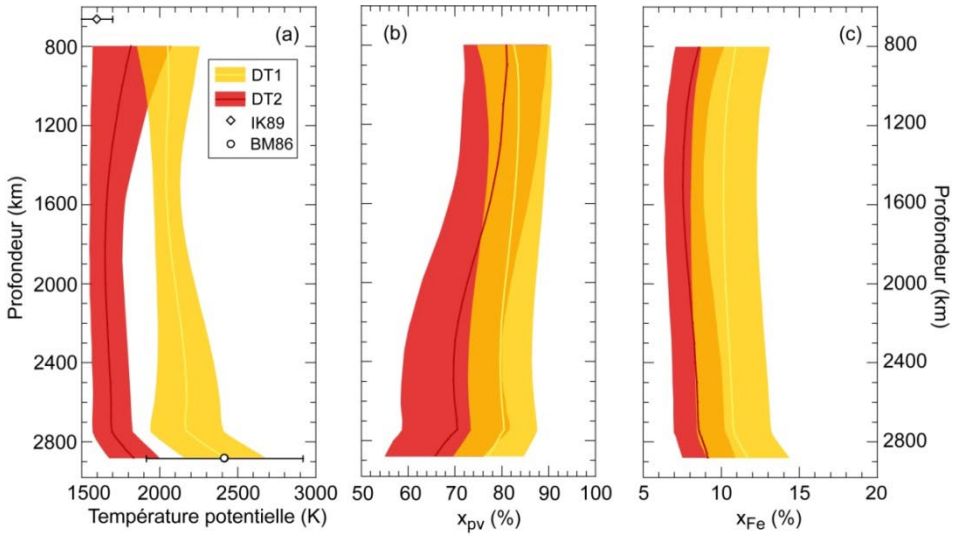

Figure 3.3 – Profiles moyens de température et de composition pour deux paramétrisations différentes. Chaque surface coloriée couvre une déviation standard autour de la valeur moyenne. DT1 (en orange) utilise les corrections pour le fer de Jackson (1998); DT2 (en rouge) utilise les corrections pour le fer de Kiefer et al. (2002) et Kung et al. (2002). Deux points d'ancrage pour la température sont également représenté, IK89 (Ito et Katsura, 1989) à 660km, et BM86 (Brown et McQueen, 1986) la base du manteau.

Pour le reste, on remarquera que les incertitudes sur la température restent élevées (de 100 à 250 K environ, selon la profondeur), ce qui empêche de conclure sans ambiguïté à la présence d'une zone super-adiabatique à la base du manteau (on y observe bien une augmentation de la température avec la profondeur, mais elle reste confinée à l'intérieur des barres d'erreurs). Avec les corrections en fer de Jackson (1998), la température potentielle à la base du manteau est de 2410 K, soit une température totale d'environ 3600 K (en première approximation, la correction adiabatique est de 0.4 K par kilomètre), en bon accord avec l'estimation de Brown et McQueen (1986). Vers 800 km, c'est au contraire la température calculée avec les corrections de Kiefer et al. (2002) et de Kung et al. (2002) qui s'accorde le mieux avec la valeur proposée par Ito et Katsura (1989). Enfin, nos profiles de composition favorisent globalement l'hypothèse d'un manteau moyen pyrolitique, avec des incertitudes d'environ 8% sur x_{pv} et 3% sur x_{Fe}. La fraction volumique de pérovskite moyenne diminue régulièrement avec la profondeur, mais de nouveau cette diminution n'est pas significative à l'intérieur de barres d'erreurs.

3.2 De l'utilisation raisonnée des rapports sismiques

Les rapports sismiques, principalement $\mathrm{d}\ln V_P/\mathrm{d}\ln V_S$ et $\mathrm{d}\ln\rho/\mathrm{d}\ln V_S$, sont des quantités très populaires parmi les géophysiciens, qui les utilisent pour diagnostiquer l'origine possible (thermique et/ou chimique) des anomalies de vitesses sismiques. L'auteur y a également succombé, notamment dans le chapitre précédent. Cet engouement est partiellement justifié. L'augmentation rapide de $\mathrm{d}\ln V_P/\mathrm{d}\ln V_S$ avec la profondeur à partir de $z = 2000$ km (van der Hilst et Kárason, 1999), par exemple, est un indice de la présence de variations latérales de composition à la base du manteau. Il masque cependant quelques difficultés inhérentes à la définition même de ces quantités (ce sont des rapports), et qui en limitent la pertinence. On pourra ainsi se poser la question de leurs significations lorsque le numérateur et/ou le dénominateur sont proches de zéro. Plus généralement, quelles valeurs prennent ces rapports si l'on considère que les $\mathrm{d}\ln V_S$, $\mathrm{d}\ln V_P$, et $\mathrm{d}\ln\rho$ en un point donné sont définis par des distributions plutôt que par des valeurs uniques? Enfin, la plupart des interprétations se basent sur une valeur moyenne de ces rapports, en ignorant leurs variations latérales. Ces dernières sont pourtant riches en enseignements (Deschamps et Trampert, 2003).

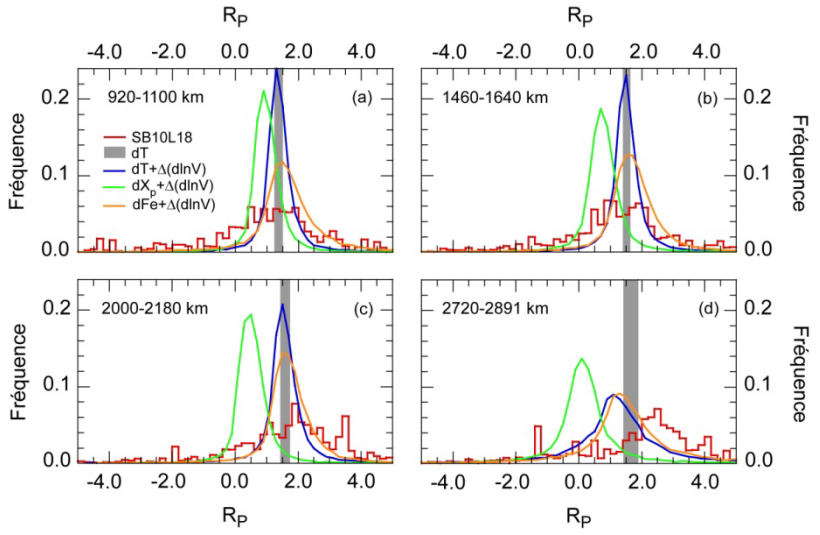

Figure 3.4 – Distribution de $R_P = \mathrm{d}\ln V_S/\mathrm{d}\ln V_P$ à différentes profondeurs selon SB10L18 (Masters et al., 2000) (histogrammes rouges). Plusieurs origines (thermique et chimiques) sont testées, ainsi que la prise en compte d'incertitudes *a priori* dans le modèle tomographique. Les histogrammes théoriques sont déduits en variant les anomalies de température et de composition à l'intérieur de bornes inférieures et supérieures fixées *a priori*, et en utilisant des sensibilités appropriées (§3.4.1).

Arrêtons-nous un instant sur ce dernier point, en prenant pour exemple le modèle global de Masters et al. (2000), SB10L18. Dans ce cas, la distribution de $\mathrm{d}\ln V_S/\mathrm{d}\ln V_P$ à une profondeur fixée est très dispersée (Figure 3.4, histogrammes rouges), ce qui contraste singulièrement avec les distributions prédites (à partir des sensibilités des vitesses

sismiques à la température, §3.4.1) par une origine purement thermique des anomalies de vitesse (Figure 3.4, bandes grises). La prise en compte d'incertitudes *a priori* sur $\mathrm{dln}\,V_S$ et $\mathrm{dln}\,V_P$, élargit les histogrammes théoriques, mais n'explique toujours pas SB10L18 (Figure 3.4, courbes bleues). Pas plus que ne le font des anomalies de compositions (en pérovskite ou en fer) prises individuellement (Figure 3.4, courbes vertes et oranges). En revanche, des variations simultanées de température et de composition (pérovskite et fer) permettent d'élargir encore les distributions théoriques de $\mathrm{dln}\,V_S/\mathrm{dln}\,V_P$, et d'expliquer relativement bien les histogrammes observés par SB10L18. La dispersion, à une profondeur donnée, de $\mathrm{dln}\,V_S/\mathrm{dln}\,V_P$, indique clairement que l'origine des anomalies sismiques est à la fois thermique et chimique. Difficile, cependant, d'être plus précis, car il apparaît très rapidement que de nombreuses combinaisons expliquent ces histogrammes également bien (en fait, n'importe quelle combinaison $a\mathrm{d}T + a\mathrm{d}x_{pv} + a\mathrm{d}x_{Fe}$, où a est une constante, conduit strictement au même résultat). Il est donc vain de vouloir contraindre quantitativement l'amplitude des variations thermochimiques à partir des rapports sismiques. L'analyse directe de la dispersion des $\mathrm{dln}\,V_S$ et $\mathrm{dln}\,V_P$ permet d'apporter des contraintes sur ces amplitudes (Deschamps et Trampert, 2003), sans toutefois briser le trade-off entre la température et la composition.

Le paragraphe suivant va introduire la tomographie probabiliste, qui défini une fonction de densité de probabilité (FDP) pour les vitesses sismiques en chaque point du modèle. Cela implique que les rapports sismiques en un point donné sont eux aussi représenté par des distributions, avec une valeur moyenne et une déviation standard (Figure 3.5d-f). Bien entendu, cette déviation standard (ou, si l'on préfère, cette incertitude) dépend des déviations standards (incertitudes) de $\mathrm{dln}\,V_S$, $\mathrm{dln}\,V_P$, et $\mathrm{dln}\rho$. La valeur moyenne de $\mathrm{dln}\,V_S$ influe également sur les déviations standards des rapports sismiques. De manière générale, plus elle est proche de zéro, plus ces déviations standards sont élevées. Un cas intéressant est celui où la FDP de $\mathrm{dln}\,V_S$ est centrée sur zéro (Figure 3.5b). Les rapports sismiques sont alors indéterminés, comme le montre leurs FDPs quasiment uniformes (Figure 3.5e).

Ces considérations doivent être gardées en mémoire lorsque l'on interprète les moyennes latérales des rapports sismiques. L'analyse de van der Hilst et Kárason (1999), par exemple, est basée sur une augmentation de $\mathrm{dln}\,V_P/\mathrm{dln}\,V_S$ d'environ 0.7 entre 2000 km et la CMB. En comparaison, la déviation standard régionale sur $\mathrm{dln}\,V_P/\mathrm{dln}\,V_S$ dans la couche la plus profonde ($2000 \leq z \leq 2891$ km) de la tomographie probabiliste est de 0.6, et la RMS de l'incertitude en chaque point du modèle est de 1.4 (0.7, si l'on ne tient compte que des points pour lesquels $\mathrm{dln}\,V_S \geq 0.2\%$).

3.3 La tomographie probabiliste

Le principe de la tomographie probabiliste, développé par Jeannot Trampert et Joe Resovsky, est relativement simple. Il s'agit de déterminer les distributions d'anomalies de de densité et de vitesses sismiques qui satisfont un ensemble de contraintes sismologiques (modes propres et ondes de surfaces), à partir d'une recherche de Monte-Carlo dans l'espace des modèles (ici les distributions d'anomalies de densité et de vitesse sismiques, auxquelles s'ajoutent, dans les modèles les plus récents, les variations de topographie de la CMB). Les

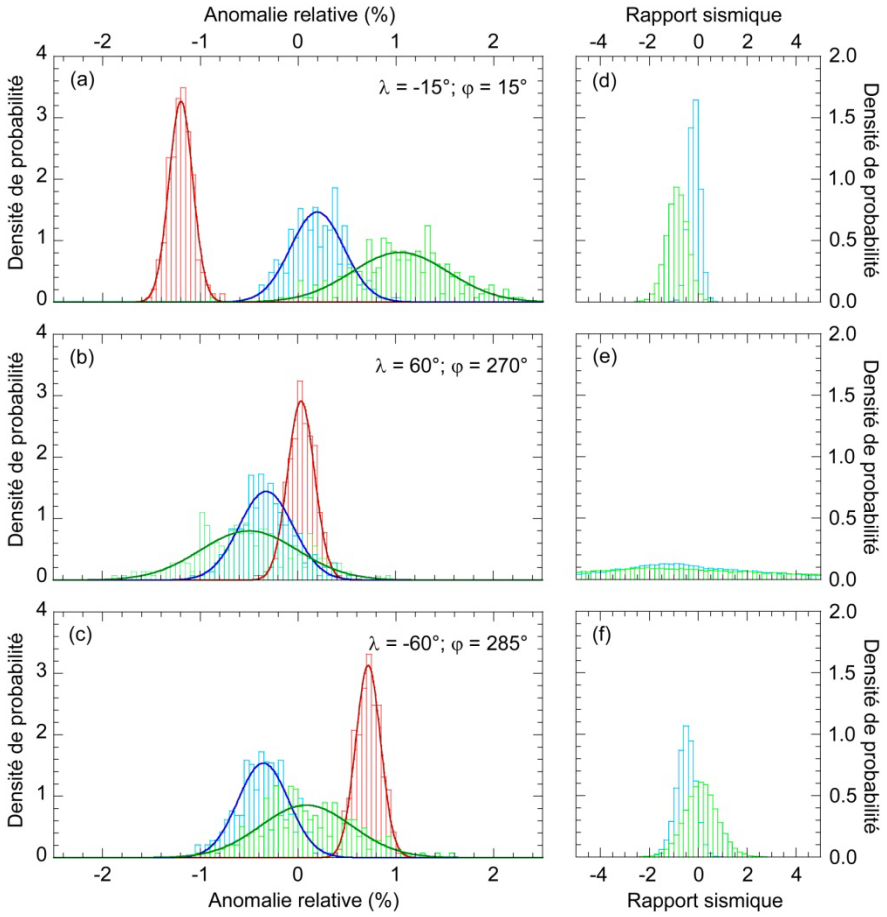

Figure 3.5 – (a-c) Densité de probabilité (FDP) pour la vitesse de cisaiilement (en rouge), la vitesse du son (en bleu), et la densité (en vert) en trois points de la couche la plus profonde (2000 ≤ *z* ≤ 2891 km) du modèle tomographique probabiliste de Trampert et al. (2004). Les histogrammes représentent les FDPs déterminées par une recherche de Monte-Carlo, et les courbes représentent les distributions gaussiennes expliquant au mieux ces distributions. (d-f) Rapports sismiques entre les anomalies relatives de vitesse du son et de vitesse de cisaillement (en bleu), et entre les anomalies relatives de densité et de vitesse de cisaillement (en vert).

modèles les plus récents (Trampert et al., 2004) sont également filtrés avec les anomalies de gravité. On trouvera une discussion détaillée sur la méthode et les données dans Resovsky et Trampert (2003). Brièvement, chaque point de l'espace modèle prédit des coefficients de structure (en fait, des coefficients d'harmonique sphériques pour une fréquence donnée), que l'on compare avec les valeurs observées de ces coefficients. On définit de plus une

fonction coût, basée sur l'accord entre les coefficients calculés et mesurés, ce qui permet de cartographier l'espace modèle en termes de probabilité d'occurrence. Pour des raisons de puissance de calcul, il est exclu d'échantillonner l'espace modèle partout avec la même densité de points. L'algorithme de voisinage (Sambridge, 1999a, 1999b) détermine les régions de l'espace modèle qui s'accordent le mieux avec les données, et focalise la recherche sur ces régions.

En chaque point du modèle, la tomographie probabiliste définit ainsi une fonction de densité de probabilité (FDP) pour les anomalies de densité et les anomalies de vitesses sismiques (cisaillement et compression). Ces FDPs sont généralement bien expliquées par des distributions gaussiennes, dont la valeur moyenne correspond au maximum de probabilité, et la déviation standard est une mesure fiable de l'incertitude. C'est en particulier le cas pour le modèle de tomographie probabiliste le plus récent, RT246g (Trampert et al., 2004) (Figure 3.5a-c), qui est développé pour les degrés d'harmoniques sphériques 2, 4, et 6, cette limitation étant liée aux mesures de modes propres disponibles. C'est de ce modèle dont il sera question dans la suite de ce mémoire (notamment dans le Chapitre 4). On notera que les anomalies de vitesses et de densité augmente significativement à la base du manteau, et que les anomalies de vitesses de cisaillement sont globalement mieux contraintes que les anomalies de densités (Table 3.2).

	$d\ln V_S$ (%)	$d\ln V_\Phi$ (%)	$d\ln\rho$ (%)	dT (K)	dx_{pv} (%)	dx_{Fe} (%)
660 ≤ z ≤ 1200 km						
Maximum	0.77	0.87	0.79	340	11.9	1.80
RMS(σ)	0.16	0.34	0.26	180	5.5	0.75
1200 ≤ z ≤ 2000 km						
Maximum	0.77	0.57	0.70	311	8.3	1.20
RMS(σ)	0.12	0.22	0.28	112	3.0	0.55
2000 ≤ z ≤ 2891 km						
Maximum	1.21	0.66	1.05	475	9.3	2.60
RMS(σ)	0.12	0.26	0.48	198	3.6	0.86

Table 3.2. Amplitude maximum et RMS de la déviation standard de RT246g dans le manteau inférieur, et des distributions thermochimiques qui en dérivent (Trampert et al., 2004).

RT246g (Trampert et al., 2004) est verticalement paramétrisé en 5 couches, $24 \leq z \leq 410$ km, $410 \leq z \leq 660$ km, $660 \leq z \leq 1200$ km, $1200 \leq z \leq 2000$ km, et $2000 \leq z \leq 2891$ km. Évidemment, on peut souhaiter mieux. La bonne nouvelle est que cette limitation est uniquement liée à la puissance de calcul. Autre bonne nouvelle, bien que grossière, cette résolution verticale permet des interprétations thermochimiques pertinentes (Trampert et al., 2004), et pose des contraintes précises et vérifiables sur le mode de convection du

manteau terrestre (Chapitre 4). Enfin, dans le manteau inférieur, RT246g (plus exactement, la distribution des anomalies moyennes) s'accorde bien avec des modèles tomographiques classiques. C'est particulièrement frappant à la base du manteau, où l'on reconnaît très clairement les deux zones de faibles vitesses de cisaillement (Figure 3.8a). Une autre observation capitale est l'absence très nette de corrélation entre les anomalies de vitesse de cisaillement et les anomalies de densité. Ce résultat hypothèque sérieusement l'hypothèse d'une origine purement thermique de ces anomalies. Il ne peut s'expliquer que par la présence de variations latérales de composition.

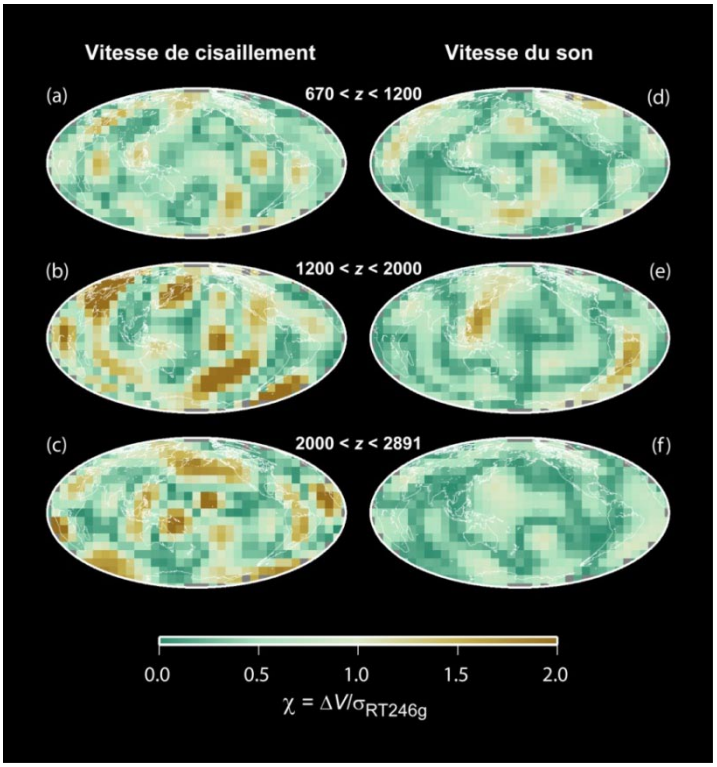

Figure 3.6 – Ecart relatif (par rapport aux incertitudes de RT246g) entre SB10L18 (Masters et al., 2000) et le modèle de tomographie probabiliste RT246g (Trampert et al., 2004). SB10L18 est moyenné selon la paramétrisation verticale définie par RT246g, et seuls les degrés d'harmoniques sphériques 2, 4, et 6 sont pris en compte.

Dans chaque couche, les anomalies de densité et de vitesse observées par RT246g représentent en fait la moyenne verticale de ces anomalies dans la couche considérée. Une comparaison plus appropriée nécessite de moyenner les modèles tomographiques classiques selon la paramétrisation de RT246g. Par exemple, lorsqu'il est filtré pour les degrés d'harmoniques sphériques 2, 4, et 6, SB10L18 (Masters et al., 2000) s'accorde bien avec RT246g dans le manteau inférieur (Figure 3.6). L'écart entre les vitesses de cisaillement prédites par les deux modèles est, en moyenne, inférieur à deux fois la barre d'erreur sur RT246g. L'accord entre les vitesses du son est sensiblement meilleur, avec un écart moyen entre les deux modèles d'environ 1.2 fois la barre d'erreur sur RT246g.

Pour terminer, revenons sur les principaux avantages apportés par la tomographie probabiliste. Tout d'abord, elle résulte d'une recherche (intelligente) de Monte-Carlo, et donc elle ne nécessite pas la prescription d'information *a priori*, cette dernière étant (comme son nom l'indique) toujours subjective. Ensuite, elle accède *de facto* à des estimations fiables sur les barres d'erreur des observables en chaque point du modèle. Enfin, et ce n'est pas son moindre intérêt, elle détermine des distributions de densité indépendantes des autres observables du modèle.

3.4 Ce qu'il advint en général des zones rouges et des zones bleues observées par les sismologues, et des 'superplumes' en particulier

Les anomalies de densité et de vitesses de cisaillement peuvent s'écrire en fonction des anomalies de température et de composition qui en sont à l'origine. Si l'on admet que, pour le manteau inférieur, les anomalies de composition sont principalement des variations des fractions volumiques de pérovskite et de fer, on a

$$\begin{cases} \mathrm{d}\ln V_S = \frac{\partial \ln V_S}{\partial T}\mathrm{d}T + \frac{\partial \ln V_S}{\partial x_{pv}}\mathrm{d}x_{pv} + \frac{\partial \ln V_S}{\partial x_{Fe}}\mathrm{d}x_{Fe} \\ \mathrm{d}\ln V_\Phi = \frac{\partial \ln V_\Phi}{\partial T}\mathrm{d}T + \frac{\partial \ln V_\Phi}{\partial x_{pv}}\mathrm{d}x_{pv} + \frac{\partial \ln V_\Phi}{\partial x_{Fe}}\mathrm{d}x_{Fe} \\ \mathrm{d}\ln\rho = \frac{\partial \ln \rho}{\partial T}\mathrm{d}T + \frac{\partial \ln \rho}{\partial x_{pv}}\mathrm{d}x_{pv} + \frac{\partial \ln \rho}{\partial x_{Fe}}\mathrm{d}x_{Fe} \end{cases}, \qquad (3.18)$$

où les dérivées partielles sont aussi appelées sensibilités. D'autres sources de variations sont aussi possibles. Citons la présence de poches de matériau partiellement fondu à la base du manteau (p.e., Labrosse et al., 2007). Dans ce cas, il faut s'attendre à de fortes variations locales de vitesse sismique, ce que détectent effectivement de nombreuses études (on en trouvera une liste récente de ces zones de vitesses sismiques ultra lentes, ULVZ, dans Thorne et Garnero, (2004)). Les modèles globaux, en revanche, diluent ces anomalies dans des volumes plus importants, et celles-ci ont peu de chance d'y apparaître. Autre source possible, la présence de $CaSiO_3$. Problème, $CaSiO_3$ a des propriétés thermo-élastiques très proches de celles de $MgSiO_3$, ce qui implique que les sensibilités des vitesses sismiques et de la densité au calcium sont faibles (Deschamps et Trampert, 2003). Les anomalies de vitesses sismiques ne peuvent ainsi pas résoudre d'éventuelles variations latérales en calcium. Enfin, les anomalies observées à la base du manteau pourraient en partie être liées à la topographie de la post-pérovskite. La prise en compte de celle-ci nécessite cependant une bonne connaissance du profile moyen de température, ce qui n'est pas la cas (§3.1). Quoiqu'il en soit, si l'on connait les sensibilités de la densité et des vitesses sismiques à la température et à la composition, il est en principe possible de résoudre le système (3.18) pour les anomalies de température, de pérovskite, et de fer. Commençons par déterminer ces sensibilités.

3.4.1 Sensibilités des observables à la température et à la composition

Le calcul des sensibilités est semblable au calcul des profiles de température et de composition (§3.1) avec une petite différence: pour chaque triplet (T,x_{pv},x_{Fe}), on réalise trois extrapolations supplémentaires pour (T+dT,x_{pv},x_{Fe}), (T,x_{pv}+dx_{pv},x_{Fe}), et (T,x_{pv},x_{Fe}+dx_{Fe}). Les incréments dT, dx_{pv}, et dx_{Fe} doivent être suffisamment petits, typiquement de l'ordre de 1.0% des valeurs de T, x_{pv}, et x_{Fe}. Chaque extrapolation supplémentaire calcule des vitesses sismiques et des densités légèrement différentes, desquelles on déduit les dérivées par

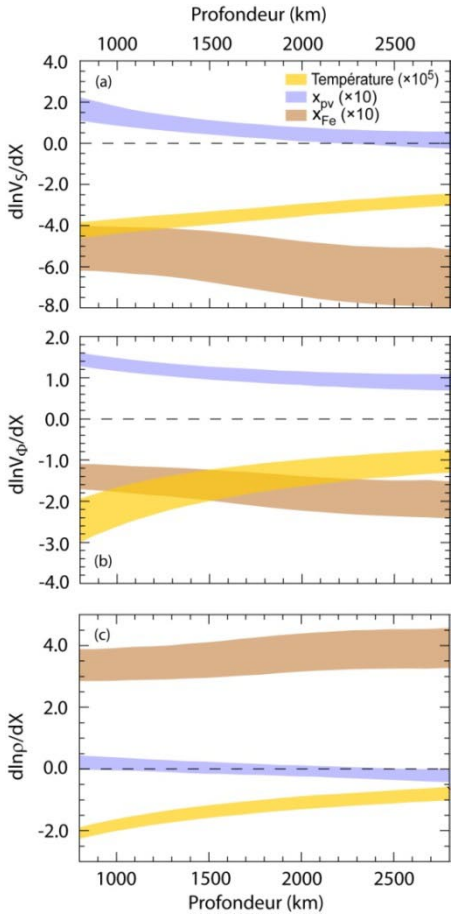

Figure 3.7 – Sensibilités de la vitesse de cisaillement (a), de la vitesse du son (b), et de la densité (c) à la température (en orange) et aux fractions volumiques de pérovskite (en bleu) et de fer (en brun), en fonction de la profondeur. Dans chaque cas, la zone colorée couvre une déviation standard autour de la sensibilité moyenne.

rapport à T, x_{pv}, et x_{Fe}. De nouveau, pour calculer les incertitudes sur les sensibilités, on utilise une méthode de Monte-Carlo en faisant varier T, x_{pv}, et x_{Fe} dans des gammes de valeurs assez larges. Pour chaque triplet (T,x_{pv},x_{Fe}), on calcule une vitesse de cisaillement, une vitesse de compression et une densité que l'on compare à PREM, ce qui permet d'attribuer un poids (équation 3.16) à chaque dérivée. Contrairement au cas du manteau supérieur, il n'a pas été tenu compte des effets éventuels de l'anélasticité. L'atténuation est

un processus thermiquement activé, et dans le manteau inférieur ces effets sont sans doute amortis par les pressions élevées. Trampert et al. (2001) ont ainsi montré que les sensibilités des vitesses sismiques à la température sont peu affectées par l'anélasticité. Brodholt et al. (2007) estime ces perturbations au plus à 30%, ce qui reste à l'intérieur des barres d'erreurs induites par d'autres paramètres. Selon d'autres auteurs, en revanche, la contribution anélastique reste importante, et pourrait modifier la valeur des rapports sismiques d'environ 50% (Matas et Bukowinski, 2007).

La Figure 3.7 représente les sensibilités de la vitesse de cisaillement, de la vitesse du son, et de la densité à la température, et aux fractions volumiques de pérovskite et de fer. Le lecteur attentif aura remarqué des différences importantes par rapport aux sensibilités publiées dans Deschamps et Trampert (2003) (de plus, dans cet article, ce sont les sensibilités de la vitesse de compression qui sont représentées, au lieu de celles de la vitesse du son). Comme dans le cas des profiles moyens (Figure 3.3), ces différences sont entièrement imputables aux corrections des modules élastiques et de leurs dérivées pour la fraction volumique de fer. La Figure 3.7 inclut les données de Kiefer et al. (2002) pour la pérovskite et de Kung et al. (2002) pour la magnésio-wüstite (Table 3.1), ce que ne fait pas Deschamps et al. (2003). Les différences les plus marquées sont bien sûr pour les sensibilitées au fer, dont les amplitudes sont plus élevées si l'on tient compte des données de Kiefer et al. (2002) et de Kung et al. (2002). De plus, les valeurs absolues des dérivées augmentent (diminuent) avec la profondeur si l'on (ne) tient (pas) compte de ces données corrections.

	V_S		V_Φ		Densité	
	Signe	Corrélation	Signe	Corrélation	Signe	Corrélation
660 ≤ z ≤ 1200 km						
Température	–	-0.564	–	0.420	–	-0.524
Pérovskite	+	-0.033	+	0.907	+	0.114
Fer	–	0.104	–	0.790	+	0.716
1200 ≤ z ≤ 2000 km						
Température	–	-0.701	–	0.089	–	-0.790
Pérovskite	+	-0.332	+	0.889	+/–	-0.281
Fer	–	-0.135	–	0.432	+	0.898
2000 ≤ z ≤ 2891 km						
Température	–	-0.302	–	-0.102	–	-0.863
Pérovskite	+/–	-0.792	+	0.933	–	0.277
Fer	–	-0.524	–	0.604	+	0.942

Table 3.3. Liens entre les observables sismologiques (vitesse de cisaillement, vitesse du son, et densité) et les variables thermochimiques (température, fractions volumiques de pérovskite et de fer). Pour chaque observable, la première et la seconde colonne indiquent respectivement le signe de la sensibilité à chacune des variables thermochimiques, et la corrélation entre les anomalies relatives de cette observable et les anomalies relatives des variables thermochimiques.

Un examen plus détaillé de ces sensibilités révèle tout l'intérêt de bien contraindre la densité. Quelque soit la profondeur, et pour un paramètre donné, les polarités (les signes) des sensibilités de la vitesse de cisaillement et de la vitesse du son sont identiques (une exception, il en faut une, est la sensibilité à la pérovskite à la base du manteau) (Table 3.3). Autrement dit, les anomalies de vitesse de cisaillement et de vitesse du son apportent quasiment la même information, et ne permettent pas de casser le trade-off entre température et composition. La densité se comporte différement. Partout dans le manteau, elle augmente lorsque la fraction volumique de fer augmente (sa sensibilité au fer est positive). Conclusion, la densité est une observable de choix pour contraindre d'éventuelles variations en fer, et le trade-off entre la température et la composition est partiellement brisé. Partiellement car la sensibilité de la densité à la température est, comme celles des vitesses sismiques, négative partout dans le manteau, et que sa sensibilité à la pérovskite n'a une polarité différente de celles des autres observables qu'à la base du manteau. Autre remarque, la sensibilité de la densité à la pérovskite change de signe dans le manteau intermédiaire, et son amplitude est faible sur toute l'épaisseur du manteau. En conséquence, les anomalies de densité ne contraignent pas d'éventuelles variations de pérovskite entre 1200 et 2000 km de profondeur. Même constat et même punition pour la vitesse de cisaillement à la base du manteau.

3.4.2 Variations latérales de température, de pérovskite, et de fer

La détermination des anomalies de température et de composition repose également sur une recherche de Monte-Carlo. On choisit de façon aléatoire, mais à l'intérieur de leurs barres d'erreur respectives, une valeur pour $\mathrm{d}\ln V_S$, $\mathrm{d}\ln V_\Phi$ et $\mathrm{d}\ln\rho$, et une valeur pour chacune des sensibilités, puis on inverse le système (3.18) pour $\mathrm{d}T$, $\mathrm{d}x_{pv}$, et $\mathrm{d}x_{Fe}$. En répétant cette opération un grand nombre de fois, on obtient des distributions (valeurs moyennes et déviations standards) pour $\mathrm{d}T$, $\mathrm{d}x_{pv}$, et $\mathrm{d}x_{Fe}$ (Trampert et al., (2004)). À la base du manteau (Figure 3.8d-f), par exemple, les anomalies de température sont au maximum de 475 K, et la RMS des barres d'erreur est de l'ordre de 200 K (Table 3.2). La fraction volumique de pérovskite varie au maximum de 9.0% (avec une RMS des erreurs de 3.5%), et celle du fer de 2.5% (avec une RMS des erreurs de 0.9%).

Un fait saute immédiatement aux yeux: il n'y-a pas de corrélation entre les anomalies de vitesse d'onde de cisaillement (Figure 3.8a) et les anomalies de température (Figure 3.8d) (voir aussi la Table 3.3). Les premières ne sont pas un bon proxy pour les secondes. Ce que voient les $\mathrm{d}\ln V_S$, c'est une combinaison des anomalies de température et des anomalies de composition, comme le suggère déjà les sensibilités représentées sur la Figure 3.7a. A vrai dire, on s'y attendait un peu, car les anomalies de densité ne sont pas

corrélées aux anomalies de vitesse sismiques (Ishii et tromp, 1999; Trampert et al., 2004). Ce qui est plus étonnant, c'est que les anomalies de vitesse du son soient très bien corrélées aux anomalies de pérovskite (Figures 3.8b et 3.8e; Table 3.2). Les anomalies de densité, quant à elles, voient principalement les anomalies de fer et, dans une moindre mesure, de température, mais pas celles de pérovskite.

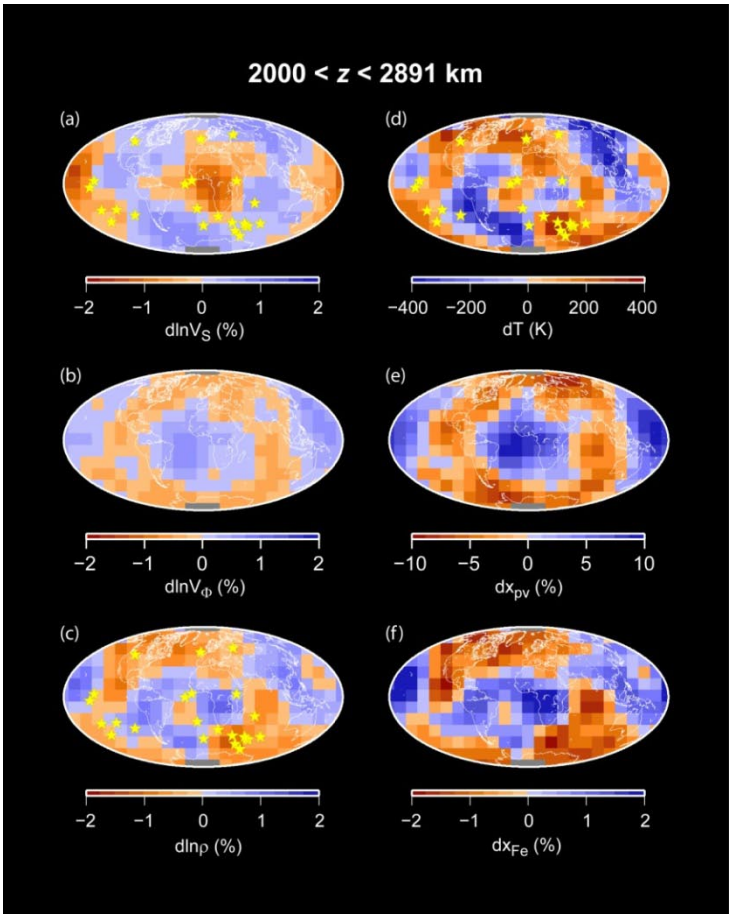

Figure 3.8 – Distributions des anomalies sismiques et thermochimiques à la base du manteau (d'après Trampert et al., 2004). (a) Vitesse de cisaillement; (b) Vitesse du son; (c) Densité; (d) Température; (e) Fraction volumique de pérovskite; (f) Fraction volumique de fer. En chaque point du modèle, on défini une densité de probabilité pour chaque variable. Sur cette figure, seule la valeur moyenne (i.e., la valeur la plus probable) est représentée par le code de couleur. En (a), (c), et (d), les étoiles jaunes localisent les emplacements des LIP (Large Igneous Provinces) calculés par Burke et Torsvik al. (2004).

On est bien loin de l'hypothèse des 'superplumes', ces zones de faibles vitesses de cisaillement assimilées à des structures thermiques présentes à la base du manteau, et dans lesquelles la majorité des hotspots trouveraient leur origine. Burke et Torsik (2004), par exemple, ont reconstruit l'emplacement des LIPs (Large Igneous Provinces) au court des 200 Ma écoulés (en supposant que, pendant ce temps, les structures liées aux anomalies de vitesses sismiques sont, elles, restées statiques), puis ils ont reporté ces localisations sur

une carte des anomalies de vitesses de cisaillement (S20RTS, Ritsema et al., 1999). Surprise!, la distribution des LIPs est bien corrélée avec la limite des zones de faibles vitesses (l'accord avec la tomographie probabiliste, Figure 3.8a, est moins évident, mais cela ne change rien à la discussion), où les gradients de vitesse sismique (transformés pour l'occasion en gradients de température) sont paraît-il les plus élevés (notons au passage que S20RTS est limité au degré d'harmonique sphérique $\ell = 20$, c'est-à-dire une résolution latérale d'environ 550 km à la CMB). Pourtant, si l'on représente ces mêmes LIPs sur une carte de la densité ou de la température (Figure 3.8cd), l'accord est tout aussi bon, sinon meilleur … à supposer, bien entendu, que la région source des LIPs soit effectivement située à la base du manteau.

3.5 Conclusions et perspectives

Le principal message de ce chapitre est le suivant: il convient d'interpréter les modèles tomographiques (en particulier pour les ondes de cisaillement) avec prudence. On ne saurait les convertir directement en anomalies de température, car les anomalies de composition (en particulier de fer) ont leur mot à dire. Séparer les contributions thermiques des contributions chimiques n'est pas une opération facile. Cela nécessite, entre autre, des contraintes indépendantes sur la distribution de la densité, et une modélisation appropriée de l'équation d'état des minéraux présents dans le manteau. Les distributions thermochimiques qui en résultent modifient notre vision de la structure et de la dynamique du manteau profond. Nous en verrons quelques exemples dans le prochain chapitre.

De nombreux problèmes restent en souffrance, cependant. La tomographie probabiliste a l'immense avantage de contraindre indépendamment la densité, mais sa résolution verticale est réduite à cinq couches, et elle ne contient que les degrés d'harmoniques sphériques 2, 4, et 6. La résolution verticale du modèle actuel est uniquement limitée par la puissance de calcul. La parallélisation de l'algorithme et l'utilisation de 'nuages de calculateurs' devrait permettre de calculer des modèles mieux résolus, avec une quinzaine de couches ou plus. La limitation aux degrés 2, 4, et 6 est plus épineuse, car elle est liée à la difficulté de détecter et de mesurer les découplages de modes propres pour les degrés impairs et les degrés plus élevés. Pour remédier à ce problème, l'idée est de compléter les catalogues de modes propres avec des catalogues d'ondes de volumes et (pour le manteau supérieur) d'ondes de surface.

Le trade-off entre la température et la composition n'est pas complètement levé par la densité, et des contraintes supplémentaires et indépendantes sont nécessaires pour le réduire encore. La conductivité électrique peut sans doute jouer ce rôle. Elle dépend de plusieurs mécanismes thermiquement activés, mais fait intéressant, le mécanisme

dominant et les mesures de laboratoire indiquent que, pour les minéraux du manteau terrestre, elle augmente avec la température (p.e., Xu et al., 2000; Vacher et Verhoeven, 2007), alors que les observables sismologiques utilisées jusqu'à présent diminuent avec la température. Bien entendu, la conductivité est également sensible à la composition, en particulier à la fraction volumique de fer. La distribution de la conductivité peut, en principe, être déduite des variations du champ magnétique. Comme dans le cas des ondes de surfaces, plus la période de ces variations est élevée, plus la région sondée par le signal géomagnétique est profonde. Pour le moment, cependant, on ne dispose pas d'observations sur une période de temps suffisamment longue pour raisonnablement échantillonner le manteau au delà de 1200 km de profondeur environ.

Enfin, se pose le problème de la distribution de la post-pérovskite à la base du manteau. Ici, le problème est que le profile thermochimique moyen dont dispose est pour le moment plutôt médiocre (la température de référence n'est connue qu'à ± 200 K, environ). Même à supposer que l'on dispose d'un modèle 3D d'anomalies de température avec une bonne résolution verticale, on ne pourrait pas en déduire une topographie de la post-pérovskite.

Bibliographie

Brodholt, J.P., G. Helffrich, et J. Trampert, 2007. Chemical versus thermal heterogeneity in the lower mantle: the most likely role of anelasticity, *Earth Planet. Sci. Lett.*, **262**, 429-437.

Brown, J.M., et R.G. McQueen, 1986. Phase transition, Grüneisen parameter, and elasticity for shocked iron between 77 and 400 GPa, *J. Geophys. Res.*, **91**, 193-211.

Bukowinski, M.S.T., et S. Akber-Knutson, 2005. The role of theoretical mineral physics in modeling the Earth's interior, in R.D. van der Hilst et al. (Eds), Earth's deep mantle: structure, composition and evolution, *Geophysical Monograph Ser.*, **160**, American Geophysical Union, Washington, DC, pp.137-163.

Burke, K., et T.H. Torsvik, 2004. Derivation of Large Igneous Provinces of the past 200 million years from long-term heterogeneities in the deep mantle, *Earth Planet. Sci. Lett.*, **227**, 531-538.

Connolly, J.A.D., 2005. Computation of phase equilibria by linear programming: a tool for geodynamic modelling and its application to subduction zone decarbonation, *Earth Planet. Sci. Lett.*, **236**, 524-541.

Deschamps, F., et J. Trampert, 2003. Mantle tomography and its relation to temperature and composition, *Phys. Earth Planet. Int.*, **140**, 277-291.

Deschamps, F., et J. Trampert, 2004. Towards a lower mantle reference temperature and composition, *Earth Planet. Sci. Lett.*, **222**, 161-175.

Dziewonski, A.M., et D.L. Anderson, 1981. Preliminary Reference Earth Model, *Phys. Earth Planet. Inter.*, **25**, 297-356.

Ito, E., et T. Katsura, 1989. A temperature profile of the mantle transition zone, *Geophys. Res. Lett.*, **16**, 425-428.

Jackson, I., 1998. Elasticity, composition, and temperature of the Earth's lower mantle: a reappraisal, *Geophys. J. Int.*, **134**, 291-311.

Karki, B.B., et J. Crain, 1998. First-principles determination of elastic properties of $CaSiO_3$ perovskite at lower mantle pressures, *Geophys. Res. Lett.*, **25**, 2741-2744.

Kiefer, B., L. Stixrude, et R.M. Wentzcovitch, 2002. Elasticity of $(Mg,Fe)SiO_3$ perovskite at high pressures, *Geophys. Res. Lett.*, **29**, doi: 10.1029/2002GL014683.

Kung, J., B. Li, D.J. Weidner, J. Zhang, et R.C. Liebermann, 2002. Elasticity of $(Mg_{0.87},Fe_{0.13})O$ ferropericlase at high pressure: ultrasonic measurements in conjunction with X-radiations techniques, *Earth Planet. Sci. Lett.*, **203**, 557-566.

Labrosse, S., J.W. Hernlund, et N. Coltice, 2007. A crystallizing dense magma ocean et the base of the Earth's mantle, *Nature*, **450**, 866-869.

Marton, F.C., et R.E. Cohen, 2002. Constraints on lower mantle composition from molecular dynamics simulations of $MgSiO_3$ perovskite, *Phys. Earth Planet. Inter.*, **134**, 239-252.

Masters, G., G. Laske, H. Bolton, et A.M. Dziewonski, 2000. The relative behavior of shear velocity, bulk sound speed, and compressional velocity in the mantle: implicationfor thermal and chemical structure, in S.-I. Karato et al. (Eds), Earth's deep interior: mineral physics and tomography from the atomic to the global scale, *Geophysical Monograph Ser.*, **117**, American Geophysical Union, Washington, DC, pp.63-87.

Matas, J., et S.T. Bukowinski, 2007. On the anelastic contribution to the temperature dependence of lower mantle seismic velocities, *Earth Planet. Sci. Lett.*, **259**, 51-65.

Matas, J., J. Bass, Y. Ricard, E. Mattern, et S.T. Bukowinski, 2007. On the bulk composition of the lower mantle: predictions and limitations from generalized inversion of radial seismic profiles, *Geophys. J. Int.*, **170**, 764-780.

Murakami, M., S.V. Sinogeikin, H. Hellwig, J.D. Bass, et J. Li, 2007. Sound velocity of $MgSiO_3$ perovskite to Mbar pressure, *Earth planet. Sci. Lett.*, **256**, 47-54.

Oganov, A.R., J.p. Brodholt, and G.D. Price, 2001a. Ab initio elasticity and thermal equation of state of $MgSiO_3$ perovskite, *Earth Planet. Sci. Lett.*, **184**, 555-560.

Oganov, A.R., J.P. Brodholt, and G.D. Price, 2001b. The elastic constants of $MgSiO_3$ perovskite at pressures and temperatures of the Earth's mantle, *Nature*, **411**, 934-937.

Poirier, J.-P., 1991. Introduction to the physics of the Earth interior, Cambridge University Press, Cambridge, 264 pp..

Poirier, J.-P., and A. Tarantola, 1998. A logarithmic equation of state, *Phys. Earth Planet. Inter.*, **109**, 1-8.

Resovsky, J.S., et J. Trampert, 2003. Using probabilistic seismic tomography to test mantle velocity-density relationships, *Earth Planet. Sci. Lett.*, **215**, 121-134.

Ricard, Y., E. Mattern, et J. Matas, 2005. Synthetic tomographic images of slabs from mineral physics, in R.D. van der Hilst et al. (Eds), Earth's deep mantle: structure, composition and evolution, *Geophysical Monograph Ser.*, **160**, American Geophysical Union, Washington, DC, pp.283-300.

Ritsema, H.J., J.H. van Heijst, et J.H. Woodhouse, 1999. Complex shear-velocity structure beneath Africa and Iceland, *Science*, **286**, 1925-1928.

Sambridge, M., 1999a. Geophysical inversion with a neighbourhood algorithm – I. Searching a parameter space, *Geophys. J. Int.*, **138**, 479-494.

Sambridge, M., 1999b. Geophysical inversion with a neighbourhood algorithm – I. Appraising the ensemble, *Geophys. J. Int.*, **138**, 479-494.

Stacey, F.D., 1995. Theory of thermal and elastic properties of the lower mantle and core, *Phys. Earth Planet. Inter.*, **89**, 219-245.

Stacey, F.D., 2000. The K-primed approach to high-pressure equations of state, *Geophys. J. Int.*, **143**, 621-628.

Thorne, M.S., et E.J. Garnero, 2004. Inferences on ultra-low velocity structures from a global analysis of *SPdKS* waves, *J. Geophys. Res.*, **109**, doi: 10.1029/2004JB003010.

Trampert, J., P. Vacher, et N. Vlaar, 2001. Sensitivities of seismic velocities to temperature, pressure and composition in the lower mantle, *Phys. Earth Planet. Inter.*, **124**, 255-267.

Trampert, J., F. Deschamps, J. Resovsky, et D.A. Yuen, 2004. Probabilistic tomography maps chemical heterogenities throughout the mantle, *Science*, **306**, 853-856.

Vacher, P., et O. Verhoeven,

van der Hilst, R.D., et H. Kárason, 1999. Compositional heterogeneity in the bottom 1000 kilometers of Earth's mantle: towards a hybrid convection model, *Science*, 283, 1885-1888.

Vinet, P., J. Ferrante, J.H. Rose, and J.R. Smith, 1987. Compressibility of solids, *J. Geophys. Res.*, **92**, 9319-9325.

Wang, Y., D.J. Weidner, et F. Guyot, 1996. Thermal equation of state of $CaSiO_3$ perovskite, *J. Geophys. Res.*, **101**, 6621-672.

Xu, Y., T.J. Shankland, et T.P. Brent, 2000. Laboratory based electrical conductivity in the Earth's mantle, *J. Geophys. Res.*, **105**, 27865-27875.

Available online at www.sciencedirect.com
SCIENCE DIRECT®
Earth and Planetary Science Letters 222 (2004) 161–175
EPSL
www.elsevier.com/locate/epsl

Towards a lower mantle reference temperature and composition

Frédéric Deschamps*, Jeannot Trampert

Department of Geophysics, Utrecht University, Budapestlaan 4, P.O. Box 80021, 3508 TA Utrecht, The Netherlands

Received 15 July 2003; received in revised form 16 February 2004; accepted 16 February 2004

Abstract

We aim to constrain the lower mantle geotherm and average composition from 1D seismic models and experimental mineralogy data, explicitly accounting for possible sources of uncertainty. We employ an isentropic third-order Birch–Murnaghan equation of state, which is in excellent agreement with recent ab initio calculations of density and bulk modulus for Mg-perovskite. Furthermore, ab initio and experimental data are reasonably consistent with each other. Modelling the shear modulus is not as straightforward, but is needed because density and the bulk modulus alone do not sufficiently constrain temperature and composition. To correctly predict ab initio calculations for the shear modulus of Mg-perovskite, we needed to prescribe a cross-derivative at zero pressure, which we determined by trial and errors. Unless this ad hoc cross-derivative is confirmed by further experimental results, there seems to be an inconsistency between ab initio and experimental data. Purely experimental data most likely require a non-adiabatic temperature profile, but it is difficult to infer the number and location(s) of the non-adiabatic increase(s). If ab initio data are used, at least one thermal boundary layer seems reasonable, but its location depends on the modelling of the iron content. A strong chemical density contrast in the mid-mantle ($\geq 2\%$) is not supported by ab initio data, but is possible with experimental data. Other major sources of uncertainty are the trade-off between thermal and compositional effects, the possible influence of aluminium perovskite, and poorly understood frequency effects.
© 2004 Elsevier B.V. All rights reserved.

Keywords: Mg-perovskite; thermal boundary layer; aluminium perovskite

1. Introduction

The Earth's average profiles of temperature and composition are key parameters to understand mantle dynamics, but to date, they are only poorly known. Anchoring points at the bottom of the upper mantle [1,2] and at the core–mantle boundary (CMB) [3,4] give a rough idea of the temperature increase through the lower mantle. A typical value for the non-adiabatic contribution is $\Delta T = 1000$ K, but the error is large, about ± 500 K. Anderson [4] used these anchoring points and different average properties of the lower mantle to compute an average temperature profile. The most detailed information about the average Earth's structure comes from radially symmetric seismic models, such as PREM [5]. These 1D-models provide a good description of the elastic moduli of the mantle, but inferring average temperature and composition from them is not straightforward. Brown and Shankland [6] computed entropies from seismic models, and deduced the mantle temperature. Alternatively, working along an adiabat

* Corresponding author. Tel.: +31-30-253-5135.
E-mail address: deschamp@geo.uu.nl (F. Deschamps).

0012-821X/$ - see front matter © 2004 Elsevier B.V. All rights reserved.
doi:10.1016/j.epsl.2004.02.024

(e.g., [7,8]) one can choose a potential temperature that fits the seismic models, and compute a temperature profile from the adiabatic gradient. For the lower mantle, Shankland and Brown [9] found an adiabatic contribution of 600 K. Average composition can also be tested against seismic models. Jeanloz and Knittle [10] used the density of PREM to estimate the temperature and the volumetric fraction of iron in the lower mantle. To date, there is still no consensus on the average temperature and composition, as illustrated by recent studies [11–13] that propose very different results.

Inferring the mantle temperature and composition from seismic models requires a careful equation of state (EOS) modelling and accurate knowledge of the thermoelastic properties of minerals [11]. Modelling the shear modulus is particularly difficult because still few data are available. Jackson [11] showed that third-order Eulerian finite strain isotherms and isentropes appear adequate for the range of strains encountered in the lower mantle. Furthermore, he showed that working along hot finite strain isentropes is consistent with the Mie–Grüneisen–Debye description of thermal pressure. Stacey [14] observed that the shear modulus varies linearly with pressure and the bulk modulus along adiabats, which is compatible with a Birch–Murnaghan adiabatic compression to third-order [11,15]. Ideally, we should move away from EOS modelling and use directly high-temperature and high-pressure data. Recent progress in ab initio calculations started to give us this possibility, but data are still scarce. da Silva et al. [12] inferred temperature from ab initio data of the bulk modulus of Mg-perovskite alone, but this resulted in large uncertainties, even for a fixed average composition. Marton and Cohen [13] used ab initio calculations for the shear modulus at high temperature and pressure, and they find a small value of the volumetric fraction of perovskite. In addition to these difficulties, seismic models cannot fully resolve the average mantle temperature and composition and as a result, trade-offs between temperature and other parameters allow a large range of temperatures and compositions to fit 1D seismic models [11,16,17].

There is mounting evidence that thermo-chemical convection is likely to occur in the mantle, but the mode of convection is still a matter of debate, in particular the location(s) and thickness of thermal boundary layer(s) and of chemical layer(s). A good candidate is the D″ layer, which culminates 200–300 km above the CMB, where oceanic crust transformed into eclogite could sediment [18,19]. In that case, D″ remains stable if the chemical density contrast ($d\rho_c$) is higher than 2% [18,20]. Alternative models proposed a more complex structure [21,22]. Davaille [21] showed that for appropriate chemical density contrasts, oscillatory domes are able to develop in a stratified fluid. Kellogg et al. [22] explained several geophysical observations with a model of descending slabs deflecting a dense lower layer.

In the present paper, we test a collection of models against density and the elastic moduli of PREM. We make no assumption on temperature or composition and determine what can actually be constrained by 1D seismic models. Our EOS modelling is partly designed to fit all recently available ab initio data. This makes results largely modelling-independent, and allows to reasonably fill existing gaps in current ab initio data. These results are compared to the classical use of third-order Birch–Murnaghan equation of state with available experimental data. We also focus on the influence of corrections for the volumetric fraction of iron in elastic moduli, which are important in some cases.

2. Method and data

We reconstruct density and seismic velocities of the lower mantle from thermoelastic properties of minerals and appropriate equations describing these properties as a function of temperature and pressure, following [15]. The density (ρ) and the adiabatic bulk modulus (K_S) of each mineral composing the rock are heated (at zero pressure) to the potential temperature T_p using:

$$\rho(T_p, P=0) = \rho_0 \exp\left[-\int_{T_0}^{T_p} \alpha(T)\mathrm{d}T\right] \quad (1)$$

$$K_S(T_p, P=0) = K_{S0} \exp\left[\frac{\rho(T_p, P=0)}{\rho_0}\right]^{\delta_{S_0}} \quad (2)$$

where α is the thermal expansion, $\delta_S = -1/(\alpha K_S)\dot{K}_{S0}$ is the Anderson–Grüneisen parameter, and $\dot{K}_{S0}$ is the

temperature derivative of K_S at constant pressure. The subscript '0' stands for ambient temperature and pressure. For the shear modulus (G), we used a linear projection:

$$G(T_p, P=0) = G_0 + \dot{G}_0(T_p - T_0) \quad (3)$$

where $\dot{G}_0$ is the temperature derivative of G at constant pressure. The justification for Eqs. (2) and (3) is given in [15] on the basis of MgO data. To extrapolate ρ, K_S and G at pressure P, we use a Birch–Murnaghan adiabatic compression to the third-order in strain (BM3). The pressure is then given by:

$$P = -3K_{S0}(1-2\varepsilon)^{5/2}\left[\varepsilon + \frac{3}{2}(4 - K'_{S0})\varepsilon^2\right] \quad (4)$$

where K'_{S0} is the pressure derivative of the bulk modulus at constant entropy, and ε the Eulerian strain. The pressure is known relatively well from PREM, which determines ε. This allows to calculate the density from:

$$\rho(T,P) = \rho(T,P=0)(1-2\varepsilon)^{3/2} \quad (5)$$

and the bulk modulus to third-order using:

$$K_S = K_{S0}(1-2\varepsilon)^{5/2} \times \left[1 + (5 - 3K'_{S0})\varepsilon - \frac{27}{2}(4 - K'_{S0})\varepsilon^2\right] \quad (6)$$

A similar equation defines the shear modulus (G) (e.g., [7]). Alternatively, Stacey [14] proposed a linear relation valid along an adiabat:

$$G = A\,K_S - BP \quad (7)$$

where the constants A and B are determined at $P=0$ and T_p. We checked that these two extrapolation methods for G lead to the same results. The density and the elastic moduli of the mineralogical assemblage are finally deduced from volumetric and Voigt–Reuss–Hill averages, respectively. Densities and elastic moduli of minerals also depend on the volumetric fraction of iron (X_{Fe}). When data are available (Table 1), we account for this dependency at $P=0$ and $T_p=298$ K. It is convenient to use the global volumetric fraction of iron in the aggregate Fe_{glob}. The values of X_{Fe} for perovskite and magnesio-wüstite are then deduced from Fe_{glob} and from the iron partitioning K_{Fe} between perovskite and magnesio-wüstite. Calcium perovskite may also enter the composition of the lower mantle and influence the density and elastic moduli of the mantle aggregate. We account for this dependence in a similar way as we do for the iron dependence, using recent experimental measurements and ab initio calculations [29,30]. Compression induces an increase of temperature, and to get the mantle (or final) temperature one must add an adiabatic contribution to the potential temperature. We calculated this increase from the adiabatic temperature gradient:

$$\left(\frac{\partial T}{\partial P}\right)_S = \frac{\gamma T}{K_S} \quad (8)$$

In the quasi-harmonic approximation, the Grüneisen parameter γ is given by:

$$\gamma = \gamma_0\left(\frac{\rho}{\rho_0}\right)^q \quad (9)$$

where q is a constant. Taking q from Table 1, and knowing ρ from Eq. (5), we can evaluate γ and thus T. The values of the thermoelastic parameters used in the present paper are listed in Table 1. When available, we indicate either the error bars on the measurements, or a range of possible values based on data published in different studies.

Error bars on the thermoelastic parameters result in uncertainties on the extrapolated elastic moduli. Other sources of uncertainty are the assumed potential temperature and the exact composition of the aggregate. When all those parameters are varied within reasonable ranges (defined below), one obtains a collection of profiles for density, the elastic moduli, and the seismic velocities. On average, we find variations of about 0.05 g/cm^3 on density and 20 GPa on the elastic moduli. Some of these models are not suitable to describe the Earth's mantle, and realistic models must fit density and elastic moduli of PREM within a given range. The choice of PREM as a reference model might influence the results. We repeated most of the calculations with the reference model ak135 [31], but did not find any significant differences. A statistical analysis of the selected models provides an estimate of the average mantle

Table 1
Thermoelastic properties of $MgSiO_3$ and MgO[a]

	Perovskite			Magnesio-wüstite	
	Experimental	Ab initio[b]	C_{Fe}[c]		C_{Fe}[c]
ρ (g/cm^3)	4.109	4.107	+1.03[d]	3.584	2.28
K_{S0} (GPa)	264.0	268.9	+20[d]	162.5	11.5[e] /+18.0[f]
K'_{S0}	3.97/3.95/3.77/3.75[e]	4.07	+0.16[d]	4.0[g] to 4.15[h]	−0.53[f]
$\dot{K}_{S0}$ (10^{-2} GPa/K)	−1.1/−1.5/−1.0/−1.5[e]	−1.2	–	−1.55[i] to 1.4[h]	–
G_0 (Gpa)	175.0	180.0	−40[g]	130.8	−75.6[e]/−108[f]
G'_0	1.8 (0.4)	–	−0.52[d]	2.4[g] to 2.5	−3.29[f]
$\dot{G}_0$ (10^{-2} GPa/K)	−2.9 (0.3)	–	–	−2.4 to −2.2[h]	–
γ_0	1.31/1.39/1.33/1.41[e]	1.51	–	1.41	–
q	1.0/2.0/1.0/2.0[e]	1.27	–	1.3	–
a_1 (10^{-5} K^{-1})	1.19 (0.17)	2.066	–	3.681	–
a_2 (10^{-8} K^{-2})	1.20 (0.10)	0.909	–	0.9283	–
a_3 (K)	0.0	0.418	–	0.7445	–

[a] All data are from the compilation of Trampert et al. [15] unless otherwise stated. When available, error bars are indicated in parenthesis. ρ is the density, K_{S0} the adiabatic bulk modulus, G_0 the shear modulus, γ_0 the Grüneisen parameter at ambient temperature and pressure, and q a constant. Primes and dots denote derivation with respect to pressure and temperature, respectively. Thermal expansion at P=0 is calculated following $\alpha=a_1+a_2T-a_3T^{-2}$.

[b] Properties of $MgSiO_3$ deduced from the ab initio calculations of Oganov et al. [23].

[c] Correction for the iron content. Given the volumetric fraction of iron X_{Fe}, the corrected value for a parameter M is $M_{Mg,Fe}=M_{Mg}+C_{Fe}X_{Fe}$.

[d] [24].

[e] Jackson [11]. Four alternative combinations of K'_{S0}, $\dot{K}_{S0}$ and γ_0 are considered, depending on the values of K'_{T0} and q. K_{S0} and G_0 of magnesio-wüstite are corrected for the volumetric fraction of iron for, but no correction is applied for perovskite.

[f] [28].

[g] [25].

[h] [26].

[i] [27].

temperature and uncertainty. At a given depth, we estimated a probability density function $f(T)$ defined by:

$$f(T)=\int_{\Omega} c(T,\omega)d\Omega, \quad \begin{cases} c(T,\omega) = 1-|x(T,\omega)| & |x(T,\omega)|\le 1 \\ c(T,\omega) = 0 & |x(T,\omega)|>1 \end{cases} \tag{10}$$

where Ω is the model space, i.e., the set of all the possible combinations ω of the thermoelastic parameters and composition, $x(T,\omega)$ is the relative difference (in percent) between PREM and the predicted velocities and density. The closer the prediction to PREM, the more weight it carries. The first order moment of $f(T)$ defines the average temperature, which is a measure of the temperature that gives the best fit to PREM, and the second-order moment defines the standard deviation, which indicates the range of temperatures that fit PREM within the given error bar. Average potential temperatures are more useful for comparison with dynamic models, whereas average mantle temperatures are more easily understood. We also calculated average and standard deviation for compositional parameters (volumetric fractions of perovskite, iron, and calcium).

3. Parameterizing the mantle density and elastic properties

Ab initio calculations started to provide values of density and elastic moduli directly at mantle temperature and pressure [13,32]. They offer the advantage of eliminating uncertainties due to EOS modelling. However, ab initio calculations are extremely time-consuming, and data points are still scarce. We propose here to combine EOS modelling and existing high temperature and pressure data points from ab initio calculations. This reduces potential errors due to EOS and allows the flexibility of a finer depth

parameterization of mantle properties. In our formulation, a thermodynamic parameterization consists of high-pressure and high-temperature extrapolations, and of a set of parameters at ambient temperature and pressure. The consistency of a given parameterization can then be compared to ab initio calculations. In all the calculations of this section, we considered pure Mg-perovskite, thus no iron correction.

We have tested BM3 against recent ab initio calculations at high temperature and pressure [23,32]. First, we used the thermoelastic parameters at ambient pressure and temperature given by ab initio calculations at zero pressure [23] (second column in Table 1). For bulk modulus, we found a very good agreement between the high-temperature extrapolation at ambient pressure (bottom curve in Fig. 1) and the ab initio calculations at zero pressure [23], which justify the use of Eqs. (1) and (2) for perovskite. High-temperature extrapolations for density are

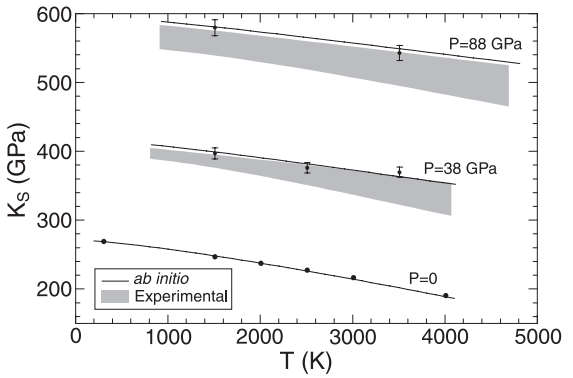

Fig. 1. Extrapolation of the bulk modulus of $MgSiO_3$ perovskite at high temperature and high pressure. Results are presented as a function of the final temperature. The bulk modulus of $MgSiO_3$ perovskite is extrapolated to high temperature and several values of the pressure ($P=0$, $P=38$ GPa and $P=88$ GPa). At $P=0$, the black dots represent ab initio calculations at zero pressure [23], and the plain curve is obtained from high-temperature extrapolation (Eq. (2)). Black dots are obtained by converting K_T values of [23] into K_S values, using the thermal expansion and Grüneisen parameter of [23]. At $P=38$ GPa and $P=88$ GPa, the black dots with error bars represent ab initio calculations at high pressures and temperatures [32], and the curves result from extrapolations at high temperature and BM3 adiabatic compressions. The thermoelastic properties of perovskite are after Oganov et al. [23], and are listed in Table 1, second column. For comparison, the grey shaded areas represent the ranges of values predicted by experimental data (Table 1, first column).

in equally good agreement with [23]. The high-pressure extrapolations for the bulk modulus (Fig. 1, middle and top curves) are in good agreement with the ab initio values of K_S reported in [32]. To estimate K_{S0} and K'_{S0}, Oganov et al. [23] fitted the Vinet EOS [33] to their athermal data, the thermal contribution being obtained with the Mie–Grüneisen–Debye description. Our results thus reconfirm that an adiabatic BM3 compression is consistent with the Mie–Grüneisen–Debye description of thermal pressure together with an isothermal part, as previously shown in [11]. We can now check the consistency between experimental and ab initio data, by using experimental data at ambient pressure and temperature (Table 1, first column) in BM3. Within error bars, there is a reasonable agreement (overlapping ranges) between these high-pressure, high-temperature extrapolations (Fig. 1, shaded areas), and the ab initio calculations (black dots with error bars). Ab initio data are close to the upper bound predicted by experimental data at both $P=38$ GPa and $P=88$ GPa, mainly because K'_{S0} for ab initio data is higher. It is interesting to note that there appears no need for a cross-derivative $\partial^2 K_S/\partial T \partial P$ to predict the bulk modulus correctly (slopes in Fig. 1 are in good agreement). For density, no error bars are given for the ab initio calculations, but the agreement is very good (within 1.0%). Finally, the effective thermal expansion calculated from the temperature derivative of density falls within the error bars in [32].

More serious problems arise when modelling the shear modulus at high pressures and temperatures. Very few experimental data exist for its derivatives. We have investigated the influence of the experimental values of the elastic moduli derivatives on the average potential temperature (Fig. 2). The most sensitive parameter is the pressure derivative, $(G'_0)_{pv}$ (Fig. 2a). The average temperature is about 1800 K if $(G'_0)_{pv}=1.4$, and 3400 K if $(G'_0)_{pv}=2.2$. If $(G'_0)_{pv}\geq 2.0$, very few models fit PREM within 1%, suggesting that high values of $(G'_0)_{pv}$ are unlikely. We then computed the shear modulus at $T_p=298$ K as a function of pressure using values of $(G'_0)_{pv}$ between 1.4 and 2.2. We compared the results with ab initio data in [23], and found that $(G'_0)_{pv}=1.5\pm0.05$ predicts ab initio data best. Note that this value of $(G'_0)_{pv}$ is close to the experimental lower bound in [34]. The temperature derivative $(\dot{G}_0)_{pv}$ is very poorly

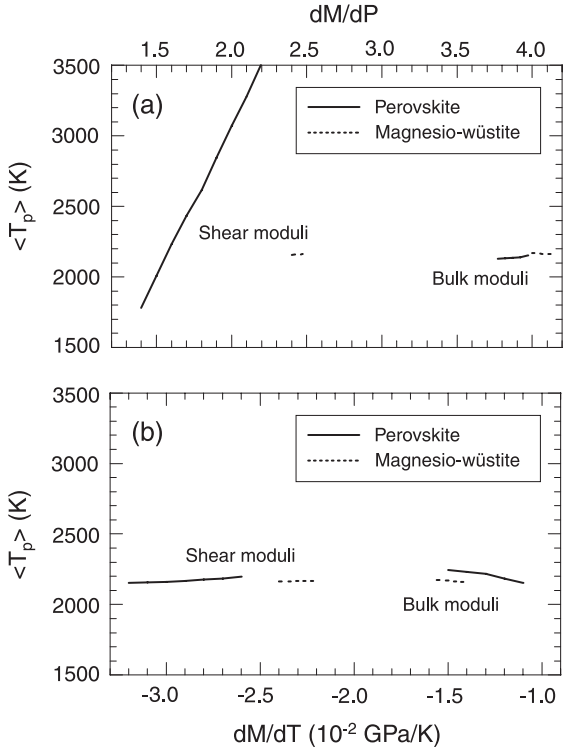

Fig. 2. Sensitivity of the average potential temperature $<T_p>$ to the derivatives of elastic moduli of perovskite (plain curves) and magnesio-wüstite (dashed curves). (a) Pressure derivatives; (b) temperature derivatives. Elastic derivatives are varied within their experimental range (Table 1), and the volumetric fraction of perovskite is equal to 0.8. The average potential temperature is estimated from a collection of models that fit PREM within 1%. Calculation are made at $P=88$ GPa ($z \sim 2000$ km).

constrained. Experimental data [34] give $(\dot{G}_0)_{pv} = -0.029 \pm 0.003$ GPa/K. Jackson [11], however, proposed a value around -0.020 GPa/K, and ab initio calculations [13] suggest an even lower value of -0.012 GPa/K. We have tested several values of $(\dot{G}_0)_{pv}$ between -0.032 and -0.012 GPa/K, but none of them could explain the ab initio calculations [32] simultaneously at $P=38$ GPa and $P=88$ GPa. At $P=38$ GPa, ab initio data are close to the upper bound predicted by experimental data, whereas at $P=88$ GPa they are close to the lower experimental bound (shaded areas in Fig. 3), but neither the data of Oganov et al. [32] nor those of Marton and Cohen [13] are correctly predicted as a function of temperature. A possible source for this disagreement could be Eq. (3). We repeated calculations using a projection similar to Eq. (2) (with $\delta_S = -1/(\alpha G)\dot{G}_0$), but the disagreement remained. This suggests that a cross-derivative $\partial^2 G/\partial T \partial P$ is needed at zero pressure to predict the ab initio shear modulus. We did a systematic search for $\partial^2 G/\partial T \partial P$, and found the best agreement with [32] for the empirical relation:

$$\partial^2 G/\partial T \partial P = a(\dot{G}_0)_{pv} + b \qquad (11)$$

where $a = -1.2 \times 10^{-2}$ GPa^{-1} and $b = -3.3 \times 10^{-4}$ K^{-1}. Taking $(\dot{G}_0)_{pv} = -0.020 \pm 0.008$ and the previous parameterization for the cross-derivative, our EOS modelling of $(G_0)_{pv}$ explain ab initio calculations in [13,32] well indeed (Fig. 3). It is worth noting, from results at $P=38$ GPa, that ab initio calculations favors low values of $(\dot{G}_0)_{pv}$ (-0.012 to -0.020 GPa/K) compared to the published experimental value (-0.029 ± 0.003 GPa/K).

Comparing this modified BM3 to predict ab initio values of G with that obtained from experimental data alone, it appears, unless $(G'_0)_{pv}$ is on the low end of the experimental data and that our ad hoc cross-

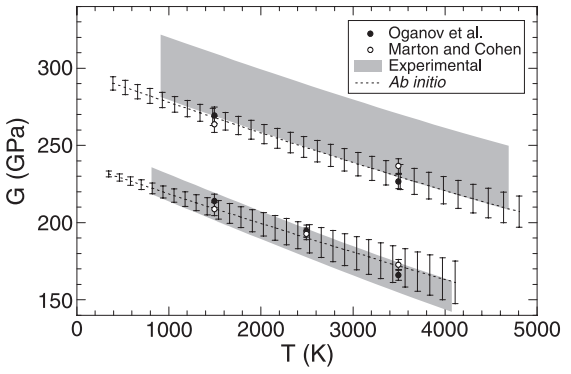

Fig. 3. Extrapolation of the shear modulus of $MgSiO_3$ perovskite at high temperature and high pressure. Results are presented as a function of the final temperature, and two values of the pressure ($P=38$ GPa and $P=88$ GPa). The black and the white dots represent the ab initio calculations at high pressure [32] and temperature [13], respectively. The dashed curves show the average values of the shear modulus predicted by an extrapolation at high temperature and an adiabatic Birch–Murnaghan compression to the third order, in which a cross-derivative is prescribed $\partial^2 G/\partial T \partial P$ (see text), and the error bars cover one standard deviation around the average. The pressure and temperature derivative are $(G'_0)_{pv} = 1.5 \pm 0.05$ and $\dot{G}_0 = -0.020 \pm 0.008$ GPa/K, respectively. The shaded areas represent the ranges of values predicted by experimental data (Table 1, first column).

derivative is confirmed by further experimental data, that there is some disagreement between ab initio and experimental data.

4. Average temperature and composition

To estimate the average potential temperature and composition and their standard deviations, we tested a whole collection of models against density and the elastic moduli of PREM. Different criteria can easily lead to different results though. Effects of anelasticity and the uncertainty on the volumetric fraction of iron persuaded da Silva et al. [12] not to use density and the shear modulus. Anelasticity could have minor consequences (see below), but uncertainty in the volumetric fraction of iron can easily be accounted for by varying it within a reasonable range. Using bulk modulus or density alone however does not give tight constraints on the temperature. With the bulk modulus, we find standard deviations of about 600 K for temperature, regardless of depth. Using simultaneously the bulk modulus and density, the standard deviation reduces to 500 K. Composition is better constrained than temperature, but standard deviations are still high (about 12% and 4.5% for perovskite and iron, respectively).

Because very little can be said if average temperature and composition are obtained from the bulk modulus and/or density alone, we decided to use the shear modulus together with the bulk modulus and the density to estimate the average temperature and composition. We varied T_p between and 1500 and 5000 K, X_{pv} between 50% and 100%, Fe_{glob} between 5% and 20%, X_{Ca} between 0% and 12%, and K_{Fe} between 0.2 and 0.5. We did calculations from $z = 800$ km down to the CMB, and omitted the lower mantle top layer ($660 \leq z \leq 800$ km). The reason is that the transformation of garnets into perovskite is probably not fully completed at these depths. Our model accounts for perovskite and magnesio-wüstite only, and may therefore not apply here. We performed three different calculations to emphasize the most important variables. The first one uses ab initio data (second column in Table 1) together with $(G_0')_{pv} = 1.5 \pm 0.05$, $(\dot{G}_0)_{pv} = -0.020 \pm 0.008$ GPa/K, and the empirical relation (11), as explained above. Elastic moduli are corrected for the volumetric fraction of iron following [11]. More recent studies for perovskite [24] and magnesio-wüstite [28] suggest that iron corrections are more significant (Table 1), and they may strongly influence the inferred average temperatures and composition [35]. The second calculation also uses the ab initio data, and accounts for the latest iron corrections [24,28]. Finally, the third calculation uses the experimental data for Mg-perovskite (first column in Table 1), and the full iron corrections. For each calculation, average temperature and composition are computed from models that fit PREM within 1%.

4.1. Statistical profiles obtained with ab initio data

4.1.1. Iron correction from [11]

The plain curves in Fig. 4 represent the mean values of T_p, X_{pv}, and Fe_{glob} obtained with ab initio data and the iron correction from [11]. The shaded grey areas cover one standard deviation around these mean values.

4.1.1.1. Potential temperature (Fig. 4a, grey shaded area). Down to $z = 1600$ km, the average potential temperature is nearly constant around 2050 K. It increases slightly ($dT/dz = 0.14$ K/km) between $z = 1600$ km and $z = 2500$ km, and very rapidly ($dT/dz = 1.8$ K/km) in the lowermost mantle ($2750 \leq z \leq 2880$ km), reaching 2410 K at the CMB. Uncertainties vary between 90 and 260 K, depending on depth. They reach 260 K at the bottom of the mantle. The smallest uncertainties are found around $z = 1600$ km. Within error bars, a purely adiabatic temperature profile could just about be accepted. A possible candidate for superadiabaticity is the lowermost layer, which extends from $z = 2750$ km down to the CMB. In this layer, the mean temperature increases strongly due to gradients in PREM. Error bars are such that robust estimates of the thickness of this layer are difficult.

Fig. 5 compares our temperature estimates together with previously published geotherms. For convenience, results are shown as final temperatures instead of potential temperatures. da Silva et al. [12] reported a strong departure from adiabaticity from $z = 1600$ km down to the CMB (black dots with error bars). Our results rule out such temperature gradients, and predict a cold lowermost mantle compared to [12]. The difference reaches about 1000 K at the CMB. A

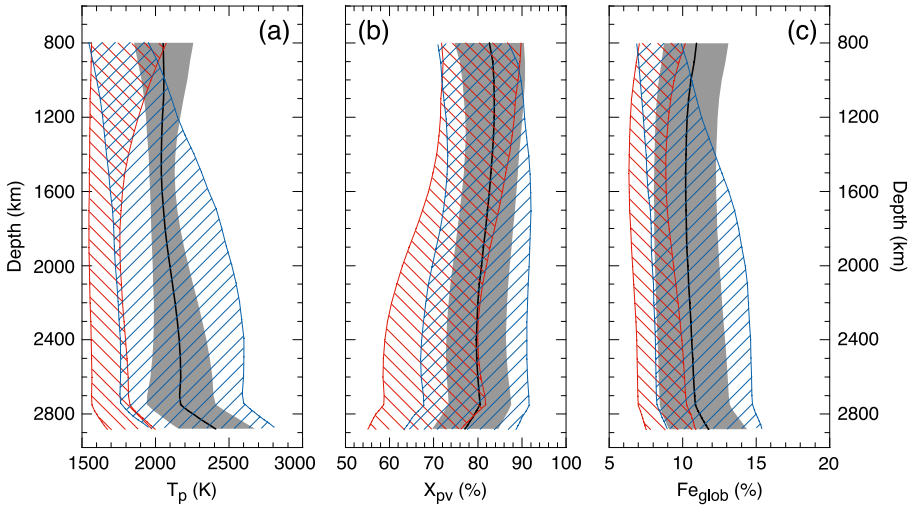

Fig. 4. Statistical profiles of potential temperature (a), volumetric fraction of perovskite (b), and volumetric fraction of iron (c). Plain curves represent the mean profiles obtained when temperature and pressure derivatives of the shear modulus of perovskite are modeled using ab initio data, with iron correction from [11]. The shaded areas cover one standard deviation around these mean profiles. The red dashed areas are obtained using the same modelling, but the correction of elastic moduli for the iron content are taken from [24,28]. The blue dashed areas represent the profiles obtained from experimental data. T_p is varied between 1500 and 5000 K, X_{pv} between 50% and 100%, and Fe_{glob} between 5% and 20%.

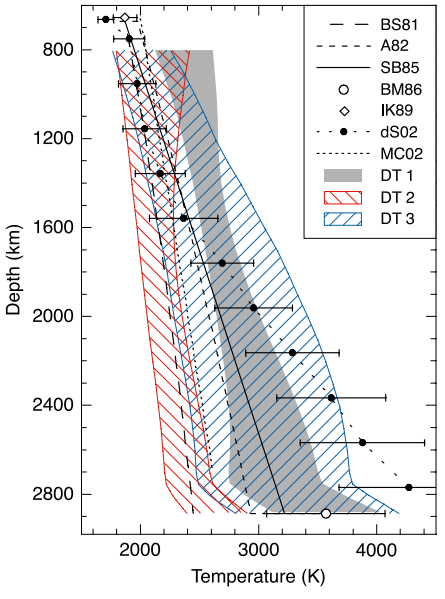

Fig. 5. Comparison between final temperature estimates (DT 1 to 3) from Fig. 4 and previous studies. The colour code is the same as in Fig. 4. BS81, Brown and Shankland [6]; A82, Anderson [4]; SB85, average profile of Shankland and Brown [9]; BM86, Brown and McQueen [3]; IK89, Ito and Katsura [1]; dS02, da Silva et al. [12]; MC02, Marton and Cohen [13].

possible reason for this difference is that da Silva et al. [12] allow much higher values for the Grüneisen parameter at ambient temperature and pressure, and that they test temperature against the bulk modulus only. The long dashed curve represents a profile of temperature reconstructed from the entropy and average seismic profiles [6]. This profile is nearly adiabatic, and because it anchors at $T=1873$ K at $z=670$ km, it is colder than our temperature estimates whatever the depth (see below). The profile calculated in [4] is also slightly colder than our lower estimates, except in the bottom layer ($z=2400$ km down to the CMB), where the agreement is good. The range of temperature proposed in [9] is globally in good agreement with our results, but their gradient is slightly higher. It is worth noting that our estimate of the temperature at the CMB is very close to that predicted in [3] (open dot with error bar), but is difficult to connect with the estimated temperature at the base of the upper mantle [1] (open diamond with error bar).

4.1.1.2. Composition (Figs. 4b–c, grey shaded areas). The mean volumetric fraction of perovskite (X_{pv}, Fig. 4b) is around 83% between 800 and 1600

km, and around 80% between 2000 and 2750 km. In the bottom layer, it decreases more rapidly, and reaches 77% at the CMB. The mean volumetric fraction of iron (Fe_{glob}, Fig. 4c) is close to 10% in most of the lower mantle ($1200 \leq z \leq 2700$ km). At $z = 800$ km and $z = 2800$ km, it is close to 11% and 12%, respectively. Again, steeper variations occur in the lowermost layer. Typically, the standard deviations are close to 6.5–7.5% for perovskite, and 2.0–2.6% for iron.

We also varied the volumetric fraction of Ca-perovskite (X_{Ca}) between 0% and 12% (not shown here). The mean value and standard deviation of X_{Ca} are constant throughout the mantle, and equal to $6 \pm 4\%$. The presence of Ca-perovskite is therefore only weakly constrained. The reason is that density and seismic velocities are not very sensitive to Ca-perovskite. Following [15], we computed sensitivities of density and seismic velocities to calcium, and found that they are one order of magnitude smaller than those for iron. The lack of resolution for X_{Ca} does not significantly change the determination of the mantle average temperature and other compositional parameters. Indeed, the mean temperature calculated with $X_{Ca} = 10\%$ is only 40 K higher than that for $X_{Ca} = 0$. Most of this difference is due to the high value of the pressure derivative of the shear modulus of Ca-perovskite reported in [30]. If, as expected, Ca-perovskite enters the composition of the lower mantle for 6–12% in volume (e.g., [2]), the effects on density and the elastic moduli would be of second-order compared to other compositional parameters. Aluminium perovskite, for which very few data are available, could have more dramatic effects (see Discussion below).

The mantle average composition derived from our calculations strongly supports the pyrolitic model ($X_{pv} = 84\%$ and $Fe_{glob} = 12\%$). Within our error bars, we do not see strong evidence for or against chemical stratification. The average composition proposed by Jackson [11] is significantly poorer in perovskite ($X_{pv} = 67\%$), but assumes an adiabatic profile with $T_p = 1600$ K. This discrepancy can be fully explained by the trade-offs existing between temperature and composition (Section 5 and Fig. 7). Marton and Cohen [13] recently proposed an even smaller value of $X_{pv} = 54\%$. Since they use a relatively cold adiabat ($T_p = 1800$ K, short dashed curve in Fig. 5), part of the discrepancy can be accounted for by the trade-offs between temperature and composition. Additional differences probably result from their low value of the iron partitioning ($K_{Fe} = 0.1$).

4.1.2. Full iron corrections

The red dashed areas in Fig. 4 cover one standard deviation around the average profiles obtained with the iron corrections from [24,28]. As expected, results are significantly different from those obtained with the iron correction from [11]. Temperatures are colder by 200 K at $z = 800$ km, and 600 K at $z = 2800$ km. The Average temperature strongly increases between 2750 and 2880 km ($dT/dz = 1.1$ K/km), but within error bars a purely adiabatic profile is possible. Additional calculations (not shown here) show that most of the difference is due to the correction for the elastic moduli of magnesio-wüstite [28]. Temperature profiles that account for the correction for the elastic moduli of perovskite [24] only are colder by 100 K at most. Inferred final temperatures (red dashed area in Fig. 5) connect well with the temperature estimates at the base of the upper mantle [1], and agree with adiabatic profiles such as in [6]. The upper bound is close to the profile derived in [13], but at the CMB it fails to connect with the range of the anchoring point [3].

Inferred composition also changes significantly, although less dramatically than temperature. Overall, the composition derived with full iron correction is less rich in perovskite and iron. On average, X_{pv} is close to 80% down to $z = 1500$ km and decreases to 65% at $z = 2800$ km, although a perovskite fraction of 75% is possible within error bars. The mean value of Fe_{glob} remains between 7.5% and 9.0% throughout the lower mantle. It is interesting to note that Fe_{glob} is better constrained (standard deviation is between 1.3 and 1.7) when corrections [24] and [28] are used.

4.2. Statistical profiles obtained with experimental data

The profiles for experimental data are represented by blue dashed areas in Fig. 4. Compared to the ab initio results, the mean potential temperature increases more rapidly with depth, and the standard deviations are higher, around 320 K. Within error bars, a purely adiabatic temperature profile is just about possible. At

$z = 800$ km, the average temperature is $T_p = 1900$ K, and it connects well with the estimated temperature at $z = 660$ km. At the CMB, the value of T_p is higher by 200 K than that obtained with ab initio data, and falls in the upper bound proposed by [3]. The mean volumetric fractions of perovskite and iron slightly increase with depth (from 81% to 86% for perovskite, and from 10% to 13% for iron), with higher standard deviations (up to 8.5% for perovskite and 3.3% for iron). In general, experimental data alone give higher uncertainties in temperature, perovskite and iron profiles, and are not very sensitive to the applied iron correction in the individual minerals.

4.3. Consequences for mantle dynamics

Our results suggest that a large collection of combinations T_p, Fe_{glob}, and X_{pv}, given the ranges of thermoelastic parameters, fit PREM as defined in Eq. (10). An accurate modelling of the shear modulus allows a significant reduction of the error bars, but the standard deviations are still high, around 300 K for temperature, 8.0% for perovskite, and 3.0% for iron. Some trade-offs exist between the parameters (in particular between temperature and composition), which is the reason why such a wide range of models fit PREM (see Discussion below). When ab initio data are used, the inferred temperatures are very sensitive to the applied correction for the iron content.

The temperature profiles plotted in Fig. 4a have different implications for mantle dynamics. Ab initio data for the elastic moduli of perovskite together with an iron correction from [11] predict a hot lower mantle. The inferred temperature at the top of the lower mantle ($z = 800$ km) does not connect to the estimates at $z = 660$ km [1,2], implying that the mantle is not adiabatic in this layer. Chemical transformations may participate to this non-adiabaticity, but a thermal boundary layer is certainly also present. Another thermal boundary layer is likely to be present somewhere in the mid- or lowermost mantle. Ab initio data together with recent iron corrections [24,28] predict a cold mantle. The inferred temperature connects to the estimates at $z = 660$ km [1,2], but not those at the CMB [3], implying the presence of a thin thermal boundary layer at the bottom of the mantle. When experimental data are used, the temperature profile connects the estimated temperatures at both $z = 660$ km and the CMB, and there is no need for a thermal boundary layer around this depth. On the other hand, the temperature gradient is such that at least one thermal boundary layer must be present somewhere between the mid–lower mantle and the CMB. Finally, all data sets predict error bars on composition that

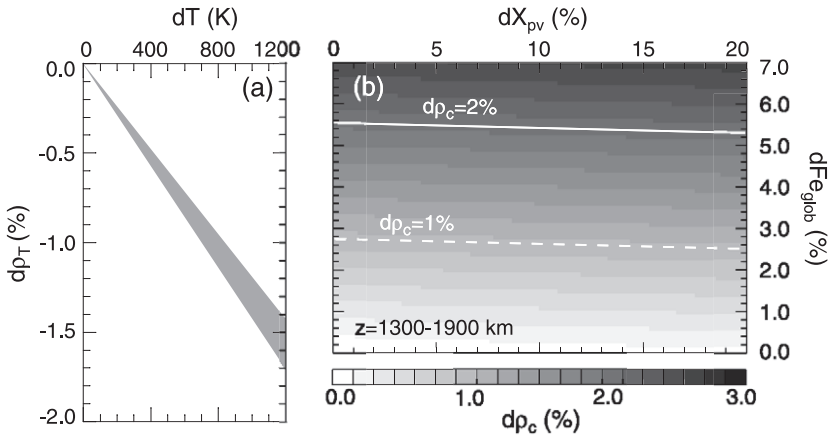

Fig. 6. Radial density variations in the mid-mantle ($1300 \le z \le 1900$ km). (a) Density variations due to temperature variations. The shaded area covers one standard deviation around the mean value of $d\rho_T$. (b) Density variations due to chemical changes (perovskite and iron). Standard deviations in $d\rho_c$ are close to 20% of the plotted values. The white dashed and plain lines denote $d\rho_c = 1\%$ and $d\rho_c = 2\%$, respectively. Sensitivity of density to temperature, perovskite, and iron are averaged between $z = 1300$ km and $z = 1900$ km. The correction of elastic moduli for iron content is taken from [24,28].

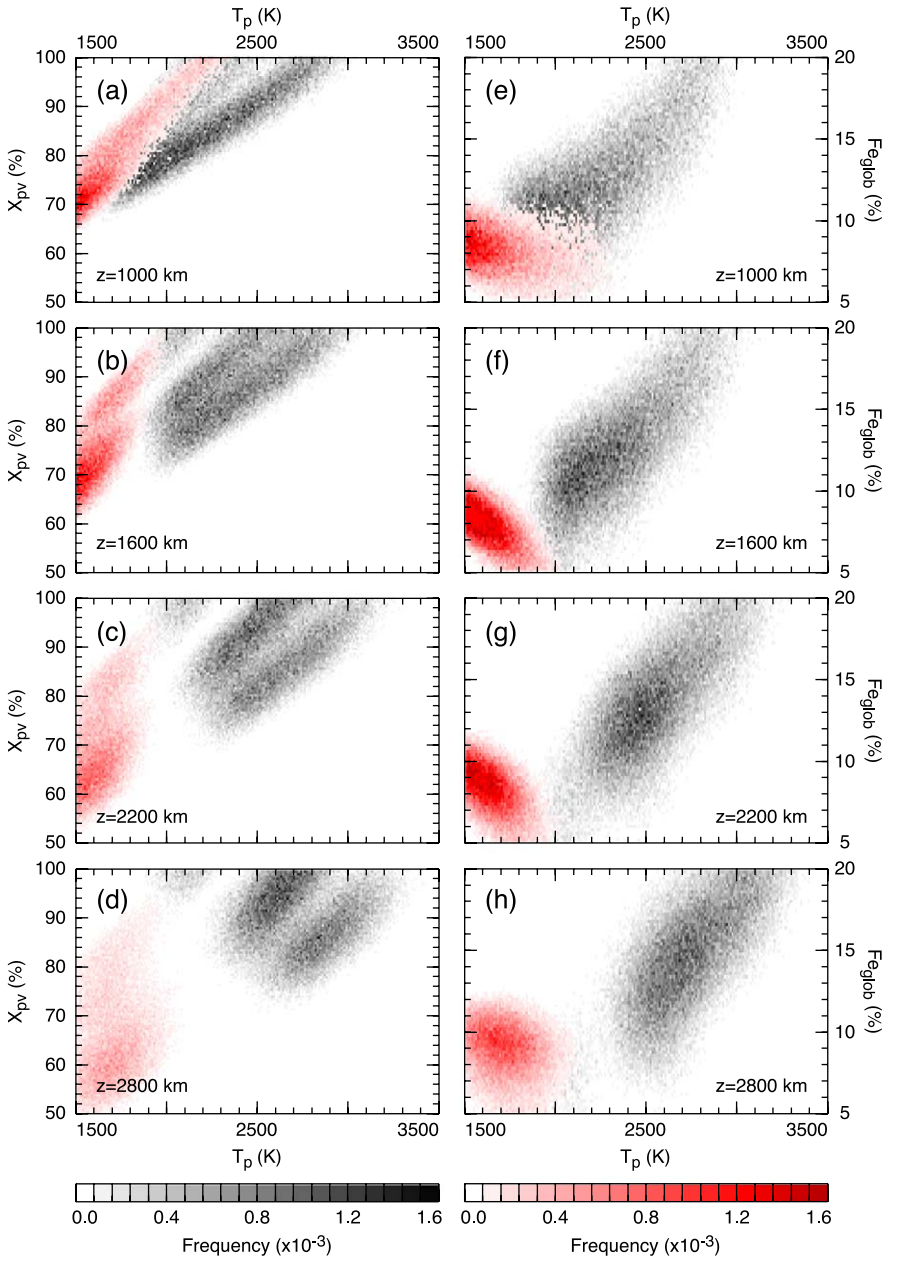

Fig. 7. (a–d) Frequency as a function of potential temperature (T_p), and volumetric fraction of perovskite (X_{pv}). (e–h) Frequency as a function of potential temperature (T_p), and global volumetric fraction of iron (Fe_{glob}). Two series of calculations are represented. One using iron correction from [11] (grey color scale), and one using full iron correction, including [24,28] (red color scale).

allow significant chemical variations (perovskite and/or iron).

It is interesting to test the hypothesis of a strongly stratified mantle against the profiles of temperature and composition shown in Fig. 4. We reconstructed variations of density from maximum allowed variations of temperature and composition, and from appropriate sensitivities of density to temperature and

composition. Using the approach of Trampert et al. [15], we have computed the sensitivities of density to temperature, perovskite and iron as a function of depth. Note that sensitivities of density (shear velocity) to perovskite and iron depend somewhat (strongly) on the applied correction for the iron content. Uncertainties in these sensitivities are used to estimate uncertainties on density.

To investigate the possible presence of a distinct mid-mantle layer, we averaged the sensitivities of density between $z=1300$ km and $z=1900$ km, and estimated density variations induced by purely thermal and compositional variations (Fig. 6). For instance, a temperature variation of 800 K across this layer would result in a thermal density contrast $d\rho_T=(-1.04\pm0.09\%)$ (Fig. 6a). From ab initio data, we see that the average temperature cannot not increase by more than 200 K between $z=1300$ km and $z=1900$ km, and therefore $d\rho_T=(-0.26\pm0.03\%)$ is an upper limit for the thermal density contrast. If experimental data are used, larger variations are possible (up to 800 K), and the maximum value of $d\rho_T$ is equal to $(-1.04\pm0.09\%)$. Density contrasts due to pure chemical variations ($d\rho_c$) are plotted in Fig. 6b. Variations in perovskite alone give small density contrasts, up to $d\rho_c=0.11\%$ for a 20% excess in perovskite. As expected, iron has stronger effects. For an excess in iron of 3% (5%), the density contrast is equal to 1.1% (1.8%). Davaille [21] showed that the doming regime should occur for a chemical density contrast around 1%. Variations in perovskite alone cannot produce such a contrast. One needs an additional 2.5–3% enrichment in iron, depending on the excess in perovskite (white dashed line in Fig. 6b). A strongly stratified convection requires a chemical density contrast higher than 2%. Assuming a maximum excess in perovskite of 20%, this value can only be reached for excess in iron higher than 5.2% (white plain line in Fig. 6b). Given the maximum ranges allowed by ab initio data between $z=1300$ km and $z=1900$ km (see red dashed areas in Fig. 4b–c), a chemical density contrast higher than 2% can hardly be obtained. The results above have been obtained for full iron corrections, including [24,28]. If only corrections from [11] are used, the values change slightly, but the conclusions remain the valid. Experimental data allow larger variations (up to 7% for iron), and therefore higher chemical density contrasts. We repeated these calculations for a distinct layer close to the CMB, and found similar results. Although the sensitivity of density to perovskite is higher, one still needs at least 5.0% enrichment in iron to create a 2% chemical density contrast.

Models of strongly stratified convection [18–22], which require average variations of thermal density bigger than 0.3% and average variations of chemical density larger than 2%, are not consistent with the average temperature and composition predicted by ab initio data. If by contrast, the average composition is inferred from experimental data, more uncertainty is obtained, and a strong stratification cannot be completely excluded ($d\rho_T$ is up to -1.0%, and $d\rho_c$ is up to 2.6%). Note that this analysis is based on average temperature and composition jumps. If lateral variations of temperature and composition are present, these conclusions can change locally.

5. Discussion

Average seismic models provide most information on the average Earth, but do not fully constrain the average mantle temperature and composition. The reason is that errors in the sensitivities of seismic velocities and density, and uncertainties in thermoelastic parameters are such that temperature and composition cannot be unambiguously determined. To quantify the trade-off between two given parameters x and y, we have calculated the frequency as a function of x and y in a similar way to the frequency for temperature (Eq. (10)). Fig. 7 shows the frequency as a function of potential temperature and volumetric fraction of perovskite (a–d) or volumic fraction of iron (e–h). The applied correction for iron is either taken from [11] (black dots), or from [24,28] (red dots). A trade-off indicates that high and low values of T_p explain PREM equally well, if they are associated with high and low values of X_{pv}, respectively. This trade-off has already been reported [11,13,16,17], and is particularly strong at the top of the lower mantle (Fig. 7a). It gets slightly smaller in the deeper mantle (Fig. 7d), but is present independently of the applied correction for iron content. Jeanloz and Knittle [10] pointed out a trade-off between the temperature and the volumetric fraction of iron. When the applied correction for iron is from [11], we also observe this

trade-off at every depth (Fig. 7e–h). Simultaneous low temperature and low volumetric fraction of iron explain as well PREM as simultaneous high temperature and high volumetric fraction of iron. When we use the corrections given in [24,28], we do not see any significant trade-off.

So far, we have only considered the effects of variations in the global volumetric fraction of iron and calcium. Aluminium oxide (Al_2O_3) may be also present for 4–5 mol%. At mantle temperature and pressure, it is thought to be incorporated into (Mg,Fe)-perovskite. The few laboratory measurements available for these phases (e.g., [36,37]) suggest that their elastic properties are significantly different from those of (Mg,Fe)-perovskite. These experimental results contrast strongly with ab initio calculations for elastic properties of aluminium oxide (Al_2O_3), which are close to those for Mg-perovskite [38]. Experimental values of the bulk modulus have important consequences on the determination of the potential temperature. If Al-perovskite is present for 4% in volume, the temperature is lower by 150–200 K, depending on the depth. However, the number of models that fit PREM within 1% decreases strongly with increasing volumetric fraction of aluminium (X_{Al}). Effects induced by variations in the derivatives of the bulk modulus are particularly dramatic. For $X_{Al}=2\%$, only a small amount of models fit PREM within 1%, and the mean potential temperature is smaller than that for $X_{Al}=0$ by more than 1000 K. For values of X_{Al} higher than 3%, we do not find any model that fit PREM within 1%. Given the experimental values to date, the presence of 4–5 mol% of Al-perovskite in the lower mantle is unlikely. The available ab initio values indicate that the presence of Al-perovskite could have a limited influence on the determination of the mantle temperature. Aluminium probably plays an important role, but additional experiments and/or ab initio calculations need to be conducted for a better knowledge of the elastic parameters of Al-perovskite.

Mineral physics measurements are made at much higher frequencies than seismic observations, If attenuation is present, this could possibly affect the comparison. It has been argued that this is important for the temperature sensitivity of seismic wave speed [39,40], but using most recent data, Trampert et al. [15] showed that this effect is modest in the lower mantle. These results cannot be used in a straightforward manner because here we are comparing calculations of absolute wave speeds to PREM. Seismic attenuation can significantly vary speed (up to 1%). This means that totally different combinations of temperature and composition will be selected to fit PREM. We introduced attenuation using the relation for dissipation of phase speed proposed by Minster and Anderson [41], and found that the estimated temperature curve would shift towards lower values by 100 K at most. Composition would also shift according to the trade-offs. This is clearly insignificant given overall errors. It is however not obvious that seismic attenuation is the right way to extrapolate dispersion from experimental studies to seismic conditions [42,43]. A recent review of measurements [43] showed complicated effects of frequency, temperature and grain size. Data are still lacking to make firm statements on the lower mantle, but it could possibly affect inferences.

6. Conclusions

The average temperature and composition of the lower mantle are key parameters for testing different possible models of mantle dynamics. We tested high pressure and temperature data from ab initio calculations and mineral physics experiments against PREM to constrain the mantle temperature and composition. We showed that, although it is least well known, the shear modulus significantly reduces uncertainty on temperature and composition, but experimental and ab initio data appear to be inconsistent. Using the ab initio data, inferred temperatures are very sensitive to the applied correction for the iron content. The temperature predicted by experimental data alone has a steeper gradient and larger uncertainties than that obtained with ab initio data, regardless of the iron correction. A strong chemical stratification ($d\rho_c \geq 2\%$) in the mid-mantle is unlikely within the error bars from ab initio data, but possible with experimental data. Other sources of uncertainty are the trade-offs between temperature and composition. An interesting remaining question concerns the presence of Al-perovskite in the mantle. If the present available measurements are correct, only very low values of temperature are able to fit PREM. Measured frequency effects in the laboratory are different from frequen-

cy effects predicted by seismic attenuation models. This could influence results, and needs to be quantified in future work.

Acknowledgements

We are grateful to Dave Yuen and Ian Jackson for useful and constructive comments on a first version of this paper. We thank Mark Bukowinski and an anonymous reviewer for their helpful reviews, and Scott King for constructive comments. This research was funded by Utrecht University. ***[SK]***

References

[1] E. Ito, T. Katsura, A temperature profile of the mantle transition zone, Geophys. Res. Lett. 16 (1989) 425–428.
[2] J. Ita, L. Stixrude, Petrology, elasticity and composition of the mantle transition zone, J. Geophys. Res. 97 (1992) 6849–6866.
[3] J.M. Brown, R.G. McQueen, Phase transitions, Grüneisen parameter, and elasticity for shocked iron between 77 and 400 GPa, J. Geophys. Res. 91 (1986) 7485–7494.
[4] O.L. Anderson, The Earth's core and the phase diagram of iron, Philos. Trans. R. Soc. Lond., A 306 (1982) 21–35.
[5] A.M. Dziewonski, D.L. Anderson, Preliminary reference Earth model, Phys. Earth Planet. Inter. 25 (1981) 297–356.
[6] J.M. Brown, T.J. Shankland, Thermodynamic parameters in the Earth as determined from seismic profiles, Geophys. J. R. Astron. Soc. 66 (1981) 579–596.
[7] G.F. Davies, A.M. Dziewonski, Homogeneity and constitution of the Earth's lower mantle and outer core, Phys. Earth Planet. Inter. 10 (1975) 336–343.
[8] T.S. Duffy, D.L. Anderson, Seismic wave speeds in mantle minerals and the mineralogy of the upper mantle, J. Geophys. Res. 94 (1989) 1895–1912.
[9] T.J. Shankland, J.M. Brown, Homogeneity and temperatures in the lower mantle, Phys. Earth Planet. Inter. 38 (1985) 51–58.
[10] R. Jeanloz, E. Knittle, Density and composition of the lower mantle, Philos. Trans. R. Soc. Lond., A 328 (1989) 377–389.
[11] I. Jackson, Elasticity, composition and temperature of the Earth's lower mantle: a reappraisal, Geophys. J. Int. 134 (1998) 291–311.
[12] C.R.S. da Silva, R.M. Wentzcovitch, A. Patel, G.D. Price, S.I. Karato, The composition and geotherm of the lower mantle: constraints from the elasticity of silicate perovskite, Phys. Earth Planet. Inter. 118 (2000) 103–109.
[13] F.C. Marton, R.E. Cohen, Constraints on lower mantle composition from molecular dynamics simulations of $MgSiO_3$ perovskite, Phys. Earth Planet. Inter. 134 (2002) 239–252.
[14] F.D. Stacey, Theory of thermal and elastic properties of the lower mantle and core, Phys. Earth Planet. Inter. 89 (1995) 219–245.
[15] J. Trampert, P. Vacher, N. Vlaar, Sensitivities of seismic velocities to temperature, pressure and composition in the lower mantle, Phys. Earth Planet. Inter. 124 (2001) 255–267.
[16] D.L. Anderson, Theory of the Earth, Blackwell, Oxford, 1989.
[17] L. Stixrude, R.J. Hemley, Y. Fei, H.K. Mao, Thermoelasticity of silicate perovskite and magnesiowüstite and stratification of the Earth's mantle, Science 257 (1992) 1099–1101.
[18] P. Olson, C. Kinkaid, Experiments on the interaction of thermal convection and compositional layering at the base of the mantle, J. Geophys. Res. 96 (1991) 4347–4354.
[19] U.R. Christensen, A. Hofmann, Segregation of subducted oceanic crust in the convecting mantle, J. Geophys. Res. 99 (1994) 19867–19884.
[20] P.J. Tackley, Three-dimensional simulations of mantle convection with a thermo-chemical basal boundary layer: D″? in: M. Gurnis, et al. (Eds.), The Core–Mantle Boundary Region, Geophys. Monogr. Ser., vol. 28, AGU, Washington, DC, 1998, pp. 231–253.
[21] A. Davaille, Simultaneous generation of hotspots and superswells by convection in a heterogeneous planetary mantle, Nature 402 (1999) 756–760.
[22] L.H. Kellogg, B.H. Hager, R.D. van der Hilst, Compositional stratification in the deep mantle, Science 283 (1999) 1881–1884.
[23] A.R. Oganov, J.P. Brodholt, G.D. Price, Ab initio elasticity and thermal equation of state of $MgSiO_3$ perovskite, Earth Planet. Sci. Lett. 184 (2001) 555–560.
[24] B. Kiefer, L. Stixrude, R.M. Wentzcovitch, Elasticity of $(Mg,Fe)SiO_3$-Perovskite at high pressures, Geophys. Res. Lett. 29 (2002) DOI: 10.1029/2002GL014683.
[25] S.V. Sinogeikin, J.D. Bass, Single crystal elasticity of MgO at high-pressure, Phys. Rev., B 59 (1999) 14141–14144.
[26] B.B. Karki, R.M. Wentzcovitch, S. de Gironcoli, S. Baroni, High-pressure lattice dynamics and thermoelasticity of MgO, Phys. Rev., B 61 (2000) 8793–8800.
[27] Y. Sumino, O.L. Anderson, I. Suzuki, Temperature coefficients of elastic constants of single crystal MgO between 80 and 1300 K, Phys. Chem. Miner. 9 (1983) 38–47.
[28] J. Kung, B. Li, D.J. Weidner, J. Zhang, R.C. Liebermann, Elasticity of $(Mg_{0.83},Fe_{0.17})O$ ferropericlase at high pressure: ultrasonic measurements in conjunction with X-radiation techniques, Earth Planet. Sci. Lett. 203 (2002) 557–566.
[29] Y. Wang, D.J. Weidner, F. Guyot, Thermal equation of state of $CaSiO_3$ perovskite, J. Geophys. Res. 101 (1996) 661–672.
[30] B.B. Karki, J. Crain, First-principles determination of elastic properties of $CaSiO_3$ perovskite at lower mantle pressures, Geophys. Res. Lett. 25 (1998) 2741–2744.
[31] B.L.N. Kennett, E.R. Engdahl, R. Bulland, Constraints on seismic velocities in the Earth from travel times, Geophys. J. Int. 122 (1995) 108–124.
[32] A.R. Oganov, J.P. Brodholt, G.D. Price, The elastic constants of MgSiO3 perovskite at pressures and temperatures of the Earth's mantle, Nature 411 (2001) 934–937.
[33] P. Vinet, J. Ferrante, J.H. Rose, J.R. Smith, Compressibility of solids, J. Geophys. Res. 92 (1987) 9319–9325.

[34] Y.D. Sinelnikov, G. Chen, D.R. Neuville, M.T. Vaughan, R.C. Liebermann, Ultrasonic shear wave velocities of $MgSiO_3$ perovskite at 8 GPa and 800 K and lower mantle composition, Science 28 (1998) 677–679.
[35] B.B. Karki, L. Stixrude, Seismic velocities of major silicate and oxide phases of the lower mantle, J. Geophys. Res. 104 (1999) 13025–13033.
[36] J. Zhang, D.J. Weidner, Thermal equation of state of aluminium-enriched silicate perovskite, Science 284 (1999) 782–784.
[37] I. Daniel, H. Cardon, G. Fiquet, F. Guyot, M. Mezouar, Equation of state of Al-bearing perovskite to lower mantle pressure conditions, Geophys. Res. Lett. 28 (2001) 3789–3792.
[38] W. Duan, B.B. Karki, R. Wentzcovitch, High-pressure elasticity of alumina studied by first principles, Am. Mineral. 84 (1999) 1961–1966.
[39] S.-I. Karato, Importance of anelasticity in the interpretation of seismic tomography, Geophys. Res. Lett. 20 (1993) 1623–1626.
[40] S.-I. Karato, B.B. Karki, Origin of lateral variation of seismic wave velocities and density in the deep mantle, J. Geophys. Res. 106 (2001) 21771–21783.
[41] J.B. Minster, D.L. Anderson, A model of dislocation-controlled rheology for the mantle, Philos. Trans. R. Soc. Lond., A. 299 (1981) 319–356.
[42] A. Dewaele, F. Guyot, Thermal parameters of the Earth's lower mantle, Phys. Earth Planet. Inter. 107 (1998) 261–267.
[43] I. Jackson, Laboratory measurement of seismic wave dispersion and attenuation: recent progress, in: S.I. Karato, et al. (Ed.), Earth's Deep Interior: Mineral Physics and Tomography From The Atomic To The Global Scale, Geophys. Monogr. Ser., vol. 117, AGU, Washington, DC, 2001, pp. 63–87.

Available online at www.sciencedirect.com
SCIENCE DIRECT®
Physics of the Earth and Planetary Interiors 140 (2003) 277–291
PHYSICS OF THE EARTH AND PLANETARY INTERIORS
www.elsevier.com/locate/pepi

Mantle tomography and its relation to temperature and composition

Frédéric Deschamps*, Jeannot Trampert

Department of Geophysics, Utrecht University, Budapestlaan 4, P.O. Box 80021, 3508 TA Utrecht, The Netherlands

Accepted 9 September 2003

Abstract

We propose a new method to constrain lateral variations of temperature and composition in the lower mantle from global tomographic models of shear- and compressional-wave speed. We assume that the mantle consists of a mixture of perovskite and magnesio-wüstite. In a first stage, we directly invert V_P and V_S anomalies for variations of temperature and composition, using the appropriate partial derivatives (or sensitivities) of velocities to temperature and composition. However, uncertainties in the tomographic models and in the sensitivities are such that variations in composition are completely unconstrained. Inferring deterministic distributions of temperature and composition being currently not possible, we turn to a statistical approach, which allows to infer several robust features. Comparison between synthetic and predicted ratios of the relative shear- to compressional-velocity anomalies indicates that the origin of seismic anomalies cannot be purely thermal, but do not constrain the amplitude of the variations of temperature and composition. We show that we can estimate these variations using histograms of the relative V_P and V_S anomalies at a given depth. We computed histograms for a large variety of cases and found that at the bottom of the mantle, variations in the volumic fraction of perovskite from -14 to 10% are essential to explain seismic tomography. In the mid-mantle, anomalies of perovskite are not required, but moderate variations (up to 6%) can explain the observed distributions equally well. These trade-offs between anomalies of temperature and composition cannot be resolved by relative velocity anomalies alone. An accurate determination of temperature and composition requires the knowledge of density variations as well. We show that anomalies of iron can then also be resolved.
© 2003 Elsevier B.V. All rights reserved.

Keywords: Shear velocity anomaly; Compressional velocity anomaly; Mantle temperature and composition

1. Introduction

One of the most challenging issues concerning the Earth's mantle is to infer its thermo-chemical structure. Variations of temperature and composition are closely related to mantle dynamics. There is little doubt that convection controls heat and mass transfers in the mantle, but the mode of mantle convection is still a matter of debate. The simplest model is whole-mantle convection driven by a strong bottom thermal boundary layer. If, on the other hand, plate tectonics is the main mode of heat transfer in the mantle, the bottom thermal boundary layer is weak (Labrosse and Tackley, 2001). A variant of whole-mantle convection is the 'blob' model (Becker et al., 1999), in which residual blobs of the primitive reservoir are dispatched throughout the lower mantle. Models of chemically stratified mantle have gained an increasing interest. Kellogg et al. (1999) proposed a model in which a dense layer surrounds the core mantle boundary. This layer peaks around a depth

* Corresponding author. Tel.: +31-30-2525135.
E-mail address: deschamp@geo.uu.nl (F. Deschamps).

0031-9201/$ – see front matter © 2003 Elsevier B.V. All rights reserved.
doi:10.1016/j.pepi.2003.09.004

of 1600 km, and is locally deflected by downwelling slabs. Analogical experiments of thermo-chemical convection (Davaille, 1999) predict two regimes, depending on the density contrast. The doming regime occurs if the density contrast is lower than 1%, whereas for higher contrasts convection is organized in two layers. Whichever the model, it creates variations of temperature and composition seismology would like to map.

Global tomographic models of the Earth started to provide good quality maps of the lower mantle, independently for compressional (V_P) and shear (V_S) velocities (e.g., Su and Dziewonski, 1997; Masters et al., 2000; Ritsema and van Heijst, 2002). Despite these recent improvements, interpretation of tomographic models is not as straightforward. The main difficulty is that seismic velocities (and density) depend simultaneously on temperature, composition and pressure. Two different lines of enquiring have been proposed in the literature. Forte and Mitrovica (2001) directly inverted models of bulk sound (V_Φ) and shear velocity anomalies for an effective temperature and composition using sensitivities they determined from existing literature. More often, studies are based on the analysis of the average of the distributions of the relative shear- to compressional-velocity anomalies (Karato and Karki, 2001, and references therein). A complicating factor in both approaches is that velocities alone cannot resolve all trade-offs between temperature and chemical variations. Density variations are needed in addition to velocity perturbations (e.g., Forte and Mitrovica, 2001; Karato and Karki, 2001).

In the present paper, we show that the deterministic approach of Forte and Mitrovica (2001) is not entirely robust given uncertainties, especially in the tomographic models. The approach based on the mean of the relative shear- to compressional-wave speed ratio (Karato and Karki, 2001) gives at best an indication of the presence of chemical heterogeneities. We propose a statistical approach, and show that the full distribution of relative velocity anomalies give robust bounds on temperature and composition.

2. Sensitivities of seismic velocities

Seismic velocity anomalies observed in the mantle can have several origins, the main contributions being anomalies of temperature and composition. At the base of the mantle, partial melt, if present, could contribute significantly to seismic anomalies (e.g., Williams and Garnero, 1996; Revenaugh and Meyer, 1997). The relative contribution of each parameter can be written as the product of a partial derivative (hereafter called the sensitivity) of seismic velocities to this parameter, and of the amplitude of the variations of this parameter. Accounting for thermal (dT) and compositional (dC) anomalies, and for the presence of partial melt (dF), the relative seismic velocity anomalies can be written as

$$\begin{aligned} \mathrm{d}\ln V_P &= \frac{\partial \ln V_P}{\partial T}\mathrm{d}T + \frac{\partial \ln V_P}{\partial C}\mathrm{d}C + \frac{\partial \ln V_P}{\partial F}\mathrm{d}F, \\ \mathrm{d}\ln V_S &= \frac{\partial \ln V_S}{\partial T}\mathrm{d}T + \frac{\partial \ln V_S}{\partial C}\mathrm{d}C + \frac{\partial \ln V_S}{\partial F}\mathrm{d}F \end{aligned} \quad (1)$$

where the compositional term can be separated in several contributions, the most important being the variations of the volumic fractions of perovskite (dX_{pv}) and iron (dX_{Fe}). The ratio R of the relavite shear to compressional seismic velocity is defined as

$$R \equiv \frac{\mathrm{d}\ln V_S}{\mathrm{d}\ln V_P} \quad (2)$$

where d ln V_S and d ln V_P are given by Eq. (1). R can be estimated from seismic tomography. Given the sensitivities of V_P and V_S, this ratio might give clues on dT, dC and dF.

Sensitivities of velocities to temperature and composition as a function of depth are calculated using mineral physics data and equation of state (EOS) modeling. We applied the method of Trampert et al. (2001) to an aggregate of perovskite ($MgSiO_3$) and magnesio-wüstite (MgO) througout the lower mantle. Each mineral of the aggregate is heated up to the potential temperature and adiabatically compressed to the required pressure. Additionally to Trampert et al. (2001), we required that our EOS fit all existing ab initio data. No modification was needed to fit density and the bulk modulus, but we had to prescribe a cross-derivative to fit the shear modulus data of Oganov et al. (2001) and Marton and Cohen (2002). Details can be found in Deschamps and Trampert (2003). Interestingly, this modification does not significantly change the sensitivities compared to those of Trampert et al. (2001). To assess sensitivities to iron and calcium, we explicitly accounted for changes in

the volumic fraction of these elements. We neglected effects of anelasticity, which appear to only have a minor influence on temperature sensitivities in the lower mantle (Trampert et al., 2001; Brodholt et al., 2003). Ignorance of the potential temperature, average composition and on thermo-elastic parameters lead to uncertainties in the sensitivities. We varied these parameters within their possible ranges, allowing a large set of reference models (temperature, composition, thermo-elastic properties). The mean values of the sensitivities and their variances are estimated from the predicted models that fit PREM within 1%. Trampert et al. (2001) performed this test on mantle-averaged profiles for V_P, V_S and density. We prefer comparisons with PREM at each depth. The reason is that high values of the potential temperature (say $T_p = 2500$ K) may fit PREM in the lowermost mantle, but not in the mid-mantle. By allowing a different reference temperature and composition at each depth, we account for eventual non-adiabatic increases of temperature. To test if the reference model might influence the results, we repeated most of the calculations with the reference model ak135 (Kennett et al., 1995), but did not find any significant differences.

Fig. 1a and b displays sensitivities of V_P (plain curves) and V_S (dashed curves) to temperature and volumic fraction of perovskite as a function of depth. Most of the input values of thermo-elastic parameters at ambient pressure are taken from the compilation of Trampert et al. (2001), where we added recent ab initio data (Table 1). Temperature, composition and pressure are varied according to Table 2, and the thermo-elastic properties are varied within their error bars (Table 1). This generated 10 million cases, from which 230 000 to 460 000 fit PREM within 1%, depending on the depth. The sensitivities to temperature are always negative, but their absolute values are decreasing with depth. The ratio R (Eq. (2)) associated with pure variations of temperature does not vary significantly with depth, and remains between 1.35 and 1.65. The sensitivity of V_P to volumic fraction of perovskite is positive throughout the lower mantle,

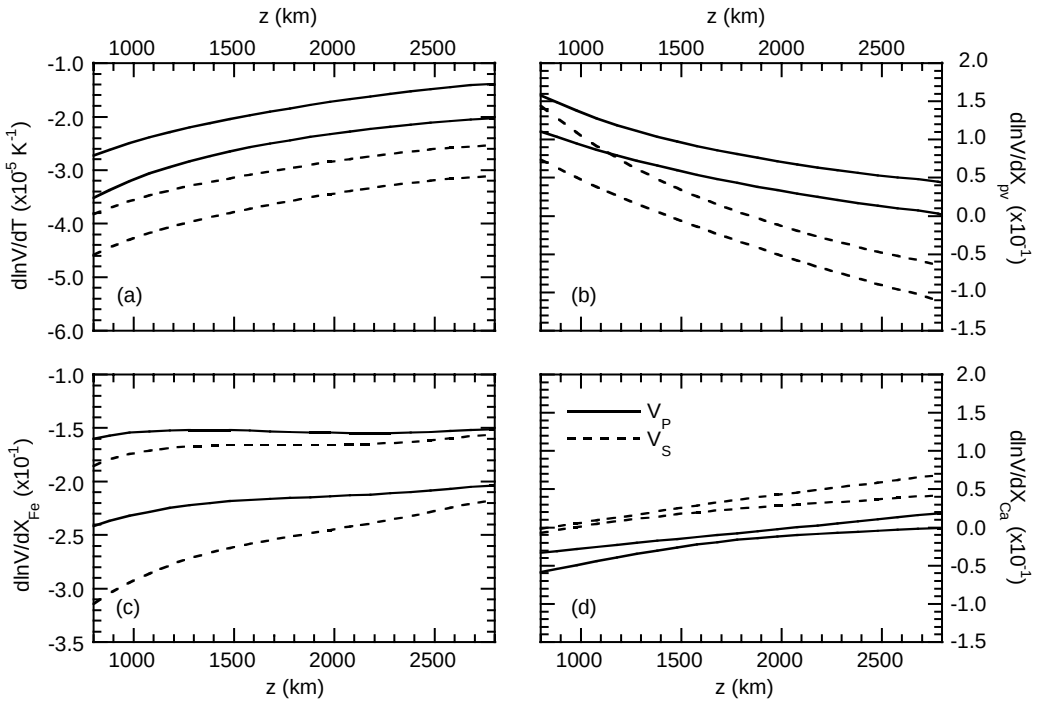

Fig. 1. Sensitivities of compressional velocity (plain curves) and shear velocity (dashed curves) to (a) temperature, (b) perovskite, (c) iron, and (d) calcium as a function of depth. In each case, we represent the upper and lower value of the sensitivity, which correspond to 1 standard deviation around the average. Averages and standard deviations are calculated from the predicted models that fit PREM within 1%.

Table 1
Thermoelastic properties of $MgSiO_3$ and MgO[a]

	Perovskite	Magnesio-wüstite
ρ (g/cm^3)	4.109 + 1.03 X_{fe}	3.584 + 2.28 X_{Fe}
K_{S0} (GPa)	264.0	162.5 + 11.5 X_{Fe}
K'_{S0}	3.97/3.95/3.77/3.75[b]	4.0[c] to 4.15[d]
$\dot{K}_{S0}$ (GPa/K)	−0.011/−0.015/ −0.010/−0.015[b]	−0.0155[e] to −0.014[d]
G_0 (GPa)	180.0[f]	130.8–75.6 X_{fe}
G'_0	1.5 (0.05)[g]	2.4[c] to 2.5
$\dot{G}_0$ (GPa/K)	−0.020 (0.008)[h]	−0.024 to −0.022[d]
γ_0	1.31/1.39/1.33/1.41[b]	1.41
q	1.0/2.0/1.0/2.0[b]	1.3
a_1 (10^{-5} K^{-1})	1.19 (0.17)	3.681
a_2 (10^{-8} K^{-2})	1.20 (0.10)	0.9283
a_3 (K)	0.0	0.7445

[a] All data are from the compilation of Trampert et al. (2001) unless otherwise stated. When available, error bars are indicated in parenthesis. ρ is the density, K_{S0} the adiabatic bulk modulus, G_0 the shear modulus, γ_0 the Grüneisen parameter at ambient temperature and pressure, and q a constant. Primes and dots denote derivation with respect to pressure and temperature, respectively. To model the shear modulus of perovskite we prescribed a cross derivative, as suggested in Deschamps and Trampert (2003). This cross-derivative is given by $\partial^2 G/\partial T\,\partial P = c_1(\dot{G}_0)_{pv} + c_2$, where $c_1 = -1.2 \times 10^{-2}$ GPa^{-1} and $c_2 = -3.3 \times 10^{-4}$ K^{-1}. Thermal expansion is calculated following $\alpha = a_1 + a_2 T - a_3 T^{-2}$.

[b] Following Jackson (1998), we consider four alternative combinations of K'_{S0}, $\dot{K}_{S0}$ and γ_0, depending on the values of K'_{T0} and q.

[c] Sinogeikin and Bass (1999).

[d] Karki et al. (2000).

[e] Sumino et al. (1983).

[f] Oganov et al. (2001).

[g] We used the value of $\dot{G}_0$ proposed by Jackson (1998). The error bar accounts for the ab initio data of Marton and Cohen (2002), and the experimental data of Sinelnikov et al. (1998).

[h] Value giving the best fit to ab initio data of Oganov et al. (2001) at room temperature. Note that this value is close to the experimental lower bound (Sinelnikov et al., 1998).

whereas the mean sensitivity of V_S to volumic fraction of perovskite gets negative at a depth of about 1600 km. Therefore, the ratios R associated with pure variations of perovskite are negative in a large part of the lower mantle. We have explicitly calculated sensitivities to the global volumic fraction of iron, X_{Fe} (Fig. 1c). This parameter is given by

$$X_{Fe} = X_{pv} x_{Fe}^{pv} + (1 - X_{pv}) x_{Fe}^{mw} \quad (3)$$

where X_{pv} is the volumic fraction of perovskite. The volumic fractions of iron in perovskite (x_{Fe}^{pv}) and in magnesio-wüstite (x_{Fe}^{mw}) can be calculated from X_{Fe} using the relation (3), and the definition of the iron partitioning between perovskite and magnesio-wüstite,

$$K_{Fe} = \frac{x_{Fe}^{pv}/(1 - x_{Fe}^{pv})}{x_{Fe}^{mw}/(1 - x_{Fe}^{mw})} \quad (4)$$

Table 2
Variations of temperature, pressure and composition[a]

Parameter	Minimal value	Maximal value
T_p (K)	1500	3000
X_{pv}	0.5	1.0
X_{Fe}	0.05	0.15
X_{Ca}	0.0	0.15
K_{Fe}	0.2	0.5
P/P_{PREM}	0.99	1.01

[a] T_p is the potential temperature, X_{pv} the volumic fraction of perovskite, X_{Fe} the global volumic fraction of iron, X_{Ca} the global volumic fraction of calcium, K_{Fe} the iron partitioning, and P the pressure.

Sensitivities to iron content are negative throughout the mantle, for both V_P and V_S. Within uncertainties, they are very close one another, at any depth. As a consequence, for pure anomalies of iron, values of R are close to 1.0, varying between 1.1 and 1.3 with depth. Because these values are close to those for pure anomalies of temperature, R cannot discriminate between anomalies of temperature and iron. On the other hand, R is useful to detect anomalies of perovskite, since pure anomalies of perovskite result in negative R in a large part of the lower mantle.

Calcium perovskite could also enter the composition of the lower mantle and influence the density and elastic moduli of the mantle aggregate. We used experimental measurements (Wang et al., 1996) and ab initio data (Karki and Crain, 1998), and found that the sensitivities of seismic velocities to calcium are small compared to other compositional parameters (Fig. 1d). On average, they are smaller than the sensitivities to iron by one order of magnitude. If, as expected, Ca-Perovskite enters the composition of the lower mantle for 6–12% in volume, the effects on seismic velocities would be of second order compared to other compositional parameters. For instance, a 12% anomaly of Ca-Perovskite at the bottom of the mantle would give relative anomalies of V_P and V_S of 0.1 and 0.2%, respectively. Aluminium perovskite, which is also expected to be present in the lower mantle, may have more dramatic effects, but very few data

(experimental or ab initio) are available. So far, we could not calculate robust sensitivities to aluminium and investigate its effects.

Sensitivities to partial melt are more delicate to estimate. A difficulty is that they strongly depend on the geometry of the melt (Hammond and Humphreys, 2000). Berryman (2000), however, suggested that the ratio R associated with partial melt does not depend on the melt geometry, and has a value close to 3. The values of sensitivities proposed by Hammond and Humphreys (2000) for the upper mantle may not be relevant at lower mantle pressure. Best estimates of sensitivities to partial melt are inferred from seismic studies of the base of the mantle. Williams and Garnero (1996) proposed values of $\mathrm{d}\ln V_P$ ($\mathrm{d}\ln V_S$) between -0.4 and -1.4% (-1.0 and -4.3%) for 1% of partial melt, depending on the melt geometry. These values agree with the assumption that $R \sim 3$ whatever the geometry (Berryman, 2000). According to Williams and Garnero (1996), partial melt is present in a volume of 5–40 km thickness, with a lateral surface of $20 \times 20^\circ$. Revenaugh and Meyer (1997), on another hand, invoke the presence of partial melt in a simple 15 km thick layer above the core–mantle boundary to explain observed PcP travel time residuals. Global tomographic models cannot yet resolve fine vertical structures. In global models, the effects of partial melt are therefore diluted, and a correction must be applied. The vertical resolution of global models of V_P and V_S (Masters et al., 2000; Ritsema and van Heijst, 2002) is 10 to 30 times larger than the thickness of pockets of partial melt. Accounting for this dilution, realistic values of the sensitivities of V_P and V_S per percent of partial melt are $\mathrm{d}\ln V_P = -0.03$ to -0.1%, and $\mathrm{d}\ln V_S = -0.1$ to -0.3%, respectively.

3. Direct inversion of global compressional- and shear- velocity anomalies

A straightforward approach to infer thermal and compositional variations in the mantle is to invert relative V_P and V_S anomalies ($\mathrm{d}\ln V_P$ and $\mathrm{d}\ln V_S$) directly using Eq. (1). Since there are only two data constraints, composition is represented by one single parameter, and partial melt is neglected. Chemically stratified models of convection (Davaille, 1999; Kellogg et al., 1999) have assumed the presence of a denser layer at the bottom of the mantle. Because perovskite is denser than magnesio-wüstite, a dense layer at the bottom could be significantly enriched in perovskite. Note that the accumulation of cold slabs issued from oceanic lithosphere would result in a depletion in perovskite, because harzburgite is preferentially transformed in magnesio-wüstite (Ringwood, 1991). A denser layer can also be explained by an excess of iron that could result from local contaminations from the outer core at the core–mantle boundary (Knittle and Jeanloz, 1991; Garnero and Jeanloz, 2000). As suggested by the analysis of R for pure variations of temperatue, perovskite and iron, V_P and V_S anomalies can only distinguish between temperature and perovskite. Iron trades off completely with temperature, and we have neglected it here.

We used the $\mathrm{d}\ln V_P$ and $\mathrm{d}\ln V_S$ from the model SB10L18 (Masters et al., 2000) and assumed in a first stage that there are no errors in the model. This model consists of 18 layers, and each layer is divided into blocks of equal area, with a dimension of 4° at the equator. It is straightforward to invert $\mathrm{d}\ln V_P$ and $\mathrm{d}\ln V_S$ in each block for $\mathrm{d}T$ and $\mathrm{d}X_{pv}$. We varied the sensitivities of seismic velocities according to their possible range, randomly generating sensitivities to temperature and perovskite with a Gaussian probability distribution (e.g. Press et al., 1989, pp. 191–203). The mean and standard deviation of the distribution at each depth are those displayed in Fig. 1a and b. This resulted in a collection of models for the anomalies of temperature and perovskite. The mean values of $\mathrm{d}T$ and $\mathrm{d}X_{pv}$ in each block are displayed in Figs. 2a and c and 3a and c at depths of $z = 1400$ km and $z = 2800$ km. We do not observe any prominent features at $z = 1400$ km depth (Figs. 2a and 3a). At this depth, the mantle seems relatively homogeneous (small temperature and perovskite variations). Anomalies of perovskite and temperature are distributed with a standard deviation equal to 3.7% and 190 K, respectively. At $z = 2800$ km depth, we clearly identify two regions of material enriched in perovskite (Fig. 3c). One is located beneath the Pacific, and the other one beneath Africa. Both are well correlated with positive anomalies of temperature (Fig. 2c). Regions strongly depleted in perovskite correspond to those of the circum-Pacific belt. In addition, anomalies of temperature and perovskite are here more pronounced than

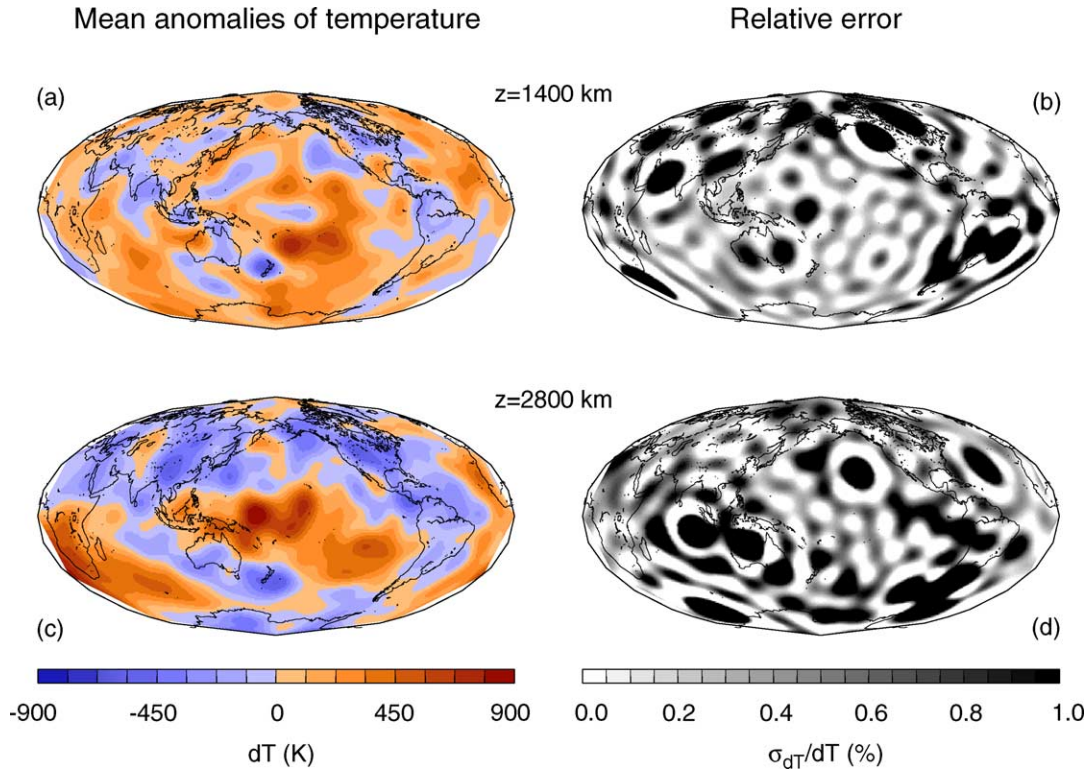

Fig. 2. Anomalies of temperature (a and c) and their relative errors (b and d) obtained with the tomographic model SB10L18 (Masters et al., 2000) at (a–b) $z = 1400$ km and (c–d) $z = 2800$ km. Relative errors are due to uncertainties in the sensitivities of seismic velocities to temperature (Fig. 1a). Maps are filtered for spherical harmonic degrees $\ell = 0$ to $\ell = 18$.

in the mid-mantle. Anomalies of perovskite (temperature) locally reach values of 12% (900 K), and the standard deviation of the distribution is 5.1% (270 K). Our results agree remarkably well with those of Forte and Mitrovica (2001), who have computed 'effective' anomalies of composition and temperature (i.e., anomalies of perovskite and temperature, including anomalies of iron) from different tomographic models and with independently calculated sensitivities.

The burning question is to know how robust these inferences are. Uncertainties on $\mathrm{d}T$ and $\mathrm{d}X_{\mathrm{pv}}$ are due to uncertainties on the tomographic models and on the sensitivities of seismic velocities to temperature and perovskite (Fig. 1a and b). Figs. 2b and d and 3b and d display the local relative errors in temperature and perovskite due to uncertainties in the sensitivities alone (errors in tomography are for the moment neglected). The relative errors are defined as the standard deviation over the mean estimated from the collection of anomalies of temperature and perovskite. Variations of temperature are relatively well constrained (Fig. 2b and d), although the relative error is close to 1.0 in some small regions. The root mean square (R.M.S.) of the relative error in temperature at each depth remains around 0.2 between $z = 1200$ km and the CMB (Fig. 4a, curve labeled 0.0). In the top layer of the lower mantle, the R.M.S. is higher, up to 0.5 at $z = 800$ km. The distributions of perovskite are much more poorly constrained (Fig. 3b and d). Between $z = 1200$ km and the CMB, the R.M.S. of the relative error for perovskite is close to 0.45, and it reaches 0.77 at $z = 800$ km (Fig. 4b, curve labeled 0.0). These errors can be viewed as conservative because only 67% of the obtained models fall within 1 standard deviation. Further, we need to include errors in the tomographic models themselves. Because tomographic models do not generally provide uncertainties, we have simulated random errors in $\mathrm{d}\ln V_{\mathrm{P}}$ and $\mathrm{d}\ln V_{\mathrm{S}}$ using Gaussian

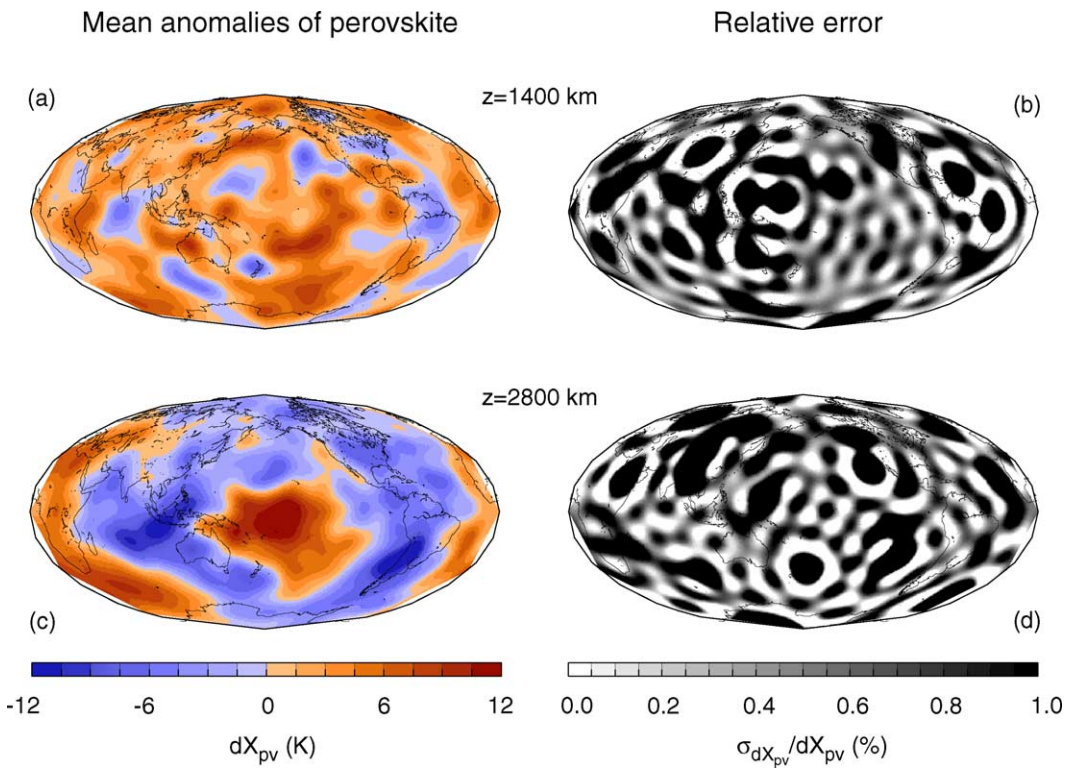

Fig. 3. Anomalies of perokskite (a and c) and their relative errors (b and d) obtained with the tomographic model SB10L18 (Masters et al., 2000) at (a–b) $z = 1400$ km and (c–d) $z = 2800$ km. Relative errors are due to uncertainties in the sensitivities of seismic velocities to perovskite (Fig. 1b). Maps are filtered for spherical harmonic degrees $\ell = 0$ to $\ell = 18$.

statistics. We simulated inversions with increasing relative error in the tomographic models, generating each time a collection of models for anomalies of temperature and perovskite. In each case, we calculated the mean and standard deviation in each block, and then computed the R.M.S. of the relative error in dT and dX_{pv} as a function of depth (Fig. 4). As previously, the sensitivities are varied within their ranges shown in Fig. 1. The R.M.S. relative error on perovskite increases very rapidly with increasing error in tomography, and becomes bigger than 1 for relative errors of the velocity anomalies close to 0.4 (Fig. 4b). A R.M.S. relative error bigger than 1 means that the average error exceeds the average signal and the inference is not robust. The R.M.S. relative error on temperature also increases with depth, but much slower. Temperature remains robust at most depths.

It is not unreasonable to assume relative errors in velocity anomalies in excess of 0.3 as has been found by directly comparing several tomographic models (Resovsky and Ritzwoller, 1999), or by full model space search (Beghein et al., 2002). Deterministic inferences of composition obtained from a direct inversion of Eq. (1) are thus not robust at present, and temperature estimates contain at least 50% errors.

Using relative V_Φ anomalies (d ln V_Φ) instead of relative V_{P} anomalies results in smallest relative errors on temperature and composition. V_Φ anomalies, however, are not inferred directly from seismic data, but are constructed from V_{P} and V_{S}. As a consequence, relative errors in d ln V_Φ are roughly twice the relative errors in d ln V_{P} and d ln V_{S}, and the final conclusion would be the same.

4. Constraints from the ratio of relative shear to compressional velocity

The ratio R of the relative V_{S} anomalies to the relative V_{P} anomalies (Eq. (2)) is often used to

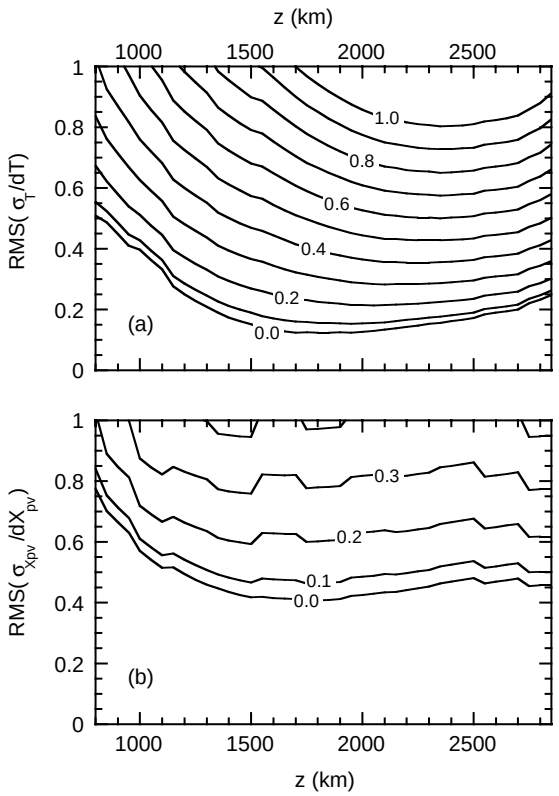

Fig. 4. Root mean square relative error in the anomalies of (a) temperature and (b) perovskite as a function of depth. In addition to the uncertainties in the sensitivities of seismic velocities, we modelled Gaussian errors in the relative V_P and V_S anomalies. The assumed relative errors are indicated on each curve.

scale compressional velocity from shear velocity as a function of depth in global tomographic models. If one has access to independent $\mathrm{d}\ln V_P$ and $\mathrm{d}\ln V_S$, R can be used as a diagnostic of the origin of these anomalies. Using P and S travel time residuals, Robertson and Woodhouse (1997) found $R = 1.58$ for the upper mantle. Masters et al. (2000) have recently compared average profiles of R for several joint models of V_P and V_S anomalies. All of them show significant variations with depth. In particular, the models of Su and Dziewonski (1997) and the model SB10L18 (Masters et al., 2000) show an increase of R with depth. For SB10L18, they found $R = 1.62$ at $z = 1400$ km, and $R = 2.52$ at $z = 2800$ km. On the basis of median values, Masters et al. (2000) proposed a thermal origin for the anomalies of velocity, except for areas beneath the Pacific and Africa at the very bottom of the mantle, where they found that ratios are different. Saltzer et al. (2001) also clearly observed laterally varying values. Full histograms of block-by-block estimates of R clearly provide more information about the lateral variations of R at a given depth. We have computed ratios for each block of the models SB10L18 (Masters et al., 2000) and 12RTS (Ritsema and van Heijst, 2002), and binned them (Fig. 5). Note that very small values in the denominator give high values of the ratio if not balanced by small values of the $\mathrm{d}\ln V_S$. We selected blocks for which the absolute value of the ratio is smaller than 10. Most blocks satisfy this condition (355 out of 408 for SB10L18 at $z = 2800$ km). The important feature is that histograms do not peak sharply around the mean value of R, but show significant dispersion. It is interesting to note that the dispersion is more important at the bottom of the mantle.

Fig. 6 shows histograms of the relative frequency of R obtained for pure variations of temperature (plain curves), perovskite (dotted curves) and iron (dashed curves). We constructed these histograms by varying the sensitivities of seismic velocities within their uncertainties (Fig. 1). For each individual case, a value of R is computed and binned. Due to uncertainties in the sensitivities, R will be dispersed even if one considers pure variations of one single parameter. Pure variations of temperature give values of R close to 1.6, regardless of the depth. The dispersion is very small (the standard deviation is around 0.2) and increases slightly with depth. Pure variations of iron lead to similar distributions. The mean value of R varies between 1.1 and 1.3, depending on the depth, with a standard deviation of about 0.2. Pure variations of perovskite show a very different behavior. At the top of the lower mantle ($z = 700$ km), they give values of R around 0.9, with a small dispersion. Dispersion then increases dramatically with depth, and the mean value of R shifts towards negative values. At the bottom of the lower mantle, the mean value of R is -4.1 and its standard deviation 2.0.

It is clear, from these results, that purely thermal or purely compositional anomalies cannot explain the observed histograms (Fig. 5). Rather, a mix of several effects, including uncertainties in the tomogarphic models, is responsible for the observed dispersion of histograms. At close inspection of Eq. (2), it becomes

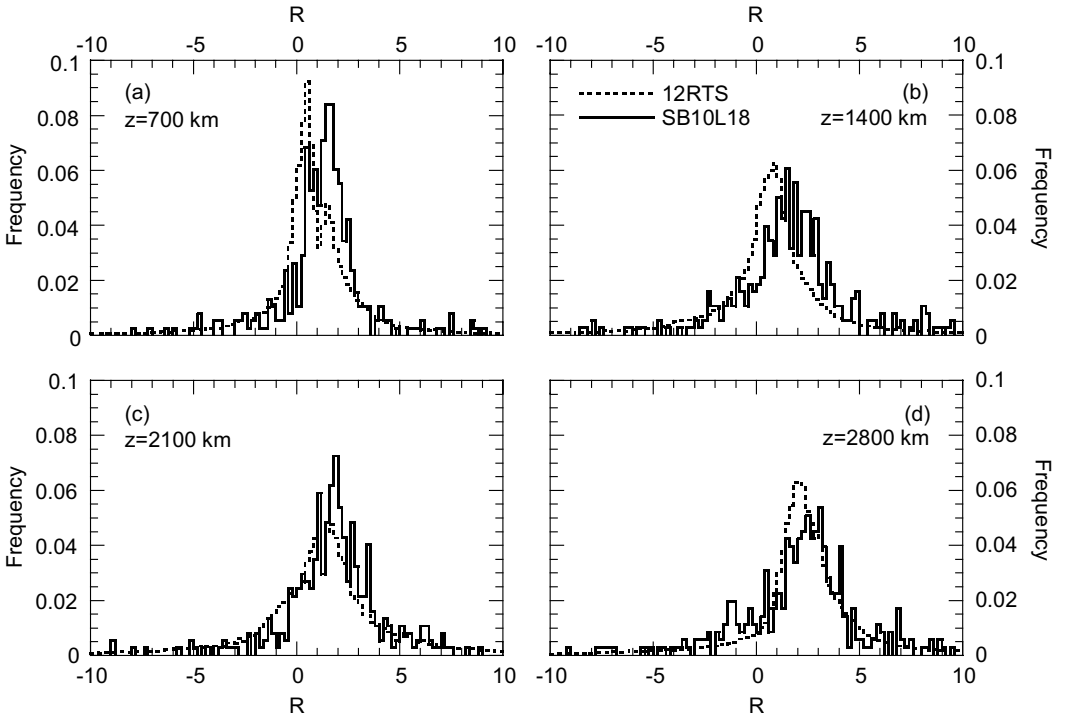

Fig. 5. Histograms of $R = \mathrm{d}\ln V_S/\mathrm{d}\ln V_P$ as a function of depth, and for two global models of V_P and V_S anomalies. Plain and dotted curves correspond to the models SB10L18 (Masters et al., 2000) and 12RTS (Ritsema and van Heijst, 2002), respectively. Depths represented are (a) $z = 700$ km, (b) $z = 1400$ km, (c) $z = 2100$ km and (d) $z = 2800$ km.

clear that the histograms of R cannot provide any quantitative statement about the bounds of $\mathrm{d}T$ and $\mathrm{d}C$. Indeed, any scaling $\alpha\,\mathrm{d}T + \alpha\,\mathrm{d}C$ will result in the same R, meaning that the amplitude of the cause remains undetermined. The histograms however contain the important qualitative information that temperature alone cannot be responsible for the observed tomographic maps.

5. Robust constraints from the observed velocity anomalies

The ambiguity found in the interpretation of R is lifted if the velocity anomalies are analysed directly. The idea is that the bounds of $\mathrm{d}T$, $\mathrm{d}C$ and $\mathrm{d}F$ are responsible for the shape of the observed histograms of $\mathrm{d}\ln V_P$ and $\mathrm{d}\ln V_S$. Using the sensitivities calculated in Section 2 together with Eq. (1), we generated synthetic values of velocity histograms for given ranges for $\mathrm{d}T$, $\mathrm{d}C$ and $\mathrm{d}F$, and compared them to the results of tomography. To make robust comparisons, we need to include possible errors in tomography. In the synthetic histograms, we have simulated these errors by adding a term on the right hand side of Eq. (1). The errors are drawn in a Gaussian distribution with a standard deviation $\Delta(\mathrm{d}\ln V_P)$ and $\Delta(\mathrm{d}\ln V_S)$ (Table 3). This standard deviation is obtained by multiplying the R.M.S. amplitude of SB10L18 by a relative error. The relative error is taken from a full model space search applied to normal mode and surface wave data (Beghein et al., 2002). Although SB10L18 also contains body wave data, the relative errors of Beghein et al. (2002) are in good agreement with direct comparisons of different tomographic models (Resovsky and Ritzwoller, 1999), and thus represent the currently best estimates of errors in global tomographic models.

We made a systematic search for bounds in temperature and composition. For each obtained synthetic histogram, we computed the variance reduction with respect to the observed histogram. A selection of combinations is listed in Table 4, and some histograms are

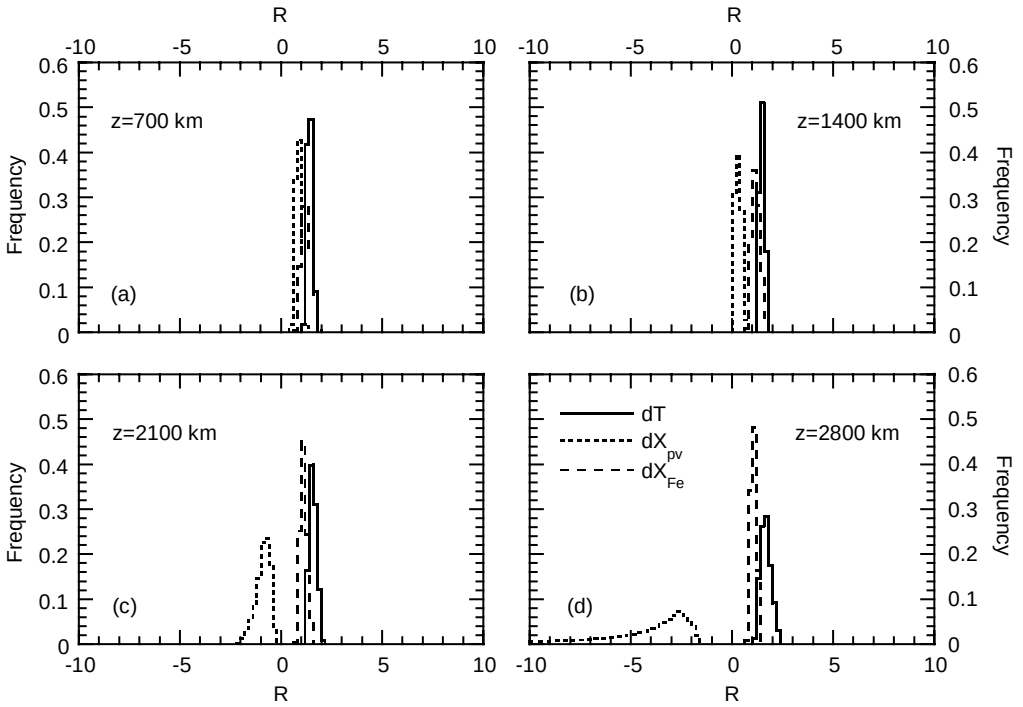

Fig. 6. Histograms of $R = \mathrm{d}\ln V_S/\mathrm{d}\ln V_P$ for different causes. Plain, dotted and dashed curves correspond to pure variations of temperature, perovskite, and iron, respectively. Depths represented are (a) $z = 700$ km, (b) $z = 1400$ km, (c) $z = 2100$ km and (d) $z = 2800$ km.

drawn in Fig. 7 (thick red curves) and compared to the observed ones (thin black curves). In the top and mid-lower mantle, moderate (up to 300 K) anomalies of temperature explain the observed histograms without the need of compositional anomalies (combinations 1, 6 and 11). For both $\mathrm{d}\ln V_P$ and $\mathrm{d}\ln V_S$, synthetic histograms fit observed histograms with a variance reduction higher than 89%. Other combinations, and in particular asymmetric combinations (e.g., 2, 7 and 12), fit observations less well. V_P and V_S anomalies therefore provide good constraints on the temperature range. Moderate (up to 6%) anomalies in the volumic fraction of perovskite also give good fits to the observed histograms (e.g., combinations 3, 9 and 13), but larger variations (8% and more) fail to explain histograms for $\mathrm{d}\ln V_P$ (e.g., combinations 5, 10 and 14, Fig. 7b, d and f). Variations in the volumic fraction of iron up to 2% do not significantly change the variance reduction, and are therefore consistent with the observations. At the bottom of the mantle,

Table 3
Errors $\Delta(\mathrm{d}\ln V)$ on the relative anomalies of seismic velocities[a]

Depth (km)	V_P			V_S		
	R.M.S. (10^{-3})	Relative errors	$\Delta(\mathrm{d}\ln V)$ (10^{-3})	R.M.S. (10^{-3})	Relative errors	$\Delta(\mathrm{d}\ln V)$ (10^{-3})
700	1.2	0.35	0.42	2.2	0.62	1.36
1400	0.7	0.65	0.46	1.7	0.31	0.53
2100	1.5	0.50	0.75	3.2	0.36	1.15
2800	1.7	0.78	1.33	6.2	0.56	3.47

[a] The $\Delta(\mathrm{d}\ln V)$ are computed from the R.M.S. amplitude of SB10L18 (Masters et al., 2000), and the relative errors from Beghein et al. (2002).

Table 4
Selected best combinations of thermal and compositional anomalies[a]

No.	dT (K)		dX_{pv} (%)		dX_{Fe} (%)		dF (%)	χ_P (%)	χ_S (%)
	Min	Max	Min	Max	Min	Max			
$z = 700$ km									
1	−300	300	0	0	0	0	0	93.0	89.4
2	−100	300	0	0	0	0	0	57.9	48.3
3	−300	300	−6	4	−2	2	0	90.1	91.1
4	−300	300	−12	6	0	0	0	72.3	81.6
5	−300	300	−12	6	−2	3	0	66.8	82.1
$z = 1400$ km									
6	−200	300	0	0	0	0	0	89.6	90.2
7	−100	400	0	0	0	0	0	67.2	77.2
8	−200	300	−4	6	0	0	0	91.0	89.8
9	−200	300	−4	6	−1	1	0	90.0	90.5
10	−200	300	−6	12	0	0	0	75.8	88.4
$z = 2100$ km									
11	−300	300	0	0	0	0	0	92.8	93.0
12	−300	100	0	0	0	0	0	47.2	39.1
13	−300	300	−6	2	−2	2	0	85.9	90.9
14	−300	300	−6	12	−2	2	0	71.9	93.6
$z = 2800$ km									
15	−400	400	0	0	0	0	0	94.3	59.6
16	−400	400	−14	6	0	0	0	93.6	81.9
17	−400	400	0	0	−3	3	0	94.1	65.6
18	−400	400	−14	6	−1	2	0	88.5	81.1
19	−400	400	−6	4	−1	2	0	92.4	65.0
20	−500	350	−14	10	−1	2	0	94.7	82.5
21	−500	350	−6	12	−1	2	0	85.8	72.7
22	−500	350	−14	6	−1	2	0	94.7	81.7
23	−500	350	−10	10	−1	2	0	94.0	78.0
24	−500	350	−10	14	−1	2	0	92.1	73.1
25	−500	350	−14	10	0	3	0	88.3	79.1
26	−500	350	−14	10	−3	0	0	61.2	76.9
27	−350	500	−14	10	−1	2	0	81.1	70.0
28	−600	300	−12	6	−1	2	0.1	94.5	80.4

[a] Each case is defined by the minimal and maximal values of the anomalies of temperature (dT) and composition (dX_{pv} and dX_{Fe}), and by the rate of partial melt (dF). χ_P and χ_S are the output variance reduction in respect with the histograms of V_P and V_S anomalies predicted by SB10L18.

temperature variations alone do not fit the observed d ln V_S histograms (combination 15, Fig. 7g). The origin of velocity anomalies can thus not be purely thermal. The compositional component is also not fully explained by variations in the volumic fraction of iron (combination 17). Furthermore, moderate (up to 6%) variations in perovskite do not fit the observation, even if variations in iron are considered (combination 19). Large variations of perovskite, with depletion (enrichment) up to 14% (10%), are required to explain the observed histogram of d ln V_S (e.g., combinations 16, 18 and 20). A large number of combinations explain the observed histograms with a variance reduction higher than 80%. Variations in perovskite and in iron can be simultaneously incorporated (combinations 18 and 20), but lead to histograms close to those obtained for anomalies of temperature and perovskite alone. Combinations for which enrichment in perovskite is stronger than depletion in perovskite do not explain SB10L18 (combination 21). Similarly, the variance reduction decreases significantly (to 75%) if the amplitude of hot anomalies is stronger than that of cold anomalies (combination 27). Finally, in combination 28 we accounted for 0.1% (locally, 1–3%) of

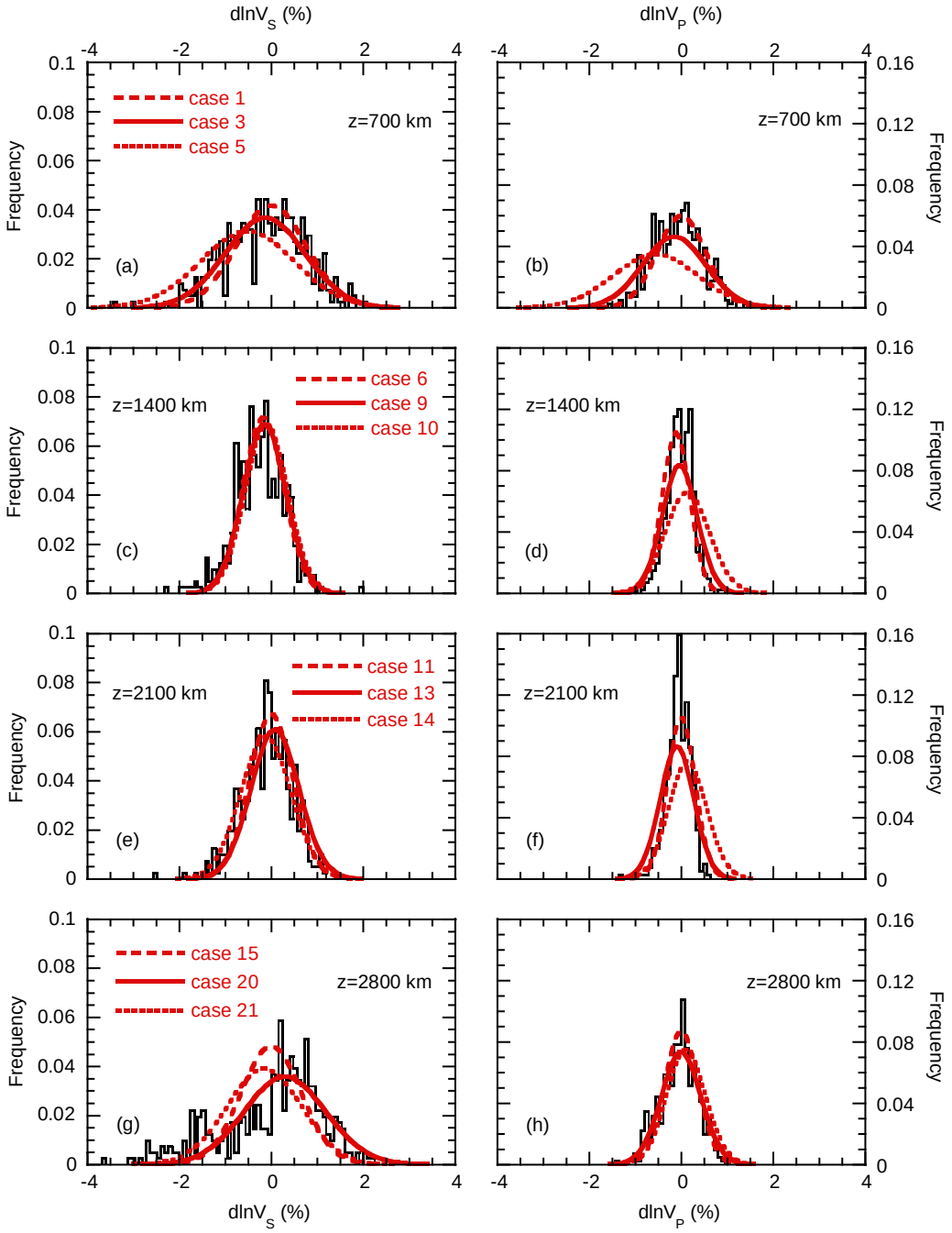

Fig. 7. Selected histograms (bold red curves) of relative V_S (left column) and V_P (right column) anomalies. The black curves represent the histograms for SB10L18. (a–b) $z = 700$ km, combinations 1, 3 and 5 in Table 4; (c–d) $z = 1400$ km, combinations 6, 9 and 10; (e–f) $z = 2100$ km, combinations 11, 13 and 14; (g–h) $z = 2800$ km, combinations 15, 20 and 21.

partial melt. A slightly different range of temperature variation is then required to fit SB10L18, but strong perovskite anomalies are still needed.

In the top and mid-lower mantle, the comparison between observed and synthetic histograms gives a relatively homogeneous image of the mantle. Temperature variations reach a maximum of ±300 K. Local variations in the volumic fractions of perovskite and iron are possible, but limited in amplitude. At the bottom of the mantle, histograms clearly suggest the presence of strong chemical heterogeneities (as variations in the volumic fraction of perovskite), and possibly iron. Large lateral anomalies of temperature (up to 500 K) are likely at these depths. Although not all variations can be distinguished unambiguously, a robust feature is the need for regions with strong depletion (up to 14%) and enrichment (up to 10%) in perovskite. Variations in iron and/or the presence of partial melt still require strong variations in perovsike. Also robust is that the variations in iron, if present, should not exceed 2 to 3%.

The shape of histograms of velocity anomalies contains important information, since it is directly related to the distributions of anomalies of temperature and composition. Using average values of the ratio R, Karato and Karki (2001) argued for significant anelastic effects and a variety of chemical components at the bottom of the mantle. Full comparisons of synthetic and predicted histograms of velocity anomalies suggest that anomalies of temperature and perovskite (and possibly iron) are enough to explain the observations.

6. Importance of the density variations

As seen above, the distribution of R qualitatively suggests that temperature anomalies alone are not able to explain the observed histograms. The shape of the histograms of relative velocity anomalies provides quantitative constraints, but some trade-offs remain. To further constrain the analysis, we suggest that density distributions are needed.

The existence of trade-offs between anomalies of temperature and composition is not so surprising, given the nature of the sensitivities of velocity (Fig. 1). Accurate determinations of lateral variations of temperature and composition require the knowledge of the density distributions, because density has

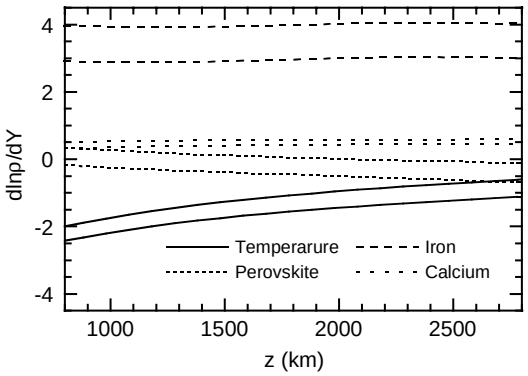

Fig. 8. Sensitivities of density to temperature ($\times 10^5$, plain curves), perovskite ($\times 10$, dotted curves), iron ($\times 10$, long dashed curves) and calcium ($\times 10$, short dashed curves) as a function of depth. In each case, we represent the upper and lower value of the sensitivity, which correspond to 1 standard deviation around the average. Averages and standard deviations are calculated from the predicted models that fit PREM within 1%.

a different sensitivity to composition than seismic velocities. The knowledge of density is particularly important for estimating iron anomalies in the upper (Forte and Perry, 2000; Deschamps et al., 2002) and lower mantle (Forte and Mitrovica, 2001; Karato and Karki, 2001). The reason is that density is an increasing function of the volumic fraction of iron, whereas seismic velocities are decreasing functions of iron content. On the other hand, both density and seismic velocities decrease with increasing temperature.

We have explicitely computed sensitivities of density to temperature, perovskite, iron and calcium in the lower mantle (Fig. 8). Again, it is worth noting that throughout the mantle the sensitivity of density to calcium is very small compared to sensitivities to other parameters. Variations of Ca-Perovskite, if present, should not influence density anomalies. Throughout the mantle, the sensitivity of density to temperature is negative, whereas the sensitivity to iron is positive. This different behaviour of density with temperature and iron content is the reason why density anomalies can discriminate between anomalies of temperature and iron, the main trade-off. Although, the sensitivity of density to perovskite is similar to that of V_S, perovskite content is better determined simply because temperature and iron are tightly constrained.

A summary of the main properties of the different sensitivities in the lowermost ($z = 2000$ km) mantle

Table 5
General characteristic of sensitivities in the lowermost mantle ($z \geq 2000$ km)[a]

	V_P		V_S		Density	
	Sign	Variation	Sign	Variation	Sign	Variation
Temperature	−	↓	−	↓	−	↓
Perovskite	+	↓	−	↑	−	↑
Iron	−	↓	−	↓	+	↑

[a] For each sensitivity, two characteristics are listed: its sign, and the variation of its absolute value with depth. The descending arrow (↓) indicates a decreasing function of depth, and the ascending arrow (↑) indicates an increasing function of depth.

can be found in Table 5. Because each unknown temperature, perovskite and iron has a different signature, the analysis of $\mathrm{d}\ln V_P$, $\mathrm{d}\ln V_S$, and $\mathrm{d}\ln \rho$ can determine temperature and the main compositional variations. Histograms of density anomalies are thus very important, since they are able to discriminate between the anomalies of iron and temperature. Mapping the density anomalies from normal modes is still controversial (Resovsky and Ritzwoller, 1999; Masters et al., 2000; Ishii and Tromp, 2001; Kuo and Romanowicz, 2002), but Resovsky and Trampert (2003) have recently proposed robust distributions of density anomalies using a neighbourhood algorithm. These distributions clearly indicate the presence of dense material at the bottom of the mantle. A preliminary comparison with synthetic histograms suggests that anomalies of iron could reach 3% in the lowermost mantle.

7. Conclusions

Distributions of velocity anomalies are, to date, the most detailed information concerning the thermal and chemical structure of the mantle. Directly inverting relative V_P and V_S anomalies for anomalies of temperature and composition within the uncertainties of current tomographic models and mineral physics data shows that compositional variations are not robust. Histograms of R, and in particular their dispersion, indicate qualitatively that the origin of V_P and V_S anomalies is not purely thermal, but also compositional. To estimate the range of temperature and compositional variations, we propose to use the histograms of the relative V_P and V_S anomalies. In the lowermost part of the mantle, this analysis suggests strong (from −14 to 10%) variations of perovskite and possible variations in iron (from −1 to 2%). This result is in agreement with the model of Kellogg et al. (1999), where a dense layer (positive variations of perovskite) is displaced by descending slabs (negative variations of perovskite). The rest of the mantle can be explained by modest temperature variations alone, but chemical variations cannot be excluded. Several combinations of perovskite, iron and temperature anomalies fit the observed histograms equally well. This trade-off is likely to be broken by additional analysis of density variations.

Acknowledgements

We thank two anonymous reviewers for very helpful suggestions. This work was financed by the Geodynamics Institute at Utrecht University.

References

Becker, T.W., Kellogg, J.B., O'Connell, R.J., 1999. Thermal constraints on the survival of primitive blobs in the lower mantle. Earth Planet. Sci. Lett. 171, 351–365.

Beghein, C., Resovsky, J.S., Trampert, J., 2002. P and S tomography using normal-mode and surface waves data with a neighbourhood algorithm. Geophys. J. Int. 149, 646–658.

Berryman, J.G., 2000. Seismic velocity decrement ratios for regions of partial melt in the lower mantle. Geophys. Res. Lett. 27, 421–424.

Brodholt, J., Alfredsson, M., Price, D., 2003. Are computational mineral physics results accurate enough to detect chemical heterogeneity in the Earth's mantle? Geophys. Res. Abs. 5, abstract #7638, CD-ROM.

Davaille, A., 1999. Simultaneous generation of hotspots and superswells by convection in a heterogeneous planetary mantle. Nature 402, 756–760.

Deschamps, F., Trampert, J., Snieder, R., 2002. Anomalies of temperature and iron in the uppermost mantle inferred from gravity data and tomographic models. Phys. Earth Planet. Inter. 129, 245–264.

Deschamps, F., Trampert, J., 2003. Towards a lower mantle reference temperature and composition. Earth Planet. Sci. Lett., in press.

Forte, A.M., Mitrovica, J.X., 2001. Deep-mantle high-viscosity flow and thermochemical structure inferred from seismic and geodynamic data. Nature 410, 1049–1056.

Forte, A.M., Perry, A.C., 2000. Seismic–geodynamic evidence for a chemically depleted continental lithosphere. Science 290, 1940–1944.

Garnero, E.J., Jeanloz, R., 2000. Fuzzy patches on the Earth's core–mantle boundary? Geophys. Res. Lett. 27, 2777–2780.

Hammond, W.C., Humphreys, E.D., 2000. Upper mantle seismic wave velocity: effects of realistic partial melt geometries. J. Geophys. Res. 105, 10975–10986.

Ishii, M., Tromp, J., 2001. Even-degree lateral variations in the Earth's mantle constrained by free oscillations and free-air gravity anomalies. Geophys. J. Int. 145, 77–96.

Jackson, I., 1998. Elasticity, composition and temperature of the Earth's lower mantle: a reappraisal. Geophys. J. Int. 134, 291–311.

Karato, S.-I., Karki, B.B., 2001. Origin of lateral variation of seismic wave velocities and density in the deep mantle. J. Geophys. Res. 106, 21771–21783.

Karki, B.B., Crain, J., 1998. First-principles determination of elastic properties of $CaSiO_3$ perovskite at lower mantle pressures. Geophys. Res. Lett. 25, 2741–2744.

Karki, B.B., Wentzcovitch, R.M., de Gironcoli, S., Baroni, S., 2000. High-pressure lattice dynamics and thermoelasticity of MgO. Phys. Rev. B 61, 8793–8800.

Kellogg, L.H., Hager, B.H., van der Hilst, R.D., 1999. Compositional stratification in the deep mantle. Science 283, 1881–1884.

Kennett, B.L.N., Engdahl, E.R., Bulland, R., 1995. Constraints on seismic velocities in the Earth from travel times. Geophys. J. Int. 122, 108–124.

Knittle, E., Jeanloz, R., 1991. Earth's core–mantle boundary: results of experiments at high pressures and temperatures. Sciences 251, 1438–1443.

Kuo, C., Romanowicz, B., 2002. On the resolution of density anomalies in the Earth's mantle using spectral fitting of normal-mode data. Geophys. J. Int. 150, 162–179.

Labrosse, S., Tackley, P.J., 2001. Heat transfer by mantle convection in plate tectonics regime: preliminary 2D results, in: Proceedings of the Seventh workshop on Numerical Modeling of Mantle Convection and Lithosphere Dynamics, http://link.springer.de/link/service/journals/10069/conferen/Aussois/index.html.

Marton, F.C., Cohen, R.E., 2002. Constraints on lower mantle composition from molecular dynamics simulations of $MgSiO_3$ perovskite. Phys. Earth Planet. Inter. 134, 239–252.

Masters, G., Laske, G., Bolton, H., Dziewonski, A.M., 2000. The relative behavior of shear velocity, bulk sound speed, and compressional velocity in the mantle: implications for chemical and thermal structure, in: Karato, S.I., et al. (Ed.), Earth's Deep Interior: Mineral Physics and Tomography from the Atomic to the Global Scale, Geophysical Monograph Series, vol. 117. AGU, Washington, DC, pp. 63–87.

Oganov, A.R., Brodholt, J.P., Price, G.D., 2001. Ab initio elasticity and thermal equation of state of $MgSiO_3$ perovskite. Earth Planet. Sci. Lett. 184, 555–560.

Press, W.H., Flannery, B.P., Teukolsky, S.A., Vetterling, W.T., 1989. Numerical Recipes. Cambridge University Press, Cambridge, 702 pp.

Resovsky, J.S., Ritzwoller, M., 1999. A degree 8 mantle shear velocity model from normal mode observations below 3 mHz. J. Geophys. Res. 104, 993–1014.

Resovsky, J.S., Trampert, J., 2003. Using probabilistic seismic tomography to test mantle velocity–density relationships. Earth Planet. Sci. Lett. 215, 121–134.

Revenaugh, J., Meyer, R., 1997. Seismic evidence of partial melt within a possibly ubiquitous low-velocity layer at the base of the mantle. Science 277, 670–673.

Ringwood, A.E., 1991. Phase transformations and their bearing on the constitution and dynamics of the mantle. Geochim. Cosmochim. Acta 55, 2083–2110.

Ritsema, J., van Heijst, H.-J., 2002. Constraint on the correlation of P- and S-wave velocity heterogeneity in the mantle from P, PP, PPP and PKPab traveltimes. Geophys. J. Int. 149, 482–489.

Robertson, G.S., Woodhouse, J.H., 1997. Comparison of P- and S-station corrections and their relationship to upper mantle structure. J. Geophys. Res. 102, 27355–27366.

Saltzer, R.L., van der Hilst, R.D., Kárason, H., 2001. Comparing P and S wave heterogeneity in the mantle. Geophys. Res. Lett. 28, 1335–1338.

Sinelnikov, Y.D., Chen, G., Neuville, D.R., Vaughan, M.T., Liebermann, R.C., 1998. Ultrasonic shear wave velocities of $MgSiO_3$ perovskite at 8 GPa and 800 K and lower mantle composition. Science 28, 677–679.

Sinogeikin, S.V., Bass, J.D., 1999. Single crystal elasticity of MgO at high-pressure. Phys. Rev. B 59, 14141–14144.

Su, W.-J., Dziewonski, A.M., 1997. Simultaneous inversion for 3D variations in shear and bulk velocity in the mantle. Phys. Earth Planet. Inter. 100, 135–156.

Sumino, Y., Anderson, O.L., Suzuki, I., 1983. Temperature coefficients of elastic constants of single crystal MgO between 80 and 1300 K. Phys. Chem. Mineral. 9, 38–47.

Trampert, J., Vacher, P., Vlaar, N., 2001. Sensitivities of seismic velocities to temperature, pressure and composition in the lower mantle. Phys. Earth Planet. Inter. 124, 255–267.

Wang, Y., Weidner, D.J., Guyot, F., 1996. Thermal equation of state of CaSiO3 perovskite. J. Geophys. Res. 101, 661–672.

Williams, Q., Garnero, E.J., 1996. Seismic evidence of partial melt at the base of the mantle. Science 273, 1528–1530.

7. B. Hetenyi, F. De Angelis, P. Giannozzi, R. Car, *J. Chem. Phys.* **120**, 8632 (2004).
8. A. Luzar, D. Chandler, *J. Chem. Phys.* **98**, 8160 (1993).
9. G. A. Jeffrey, *Introduction to Hydrogen Bonding* (Oxford Univ. Press, New York, 1997), pp. 11–12.
10. K. R. Wilson *et al.*, *J. Phys. Condens. Matter* **14**, L221 (2002).
11. S. Myneni *et al.*, *J. Phys. Condens. Matter* **14**, L213 (2002).
12. H. Bluhm *et al.*, *J. Phys. Condens. Matter* **14**, L227 (2002).
13. J.-H. Guo *et al.*, *Phys. Rev. Lett.* **89**, 137402 (2002).
14. K. R. Wilson *et al.*, *Rev. Sci. Instrum.* **75**, 725 (2004).
15. U. Bergmann *et al.*, *Phys. Rev. B* **66**, 092107 (2002).
16. See supporting data on *Science* Online.
17. R. Corban, M. D. Zeidler, *Ber. Bunsenges. Phys. Chem.* **96**, 1463 (1992).
18. We caution that this method for determining ΔE could imply an oversimplification of the actual spectrum. We have assumed that the pre-edge intensity arises exclusively from molecules with one or two broken-donor H bonds, whereas the post-edge intensity is a result of fully coordinated species. Under this assumption, the pre-edge intensity can be expressed as

$$I_{pre} \propto \sigma_{pre} \exp(-E_{pre}/RT)$$

where σ_{pre} is the cross section at 535 eV for the broken-donor bond configurations, and E_{pre} is the average energy of molecules in these configurations. A similar expression can be written for the post-edge intensity, and the ratio of intensities can then be written as

$$\ln(I_{post}/I_{pre}) = -\Delta E/RT + \ln(a)$$

where a is a constant with respect to temperature. If other H-bonding configurations also produce appreciable absorption in these regions, we would expect deviations from linearity. Therefore, the quality of the linear fit evident in Fig. 2 is an indication that this simple model is appropriate, at least as a first approximation. This type of analysis is similar to that used to interpret the temperature-dependent Raman spectrum of liquid water (*19*, *20*).
19. D. E. Hare, C. M. Sorenson, *J. Chem. Phys.* **93**, 6954 (1990).
20. G. E. Walrafen, in *Water: A Comprehensive Treatise*, F. Franks, Ed. (Plenum, New York, 1972), vol. 1.
21. S. J. Suresh, V. M. Naik, *J. Chem. Phys.* **113**, 9727 (2000).
22. R. L. Blumberg *et al.*, *J. Chem. Phys.* **80**, 5230 (1984).
23. The energetic cutoff is defined such that two molecules are considered H-bonded to one another only if the computed pair potential is less than –4 kcal/mol. Furthermore, if any molecule has more than four H bonds according to the cutoff, only the four strongest bonds are considered.
24. F. H. Stillinger, A. Rahman, *J. Chem. Phys.* **60**, 1545 (1974).
25. J. M. Sorenson *et al.*, *J. Chem. Phys.* **113**, 9149 (2000).
26. Supported by the National Defense Science and Engineering Graduate Fellowship Program (C.D.C.) and by the Chemical Sciences Division of the U.S. Department of Energy. This research was carried out at the Advanced Light Source (ALS) beamline 8.0.1, Lawrence Berkeley National Laboratory. The Advanced Light Source is supported by the Office of Basic Energy Sciences, Materials Sciences Division, of the U.S. Department of Energy under contract DE-AC03-76SF00098 at Lawrence Berkeley National Laboratory. We thank the ALS staff, including M. Gilles, B. Rude, and J. Denlinger, for assistance.

Supporting Online Material
www.sciencemag.org/cgi/content/full/306/5697/851/DC1
Materials and Methods
Figs. S1 and S2
References

9 July 2004; accepted 23 September 2004

Probabilistic Tomography Maps Chemical Heterogeneities Throughout the Lower Mantle

Jeannot Trampert,[1]* Frédéric Deschamps,[1] Joseph Resovsky,[1] Dave Yuen[2]

We obtained likelihoods in the lower mantle for long-wavelength models of bulk sound and shear wave speed, density, and boundary topography, compatible with gravity constraints, from normal mode splitting functions and surface wave data. Taking into account the large uncertainties in Earth's thermodynamic reference state and the published range of mineral physics data, we converted the tomographic likelihoods into probability density functions for temperature, perovskite, and iron variations. Temperature and composition can be separated, showing that chemical variations contribute to the overall buoyancy and are dominant in the lower 1000 kilometers of the mantle.

To understand the nature of mantle convection, it is essential to quantify thermal and compositional contributions to the density variations that drive the solid-state flow. Although seismic tomography is probably the best probe for Earth's three-dimensional structure, its main constraint is on wave speeds rather than density. It has therefore been common practice in tomography to prescribe a scaling between density and velocity variations (*1*) and invert for velocity only. Such a scaling is justified if a single cause is responsible for the observed variations. Temperature-induced ratios of relative density to relative shear wave speed variations between 0.2 to 0.4 have been measured (*2*, *3*) and are compatible with geodynamic data, combined with specific viscosity profiles (*4*, *5*). This, together with evidence from seismology that slabs penetrate deep into the mantle (*6*, *7*), led to the view that mantle dynamics is dominated by thermally driven whole-mantle convection (*8*). Chemical buoyancy (*9*) was introduced mainly to explore the possible thermochemical nature of D″ in terms of a primordial layer (*10–14*), subducted oceanic crust (*14–16*), or chemical reactions with the core (*17*). These Boussinesq calculations, however, are not realistic, because the simulated high-density contrasts are not compatible with the observed seismic velocities and a plausible mineralogic model (*18*). When an extended Boussinesq or compressible calculation is used, the required density contrasts are reduced (*19–21*). More interestingly, in models where thermal expansivity decreases with depth, thermochemical superplumes are seen to develop (*20–22*), not unlike those found under Africa and the Pacific in tomography (*23*, *24*). With improving resolution of seismic velocities and, especially, of density, indirect evidence has emerged suggesting that compositional heterogeneity is present in the lower mantle (*5*, *25–32*). In an effort to reconcile evidence from various research fields, dynamical models with a strong compositional component (*33–35*) have challenged the classic view of thermally driven mantle convection.

Owing to trade-offs between temperature and composition, wave speeds alone are not sufficient to infer their variations, and density constraints should be included (*5*, *31*, *36*). Normal modes require weak and/or negative correlations between density and shear wave speed variations throughout most of the lower mantle (*28*), but amplitudes of density are difficult to infer (*37*). We represent the seismic constraints with more complete likelihoods, rather than individual models, and have extended the work of Resovsky and Trampert (*32*) to spherical harmonic degree 6 for relative variations of bulk sound ($d\ln V_\Phi$) and shear wave speed ($d\ln V_s$), density ($d\ln\rho$), and topography at the 670-km discontinuity and at the core-mantle boundary (CMB). In addition to providing a full uncertainty analysis (errors and trade-offs), representing the data as likelihoods of seismic parameters allows a subsequent incorporation of additional data constraints. Most often, geodynamic data are jointly inverted with the seismologic data (*5*, *28*), but in our approach, it is more efficient to filter a posteriori the purely seismic models by retaining only those that fit the gravity field within

[1]Department of Earth Sciences, Utrecht University, Post Office Box 80021, 3508 TA Utrecht, Netherlands. [2]Minnesota Supercomputer Institute, Department of Geophysics University of Minnesota, Minneapolis, MN 55455–0219, USA.

*To whom correspondence should be addressed. E-mail: jeannot@geo.uu.nl

its error bars (*37*). The final likelihoods for wave speeds and density variations are close to Gaussian and can thus be represented by a mean and standard deviation (Table 1). They are a complete and compact representation of all long-period seismic data, compatible with the observed gravity field, and robust (defined here as >1 SD) mean variations of wave speeds agree with previous work (*28*, *29*) (Fig. 1).

Although correlations and average amplitudes can be a good indicator of chemical heterogeneities (*37*), we directly inverted the seismic likelihoods for variations of temperature (*dT*) and composition. Describing the chemical variations by the relative variations of total perovskite (*dPv*) and total iron (*dFe*) content in the lower mantle (*37*), the seismic likelihoods are related to probability density functions (pdfs) for temperature and composition by:

$$d\ln V_s = (\partial \ln V_s/\partial T)dT + (\partial \ln V_s/\partial Pv)dPv + (\partial \ln V_s/\partial Fe)dFe \quad (1)$$

$$d\ln V_\Phi = (\partial \ln V_\Phi/\partial T)dT + (\partial \ln V_\Phi/\partial Pv)dPv + (\partial \ln V_\Phi/\partial Fe)dFe \quad (2)$$

$$d\ln \rho = (\partial \ln \rho/\partial T)dT + (\partial \ln \rho/\partial Pv)dPv + (\partial \ln \rho/\partial Fe)dFe \quad (3)$$

where the partial derivatives are the sensitivities of velocities and density to temperature and composition. We calculated sensitivities (fig. S1) using available mineral physics data and a reasonable range for the thermal and chemical reference state of the mantle (*37*). This leads to uncertainties in the sensitivities that are also close to Gaussian.

Solving the algebraic system (Eqs. 1 to 3) would be trivial if some quantities were not pdfs. No routine mathematical tools are available to solve such a system. We solved the system for fixed sensitivities, which implies that the lateral variations in *dT*, *dPv*, and *dFe* are Gaussian distributed. In this case, the system can be written in vector form as $d = Gm$, where d represents the mean of the seismic likelihoods and G the partial derivatives in the system (Eqs. 1 to 3). The mean thermochemical model is found by $\overline{m} = G^{-1}d$ and the variance is given by $C_{\overline{m}} = G^{-1}C_d(G^{-1})^*$ (*38*), where C_d represents the variance of the seismic likelihoods and * denotes the matrix transpose. Of course, G is not a constant matrix, but each sensitivity is a pdf itself. We therefore solved the system a million times, drawing randomly in the Gaussian distributions of the partial derivatives. We then averaged the mean models $\overline{m}$ and their variances $C_{\overline{m}}$ and determined the corresponding spread. This allows us to distinguish between contributions from the widths of the seismic likelihoods and from uncertainties in the sensitivities in the final model. The average model variance is taken as the sum of all variances; however, the variance in all cases is dominated by C_d. Uncertainties in the sensitivities contribute less than 10% to the total model uncertainties.

For each step (seismic models, sensitivities, thermo-chemical models), we determine complete uncertainties, providing the tools to quantify how meaningful the results are. Robust mean variations of temperature, perovskite, and iron are shown in Fig. 2. Uncertainties in these maps are uniform within a given layer and are listed in Table 1. The large uncertainties in temperature are mainly due to the large uncertainties in density. Nevertheless, density is indispensable to infer the compositional variations. Previous estimates of thermal and chemical parameters without density (*5*, *31*) were not robust (*31*). We obtained robust temperature and compositional anomalies in many places (Fig. 2). Iron and temperature variations are largest in the bottom 1000 km of the mantle. Perovskite variations are smallest in our mid-mantle layer. These characteristic changes with depth are consistent with previous suggestions based on seismologic (*27*) and rheologic (*5*) properties of the mantle. Our estimates are valid for long wavelengths (spherical harmonic degrees 2, 4, 6, and vertical layers of ≈1000 km). Because current tomographic models do not show much power beyond degree 6 (*39*), we do not expect significant lateral changes, but a finer vertical resolution could concentrate the thermochemical signal

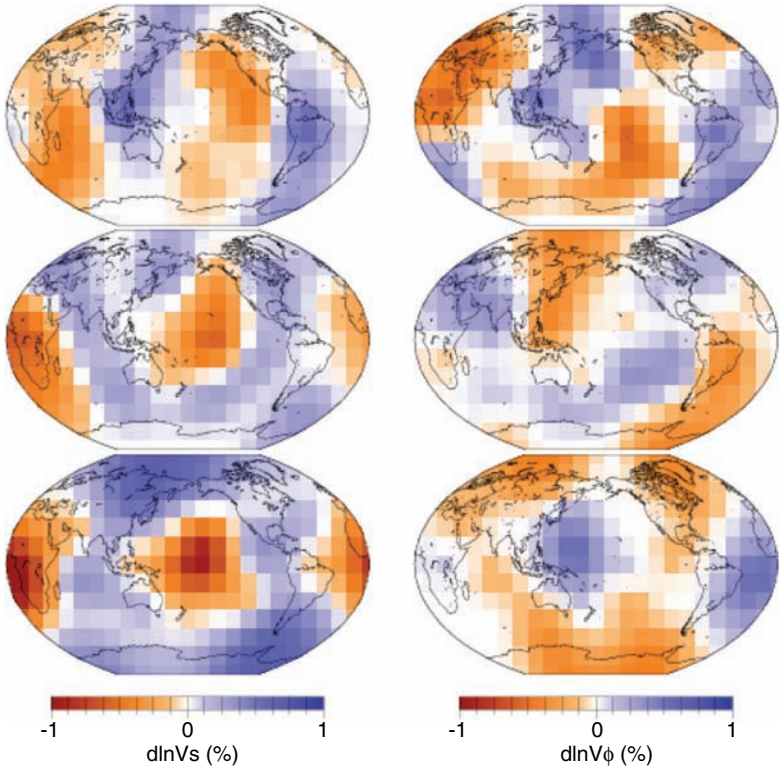

Fig. 1. Lateral variations in shear wave and bulk sound speed in the lower mantle relative to the spherical average. The lower mantle is parameterized in three layers (from the top: 670 to 1200, 1200 to 2000, and 2000 to 2891 km depth). The coarse layering is determined not by data resolution, but by computational requirements. Because no explicit regularization is used, results for thick layers are correct averages over any finer parameterization. This has been tested, and details of the technique are given in (*32*). Shown is the mean (or most likely) model averaged over equal-area caps of 15° by 15°. The standard deviation is uniform in each layer and is a reliable estimate of the uncertainty in the seismic model (Table 1). The model is set to zero when its absolute amplitude is <1 SD and plots in white.

Table 1. Root mean square (rms) uncertainties per layer. Within a given layer, location-specific uncertainties deviate by less than 10% from the corresponding rms value. In the absence of error estimates in most tomographic studies, we suggest using these values as a good first-order estimate.

Layer (km depth)	*dT* (K)	*dPv* (%)	*dFe* (%)	$d\ln V_s$ (%)	$d\ln V_\Phi$ (%)	$d\ln\rho$ (%)
670–1200	180	5.5	0.75	0.16	0.34	0.26
1200–2000	112	3.0	0.55	0.12	0.22	0.28
2000–2891	198	3.6	0.86	0.12	0.26	0.48

over smaller vertical length scales. The recent discovery of a postperovskite phase at the bottom of the mantle (*40*) is not likely to change our inferences, because the expected change in elastic properties (*41*) falls inside our range of input parameters used for the calculation of the sensitivities. In most interpretations of tomography, it is assumed that wave speeds, and in particular shear wave speeds, can be scaled to temperature. Our results show that this is not the case (*37*) (fig. S2) and explain why thermochemical inferences obtained without density (*5*, *31*) are so different from those presented here.

Density anomalies generate buoyancy forces that drive mantle flow. Because we determined independent likelihoods for thermochemical variations in the mantle, we are in a position to separate the driving force into thermal and chemical contributions. We resampled the pdfs for *dT*, *dPv*, and *dFe* and

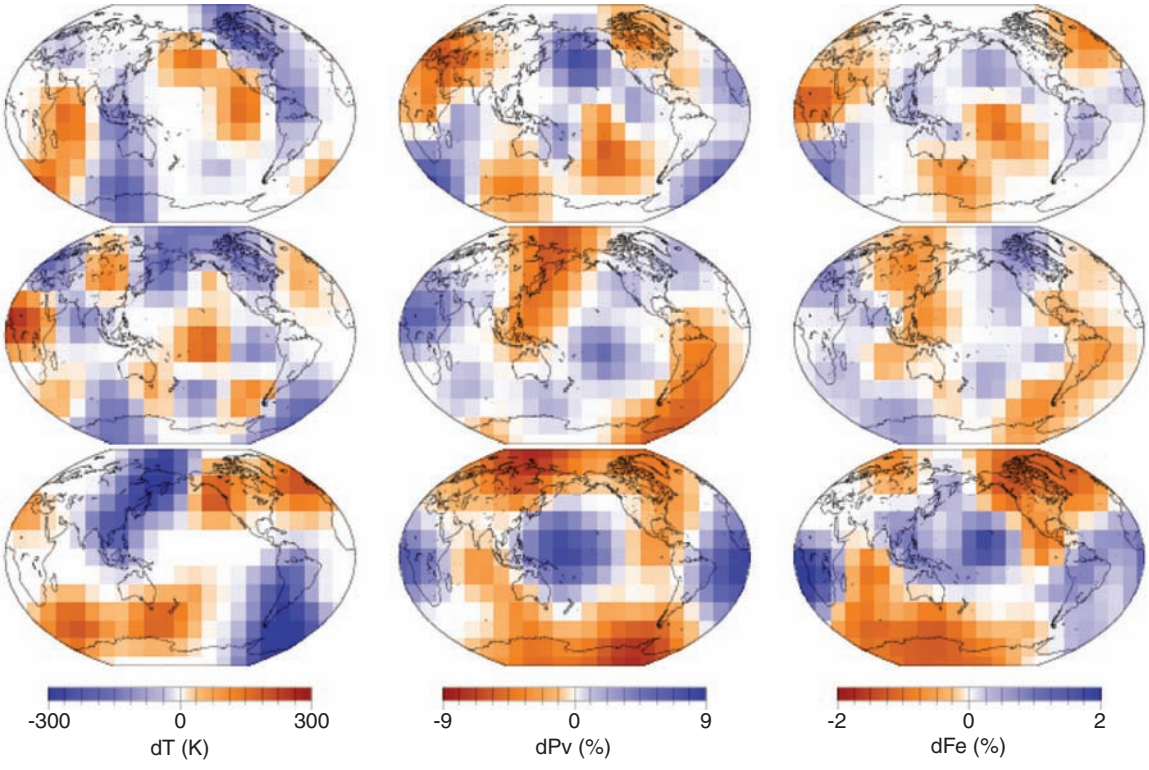

Fig. 2. Variations of temperature, perovskite, and iron in the lower mantle relative to an average (unspecified) reference state. From the top, layers are between 670 and 1200, 1200 and 2000, and 2000 and 2891 km depth. Within each cell, the variables are represented by Gaussian distributions. Shown are the mean models >1 SD (Table 1). The white areas cover anomalies that are not robust and have been set to zero for plotting purposes. They are likely to be smaller in amplitude than the uncertainty.

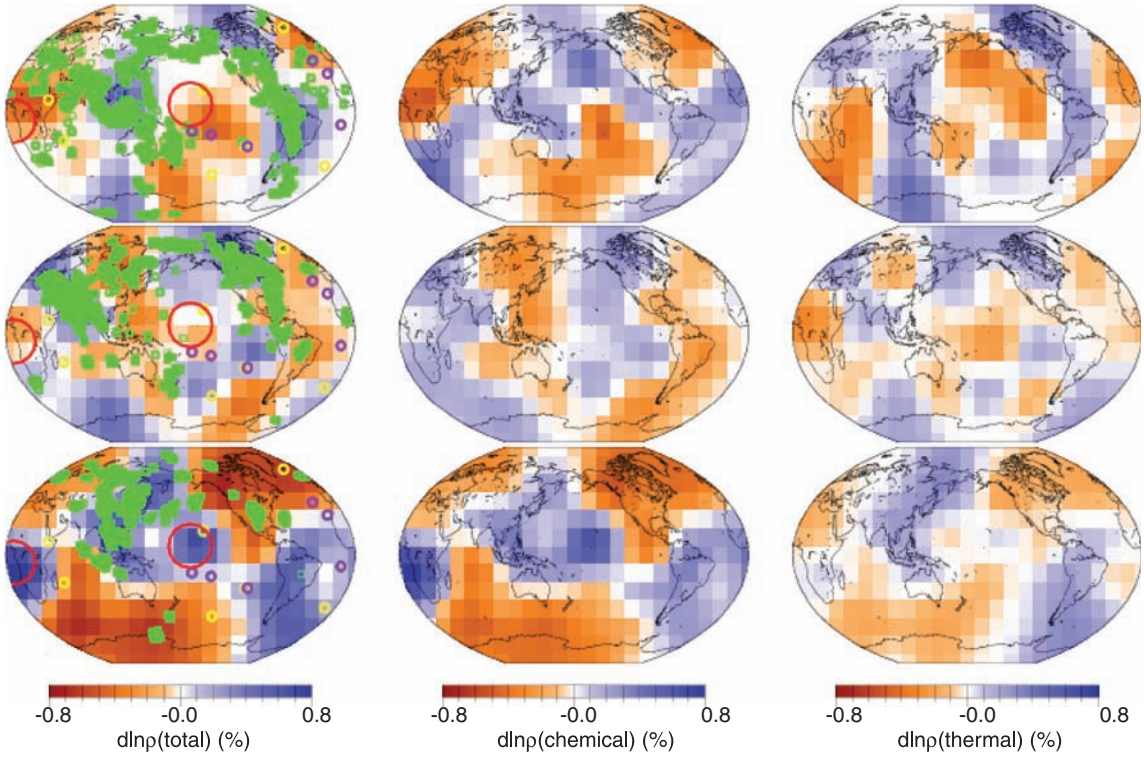

Fig. 3. Total, chemical, and thermal contributions to relative density variations with respect to the average in the lower mantle. From the top, layers are between 670 and 1200, 1200 and 2000, and 2000 and 2891 km depth. Large red circles indicate locations of the superplumes as identified from *dlnVs* (Fig. 1). Green squares denote *P*-wave amplitudes >0.2% from (*44*), which we consider to be slabs. Yellow circles correspond to hotspots originating near the CMB proposed by Courtillot *et al*. (*45*) and purple circles to CMB hotspots identified by Montelli *et al*. (*46*).

the corresponding density sensitivities to obtain separate likelihoods for thermal and compositional parts of the density (Fig. 3). In the lower 1000 km of the mantle, thermal buoyancy is weak compared to chemical buoyancy, even though temperature variations are highest in this layer. This is because the thermal expansivity decreases with increasing depth (fig. S1). The Pacific and African superplumes, identified in global tomography (*23*, *24*), are dense and have a chemical origin as previously suggested (*20*–*22*, *28*, *29*, *42*). Unless complex, as-yet-unmodeled processes are at play, our findings rule out that superplumes are thermally buoyant, as has often been proposed (*5*, *43*). In the mid- and upper-lower mantle layers, thermal and chemical buoyancies are equally important. Other important concepts of mantle flow are slabs and hotspots. Very few slabs, identified from seismic tomography (*44*), continuously plot on heavier-than-average material down to the CMB, and hardly any hotspots, recently classified as coming from the CMB (*45*, *46*), continuously plot on buoyant material throughout the lower mantle.

Our results demonstrate that long-wavelength chemical heterogeneities exist and play an important role throughout the mantle. Our ability to separate the total buoyancy into thermal and chemical components further shows that compositional variations play a first-order role in large-scale mantle dynamics and cannot be ignored. Recent experimental (*47*) and numerical (*35*) models of thermochemical convection show a variety of structures, depending on input parameters. Whether the structures identified in our models are chemically stable (*33*), organized in piles (*20*), or in a doming regime (*47*) will crucially depend on the input parameters of the simulations: the initial composition of Earth; depth-dependent parameters such as thermal expansivity, thermal conductivity, viscosity; and many other parameters.

References and Notes

1. J. H. Woodhouse, A. M. Dziewonski, *J. Geophys. Res.* **89**, 5953 (1984).
2. O. L. Anderson, E. Schreiber, R. C. Liebermann, N. Soga, *Rev. Geophys. Space Phys.* **6**, 491 (1964).
3. S.-I. Karato, *Geophys. Res. Lett.* **20**, 1623 (1993).
4. B. H. Hager, R. W. Clayton, M. A. Richards, R. P. Comer, A. M. Dziewonski, *Nature* **313**, 541 (1985).
5. A. M. Forte, J. X. Mitrovica, *Nature* **140**, 1049 (2001).
6. R. D. van der Hilst, S. Widiyantoro, E. R. Engdahl, *Nature* **386**, 578 (1997).
7. S. Grand, R. D. van der Hilst, S. Widiyantoro, *GSA Today* **7**, 1 (1997).
8. G. Schubert, D. L. Turcotte, P. Olsen, *Mantle Convection in the Earth and Planets* (Cambridge Univ. Press, Cambridge, 2001).
9. P. Olson, D. A. Yuen, *J. Geophys. Res.* **87**, 3993 (1982).
10. U. R. Christensen, *Ann. Geophys.* **2**, 311 (1984).
11. G. F. Davies, M. Gurnis, *Geophys. Res. Lett.* **13**, 1517 (1986).
12. U. Hansen, D. A. Yuen, *Nature* **334**, 237 (1988).
13. N. H. Sleep, *Geophys. J.* **95**, 437 (1988).
14. P. Olson, C. Kincaid, *J. Geophys. Res.* **96**, 4347 (1991).
15. M. Gurnis, *J. Geophys. Res.* **91**, 1407 (1986).
16. U. R. Christensen, *Philos. Trans. R. Soc. London A* **328**, 417 (1989).
17. L. H. Kellogg, S. D. King, *Geophys. Res. Lett.* **20**, 379 (1993).
18. I. Sidorin, M. Gurnis, in *Observational and Theoretical Constraints on the Core-Mantle Boundary Region*, M. Gurnis *et al.*, Eds. (American Geophysical Union, Washington, DC, 1998), pp. 209–230.
19. U. Hansen, D. A. Yuen, in *Double-Diffuse Convection*, A. Brandt, H. J. S. Fernando, Eds. (American Geophysical Union, Washington, DC, 1995), pp. 135–149.
20. P. Tackley, in *Observational and Theoretical Constraints on the Core-Mantle Boundary Region*, M. Gurnis *et al.*, Eds. (American Geophysical Union, Washington, DC, 1998), pp. 231–253.
21. B. Schott, D. A. Yuen, *Phys. Earth Planet. Int.* **146**, 139 (2004).
22. D. A. Yuen, O. Cadek, A. Chopelas, C. Matyska, *Geophys. Res. Lett.* **20**, 889 (1993).
23. W. J. Su, R. L. Woodward, A. M. Dziewonski, *J. Geophys. Res.* **99**, 6945 (1994).
24. J. Ritsema, H. J. van Heijst, J. H. Woodhouse, *Science* **286**, 1925 (1999).
25. W. J. Su, A. M. Dziewonski, *Phys. Earth Planet. Int.* **100**, 135 (1997).
26. B. L. N. Kennett, S. Widiyantoro, R. H. van der Hilst, *J. Geophys. Res.* **103**, 12,469 (1998).
27. R. D. van der Hilst, H. Karason, *Science* **283**, 1885 (1999).
28. M. Ishii, J. Tromp, *Science* **285**, 1231 (1999).
29. G. Masters, G. Laske, H. Bolton, A. M. Dziewonski, in *Earth's Deep Interior: Mineral Physics and Tomography from the Atomic to the Global Scale*, S.-I. Karato *et al.*, Eds. (American Geophysical Union, Washington, DC, 2000), pp. 66–87.
30. R. L. Saltzer, R. D. van der Hilst, H. Karason, *Geophys. Res. Lett.* **28**, 1335 (2001).
31. F. Deschamps, J. Trampert, *Phys. Earth Planet. Int.* **140**, 277 (2003).
32. J. Resovsky, J. Trampert, *Earth Planet. Sci. Lett.* **215**, 121 (2003).
33. L. H. Kellogg, B. H. Hager, R. D. van der Hilst, *Science* **283**, 1881 (1999).
34. D. L. Anderson, *Science* **293**, 2016 (2001).
35. P. J. Tackley, *Geochem. Geophys. Geosyst.* **3**, 10.1029/2001GC000167 (2002).
36. S.-I. Karato, B. B. Karki, *J. Geophys. Res.* **106**, 21771 (1999).
37. Materials and Methods are available as supporting material on *Science* Online.
38. A. Tarantola, *Inverse Problem Theory* (Elsevier, Amsterdam, 1987).
39. Y. J. Gu, A. M. Dziewonski, W. J. Su, G. Ekström, *J. Geophys. Res.* **106**, 11,169 (2001).
40. M. Murakami, K. Hirose, K. Kawamura, N. Sato, Y. Ohishi, *Science* **304**, 855 (2004).
41. T. Tsuchiya, J. Tsuchiya, K. Umemoto, R. M. Wentzcovitch, *Geophys. Res. Lett.* **31**, L14603, 10.1029/2004GL020278 (2004).
42. S. Ni *et al.*, *Science* **296**, 1850 (2002).
43. B. Romanowicz, Y. Gung, *Science* **296**, 513 (2002).
44. H. Bijwaard, W. Spakman, E. R. Engdahl, *J. Geophys. Res.* **103**, 20,055 (1998).
45. V. Courtillot, A. Davaille, J. Besse, J. Stock, *Earth Planet. Sci. Lett.* **205**, 295 (2003).
46. R. Montelli *et al.*, *Science* **303**, 338 (2004).
47. A. Davaille, *Nature* **402**, 756 (1999).

48. We acknowledge discussions and suggestions from D. Anderson, R. van der Hilst, A. Hoffmeister, H. Paulssen, and R. Wenzcowitch. This work was partly funded by the Dutch National Science Foundation (grant NWO:Vici:865.03.001). D.Y. acknowledges support from the Earth Science Program of the NSF.

Supporting Online Material

www.sciencemag.org/cgi/content/full/306/5697/853/DC1
Materials and Methods
Figs. S1 and S2
Table S1
References

25 June 2004; accepted 30 August 2004

Runcaria, a Middle Devonian Seed Plant Precursor

P. Gerrienne,[1]* B. Meyer-Berthaud,[2] M. Fairon-Demaret,[1] M. Streel,[1] P. Steemans[1]

The emergence of the seed habit in the Middle Paleozoic was a decisive evolutionary breakthrough. Today, seed plants are the most successful plant lineage, with more than 250,000 living species. We have identified a middle Givetian (385 million years ago) seed precursor from Belgium predating the earliest seeds by about 20 million years. *Runcaria* is a small, radially symmetrical, integumented megasporangium surrounded by a cupule. The megasporangium bears an unopened distal extension protruding above the multilobed integument. This extension is assumed to be involved in anemophilous pollination. *Runcaria* sheds new light on the sequence of character acquisition leading to the seed.

The seed habit is a heterosporous means of reproduction involving a single megaspore that germinates within an indehiscent megasporangium (nucellus) retained on the maternal sporophyte, enclosure of the nucellus within an integument, and the capture of pollen before seed dispersal. Contrasting hypotheses about the origin of the seed habit and the identification of the closest relatives to seed plants (*1*–*7*) are matters of considerable debate and are issues that cannot be resolved without substantial investigation of the fossil record.

The earliest known seeds are Late Devonian [Famennian, 365 million years ago (Ma)] (*8*–*10*). Most are borne within a cupule, either singly or in small groups. Their general organization consists of a radially symmetrical nucellus surrounded by an integument dissected

[1]Département de Géologie, B18, Université de Liège, Sart Tilman, Liège 1, Belgique. [2]Botanique et Bioinformatique de l'Architecture des Plantes, Centre de Coopération Internationale en Recherche Agronomique pour le Développement, TA40/PS2, Boulevard de la Lironde, 34398 Montpellier Cedex 5, France.

*To whom correspondence should be addressed. E-mail: p.gerrienne@ulg.ac.be

Probabilistic Tomography Maps Chemical Heterogeneities Throughout the Lower Mantle

Jeannot Trampert, Frédéric Deschamps, Joseph Resovsky, Dave Yuen

Materials and Methods

Density modeling

In a pioneering study, Ishii and Tromp (*S1*) showed that it was possible to obtain density models from normal mode data. The nature of the inverse problem, however, is such that the density part is heavily dependent on the employed regularization. This led to criticism of their study (*S2*-*S4*), but an extended data set and a new approach (*S5*), referred to as probabilistic tomography, can unambiguously isolate the density signal in the long period seismic data. We realized that the normal mode data used in (*S1*) suffered from trade-offs between upper and lower mantle signals, which could easily be broken by adding existing high quality fundamental mode and overtone surface wave data (*S6*). The probabilistic approach established that individual models are not necessarily meaningful, but the whole family of models (represented by a joint probability density function (pdf)), compatible with the data, has well defined properties (*S6*). Likelihoods of individual seismic parameters are found by marginalizing the joint pdfs obtained from a full model space search. These likelihoods contain no explicit regularization and are not biased by a chosen parameterization. They can thus be seen as a complete representation of the seismological constraints. We confirm that the probability p of a positive correlation between $d\ln\rho$ and $d\ln V_s$ is small ($p = 0.02$), and that the commonly used scalings between the two quantities are not justified ($p[0 < d\ln\rho/d\ln V_s < 0.5] = 0.08$). Using a similar data set to ours,

Ishii and Tromp (*S7*) obtained a density model which is close to ours in pattern in the lowermost mantle. Their amplitude is half of that of our most likely model and is a consequence of the damping which they have to prescribe.

Gravity filtering

The gravity field can be obtained by a simple static calculation (*S1*), independent of uncertain viscosity profiles, provided we have compatible information on density and topography. In the joint pdfs, an individual realization is a single compatible density-topography-velocity model fitting the seismic data. We drew randomly in these joint pdfs and calculated the corresponding non-hydrostatic gravity potential without crust and surface topography. We only kept those compatible models fitting the observed gravity potential within its error bars. These errors are dominated by the uncertainty of removing a crustal model including surface topography (*S5*). The posterior filtering has the advantage of identifying inconsistencies between seismic and gravity inferences on density rather than concealing them by merging the two for a joint inversion. Only a few extreme (low probability) models are eliminated, and modest changes (mainly narrowing of the likelihoods) occur in the density model distribution. The correlation between the most likely density models before and after gravity filtering varies between 0.60 and 0.67 depending on depth and the root-mean square (rms) amplitudes increase in the lowermost mantle while they decrease elsewhere. The most likely velocity models are hardly affected by this filtering (correlations vary between 0.90 and 0.98 and approximately no change in rms amplitudes). Which effect our models will have on inferences of viscosity, and how well they will explain other geodynamic data, remains to be tested using dynamic modeling. Current scaled density models together with published boundary topographies certainly give a significantly worse fit ($\chi^2/N > 3$) to our dataset than the models presented here ($\chi^2/N < 2$).

Correlation between seismic likelihoods

The width of the likelihoods of correlation serve as a reminder that interpreting a single tomographic model can be misleading, whereas the whole family of models compatible with the data, can present useful properties. For instance, the likelihood of correlation between bulk sound and shear wave speed (example shown in *S5*) in the lower 1000 km of the mantle is sufficiently wide to incorporate those of all recent tomographic models (reviewed in *S8*). This suggests that much of the debate on the cause of tomographic images (chemical for a negative correlation, thermal for a positive correlation) is generated by different ways of solving the inverse problem rather than by data constraints. Our integrated likelihood has a probability of 0.95 for a negative correlation, and hence a very likely chemical origin.

Mineral physics modeling

The lower mantle is assumed to be a mixture of (Mg,Fe,Ca)perovskite and magnesiowüstite. Aluminum content could be important, but published mineral physics data are not in sufficient agreement to calculate the effect (*S9*). Even very recent measuring attempts remain inconclusive (*S10-S12*) so that we chose to neglect aluminum. To calculate density and all elastic moduli at high temperature and pressure, we used the method of Trampert et al. (*S13*). The equation-of-state modeling has been extended to accommodate the simultaneous use of experimental and ab initio data. There seems to be an inconsistently in the shear data, and a cross-derivative has been introduced at zero pressure to ensure compatibility of all data (*S9*). The iron dependence is introduced at the individual mineral level by corrections to the magnesium end-member at ambient conditions. Iron is shared between perovskite and magnesiowüstite via a partitioning coefficient. Calcium is modeled in a similar way, but Ca enters perovskite only. The mineral physics data used to calculate the sensitivities of seismic parameters to thermo-chemical parameters are shown in Table S1. The sensitivities have some dependence on the assumed reference

state. We therefore do not fix a reference state, but vary all parameters within reasonable ranges (*S13*) for the lower mantle. The total iron content is varied between 5 and 15 %, the iron partitioning between 0.2 and 0.5. Calcium content changes between 0 and 12 %. The foot of the adiabat is taken between 1500 and 2500 K, and the total perovskite content in the lower mantle is assumed to be between 50 and 100 %. These ranges together with uncertainties in the input parameters (Tab. S1) allow to generate many seismic profiles. Only those compatible with a seismic reference model are retained (*S13, S9*). For all profiles fitting the seismic reference model, we calculate the sensitivities by straightforward numerical differentiation (*S13, S9*). We then average the sensitivities and determine their standard deviation. This is a natural way to assess uncertainties in sensitivities simultaneously due to our ignorance of the Earth's thermo-chemical reference state and uncertainties in mineral physics data. Partial derivatives for many different parameters may be calculated. We retain only those which are large for at least one of the seismic parameters $d\ln V_s$, $d\ln V_\Phi$ or $d\ln\rho$ (Fig. S1). This leaves us with sensitivities for the total perovskite content. Note that its uncertainty reflects the fact that it may contain iron and calcium, but not aluminum. The other significant sensitivity is for the total iron content. Part of its uncertainty comes from our ignorance on how exactly iron is partitioned between perovskite and magnesiowüstite. Calcium variations induce small variations on all seismic parameters and hence cannot reliably be resolved. Given existing error bars on seismic parameters and sensitivities, neglecting calcium will probably not bias the results. Some partial derivatives are different from Deschamps and Trampert (*S14*) due to the fact that we included the latest published data for iron content in perovskite (*S15*) and magnesiowüstite (*S16*). Indeed, shear wave sensitivities to iron and perovskite depend on the assumed effect of iron at zero temperature and pressure (*S9*). We tested that this only slightly affects amplitudes of the inferred thermo-chemical variations, but not their sign and location.

Correlation between seismic and thermo-chemical parameters

In most interpretations of tomography, it is assumed that wave speeds, and in particular shear wave speeds, can be scaled to temperature. We have independent estimates (with almost no observed covariance) of likelihoods for $d\ln V_s$, $d\ln V_\Phi$ and $d\ln\rho$. System (1-3) is a perfectly determined problem and hence the pdfs for the thermo-chemical parameters dT, dPv or dFe are independent as well. We can thus calculate the likelihoods of correlation between any of these parameters. In our lowermost layer (`Fig. S2`), the correlation between $d\ln V_s$ and dT is indeed very low and shear wave speeds correlate much better with iron or perovskite variations. Temperature cannot be obtained by scaling shear wave speed, but is to a large extend determined by density. Although the correlation between $d\ln V_s$ and dT improves higher in the mantle, it never exceeds 0.7 in absolute value for a given pair drawn in the Gaussian distributions of the models. Notable very high correlations throughout the mantle (only shown for our lowermost layer) are between $d\ln V_\Phi$ and dPv, and between $d\ln\rho$ and dFe.

References

S1 M. Ishii, J. Tromp, *Science* **285**, 1231 (1999).

S2 J. S. Resovsky, M. H. Ritzwoller, *Geophys. Res. Lett.* **26**, 2319 (1999).

S3 B. Romanowicz, *Geophys. Res. Lett.* **28**, 1107 (2001).

S4 C. Kuo, B. Romanowicz, *Geophys. J. Int.* **150**, 162 (2002).

S5 J. Resovsky, J. Trampert, *Earth Planet. Sci. Lett.* **215**, 121 (2003).

S6 J. S. Resovsky, J. Trampert, *Geophys. J. Int.* **150**, 665 (2002).

S7 M. Ishii, J. Tromp, *Phys. Earth Planet. Int.* **146**, 113 (2004).

S8 G. Masters, G. Laske, H. Bolton, A. M. Dziewonski, in *Earth's Deep Interior: mineral Physics and Tomography From the Atomic to the Global Scale*, S.-I.

Karato et al., Eds. (American Geophysical Union, Washington, DC, 2000) pp. 66-87.

S9 F. Deschamps, J. Trampert, *Earth Planet. Sci. Lett.* **222**, 161 (2004).

S10 I. Daniel, J. D. Bass, G. Fiquet, H. Carden. J. Zhang, M. Hanfland, *Geophys. Res. Lett.* **31**, doi: 10.1029/2004GL020213 (2004).

S11 J.M. Jackson, J. Zhang, J.D. Bass, *Geophys. Res. Lett.* **31**, doi: 10.1029/2004GL019918 (2004).

S12 T. Yagi, K. Okabe, N. Nishiyama, A. Kubo, T. Kikegawa, *Phys. Earth Planet. Inter.* **81**, 143 (2004).

S13 J. Trampert, P. Vacher, N. Vlaar, *Phys. Earth Planet. Int.* **124**, 255 (2001).

S14 F. Deschamps, J. Trampert, *Phys. Earth Planet. Int.* **140**, 277 (2003).

S15 B. Kiefer, L. Stixrude, R. M. Wentzcovitch, *Geophs. Res. Lett.* **29** doi:10.1029/2002GL014683 (2002).

S16 J. Kung, B. Li, D. J. Weidner, J. Zhang, R. C. Liebermann, *Earth Planet. Sci. Lett.* **203**, 557 (2002).

S17 A.R. Oganov, J.P. Brodholt, G.D. Price, *Earth Planet. Sci. Lett.* **184**, 555 (2001).

S18 Y. Wang, D.J. Weidner, F. Guyot, *J. Geophys. Res.* **101**, 661 (1996)

S19 B.B. Karki, J. Crain, *Geophys. Res. Lett.* **25**, 2741 (1998).

S20 S.V. Sinogeikin, J.D. Bass, *Phys. Res.* **B59**, 14141 (1999).

S21 B.B. Karki, R. M. Wentzcovitch, S. de Gironcoli, S. Baroni, *Phys. Res.* **B61**, 8793 (2000).

S22 Y. Sumino, O.L. Anderson, I. Suzuki, *Phys. Chem. Miner.* **9**, 38 (1983).

	perovskite (pv)			magneiowüstite (mw)	
	$MgSiO_3$	C_{Fe}^{pv}	C_{Ca}^{pv}	MgO	C_{Fe}^{mw}
ρ (g/cm3)	4.109	1.03 (*S15*)	0.122 (*S18*)	3.584	2.28
K_{S0} (GPa)	264.0	20.0 (*S15*)	-30.2 (*S18*)	162.5	18.0 (*S16*)
K'_{S0}	3.97/3.95/3.77/3.75	0.16 (*S15*)	0.73 (*S18*)	4.0 (*S20*) to 4.15 (*S21*)	-0.53 (*S16*)
$\dot{K}_{S0}$ (10^{-2} GPa/K)	-1.1/-1.5/-1.0/-1.5		-0.014 (*S18*)	-1.55 (*S22*) to -1.4 (*S21*)	
G_0 (GPa)	180.0 (*S17*)	-40.0 (*S15*)	-10.0 (*S19*)	130.8	-108.0 (*S16*)
G'_0	1.5 [0.05] (*S17*)	-0.52 (*S15*)	0.66 (*S19*)	2.4 (*S20*) to 2.5	-3.29 (*S16*)
$\dot{G}_0$ (10^{-2} GPa/K)	-2.0 [0.08] (*S17*)			-2.4 to -2.2 (*S21*)	
γ_0	1.31/1.39/1.33/1.41			1.41	
q	1.0/2.0/1.0/2.0			1.3	
a_1 ($10^{-5}K^{-1}$)	1.19 [0.17]			3.681	
a_2 ($10^{-8}K^{-2}$)	1.20 [0.10]			0.9283	
a_3 (K)	0.0			0.7445	

Table S1: All data are from Trampert et al. (*S13*), unless otherwise stated. When available, error bars are indicated in square brackets. ρ is the density, K_{S0} the abibatic bulk modulus, G_0 the shear modulus and γ_0 the Grüneisen parameter at ambient temperature and pressure. q is a constant. Primes and dots denote derivation with respect to pressure and temperature, respectively. Thermal expansitvity at zero pressure is given by $\alpha = a_1 + a_2 T - a_3 T^{-2}$. Where available, parameters are corrected for iron and calcium content X using $M = M_{Mg} + C_{Fe} X_{Fe} + C_{Ca} X_{Ca}$.

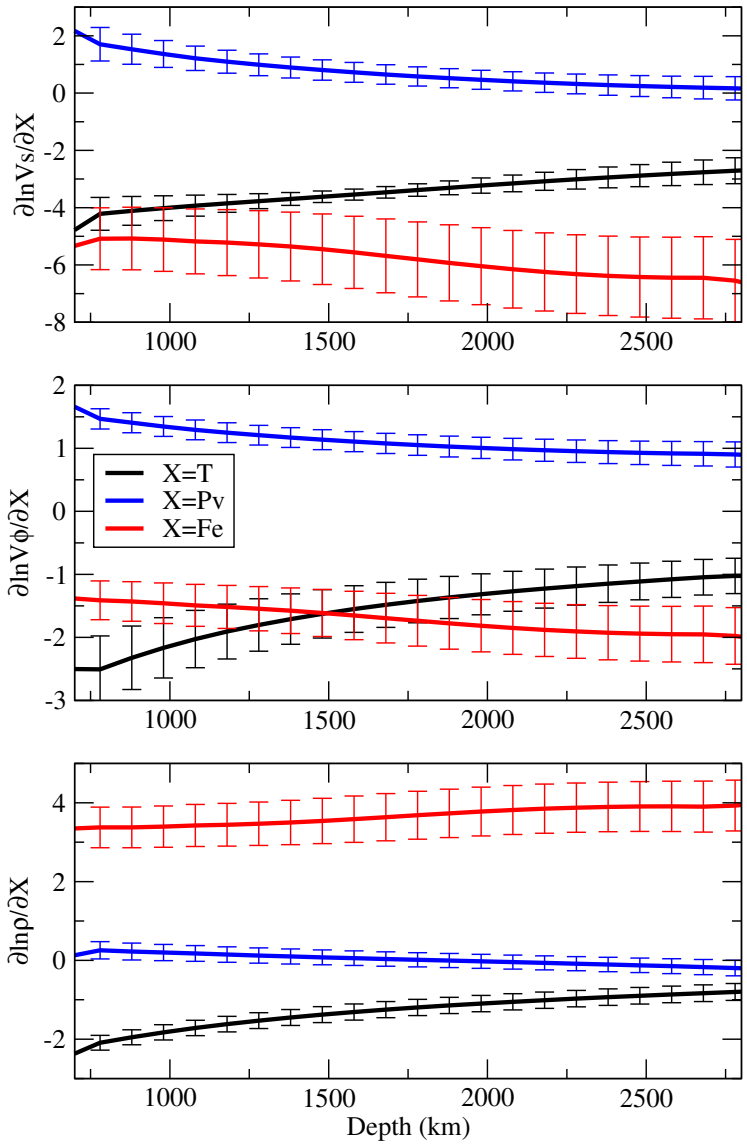

Figure S1: Sensitivities used in this study. Shown is the mean and standard deviation. For display only, the temperature derivatives are pre-multiplied by 10^5 all other derivatives by a factor of 10. Thermal expansivity $-\alpha = \partial \ln \rho / \partial T$ is seen on the black curve of the bottom panel.

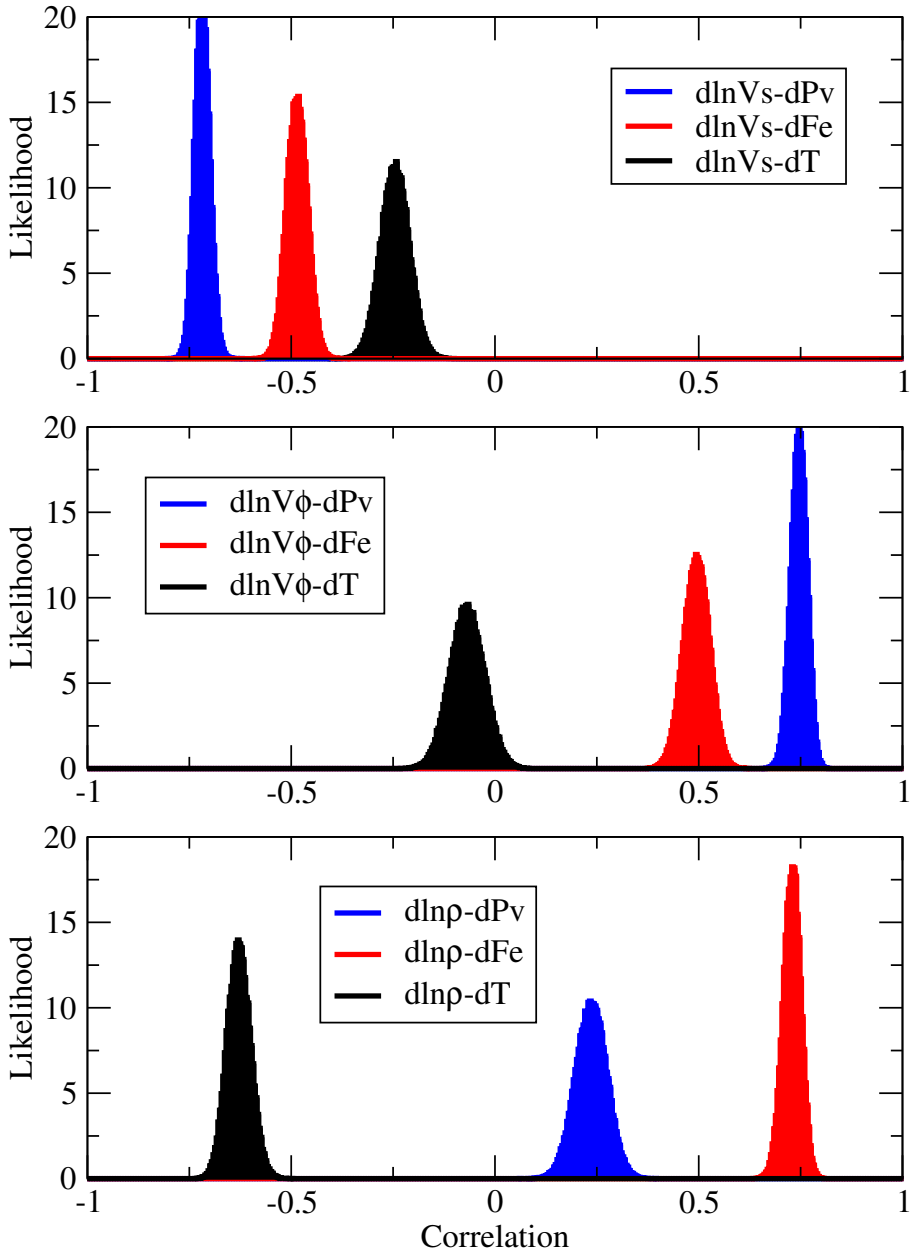

Figure S2: Likelihoods for correlations in the lowermost mantle layer [2000-2891 km].

Chapitre 4

Quelques modèles de convection thermochimique

L'information sismologique met en évidence de fortes variations latérales des vitesses sismiques et de la densité dans le manteau inférieur. Nous l'avons vu dans le chapitre précédent, l'interprétation de ces variations n'est pas exempte d'ambiguïté. Sans doute, l'interprétation classique, qui consiste à convertir ces variations en structures purement thermiques, est erronée. C'est en tout cas ce que suggère la mauvaise corrélation entre les anomalies de vitesse de cisaillement et de densité observées. Cette mauvaise corrélation ne peut s'expliquer que si des anomalies de composition contribuent de manière significative aux anomalies de vitesse et de densité. Reste maintenant à évaluer les conséquences de ces anomalies thermochimiques sur la structure et la dynamique du manteau. En particulier, quel(s) ingrédient(s) faut-il inclure dans les modèles de convection pour expliquer convenablement les observations sismologiques ? Le but de ce chapitre est d'apporter des réponses préliminaires à ces questions. Trois des articles rassemblés dans ce mémoire sont consacrés à ce sujet (Deschamps et al., 2007; Deschamps et al., 2008a, 2008b).

4.1 Quel(s) modèle(s) de convection pour le manteau terrestre?

Les premiers modèles de convection numériques censés modéliser le transfert de masse et de chaleur dans le manteau terrestre ont plus de trente ans (p.e., Moore et Weiss, 1973 ; McKenzie et al., 1974). De nombreux modèles leurs ont succédés. Aujourd'hui, le bilan de ces recherches est mitigé. D'un côté, les modèles développés pendant ces trois décades ont indiscutablement validé l'hypothèse d'un transfert de chaleur et de matière par convection.

D'un autre côté, ils n'ont pas encore permis de préciser le mode de convection effectivement à l'œuvre dans le manteau terrestre. C'est que la convection y est plus compliquée que le cas classique de Rayleigh-Bénard. Elle inclut de nombreuses complexités auxquelles l'écoulement et le transfert de chaleur sont sensibles, par exemple, un mode de chauffage mixte, la présence de transitions de phases, et une viscosité dépendant de la température. Et puis la Terre est ronde. Des progrès majeurs sur les algorithmes et la puissance de calcul ont jalonnés ces trois décades, et ont permis de prendre en compte ces complexités (Figure 4.1). Avec l'aide d'un cluster informatique (en français, Wikipédia recommande l'utilisation de l'expression 'grappe de calculateurs' ou 'ferme de calcul'. J'avais aussi pensé à 'nuage' ou 'essaim' de calculateurs, qui sonnent plutôt bien), il est maintenant possible de résoudre un cas relativement complexe dans un temps raisonnable (par exemple, 2 ou 3 jours de calculs sur 16 processeurs sont suffisants pour obtenir un modèle semblable à ceux décrits dans ce chapitre). Malgré cela, on ne sait toujours pas quels sont les paramètres qui contrôlent la convection du manteau terrestre, ni quelles valeurs attribuer à ces paramètres. Le nombre de Rayleigh, par exemple, dépend de la viscosité moyenne du manteau qui n'est connue qu'à un facteur 10 près. Sa définition même devient ambiguë lorsque certains paramètres (la viscosité, de nouveau, mais aussi l'expansion thermique et la densité) varient d'un point à l'autre du système. À la complexité du système s'ajoutent des contraintes observationnelles – sismologiques, gravimétriques, géochimiques, et de physique des minéraux – qu'il faut satisfaire, si possible simultanément.

4.1.1 Variations latérales de composition et paramètres chimiques

Une contrainte majeure apparue récemment est la présence de fortes variations latérales de densité à la base du manteau (Ishii et Tromp, 1999; Resovsky et Trampert, 2003; Trampert et al., 2004), vraisemblablement dues à de fortes variations latérales de composition (van der Hilst et Kárason, 1999; Deschamps et Trampert, 2003; Trampert et al., 2004). Très clairement, la convection dans le manteau terrestre est thermochimique, et l'équation de conservation de la composition est un ingrédient indispensable pour bien décrire ce qu'il s'y passe. Une question importante à laquelle il faudra répondre est comment maintenir un réservoir de matériau dense à la base du manteau. Plusieurs études ont montré qu'une couche de matériau dense peut rester stable pendant de très longues périodes de temps (comparable à l'âge de la Terre), pourvu que le contraste de densité chimique soit suffisamment élevé (p.e., Tackley, 2002; Zhong et Hager, 2003; van Thienen et al., 2005). En fait, ce type de modèle n'est pas souhaitable, car il n'explique pas les observations sismologiques (Deschamps et al., 2007). Ce que l'on souhaiterait plutôt, c'est un ensemble de réservoirs discontinus ancrés à la base du manteau et culminant à

quelques centaines de kilomètres (nous verrons qu'il est possible d'obtenir ce genre de structures), ou un réservoir continu mais ayant une forte topographie (semblable au modèle de Kellogg et al. (1999), ou aux dômes observés par Davaille (1999)).

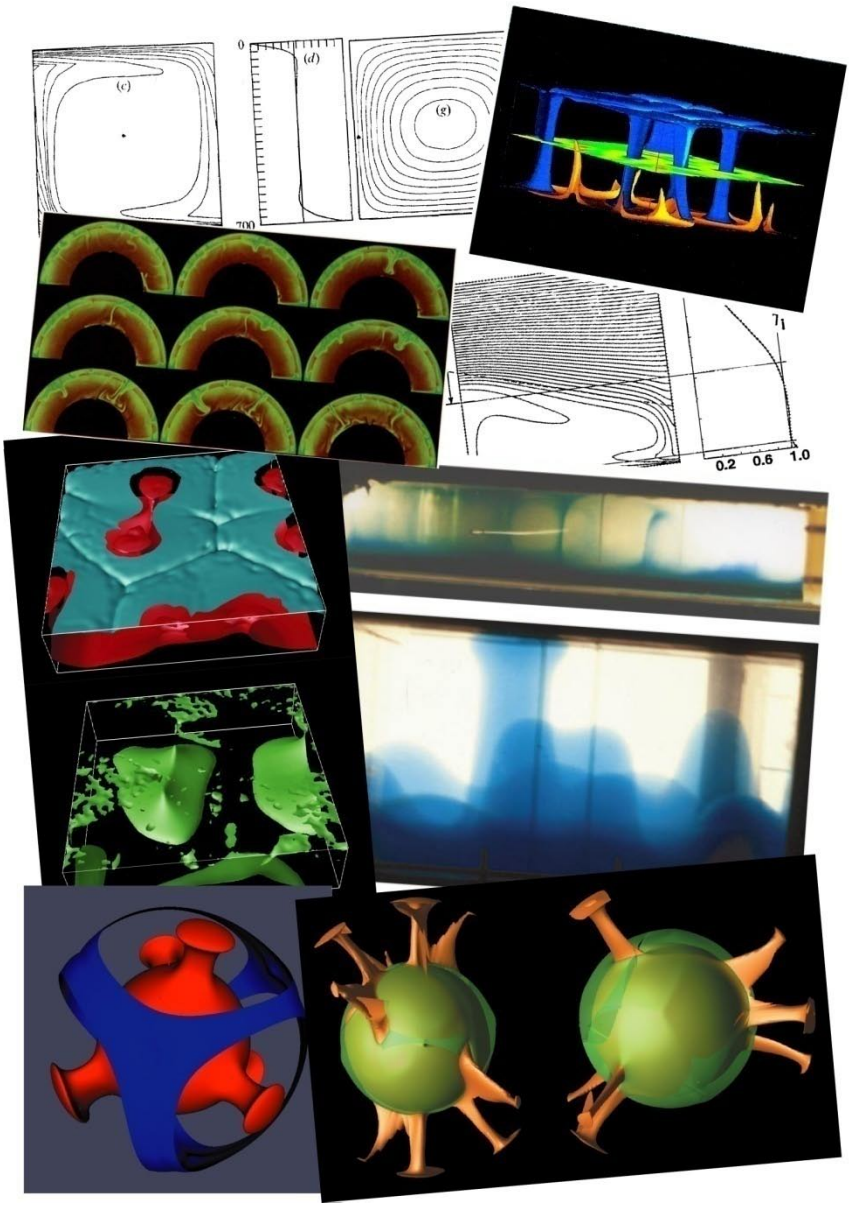

Figure 4.1 – Plus de trente ans se sont écoulés entre les modèles représentés en haut à gauche et en bas à droite. Des progrès techniques et théoriques incontestables … mais toujours pas de modèle expliquant de façon complètement satisfaisante le transfert de matière et de chaleur dans le manteau terrestre.

Le paramètre chimique le plus important est la flottaison B (buoyancy ratio, en anglais), c'est-à-dire le rapport entre le contraste de densité chimique et le contraste de densité thermique super-adiabatique. La flottaison joue pour le chimique le même rôle que le nombre de Rayleigh pour le thermique. Elle contrôle l'amplitude de la distorsion de la couche de matériau dense (Davaille, 1999; McNamara et Zhong, 2004; Jaupart et al., 2007),

et bien sûr le mode de convection en dépend fortement. Pour de fortes valeurs de B, le fluide reste stratifié, tandis que pour de faibles valeurs de B la couche initiale de matériau dense est rapidement déstabilisée. Pour des valeurs intermédiaires, des dômes de matériau dense se forment à partir de la couche initiale et oscillent verticalement (Davaille, 1999). De plus, les expériences analogiques de Jellinek et Manga (2002) suggèrent que la présence de matériau dense à la base d'un fluide contrôle la localisation des panaches thermiques. Un second paramètre est la fraction volumique de matériau dense, X, c'est-à-dire la quantité de matériau dense présente dans le système. Si l'on en croit l'analyse de stabilité linéaire et les expériences analogiques (Jaupart et al., 2007), ainsi que les modèles numériques (p.e., McNamara et Zhong, 2004), son influence est cependant de second ordre.

4.1.2 Viscosité

La viscosité du système et ses variations jouent un rôle clé, à la fois en contrôlant (partiellement) le nombre de Rayleigh, et l'équation de conservation de la quantité de mouvement. Les variations de viscosité avec la profondeur et la température ont été introduites pour tenir compte du fait que les lois de fluage des minéraux du manteau dépendent de la pression et de la température (p.e., Weertman, 1970). À noter que ces lois dépendent aussi de la taille des grains, de la présence de fluides, et de l'exposant de la contrainte. Les variations thermiques de la viscosité sont particulièrement intéressantes, car elles conduisent à la formation d'un couvercle rigide et (thermiquement) conductif au sommet du fluide (p.e., Davaille et Jaupart, 1993; Moresi et Solomatov, 1995; Deschamps et Sotin, 2000). Le régime de couvercle conductif est pertinent pour décrire la convection dans les planètes mono-plaque, comme Vénus (Solomatov et Moresi, 1996) et les satellites de glace des planètes géantes (Deschamps et Sotin, 2001), mais il ne parvient pas à expliquer un régime de tectonique des plaques, tel que celui observé sur Terre. Pour cela, il est nécessaire d'imposer des rhéologies plus complexes près de la surface du système (Tackley, 1998a). Pour l'étude de la convection globale, on peut cependant, en première approximation, négliger ces rhéologies complexes, et supposer que le manteau se comporte comme un fluide newtonien (Karato et Wu, 1993).

En plus des variations régulières avec la profondeur, la viscosité semble augmenter brutalement autour de 660 km de profondeur. C'est en tout cas ce que suggèrent les variations du géoïde (Hager et Richards, 1989) et les données du rebond post-glaciaire (Nakada et Lambek, 1989; Forte et Mitrovica, 1996). Le contraste de viscosité supplémentaire pourrait atteindre un ou deux ordres de grandeur.

Dans cette étude, on ne défini pas précisément la nature du matériau dense. Difficile, donc, d'estimer d'éventuelles variations de viscosité en fonction de la composition.

Pour le moment, il n'existe de toute façon pas de données fiables concernant les contrastes de viscosité entre les différentes phases potentiellement présentes dans le manteau inférieur, par exemple entre les pôles magnésien et ferreux de la pérovskite. Devant cette indétermination, il est préférable de mener une étude systématique dans un intervalle de contraste de viscosité assez grand.

4.1.3 Paramètres physiques

J'en ai déjà dit deux mots un peu plus haut, le nombre de Rayleigh n'est pas si bien défini que cela. C'est pourtant lui qui contrôle la vigueur de la convection thermique. Pour palier à la non-unicité induite par les variations de viscosité et, dans le cas d'un fluide compressible, à la dépendance vertical du modèle thermochimique de référence (Figure 4.4), il faut définir un nombre de Rayleigh de référence. Le nombre de Rayleigh défini dans ce chapitre, Ras, est calculé avec les valeurs de surface de la densité, de l'expansion et de la diffusivité thermique, et pour une température adimensionnée $T_{\mathrm{ref}} = 0.9$. Reste que les incertitudes sur les valeurs de ces paramètres (principalement sur la viscosité) induisent une incertitude d'un ordre de grandeur sur la valeur terrestre du nombre de Rayleigh.

Dans le cas de la convection purement thermique avec chauffage mixte, une augmentation du taux de chauffage interne, H_c, réduit la force de la couche limite thermique chaude (p.e., Sotin et Labrosse, 1999). Les panaches thermiques sont moins vigoureux, et si la quantité de chauffage interne est suffisante, ils n'atteignent pas la surface du fluide. Il n'est pas certain que ces effets soient aussi marqués dans le cadre de la convection thermochimique. Un second paramètre lié au chauffage interne et qui semble avoir de l'influence en géométrie 2D-Cartésienne (van Thienen et al., 2005) est le rapport RH_c entre les taux de chauffage interne des matériaux dense et régulier. Afin d'expliquer le manque d'éléments radioactifs dans le matériau source des MORB, il a été proposé que la concentration en éléments radiogéniques était plus élevée dans les réservoirs de matériau dense que dans le matériau régulier (Kellogg et al., 1999).

La discontinuité sismique observée vers 660 km de profondeur est associée à la transformation de la ringwoodite en pérovskite et en magnésio-wüstite, dont la pente de Clapeyron est négative et de l'ordre de -2.5 MPa/K (Bina et Helffrich, 1994). L'influence d'une transition de phase endothermique a été largement étudiée en différentes géométries (p.e., Christensen et Yuen, 1985; Machetel et Weber, 1991; Tackley et al., 1994). La présence d'une transition de phase endothermique modifie la structure de l'écoulement, le fait le plus marquant étant une forte réduction du transfert de masse de part et d'autre de la transition de phase. Il existe cependant des différences importantes entre les structures observées par les modèles 2D et 3D. Les modèles 2D observent une stratification périodique

entrecoupée d'avalanches épisodiques. Dans les modèles 3D, par contre, l'écoulement n'est jamais complètement stratifié. Des avalanches s'y produisent constamment, bien qu'en des endroits différents.

Voilà pour une liste des paramètres potentiellement influents. N'oublions pas la géométrie (évidemment sphérique dans le cas du manteau terrestre; ce sera pour une prochaine étape), et la présence de post-pérovskite, bien que celle-ci ne soit pas certifiée (Lay et Garnero, 2007). Même en se limitant à notre liste initiale, le nombre de modèles possibles est très élevé. Une exploration systématique et aussi exhaustive que possible dans l'espace de ces modèles devrait nous indiquer les paramètres les plus influents et, par comparaison avec la tomographie probabiliste, délimiter des intervalles de valeur possibles pour ces paramètres.

4.2 À la recherche d'un modèle de convection compatible avec la tomographie probabiliste

4.2.1 Principe

Les modèles de convection thermochimique prédisent des variations de température et de composition. L'approche directe consisterait à calculer des anomalies de vitesses sismiques (cisaillement et compression) et de densité à partir de ces variations, puis de les comparer à celles modèles tomographiques. Cette opération nécessite des hypothèses quant à la nature de ce matériau dense. Par exemple, le matériau dense est lié à un excès de fer et/ou à la présence de la phase post-pérovskite. L'approche directe n'est pas complètement inconcevable (elle permettrait, justement, de tester certains scénarios concernant la nature

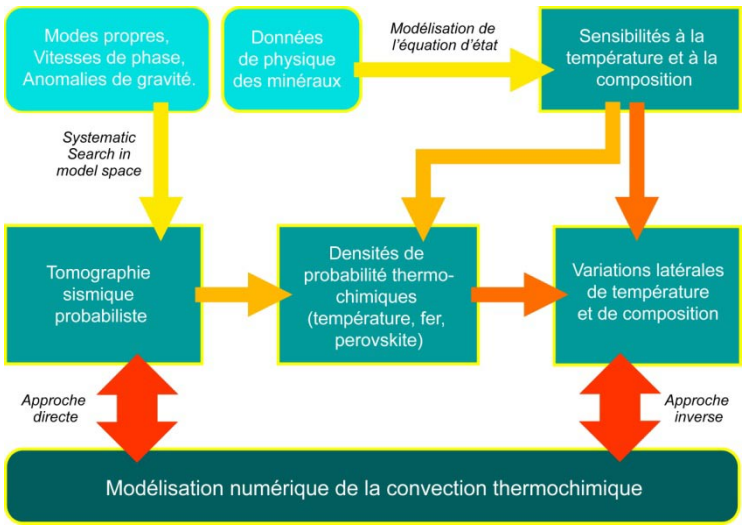

Figure 4.2 - Comparaison entre les modèles de tomographie sismique et les modèles de convection thermochimique.

des anomalies de composition), mais on lui préférera une approche inverse, plus générale. Inverse, car elle nécessite d'inverser les modèles tomographiques pour des anomalies de température et de composition (Chapitre 3), puis d'en déduire les anomalies de densité 'thermiques', $d\ln\rho_T$, et 'chimiques', $d\ln\rho_c$,

$$d\ln\rho_T = \frac{\partial \ln\rho}{\partial T} dT \qquad (4.1a)$$

et

$$d\ln\rho_c = \frac{\partial \ln\rho}{\partial x_{Fe}} dx_{Fe} + \frac{\partial \ln\rho}{\partial x_{pv}} dx_{pv}, \qquad (4.1b)$$

que l'on peut ensuite comparer à celle prédites par les modèles de convection thermochimique. La Figure 4.2 résume les deux approches, et la Figure 4.3 montre les distributions de densité thermiques chimiques déduites du modèle de tomographie probabiliste RT246g (Trampert et al., 2004).

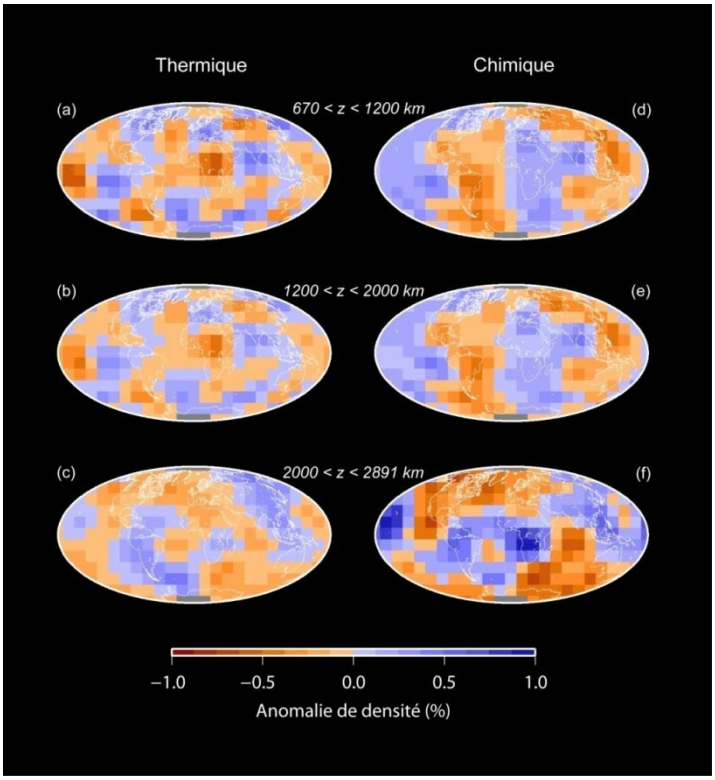

Figure 4.3 – Anomalies de densité thermiques et chimiques prédites par le modèle de tomographie probabiliste RT246g et une modélisation appropriée des propriétés thermo-élastiques de la pérovskite et de la magnésio-wüstite à hautes pressions et températures (Trampert et al., 2004).

En plus de tester les distributions thermochimiques des modèles numériques, on s'attachera à décrire l'évolution de la couche initiale de matériau dense. Pour cela, on pourra s'appuyer sur plusieurs observables, dont l'altitude moyenne des particules de matériau dense, définie par

$$\langle h_C \rangle = \frac{1}{\vartheta} \iiint_{\vartheta} (1 - z) C(x, y, z) \mathrm{d}\vartheta \,, \qquad (4.2)$$

où ϑ est le volume total du système. L'évolution de $\langle h_C \rangle$ permet d'estimer à quel instant la couche de matériau dense devient instable. Au départ du calcul, $\langle h_C \rangle$ est égal à la moitié de l'épaisseur initiale de la couche de matériau dense, puis elle augmente rapidement lorsque la courbe devient instable. La RMS de la vitesse du fluide, RMS(v) est indirectement liée à l'efficacité du mélange. Plus elle est élevée, plus le mélange est efficace. Son évolution constitue un indicateur supplémentaire de l'efficacité du mélange. Un indicateur similaire est le taux de déformation Lagragien, utilisé notemment par Coltice (2005). Dans certain cas, le mélange entre le matériau dense et le matériau régulier est accompli avant la fin du calcul, et il est possible d'estimer le temps nécessaire pour obtenir ce mélange. Le point de départ est, comme dans Ferrachat et Ricard (2001), l'évolution de la variance de la distribution chimique, plus exactement de la fonction

$$e(t) = 1 - \frac{var_C(t)}{var_C(t=0)} \qquad (4.3)$$

qui en est dérivée, mais la configuration de notre implique un traitement différent par la suite. On trouvera plus de détails à ce sujet, ainsi que des exemples d'évolution temporelles de $\langle h_C \rangle$ et de RMS(v) dans Deschamps et Tackley (2008a, 2008b).

4.2.2 Modèles de convection thermochimique

Pour explorer l'espace des modèles de convection thermochimiques, j'ai utilisé la version 3D-Cartésienne du code STAG3D développé par Paul Tackley (Tackley 1998b, 2002). Ce modèle inclut la plupart des complexités discutées dans le paragraphe 5.1. Il résout les équations adimensionnées de conservation de la quantité de mouvement, de l'énergie, de la masse et de la composition pour un fluide anélastique compressible à nombre de Prandtl infini (et je crois n'avoir oublié personne). On trouvera des détails concernant STAG3D et le dispositif expérimental dans plusieurs publications (p.e., Tackley, 1998b, Tackley, 2002, Deschamps et Tackley, 2008a). Les paramètres, leurs définitions, et les plages de valeurs explorées sont résumées dans la Table 4.1.

Brièvement, les calculs sont effectués sur des grilles imbriquées (certains dirons entrelassées) de 128×128×64 nœuds, et de rapport d'aspect égal à 4. La grille est affinée au sommet et à la base du système, ce qui permet de mieux décrire les couches limites thermiques. Les calculs sont stoppés pour un temps adimensionné $t_{\mathrm{run}} = 0.0106$, équivalent à 4.5 milliard d'années en temps dimensionné. Toutes les frontières sont à bord libre (la contrainte tangentielle est nulle), et le système est refroidi par le haut et chauffé à la fois par le bas et en volume, avec des taux de chauffage interne entre 0 et 50 (équivalents à des

flux de surface entre 0 et 130 mW/m²), selon le calcul. Contrairement aux modèles 2D (van Thienen et al., 2005), le rapport de chauffage interne entre matériau dense et matériau régulier n'a pas ou peu d'influence en 3D. Ce paramètre est fixé à la même valeur ($R H_C$ = 10) dans toutes les expériences. La compressibilité induit des sources et des puits d'énergie supplémentaires qui sont contrôlés par le nombre dissipatif. De nouveau, la définition de ce paramètre n'est pas unique, car elle dépend de l'expansion thermique qui varie avec la profondeur. On peut toutefois définir un nombre dissipatif de surface et un nombre dissipatif moyen qui, dans nos expériences, valent respectivement 1.2 et 0.43.

Paramètre	Symbole	Valeur	Unité	Valeur adimensionnée
Paramètres adimensionnés				
Nombre de Rayleigh de référence	Ra_S			10^6 - 10^9
Flottaison	B			0.1 - 0.5
Fraction volumique de matériau dense	X			0.05 - 0.30
Epaisseur initial de la couche dense	h_{DL}			0.05 - 0.30
Nombre dissipatif en surface	Di_S			1.2
Moyenne volumique du nombre dissipatif	Di			0.43
Paramètres physiques & thermodynamiques				
Acceleration de la gravité	g	9.81	m s^{-2}	1.0
Epaisseur du manteau	D	2891	km	1.0
Chauffage interne	H_C	0 - 130	mW m^{-2}	0 - 50
Rapport de chauffage chimique	RH_C	10		
Pente de Clapeyron à d = 660 km	Γ	-3.2 – 0.0	MPa K^{-1}	-0.12 – 0.0
Contraste de température super-adiabatique	ΔT_S	2500	K	1.0
Géotherme de référence	T_{as}	1600	K	0.64
Densité en surface	ρ_S	3300	kg m^{-3}	1.0
Contraste de densité à d = 660 km	$\Delta\rho_{660}$	400	kg m^{-3}	0.1212
Expansion thermique en surface	α_S	5.0×10^{-5}	K^{-1}	1.0
Diffusivité thermique en surface	κ_S	6.24×10^{-7}	m^2 s^{-1}	1.0
Capacité calorifique	C_P	1200	J kg^{-1} K^{-1}	1.0
Conductivité thermique en surface	k_S	3.0	W m^{-1} K^{-1}	1.0
Paramètre de Grüneisen en surface	γ_S	1.091		
Loi de viscosité				
Viscosité en surface	μ_S	1.6×10^{21}	Pa s	1.0
Rapport de viscosité à d = 660 km	$R\mu_{660}$	1.0 - 300		
Rapport de viscosité chimique	$R\mu_c$	3.2×10^{-3} - 10^3		
Rapport de viscosité radial	$R\mu_z$	1.0 - 10^4		
Rapport de viscosité thermique	$R\mu_T$	1.0 - 10^7		
Grandeurs caractéristiques				
Vitesse	v	1.0	cm yr^{-1}	1468
Temps	t	424	Ga	1.0
Flux de chaleur	Φ	2.6	mW m^{-2}	1.0
Production de chaleur interne	H	2.72×10^{-13}	W kg^{-1}	1.0

Table 4.1. Paramètres et dimensionnements.

Le champ de composition est modélisé à l'aide de 10 million de traceurs de deux types, l'un pour le matériau régulier, l'autre pour le matériau dense. Le nombre de particules denses est réglé en imposant la fraction volumique de matériau dense, X. Ces particules denses sont initialement distribuées à la base du système dans une couche d'épaisseur adimensionnée h_{DL} (pour des raisons géométriques, h_{DL} est numériquement égale à X). La quantité mesurée est la concentration C en particule denses dans chaque cellule du modèle. Elle varie entre 0 et 1 selon que la cellule ne contient que des particules régulières ou que des particules denses. Le contraste de densité chimique crée une flottabilité chimique qui s'oppose à la flottabilité thermique. L'importance relative de la flottabilité chimique est habituellement mesurée par la flottaison,

$$B = \frac{\Delta\rho_c}{\alpha_S \rho_S \Delta T_S}. \qquad (4.4)$$

où α_S et ρ_S sont l'expansion thermique et la densité en surface, et ΔT_S le saut de température super-adiabatique à travers le système. Dans cette recherche, j'ai varié la flottaison entre 0.1 et 0.5 ce qui correspond, en supposant $\alpha_S = 5.0\times10^{-5}$ K^{-1}, $\rho_S = 3300$ kg/m^3, et $\Delta T_S = 2500$ K, à des contrastes de densité compris entre 41.3 et 206.3 kg/m^3, valeurs tout-à-fait pertinentes dans le cas du manteau terrestre.

La loi de viscosité tient compte des propriétés discutées dans le paragraphe 5.1.2 et s'écrit

$$\mu(T,z,C) = \begin{cases} \mu_S \exp[V_a z - E_a(T - T_{ref}) + \Lambda_a C], & z < 0.228 \\ \mu_S R\mu_{660} \exp[V_a z - E_a(T - T_{ref}) + \Lambda_a C], & z \geq 0.228 \end{cases} \qquad (4.5)$$

où T et z sont la température et la profondeur adimensionnés, et μ_S est la viscosité de surface, et $T_{ref} = 0.9$. $R\mu_{660}$ est le rapport de viscosité à $d = 660$ km ($z = 0.228$). L'augmentation de viscosité avec la profondeur est contrôlée par V_a qui représente le volume d'activation. De même, l'augmentation de viscosité avec la température est contrôlée par E_a qui représente l'énergie d'activation. On a bien sûr $R\mu_z = \exp(V_a)$ et $R\mu_T = \exp(E_a)$. Par analogie, on peut aussi définir un potentiel chimique, Λ_a, qui contrôle les variations de viscosité avec la composition.

La transition de phase à 660 km est modélisée par une discontinuité définie par un point d'ancrage en température et profondeur ($d = 660$ km et $T_{660} = 1900$ K, ou, en valeurs adimensionnées, $z = 0.228$ et $T_{0.228} = 0.76$), et une pente de Clapeyron Γ, dont la grandeur caractéristique est

$$\Gamma_0 = \frac{\rho_S g D}{\Delta T_S}, \qquad (4.6)$$

où g est l'accélération de la gravité et D l'épaisseur du manteau. Avec $\rho_S = 3300$ kg/m^3, et $\Delta T_S = 2500$ K, on a $\Gamma_0 = 38.2$ MPaK^{-1}. Le contraste de densité au passage de cette transition

est $\Delta\rho_{660}$ = 400 kg/m^3. Enfin, il ne sera pas tenu compte des transitions de phase à 410 et 520 km, qui semblent avoir peu d'effets sur l'écoulement (Tackley et al., 1994).

Dans le cas d'un fluide compressible, les équations de conservation font intervenir un modèle thermodynamique radial de référence (notamment pour la densité, l'expansion thermique et la diffusivité thermique, Figure 4.4), que l'on calcule à partir de relations appropriées (Tackley, 1998b). Ces quantités sont adimensionnées avec leurs valeurs de surface, que l'on trouvera dans la Table 4.1. Le profil d'expansion thermique revêt une importance particulière. Il décroit régulièrement avec la profondeur jusqu'à la base du système, où il atteint 20% de sa valeur en surface. Cela a pour effet de réduire la flottabilité thermique (à variation de température égale, le contraste de densité thermique diminue), et de renforcer la stratification chimique.

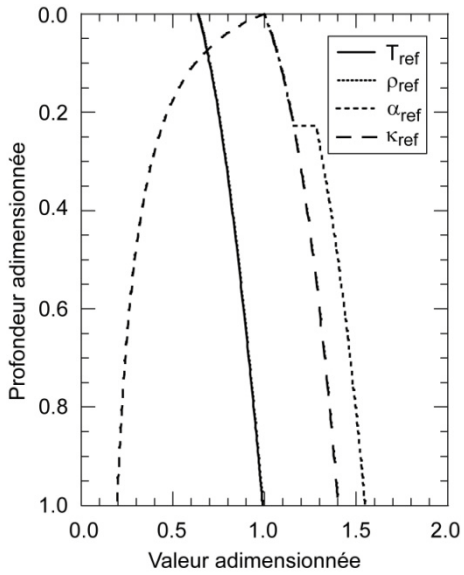

Figure 4.4 – Modèle thermodynamique radial de référence en valeurs adimensionnées. T est la température, ρ la densité, et α et κ l'expansion et la diffusivité thermique.

4.2.3 Comparaison avec la tomographie sismique

Pourquoi utiliser le modèle de tomographie probabiliste RT246g (Resovsky et Trampert, 2003; Trampert et al., 2004) pour tester les modèles de convection thermochimiques ? Sa résolution verticale (5 couches, dont trois dans le manteau inférieur) et sa résolution latérale (limitée aux degrés d'harmoniques sphériques 2, 4, et 6) ne sont en effet pas exceptionnelles. Trois raisons principales à ce choix. D'abord, RT246g apporte des contraintes indépendante sur la distribution de densité, ce qui permet de lever en grande partie le trade-off entre la température et la composition. Ensuite, il défini une fonction de densité de probabilité (pour V_S, V_Φ et la densité) en chaque point du modèle, c'est-à-dire une estimation fiable des incertitudes. Enfin, il est basé sur une méthode de Monte-Carlo

(l'algorithme de voisinage), c'est-à-dire qu'il s'affranchi de toute information *a priori* et de la subjectivité qui l'accompagne.

Les comparaisons entre tomographie probabiliste et modèles thermochimiques sont basées sur les distributions de densité thermiques et chimiques. Celles-ci sont calculées par rapport aux profils moyens de température et de composition ($\langle T \rangle_z$ et $\langle C \rangle_z$), et font intervenir le modèle thermodynamique de référence (T_{ref}, ρ_{ref}, et α_{ref}), la densité ρ_T à la température T et pour $C = 0$ (matériau régulier), et la densité ρ_c à la température T_{ref} et pour une concentration de particule dense C. On a :

$$d\ln\rho_T = \frac{\rho_T(T) - \rho_T(\langle T \rangle_z)}{\rho_T(\langle T \rangle_z)} = -\frac{\alpha_{ref}(T - \langle T \rangle_z)}{[1 - \alpha_{ref}(\langle T \rangle_z - T_{ref})]} \quad (4.7a)$$

et $$d\ln\rho_c = \frac{\rho_c(C) - \rho_c(\langle C \rangle_z)}{\rho_c(\langle C \rangle_z)} = -\frac{\alpha_S \Delta T_S B(C - \langle C \rangle_z)}{[1 + \alpha_S \Delta T_S B\langle C \rangle_z]}, \quad (4.7b)$$

avec $$\rho_T = \rho_{ref}[1 - \alpha_{ref}(T - T_{ref})] \quad (4.8a)$$

et $$\rho_c = \rho_S[1 + \alpha_S \Delta T_S BC] \quad (4.8a)$$

où l'on aura aussi reconnu la flottaison B, l'expansion thermique en surface α_S, et le gradient super-adiabatique ΔT_S.

Les profils de RMS de $d\ln\rho_T$ et $d\ln\rho_c$ donnent une première idée sur la structure thermochimique du modèle. La présence d'une couche de matériau dense à la base du système se traduit par un pic de RMS autour de l'interface, et zéro ailleurs. Pour des structures telles que les panaches thermochimiques ou les réservoirs de matériau dense (Figure 4.5), les profils de RMS décroissent régulièrement avec la profondeur jusqu'à la base du système. Si, par contre, les matériaux denses et réguliers sont bien mélangés, le profil de RMS est constant et proche de zéro sur toute l'épaisseur du système. Cependant, les incertitudes sur la tomographie probabiliste et sa paramétrisation verticale ne permettent pas d'opérer une sélection parmi les modèles de convection thermochimique (Deschamps et al., 2007). Les cartes d'hétérogénéïtés spectrales (CHS, Tackley et al., 1994) donnent une information plus détaillée sur la structure thermodynamique. Pour une distribution 3D données, elles sont obtenues en calculant le spectre de puissance de l'expansion de Fourier (2D) de cette distribution, puis en représentant cette puissance en fonction du nombre d'onde ($k = \sqrt{k_x^2 + k_y^2}$) et de la profondeur.

La comparaison de ces spectres de puissances avec ceux de la tomographie probabiliste nécessite deux opérations supplémentaires. Il faut d'abord les convertir en spectres d'harmoniques sphériques (la plupart des modèles tomographiques globaux, dont RT246g, est développé en harmoniques sphériques). Si l'on impose que la puissance par unité de surface doit être la même pour les deux expansions, le signal contenu dans le degré

d'harmonique sphérique ℓ est calculée en additionnant les signaux contenus dans les nombre d'onde k qui satisfont (Chevrot et al., 1998)

$$\ell + \frac{1}{2} \leq ka \leq \ell + \frac{3}{2}, \tag{4.9}$$

où a est le rayon de la Terre. Suivant cette règle, on peu décomposer les distributions issues des modèles de convection jusqu'au degré d'harmonique sphérique 32, ce qui est largement suffisant pour une comparaison avec RT246g. Ensuite, il faut bien-sûr dégrader la résolution verticale des modèles de convection en moyennant les distributions issues ces modèles selon la paramétrisation verticale de RT246g (soit 5 couches, $24 \leq z \leq 410$ km, $410 \leq z \leq 660$ km, $660 \leq z \leq 1200$ km, $1200 \leq z \leq 2000$ km, $2000 \leq z \leq 2891$ km). Notons que les anomalies de composition étant paramétrisées en termes de fractions volumiques de fer et de pérovskite, la comparaison avec RT246g n'a de sens que dans le manteau inférieur.

4.2.4 Une petite remarque et un point de référence avant de continuer

Le nombre de paramètres explorés dans cette étude est grand, ce qui est sympathique car on peut ainsi définir des modèles relativement complexes. Cette approche comporte toutefois des désavantages. À tout vouloir faire varier on risque de ne plus savoir 'qui fait quoi'. Pour mieux appréhender le rôle de chaque paramètre il conviendra de varier indépendamment chacun des paramètres considérés. Plus ennuyeux, on se prive de méthodes d'analyses puissantes, telles que l'analyse de stabilité linéaire, qui délimite le domaine de stabilité du système en fonction des paramètres du modèle. Difficile aussi, avec tant de paramètres, de déterminer des lois d'échelles (p.e., pour le flux de chaleur, la température interne, ou encore le temps nécessaire au mélange), pourtant si utiles quantitativement. Quelques conclusions importantes peuvent néanmoins être tirées d'une recherche exhaustive.

Avant de commencer la recherche, il faut définir un cas de référence – en quelque sorte le point d'origine de la recherche dans l'espace des modèles – sans toutefois lui accorder une importance ou une signification particulière. Dans chaque expérience, on ne variera qu'un seul paramètre par rapport à ce cas. Prenons pour cas de référence une flottaison égale à 0.2, pas de variation thermique de la viscosité, un saut de viscosité à 660 km égal à 30, et un matériau dense 100 fois moins visqueux que le matériau régulier (les autres paramètres sont listés dans la Table 4.2). Avec ces valeurs, la couche dense initiale est rapidement déstabilisée, ce qui génère des panaches thermochimiques de grande taille (Figure 2 de l'article Deschamps et Tackley, 2008a). Ces structures expliquent assez bien les spectres de puissances des distributions observées par la tomographie probabiliste, mais leur durée de vie est très courte. Après cet épisode, le mélange entre les matériaux denses et régulier est efficace, ce qui signifie que sur le long terme, le cas de référence n'explique

pas la tomographie probabiliste. Ce que l'on cherche, au contraire, ce sont les ingrédients capables de maintenir de fortes variations de composition dans le manteau profond. De ce point de vue, le cas discuté plus haut constitue une référence acceptable.

Paramètre	Symbole	Cas de référence	Cas composite
Nombre de Rayleigh de référence	Ra_S	10^8	10^8
Flottaison	B	0.2[a]	0.2[a]
Fraction volumique de matériau dense	X	0.1	0.1
Chauffage interne	H_C	25[b]	25[b]
Rapport de chauffage chimique	RH_C	10	10
Pente de Clapeyron à d = 660 km	Γ	0.0	-0.0668[c]
Rapport de viscosité à d = 660 km	$R\mu_{660}$	30	30
Rapport de viscosité chimique	$R\mu_c$	10^{-2}	0.5
Rapport de viscosité radial	$R\mu_z$	10	10
Rapport de viscosité thermique	$R\mu_T$	1.0	10^6

Table 4.2. Deux cas particuliers. Le cas de référence, point d'origine de la recherche dans l'espace modèle, et un cas composite qui rassemble les ingrédients essentiels pour maintenir des variations latérales de composition à la base du système (§ 4.3). On trouvera un instantané du cas de référence (pour un temps proche du début du calcul) sur la Figure 2 de Deschamps et al. (2008a), et un instantané du cas composite (pour un temps proche de la fin du calcul) sur la Figure 11 de Deschamps et al. (2008b).
[a] Equivalent à un contraste de densité chimique de 82.5 kg/m^3.
[b] Equivalent à un flux de chaleur en surface de 65 mW/m^2.
[c] Soit, en valeur dimensionnée, -2.5 MPa/K.

4.3 Quelques ingrédients essentiels

Dans le paragraphe précédent, j'ai détaillé quelques points importants de la recherche systématique dans l'espace des modèles de convection thermochimiques. Que nous apprend cette recherche, et comment ces conclusions s'accordent-elles avec d'autres contraintes disponibles (et indépendantes de l'information sismologique) sur le manteau inférieur ?

La flottaison doit être choisie dans une fourchette raisonnable, typiquement entre 0.15 et 0.25, c'est-à-dire pour un contraste de densité chimique compris entre 60 et 100 kg/m^3). Des contrastes de densité chimiques plus forts conduisent à une stratification du système, où le matériau dense peut toutefois être entraîné par les panaches thermiques. Cette érosion diminue lorsque B augmente, et elle contrôle la topographie de la couche dense. Dans le meilleur des cas (B = 0.3) cette topographie est suffisante pour créer des trous dans la couche dense (Deschamps et Tackley, 2008b, Figure 8a-f), mais reste trop faible (h ~0.1, soit en valeur dimensionnée ~300 km) pour expliquer les anomalies de densité chimiques observées par la tomographie probabiliste. Estimons maintenant la flottaison pour le manteau terrestre. Supposons que le manteau 'régulier' soit pyrolitique (Si/Mg ~ 0.8, et Fe/Mg ~ 0.11), et que les excès de densité observés à la base du manteau soient liés à la présence de pérovskite (et/ou de post-pérovskite) riche en fer. À partir des données thermo-élastiques disponibles (y compris celle de Tsuchiya et al. (2004) pour la

post-pérovskite), et d'une modélisation appropriée de l'équation d'état (Deschamps et Trampert, 2004), on trouve qu'un excès de fer de 2.0 à 2.5% (c'est à peu près ce que prévoit la tomographie probabiliste), se traduit par un contraste de densité chimique entre 80 et 96 kg/m^3, soit (avec les paramètres de la Table 4.1) une flottaison comprise entre 0.19 et 0.22.

Le rapport entre la viscosité du matériau dense et celle du matériau régulier ne doit être ni trop faible ni trop fort, disons entre 0.1 et 10. De faibles valeurs de $R\mu_c$ (par exemple, pour le cas de référence, 10^{-2}) favorisent un mélange rapide et efficace entre les matériaux dense et régulier, tandis des valeurs élevées (30 et plus) conduisent à une stratification du système. Dans ce dernier cas, de nouveau, une petite fraction du matériau dense est entraînée vers la partie supérieure du système par érosion thermique. Il est difficile d'estimer quel pourrait être la valeur de $R\mu_c$ pour le manteau terrestre. Tout d'abord, on n'a pas de certitude concernant la nature des anomalies de composition à la base du manteau. Même en supposant qu'il s'agit d'un excès de fer combiné, éventuellement, à la présence de post-pérovskite, on ne dispose pas, pour le moment, de données fiables sur la viscosité de la post-pérovskite et des pôles ferreux des minéraux du manteau inférieur.

Un rapport de viscosité thermique élevé, 10^4 ou plus, se traduit par la formation de réservoirs de matériau dense à la base des panaches thermiques (Figure 4.5). Ces structures sont particulièrement intéressantes. Elles sont de grande taille (et ont donc une signature spectrale très marquée pour les petits nombres d'onde et les petits degrés d'harmoniques sphériques); elles ont une topographie très développée (1000 km et plus); et elles survivent à la convection pendant un très long intervalle de temps. En fait, elles sont même très stables, puisqu'elles sont toujours présentes à la fin d'un calcul volontairement poussé jusqu'à $t = 0.0212$ (9.0 Ga). Enfin, les spectres de puissances des anomalies de densité associées à ces structures expliquent remarquablement bien les spectres observés par la tomographie probabiliste (Figure 4.7), excepté pour les anomalies chimiques dans la couche $660 \leq z \leq 1200$ km. La viscosité du manteau inférieur dépend de la température, et elle est bien expliquée par une loi d'Arrhénius. En prenant un géotherme de référence de 1200 °C et un saut de température super-adiabatique de 2500 K, un rapport de viscosité thermique compris entre 10^5 et 10^7 implique une énergie d'activation comprise entre 220 et 310 kJ/mol. Ces valeurs sont compatibles avec les énergies d'activation mesurées en laboratoire pour la pérovskite et la magnésio-wüstite (Yamazaki et Karato, 2001).

Le rapport de viscosité à 660 km de profondeur doit être de un à deux ordres de grandeur. Si $R\mu_{660}$ est trop petit, l'écoulement est dominé par de petites structures thermochimiques, et le mélange est très rapide (Figure 7 de Deschamps et al., 2008a). Des valeurs élevées (> 100) de $R\mu_{660}$ permettent de maintenir (même pour de faibles valeurs de $R\mu_T$) des structures thermochimiques à grande échelles pendant des périodes de temps

raisonnables, mais le prix à payer est une réduction drastique de la vigueur de l'écoulement. De plus ces structures finissent par disparaître sur le long terme. La fourchette de valeurs de suggérée par notre recherche n'est pas vraiment une surprise. La plupart des estimations géophysiques de ce paramètre donnent également une valeur comprise entre 10 et 30 (p.e., Nakada et Lambek, 1989; Forte et Mitovica, 1996).

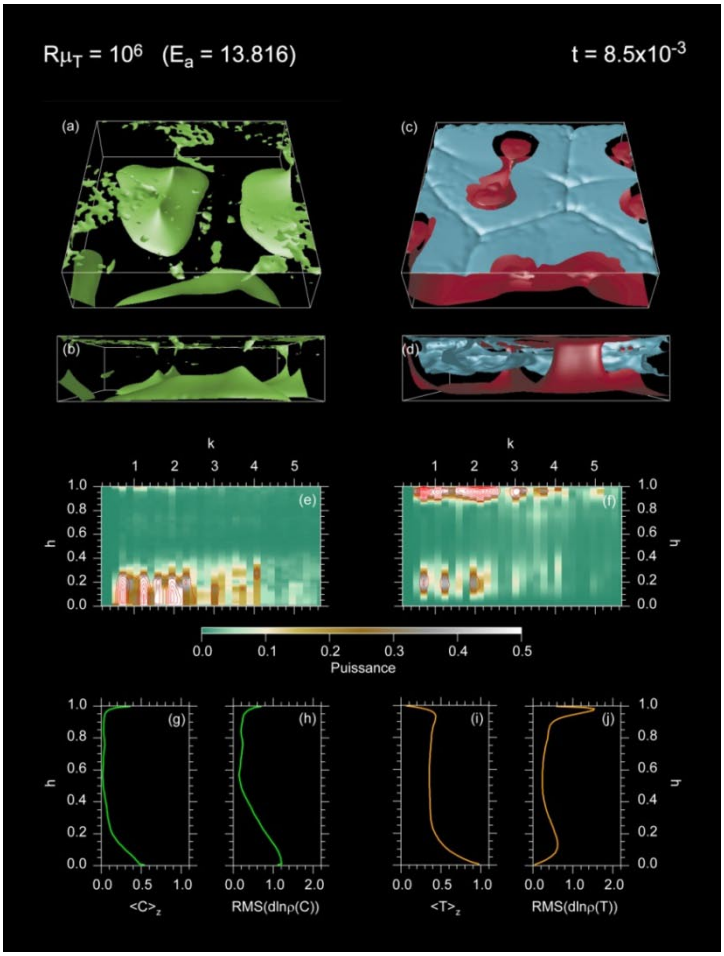

Figure 4.5 – Un instantané à t = 8.5×10^{-3} (3.6 Ga) pour le cas Rμ$_T$ = 10^6. Les autres paramètres sont les mêmes que pour le cas de référence. (a et b) Isosurfaces de la concentration en particules denses pour C = 0.5. (c et d) Isosurfaces de la température résiduelle adimensionnée pour $T - \langle T \rangle$ = -0.25 (en bleu) et $T - \langle T \rangle$ = 0.15 (en rouge). (e) Carte d'hétérogénéïté spectrale (CHS) pour les anomalies de densité chimiques, dlnρ$_c$. (f) Carte d'hétérogénéïté spectrale pour les anomalies de densité thermiques, dlnρ$_T$. Ces cartes sont représentés à la fois avec un code de couleur et des courbes de niveau (avec un intervalle de 0.2). h est l'altitude adimensionnée. (g) Profil vertical moyen de la concentration en particule dense, $\langle C \rangle_z$. (g) Profil vertical de la RMS des anomalies de densité chimiques, dlnρ$_c$. (h) Profil vertical moyen de la température adimensionnée, $\langle T \rangle_z$. (g) Profil vertical de la RMS des anomalies de densité thermiques, dlnρ$_T$.

Enfin, la pente de Clapeyron de la transition de phase à 660km doit être comprise entre -3.0 et -1.5 MPa/K. L'effet (et l'intérêt) principal de cet ingrédient est de maintenir le matériau dense sous la transition de phase. Au contraire des slabs, qui traversent (vers le bas) cette transition de phase, le matériau dense ne parvient quasiment pas à la franchir

(vers le haut). Le matériau dense se trouve majoritairement piégé dans la partie inférieure du système (Figure 4.6), avec pour conséquence de fortes variations latérales de composition à la base système ($z \geq 0.85$), et des variations plus modérées immédiatement sous la transition. Celles-ci expliquent bien les spectres de puissance observés par la tomographie probabiliste (Figure 4.7). Une pente de Clapeyron trop négative ($\leq$ -3.0 MPa/K) n'est pas souhaitable, car elle maintient le matériau dense proche de la base système. Enfin, rappelons que la transformation de ringwoodite en pérovskite et en magnésio-wüstite est endothermique, et que sa pente de Clapeyron est estimée autour de -3.0 à -2.0 MPa/K (Bina et Helffrich, 1994).

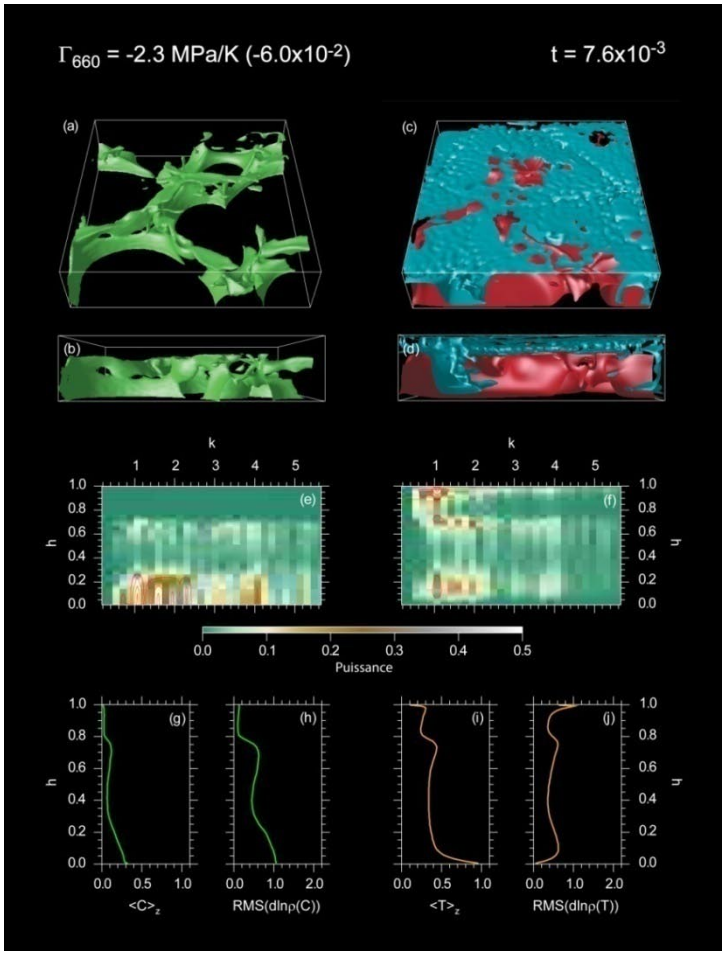

Figure 4.6 – Un instantané à t = 7.6×10^{-3} (3.2 Ga) pour le cas Γ_{660} = -2.3 MPa/K (-0.06 en adimensionné). Les autres paramètres sont les mêmes que pour le cas de référence. Le descriptif des différents graphes est le même que sur la Figure 4.5. Sur les graphes c et d, les valeurs des isosurfaces de la température résiduelle sont $T - \langle T \rangle$ = -0.15 (en bleu) et $T - \langle T \rangle$ = 0.15 (en rouge).

Reste à tester un modèle composite, comportant simultanément les ingrédients que l'on vient de discuter. Les propriétés de ce cas sont listées dans la Table 4.2. Un instantané de ce modèle est représenté sur la Figure 11 de Deschamps et Tackley (2008b). Ce modèle ressemble comme deux gouttes d'eau à celui obtenu pour un rapport de viscosité thermique

élevé (Figure 4.5). La topographie des réservoirs est cependant plus marquée, ainsi que les variations latérales de température dans la partie inférieure du système. Globalement, ce modèle explique très bien les spectres des anomalies de densité observé par la tomographie probabiliste (Figure 4.7), sauf ceux des anomalies chimiques entre 660 et 1200 km. Celles-ci pourraient être liées à l'accumulation momentanée de slabs entre 660 et ~1000 km de profondeur, comme le suggère des modèles tomographiques régionaux récent (Fukao et al., 2001). Dans nos modèles, la modélisation du champ chimique ne tient pas compte des variations de compositions induites par les slabs. Ceux-ci ne laissent donc pas de signature chimique particulière, au passage de la transition de phase à 660 km (les fortes anomalies observées pour le cas $\Gamma = -6.0\times10^{-2}$ sont simplement liés à l'accumulation de matériau dense sous la transition de phase). En revanche, les anomalies de densités thermiques dans la couche 660-1200 km sont elles très nettes.

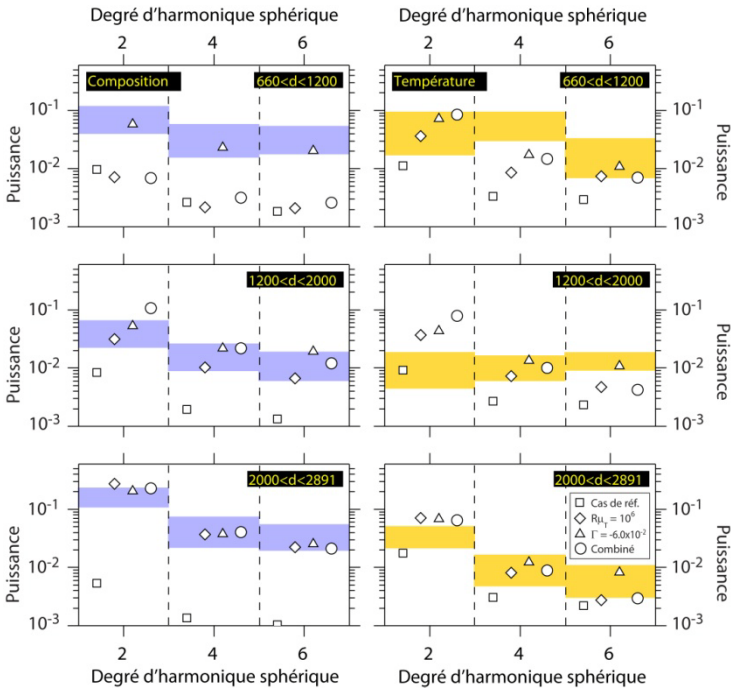

Figure 4.7 – Spectres de puissance des anomalies de densité chimiques (à gauche) et thermique (à droite) pour quelques cas. Les anomalies ont été moyennées dans le temps entre 0.85×10^{-3} et 1.06×10^{-2} (3.5 - 4.5 Ga), et verticalement dans trois couches. Les bandes bleues (oranges) représentent les spectres observés par la tomographie probabilistes à l'intérieur de deux barres d'erreur.

4.4 Un réservoir de matériau dense à la base du manteau ?

La condition initiale qui consiste à imposer une couche dense à la base du système apparaît quelque peu *ad hoc*. Il existe cependant plusieurs mécanismes capables d'expliquer la présence d'une couche de matériau dense à la base du manteau. Le modèle le plus récent, et sans doute l'un des plus séduisant, est celui de Labrosse et al. (2007). Selon ce modèle, la

cristallisation d'un océan magmatique à la base du manteau, lui même issu de la migration de poches de silicates riches en fer, pourrait être à l'origine d'un réservoir de matériau dense (car riche en fer) à la base du manteau. Ce modèle est compatible avec des contraintes géochimiques récentes basées sur les différences isotopiques entre les chondrites et les roches du manteau (Boyet et Carlson, 2006). Il donne également une explication élégante des zones de très faibles vitesses sismiques (plus connues sous leur acronyme anglais, ULVZ) observées localement à la base du manteau (p.e., Williams et Garnero, 1996). Ces zones seraient des poches de fusion partielle rescapées de la cristallisation de l'océan initial.

Un autre scénario, également attractif, fait appel au recyclage d'une croûte primitive qui serait formé très tôt dans l'histoire de la Terre. Des données géochimiques basées sur le système Sm-Nd (Caro et al., 2003) indiquent clairement que les plus anciennes roches de la croûte actuelle se sont formées à partir d'un manteau déjà en partie appauvri en certains éléments. La différenciation se serait produite vers 4.46 Ga. D'autres mesures plus récentes (Caro et al., 2005) sont venu étayer cette hypothèse, en montrant que le réservoir complémentaire aurait cristallisé à partir d'un océan magmatique pour former une croûte primitive. Celle-ci aurait ensuite été subductée, et résiderait de nos jours dans le manteau profond, où elle resterait piégée (Boyet et Carlson, 2006). Les modèles de convection thermochimique de van Thienen et al. (2004) ont montré que ce scénario est viable d'un point de vu dynamique, et que sous certaines conditions une croûte primitive peut migrer vers la base du manteau en 0.5 Ga.

4.5 Conclusions et perspectives

Supposons, comme dans le paragraphe précédent, qu'une couche de matériau dense se soit formée tôt dans l'histoire de la Terre. Une question cruciale est maintenant de savoir si un ou des réservoirs de matériau dense issus de cette couche ont pu survivre à la convection pendant 4 milliard d'années. La recherche systématique dans l'espace des modèles de convection thermochimique nous a apporté des réponses préliminaires en soulignant les rôles cruciaux joués par le rapport de viscosité thermique et la pente de Clapeyron de la transition de phase à 660 km pour maintenir de tels réservoirs à la base du manteau. Bien que relativement exhaustive, cette recherche ne prétend pas avoir fait le tour du sujet. D'autres paramètres doivent encore être explorés.

Par rapport à la convection de Rayleigh-Bénard, la géométrie sphérique modifie la symétrie entre les couches limites thermiques chaude et froide. On peut donc s'attendre à des effets dynamiques supplémentaires non négligeables en comparaison des cas 3D-Cartésiens, peut-être une stabilisation accrue de la couche de matériau dense (toutes choses

égales par ailleurs). De futurs modèles devraient également tenir compte de la phase post-pérovskite à la base du système. Ce faisant, Nakagawa et Tackley (2006) ont remarqué que les spectres des anomalies de composition sont fortement influencés par la topographie de la post-pérovskite. Notons toutefois que la présence de post-pérovskite à la base du manteau n'est pas absolument avérée, et que la couche D" est sans doute plus complexe qu'une simple couche de post-pérovskite (Lay et Garnero, 2007). Un paramètre dont il a été peu question jusqu'à présent est le profil de référence de l'expansion thermique. Question capitale, pourtant, car l'expansion thermique contrôle la flottabilité thermique. Il ne sera pas inutile, lors de futurs travaux, de calculer des modèles pour différents profils de référence, notamment pour des profils issus de la modélisation de l'équation d'état du manteau inférieur (Deschamps et Trampert, 2004). Enfin, une modélisation plus fine du champ chimique, tenant compte de sources et de puits de matériau dense, par exemple la création (par fusion partielle et ségrégation) et le recyclage (par subduction) de MORB, est souhaitable. Une amélioration relativement simple serait de modéliser le champ chimique avec trois types de particules (pour la pyrolite, les MORB, et l'harzburgite) au lieu de deux. Cela permettrait aussi de définir une composition différente pour les slabs et peut-être d'expliquer le désaccord entre les spectres des anomalies chimiques prédits par les modèles de convection dans la couche 660-1200 km, et ceux observés par la tomographie probabiliste.

Beaucoup reste encore à faire dans ce domaine. Il n'en reste pas moins que les modèles de convection thermochimique, lorsque l'on choisit soigneusement quelques paramètres importants, s'accordent remarquablement bien avec la tomographie probabiliste. La piste est ouverte.

Bibliographie

Bina, C.R., et G. Helffrich, 1994. Phase transitions Clapeyron slopes and transition zone seismic discontinuity tomography, *J. Geophys. Res.*, **99**, 15853-15860.

Boyet, M., et R.W. Carlson 2006. ^{142}Nd evidence for early (>4.53 Ga) global differentiation of the silicate Earth, *Science*, **309**, 576-581.

Caro, G., B. Bourdon, J.-L. Birck, et S. Moorbath, 2003. ^{146}Sm-^{142}Nd evidence from Isua metamorphosed sediments for early differentiation of the Earth's mantle, *Nature*, **423**, 428-432.

Caro, G., B. Bourdon, B.J. Wood, et A. Corgne, 2005. Trace-element fractionation in Hadean mantle generated by melt segregation from a magma ocean, *Nature*, **436**, 246-249.

Christensen, U.R., et D.A. Yuen, 1985. Layered convection induced by phase transitions, *J. Geophys. Res.*, **90**, 10291-10300.

Chevrot, S., J.-P. Montagner, et R. Snieder, 1998. The spectrum of tomographic Earth models. *Geophys. J. Int.*, **133**, 783–788.

Coltice, N., 2005. The role of convective mixing in degassing the Earth's mantle, *Earth Planet. Sci. Lett.*, **234**, 15-25.

Davaille, 1999. Simultaneous generation of hotspots and superswells by convection in a heterogeneous planetary mantle, *Nature*, **402**, 756-760.

Davaille, A., et C. Jaupart, 1993. Transient high-Rayleigh number thermal convection with large viscosity variations, *J. Fluid Mech.*, **253**, 141-166.

Deschamps, F., et C. Sotin, 2000. Inversion of two-dimensional numerical experiments for a fluid with strongly temperature-dependent viscosity, *Geophys. J. Int.*, **143**, 204-218.

Deschamps, F., et C. Sotin, 2001. Thermal convection in the outer shell of large icy satellites, *J. Geophys. Res.*, **106**, 5107-5121.

Deschamps, F., et J. Trampert, 2004. Towards a lower mantle reference temperature and composition, *Earth Planet. Sci. Lett.*, **222**, 161-175.

Deschamps, F., J. Trampert, et P.J. Tackley, 2007. Thermo-chemical structure of the lower mantle: seismological evidences and consequences for geodynamics, in D.A. Yuen et al. Eds., *Superplumes: beyond plate tectonics*, Springer, pp. 293-320.

Deschamps, F., et P.J. Tackley, 2008a. Searching for models of thermo-chemical convection that explain probabilistic tomography. I. Principles and influence of rheological parameters, *Phys. Earth Planet. Inter.*, **171**, 357-373.

Deschamps, F., et P.J. Tackley, 2008b. Searching for models of thermo-chemical convection that explain probabilistic tomography. II. Influence of physical and compositional parameters parameters, soumis à *Phys. Earth Planet. Inter.*.

Ferrachat, S., et Y. Ricard, 2001. Mixing properties in the Earth's mantle: effect of the viscosity stratification and oceanic crust segregation, *Geochem. Geophys. Geosys.*, **2**, doi:10.1029/2000GC000092.

Forte, A.M., et J.X. Mitrovica, 1996. New inferences of mantle viscosity from joint inversion of long-wavelength mantle convection and post-glacial rebound data, *Geophys. Res. Lett.*, **23**, 1147-1050.

Fukao, Y., S. Widiyantoro, et M. Obayashi, 2001. Stagnant slabs in the upper and lower transition regions, *Rev. Geophys.*, **39**, 291-323.

Hager, B.H., et M.A. Richards, 1989. Long-wavelength variations in Earth's geoid: physical models and dynamical implications, *Phil. Trans. Roy. Soc. London A*, **328**, 309-327.

Ishii, M., et J. Tromp, 1999. Normal-mode and free-air gravity constraints on lateral variations in velocity and density of Earth's mantle, *Science*, **285**, 1231-1236.

Jaupart, C., P. Molnar, et E. Cottrell, 2007. Instability of a chemically dense layer heated from below and overlain by a deep less viscous fluid, *J. Fluid Mech.*, **572**, 433-469.

Jellinek, A.M., et M. Manga, 2002. The influence of a chemical boundary layer on the fixity, spacing and lifetime of mantle plumes, *Nature*, **418**, 760-763.

Karato, S.-I., et P. Wu, 1993. The rheology of the upper mantle: a synthesis, *Science*, **260**, 771-778.

Kellogg, L.H., B.H. Hager, et R.D. van der Hilst, 1999. Compositional stratification in the deep mantle, *Science*, **283**, 1881-1884.

Labrosse, S., J.W. Hernlund, et N. Coltice, 2007. A crystallizing dense magma ocean et the base of the Earth's mantle, *Nature*, **450**, 866-869.

Lay, T., et E.J. Garnero, 2007. Reconciling the post-perovskite phase transition with seismological observations of the lowermost mantle structure, in K. Hirose et al. (Eds.), Post-perovskite: the last mantle phase transition, *Geophys. Monograph*, **174**, American Geophysical Union, Washington, DC, pp. 129-153.

Machetel P., et P. Weber, 1991. Intermittent layered convection in a model mantle with an endothermic phase change at 670 km, *Nature*, **350**, 55-57.

McKenzie, D.P, J.M. Roberts, et N.O. Weiss, 1974. Convection in the Earth's mantle: towards a numerical simulation, *J. Fluid. Mech.*, **62**, 465-538.

McNamara, A.K., et S. Zhong, 2004. Thermochemical structures within a spherical mantle, *J. Geophys. Res.*, **109**, doi: 10.1029/2003JB002847.

Moore, D.R., et N.O. Weiss, 1973. Two-dimensional Rayleigh-Bénard convection, *J. Fluid. Mech.*, **58**, 289-312.

Moresi, L.-N., et V.S. Solomatov, 1995. Numerical investigation of 2D convection with extremely large viscosity variations, *Phys. Fluids*, **7**, 2154-2162.

Nakada M., et K. Lambeck, 1989. Late Pleistocene and Holocene sea-level change in the Australian region and mantle rheology, *Geophys. J. Int.*, **96**, 497-517.

Solomatov, V.S., et L.-N. Moresi, 1996. Stagnant lid convection on Venus, *J. Geophys. Res.*, **101**, 4737-4753.

Tackley, P.J., 1998a. Self-consistent generation of tectonic plates in three-dimensional mantle convection, *Earth Planet. Sci. Lett.*, **157**, 9-22.

Tackley, P.J., 1998b. Three-dimensional simulations of mantle convection with a thermo-chemical CMB boundary layer: D"?, in M. Gurnis et al. (Eds.), The Core-Mantle Boundary Region, *Geodynamical Ser.*, **28**, American Geophysical Union, Washington, DC, pp. 231-253.

Tackley, P.J., 2002. Strong heterogeneity caused by deep mantle layering, *Geochem. Geophys. Geosys.*, **3**, doi: 10.1029/2001GC000167.

Tackley, P.J., D.J. Stevenson, G.A. Glatzmaier, et G. Schubert, 1994. Effects of multiple phase transitions in three-dimensional spherical model of convection in the Earth's mantle, *J. Geophys. Res.*, **99**, 15877-15901.

Tsuchiya, T., J. Tsuchiya, K. Umemoto, et R.M. Wentzcovitch, 2004. Phase transition in $MgSiO_3$ perovskite in the lower mantle, *Earth Planet. Sci. Lett.*, **224**, 241-248.

Trampert, J., F. Deschamps, J.S. Resovsky, et D.A. Yuen, 2004. Probabilistic tomography maps significant chemical heterogeneities in the lower mantle, *Science*, **306**, 853-856.

van der Hilst, R.D., et H. Kárason, 1999. Compositional heterogeneity in the bottom 1000 kilometers of Earth's mantle: towards a hybrid convection model, *Science*, 283, 1885-1888.

van Thienen, P., J. van Summeren, R.D. van der Hilst, A.P. van den Berg, et N. J. Vlaar, 2005. Numerical study of the origin and stability of chemically distinct reservoirs deep in Earth's mantle, in: R.D. van der Hilst et al. (Eds.), Earth's deep mantle: structure, evolution and composition, *Geophys. Monograph*, **160**, American Geophysical Union, Washington, DC, pp. 117-136.

Weertman, J., 1970. The creep strength of the Earth's mantle, *Rev. Geophys. Space Phys.*, **8**, 145-168.

Williams, Q., et E.J. Garnero, 1996. Seismic evidence for partial melt at the base of the Earth's mantle, *Science*, **273**, 1528-1530.

Yamazaki, D., et S.-I. Karato, 2001. Some mineral physics constraints on the rheology and geothermal structure of Earth's lower mantle, *Amer. Mineral.*, **86**, 385-391.

Zhong, S., et B.H. Hager, 2003. Entrainment of a dense layer by thermal plumes, *Geophys. J. Int.*, **154**, 666-676.

CHAPTER 11

THERMO-CHEMICAL STRUCTURE OF THE LOWER MANTLE: SEISMOLOGICAL EVIDENCE AND CONSEQUENCES FOR GEODYNAMICS

FRÉDÉRIC DESCHAMPS[1,3], JEANNOT TRAMPERT[1], AND PAUL J. TACKLEY[2]

[1] *Department of Earth Sciences, Utrecht University, Budapestlaan 4, PO Box 80021, 3508 TA Utrecht, The Netherlands;*
E-mail: frederic.deschamps@erdw.ethz.ch

[2] *Department of Earth and Space Sciences, University of California, 595 Charles Young Drive East, Los Angeles, California 90095, USA*

[3] *Now at Institute of Geophysics, Swiss Federal Institute of Technology, HPP Honggerberg L8.1, 8083 Zurich, Switzerland*

Abstract

We combine recent progress in seismic tomography and numerical modeling of thermo-chemical convection to infer robust features on mantle structure and dynamics. First, we separate the observed density anomalies into their thermal and compositional contributions. The tomographic maps of thermo-chemical variations were computed using a new approach that combines a careful equation of state modeling of the lower mantle, independent constraints on density from probabilistic tomography, and a full statistical treatment for uncertainties analyses. We then test models of thermo-chemical convection against these density components. We compute synthetic anomalies of thermal and compositional density from models of thermo-chemical convection calculated with the anelastic approximation. These synthetic distributions are filtered to make meaningful comparisons with the observed density anomalies. Our comparisons suggest that a stable layer (i.e., that no domes or piles are generated from it) of dense material with buoyancy ratio $B \geq 0.3$ is unlikely to be present at the bottom of the mantle. Models of piles entrained upwards from a dense, but unstable layer with buoyancy ratio $B \sim 0.2$, explain the observation significantly better, but discrepancies remain at the top of the lower mantle. These discrepancies could be linked to the deflection of slabs around 1000 km, or to the phase transformation at 670 km, not included yet in the thermo-chemical calculations.

D. A. Yuen et al. (eds.), Superplumes, 293–320.
© 2007 *Springer.*

1 INTRODUCTION

Inferring the thermo-chemical structure of the mantle is a key problem in geophysics. Both thermal and chemical sources contribute to lateral variations in density, and the mode of mantle convection strongly depends on the relative strength of these two sources. It is the goal of seismology to map and quantify these contributions. Although seismic data represent our most detailed information on Earth structure, their interpretation raises difficulties that are often underestimated (Trampert and van der Hilst, 2005). For instance, the low shear-wave velocity structures in the deep mantle observed beneath Africa and the Pacific in many tomographic models (e.g., Su and Dziewonski, 1997; Vasco and Johnson, 1998; Masters et al., 2000) are usually referred to as "superplumes" and interpreted as hotter than average, and hence buoyant material (Forte and Mitrovica, 2001; Romanowicz and Gung, 2002). This interpretation implicitly assumes that shear-wave velocity anomalies are a reasonable proxy for temperature and density. It has been argued that in the uppermost mantle compositional effects do not strongly influence seismic velocity (Goes et al., 2000). In the lower mantle, however, pressure effects reduce the influence of temperature, and compositional effects may dominate seismic velocity anomalies (Anderson, 2001). Moreover, we should not forget that even if chemical anomalies do not significantly contribute to seismic velocity anomalies, they may still contribute to density anomalies, which are the important parameters in terms of dynamics.

Lateral variations of temperature and composition play a key role in linking geophysical observations and geodynamics. In recent years, mounting evidence suggested that chemical variations are present in the lower mantle (Ishii and Tromp, 1999; Kellogg et al., 1999; Forte and Mitrovica, 2001; Karato and Karki, 2001; Saltzer et al., 2001; Deschamps and Trampert, 2003), but difficulties remain to quantify thermo-chemical variations from seismology, and to relate them to thermo-chemical convection. Unless independent constraints on mass density are available, the distributions of temperature and composition inferred from tomographic models are not robust (Deschamps and Trampert, 2003).

Recent progresses shed new light on the link between seismology and geodynamics. Probabilistic tomography (Resovsky and Trampert, 2003) estimated independent and robust constraints on the lateral variations of density and seismic velocities, which can be converted into thermo-chemical variations (Trampert et al., 2004). Models of thermo-chemical convection that include the anelastic (e.g., Tackley, 1998) or extended Boussinesq (e.g., Schott and Yuen, 2004) approximation predict more realistic density contrasts. In this chapter, we investigate the geodynamical consequences of these improvements.

2 DENSITY ANOMALIES FROM THERMO-CHEMICAL CONVECTION

A variety of experimental (Olson and Kincaid, 1991; Davaille, 1999) and numerical (Hansen and Yuen, 1988; Christensen and Hofmann, 1994; Kellogg et al., 1999; Tackley, 1998, 2002; Schott and Yuen, 2004) models of thermo-chemical convection

have been developed, showing strong stratification or a more complex structure, depending on the fluid properties and on the buoyancy ratio. A major improvement was to perform calculations that account for fluid compressibility, either using the anelastic (Tackley, 1998), or extended Boussinesq (Schott and Yuen, 2004) approximation. In these approximations, some dissipation is present, and thermo-chemical properties are allowed to vary with depth through the prescription of a reference model. The decrease of thermal expansion with depth, which is well documented from mineral physics data (e.g., Anderson, 1995), is particularly important because it weakens the thermal buoyancy in the lowermost mantle. As a result, chemical stratification and the development of thermo-chemical domes require a smaller buoyancy ratio than in the classical Boussinesq approximation. The mode of convection is therefore controlled by several key parameters, including the buoyancy ratio, the thermal expansion, and the initial composition. Each convection regime predicts a distribution of temperature and composition that we want to test against seismological observations. In this section, we show how to compute the density variations due to the variations of temperature and composition predicted by several models of thermo-chemical convection (Tackley, 2002).

Details of the numerical modeling are described in Tackley (1998, 2002). The equations of conservation of mass, energy and momentum are solved for an anelastic, compressible fluid with infinite Prandlt number. Calculations are made in a 3-D Cartesian box of dimensions $4 \times 4 \times 1$. The fluid is cooled on the top, and heated both from below and from within. The top and bottom boundaries are isothermal, but some cases with zero heat flow at each point (i.e., no bottom heating) have also been considered. The viscosity depends on depth and composition. The viscosity increases smoothly by a factor of 10 across the fluid layer, and an additional viscosity jump equal to 30 is imposed at $z = 660$ km. The dense material is less viscous than the light material by a factor of 100. Calculations involve a depth-dependent reference thermodynamic model (Tackley, 1998), including temperature, density, thermal expansion, and thermal conductivity. The chemical field is represented using 10 million tracer particles dispatched everywhere in the box. Two types of particles are considered, one for regular material, and one for dense material. The fraction of dense particles C in each cell varies between $C = 0$ when the cell is filled with regular material only, and $C = 1$ when the cell is filled with particles of dense material only. The chemical density contrast $\Delta\rho_c^{\max}$ between dense and regular material is acting against the thermal buoyancy due to the thermal density contrast across the fluid layer $\Delta\rho_T^{\max} = \alpha_s \rho_s \Delta T_s$, where α_s and ρ_s are the thermal expansion and density at zero pressure, and ΔT_s the superadiabatic temperature difference between the top and the bottom of the layer. The relative strength of chemical and thermal buoyancies is measured by the global buoyancy ratio

$$B \equiv \frac{\Delta\rho_c^{\max}}{\alpha_s \rho_s \Delta T_s}, \tag{1}$$

which is used to define the chemical Rayleigh number.

The density at temperature T and regular material ($C = 0$) can be computed using the depth-dependent reference state (temperature $T_{\rm ref}$ and thermal expansion $\alpha_{\rm ref}$),

$$\rho_T = \rho_{\rm ref}[1 - \alpha_{\rm ref}(T - T_{\rm ref})]. \tag{2}$$

The density at temperature $T_{\rm ref}$ and fraction of dense material C can be expressed as a function of the buoyancy ratio (Eq. 1),

$$\rho_c = \rho_s[1 + BC\alpha_s\Delta T]. \tag{3}$$

If $\overline{T}$ and $\overline{C}$ are the average temperature and the average fraction of dense particles at a given depth, the relative thermal and chemical density anomalies are

$$\mathrm{d}\ln\rho_T = -\frac{\alpha_{\rm ref}(T - \overline{T})}{[1 - \alpha_{\rm ref}(\overline{T} - T_{\rm ref})]}, \tag{4}$$

$$\text{and} \quad \mathrm{d}\ln\rho_c = -\frac{B(C - \overline{C})}{(1 + B\overline{C}\alpha_s\Delta T)}\alpha_s\Delta T_s. \tag{5}$$

We computed synthetic $\mathrm{d}\ln\rho_T$ and $\mathrm{d}\ln\rho_c$ for four numerical models with buoyancy ratio equal to 0.2, 0.3 or 0.4 and percentage of dense material equal to 10% or 30% (Table 1). The bottom boundary is isothermal in all cases, except for $B = 0.4$, $X = 10\%$, in which the heat flow is put to zero everywhere on the boundary. Calculations were initialized with a geotherm from similar 2-D calculations that have reached a secular equilibrium. The models we tested are snapshots representative of long-term evolution, and the dimensional evolution times are listed in Table 1. Figure 1 shows isosurfaces of the fraction of dense particles and the non-dimensional temperature, and Figure 2 shows $\overline{T}, \overline{C}$, and the root mean square (RMS) of $\mathrm{d}\ln\rho_T$ and $\mathrm{d}\ln\rho_c$ as a function of depth. For $B = 0.3$, $X = 30\%$, a thick (~ 500 km) stable layer of dense and hot material sediments at the bottom of the fluid (Fig. 1, plots i–l). The RMS of $\mathrm{d}\ln\rho_T$ and $\mathrm{d}\ln\rho_c$ (Fig. 2, green curves) indicate that this layer is thermally and chemically homogeneous, and that most of the lateral variations of temperature and composition are located between 1600 and 2400 km. In the case $B = 0.4$, $X = 10\%$, a stable layer is also present at the bottom of the fluid, but it is much thinner and does not completely cover the bottom boundary (Fig. 1, plots m–p). The Strongest lateral variations of thermal and chemical density are found

Table 1. Four models of thermo-chemical convection[a]

B	X (%)	t (Gy)	Bottom boundary condition	Convective pattern
0.2	10	1.1	Isothermal	Piles
0.3	10	6.0	Isothermal	Discontinuous spokes
0.3	30	2.7	Isothermal	Thick stable layer
0.4	10	4.2	Zero heat flux at each point	Thin stable layer

[a] B is the buoyancy ratio, X the fraction of dense material and t the evolution time.

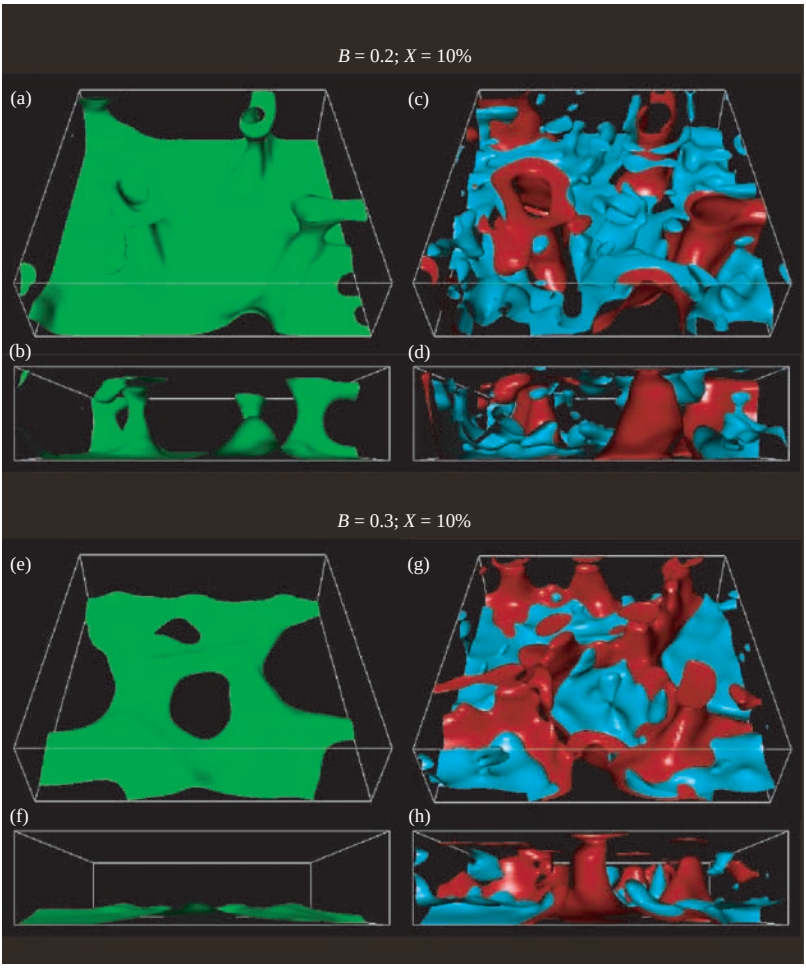

Figure 1. Isosurfaces of non-dimensional temperature (red and blue) and fraction of dense particles (green) for thermo-chemical convection models for various buoyancy ratios (B) and fractions of dense particles (X). Contour levels are $T = 0.0375$ (red), $T = -0.0375$ (blue), and $C = 0.5$ (green). The cases considered are (a–d) $B = 0.2$ and $X = 10\%$; (e–h) $B = 0.3$ and $X = 10\%$; (i–l) $B = 0.3$ and $X = 30\%$ (green curves); and (m–p) $B = 0.4$ and $X = 10\%$.

between 2500 and 2750 km (Fig. 2, blue curves). For $B = 0.3$, $X = 10\%$, the fluid is organized in a discontinuous spoke pattern of dense and hot material (Fig. 1, plots e–h). Strong lateral variations of density are present from $z = 2400$ km down to the bottom of the fluid (Fig. 2, red curves). Note that the two previous cases do not show significant lateral variations of composition for depths shallower than 2000 km. Finally, for $B = 0.2, X = 10\%$, piles are generated in the deep mantle from

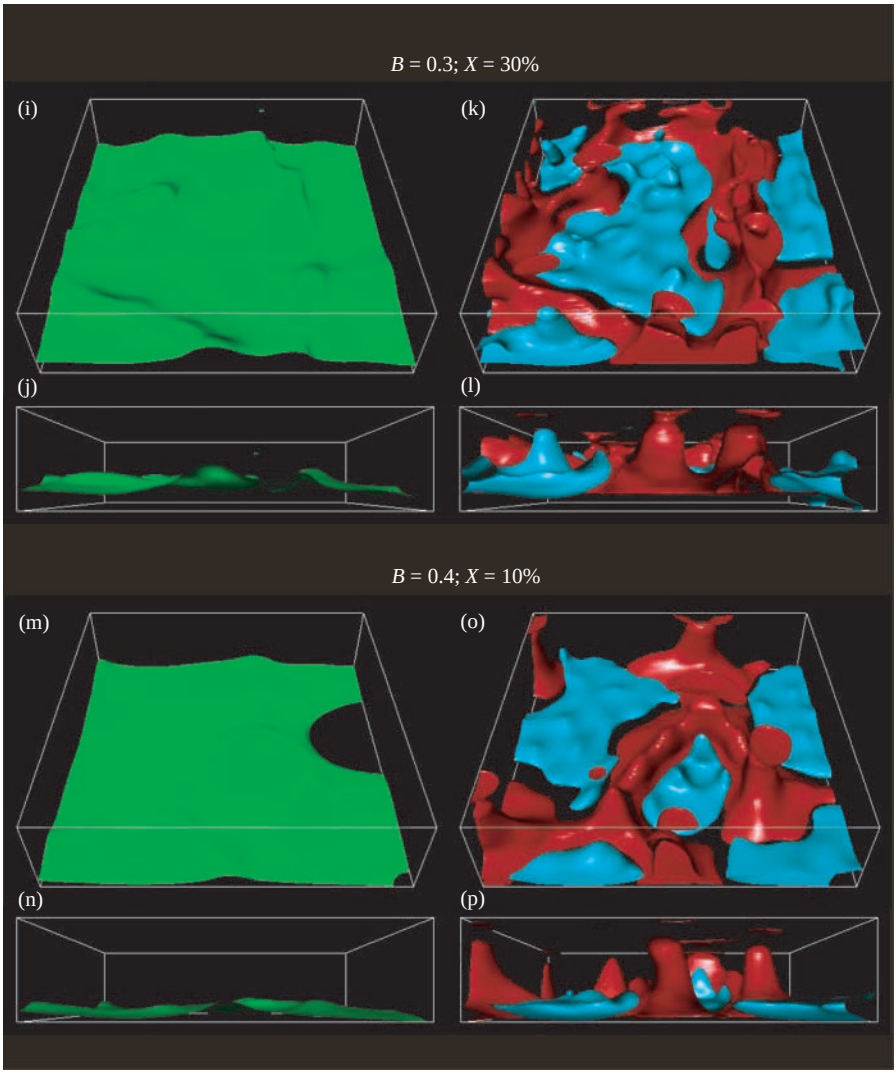

Figure 1. (*Continued*).

a layer of dense material, and are entrained upwards (Fig. 1, plots a–d). Chemical density anomalies are increasing progressively with depth, and drop dramatically to zero in the last 100 km (Fig. 2, orange curve). Some significant variations of density (thermal and chemical) are also observed in the upper half layer of the fluid. It is interesting to note that only this case predicts chemical variations throughout the fluid layer.

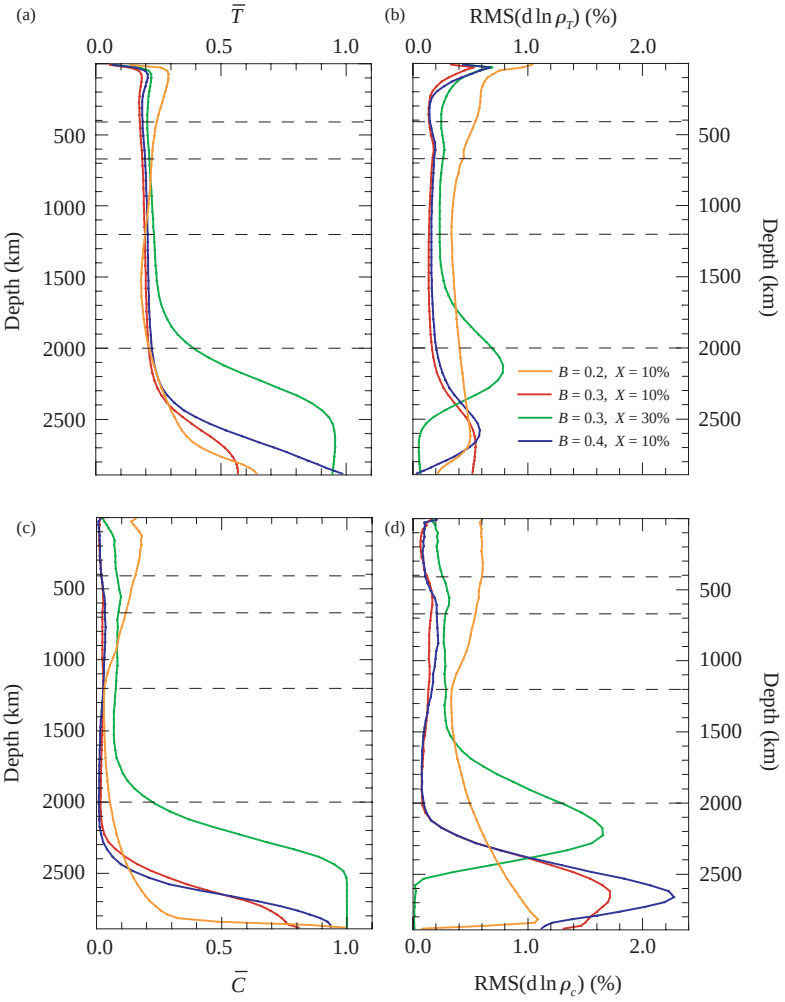

Figure 2. Profiles of (a) average temperature, (b) RMS of lateral variations of thermal density, (c) average fraction of dense particles, and (d) RMS of lateral variations of chemical density, for each model of thermo-chemical convection plotted in Figure 1. Orange curves are for $B = 0.2$ and $X = 10\%$, red curves for $B = 0.3$ and $X = 10\%$, green curves for $B = 0.3$ and $X = 30\%$, and blue curves for $B = 0.4$ and $X = 10\%$.

3 PROBABILISTIC SEISMIC TOMOGRAPHY

Seismic velocities alone cannot resolve the interconnection between temperature and composition. Independent constraints on density anomalies are needed to infer correct variations of temperature and composition. Early constraints on density from normal

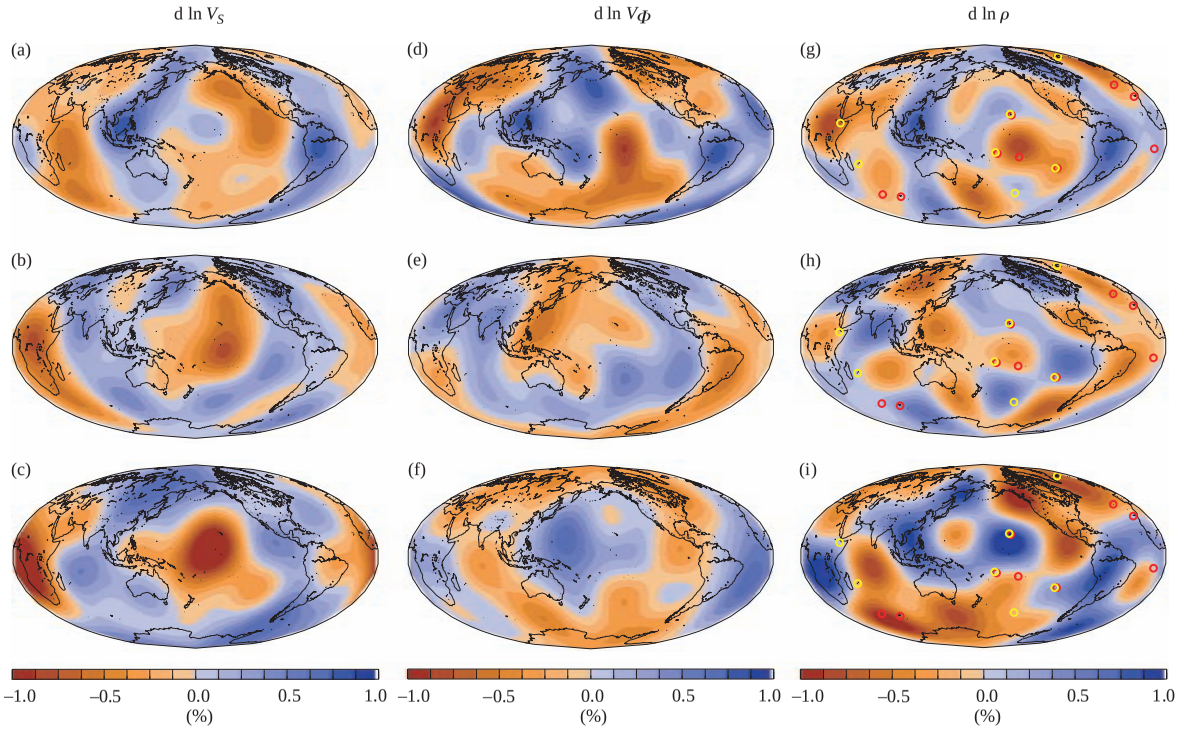

Figure 3. Mean relative anomalies of shear-wave velocity, bulk-sound velocity and density in the lower mantle predicted by probabilistic tomography (Trampert et al., 2004). The lower mantle is parameterized in three layers, from top to bottom $670 \leq z \leq 1200$ km, $1200 \leq z \leq 2000$ km, and $2000 \leq z \leq 2891$ km. Yellow and red dots on density anomalies maps locate hotspots that possibly originate in the deep lower mantle ($z \geq 2000$ km), as identified by Courtillot et al. (2003) and Montelli et al. (2004), respectively.

Table 2. Statistics for tomographic observables and thermo-chemical parameters[a]

Layer (km)		d ln V_S (%)	d ln V_Φ (%)	d ln ρ (%)	dT (K)	dX_{pv} (%)	dFe (%)	d ln ρ_T (%)	d ln ρ_c (%)
670–1200	A	0.77	0.87	0.79	340	11.9	1.8	0.64	0.80
	RMS(σ)	0.16	0.34	0.26	180	5.5	0.75	0.38	0.34
1200–2000	A	0.77	0.57	0.70	311	8.3	1.2	0.41	0.45
	RMS(σ)	0.12	0.22	0.28	112	3.0	0.55	0.15	0.22
2000–2891	A	1.21	0.66	1.05	475	9.3	2.6	0.44	0.95
	RMS(σ)	0.12	0.26	0.48	198	3.6	0.86	0.19	0.37

[a] A is the maximum amplitude of the average model, and RMS(σ) is the root mean square of the uncertainty.

modes were inferred by Ishii and Tromp (1999). More recent studies (Resovsky and Trampert, 2003) have developed the technique of probabilistic seismic tomography, which gives robust likelihoods for long wavelength models (spherical harmonic degree 2, 4, and 6) bulk-sound speed, shear wave speed, density and boundary topography in the mantle, from normal mode splitting and surface wave data. Probabilistic tomography explores the model space using a neighborhood algorithm (Sambridge, 1999a, 1999b) and estimates the likelihood of points in the model space by testing them against observables. The likelihoods of Resovsky and Trampert (2003), hereafter referred to as RT246g, are fully compatible with the observed gravity anomalies, and can thus be seen as a compact representation of the available seismic and gravity data. To a very good approximation, they can be represented as Gaussian distributions, and their standard deviation is remarkably stable within each layer. Figure 3 shows the mean of the distributions for d ln V_S, d ln V_Φ and d ln ρ in each layer, and Table 2 lists the root mean square (RMS) of the uncertainties (defined as one standard deviation around the mean value). In the deepest layer ($2000 \leq z \leq 2891$), there is a general agreement between the d ln V_S, d ln V_Φ of RT246g and those predicted by previous models (Su and Dziewonski, 1997; Vasco and Johnson, 1998; Masters et al., 2000). Like previous studies, RT246g shows regions of low shear-wave velocity beneath Africa and the Pacific. Assuming that d ln V_S scales with lateral variations of temperature, these regions are usually interpreted as "superplumes". However, a quick look to the density anomalies of RT246g (Fig. 3i) clearly shows that these features are denser than the surrounding mantle, and hence not buoyant.

4 LINKING OBSERVABLES TO THERMO-CHEMICAL PARAMETERS

4.1 Sensitivities of density and seismic velocities to temperature and composition

Density and thermo-elastic properties of a lower mantle aggregate depend on temperature, pressure and composition. A careful modeling of these effects is essential to correctly interpret seismological observations. The basic ingredients are the density

and elastic parameters at ambient temperature and pressure, and a set of relations (the equation of state, EOS) that extrapolate these ambient values at mantle temperature and pressure. To calculate thermo-elastic properties at any depth and temperature, we have built a parameterization that combines EOS modeling, experimental values of thermo-elastic parameters at ambient conditions, and existing *ab initio* data calculations (Deschamps and Trampert, 2004). The latter are used to check the consistency of high-temperature and high pressure extrapolations. We are thus able to calculate velocities and density of a given mineralogical composition at mantle pressures and temperatures. Several sources of uncertainties, mainly the error bars on the ambient thermo-elastic parameters and the assumed potential temperature and assemblage composition, contribute to uncertainties on the extrapolated thermo-elastic parameters. The latter are obtained by varying thermo-elastic parameters within their error bars, and average temperature and composition within reasonable range. PREM is used as an additional constraint to reduce the uncertainty range.

By repeating the calculations of elastic moduli and density at high-temperature and high-pressure for slightly different values of temperature and composition, we estimate the partial derivatives (or sensitivities) of density and seismic velocities to temperature and several compositional parameters as a function of depth. The sensitivities plotted in Figure 4 (used in Trampert et al., 2004) account for the most recent corrections for iron (Kiefer et al., 2002; Kung et al., 2002). Compared to previous work (Trampert et al., 2001; Deschamps and Trampert, 2003), sensitivities of shear-wave velocities to composition are different, mainly due to the iron correction for the pressure derivatives of the moduli of magnesio-wüstite (Kung et al., 2002), not included in previous work.

Sensitivities of both shear and bulk sound velocities have similar properties (sign and variation with depth): sensitivities to temperature are negative throughout the mantle and increase with depth; sensitivities to perovskite are positive and decrease with depth; and sensitivities to iron are negative and decrease with depth. A consequence of this similarity is that seismic velocities alone cannot discriminate between thermal and compositional effects. Sensitivities of density (Fig. 4c) are clearly different. The sensitivity to perovskite is negligible, whereas the sensitivity to iron is positive throughout the mantle and increases with depth. Density therefore carries essential information to separate thermal and compositional effects. Another important feature in Figure 4c is that the sensitivity of density to temperature (i.e., the thermal expansion of the aggregate) is decreasing in amplitude with depth. As a consequence, for a fixed temperature anomaly, the strength of the thermal buoyancy is also decreasing with depth.

4.2 Converting density and seismic velocities

Several thermo-chemical sources contribute to the observed anomalies of density and seismic velocities. Knowing the sensitivities of density and seismic velocities

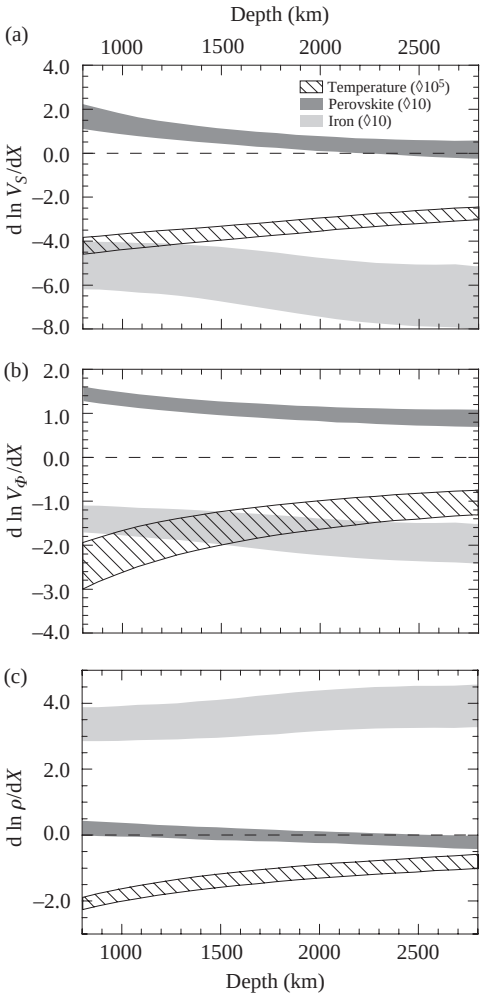

Figure 4. Sensitivities of seismic velocities and density to temperature (dashed areas), perovskite (dark grey areas) and iron content (light grey areas) as a function of depth. Dashed and shaded areas cover one standard deviation around the mean values. Mean and standard deviations are estimated from a collection of possible models that fit PREM within 1%, and are generated by varying thermo-elastic parameters within their error bars, and the average temperature and composition within reasonable ranges. For plotting convenience, sensitivities to temperature are multiplied by 10^5, and sensitivities to perovskite and iron by 10.

to these sources, one can reconstruct synthetic anomalies by adding possible contributions, and compare them to the observed anomalies. A difficulty is to decide which contributions are significant, and which are not. Lateral variations of temperature (dT) are of course a major source. Partial melt is locally generating dramatic

effects, but is limited in extension (Williams and Garnero, 1996) and has therefore limited effects on the global tomography (Deschamps and Trampert, 2003). Compositional (or chemical) variations are a significant contribution, but they consist in a variety of sources that must be treated independently. Since the mantle aggregate consists in a silicate phase (perovskite) and magnesio-wüstite, it is natural to consider the variations in silicate. In the remainder of the chapter, we refer to these variations as variations in the volumetric fraction of perovskite dX_{pv}. In the lower mantle, iron is incorporated in both perovskite and magnesio-wüstite, and induces strong changes in the properties of these minerals. Changes in the elastic moduli (and their derivatives) are moderate for perovskite (Kiefer et al., 2002), but very strong for magnesio-wüstite (Kung et al., 2002). In addition, the density of both perovskite and magnesio-wüstite strongly increases with the iron fraction. Figure 4 clearly shows that the variations in the global volumetric fraction of iron *dFe* strongly contribute to the anomalies of density and seismic velocity. At lower mantle pressure, subducted oceanic crust results in material enriched in calcium compared to average aggregate. If oceanic slabs reach the bottom of the mantle, the fraction of calcium (X_{Ca}) may vary laterally. Calcium is incorporated in perovskite, and induces moderate changes in the elastic properties and very small changes in density. Because in our modeling we considered $CaSiO_3$ as a pole of perovskite, the sensitivities shown in Figure 4 implicitly account for variations in calcium. Practically, however, the differences between these sensitivities and those obtained for $X_{\mathrm{Ca}} = 0$ are not significant. In addition, the sensitivities of density and seismic velocities to calcium are one order of magnitude smaller than those for iron. For these reasons we neglected the contribution of the variations in calcium to the relative anomalies of density and seismic velocities. The fraction of aluminum in perovskite is also expected to vary if subducted crust reaches the lower mantle. The effects of aluminum on the thermo-elastic properties of perovskite are still debated. Jackson et al. (2004) reported important modification in the shear modulus, but no agreement could be found for the bulk modulus (Daniel et al., 2004; Jackson et al., 2004; Yagi et al., 2004). In addition, there are presently no robust estimates for the pressure and temperature derivatives of the elastic moduli. Because the real effects of aluminum are still uncertain, we did not account for them, but potentially they can have a large influence. At first order, it is therefore reasonable to parameterize compositional variations as a function of the variations in perovskite and iron, and the relative anomalies of shear-wave velocity ($\mathrm{d}\ln V_S$), bulk sound velocity ($\mathrm{d}\ln V_\Phi$), and density ($\mathrm{d}\ln \rho$) can be written

$$
\begin{aligned}
\mathrm{d}\ln V_S &= \frac{\partial \ln V_S}{\partial T} dT + \frac{\partial \ln V_S}{\partial X_{pv}} dX_{pv} + \frac{\partial \ln V_S}{\partial Fe} dFe, \\
\mathrm{d}\ln V_\Phi &= \frac{\partial \ln V_\Phi}{\partial T} dT + \frac{\partial \ln V_\Phi}{\partial X_{pv}} dX_{pv} + \frac{\partial \ln V_\Phi}{\partial Fe} dFe, \\
\mathrm{d}\ln \rho &= \frac{\partial \ln \rho}{\partial T} dT + \frac{\partial \ln \rho}{\partial X_{pv}} dX_{pv} + \frac{\partial \ln \rho}{\partial Fe} dFe.
\end{aligned}
\tag{6}
$$

Alternatively, one can use the relative anomalies of compressional-wave velocity ($\mathrm{d}\ln V_P$) instead of $\mathrm{d}\ln V_\Phi$. Equations (6) are the basis for a thermo-chemical interpretation of seismic observations. They can either be used by combining two observables (seismic ratios), or be directly inverted for anomalies of temperature and composition.

5 THERMO-CHEMICAL STRUCTURE: SEISMOLOGICAL EVIDENCES

5.1 First hints from seismic ratios

Several tomographic models based on joint inversion of different seismic data now provide independent constraints on shear and compressive (or bulk sound) velocity anomalies (e.g., Su and Dziewonski, 1997; Kennett et al., 1998; Vasco and Jonhson, 1998; Masters et al., 2000). Seismic ratios combine this information to make a diagnostic of the origin of the observed velocity anomalies. The most commonly used is the ratio of relative shear to compressional velocity anomalies,

$$R_P \equiv \frac{\mathrm{d}\ln V_S}{\mathrm{d}\ln V_P}. \tag{7}$$

Since any scaling $adT + adC$ will result in the same value of R_P, no quantitative information about the amplitude of the variations of temperature (dT) and composition (dC) can be accessed. However, lateral variations of R_P provide clear qualitative evidence for compositional variations in the deep mantle (Master et al., 2000; Saltzer et al., 2001). In a previous study (Deschamps and Trampert, 2003), we showed that a full statistical analysis of the histograms of block-by-block values of R_P provides useful information on the origin of seismic velocity anomalies.

Figure 5 compares histograms predicted by the global model SB10L18 and synthetic histograms computed for several origins of the velocity anomalies using sensitivities from Figure 4. If only temperature variations contribute to the velocity anomalies, the possible ranges of values of R_P are obtained by varying the sensitivities of V_S and V_P to temperature within their error bars. The results (shaded areas) clearly differ from the observed histograms (red curves), which show a strong dispersion at all depths. Accounting for reasonable errors in the tomographic model (Beghein et al., 2002) increases the dispersion in the distribution of R_P (blue curves), but still do not explain the observed dispersion. The observed velocity anomalies can thus not be purely thermal in origin. We also computed distributions of R_P for pure compositional effects, including errors in the tomographic models. For perovskite (green curves), the distributions of R_P have a similar dispersion than for temperature, but peak at smaller values. For iron (orange curves) they are slightly more dispersed than for temperature, and peak at similar values, suggesting that R_P cannot discriminate between temperature and iron variations, hence the need for density information. None of the compositional effects alone can explain

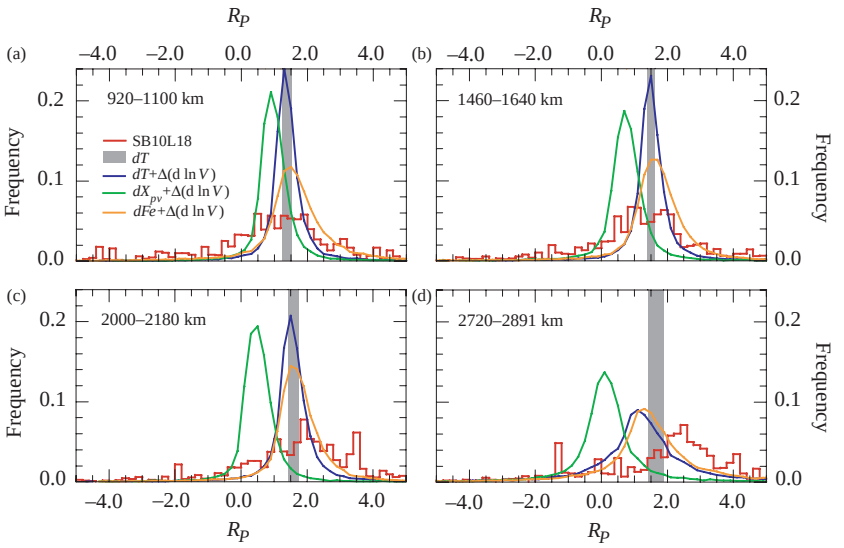

Figure 5. Seismic ratios $R_P = \mathrm{d}\ln V_S/\mathrm{d}\ln V_P$ in the lower mantle. Red curves are block-by-block histograms predicted by SB10L18 (Masters et al., 2000). Dashed areas cover one standard deviation around the mean value obtained for velocity anomalies of a purely thermal origin. Blue curves are obtained by adding simulated errors $\Delta(\mathrm{d}\ln V)$ in the tomographic model to the thermal contribution. Simulated errors have a Gaussian distribution with standard deviation obtained by multiplying the RMS of SB10L18 by the relative error from Beghein et al. (2002). From top to bottom, $\Delta(\mathrm{d}\ln V_S)$ is equal to 2.66×10^{-3}, 1.66×10^{-3}, 1.93×10^{-3}, and 5.84×10^{-3}, and $\Delta(\mathrm{d}\ln V_P)$ is equal to 1.83×10^{-3}, 2.57×10^{-3}, 1.26×10^{-3}, and 3.12×10^{-3}. Green and orange curves are obtained by adding simulated errors $\Delta(\mathrm{d}\ln V)$ to the velocity anomalies due to pure perovskite and pure iron variations, respectively.

the observed histograms, but a combination of thermal and compositional effects might.

Ideally, one would like to vary dT, dX_{pv} and dFe within reasonable ranges, compute associated histograms, and compare them with the observed histograms to decide on bounds for dT, dX_{pv} and dFe that fit the observations best. As noted above, however, combinations of dT, dX_{pv} and dFe that differ by a multiplicative factor give the same value of R_P. While the full histograms of seismic ratios are a good indicator of chemical heterogeneities, a quantitative estimate remains impossible.

5.2 Deterministic inversions of probabilistic seismic tomography

Deterministic inversions of shear-wave and compressional-wave (or bulk-sound) velocity have reported lateral variations of composition in the deep mantle (Forte and Mitrovica, 2001; Deschamps and Trampert, 2003), but a close inspection of the possible sources of uncertainties (including the uncertainties in the sensitivities

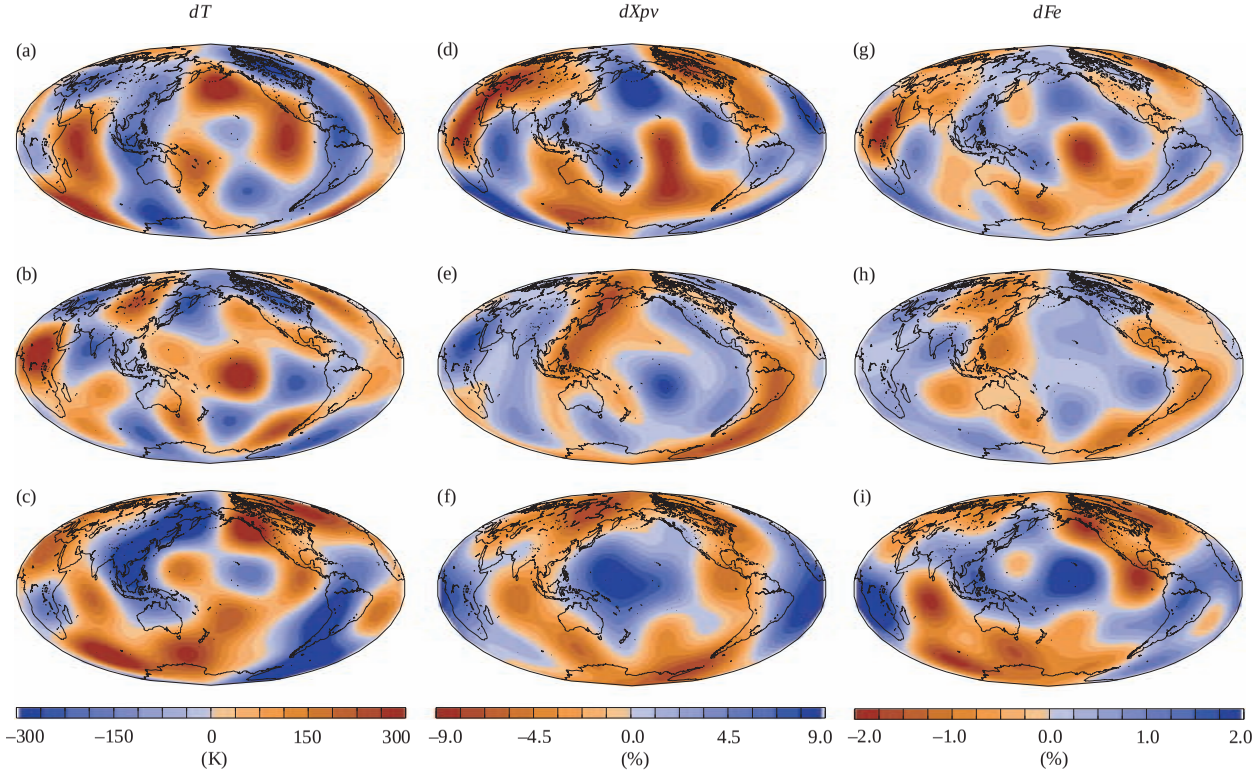

Figure 6. Mean anomalies of temperature, perovskite and iron in the lower mantle derived from Equation 6 and probabilistic seismic tomography (Trampert et al., 2004). The lower mantle is parameterized in three layers, from top to bottom $670 \leq z \leq 1200$ km, $1200 \leq z \leq 2000$ km, and $2000 \leq z \leq 2891$ km.

and reasonable uncertainties in the tomographic model) revealed that these variations are not robust (Deschamps and Trampert, 2003) because of a lack of density information.

In a previous paper (Trampert et al., 2004), we inverted the density and seismic velocity anomalies of RT246g for lateral variations of temperature, perovskite and iron. Since seismic observable and sensitivities are probability density functions, we performed a search that returned likelihoods for anomalies of temperature and composition. Assuming the likelihoods to be Gaussian, they can be represented by a mean and a standard deviation. The error bars on temperature and composition account for errors in the data and in the sensitivities. The latter, however, contribute for less than 10% to the total uncertainties, which are dominated by data errors. The resulting uncertainties are remarkably uniform within each layer (RMS uncertainties are listed in Table 2).

Figure 6 shows the mean of the lateral variations in dT,dX_{pv} and dFe in each layer. Note that, in the deepest layer, the strongest excess in perovskite and iron are found beneath Africa and the Pacific. In the top and mid mantle, amplitudes of temperature and composition anomalies are globally smaller (Table 2). A notable exception are the anomalies of perovskite in the top layer ($670 \leq z \leq 1200$ km), which vary between -8.5% and 11.9% (Fig. 6d). A comparison between Figure 3 and Figure 6 do not show striking similarities between the distributions of $\mathrm{d}\ln V_S$ and dT. The correlations between $\mathrm{d}\ln V_S$ and dT (Table 3) are clearly too low to obtain temperature variations from $\mathrm{d}\ln V_S$ scaling. Further comparisons (Table 3) suggest that $\mathrm{d}\ln V_\Phi$ is an excellent proxy for perovskite variations independent of depth, and that $\mathrm{d}\ln \rho$ maps iron variations very well below $z = 1200$ km.

A striking result is that low velocities in the deep mantle beneath Africa and the Pacific are due to an enrichment in perovskite and iron, which makes them denser than the surrounding mantle. Because sensitivities of shear-wave velocity to iron

Table 3. Correlation between tomographic observables and thermo-chemical parameters[a]

Layer		$\mathrm{d}\ln V_S$	$\mathrm{d}\ln V_\Phi$	$\mathrm{d}\ln \rho$
670–1200 km	dT	−0.564	0.420	−0.524
	dX_{pv}	−0.033	0.907	0.114
	dFe	0.104	0.790	0.716
1200–2000 km	dT	−0.701	0.089	−0.790
	$\mathrm{d}X_{pv}$	−0.332	0.889	−0.281
	dFe	−0.135	0.432	0.898
2000–2891 km	dT	−0.302	−0.102	−0.863
	dX_{pv}	−0.792	0.933	0.277
	dFe	−0.524	0.604	0.942

[a]Correlations are computed for mean values, on the original grid $15° \times 15°$.

(Fig. 4a, light grey area) are negative throughout the lower mantle, this excess in iron results in low V_S-anomalies and could erroneously be interpreted as a temperature increase.

6 THERMO-CHEMICAL STRUCTURE: GEODYNAMICAL CONSEQUENCES

6.1 Observed variations of density

Trampert et al. (2004) clearly demonstrated that strong lateral variations of composition are present throughout the lowermost mantle. It is crucial, from a dynamical point of view, to separate and compare chemical (d ln ρ_c) and thermal (d ln ρ_T) contributions to the density anomalies. At each model point, we randomly sampled the anomalies of temperature and composition (perovskite and iron) within their Gaussian distributions. We similarly sampled the sensitivities of density and generated 20 million models of d ln ρ_T and d ln ρ_c density. Figure 7 shows the average maps of d ln ρ_T and d ln ρ_c in each layer. Again, uncertainties (defined as one standard deviation) are remarkably homogeneous within each layer (RMS of these uncertainties are given in Table 2).

In the bottom layer, d ln ρ_T is small, and varies between -0.31 and 0.44% (Fig. 7c). As previously noted, the small values of d ln ρ_T are due to the decrease of the thermal expansion at great depths (Fig. 4c, dashed area). In comparison, d ln ρ_c are on average twice as large (Fig. 7f), and vary between -0.71% and 0.95%. Due to the small values of the sensitivity of density to perovskite (Fig. 4c, light grey area), variations in perovskite contribute less than 10% to the total d ln ρ_c. The chemical density anomalies are therefore dominated by iron anomalies, as also suggested by the high correlation between the relative density anomalies and the iron anomalies (Table 3). Excess in iron increases the density up to 1.0%, the largest anomalies being observed beneath Africa and the Pacific. Since thermal density anomalies in these regions are of the order of 0.2%, the material is not buoyant. Power spectra of d ln ρ_T and d ln ρ_c reveal that each degree of the spherical harmonic expansion is dominated by chemical density anomalies (Fig. 8c). Moreover, most of the chemical and thermal signals are contained in degree 2. Degrees 4 and 6 are weaker than degree 2 by a factor 4.

Although weaker than in the bottom layer, the chemical density anomalies in the intermediate layer ($1200 \leq z \leq 2000$ km) are of the same order as the thermal density anomalies, and are dominated by degree 2. In general, this layer has small anomalies of temperature and composition.

Thermal and chemical buoyancies become stronger at the top of the lower mantle ($670 \leq z \leq 1200$ km). d ln ρ_T varies between -0.64% and 0.57%, and is stronger, on average, than in the bottom layer. Degree 2 is slightly stronger than in the lowermost layer, but, interestingly, there is more power in the degree 4 than in the degree 2 (Fig. 8a). d ln ρ_c is not as strong as in the lowermost layer, but still varies between -0.80% and 0.67%. Most of the difference in amplitude is due to the degree 2, which

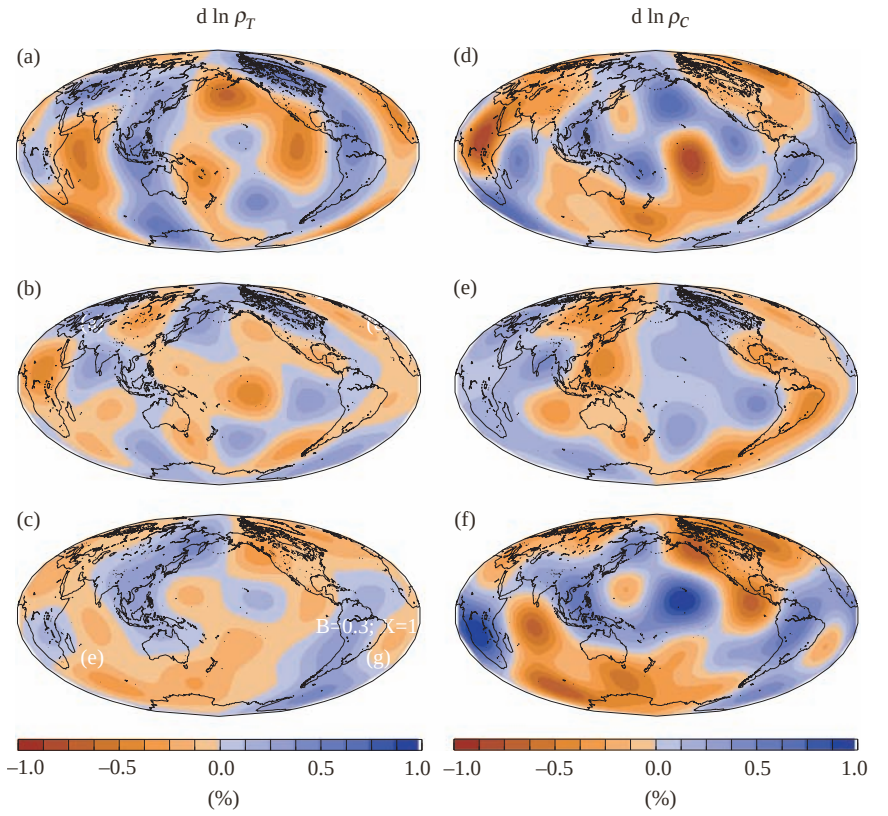

Figure 7. Thermal (a–c) and chemical (d–f) contributions to the relative anomalies of density in the lower mantle. The lower mantle is parameterized in three layers, from top to bottom $670 \leq z \leq 1200$ km, $1200 \leq z \leq 2000$ km, and $2000 \leq z \leq 2891$ km.

is half of that the bottom layer. Note that the anomalies of perovskite now make up 30% of the total d ln ρ_c.

6.2 Comparison with thermo-chemical convection

The numerical models of convection we used are defined on Cartesian grids (see Section 2) and can therefore be transferred to the Fourier domain. To compare them with global tomographic models, which are expanded in spherical harmonics, one must carefully compute the power spectra for each expansion. We did this using a method developed by Chevrot et al. (1998). From the convection models, we first performed a Fourier transform of the d ln ρ_T and d ln ρ_c at each depth, and computed the signal contained in each wave number $k = \sqrt{k_x^2 + k_y^2}$, where k_x and k_y are the

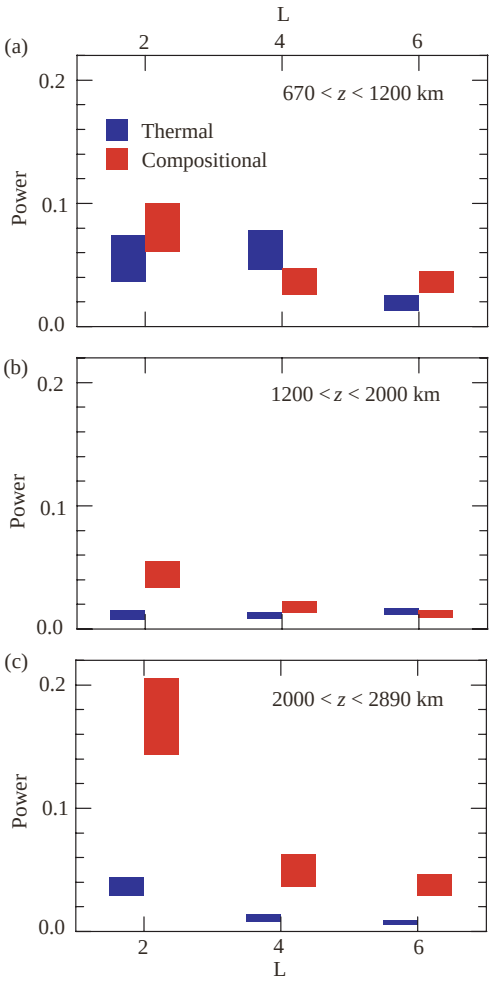

Figure 8. Power spectra of thermal (blue histograms) and chemical (red histograms) density anomalies predicted by probabilistic tomography model RT246g (Trampert et al., 2004) for degrees 2, 4 and 6. Each histogram covers one standard deviation around the mean value of the power.

wave numbers along the x- and y-axis. The signal contained in the spherical harmonic degree ℓ is equal to the sum of the signals contained in the wave numbers k that satisfy $(\ell + 1/2) \leq ka \leq (\ell + 3/2)$ (Chevrot et al., 1998):

$$P(\ell) = \frac{2\pi}{N_x^2 N_y^2 (\ell + 1/2)} \sum_{(\ell+1/2) \leq ka \leq (\ell+3/2)} |\mathrm{d} \ln \rho(k)|^2, \tag{8}$$

where a is the Earth's radius, and N_x and N_y the number of grid points in x and y directions. The tomographic model RT246g represents the lower mantle in three layers, and contains spherical harmonic degrees 2, 4 and 6 only, whereas the numerical models of Tackley (2002) sample the lower mantle with 50 points, and contains signal up to degree 32. To make meaningful comparisons, we averaged the synthetic d ln ρ_T and d ln ρ_c (Eqs. 4–5) in comparable layers as defined by RT246g, and filtered them for spherical harmonic degrees 2, 4 and 6.

The RMS of d ln ρ_T and d ln ρ_c from seismology and convection models are plotted in Figure 9. All the numerical models we considered predicted the RMS of d ln ρ_T and d ln ρ_c that fitted within one standard deviation of the observed RMS. The best fit is obtained for $B = 0.2, X = 10\%$. In the intermediate layer, the RMS of d ln ρ_c for the cases $B = 0.3, X = 10\%$, and $B = 0.4, X = 10\%$ are close to the observed lower bound, but cannot be excluded. Analysis of the RMS is therefore not a conclusive test, at least with the current depth parameterization of probabilistic seismic tomography. Models with finer parameterization will certainly provide a better test, but are not yet available. Clearer conclusions can be drawn from comparing the power spectra of observed and synthetic distributions (Fig. 10). In case of a stable layer of dense material ($B = 0.3$, $X = 30\%$, green histograms), the strongest chemical density anomalies are found between the intermediate and lower layers (Fig. 1d). As a result, spectra of d ln ρ_c in the bottom and intermediate layers are similar one another, which is not observed by RT246g. In particular, degree 2 has too little power in the bottom

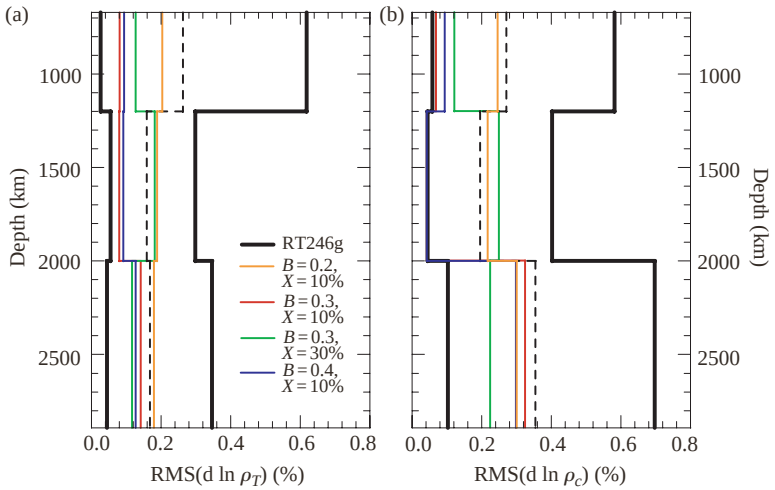

Figure 9. RMS of relative density anomalies due to (a) thermal and (b) compositional effects. The thin dashed curve represents the RMS of the average observed models (Fig. 7), and the thick curves represent de RMS of the models with one standard deviation around these models. Colored curves represent the RMS predicted by 3-D Cartesian numerical models of thermo-chemical convection (Tackley, 2002) with several buoyancy ratio (B) and volumetric fraction of dense material (X). Density anomalies from numerical models of convection are filtered for degrees 2, 4, and 6.

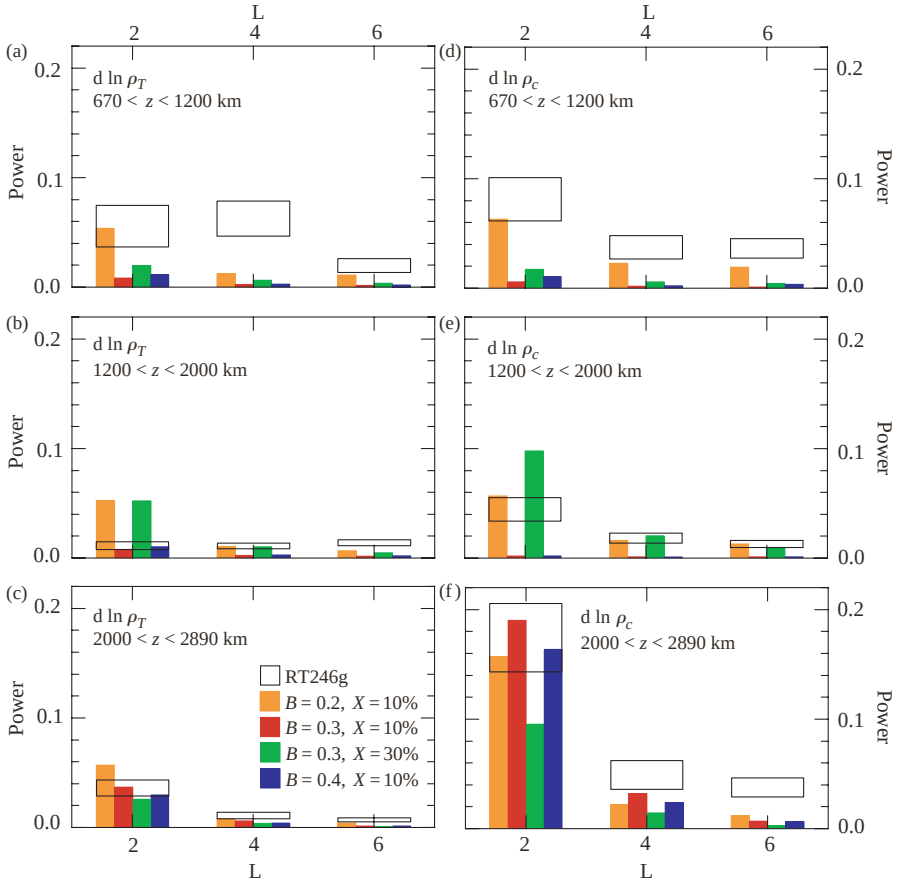

Figure 10. Power spectra of thermal and chemical contributions to the density anomalies derived from numerical models of thermo-chemical convection (Tackley, 1998, 2002), for degrees 2, 4 and 6, and for several buoyancy ratio (B) and volumetric fraction of dense material (C). Because numerical models are defined on a 3-D Cartesian grid, we used the method of Chevrot et al. (1998) to compute their spherical harmonic coefficients (see text). For comparison, the white rectangles cover one standard deviation around the means of the observed power (see Fig. 8).

layer, and too much in the intermediate layer. This case also fails to explain the observed power spectrum of d ln ρ_T and d ln ρ_c in the upper layer, and the degree 2 of d ln ρ_T in the intermediate layer. The thin stable layer ($B = 0.4$, $X = 10\%$, blue histograms) and discontinuous spoke pattern ($B = 0.3$, $X = 10\%$, red histograms) show strong lateral variations of temperature and composition below 2000 km, but not at shallower depths. They explain the observed power spectra in the bottom layer, but not in the intermediate (except the degree 2 of d ln ρ_T) and top layers. Finally, the case $B = 0.2$, $X = 10\%$ (orange histograms) explains most of the power spectra

of d ln ρ_c, at least within two standard deviations (95% certainty). It fits d ln ρ_T less well, most of the discrepancies being due to the degree 2 in the intermediate layer, and to the degree 4 in the top layer.

The previous comparisons suggest that the model with $B = 0.2$ gives the best agreement to the observed density anomalies. As an additional test, we estimated the global buoyancy ratio associated with the observed d ln ρ_T and d ln ρ_c. We considered that the iron fraction of the regular material is equal to 11%, and that the dense material is enriched in iron by 2.0–2.5%, as reported in Section 5. If the mantle aggregate consists in 80% perovskite and 20% magnesio-wüstite, the density and thermal expansion at the surface are $\rho_s = 4240$ kg/m^3 and $\alpha_s = 2 \times 10^{-5}$ K^{-1}, and the chemical density contrast due to the enrichment in iron varies between $\Delta\rho_c^{\max} = 40$ kg/m^3 and $\Delta\rho_c^{\max} = 49$ kg/m^3 (Deschamps and Trampert, 2004). Taking $\Delta T_s = 2500$ K, the thermal density contrast is $\Delta\rho_T^{\max} = 213$ kg/m^3, and the buoyancy ratio varies between $B = 0.19$ and $B = 0.23$.

7 DISCUSSION

The low shear wave velocities observed in the deep mantle below Africa and the Pacific are fully explained by long wavelength lateral variations of composition. Iron increases are responsible for strong (up to 1%) anomalies of density, and variations in perovskite are significant (up to 9%) and explain bulk-sound velocity very well. The comparisons performed in the previous section, however, suggest that these variations are not large enough to maintain a stable chemical layering. If a dense layer is present it must be unstable, i.e., the domes or piles of dense material are generated in the bottom of the mantle and oscillate or are entrained upwards. The current parameterization of probabilistic seismic tomography, however, cannot resolve these structures.

A question that is not addressed in this paper is the origin of the compositional variations. We easily identify three different scenarios. First, early differentiation may have created a dense layer at the bottom of the mantle. Because the buoyancy ratio is not large enough ($B < 0.3$), this layer is unstable, and the material is entrained upwards. A major disadvantage of this scenario is that the layer must have been rapidly entrained and mixed in the mantle, unless it is regularly fed with new material. Gonnerman et al. (2002) showed that even if the initial layer is stable, entrainment of material would progressively decrease the density contrast and lead to a present unstable layer. Second, slabs may penetrate in the lower mantle and reach the CMB, where they sediment in pools (e.g., Christensen and Hofmann, 1994). Again, the density contrast and quantity of sinking material should not be too large to allow the development of instabilities. Slabs could temporarily stack in the mid-mantle, and reach the bottom of the mantle in occasional avalanches (Tackley et al., 1994). There are indeed some indications from classical tomography that significant amounts of slabs are deflected in the top of the lower mantle, around 1000 km (Fukao et al., 2001). The variations of temperature and composition (mainly perovskite) observed by probabilistic tomography at the top of the lower mantle could also be due to

deflected slabs. Finally, iron excess may result from percolation from the core (e.g., Knittle and Jeanloz, 1991). A recent study (Humayun et al., 2004) suggests that the lower mantle beneath Hawaii is enriched in iron by 1–2%. Interestingly, the largest iron anomalies we found are close to 2%, and are located beneath Hawaii (Fig. 6i). The actual influence of iron percolation from the core remains however difficult to estimate. These scenarios are end-members, and a mix of them is more likely required to describe the Earth's mantle. Discriminating between the previous scenarios (or a mix of them) is not possible from the results presented in this paper only, but needs to integrate other types of information, in particular geochemical constraints.

The thermo-chemical distributions from convection we have tested are snapshots of time-dependent calculations, which do not necessarily correspond to the present state of the mantle. A full comparison requires to test series of snapshots at different times. For $B = 0.3$, $X = 30\%$, the layer of dense material remains stable for a long period of time (3 Gy), with similar spectral signature. The spokes pattern ($B = 0.3$, $X = 10\%$) and thin dense layer ($B = 0.4$, $X = 10\%$) modes are also stable over long periods of time (5 Gy and more). For $B = 0.2$, $X = 10\%$, mature piles (such as those plotted in Fig. 1) develop in about 200 My. Once they are formed, piles feed the mantle with dense material until the fluid is chemically homogeneous. Spectral signatures for early stages do not explain the observation as well as mature piles.

Hotspots are a major ingredient of mantle dynamics, but their origin is still debated. Recent tomographic studies (Zhao, 2001, 2004; Montelli et al., 2004) image hotspot tails down to various depths. Several hotspots, including Hawaii, seem to originate in the lowermost mantle, close to the CMB. The resolution of RT246g does not allow detailed inferences on the origin of hotspots, but maps of density anomalies (Fig. 3g–i) clearly show that deep-rooted hotspots, as defined by and Courtillot et al. (2003) and Montelli et al. (2004), do not systematically plot continuously on buoyant material throughout the lower mantle. Within error bars in density anomalies, only one third of these deep hotspots correlate with negative density anomalies in the lowermost mantle, and only two (Iceland and Azores) plot on buoyant material throughout the mantle. It is important to keep in mind that Zhao (2001, 2004) and Montelli et al. (2004) map compressional seismic velocity anomalies only, but not density. Neglecting compositional variations, they assume that the seismic velocity anomalies are purely thermal in origin, i.e., that low velocity regions are related to hot, hence buoyant material. As shown in this chapter and elsewhere (Trampert et al., 2004), chemically dense material dominates thermal buoyancy in the lower mantle, and still results in low velocities. For instance, in the lowermost mantle, the Hawaiian region is associated with dense, non-buoyant material (Fig. 3i) and low shear-wave velocities (Fig. 3c).

The thermo-chemical structure we inferred is based on a parameterization of composition that consists in perovskite and iron variations. Recent developments in mineral physics, which are not accounted for in this study, may complicate the interpretation of seismic information, and modify our inferences. Murakami et al.

(2004) reported a new phase transition from perovskite to post-perovskite around 2700 km. We did preliminary tests using available thermo-elastic data for post-perovskite (Tsuchiya et al., 2004a,b), but we did not find any dramatic differences compared to the sensitivities plotted in Figure 4. The biggest change is for the sensitivities of density to perovskite, which are positive from the depth of the transition down to the CMB. The amplitudes of the sensitivities, however, remain small. Thus, the phase transition to post-perovskite should not dramatically modify the thermo-chemical structure inferred from probabilistic tomography. Still, it may have significant consequences on the lower mantle dynamics (Nakagawa and Tackley, 2005). Interestingly, the large value of its Clapeyron slope (around 8–10 MPa/K) could explain the good correlation (equal to 0.7) between the observed thermal and compositional contributions to density at the bottom of the mantle, which is not predicted by the models of thermo-chemical convection we used. In cold regions (e.g., slabs) perovskite may transform to post-perovskite at shallower depths than in hot regions (if they transform at all before the CMB). In addition, there are indications that Fe-perovskite may transform at shallower depths than Mg-perovskite (Spera et al., 2006). In that case, the chemically dense and cold regions observed in the lowermost mantle would correspond to iron-rich post-perovskite.

Due to heavy computational requirements, the vertical parmeterization of RT246g is limited to three layers in the lower mantle, which reduces the effects of a post-perovskite phase on this study. Further, averaging models of thermo-chemical convection in these layers, we lose important information (compare Figs. 2b and 2d against Fig. 9). A careful statistical analysis, however, allows robust conclusions concerning the lower mantle structure. A thick stable layer of dense material, for instance, implies that the chemical signatures in the mid-mantle ($1200 \leq z \leq 2000$ km) and in the lowermost mantle ($2000 \leq z \leq 2891$ km) are comparable. On the contrary, a thin stable layer would result in no notable chemical signal down to 2000 km. Since none of these features fit within the observed error bars (Fig. 10), a stable layer of dense material is unlikely to be present at the bottom of the mantle. Probabilistic models of seismic tomography with a better vertical parameterization should be available in the near future by performing more efficient parallel calculations. A more serious problem is that RT246g does not include odd degrees, which potentially contain important information. Including odd spherical harmonic degrees is a difficult task because normal mode splitting cannot access these degrees very easily. A last point is that a finer lateral resolution, including degrees higher than 6, is not so essential to correctly understand the lower mantle. The power spectrum of relative density anomalies predicted by models of thermo-chemical convection strongly decreases for degrees higher than 7, as shown in Figure 11 for the case $B = 0.2$ and $X = 10\%$. The power spectra for other models of thermo-chemical convection (not shown here), have a similar decrease. If mantle convection is similar to one of these models, we would expect that degrees higher than 7 are weak, and do not significantly participate to the nature of tomographic models. This is confirmed by recent tomographic models (Gu et al., 2001).

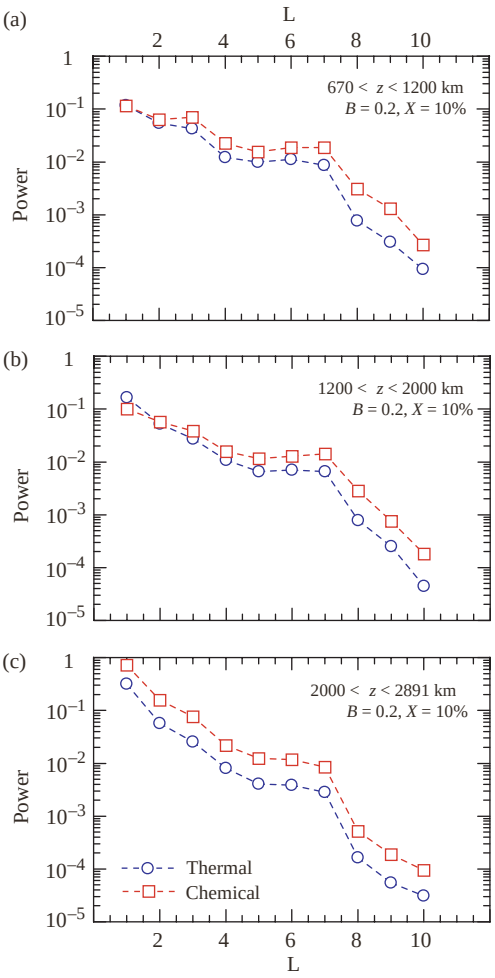

Figure 11. Power spectrum of thermal (blue curves) and chemical (red curves) contributions to the density anomalies predicted by a 3-D Cartesian numerical model of thermo-chemical convection (Tackley, 2002) with buoyancy ratio $B = 0.2$, and volumetric fraction of dense material $X = 10\%$. The power in each spherical harmonic degree is calculated following Chevrot et al. (1998). Degrees $\ell = 1$–10 are represented, and the signal is averaged within each layer defined by the probabilistic model of seismic tomography RT246g.

8 CONCLUSION

Our view of mantle structure and dynamics has rapidly changed during the last decade. A strong indication of dense material (Ishii and Tromp, 1999) or chemical variations in the lower mantle (Forte and Mitrovica, 2001; Saltzer et al., 2001) has now turned

to robust quantitative estimates of the variations of temperature and composition (Trampert et al., 2004). Chemical heterogeneities are clearly present throughout the mantle. In the top layer ($670 \leq z \leq 1200$ km), thermal and chemical signatures could be related to slab deflection. In the lowermost mantle ($2000 \leq z \leq 2891$ km) strong anomalies of iron, whose origin is still to be determined, are present in regions usually referred to as "superplumes". From a geodynamical point of view, the presence of lateral variations of composition is observed in recent models of thermo-chemical convection, which now account for fluid compressibility. Robust comparisons between geophysical observations, mainly seismology, and geodynamical models can now be attempted in order to discriminate between certain modes of convection in the mantle. Preliminary results discussed in this chapter indicate that a stable layer of dense material is unlikely to be present at the bottom of the mantle. Piles of dense material entrained upwards from a dense, unstable layer statistically explain probabilistic tomography better, but discrepancies remain in the top of the lower mantle, possibly linked to the phase transformation around 670 km and/or slabs deflection around 1000 km. Future researches should focus on estimating the influence of recent mineral physics findings on lower mantle seismic velocity and density, exploring and testing scenarios that can produce strong lateral variations of iron at the bottom of the mantle, computing probabilistic models of tomography with finer vertical parameterization, and testing models of thermo-chemical convection that include more complexities, such as a phase transformation at 670 km, or the post-perovskite phase transition in the lowermost mantle.

ACKNOWLEDGEMENTS

We appreciated the constructive reviews of an anonymous reviewer. This research was funded by the Netherlands Research Center for Integrated Solid Earth Sciences (ISES) and Utrecht University.

REFERENCES

Anderson, O.L. (1995) Equations of State of Solids for Geophysics and Ceramic Sciences, Oxford University Press, Oxford, 405pp.

Anderson, D.L. (2001) Top-down tectonics. *Science*, 293, 2016–2018.

Beghein, C., J.S. Resovsky, and J. Trampert (2002) P and S tomography using normal-mode and surface waves data with a neighbourhood algorithm. *Geophys. J. Int.*, 149, 646–658.

Chevrot, S., J.P. Montagner, and R. Snieder (1998) The spectrum of tomographic Earth models. *Geophys. J. Int.*, 33, 783–788.

Christensen, U.R., and A. Hofmann (1994) Segregation of subducted oceanic crust in the convecting mantle. *J. Geophys. Res.*, 99, 19867–19884.

Courtillot, V., A. Davaille, J. Besse, and J. Stock (2003) Three distinct types of hotspots in the Earth's mantle. *Earth Planet. Sci. Lett.*, 205, 295–308.

Daniel, I., J.D. Bass, G. Fiquet, H. Cardon, J. Zhang, and M. Hanfland (2004) Effect of aluminium on the compressibility of silicate perovskite. *Geophys. Res. Lett.*, 31, doi: 10.1029/2004GL020213.

Davaille, A. (1999) Simultaneous generation of hotspots and superswells by convection in a heterogeneous planetary mantle. *Nature*, 402, 756–760.

Deschamps, F., and J. Trampert (2003) Mantle tomography and its relation to temperature and composition. *Phys. Earth Planet. Inter.*, 140, 277–291.

Deschamps, F., and J. Trampert (2004) Towards a lower mantle reference temperature and composition. *Earth Planet. Sci. Lett.*, 222, 161–175.

Forte, A.M., and J.X. Mitrovica (2001) Deep-mantle high-viscosity flow and thermo-chemical structure inferred from seismic and geodynamic data. *Nature*, 410, 1049–1056.

Fukao, Y., S. Widiyantoro, and M. Obayashi (2001) Stagnant slabs in the upper and lower mantle transition region. *Rev. Geophys.*, 39, 291–323.

Goes, S., R. Govers, and P. Vacher (2000) Shallow mantle temperature under Europe from P and S wave tomography. *J. Geophys. Res.*, 105, 11153–11169.

Gonnerman, H.M., M. Manga, and A.M. Jellinek (2002) Dynamics and longevity of an initially stratified mantle. *Geophys. Res. Lett.*, 29, doi:10.1029/2002GL014851.

Gu, Y.J., A.M. Dziewonski, W.J. Su, and G. Ekstrom (2001) Models of the mantle shear velocity and discontinuities in the pattern of lateral heterogeneities. *J. Geophys. Res.*, 106, 11169–11199.

Hansen, U., and D.A. Yuen (1988) Numerical simulations of thermo-chemical instabilities at the core-mantle boundary. *Nature*, 334, 237–240.

Humayun, M., L. Qin, and M.D. Norman (2004) Geochemical evidence for excess iron in the lower mantle beneath Hawai. *Science*, 306, 91–94.

Ishii, M., and J. Tromp (1999) Normal-mode and free-air gravity constraints on lateral variations in velocity and density of Earth's mantle. *Science*, 285, 1231–1236.

Jackson, I. (1998) Elasticity, composition and temperature of the earth's lower mantle: A reappraisal. *Geophys. J. Int.*, 134, 291–311.

Jackson, J.M., J. Zhang, and J.D. Bass (2004) Sound velocities and elasticity of aluminous $MgSiO_3$ perovskite: Implications for aluminium heterogeneity in Earth's lower mantle. *Geophys. Res. Lett.*, 31, doi: 10.1029/2004GL019918.

Jeanloz, R., and E. Knittle (1989) Density and composition of the lower mantle. *Philos. Trans. R. Soc. Lond. A*, 328, 377–389.

Karato, S.I., and B.B. Karki (2001) Origin of lateral variation of seismic wave velocities and density in the deep mantle. *J. Geophys. Res.*, 106, 21771–21783.

Kellogg, L.H., B.H. Hager, and R.D. van der Hilst (1999) Compositional stratification in the deep mantle. *Science*, 283, 1881–1884.

Kennett, B.L.N., S. Widiyantoro, and R.D. van der Hilst (1998) Joint seismic tomography for bulk sound and shear wave speed in the Earth's mantle. *J. Geophys. Res.*, 103, 12469–12493.

Kiefer, B., L. Stixrude, and R.M. Wentzcovitch (2002) Elasticity of $(Mg,Fe)SiO_3$ perovskite at high-pressures. *Geophys. Res. Lett.*, 29, doi: 10.1029/2002GL014683.

Knittle, E., and R. Jeanloz (1991) Earth's core-mantle boundary: Results of experiments at high pressures and temperatures. *Science*, 251, 1438–1443.

Kung, J., B. Li, D.J. Weidner, J. Zang, and R.C. Liebermann (2002) Elasticity of $(Mg_{0.83},Fe_{0.17})O$ ferropericlase at high pressure: Ultrasonic measurements in conjunction with X-radiation techniques. *Earth Planet. Sci. Lett.*, 203, 557–566.

Masters G., G. Laske, H. Bolton, and A.M. Dziewonski (2000) The relative behavior of shear velocity, bulk sound speed, and compressional velocity, in the mantle: Implications for chemical and thermal structure. In Karato, S.I. et al. (eds.) Earth's Deep Interior: Mineral Physics and Tomography from the Atomic to the Global Scale, Geophys. Mon. Ser., 117, pp. 63–87.

Montelli, R., G. Nolet, F.A. Dahlen, G. Masters, E.R. Engdahl, and S.H. Hung (2004) Finite frequency tomography reveals a variety of plumes in the mantle. *Science*, 303, 338–343.

Murakami, M., K. Hirose, K. Kawamura, N. Sata, and Y. Ohishi (2004) Post-perovskite phase transition in $MgSiO_3$. *Science*, 304, 855–858.

Nakagawa, T., and P.J. Tackley (2005) The interaction between the post-perovskite phase change and a thermo-chemical boundary layer near the core-mantle boundary. *Earth Planet. Sci. Lett.*, 238, 204–216.

Olson, P., and C. Kinkaid (1991) Experiment on the interaction of thermal convection and compositional layering at the base of the mantle. *J. Geophys. Res.*, 96, 4347–4354.

Resovsky, J.S., and J. Trampert (2003) Using probabilistic seismic tomography to test mantle velocity-density relationships. *Earth Planet. Sci. Lett.*, 215, 121–134.

Romanowicz, B., and Y. Gung (2002) Superplumes from the core-mantle boundary to the lithosphere: Implications for heat flux. *Science*, 296, 513–516.

Saltzer, R.L., R.D. van der Hilst, H. Kárason (2001) Comparing P and S wave heterogeneity in the mantle. *Geophys. Res. Lett.*, 28, 1335–1338.

Sambridge, M. (1999a) Geophysical inversion with a neighbourhood algorithm—I. Searching a parameter space. *Geophys. J. Int.*, 138, 479–494.

Sambridge, M. (1999b) Geophysical inversion with a neighbourhood algorithm—II. Apraising the ensemble. *Geophys. J. Int.*, 138, 727–746.

Schott, B., and D.A. Yuen (2004) Influences of dissipation and rheology on mantle plumes coming from the D″-layer. *Phys. Earth Planet. Inter.*, 146, 139–145.

Spera, F.J., D.A. Yuen, and G. Giles (2006) Tradeoffs in chemical and thermal variations in the post-perovskite phase transition: Mixed phase regions in the deep lower mantle? *Phys. Earth Planet. Inter.*, 159, 234–246.

Su, W.J., and A.M. Dziewonski (1997) Simultaneous inversion of 3D variations in the shear and bulk velocity in the mantle. *Phys. Earth Planet. Inter.*, 100, 135–156.

Tackley, P.J. (1998) Three-dimensional simulations of mantle convection with a thermo-chemical CMB boundary layer: D″? In Gurnis M. et al. (eds.) The Core-Mantle Boundary Region, Geodynamical Ser., 28, pp. 231–253.

Tackley, P.J. (2002) Strong heterogeneity caused by deep mantle layering. *Geochem. Geophys. Geosys.*, 3, doi: 10.1029/2001GC000167.

Tackley, P.J., D.J. Stevenson, G.A. Glatzmaier, and G. Schubert (1994) Effects of multiple phase transition in a three-dimensional spherical model of convection in Earth's mantle. *J. Geophys. Res.*, 99, 15877–15902.

Trampert, J., P. Vacher, and N. Vlaar (2001) Sensitivities of seismic velocities to temperature, pressure and composition in the lower mantle. *Phys. Earth Planet. Inter.*, 124, 255–267.

Trampert, J., F. Deschamps, J.S. Resovsky, and D.A. Yuen (2004) Probabilistic tomography maps significant chemical heterogeneities in the lower mantle. *Science*, 306, 853–856.

Trampert, J., and R.D. van der Hilst (2005) Quantitative interpretation of global seismic tomography. In van der Hilst et al. (eds) Earth's Deep Mantle: Structure, Composition, and Evolution, Geophys Mon. Ser., 160, pp. 47–62.

Tsuchiya, T., J. Tsuchiya, K. Umemoto, and R.M. Wentzcovitch (2004a) Phase transition in $MgSiO_3$ perovskite in the Earth's lower mantle. *Earth Planet. Sci. Lett.*, 224, 241–248.

Tsuchiya T., J. Tsuchiya, K. Umemoto, and R.M. Wentzcovitch (2004b) Elasticity of post-perovskite $MgSiO_3$. *Geophys. Res. Lett.*, 31, doi: 10.1029/2004GL020278.

Vasco, D.W., and L.R. Johnson (1998) Whole Earth structure estimated from seismic arrival times. *J. Geophys. Res.*, 103, 2633–2671.

Williams, Q., and E.J. Garnero (1996) Seismic evidence of partial melt at the base of the mantle. *Science*, 273, 1528–1530.

Yagi, T., K. Okabe, N. Nishiyama, A. Kubo, and T. Kikegawa (2004) Complicated effects of aluminum on the compressibility of silicate perovskite. *Phys. Earth Planet. Inter.*, 143–144, 81–91.

Zhao, D. (2001) Seismic structure and origin of hotspots and mantle plumes. *Earth Planet. Sci. Lett.*, 192, 251–265.

Zhao, D. (2004) Global tomographic images of mantle plumes and subducting slabs: Insight into deep Earth dynamics. *Phys. Earth Planet. Inter.*, 146, 3–34.

Physics of the Earth and Planetary Interiors 171 (2008) 357–373

Contents lists available at ScienceDirect

Physics of the Earth and Planetary Interiors

journal homepage: www.elsevier.com/locate/pepi

Searching for models of thermo-chemical convection that explain probabilistic tomography
I. Principles and influence of rheological parameters

Frédéric Deschamps*, Paul J. Tackley

Institute of Geophysics, Swiss Federal Institute of Technology Zurich, HPP L8.1, 8093 Zurich, Switzerland

ARTICLE INFO

Article history:
Received 26 October 2007
Received in revised form 25 February 2008
Accepted 25 April 2008

Keywords:
Mantle convection
Seismic tomography
Mantle rheology
Chemical anomalies

ABSTRACT

Recent seismological observations indicate that strong lateral density anomalies, likely due to compositional anomalies, are present in the deep mantle. We aim to identify models of thermo-chemical convection that can generate strong thermo-chemical density anomalies. For this, we explore the model space of thermo-chemical convection, determine the thermal and chemical density distributions predicted by these models, and compare their power spectra against those from probabilistic tomography. We conduct 3D-Cartesian numerical experiments using STAG3D, in which we prescribed an initial layer of dense material at the bottom of the system. We focus on the parameters of the viscosity law, including the compositional ($R\mu_c$), 660 km ($R\mu_{660}$), depth ($R\mu_z$), and thermal ($R\mu_T$) viscosity contrasts, and report strong differences in the pattern of thermo-chemical convection depending on the values of these ratios. For small (≤ 0.1) values of $R\mu_c$ dense and regular materials quickly mix, whereas for large ($\geq 10^2$) values of $R\mu_c$ the layer of dense material remains stable. Only moderate (0.1–10) $R\mu_c$ predict patterns that can maintain chemical density anomalies that fit seismic observations over long periods of time. A large ($\geq 10^2$) $R\mu_{660}$ acts as a filter for dense material, maintaining strong lateral chemical density anomalies in the lower mantle, but the power spectra of these distributions do not fit seismic tomography in the long term. A large ($\geq 10^4$) $R\mu_T$ maintains strong density anomalies everywhere in the lower mantle, including pools of dense material at the bottom of mantle, which fits seismic tomography well. A successful model of thermo-chemical convection (in the sense that it fits seismological observations well) might thus include a moderate (0.1–10) compositional density contrast and/or a strong ($\geq 10^4$) thermal viscosity contrast. The influence of other important parameters, including the buoyancy ratio, the Clapeyron slope at $d = 660$ km and the fraction of dense material, are explored in a companion paper.

© 2008 Elsevier B.V. All rights reserved.

1. Introduction

More than three decades have passed since the first numerical models of mantle convection were designed (e.g., Moore and Weiss, 1973; McKenzie et al., 1974). However, the mode of mantle convection is still highly debated. A major difficulty in finding a successful model is that the Earth's mantle includes numerous complexities compared to classical Rayleigh–Bénard convection (e.g., among the most important, viscosity variations with temperature, phase transitions, mode of heating). In addition, a successful model must be consistent with observations and constraints from various fields, including geochemistry, seismology, gravimetry, and mineral physics.

A major constraint, which arose and gained increasing support in the past decade, is the presence of strong density variations in the lower mantle (Ishii and Tromp, 1999; Resovsky and Trampert, 2003; Trampert et al., 2004), likely due to chemical variations (Forte and Mitrovica, 2001; Karato and Karki, 2001; Saltzer et al., 2001; Deschamps and Trampert, 2003). Thermo-chemical convection might thus be a key ingredient for a successful model of mantle convection. Analogical experiments (Olson and Kincaid, 1991; Davaille, 1999; Jellinek and Manga, 2002) and numerical models (Christensen and Hofmann, 1994; Kellogg et al., 1999; Tackley, 1998b; Tackley, 2002) observed a variety of flow patterns, from strong stratification to more complex structures, depending on the chemical density contrast between the dense and regular material and the fluid properties.

The increase in complexity of convection models opened new perspectives in the comparison between geophysical observations and models of mantle convection. Global tomography provides so far the best constraints on the 3D structure of the lower mantle, but

* Corresponding author. Tel.: +41 446336906; fax: +41 446331065.
E-mail address: frederic.deschamps@erdw.ethz.ch (F. Deschamps).

0031-9201/$ – see front matter © 2008 Elsevier B.V. All rights reserved.
doi:10.1016/j.pepi.2008.04.016

its interpretation is not unambiguous (Trampert and van der Hilst, 2005). Two crucial ingredients are independent constraints on the mass density, and a careful equation of state modeling (Deschamps and Trampert, 2003; Trampert et al., 2004). In a previous paper (Deschamps et al., 2007), we developed a method to test density distributions predicted by thermo-chemical convection against those from probabilistic tomography, which we applied to snapshots from various runs. These comparisons showed that a stable layer of dense material does not explain probabilistic tomography. Piles of dense material entrained upward provide a better explanation, but are short-lived structures that develop early in the run history. They may not explain the present tomography.

Searching for successful model(s) of mantle convection requires an extensive exploration of the model space of thermo-chemical convection over time sequences comparable to the age of the Earth, and careful comparison with available geophysical constraints. An important question is how to maintain density anomalies in the bottom of the mantle for a long period of time. Previous studies showed that a dense layer is able to survive thermal convection over 4.5 Gyr and more, provided that the buoyancy ratio is large enough (Tackley, 2002; Samuel and Farnetani, 2003; Zhong and Hager, 2003; van Thienen et al., 2005). However, a stable layer of dense material with no or weak topography does not fit seismic tomography (Deschamps et al., 2007). In this paper, we extend the approach of Deschamps et al. (2007). We then explore the influence of the parameters of the viscosity law on the flow pattern and the distribution of thermal and chemical density anomalies, and compare these distributions against those from probabilistic tomography (Trampert et al., 2004).

Parameters of the viscosity law control the viscosity variations with depth, temperature and composition. Depth- and temperature-dependence were introduced to model the pressure and thermal dependence of mantle minerals creeping laws (e.g., Weertman, 1970). Additional complexities of creep laws include the grain-size dependence, the role of fluids, and the stress exponent. Temperature-dependent viscosity attracted a particular attention (e.g., Christensen, 1984; Ogawa et al., 1991; Moresi and Solomatov, 1995). High viscosity contrasts due to temperature variations result in a stagnant lid regime (e.g., Davaille and Jaupart, 1993; Moresi and Solomatov, 1995; Deschamps and Sotin, 2000) that is relevant to model convection in the mantles of Venus (Solomatov and Moresi, 1996) and icy satellites (Deschamps and Sotin, 2001), but fails to explain plate tectonics regime as observed on the Earth. Self-consistent modeling of plate tectonics requires the prescription of more complex rheologies at the top of the system (Tackley, 1998a). When studying whole mantle convection, such complex rheologies can be neglected, and a Newtonian rheology, associated with diffusion creep, is well suited (Karato and Wu, 1993). Temperature- and depth-dependent viscosity remain however important ingredients, in particular for thermo-chemical convection (McNamara and Zhong, 2004). In addition, both geoid (Hager and Richards, 1989) and post-glacial rebound (Nakada and Lambeck, 1989; Forte and Mitrovica, 1996) data suggest that the lower mantle is more viscous than the upper mantle by about one order of magnitude. Finally, it is reasonable to consider that dense and regular materials have different viscosities.

Other important parameters include the Rayleigh number, the buoyancy ratio, and the Clapeyron slope of the 660 km phase transition. We explore these parameters in a companion paper (Deschamps and Tackley, submitted for publication).

2. Experimental setup

We conducted numerical experiments using a 3D-Cartesian version of STAG3D (Tackley, 1998b; Tackley, 2002), which solves the non-dimensional conservative equations of mass, momentum, energy, and composition for an anelastic, compressible fluid with an infinite Prandtl number. Calculations are made on staggered grids of $128 \times 128 \times 64$ points, with aspect ratio equal to 4. Grids are vertically refined at the top and at the bottom of the box. Scalar and vectorial quantities are calculated at the center and on the sides of each cell, respectively. At each time step, the conservative equations are solved using a Jacobi relaxation method. In addition, to speed up the convergence of the momentum equation, we used a multigrid algorithm (e.g., Stüben and Trottenberg, 1982). Time-stepping (in conservations of energy and composition) is achieved by an explicit MPDATA (Smolarkiewicz, 1984) algorithm for advective terms, and a second-order finite difference scheme for diffusive and other terms. Runs are stopped at a non-dimensional time $t = 0.0106$, which correspond to a dimensional time of 4.5 Gyr. Previous studies (e.g., Davies, 2002) performed runs over longer periods of time to account for the possibility that convection was more vigorous in the past. In many cases, however, a quasi-stationary pattern (i.e., the average altitude of dense particles, Eq. (6), and the RMS of velocity are oscillating around constant values) is reached before the end of the run, and extending the run further in time would not significantly modify the thermal and chemical structures.

All boundaries are free-slip. The system is cooled on the top and heated both from below and from within. The heating rate for dense material is increased by a factor 10 compared to regular material, and the heating rate of the mantle is adjusted to give a total heat production equivalent to a heat flux of 65 mW/m^2. Because the MORB source region appears depleted in heat-producing elements, it is reasonable to assume that the concentration in radiogenic elements is higher in dense material that in regular material (Kellogg et al., 1999). The value of the compositional heating ratio ($\mathrm{R}H_\mathrm{c}$) we imposed is somewhat arbitrary, and one may wonder about the influence of $\mathrm{R}H_\mathrm{c}$ on the mode of convection. We explored values of $\mathrm{R}H_\mathrm{c}$ in the range 10^{-1} to 10^3, and found that the influence of $\mathrm{R}H_\mathrm{c}$ is small compared to that of other parameters. The flow patterns of these cases are similar to that for the reference case, the time averaged of the RMS velocity are nearly constant around 1300, and the estimated mixing times (defined in Section 4.1) vary between 5.7×10^{-3} and 4.8×10^{-3}. This result contrasts with a recent study in 2D-Cartesian geometry (van Thienen et al., 2005), which reports a moderate but significant dependence on $\mathrm{R}H_\mathrm{c}$. This discrepancy might be explained by the difference in geometry.

The chemical field is modeled using 10 million tracer particles of two types, one for the regular material, and one for the dense material (Tackley and King, 2003). Tracers are advected following a 4th order Runge–Kutta method. The number of particles of dense material is fixed by prescribing the fraction of dense material, X. Dense particles are initially distributed in the bottom of the system, leading to a dense layer of (non-dimensional) thickness h_DL. Numerically, h_DL is equal to the initial volume fraction of dense material, X. The concentration of dense particles C is measured in each cell, and varies between $C = 0$ and $C = 1$ for a cell fully filled with regular and dense material, respectively. The density contrast between dense and regular material, $\Delta\rho_\mathrm{c}$, creates negative buoyancy that acts against the positive thermal buoyancy. The relative strength of chemical buoyancy is usually measured by the buoyancy ratio

$$B \equiv \frac{\Delta\rho_\mathrm{c}}{\Delta\rho_T}, \tag{1}$$

where $\Delta\rho_T = \alpha_\mathrm{S}\rho_\mathrm{S}\Delta T_\mathrm{S}$, α_S and ρ_S are the thermal expansion and density at zero pressure, and ΔT_S the superadiabatic temperature difference across the system. In the present study, we fixed the fraction of dense material and buoyancy ratio to $X = 10\%$ and $B = 0.2$, respectively. Taking $\alpha_\mathrm{S} = 5.0 \times 10^{-5}\,\mathrm{K}^{-1}$, $\rho_\mathrm{S} = 3300\,\mathrm{kg\,m}^{-3}$,

and $\Delta T_S = 2500$ K, the density contrast between dense and regular material is thus $\Delta\rho_c = 82.5\,\mathrm{kg\,cm^{-3}}$.

Viscosity depends on temperature, depth, and composition. Depth-dependence consists of an exponential increase with depth, and a viscosity jump $R\mu_{660}$ at $d = 660$ km depth (non-dimensional depth $z = 0.228$). The exponential increase is controlled by a non-dimensional parameter V_a, which models the activation volume. Temperature-dependence is exponential and controlled by a non-dimensional parameter E_a representing the activation energy. Finally, the compositional dependence is also exponential and controlled by the ratio between the viscosities of the dense and regular materials, $R\mu_c$. By analogy with the thermal and depth dependences, it is convenient to define a chemical potential Λ_a, which in our case is numerically equal to $\ln(R\mu_c)$. The non-dimensional viscosity (with respect to the surface viscosity, μ_S) can thus be written:

$$\begin{cases} \mu(z,T,C) = \exp[V_a z - E_a T + \Lambda_a C] & z < 0.228 \\ \mu(z,T,C) = \Delta\mu_{660}\exp[V_a z - E_a T + \Lambda_a C)] & z > 0.228 \end{cases}, \quad (2)$$

where T is the non-dimensional temperature, and z the non-dimensional depth.

Because the fluid viscosity, thermal expansion, thermal diffusivity and density are allowed to vary throughout the system, the definition of the Rayleigh number is non-unique. As input, we prescribe the surface Rayleigh number:

$$Ra_S = \frac{\alpha_S g \rho_S \Delta T_S D^3}{\mu_S \kappa_S}, \quad (3)$$

where g is the acceleration of gravity, D the mantle thickness, and κ_S the surface thermal diffusivity. The surface Rayleigh number remains constant during the entire run (surface values of all parameters are assumed constant with time), and in all the calculations shown in this paper we prescribed $Ra_S = 10^8$. In contrast, the effective Rayleigh number Ra_{eff}, calculated with the properties of the material of the well-mixed interior, does vary with time. The value and time evolution of the effective Rayleigh number strongly depends on the model parameters. In the reference case, Ra_{eff} drops by 15% after the onset of instability of the dense layer, and remains constant around 10^6 during the rest of the run. For a large (≥ 10) compositional viscosity contrasts, Ra_{eff} is smaller, around 10^5, and slightly increases with time. The effect of temperature-dependent viscosity is more significant. In the case $R\mu_T = 10^6$, for instance, Ra_{eff} increases from 1.4×10^5 to 2.2×10^5 during the run duration. Variations in time of the surface Rayleigh number (due to variations in the surface viscosity, density, and thermal expansion) are however not accounted for in our calculations. This may induce small biases in the evolution of the system, in particular if the Rayleigh number was larger in the past (Davies, 2002).

Compressibility induces an additional sources and sinks of heat that are controlled by the dissipation number. Again, the definition of this number is non-unique. The dissipation number as a function of depth is given by

$$Di(d) = \frac{\alpha(d) g D}{C_P}, \quad (4)$$

where C_P is the heat capacity, which we assumed to be constant with depth. In all our experiments, the surface and volume average dissipation numbers are $Di_S = 1.2$ and $\langle Di\rangle = 0.43$, respectively. A phase transition at $d = 660$ km is implemented, but we imposed a zero Clapeyron slope.

Conservative equations involve reference profiles for thermodynamic parameters, including density, thermal expansion, and temperature. Reference profiles are calculated using an appropriate thermodynamic model (Tackley, 1996; Tackley, 1998b), and scaled

Table 1
Parameters and scalings

Parameter	Symbol	Value	Units	Non-dimensional
Non-dimensional parameters				
Surface Rayleigh number	Ra_S			10^8
Buoyancy ratio	B			0.2
Volume fraction of dense material	X			0.10
Initial thickness of the dense layer	h_{DL}			0.10
Surface dissipation number	Di_S			1.2
Volume average dissipation number	Di			0.43
Total internal heating	H_c	65	$\mathrm{mW\,m^{-2}}$	25
Compositional heating ratio	RH_c			10
Physical and thermo-dynamical parameters (dimensional)				
Acceleration of gravity	g	9.81	$\mathrm{m\,s^{-2}}$	1.0
Mantle thickness	D	2891	km	1.0
Superadiabatic temperature difference	ΔT_S	2500	K	1.0
Reference geotherm	T_{as}	1600	K	0.64
Surface density	ρ_S	3300	$\mathrm{kg\,m^{-3}}$	1.0
Density jump at $d = 660$ km	$\Delta\rho_{660}$	400	$\mathrm{kg\,m^{-3}}$	0.1212
Surface thermal expansion	α_S	5.0×10^{-5}	$\mathrm{K^{-1}}$	1.0
Surface thermal diffusivity	κ_S	6.24×10^{-7}	$\mathrm{m^2\,s^{-1}}$	1.0
Heat capacity	C_P	1200	$\mathrm{J\,kg^{-1}\,K^{-1}}$	1.0
Surface conductivity	k_S	3.0	$\mathrm{W\,m^{-1}\,K^{-1}}$	1.0
Surface Grüneisen parameter	γ_S	1.091		
Viscosity law				
Surface thermal viscosity	μ_S	1.6×10^{21}	Pa s	1.0
Viscosity ratio at $d = 660$ km	$R\mu_{660}$	1.0–300		
Compositional viscosity ratio	$R\mu_c$	3.2×10^{-3}–10^3		
Depth viscosity ratio	$R\mu_z$	1.0–10^4		
Thermal viscosity ratio	$R\mu_T$	1.0–10^7		
Dimensional scalings				
Velocity	v	1.0	$\mathrm{cm\,yr^{-1}}$	1468
Time	t	424	Gyr	1.0
Heat flux	Φ	2.6	$\mathrm{mW\,m^{-2}}$	1.0
Internal heating rate	H	2.72×10^{-13}	$\mathrm{W\,kg^{-1}}$	1.0

with respect to their surface value (except temperature, which is scaled to ΔT_S). The thermodynamic parameters we used to build the reference state are listed in Table 1, together with other physical parameters and scalings. Note that we assumed a density jump at $d = 660$ km, but not at $d = 410$ km.

To avoid the transient phase in which the dense layer heats up, the temperature field is initialized with a geotherm taken from 2D calculations that have reached secular equilibrium, to which we added random 3D perturbations. 2D calculations have similar boundary conditions as the 3D cases, and include a dense layer at the bottom. This initial condition does not influence the flow evolution after the onset of instability of the dense layer.

3. Stability of the dense layer

The layer of dense material at the bottom of the system creates negative buoyancy that stabilizes it. To generate instabilities from this layer, thermal buoyancy must overcome the chemical negative buoyancy. This can be achieved by heating the system during a long enough period of time. Howard (1966) pointed out that a thermal boundary layer becomes unstable if its thickness exceeds a critical value that is determined from a local Rayleigh number. Furthermore, the onset time for the rise of instabilities depends on the properties of the system. A larger viscosity increases the critical thickness of the thermal boundary layer, thus delaying the onset of instability. It is also useful to define a proper Rayleigh number for the dense layer:

$$Ra_{DL} = \frac{\alpha \rho g \, \Delta T_{DL} h_{DL}^3}{\mu_{DL} \kappa}, \tag{5}$$

and compare it to a critical Rayleigh number, estimated from linear stability analysis. LeBars and Davaille (2002) and Jaupart et al. (2007) performed such analysis and showed that the critical Rayleigh number mainly depends on the buoyancy ratio and, to a lesser extent, on the compositional viscosity contrast.

From Eq. (5), it is clear that a small (large) value of the viscosity of the dense layer is decreasing (increasing) Ra_{DL}. A compositional viscosity contrast smaller than 1 (the dense material is less viscous than the regular material) will oppose the action of dense material and decrease the time for the onset of instability. On the contrary, a compositional viscosity contrast larger than 1 or an increase of viscosity with depth will enhance the stability of the layer of dense material. Because our calculations include more complexities (depth- and temperature-dependent viscosity, compressibility) than the linear stability analysis in LeBars and Davaille (2002) and Jaupart et al. (2007), their results might not valid in our case. However, it is worth noting that for $B = 0.2$, they found a critical Rayleigh number of about 125. Taking $Ra = 10^8$, $h_{DL} = 0.1D$, and $\Delta T_{DL} = 0.5\Delta T_S$, Ra_{DL} is larger than the critical Rayleigh number if the viscosity of the dense layer is smaller than the surface viscosity by a ratio of about 400.

To estimate the time of the onset of instability of the dense layer (t_{onset}), we calculated the average non-dimensional altitude of dense material:

$$\langle h_c \rangle = \frac{1}{V} \int_V (1 - z) C(x, y, z) \, dV, \tag{6}$$

as a function of time. Initially, $\langle h_c \rangle$ is equal to half the thickness of the dense layer, h_{DL}, i.e., it is numerically equal to $X/2$, where X is the volume fraction of dense material. As long as the dense layer is stable $\langle h_c \rangle$ remains equal to $X/2$, but when the dense layer gets unstable it increases. Time evolutions of $\langle h_c \rangle$ (Section 5, Figs. 3a, 6a and 9a), clearly show that t_{onset} increases with increasing compositional ($R\mu_c$), 660 km ($R\mu_{660}$), and depth ($R\mu_z$) viscosity contrasts. Note that for $R\mu_c = 10^2$, the dense layer remains stable during the entire run. t_{onset} also increases with increasing thermal viscosity contrast ($R\mu_T$), but the layer gets unstable even for large (at least 10^7) values of $R\mu_T$.

4. Processing the numerical results

4.1. Estimated mixing time

Mixing time is estimated from the time evolution of the variance in the distribution of composition, var(t). Following previous studies (Ferrachat and Ricard, 2001; Olson et al., 1984), we first defined the function:

$$e(t) = 1 - \frac{\mathrm{var}(t)}{\mathrm{var}(t = 0)}, \tag{7}$$

and its time integral over the duration of the run, $f(t_{run})$. The function $e(t)$ varies between zero at $t = 0$ and its statistical limit

$$e_{max} = 1 - \frac{N - 1}{n_{part}}, \tag{8}$$

where n_{part} and N are the number of particle tracers and the number of cells, respectively. The integral $f(t_{run})$ varies between $f_{min} = 0$, for a bottom layer that remains strictly stable, and $f_{max} = e_{max} t_{run}$, in

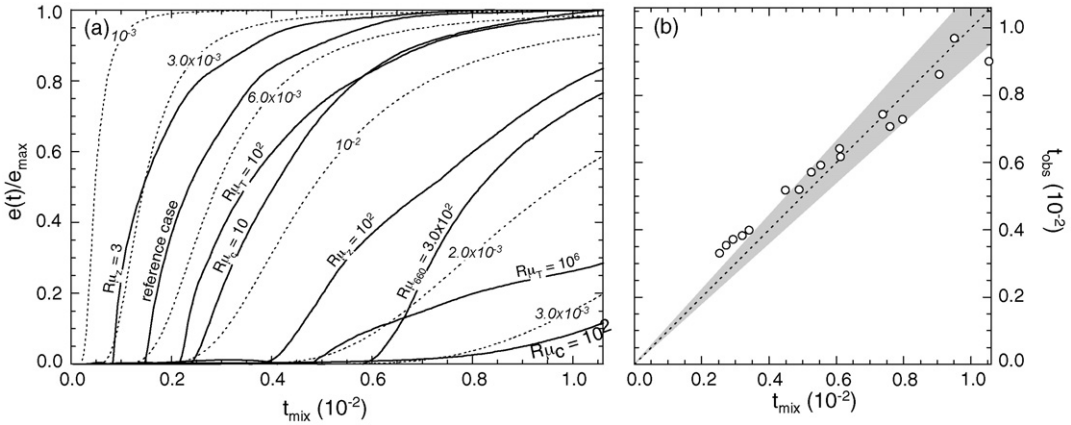

Fig. 1. Estimating the mixing time. (a) Comparison between the function $\xi^2 \exp(\xi)/[\exp(\xi) - 1]^2$, where $\xi = (t_0/t)^{1.5}$ (dotted curves; the value of t_0 is indicated with italic numbers), and the ratio $e(t)/e_{max}$ for various cases (thick plain curves; the case considered is indicated on each curve). (b) Comparison between the mixing time estimated from Eq. (9), and the 'observed' mixing time, defined as the time at which the function $e(t)$ (Eq. (7)) reaches 92% of its statistical limit. The gray shaded area covers ±10% around the estimated mixing time.

the (hypothetical) case of a system instantaneously homogenized at $t = 0$. Interestingly, $e(t)$ fits reasonably well the family of functions $g(\xi) = c\xi^2 \exp(\xi)/[\exp(\xi) - 1]^2$, where c is a constant and $\xi = (t_0/t)^{1.5}$, except for large values of $R\mu_{660}$ and $R\mu_T$ (Fig. 1a). The function $g(\xi)$ reaches 92% of its maximum value at time $t = t_0$ and tends towards c when t goes to infinity. Note that exponential functions are also used to estimate the mantle degassing time by convective mixing (Coltice, 2005). It is not clear why $e(t)$ is well described by $g(\xi)$. This function is however well known in statistical physics. It describes the temperature dependence of the specific heat of a collection of atoms (modeled by harmonic oscillators) distributed between discrete energy levels. As the temperature of the assembly of atoms increases, a larger number of energetic levels are populated, and the specific heat (which measures the increase in the entropy of the system for a given increment of temperature), increases. We suggest the following analogy. The distribution of particles of dense material is obviously discrete (due to the finite difference scheme we use), and the initial condition (the particles of dense material are all distributed in a basal layer) may correspond to a fundamental, frozen state (all atoms are in the lower energy level). As time increases, convective flow allows the particles of dense material to reach a larger number of locations, and the function $e(t)$ (which measures the time evolution of the mixing efficiency of the system, and therefore of its entropy) increases. To estimate the mixing time t_{mix}, we thus solve the equation:

$$f(t_{\mathrm{run}}) = e_{\max} \int_0^{t_{\mathrm{run}}} \xi^2 \frac{\exp(\xi)}{[\exp(\xi) - 1]^2}\, \mathrm{d}t, \quad \xi = \left(\frac{t_{\mathrm{mix}}}{t}\right)^{1.5}, \tag{9}$$

following a Newton–Raphson method.

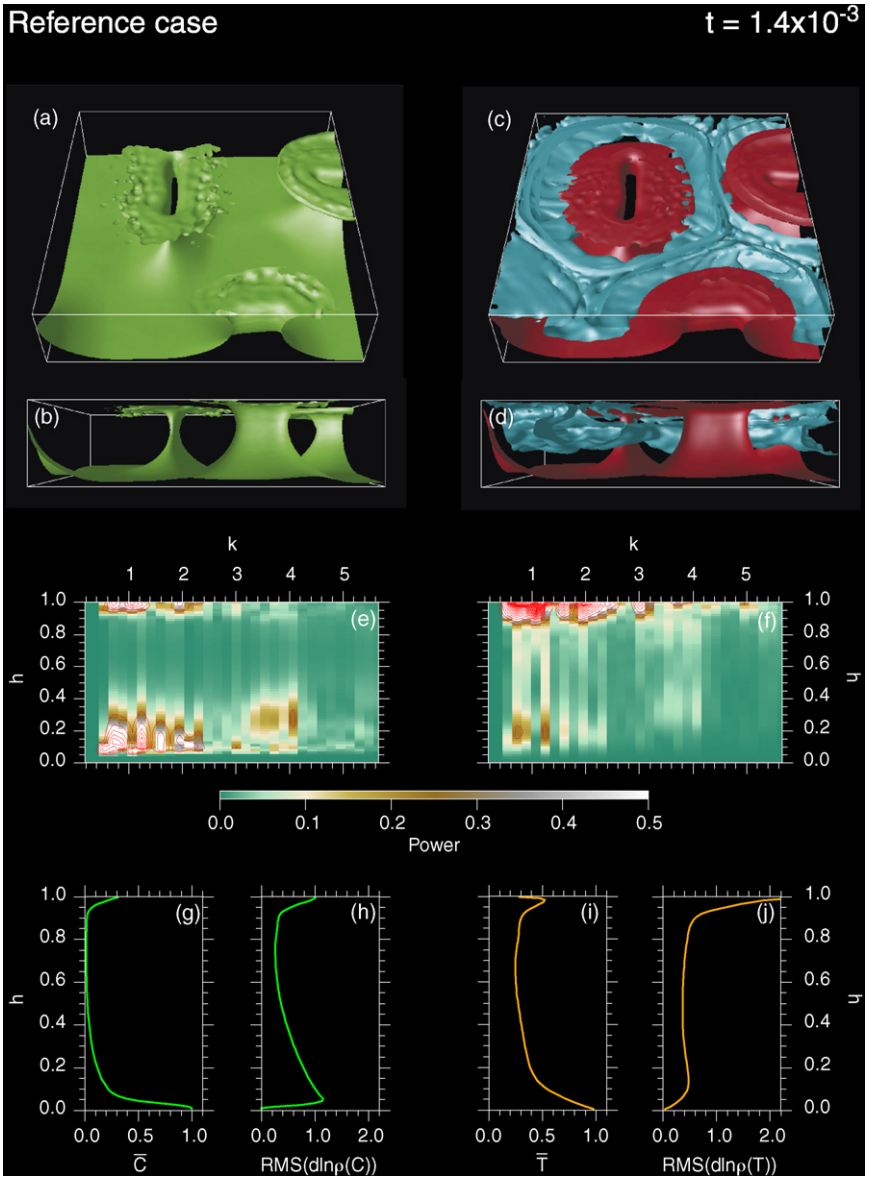

Fig. 2. Snapshot of the reference case at $t = 1.4 \times 10^{-3}$ (0.6 Gyr). Parameters of the viscosity law are $R\mu_c = 10^{-2}$, $R\mu_{660} = 30$, $V_a = 2.303$ ($R\mu_z = 10$), and $E_a = 0$ ($R\mu_T = 1$). (a and b) Isosurface of the concentration in dense particle, with contour level $C = 0.5$. (c and d) Isosurfaces of the non-dimensional temperature (relative to average), with contour levels $T - \langle T \rangle = -0.15$ (blue) and $T - \langle T \rangle = 0.15$ (red). (e) Spectral heterogeneity map (SHM) of the chemical density anomalies, $d \ln \rho_c$ (Eq. (11)). (f) SHM of the thermal density anomalies, $d \ln \rho_T$ (Eq. (10)). SHMs are plotted with both a color scale and contour levels (red curves, interval is 0.2). h is the non-dimensional altitude. (g) Profile of the horizontally average concentration in dense particle, $\bar{C}$. (h) Profile of the RMS of the chemical density anomalies $d \ln \rho_c$. (i) Profile of the horizontally average non-dimensional temperature, $\bar{T}$. (j) Profile of the RMS of the thermal density anomalies $d \ln \rho_T$. (For interpretation of the references to color in this figure legend, the reader is referred to the web version of the article.)

An advantage of Eq. (9), compared to previous studies (Ferrachat and Ricard, 2001; Olson et al., 1984), is to provide estimates of the mixing time even if the mixing is not completed at the end of the run. However, this approach fails to predict a mixing time when the dense layer remains stable, e.g., for a large compositional viscosity contrast ($R\mu_c = 30$ and more). Similarly, our estimates are strongly underestimated if the mass transfer around $d = 660$ km is reduced (large values of $R\mu_{660}$), or if pools of dense material generate at the bottom of the system (large values of $R\mu_T$). In cases for which mixing is completed before the end of the run, the value of t_{mix} predicted by Eq. (9) agrees very well with the observed time at which $e(t)$ reaches 92% of the statistical limit e_{max} (Fig. 1b).

4.2. RMS flow velocity

The RMS of the flow velocity, RMS(v), does not provide a direct measure of the mixing, but is indirectly related to it. The faster the flow, the more efficient the mixing. Another measure of the mixing efficiency is the bulk Lagrangian strain rate (Coltice, 2005). For instance, in the case of a 2D-Cartesian fluid, Coltice (2005) established scaling laws of the processing time as a function of this strain rate. Flow velocity is controlled by various parameters, including the parameters of the viscosity law. All other parameters being equal, a fluid flows more slowly as its viscosity increases. Thus, if the viscosity of the dense material increases, the velocity of thermo-chemical plumes decreases, and mixing gets less efficient. It is difficult to predict *a priori* the influence of the various viscosity variations on RMS(v). In the case of a temperature-dependent viscosity, for instance, the top of the system is more viscous and flows slower than average, but the bottom is less viscous and flows faster than average. In most cases (Section 5, Figs. 3b, 6b and 9b), RMS(v) sharply increases immediately after the onset of instability, reaches a peak, and decreases again to an intermediate values around which it oscillates during the rest of the run. The amplitude of the maximum of RMS(v) strongly depends on the type and amplitude of the viscosity variation. Overall, the time average of RMS(v), $\langle \mathrm{RMS}(v) \rangle_t$, provide a good estimate of the characteristic amplitude of the flow velocity for each case (Section 5, Figs. 3d, 6d and 9d).

4.3. Lateral chemical and thermal heterogeneities

Thermo-chemical convection provides distributions of temperature and composition that we use to compute relative density variations. At each depth, the lateral density anomalies due to thermal and compositional variations around the average temperature $\bar{T}(z)$ and fraction of dense particles $\bar{C}(z)$ at this depth are (Deschamps et al., 2007)

$$d\ln\rho_T = \frac{\alpha_{ref}[T - \bar{T}(z)]}{1 - \alpha_{ref}[\bar{T}(z) - T_{ref}]}, \tag{10}$$

and

$$d\ln\rho_c = -\alpha_S \Delta T_S \frac{B[C - \bar{C}(z)]}{1 + \alpha_S \Delta T_S B\bar{C}(z)}. \tag{11}$$

Profiles of the RMS of $d\ln\rho_T$ and $d\ln\rho_c$ provide the first hints of the thermo-chemical structure. A stable layer of dense material results in a RMS that peaks around the interface between regular and dense material, and is zero elsewhere. Piles of dense material rising from a dense layer predict a RMS of $d\ln\rho_c$ that increases with depth down to the top of the dense layer. If dense and regular materials are well mixed, the RMS of $d\ln\rho_c$ is constant with depth and close to zero. Unfortunately, uncertainties and the vertical parameterization of tomographic models are such that the comparison of RMS profiles from tomography and thermo-chemical convection alone cannot provide a full diagnostic for the mantle convection (Deschamps et al., 2007).

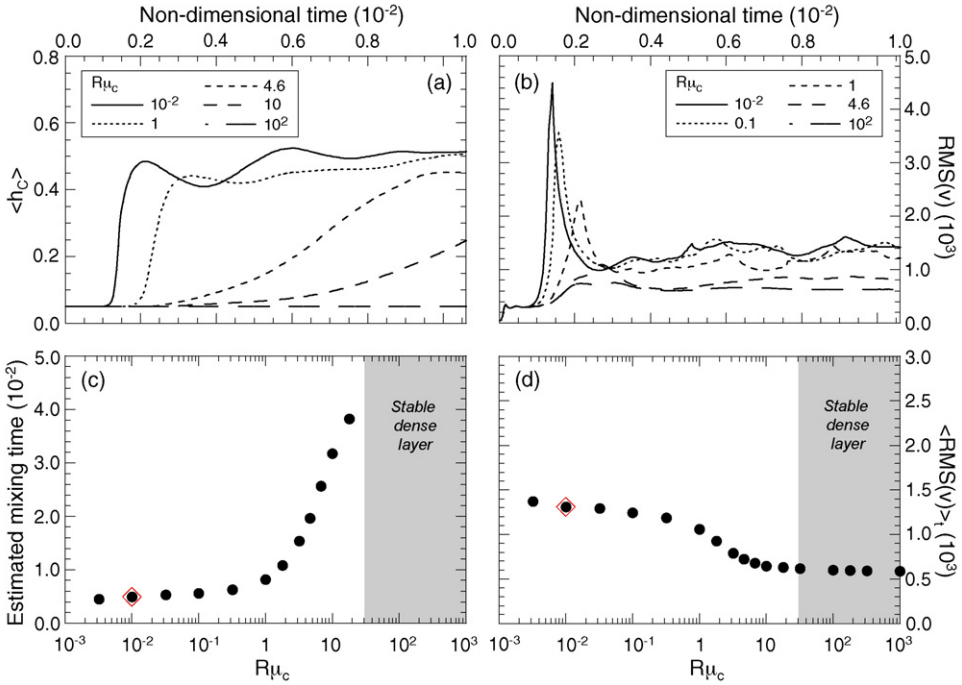

Fig. 3. Influence of the compositional viscosity ratio, $R\mu_c$. (a) Average altitude of dense material, $\langle h_c \rangle$ (Eq. (6)), as a function of time and for various values of $R\mu_c$. (b) RMS of the flow velocity as a function of time and for various values of $R\mu_c$. (c) Estimated mixing time as a function of $R\mu_c$. For $R\mu_c \geq 30$, dense layer is stable during the entire run, and we cannot give estimate of the mixing time. (d) Time average RMS of the flow velocity as a function of $R\mu_c$. In plots (c) and (d), the reference case is indicated by the red diamond. (For interpretation of the references to color in this figure legend, the reader is referred to the web version of the article.)

More detailed information can be inferred from spectral heterogeneity maps (SHMs, Tackley et al., 1994) of $d\ln\rho_T$ and $d\ln\rho_c$. The SHM of a given 3D distribution is obtained by calculating the 2D Fourier expansion of this distribution at each depth and plotting the resulting power spectrum as a function of the wave number ($k = \sqrt{k_x + k_y}$) and the depth.

4.4. Comparison with probabilistic tomography

We decided to test our models of thermo-chemical convection against probabilistic tomography (Resovsky and Trampert, 2003; Trampert et al., 2004) because this model includes a distribution of density anomalies in the lower mantle. Density anomalies are

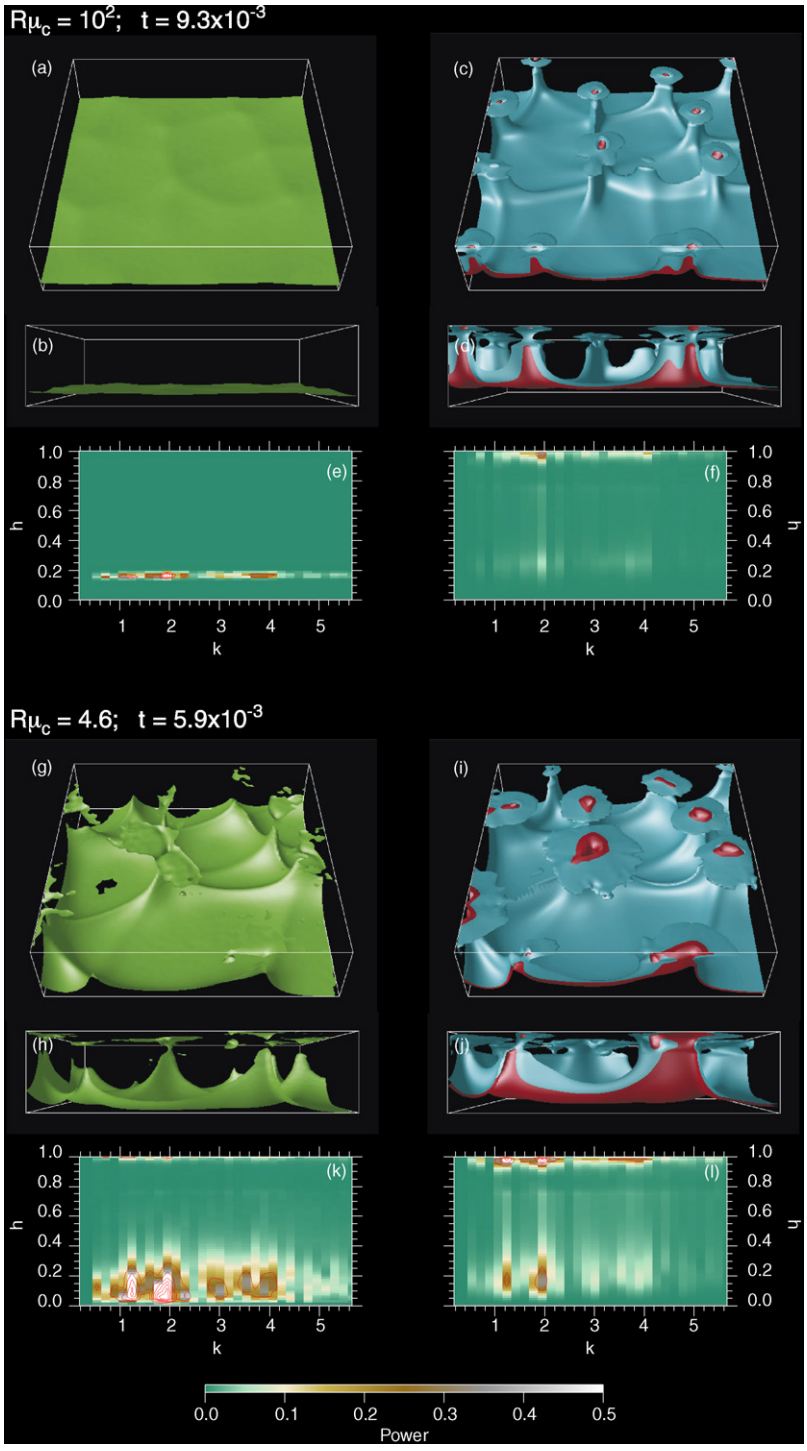

Fig. 4. (a–f) Snapshot of the case $R\mu_c = 10^2$ at $t = 9.3 \times 10^{-3}$ (2.5 Gyr). Other parameters are as in the reference case. (a and b) Isosurface of the concentration in dense particle, with contour level $C = 0.5$. (c and d) Isosurfaces of the non-dimensional temperature (relative to average), with contour levels $T - \langle T\rangle = -0.05$ (blue) and $T - \langle T\rangle = 0.05$ (red). (e) Spectral heterogeneity map (SHM) of the chemical density anomalies, $d\ln\rho_c$ (Eq. (11)). (f) SHM of the thermal density anomalies, $d\ln\rho_T$ (Eq. (10)). SHMs are plotted with both a color scale and contour levels (red curves, interval is 0.2). h is the non-dimensional altitude. (g–l) Snapshot of the case $R\mu_c = 4.6$ at $t = 5.9 \times 10^{-3}$ (3.9 Gyr). Other parameters are as in the reference case. Plots description is similar to that for plots (a–f). (For interpretation of the references to color in this figure legend, the reader is referred to the web version of the article.)

essential to resolve the trade-off that exists between temperature and composition. Furthermore, probabilistic tomography provides full probability density functions (rather than mean values only) for anomalies in density and seismic velocity at each point of the model.

A convenient way to compare the distributions of density anomalies predicted by tomography and thermo-chemical convection is to compare their power spectra. Global tomographic models, including probabilistic tomography from Trampert et al. (2004) (hereafter referred to as RT246g), are developed in spherical harmonics, and relevant comparisons requires that we appropriately sum up the Fourier spectra of density anomalies obtained by thermo-chemical convection over the wave number k. Assuming that the power per surface unit is the same in the Fourier and harmonic expansions, the signal contained in spherical harmonic degree ℓ is obtained by summing the wave numbers that satisfies (Chevrot et al., 1998)

$$\ell + \frac{1}{2} \leq ka \leq \ell + \frac{3}{2}, \quad k = \sqrt{k_x + k_y}, \tag{12}$$

where a is the Earth's radius, and k_x and k_y the wave number along the x-axis and y-axis. Following this rule, one can expand density anomalies from thermo-chemical convection up to spherical harmonic 32. This is far enough for compar-

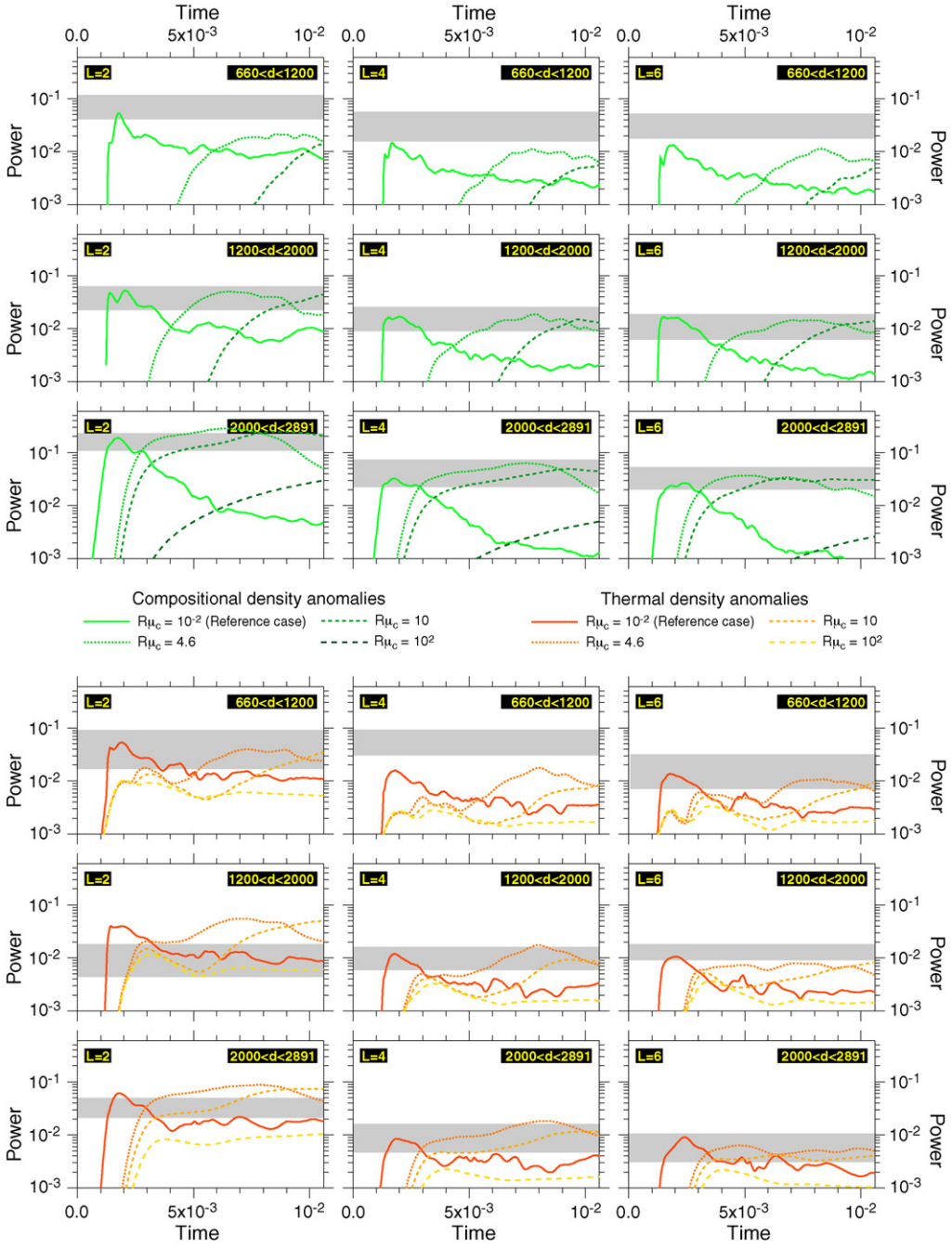

Fig. 5. Power of chemical (three top rows) and thermal (three bottom rows) density anomalies as a function of time and for various values of the chemical viscosity ratio, Rμ_c. Anomalies are averaged within three layers ($660 \leq d \leq 1200$ km, $1200 \leq d \leq 2000$ km, and $2000 \leq d \leq 2891$ km), and we considered three spherical harmonics ($L = 2$, $L = 4$, and $L = 6$). Gray bands indicate the power spectrum predicted by RT246g within twice its standard deviation.

ison with RT246g, which contains degrees 2, 4 and 6 only. Furthermore, one must vertically average the density anomalies from thermo-chemical convection according to the radial parameterization of RT246g. This includes two layers in the upper mantle ($24 \le d \le 410$ km and $410 \le d \le 660$ km), and three in the lower mantle ($660 \le d \le 1200$ km, $1200 \le d \le 2000$ km, and $2000 \le d \le 2891$ km). Note that because compositional anomalies are parameterized in terms of iron and perovskite anomalies (Trampert et al., 2004), the comparison with RT246g is meaningful only in the lower mantle.

5. Model space search: viscosity law parameters

To illustrate the method described in Section 4, we studied the influence of the parameters of the viscosity law (Eq. (2)) on the convective flow and on the efficiency of mixing. We define a reference case, and vary one parameter at a time, other parameters having values similar to those of the reference case. The surface Rayleigh number, fraction of dense material, and buoyancy ratio are the same for all the experiments reported in this paper, with $Ra_S = 10^8$, $X = 0.1$ and $B = 0.2$, respectively. We performed 46 runs in total, but only display snapshots from a few runs. Additional snapshots and movies from all cases are available as supplementary online material or by the authors on demand.

5.1. Reference case

For comparisons, we defined a reference case with the following properties. Viscosity varies with depth ($V_a = 2.303$, corresponding to a bottom to top viscosity ratio equal to 10), but not with temperature ($E_a = 0$). The viscosity jump at the upper/lower mantle boundary ($R\mu_{660}$) is equal to 30, and the dense material is less viscous than the regular material by two orders of magnitude ($R\mu_c = 10^{-2}$). As discussed below, this case generates large thermo-chemical plumes that lead to efficient mixing between dense and regular material. It may thus be used as a reasonable reference to better understand the influence of each parameter.

In this case, the time for the onset of instability of the dense layer (t_{onset}) is around 0.9×10^{-3} (i.e., a dimensional time around 0.4 Gyr). Large plumes are generated from the dense layer, entraining dense and hot material upwards (Fig. 2, plots a–d). This pattern is associated with strong chemical heterogeneities at the bottom and, to a lesser extent, at the top of the system (Fig. 2, plots e and h). Strong thermal heterogeneities are also present at the top of the system (Fig. 2, plots f and j). The power spectrum of chemical anomalies is dominated by large-scale structures with (non-dimensional) wave number up to $k = 2.5$ (Fig. 2e). Thermal anomalies have a wider spectrum, with wave number up to $k = 3.5$ (Fig. 2f). The distributions of these anomalies agree well with those from probabilistic tomography (Deschamps et al., 2007). However, piles are generated early in the run history and remain stable for a short period of time only, in the range $10^{-3} \le t \le 2.0 \times 10^{-3}$ (0.42–0.84 Gyr). During this episode, most of the dense layer is swept out. Thermal plumes, in contrast, remain present until the end of the run. Piles are thus an efficient way to mix dense and regular material, with an estimated mixing time $t_{mix} = 5.0 \times 10^{-3}$ (2.1 Gyr). An important consequence is that the amplitude of chemical density anomalies rapidly decreases with time.

5.2. Compositional viscosity contrast

We first explored the influence of the viscosity contrast between the dense and regular materials, varying $R\mu_c$ in the range 3.2×10^{-3}–10^3. Based on the variations of $\langle \mathrm{RMS}(v) \rangle_t$ and t_{mix}, we identify three regimes.

For $R\mu_c \le 0.1$, the dense layer reaches the onset of instability within a short time (Fig. 3a). As in the reference case, we observe thermo-chemical plumes, but their size and velocity slightly decrease with increasing $R\mu_c$, and they remain present for a longer time. $\langle \mathrm{RMS}(v) \rangle_t$, slowly decreases (from ~1400 to ~1200) with increasing $R\mu_c$ (Fig. 3d). The mixing time is thus slightly increasing, but is always smaller than the time of the run (Fig. 3c). Again, piles are associated with strong lateral density anomalies, but these anomalies sharply decrease in amplitude with time, as

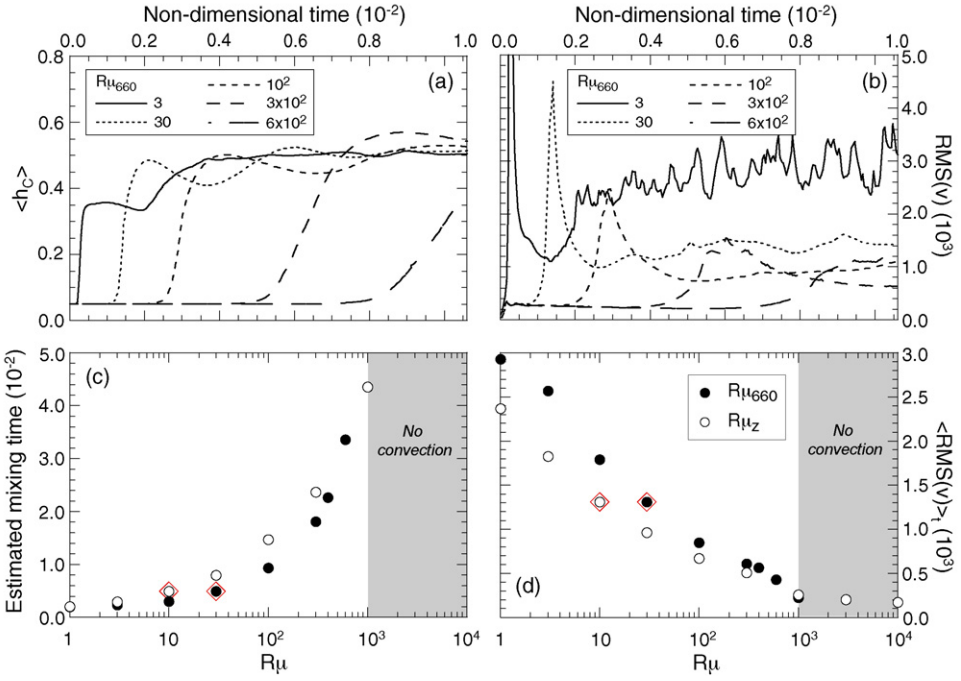

Fig. 6. Same as Fig. 3, but for various values of the viscosity ratio at $d = 660$ km, $R\mu_{660}$. Plots (c) and (d) also display the estimated mixing time and average RMS of the flow velocity for the depth viscosity ratio, $R\mu_z$ (open circles).

dense and regular material get mixed. The spherical harmonics power spectra of density anomalies fit RT246g well during a short period of time, but strongly disagree with them in the long term (Fig. 5, plain curves).

For $R\mu_c \geq 30$, the layer of dense material remains stable over long periods of time (Fig. 4, plots g and h). The layer of regular material is unstable with respect to thermal convection, and small plumes rises from a thermal boundary layer located at the top of the dense material (Fig. 4, plots i and j). These thermal plumes entrain small amounts of dense material upwards, but thermal erosion is a slow process and is not completed before the end of the run. Lateral chemical anomalies are present, but strongly localised around the boundary between the dense and regular materials (Fig. 4k). Whatever the time, models with a stable layer of dense material do not fit

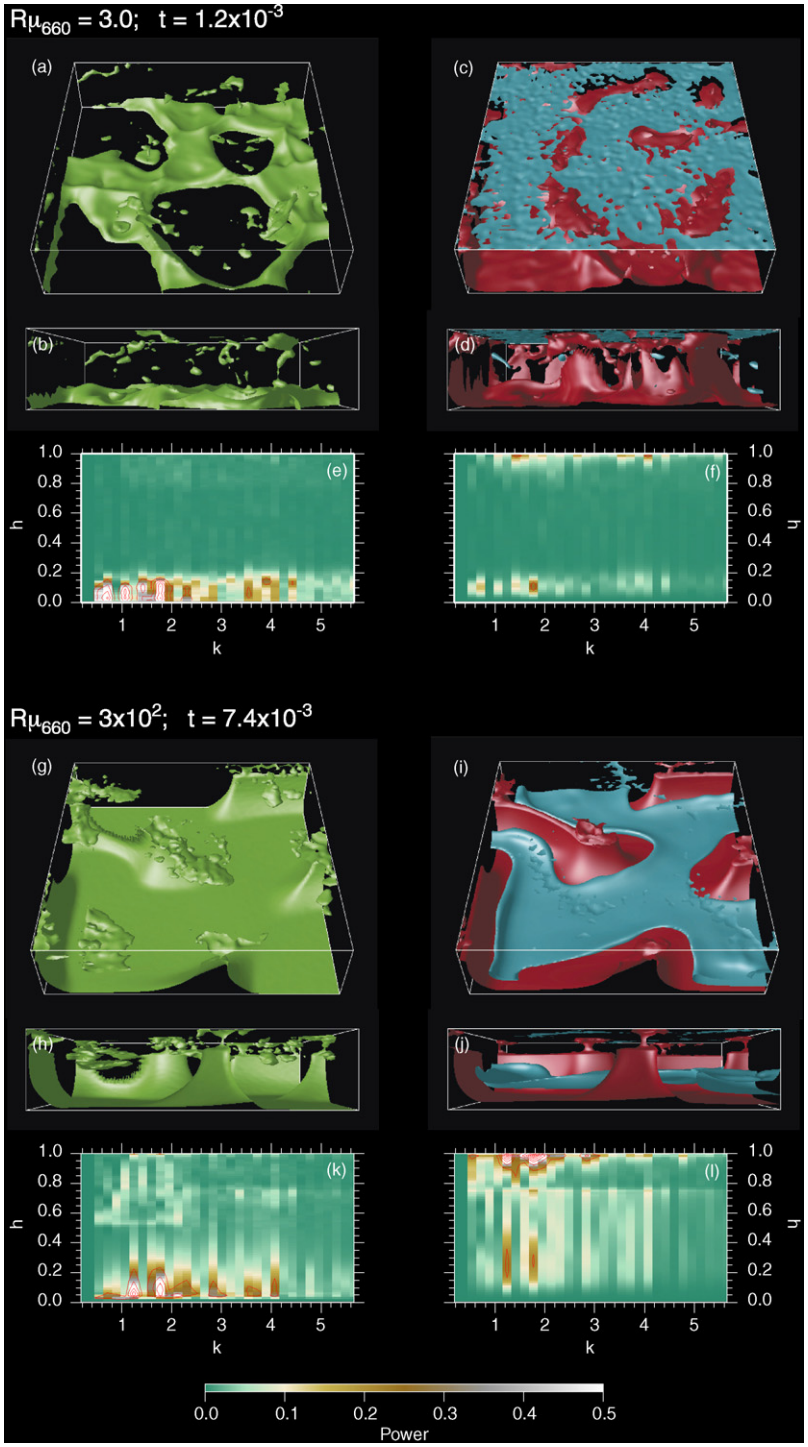

Fig. 7. (a–f) Snapshot of the case $R\mu_{660} = 3.0$ at $t = 1.2 \times 10^{-3}$ (0.5 Gyr). Other parameters are as in the reference case. Plots description is similar to that in plots (a–f) of Fig. 4. In plots (c) and (d), contour levels for temperature isosurfaces are $T - \langle T \rangle = -0.125$ (blue) and $T - \langle T \rangle = 0.075$ (red). (g–l) Snapshot of the case $R\mu_{660} = 3.0 \times 10^2$ at $t = 7.4 \times 10^{-3}$ (3.1 Gyr). Other parameters are as in the reference case. Plots description is similar to that in plots (a–f) of Fig. 4. In plots (i) and (j), contour levels for temperature isosurfaces are $T - \langle T \rangle = -0.2$ (blue) and $T - \langle T \rangle = 0.2$ (red). (For interpretation of the references to color in this figure legend, the reader is referred to the web version of the article.)

RT246g (Fig. 5, long dashed curves). In the layers $660 \leq d \leq 1200$ km and $1200 \leq d \leq 2000$ km, the power of chemical density anomalies is negligible. In the layer $2000 \leq d \leq 2891$ km, it slowly increases with time, but never reaches the value observed by RT246g.

For intermediate (0.1–10) values of $R\mu_c$, we observe transitional patterns, in which small fingers of dense, viscous, material are entrained upwards by thermal plumes (Fig. 4, plots a and b). The number and size of thermal plumes (Fig. 4, plots c and d) are intermediate between those observed for high and low $R\mu_c$. t_{onset} increases (Fig. 3a), whereas $\left\langle \mathrm{RMS}(v) \right\rangle_t$ drops by ~500 (Fig. 3d). The thermo-chemical plumes remain stable for a longer period of time. The estimated mixing time sharply increases with increasing $R\mu_c$ (Fig. 3c). Interestingly, this pattern implies strong lateral anomalies of composition at the bottom of the system (Fig. 4e). The Fourier power spectra are wider than in the reference case, and we observe strong anomalies up to $k = 4.2$. More importantly, these anomalies are maintained for a long period of time, and agree with seismic tomography in the long term. By the end of the run, the spherical harmonics power spectra of thermal density anomalies still fit RT246g reasonably well (Fig. 5, dotted and short-dashed curves), although some discrepancies remain in the layer 660–1200 km for all degrees of the chemical density anomalies, and for the degree 4 of the thermal density anomalies.

Three important conclusions can be drawn from this series of experiments. First, an increase in compositional viscosity contrast favours the development of small-scale structures. This observation is consistent with linear theory for Rayleigh–Taylor instabilities, which predict that plumes size and spacing increase as the plumes

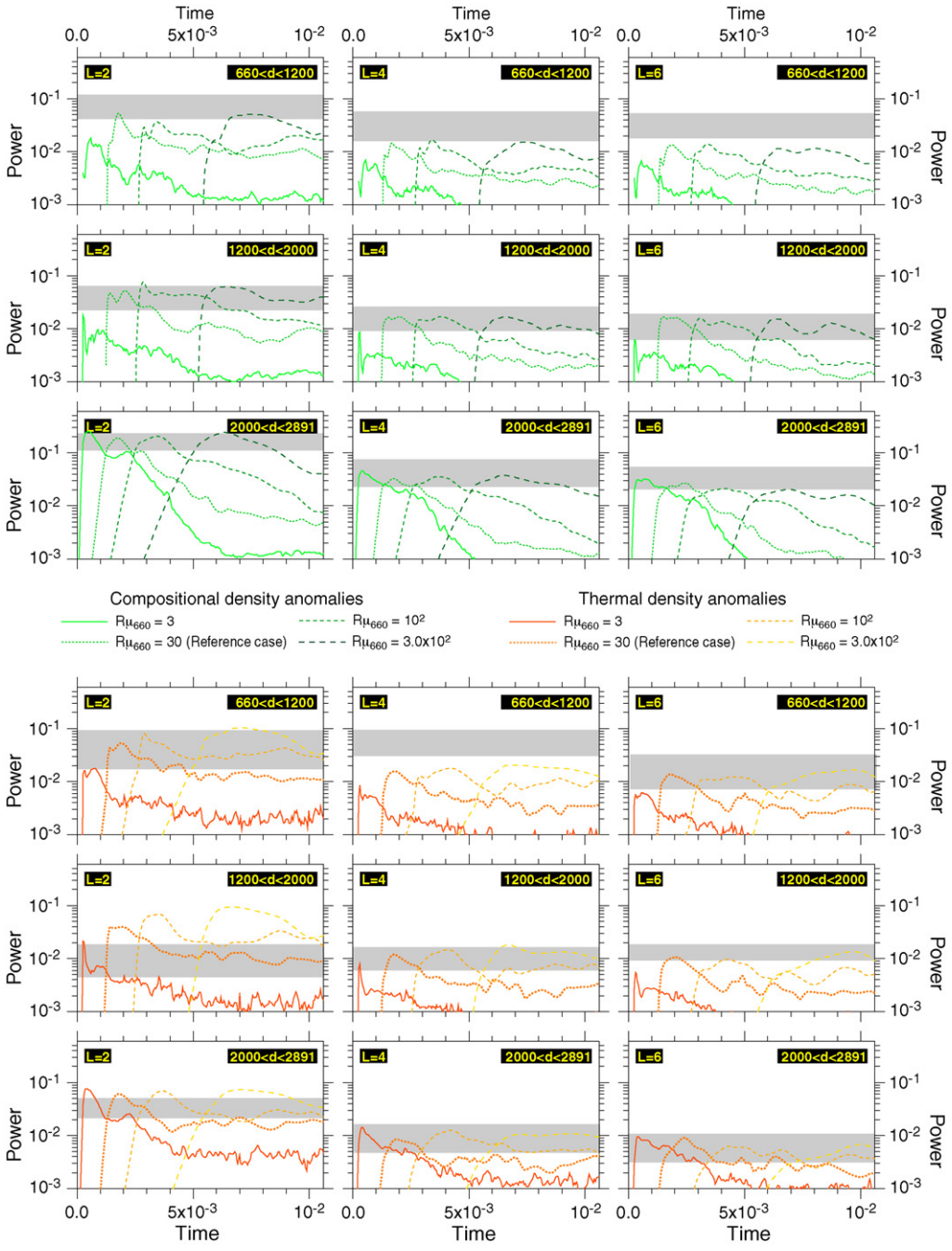

Fig. 8. Same as Fig. 5, but for various values of the viscosity ratio at $d = 660$ km, $R\mu_{660}$.

viscosity decrease (Whitehead and Luther, 1975). Second, thermo-chemical plumes, and therefore lateral density anomalies, can be maintained for longer period of time as $R\mu_c$ increases. In other words, the mass flux within thermo-chemical plumes decreases with increasing $R\mu_c$. Again, this observation agrees with linear theory for Rayleigh–Taylor instabilities. Finally, for high enough values of $R\mu_c$ (30 and more), the dense layer remains stable during the whole run, i.e., for period of time comparable to the age of the Earth.

5.3. Depth-dependent viscosity

Viscosity variations with depth are controlled by an exponential increase with depth and a viscosity contrast at $d = 660$ km ($z = 0.228$). We independently explored the influence of these two parameters, varying $R\mu_{660}$ between 1 and 10^3, and $R\mu_z$ between 1 and 10^4 ($0 \leq V_a \leq 9.210$). Note that for $R\mu_{660}$ and $R\mu_z$ larger than critical values, which, in this series of experiments, are around 10^3 and 3.0×10^3, respectively, the whole system is stable and does not convect.

For small (≤ 10) values of $R\mu_{660}$ we observe fast, small-scale plumes entraining dense material upwards (Fig. 7, plots c and d). t_{onset} is small (Fig. 6a), around 5.0×10^{-4} (0.2 Gyr) for $R\mu_{660} = 3$, and the plume velocity reaches extremely large values, up to 10^4 (~ 6.8 cm/yr) (Fig. 6b). Similarly, $\langle \mathrm{RMS}(v) \rangle_t$ is large, up to 3000 for $R\mu_{660} = 1$ (Fig. 6d). The dense layer mixes with the regular material, with $t_{mix} \leq 3.0 \times 10^{-3}$ (2.7 Gyr) (Fig. 6c). In the early stages, interconnected ridges of dense material are present at the bottom of the system (Fig. 7, plots a and b). These structures are associated with moderate density anomalies up to $k = 4.5$ (Fig. 7e), which are very short-lived and poorly fit RT246g (Fig. 8).

On the contrary, for $R\mu_{660} \geq 10$, large-scale structures dominate the flow. For moderate (10–50) values of $R\mu_{660}$, we observe large thermo-chemical plumes surrounded by downwelling sheets, similar to those seen in the reference case (Fig. 2). For larger (10^2 to 6.0×10^2) values of $R\mu_{660}$, large-scale structures are still present, but we note major changes in the flow pattern (Fig. 7g–j). The average flow velocity is strongly attenuated (Fig. 6b and d). Thermo-chemical plumes are interconnected with ridges of hot, dense material. More importantly, the viscosity contrast strongly attenuates the upward mass transfer. Thermo-chemical plumes dramatically narrow as they cross the 660 km boundary. In addition, t_{onset} sharply increases with $R\mu_{660}$ (Fig. 6a). The mixing of dense and regular materials is thus severely inhibited. Note that in this case, the variance in the concentration of dense particle does not fit well the function $\xi^2 \exp(\xi)/[\exp(\xi) - 1]^2$ (Fig. 1a), and that our estimates of the mixing time are underestimated. Strong lateral chemical density anomalies are present in the lower part of the system (Fig. 7k). Thermal density anomalies are also present, but mostly concentrate below the surface (Fig. 7l). Compared to those obtained for moderate $R\mu_{660}$, these anomalies are smaller in amplitude, but they are maintained for longer periods of time. Globally, their power spectra fit RT246g well (Fig. 8, short and long dashed curves). However, the power spectra of chemical density anomalies slowly decrease with time and, in the long term, disagree with RT246g.

The convective pattern sensitivity to $R\mu_z$ is similar to that to $R\mu_{660}$, with some differences (Fig. 6c and d, open circles). For small (≤ 5) values of $R\mu_z$, the flow is dominated by fast, small-scale structures, which quickly mix dense and regular materials. For large (10^2 to 10^3) $R\mu_z$, thermo-chemical plumes progressively narrow with altitude, and anomalies of density at the bottom of the system are maintained for long period of time.

Increasing $R\mu_{660}$ (or $R\mu_z$) has two main effects. First, the dense layer gets more viscous, and thus more stable (Fig. 6a). Second, it favours the development of large-scale structures, as pointed out in previous studies (Bunge et al., 1996; Tackley, 1996). Furthermore, for large ($\geq 10^2$) values of $R\mu_{660}$, the transfer of dense material around 660 km depth is strongly attenuated, and density anomalies are maintained in the lower part of the system for moderate periods of time.

5.4. Temperature-dependent viscosity

Finally, we performed numerical experiments for thermal viscosity contrasts between 1 ($E_a = 0$) and 10^7 ($E_a = 16.118$). t_{onset}

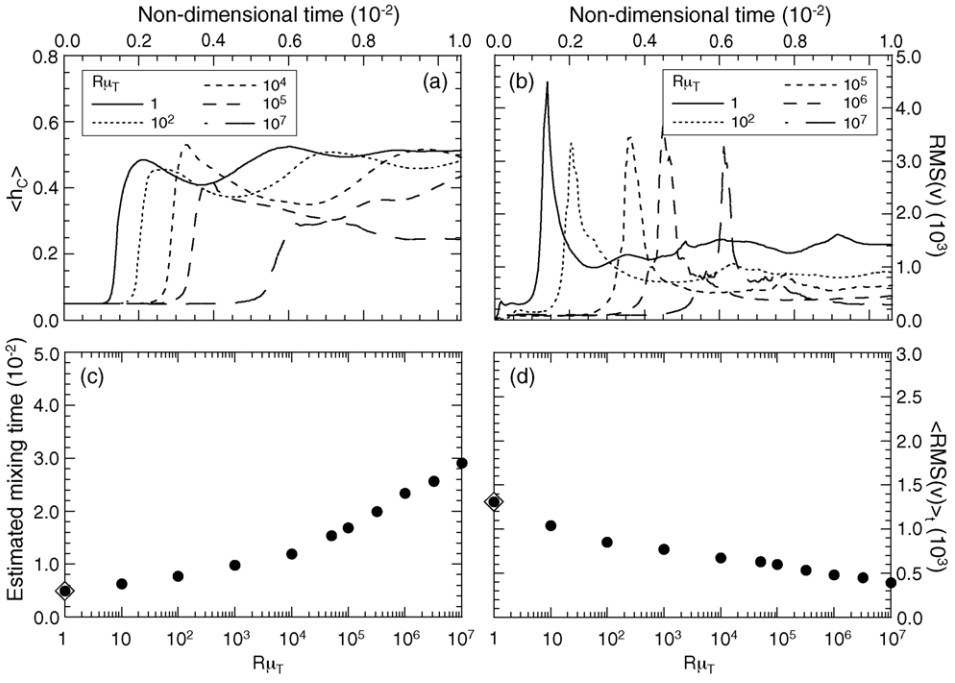

Fig. 9. Same as Fig. 3, but for various values of the thermal viscosity ratio, $R\mu_T$.

increases with $R\mu_T$ (Fig. 9a), but is smaller than the run duration in all cases. The flow pattern immediately after the onset of instability depends very little on $R\mu_T$. In all cases, we see large thermo-chemical plumes surrounded by downwelling sheets. The peak of RMS(v) that follows the onset of instability remains approximately constant with $R\mu_T$ (Fig. 9b).

In later stages, however, the flow patterns strongly differ, depending on $R\mu_T$. Furthermore, RMS(v) decreases with increasing $R\mu_T$. Overall, $\langle \mathrm{RMS}(v) \rangle_t$ drops by a factor 3 between $R\mu_T = 1$ and $R\mu_T = 10^7$ (Fig. 9d) (note that this decrease also account for the increase in t_{onset}). For $R\mu_T \leq 10^4$, dense material concentrates in narrow ridges and is rapidly entrained upwards. Convection is efficient enough to sweep out and mix the layer of dense material within the run duration (Fig. 9c). McNamara and Zhong (2004) observed similar patterns and evolutions in spherical geometry. For larger values of $R\mu_T$, on the contrary, pools of dense material are generated at the foot of hot thermal plumes and survive thermal convection during the entire run (Fig. 10, plots a–d). Note that we do not observe such pools for $R\mu_T \leq 10^4$, even temporarily. Again, the formation of pools severely inhibits the mixing of dense and regular materials, and the mixing times calculated by Eq. (9) are strongly underestimated. The presence of pools induces strong chemical density anomalies with wave number up to $k = 4.0$ throughout the lower half of the system (Fig. 10, plots e and h). Moderate thermal density anomalies are also present at the bottom of the system, but the largest thermal anomalies are found below the surface (Fig. 10, plots f and j).

Globally, the spherical harmonics power spectra of thermal and chemical density anomalies fit RT246g better as $R\mu_T$ increases (Fig. 11). In particular, for $R\mu_T \geq 10^5$ the power spectra of chemical density anomalies in the bottom and intermediate layers remain close to those of RT246g over long periods of times. Some important discrepancies remain in the layer 660–1200 km, where the power of chemical density anomalies for all spherical harmonic degrees strongly decrease after reaching a peak, and the power of thermal density anomalies for degree 4 remain too small at any time.

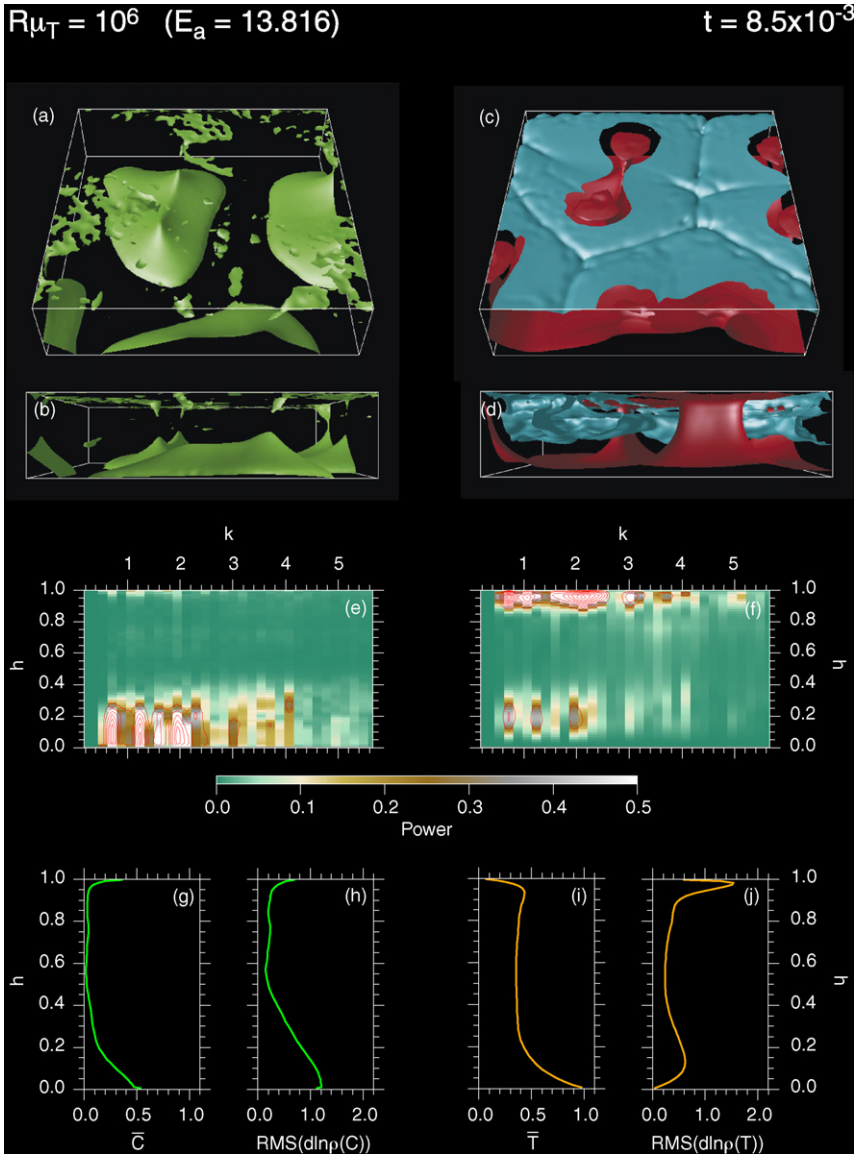

Fig. 10. Snapshot of the case $R\mu_T = 10^6$ at $t = 8.5 \times 10^{-3}$ (3.6 Gyr). Other parameters are as in the reference case. Plots description is similar to that in Fig. 2. In plots (c) and (d), contour levels for temperature isosurfaces are $T - \langle T \rangle = -0.25$ (blue) and $T - \langle T \rangle = 0.15$ (red). (For interpretation of the references to color in this figure legend, the reader is referred to the web version of the article.)

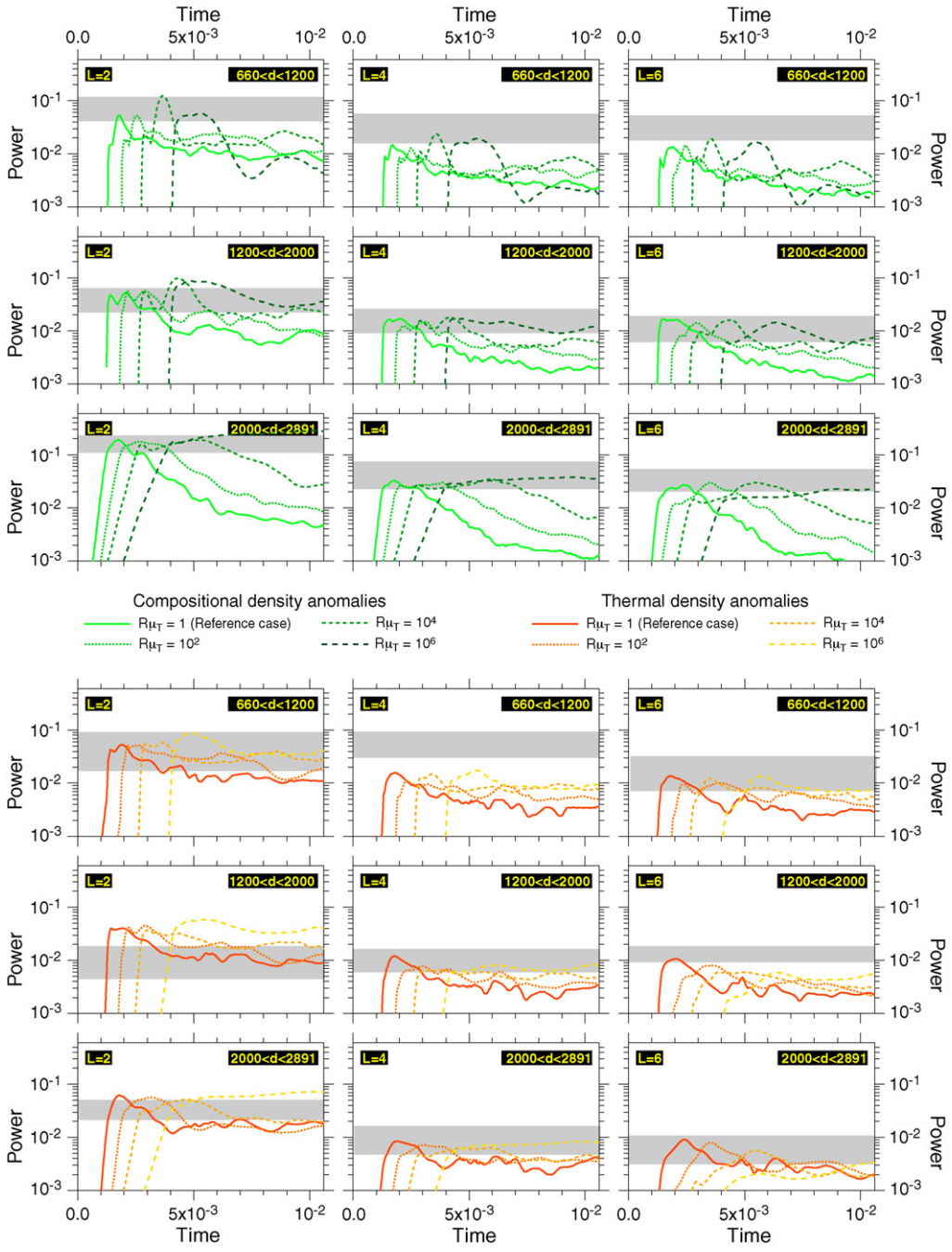

Fig. 11. Same as Fig. 5, but for various values of the thermal viscosity contrast, Rμ_T.

A well-known effect of temperature-dependent viscosity is to weaken the vigor and efficiency of convection, especially when a stagnant lid regime is reached, i.e., for high enough values of Rμ_T (Davaille and Jaupart, 1993; Moresi and Solomatov, 1995; Deschamps and Sotin, 2000). The critical Rayleigh number for the onset of instability increases with Rμ_T, and the heat and flow transfers are less efficient. We observe similar effects in this series of experiments, but because we prescribed a high enough Rayleigh number and included additional complexities that partly balance the thermal viscosity variations, the conditions for a stagnant lid were not reached. The decrease in the vigor and efficiency of convection is however strong enough to maintain pools of dense material at the bottom of the system for periods of time larger than the run duration.

6. Discussion and conclusions

Our goal was to start an extensive exploration of the model space of thermo-chemical convection, and identify models that explain seismic observations well, an important constraint being the presence of large density anomalies in the deep mantle (Ishii and Tromp, 1999; Resovsky and Trampert, 2003; Trampert et al., 2004). For this, we varied the parameters of the viscosity law (other important parameters are explored in a companion paper), and studied their influence on the flow pattern and on the mixing of dense and regular materials. Our approach has however some disadvantages. Linear stability analysis is a powerful tool to analytically describe the results of experiments, but it usually considers two or three parameters at a time. Because we considered too many parameters,

we did not attempt to perform such analysis. For similar reasons, we also did not build any scaling laws.

One may point out that the initial condition that consists in imposing a layer of dense material at the bottom of the system, is somewhat *ad hoc*. Several mechanisms, however, could explain the presence of reservoirs of dense material at the bottom of the mantle, including interactions between the liquid iron of the outer core and the silicates of the lowermost mantle (Knittle and Jeanloz, 1991), and the early differentiation of a magma ocean (Agee and Walker, 1988). Recently, Labrosse et al. (2007) showed that the crystallization of a magma ocean at the base of the mantle (resulting from the sinking of iron-rich droplets) would also result in a reservoir of dense, iron-rich material buried at the bottom of the mantle. Furthermore, this model is consistent with geochemical differences observed between chondrites and mantle rocks (Boyet and Carlson, 2006), and it explains the ultra-low seismic velocities zones (ULVZs) observed locally at the bottom of the mantle (Williams and Garnero, 1996). Another attractive scenario is the recycling of a primitive crust. Recent Sm–Nd data (Caro et al., 2003, 2005) clearly indicate that the oldest crustal rocks observed today were formed from an already depleted mantle, with an age of differentiation around 4.46 Gyr. Further geochemical constraints suggest that the complementary, enriched reservoir crystallized from a magma ocean (Caro et al., 2005) to form an early crust that has then subducted and currently reside in the deep mantle (Boyet and Carlson, 2006). This scenario is supported by recent numerical models of thermo-chemical convection (van Thienen et al., 2004, 2005), which showed that under certain conditions, a primitive crust would delaminate and sink to the bottom of the mantle within about 0.5 Gyr. Earlier models (e.g., Christensen and Hofmann, 1994) also showed that a significant amount of delaminated crust piles up in the deep mantle.

Assuming that a layer of dense material formed early in the Earth's history, a crucial question is to figure out whether this reservoir could survive (at least partially) thermal convection over time intervals comparable to the age of the Earth. Many studies focused on the role of the buoyancy ratio (Davaille, 1999; Tackley, 2002; Samuel and Farnetani, 2003; Zhong and Hager, 2003; van Thienen et al., 2005; Jaupart et al., 2007), which is undoubtedly a major controlling parameter. For values of B larger than a critical value, which varies from one study to another because of differences in the experimental setups and model ingredients, the layer of dense material remains stable over 4.5 Gyr and more. We reach similar conclusions in our companion paper. However, the complete survival a thick ($\delta_{DL} = 0.1D$, and more), stable layer is not desirable, because it does not fit seismic observations (Deschamps et al., 2007; this study). On the contrary, disconnected pools or a layer with strong topography explain seismic tomography better. The 2D-Cartesian model of van Thienen et al. (2005) maintains a layer with strong (up to 10^3 km) topography. 3D-Cartesian models, however, do not predict dense layer with strong topography. For $0.25 \leq B \leq 0.35$ (and $X = 10\%$) the observed patterns are connected ridges of dense material with moderate topography (Tackley, 2002) that does not explain RT246g well (Deschamps et al., 2007), and for $B \geq 0.4$ the layer of dense material fully covers the bottom of the box but has small topography.

As discussed above, it is not unreasonable to impose a basal layer of dense material as initial condition. A more realistic modeling, however, should also include sources and sinks of dense material. This might be achieved by using three types of particles (representing the pyrolitic, MORB, and harzburgitic compositions, respectively) rather than two, and by segregating the material at the top of the system into crustal and residual materials. This more complex modeling may allow part of the dense material entrained upwards to be trapped in the crust, and new MORB material to be recycled in the deep mantle, where it would feed reservoirs of dense material and contribute to their survival.

Cold downwellings are present in our models, but we did not specifically account for the effect of slabs on the stability of the initial layer of dense material and on the distribution of density anomalies. Slab avalanches impacting either a layer or pools of dense material are likely to deflect and destabilize these structures, which may induce strong topography (Kellogg et al., 1999). Furthermore, slabs penetrating in the lower mantle are likely to participate to the density anomalies (thermal and chemical) observed by seismic tomography. For instance, the strong discrepancies that remain between the observed (RT246g) and modeled power spectra of density anomalies in the layer 660–1200 km might be explained by slab stacking below the 660 km discontinuity and down to ~1000 km depth, as observed by regional tomography (Fukao et al., 2001).

Spherical geometry is likely to have a strong effect on the flow pattern. Compared to the 3D-Cartesian case, the stability of the bottom thermal boundary layer is increased, and the ingredients that stabilize the dense layer (large compositional viscosity ratio, large buoyancy ratio) might have more pronounced effects in spherical geometry. Note that the comparison of our 3D-Cartesian models with global seismic tomography models (which are spherically distributed) does not generate additional discrepancies because we converted Fourier spectra into spherical harmonic spectra assuming that the power per surface unit is the same in both expansion (Chevrot et al., 1998).

Due to the simplifications discussed above, the models presented in this study are still far from an accurate description of convection in the real Earth. Our approach, however, allowed identification of possible ingredients for a successful (in the sense that it fits seismic observations well) model of thermo-chemical convection. From this point of view, it is essential for a successful model to maintain pools or layer of dense material with a strong topography in the deep mantle. Too small values of $R\mu_c$ induce fast mixing between dense and regular materials, whereas too large values of $R\mu_c$ induce long-term stability of the dense layer. None of these cases is compatible with seismic observations. A moderate compositional viscosity contrast (typically, between 0.1 and 10) maintain strong density anomalies that fit well RT246g for a long period of time. Possible candidate for the dense material include Fe-rich perovskite and post-perovskite. To date, however, there are no estimates concerning the viscosity of these phases. A large ($\geq 10^2$) viscosity contrast at $d = 660$ km inhibits the mass transfer around this depth, and maintain strong lateral chemical density anomalies over moderate (~1.5 Gyr) time intervals. However, the distributions of these anomalies do not fit RT246g in the long term. The range of value usually assumed for the 660 km viscosity jump (around 10–30) is thus acceptable, provided that other ingredients maintain strong density anomalies in the deep mantle. Large thermal viscosity contrast maintain pools of dense material at the bottom of mantle and significant density anomalies elsewhere in the lower mantle for long periods of time. Again, the distribution of these anomalies fit well those observed by RT246g. It is usually accepted that the mantle viscosity strongly depends on temperature, but this ingredient is sometimes omitted because it induces a stagnant lid at the top of the system. In our case, however, the high Rayleigh number and the additional complexities included in our calculations prevent the development of a stagnant lid at the top of the system.

The main criteria we used to decide the validity of a convection model is its agreement with seismic tomography. It is important to test whether these models also fit other available constraints, in particular the upper mantle geotherm and the surface heat flow (Pollack et al., 1993). Table 2 lists the mean upper mantle potential temperature (T_{UM}) and surface heat flow (Φ_{surf}) averaged over the

Table 2
Predicted upper mantle temperature and surface heat flow for selected cases[a]

Case	T_{UM} (K)[b]	Φ_{surf} (mW/m^2)[c]
Reference case	970	77.5
$R\mu_c = 1.0$	920	77.3
$R\mu_c = 10$	820	52.6
$R\mu_c = 10^2$	760	43.4
$R\mu_{660} = 3.0$	1140	100.0
$R\mu_{660} = 3.0 \times 10^2$	840	61.0
$R\mu_T = 10^2$	1140	73.0
$R\mu_T = 10^4$	1280	69.7
$R\mu_T = 10^6$	1280	46.5

[a] Average values over the last Gyr of the run. Possible values for the Earth upper mantle temperature are in the range 1200–1400 K. Surface heat flow strongly varies with location. The compilation of Pollack et al. (1993) proposes a global value around 87 mW/m^2, with oceanic and continental values around 101 mW/m^2 and 65 mW/m^2, respectively.

[b] The upper mantle potential temperature is averaged in the layer $200 \le d \le 660$ km ($0.07 \le z \le 0.228$), and scaled with a superadiabatic temperature difference $\Delta T_S = 2500$ K and a surface temperature $T_{surf} = 300$ K. The real temperature can be estimated by assuming that the adiabatic gradient in this layer is 0.4 K/km, i.e., by adding an adiabatic contribution of about 100 K.

[c] Surface heat flow includes a contribution from the adiabatic gradient of temperature. In the reference state we used (Tackley, 1996; Tackley, 1998b), the adiabatic gradient below the surface gradient is about 0.8 K/km. Taking $k_S = 3.0$ W/(m K), the adiabatic contribution to the surface heat flow is thus 2.4 mW/m^2.

last Gyr of each run for selected cases. The reference case explains well the observed surface heat flow, but has a too low temperature. Both T_{UM} and Φ_{surf} decrease with increasing compositional viscosity contrast, and for $R\mu_c \ge 5$ Φ_{surf} is too low. Increasing the 660 km viscosity contrast has similar effect, but the surface heat flow remains comparable to the observed continental value even for large (3.0×10^2) values of $R\mu_{660}$. With increasing thermal viscosity contrast the upper mantle temperature increases to reasonable values, but in the meantime heat flow decreases and its value for $R\mu_T = 10^6$ is too low. Comparisons with heat flow should however be taken with care because published values (including the compilation by Pollack et al., 1993) are usually not corrected for the crustal heat production, and may thus overestimate the mantle heat flux. In provinces where the crust is thick (e.g., beneath cratons) the crustal contribution to the surface heat flow is likely large, and in some locations the mantle heat flux may not be higher than 15–20 mW/m^2 (Jaupart and Mareschal, 2007).

We did not run models that simultaneously include high thermal and moderate compositional viscosity contrasts. The combination of these two parameters is likely to induce and maintain strong chemical heterogeneities in the deep mantle. McNamara and Zhong (2004) conducted numerical experiments in spherical geometry with thermal and compositional viscosity contrasts equal to 10^3 and 10^2, respectively, and observed large oscillating plumes of dense material similar to those reported by Davaille (1999). This pattern induces strong topography and might thus explain seismic tomography well.

Finally, more parameters need to be explored. The phase change at $d = 660$ km is endothermic, and for large enough absolute values of its Clapeyron slope, is likely to inhibit the mass transfer, which would help maintaining strong heterogeneities in the lower mantle. Spherical geometry is certainly an important parameter, because it modifies the stability of the hot and cold thermal boundary layers. Finally, the phase transition to post-perovskite, which is not included in the present study, is also likely to influence the flow pattern (Nakagawa and Tackley, 2005), create structures such as double-crossings (Hernlund et al., 2005), and predict specific seismic velocity distributions (Nakagawa and Tackley, 2006). The strong Clapeyron slope of this phase transition implies that cold material transforms at shallower depths, which might explain the correlation between cold and chemically dense material observed by RT246g (Trampert et al., 2004; Deschamps et al., 2007). In addition, there are indications that the Fe–perovskite transforms to post-perovskite at shallower depths than Mg–perovskite (Ono and Oganov, 2005). Thus, the dense, cold, material observed by RT246g could correspond to pools of Fe-rich post-perovskite resulting, for instance, from the recycling of an early crust.

Acknowledgments

We are grateful to Pieter van Thienen and an anonymous colleague for their constructive reviews that helped to clarify some parts of this paper.

Appendix A. Supplementary data

Supplementary data associated with this article can be found, in the online version, at doi:10.1016/j.pepi.2008.04.016.

References

Agee, C.B., Walker, D., 1988. Mass balance and phase density constraints on early differentiation of chondritic mantle. Earth Planet. Sci. Lett. 90, 144–146.
Boyet, M., Carlson, R.W., 2006. ^{142}Nd evidence for early (>4.53 Ga) global differentiation of the silicate Earth. Science 309, 576–581.
Bunge, H.-P., Richards, M.A., Baumgardner, J.R., 1996. Effects of depth-dependent viscosity on the planform of mantle convection. Nature 379, 436–438.
Caro, G., Bourdon, B., Birck, J.-L., Moorbath, S., 2003. ^{146}Sm–^{142}Nd evidence from Isua metamorphosed sediments for early differentiation of the Earth's mantle. Nature 423, 428–432.
Caro, G., Bourdon, B., Wood, B.J., Corgne, A., 2005. Trace-element fractionation in Hadean mantle generated by melt segregation from a magma ocean. Nature 436, 246–249.
Chevrot, S., Montagner, J.-P., Snieder, R., 1998. The spectrum of tomographic Earth models. Geophys. J. Int. 133, 783–788.
Christensen, U.R., 1984. Heat transport by variable viscosity convection and implications for the Earth's thermal evolution. Phys. Earth Planet. Inter. 35, 264–282.
Christensen, U.R., Hofmann, A., 1994. Segregation of subducted oceanic crust in the convecting mantle. J. Geophys. Res. 99, 19867–19884.
Coltice, N., 2005. The role of convective mixing in degassing the Earth's mantle. Earth Planet. Sci. Lett. 234, 15–25.
Davaille, 1999. Simultaneous generation of hotspots and superswells by convection in a heterogeneous planetary mantle. Nature 402, 756–760.
Davaille, A., Jaupart, C., 1993. Transient high-Rayleigh number thermal convection with large viscosity variations. J. Fluid Mech. 253, 141–166.
Davies, G.F., 2002. Stirring geochemistry in mantle convection models with stiff plates and slabs. Geochem. Cosmochem. Acta 66, 3125–3142.
Deschamps, F., Sotin, C., 2000. Inversion of two-dimensional numerical experiments for a fluid with strongly temperature-dependent viscosity. Geophys. J. Int. 143, 204–218.
Deschamps, F., Sotin, C., 2001. Thermal convection in the outer shell of large icy satellites. J. Geophys. Res. 106, 5107–5121.
Deschamps, F., Trampert, J., 2003. Mantle tomography and its relation to temperature and composition. Phys. Earth Planet. Inter. 140, 277–291.
Deschamps, F., Trampert, J., Tackley, P.J., 2007. Thermo-chemical structure of the lower mantle: seismological evidence and consequences for geodynamics. In: Yuen, D.A., et al. (Eds.), Superplumes: Beyond Plate Tectonics. Springer, pp. 293–320.
Deschamps, F., Tackley, P.J., submitted for publication. Exploring the model space of thermo-chemical convection. II. Physical and compositional parameters. Phys. Earth Planet. Inter.
Ferrachat, S., Ricard, Y., 2001. Mixing properties in the Earth's mantle: effects of the viscosity stratification and oceanic crust segregation. Geochem. Geophys. Geosys. 2, doi:10.1029/2000GC000092.
Forte, A.M., Mitrovica, J.X., 1996. New inferences of mantle viscosity from joint inversion of long-wavelength mantle convection and post-glacial rebound data. Geophys. Res. Lett. 23, 1147–1150.
Forte, A.M., Mitrovica, J.X., 2001. Deep-mantle high-viscosity flow and thermochemical structure inferred from seismic and geodynamic data. Nature 410, 1049–1056.
Fukao, Y., Widiyantoro, S., Obayashi, M., 2001. Stagnant slabs in the upper and lower transition regions. Rev. Geophys. 39, 291–323.
Hager, B.H., Richards, M.A., 1989. Long-wavelength variations in Earth's geoid: physical models and dynamical implications. Phil. Trans. Roy. Soc. Lond. A 328, 309–327.
Hernlund, J., Thomas, C., Tackley, P.J., 2005. A doubling of the post-perovskite phase boundary and structure of the Earth's lower mantle. Nature 434, 882–886.

Howard, L.N., 1966. Convection at high Rayleigh number. In: Gortlet, H. (Ed.), Proceedings of the Eleventh International Congress of Applied Mathematics. Springer-Verlag, New York, pp. 1109–1115.
Ishii, M., Tromp, J., 1999. Normal-mode and free-air gravity constraints on lateral variations in velocity and density of Earth's mantle. Science 285, 1231–1236.
Jaupart, C., Mareschal, J.-C., 2007. Heat flow and thermal structure of the lithosphere. In: Schubert, G., et, al. (Eds.), Treatise on Geophysics, vol. 3: Crust and Lithosphere Dynamics. Elsevier, pp. 218–251.
Jaupart, C., Molnar, P., Cottrell, E., 2007. Instability of a chemically dense layer heated from below and overlain by a deep less viscous fluid. J. Fluid Mech. 572, 433–469.
Jellinek, A.M., Manga, M., 2002. The influence of a chemical boundary layer on the fixity, spacing and lifetime of mantle plumes. Nature 418, 760–763.
Karato, S.-I., Wu, P., 1993. The rheology of the upper mantle: a synthesis. Science 260, 771–778.
Karato, S.-I., Karki, B.B., 2001. Origin of lateral variation of seismic wave velocity and density in the deep mantle. J. Geophys. Res. 106, 21771–21783.
Kellogg, L.H., Hager, B.H., van der Hilst, R.D., 1999. Compositional stratification in the deep mantle. Science 283, 1881–1884.
Knittle, E., Jeanloz, R., 1991. Earth's core–mantle boundary: results of experiments at high pressures and temperatures. Science 251, 1438–1443.
Labrosse, S., Hernlund, J.W., Coltice, N., 2007. A crystallizing dense magma ocean at the base of the Earth's mantle. Nature 450, 866–869.
LeBars, M., Davaille, A., 2002. Stability of thermal convection in two superimposed miscible viscous fluids. J. Fluid Mech. 471, 339–363.
McKenzie, D.P., Roberts, J.M., Weiss, N.O., 1974. Convection in the Earth's mantle: towards a numerical simulation. J. Fluid Mech. 62, 465–538.
McNamara, A.K., Zhong, S., 2004. Thermochemical structures within a spherical mantle. J. Geophys. Res. 109, doi:10.1029/2003JB002847.
Moore, D.R., Weiss, N.O., 1973. Two-dimensional Rayleigh–Bénard convection. J. Fluid Mech. 58, 289–312.
Moresi, L.-N., Solomatov, V.S., 1995. Numerical investigation of 2D convection with extremely large viscosity variations. Phys. Fluids 7, 2154–2162.
Nakada, M., Lambeck, K., 1989. Late pleistocene and holocene sea-level change in the Australian region and mantle rheology. Geophys. J. Int. 96, 497–517.
Nakagawa, T., Tackley, P.J., 2005. The interaction between the post-perovskite phase change and a thermo-chemical boundary layer near the core–mantle boundary. Earth Planet. Sci. Lett. 238, 204–216.
Nakagawa, T., Tackley, P.J., 2006. Three-dimensional structures and dynamics in the deep mantle: effects of post-perovskite phase change and deep mantle layering. Geophys. Res. Lett. 33, doi:10.1029/2006GL025719.
Ogawa, M., Schubert, G., Zebib, A., 1991. Numerical simulations of three-dimensional thermal convection in a fluid with strongly temperature-dependent viscosity. J. Fluid Mech. 233, 299–328.
Olson, P., Yuen, D.A., Balsiger, D., 1984. Mixing of passive heterogeneities by mantle convection. J. Geophys. Res. 89, 425–436.
Olson, P., Kincaid, C., 1991. Experiment on the interaction of thermal convection and compositional layering at the base of the mantle. J. Geophys. Res. 96, 4347–4354.
Ono, S., Oganov, A.R., 2005. In situ observations of phase transition between perovskite and $CaIrO_3$-type phase in $MgSiO_3$ and pyrolitic mantle composition. Earth Planet. Sci. Lett. 236, 914–932.
Pollack, H.N., Hurter, S.J., Johnson, J.R., 1993. Heat flow from the earth interior: analysis of global data set. Rev. Geophys. 31, 267–280.
Resovsky, J., Trampert, J., 2003. Using probabilistic seismic tomography to test mantle velocity–density relationships. Earth Planet. Sci. Lett. 215, 121–134.
Saltzer, R.L., van der Hilst, R.D., Kárason, H., 2001. Comparing P and S wave heterogeneity in the mantle. Geophys. Res. Lett. 28, 1335–1338.
Samuel, H., Farnetani, C., 2003. Thermochemical convection and helium concentrations in mantle plumes. Earth Planet. Sci. Lett. 207, 39–56.
Smolarkiewicz, P.K., 1984. A fully multidimensional positive definite advection transport algorithm with small implicit diffusion. J. Comput. Phys. 54, 325–362.
Solomatov, V.S., Moresi, L.-N., 1996. Stagnant lid convection on Venus. J. Geophys. Res. 101, 4737–4753.
Stüben, K., Trottenberg, U., 1982. Multigrids methods: fundamental algorithms, model problem analysis and applications. In: Hackbusch, W., Trottenberg, U. (Eds.), Multigrids Methods. Springer-Verlag, pp. 1–175.
Tackley, P.J., 1996. On the ability of phase transitions and viscosity layering to induce long wavelength heterogeneity in the mantle. Geophys. Res. Lett. 23, 1985–1988.
Tackley, P.J., 1998a. Self-consistent generation of tectonic plates in three-dimensional mantle convection. Earth Planet. Sci. Lett. 157, 9–22.
Tackley, P.J., 1998b. Three-dimensional simulations of mantle convection with a thermo-chemical CMB boundary layer: D? In: Gurnis, M., et al. (Eds.), The Core–Mantle Boundary Region, Geodynamical Ser. 28. American Geophysical Union, Washington, DC, pp. 231–253.
Tackley, P.J., 2002. Strong heterogeneity caused by deep mantle layering. Geochem. Geophys. Geosys. 3, doi:10.1029/2001GC000167.
Tackley, P.J., King, S.D., 2003. Testing the tracer ratio method for modeling active compositional fields in mantle convection simulations. Geochem. Geophys. Geosys. 4, doi:10.1029/2001GC000214.
Tackley, P.J., Stevenson, D.J., Glatzmaier, G.A., Schubert, G., 1994. Effects of multiple phase transitions in a three dimensional spherical model of convection in the Earth's mantle. J. Geophys. Res. 99, 15877–15901.
Trampert, J., van der Hilst, R.D., 2005. Towards a quantitative interpretation of global seismic tomography. In: van der Hilst, R.D., et al. (Eds.), Earth's Deep Mantle: Structure, Evolution and Composition, Geophysical Monograph Ser. 160. American Geophysical Union, Washington, DC, pp. 47–62.
Trampert, J., Deschamps, F., Resovsky, J.S., Yuen, D.A., 2004. Probabilistic tomography maps significant chemical heterogeneities in the lower mantle. Science 306, 853–856.
van Thienen, P., van den Berg, J.A.P., Vlaar, N.J., 2004. Production and recycling of oceanic crust in the early Earth. Tectonophysics 386, 41–65.
van Thienen, P., van Summeren, J., van der Hilst, R.D., van den Berg, A.P., Vlaar, N.J., 2005. Numerical study of the origin and stability of chemically distinct reservoirs deep in Earth's mantle. In: van der Hilst, R.D., et al. (Eds.), Earth's Deep Mantle: Structure, Evolution and Composition, Geophysical Monograph Ser. 160. American Geophysical Union, Washington, DC, pp. 117–136.
Weertman, J., 1970. The creep strength of the Earth's mantle. Rev. Geophys. Space Phys. 8, 145–168.
Whitehead, J.A., Luther, D.S., 1975. Dynamics of laboratory diapirs and plume models. J. Geophys. Res. 80, 705–717.
Williams, Q., Garnero, E.J., 1996. Seismic evidence for partial melt at the base of the Earth's mantle. Science 273, 1528–1530.
Zhong, S., Hager, B.H., 2003. Entrainment of a dense layer by thermal plumes. Geophys. J. Int. 154, 666–676.

Searching for models of thermo-chemical convection that explain probabilistic tomography II. Influence of physical and compositional parameters

Frédéric Deschamps and Paul J. Tackley

Institute of Geophysics, Swiss Federal Institute of Technology Zurich, HPP L8.1, 8093 Zurich, Switzerland. Email: frederic.deschamps@erdw.ethz.ch

Submitted to *Physics of the Earth and Planetary interiors*, April 2008

Abstract. We continue the exploration of the model space of thermo-chemical convection that we started in a previous study (Deschamps and Tackley, *in press*). In this second part, we study the influence of the Rayleigh number, the internal heating, the Clapeyron slope of the 660-km transition, the chemical density contrast between dense and regular materials (buoyancy ratio), and the volume fraction of dense material. We apply the same analysis and test the chemical and thermal density distributions predicted by various thermo-chemical models against those predicted by probabilistic tomography. Varying the reference Rayleigh number within a reasonable range of values for the Earth's mantle, we find significant differences in the flow pattern and efficiency of mixing. A Rayleigh number equal to one third only of the standard value (10^8) helps to maintain compositional anomalies throughout the system during a long period of time. The internal heating has no or very little influence on the flow pattern and the efficiency of mixing. An endothermic phase transition with a (non-) dimensional Clapeyron slope lower than –1.0 MPa/K (-4.0×10^{-2}) strongly inhibits the mass exchange and thus the efficiency of mixing. It provides a convenient way to maintain strong compositional anomalies in the lower mantle during a long period of time. The stability of the layer of dense material is mainly controlled by the buoyancy ratio, and the influence of the volume fraction of dense material is only of second order. These experiments, together with those performed in our previous study, suggest that five ingredients may enter a successful thermo-chemical model of convection for the Earth's mantle: (1) a buoyancy ratio between 0.15 and 0.25, which is equivalent to a chemical density contrast in the range 60-100 kg/m^3; (2) A moderate chemical viscosity contrast, typically in the range 0.1-10. (3) A large ($\geq 10^4$), thermal viscosity contrast, which creates and maintains pools of dense material at the bottom of the mantle. (4) a viscosity contrast at d = 660 km around 30; (5) and a Clapeyron slope of the phase transition at d = 660 km of about –3.0 to –1.5 MPa/K. Interestingly, additional, independent geophysical constraints support these conclusions.

1. Introduction

Because the Earth's mantle includes numerous complexities and uncertain parameters, the model space of mantle convection is huge. Comparisons against observational constraints (mainly from seismology, mineral physics, and geochemistry), reduce the size of the space of possible models, but so far no consensus could be reached on a successful model. Recently, a number of studies pointed out that seismological observations are not fully explained by temperature variations alone (Karato and Karki, 2001; Saltzer et al., 2001; Deschamps and Trampert, 2003; Trampert et al., 2004). The strong density variations observed in the lower mantle (Ishii and Tromp, 1999; Trampert et al., 2004) might be partly compositional in origin. A successful model of mantle convection (in the sense that it fits seismological observations) must therefore predict strong lateral variations of composition in the lower mantle, and maintain them over long periods of time. In a companion paper (Deschamps and Tackley,

in press), we started an extensive search in the model space of thermo-chemical convection to identify ingredients that are needed to maintain compositional anomalies in the lower mantle, and found that a moderate compositional viscosity ratio and a strongly temperature dependent viscosity are two of these ingredients. In the present paper, we continue this search and explore the influence of physical (Rayleigh number, internal heating, 660-km phase transition) and compositional (buoyancy ratio and fraction of dense material) parameters.

The Rayleigh number, *Ra*, controls the vigor of convection. When complexities like variable viscosity and depth-dependent thermal expansion are accounted for, the definition of the Rayleigh number is not trivial. One usually defines a reference Rayleigh number, Ra_S, using reference values (e.g., surface values) of the parameters. Of course, one expects the mixing between dense and regular materials to be more efficient with increasing Ra_S. Because of uncertainties in mantle properties (mainly its viscosity), however, possible values for the Rayleigh number of the Earth's mantle may vary within one order of magnitude, and it is important to quantify this effect.

In the case of purely thermal convection with mixed heating, increase in the amount of internal heating, H_c, is known to reduce the strength of the bottom thermal boundary layer (e.g., Travis and Olson, 1994; Sotin and Labrosse, 1999; McNamara and Zhong, 2005). Thermal plumes are less vigorous, and if internal heating is large enough they do not reach the top of the system. It is important to check whether similar effects are also observed in thermo-chemical convection.

The 660-km discontinuity is associated with the transformation of ringwoodite into perovskite and magnesio-wüstite, which has a negative Clapeyron slope. The effect of an endothermic phase transition on thermal convection has been extensively studied in various geometries (e.g., Christensen and Yuen, 1985; Machetel and Weber, 1991; Tackley et al., 1993, 1994; Solheim and Peltier, 1994; Yuen et al., 1994). An endothermic phase change strongly modifies the flow pattern, the main change being the reduction of mass exchange between the upper and lower mantle. There are however significant differences between the patterns observed by 2D- and 3D-simulations. The former predict intermittent layering with slab avalanches occurring from time to time. The later, on the contrary, predict that the flow is never completely layered, with slab avalanches occurring not necessarily at the same location, but at any time.

The two important compositional parameters are the buoyancy ratio *B* (i.e., the chemical density contrast between dense and regular material relatively to the total thermal density contrast), and the volume fraction of dense material, *X*. The buoyancy ratio controls the amplitude of the deformation of the dense layer (e.g., Davaille, 1999; McNamara and Zhong, 2004; Jaupart et al., 2007). Variations in *B* lead to different patterns, from a stable layer (large *B*), to a fully unstable layer (small *B*). Linear stability analysis and analogical experiments (Jaupart et al., 2007) and numerical experiments with spherical geometry (McNamara and Zhong, 2004) suggest that the effects of the volume fraction are of second order compared to those of the buoyancy ratio.

Gathering the results from these new series of experiments and from our companion paper, we identify sensitive parameters and their possible values for the Earth's mantle. Interestingly, these values are consistent with additional, independent geophysical constraints.

2. Numerical modeling and results analysis

2.1 Numerical modeling

As in our companion paper, numerical experiments are performed with a 3D-Cartesian version of STAG3D (Tackley, 1998a, 2002). All runs are stopped at non-dimensional time t = 0.0106, which correspond to a dimensional time equal to 4.5 Gyr. The size of the box is 4×4×1, with 128 points in each horizontal direction, and 64 points in vertical direction (the grid spacing is vertically refined at the top and bottom of the system).

The system is heated both from the bottom and from within, and the internal heating rate is varied between 0 and 50, which is equivalent to dimensional heat flow between 0 and 130 mWm^{-2}. We accounted for the possibility that the MORB source region is depleted in radiogenic elements by increasing the heating rate of dense material by a factor 10 (RH_C = 10). The mantle heating rate is then adjusted to obtained the prescribed total heat production. Compressibility induces additional sources and sinks of heat that are controlled by the dissipation number, Di. This number depends on the thermal expansion and thus varies with depth. In all our calculations, the surface and volume average values of the dissipation number are Di_S = 1.2 and $<Di>$ = 0.43, respectively.

The conservative equations require definition of reference radial profiles for the density, the thermal expansion, and the temperature. These profiles are calculated using appropriate thermodynamic relationships (Tackley, 1996, 1998). Density and thermal expansion are scaled with respect to their surface value, and temperature with respect to the super-adiabatic temperature difference across the system ΔT_S (Table 1).

The viscosity depends on depth and composition, but not on temperature (except the combined case in section 5, for which $R\mu_T = 10^6$). Viscosity increases exponentially with depth by a factor $R\mu_z$ = 10, and an additional contrast of $R\mu_{660}$ = 30 is imposed at d = 660 km (z = 0.228). The dense material is less viscous than the regular material by two orders of magnitude ($R\mu_c = 10^{-2}$) (except, again, for the combined case, for which $R\mu_c$ = 0.5). Because thermal expansion and viscosity are not uniform, the definition of the Rayleigh number is non-unique. In the present study, we prescribed a reference Rayleigh number, Ra_S, using the reference (surface) values of viscosity, density, and thermal expansion (Table 1), and performed experiments for values of Ra_S in the range 10^6-10^9. This reference Rayleigh number does not vary with time. On the contrary, the effective Rayleigh number, measured in the well-mixed interior, is time-dependent. Note that because the viscosity increases with depth and the thermal expansion decreases with depth, this Rayleigh number is smaller than Ra_S.

Parameter	Symbol	Value	Units	Non-dimensional
Non-dimensional parameters				
Reference Rayleigh number	Ra_S			10^6-10^9
Buoyancy ratio	B			0.1-0.5
Volume fraction of dense material	X			0.05-0.30
Initial thickness of the dense layer	h_{DL}			0.05-0.30
Surface dissipation number	Di_S			1.2
Volume average dissipative number	Di			0.43
Total internal heating	H_C	0-130	mW m^{-2}	0-50
Compositional heating ratio	RH_C	10		
Physical & thermo-dynamical parameters (dimensional)				
Acceleration of gravity	g	9.81	m s^{-2}	1.0
Mantle thickness	D	2891	km	1.0
Super-adiabatic temperature difference	ΔT_S	2500	K	1.0
Reference adiabat	T_{as}	1600	K	0.64
Surface density	ρ_S	3300	kg m^{-3}	1.0
Density jump at z = 660 km	$\Delta\rho_{660}$	400	kg m^{-3}	0.1212
Surface thermal expansion	α_S	5.0×10^{-5}	K^{-1}	1.0
Surface thermal diffusivity	κ_S	6.24×10^{-7}	m^2 s^{-1}	1.0
Heat capacity	C_P	1200	J kg^{-1} K^{-1}	1.0
Surface conductivity	k_S	3.0	W m^{-1} K^{-1}	1.0
Surface Grüneisen parameter	γ_S	1.091		
Clapeyron slope at z = 660 km	Γ	-4.6 - 0.0	MPa K^{-1}	-1.2×10^{-1} - 0.0
Viscosity law				
Surface thermal viscosity	μ_S	1.6×10^{21}	Pa s	1.0
Viscosity ratio at z = 660 km	Rμ_{660}	30		
Compositional viscosity ratio	Rμ_c	10^{-2}		
Thermal viscosity ratio	Rμ_T	1		
Vertical viscosity ratio	Rμ_z	10		
Dimensional scallings				
Velocity	v	1.0	cm yr^{-1}	1468
Time	t	424	Gyr	1.0
Heat flux	Φ	2.6	mW m^{-2}	1.0
Internal heating rate	H	2.72×10^{-13}	W kg^{-1}	1.0

Table 1. Parameters and scallings

The compositional field is modeled with a collection of particle tracers (Tackley and King, 2003). We defined two types of particles, for dense and regular material, respectively, and used a total of 10 million particles in each experiment. The fraction of dense material, *X*, is controlled by prescribing the fraction of dense particles. We varied this parameter between 5 and 30 %. The compositional field is obtained by calculating the concentration *C* of dense particles in each cell. *C* varies between 0 for a cell filled with regular material only, and 1 for a cell filled with dense particle only. Dense particles

are initially concentrated at the bottom of the box in a layer of non-dimensional thickness h_{DL}. For geometrical reasons, h_{DL} is numerically equal to the volume fraction of dense material, X. The density difference between the dense and regular materials is controlled by the buoyancy ratio,

$$B \equiv \frac{\Delta\rho_c}{\alpha_S \rho_S \Delta T_S} \quad (1)$$

where α_S and ρ_S are the thermal expansion and density at zero pressure, and ΔT_S the superadiabatic temperature difference across the system. The chemical density contrast creates a negative buoyancy that opposes the positive buoyancy due to the thermal density contrast $\Delta\rho_T = \alpha_S \rho_S \Delta T_S$. We carried out experiments for buoyancy ratios between 0.1 and 0.5. Taking $\alpha_S = 5.0\times10^{-5}$ K^{-1}, $\rho_S = 3300$ kg m^{-3}, and $\Delta T_S = 2500$ K, the density contrast between dense and regular material thus varies between 41.3 and 206.3 kg m^{-3}.

The 660 km chemical change is modeled with a discontinuous phase transition that is controlled by defining a point on the phase boundary and a Clapeyron slope, Γ. We imposed $z = 660$ km and $T = 1900$ K as anchor point, and varied the Clapeyron slope between –3.2 and 0 MPa/K. The Clapeyron slope is scaled with

$$\Gamma_0 = \frac{\rho_S g D}{\Delta T_S} \quad (2)$$

where g is the gravity acceleration and D the mantle thickness. Taking $\rho_S = 3300$ kg m^{-3} and $\Delta T_S = 2500$ K, we have $\Gamma_0 = 38.2$ MPa K^{-1}. The density contrast at the phase transition is $\Delta\rho_{660} = 400$ kg m^{-3} and is scaled with the surface density. A measure of the strength of the phase transition is the phase buoyancy ratio P, i.e. the ratio of the buoyancy induced by the phase transition to the thermal buoyancy,

$$P = \frac{(\Gamma \Delta T_{pt} \Delta\rho_{pt})/\rho_{pt} g D}{\alpha_{pt} \rho_{pt} \Delta T_{pt}} = \frac{\Gamma \Delta\rho_{pt}}{\alpha_{pt}^2 \rho_{pt} g D} \quad , \quad (3)$$

where α_{pt}, ρ_{pt}, $\Delta\rho_{pt}$, and ΔT_{pt}, are the thermal expansion, density, density jump, and temperature difference at the phase transition. The thermodynamic reference model we used indicate that $\alpha_{660}/\alpha_S = 0.44$ and $\rho_{660}/\rho_S = 0.12$. Taking $\alpha_S = 5.0\times10^{-5}$ K^{-1}, $\rho_S = 3300$ kg m^{-3}, and $\Delta\rho_{660} = 400$ kg m^{-3}, the range of values of Clapeyron slope we explored leads to values of P between –0.04 and 0.

2.2 Results analysis

We focused our analysis on the mapping of thermal and chemical anomalies and their time evolution. These are of course closely related to the flow pattern. Our analysis is based on several observations.

First, model parameters influence the stability of the bottom layer of dense material. We estimated the time for the onset of instability of this layer (t_{onset}) from the average depth of dense material, $\langle h_C \rangle$,

which varies between $h_{DL}/2$ (numerically equal to $X/2$, where X is the volume fraction of dense material) for a stable layer, and ½ for a well-mixed system. A sharp increase of $<h_C>$ from its initial value $X/2$ clearly indicates that the dense layer became unstable.

We then estimated the mixing time from the evolution of the variance in the compositional field. More precisely, we calculated the time integral

$$E = \int_0^{t_{run}} \left[1 - \frac{var(t)}{var(t=0)} \right] dt \ , \qquad (4)$$

where $var(t)$ is the variance at time t, and t_{run} the run duration. We then compare this integral to the integral (in the same interval of time) of the function

$$f(\xi) = e_{max} x^2 \frac{\exp(\xi)}{[\exp(\xi) - 1]^2} \qquad \xi = (t_0/t)^{1.5}, \qquad (5)$$

where e_{max} is the statistical limit of $1\text{-}var(t)/var(t = 0)$, and t_0 the time at which $f(\xi)$ reaches 92% of its maximum value, e_{max}. We defined the mixing time t_{mix} as the value of t_0 that provides best fit to Eq. 4 best. This approach allows estimates of the mixing time even if mixing is not completed before t_{run}. In cases for which mixing is completed before t_{run}, the calculated mixing time agrees well with the observed time at which $e(t)$ reaches 92% of its statistical limit (Deschamps and Tackley, *in press*). However, when mixing is strongly inhibited, our approach poorly estimates the mixing time. Such cases include models with large (≥ 0.35) values of the buoyancy ratio, for which the dense layer remains stable, and models with large values of the 660-km transition Clapeyron slope, for which dense material is filtered at $d = 660$ km.

An alternative measure of mixing efficiency is the time average of the average depth of dense material, $\overline{< h_C >}$, which varies between ½ (the dense and regular material are well mixed during the entire run) and $h_{DL}/2$ (the layer of dense material remain stable during the entire run). It is convenient to define a non-dimensional version of this parameter from its upper and lower values,

$$\zeta = \frac{2\overline{< h_C >} - h_{DL}}{1 - h_{DL}} . \qquad (6)$$

The RMS of the flow velocity, RMS(v), and its time average, $< RMS(v)>_t$, provide good estimates of the amplitude of the flow velocity, and thus give indirect estimate of the mixing efficiency. Note that the bulk Lagrangian strain rate may also be used for similar purpose (Coltice, 2005). In most cases, the onset of instability is followed by a sharp increase in RMS(v), up to a maximum value that depends on the model parameters. RMS(v) then decreases again and oscillates around a constant value during the rest of the experiment.

At each time step, we calculate the lateral density anomalies due to lateral variations in temperature and composition. Thermal and chemical density anomalies are relative to radial density profiles

derived from the radial profiles of temperature and composition, respectively. First order properties of the thermo-chemical structure of the flow, e.g., the presence of a stable layer of dense material, or two-layered convection, can be deduced from the radial profiles of average composition and temperature and of the RMS of density anomalies. Spectral heterogeneity maps (SHM) of chemical and thermal density anomalies provide more detailed information on this structure. Furthermore, to test our models of thermo-chemical convection against seismic tomography, we converted the Fourier power spectra of the density anomalies into spherical harmonics power spectra following Chevrot et al. (1998). These comparisons also require radial averaging of the convection models according to the vertical parameterization of the tomographic model (in our case, RT246g (Trampert et al., 2004), which includes three layers in the lower mantle).

2.3 Reference case

For comparison, we defined a reference case with the following properties. The mantle non-dimensional heating rate is equal to 25 (equivalent to a dimensional heat flow of 65 mWm^{-2}), and the Rayleigh number is equal to 10^8. The buoyancy ratio and volume fraction of dense material are $B = 0.2$ and $X = 10$ %, respectively. The Clapeyron slope of the 660km-transition is set to zero. Note that the parameters of the viscosity law are the same for all the calculations shown in this paper, with values listed in Table 1.

After the onset of instability of the layer of dense material, at $t_{onset} \sim 0.9\times10^{-3}$ (0.4 Gyr), large thermo-chemical plumes rise from the dense layer and entrain dense material upwards. This 'piles' pattern explain probabilistic tomography well (Deschamps et al., 2007), but is short-lived, about $\delta t \sim 10^{-3}$ (0.4 Gyr) (Deschamps and Tackley, *in press*). The thermal plumes, on the contrary, remain present until the end of the run. Dense and regular material quickly mix, with an estimated mixing time $t_{mix} = 5.0\times10^{-3}$ (2.1 Gyr). As a result, the amplitude of the lateral variations of composition rapidly decreases with time. The reference case is thus unable to maintain lateral anomalies of composition over a long period of time.

3. Influence of physical parameters

3.1 Rayleigh number

We first explored the influence of the Rayleigh number, varying Ra_S between 10^6 and 10^9. due to the presence of dense material at the bottom of the system and to the decrease of the thermal expansion with depth, t_{onset} increases with decreasing Ra_S (Figure 1a). If the prescribed Ra_S is too small, the whole layer remains stable during the entire run. Of course, the critical Rayleigh number depends on the input parameters, mainly the parameters of the viscosity law. For values similar to those of the reference case, we found that the critical Rayleigh number is around 7.0×10^6. This value may sound a

bit large, but one may recall that the presence of dense material at the bottom of the system and the decrease of thermal expansion increase the stability of the system. Convection gets more vigorous with increasing Rayleigh number and unsurprisingly, the mixing between dense and regular material is more efficient (Figs. 1c and 1d). For instance, the values of the estimated mixing time, t_{mix}, and of The time average of the RMS of the velocities, $\langle RMS(v)\rangle_t$, for $Ra_S = 6.0\times10^8$ are smaller than those for $Ra_S = 10^8$ (reference case) by a factor 4 and 2, respectively. As in the reference case, the onset of instability is followed by the rise of thermo-chemical plumes. The duration of this episode decreases

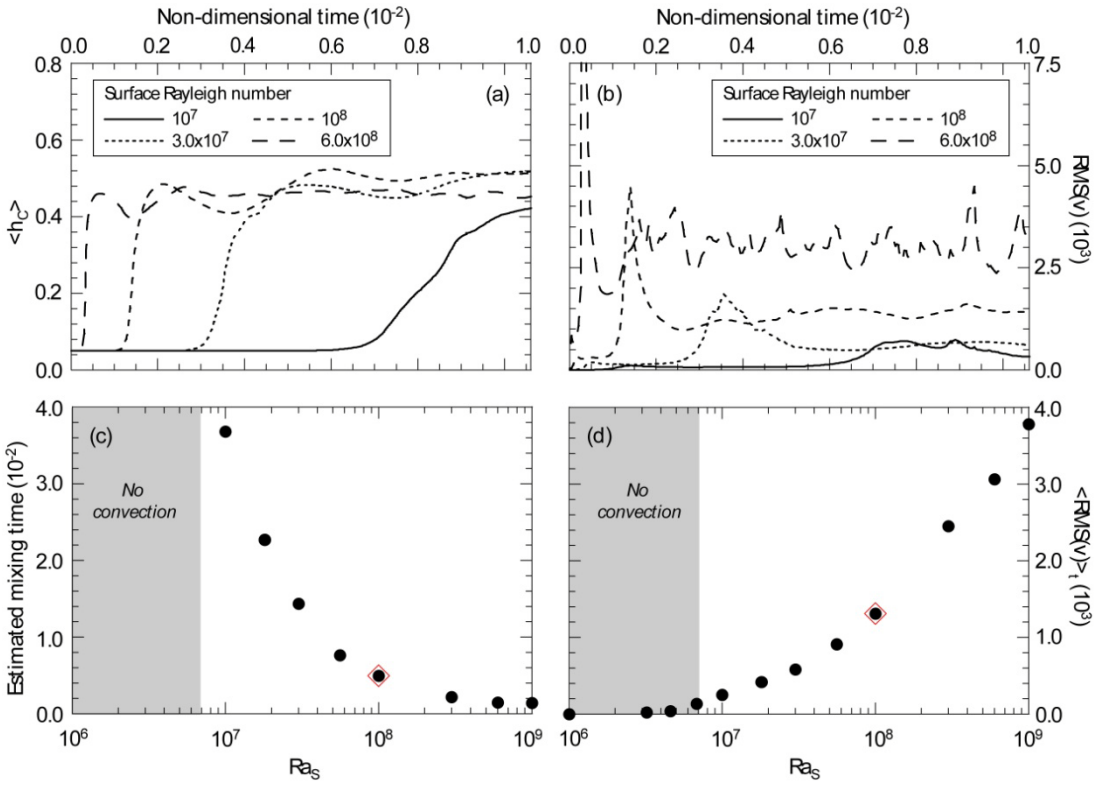

Figure 1. Influence of the reference Rayleigh number, Ra_S. (a) Average depth of dense material, $\langle h_C\rangle$, as a function of time and for various values of Ra_S. (b) RMS of the flow velocity as a function of time and for various values of Ra_S. (c) Estimated mixing time as a function of Ra_S. (d) Time average RMS of the flow velocity as a function of Ra_S. Note that for $Ra_S \leq 7.0\times10^6$, the whole system remain stable during the entire duration of the run. In plots (c) and (d), the reference case is indicated by the red diamond.

with increasing Ra_S. Lateral variations of composition at low Ra_S are maintained during longer periods of time than at high Ra_S, and the power spectra of these compositional anomalies decreases with time more smoothly (Figure 2).

A typical value of Ra_S for the Earth's mantle is 10^8. This value is derived from the data reported in Table 1, but due to uncertainties in some parameters (mainly, the uppermost mantle viscosity, thermal expansion and thermal diffusivity) it is reasonable to consider values of Ra_S between 3.0×10^7 and 3.0×10^8. The series of experiences presented in this section show that the efficiency of mixing significantly varies within this range of values. In particular, a value of Ra_S close to the lower bound (e.g., due to an upper mantle viscosity larger than the usual value by a factor 3) would help

maintaining compositional anomalies in the lower mantle for a long period of time, and explain probabilistic tomography better.

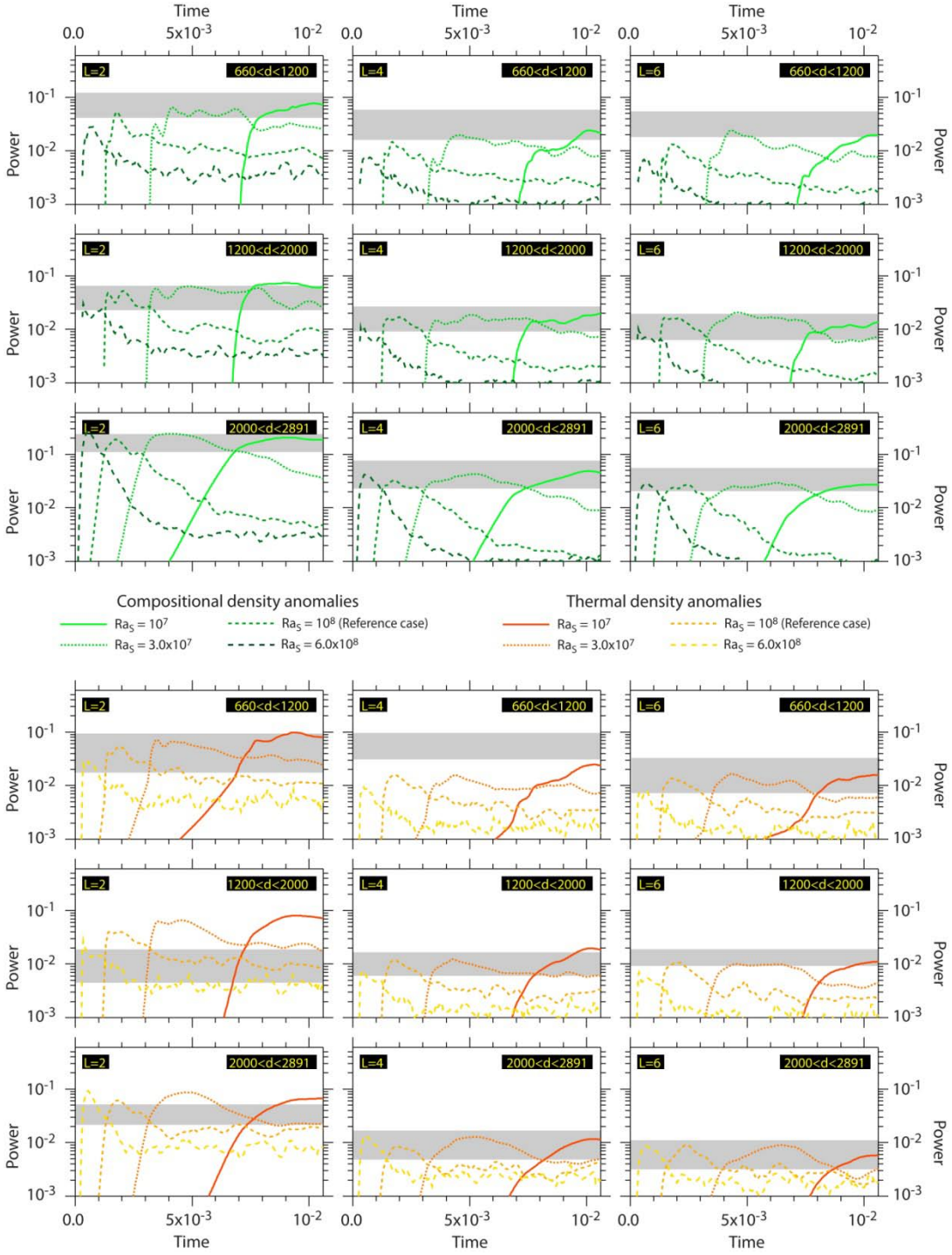

Figure 2. Power of chemical (three top rows) and thermal (three bottom rows) density anomalies as a function of time and for various values of the reference Rayleigh number, Ra_S. Anomalies are averaged within three layers ($660 \leq d \leq 1200$ km, $1200 \leq d \leq 2000$ km, and $2000 \leq d \leq 2891$ km), and we considered three spherical harmonics ($L = 2$, $L = 4$, and $L = 6$). Gray bands indicate the power spectrum predicted by RT246g within twice its standard deviation.

3.2 Internal heating

We have then varied the amount of internal heating between 0 and 50 (equivalent to a heat flux of 130 mW/m^2), but did not find substantial differences depending on this parameter. For all the values of H_c we explored, the flow pattern and its time evolution are similar, with large thermo-chemical plumes generating early in the run history (see reference case). $<RMS(v)>_t$,is nearly constant with H_c (Figure 3, open dots). Variations in t_{mix} with H_c are very small (Figure 3, black dots), and mixing is efficient in all cases. We conducted additional experiments for buoyancy ratios B = 0.1 and B = 0.4 and three values of the internal heating (0, 25, and 50), and found that the variations in t_{mix} and $<RMS(v)>_t$ with H_c are still very small.

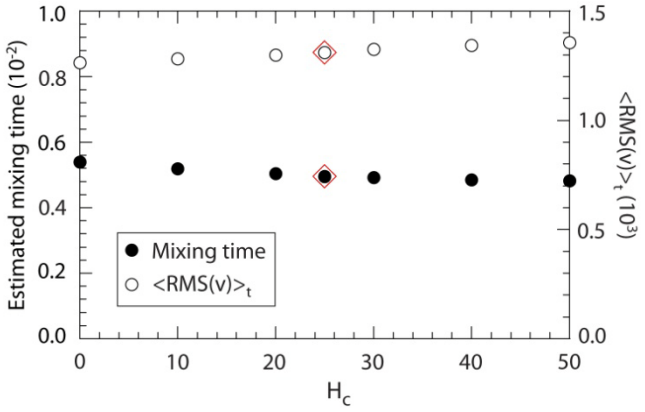

Figure 3. Influence of internal heating, H_c. Plain and open circles show the estimated mixing time and the time average RMS of the flow velocity, respectively, as a function of H_c. The reference case is indicated by the red diamond.

Numerical experiments of purely thermal convection in various geometries showed that the presence of internal heating strongly reduces the vigor of thermal plumes (Travis and Olson, 1994; Sotin and Labrosse, 1999; McNamara and Zhong, 2005). By contrast, the results of our experiments suggest that the amount of internal heating does not significantly influence thermo-chemical convection. This disagreement may be explained by the fact that part of the energy provided by internal heating is used as potential energy for the particles of dense material. In addition, because we imposed a compositional heating ratio (RH_C) of 10, part of internal heating may also be used to heat up the dense material. These explanations are consistent with the observation that the surface heat flow is smaller than the sum of the bottom and internal heating heat flows.

3.3 Phase transition at z = 660 km

We conducted numerical experiments with Clapeyron slope Γ_{660} of the phase transition at d = 660 km (i.e, a non-dimensional altitude h = 0. 771) between –4.6 and 0 MPa/K (i.e., non-dimensional values between $–1.2\times10^{-1}$ and 0). In agreement with previous studies (Christensen and Yuen, 1985; Machetel

and Weber, 1991; Tackley et al., 1993, 1994; Solheim and Peltier, 1994; Yuen et al., 1994), we find that the presence of an endothermic phase transition with low enough (≤ –1.5 MPa/K, i.e. a non-dimensional value of -4.0×10^{-2}) Clapeyron slope inhibits the mass exchange between the upper and lower layers. Furthermore, the RMS of velocity strongly decreases (Fig. 4, plots b and c). Consequently, mixing between dense and regular materials is much less efficient, as indicated by the time evolution of the average altitude of dense material, $\langle h_c \rangle$ (Fig. 4a). Note that the mixing time estimated by Eq. 4 is not accurate in this case, because the function $e(t) = 1 - var(t)/var(t=0)$ do not fit Eq. 5 well.

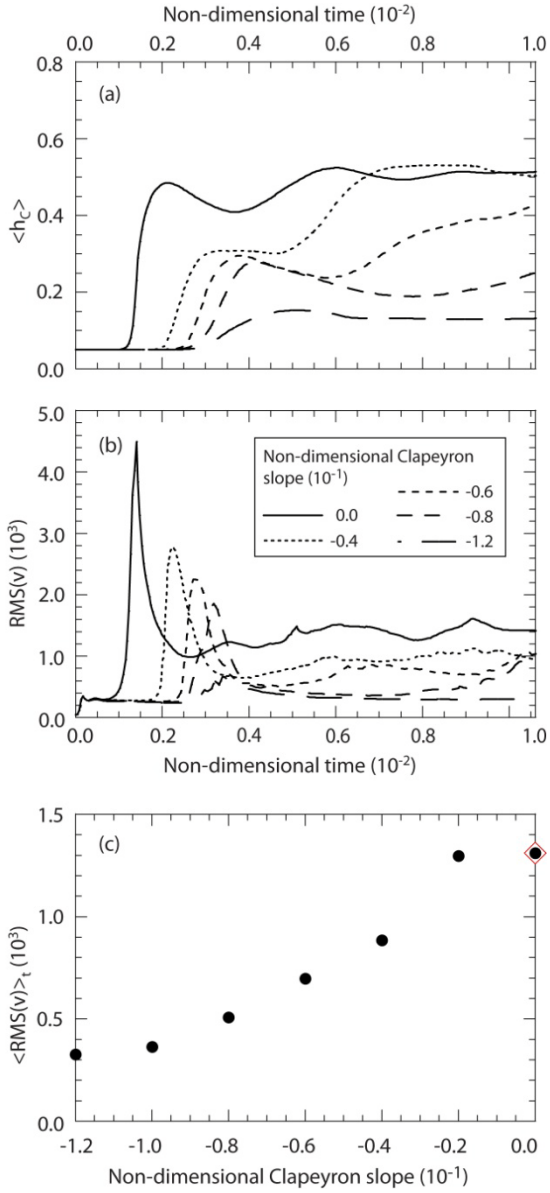

Figure 4. Influence of the Clapeyron slope at d = 660 km, Γ_{660}. (a) Average depth of dense material, $\langle h_C \rangle$, as a function of time and for various values of Γ_{660}. (b) RMS of the flow velocity as a function of time and for various values of Γ_{660}. (c) Time average RMS of the flow velocity as a function of Γ_{660}. In plot (c), the reference case is indicated by the red diamond.

The influence of phase transition on cold downwellings and on hot plumes is radically different. Cold downwellings are temporally stacked above the phase transition. When the mass of accumulated cold material is large enough, this accumulated material crosses the phase boundary and sinks to the bottom of the system. These avalanches are locally intermittent, but at any time of the run there is one occurring somewhere. The system is thus never fully stratified. Hot plumes rising from the bottom, on the contrary, are stopped below the phase transition, and smaller, secondary plumes are generated above the phase transition, as suggested by the temperature profile (Fig. 5i). The upward mass transfer is strongly inhibited, and most of the dense material remains trapped below the phase transition during a long period of time (Fig. 5, plots a and b). Filtering effects have been previously noted in 2D-Cartesian geometry (Weinstein, 1992). The dense material concentrates along hot ridges that interconnect the hot plumes, leading to large holes in the initial layer of dense material. Interestingly, the phase transition is not strictly impermeable and small amounts of dense material are entrained upwards by secondary plumes. Permeability increases with decreasing absolute value of the Clapeyron slope. In the case Γ_{660} = –1.5 MPa/K (-4.0×10^{-2}), for instance, mixing is nearly completed by the end of the run, as indicated by the time evolution of $<h_c>$ (Fig. 4a). In the case Γ_{660} = –2.3 MPa/K (-6.0×10^{-2}), on the contrary, $<h_c>$ only reaches 0.4 by the end of the run, meaning that dense material is distributed nearly completely below the phase transition.

An important consequence of trapping the dense material in the lower mantle is to create strong chemical density anomalies at the bottom of the system ($z \geq 0.85$), and moderate ones below the phase transition (Fig. 5, plots e and h). Moderate thermal density anomalies are also present at the bottom of the system and below the phase transition (Fig. 5, plots f and j), but the strongest thermal density anomalies are seen at the top of the system. These anomalies are maintained for a long period of time, and their power spectra fit very well those predicted by probabilistic tomography (Figure 6), even in the layer 660-1200 km. Note however that a Clapeyron slope lower than –2.7 MPa/K (-7.0×10^{-2}) is not desirable because it keeps dense material at the very bottom of the system. As a consequence, the power of chemical density anomalies for depths in the range $0.23 \leq z \leq 0.85$ ($660 \leq d \leq 2500$ km) is small and does fit probabilistic tomography, even for spherical harmonic degree 2.

We did not account for the olivine to wadsleyite phase transition at the d = 410 km depth. Because this transition is exothermic, it may partly balances the effects of the 660-km transition. However, its phase buoyancy parameter is likely much smaller than that of the 660-km transition (assuming that this transition is well approximated by the transformation of ringwoodite into perovskite and magnesio-wüstite). First the amplitude of the Clapeyron slope 410-km phase transition is smaller than that of the 660-km phase transition, between 1.5 and 2.5 MPa/K (Katsura and Ito, 1989). Note that Bina and Helffrich (1994) proposed a slightly larger value, 3.0 MPa/K, i.e., comparable to that at 660-km. Second, the relative density jump at 410 km is only half that at 660-km. Finally, the thermal expansion decreases with depth, i.e. that the thermal buoyancy (for a given temperature change) is

larger at 410 km than at 660 km. Numerical experiments (Tackley, 1994) confirmed that the effect of the 410-km phase transition are small compared to those of the 660-km transition.

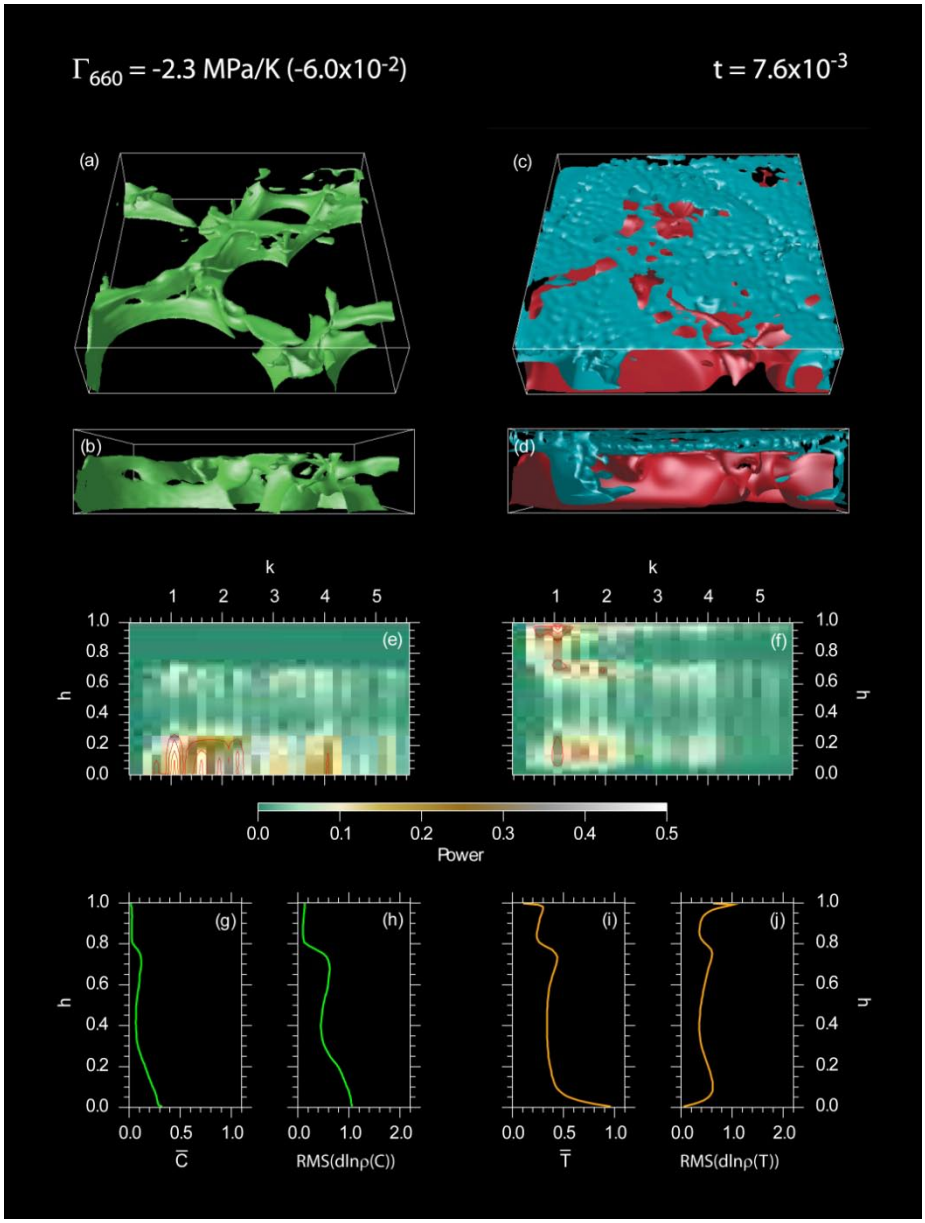

Figure 5. Snapshot of the case Γ_{660} = -2.3 MPa/K (i.e., a non-dimensional value of -6.0×10^{-2}) at t = 7.6×10^{-3} (3.2 Gyr). Other parameters are $Ra_S = 10^8$, H_c = 25 (corresponding to Φ_{surf} = 65 mW/m^2), B = 0.2, and X = 10%. (a-b) Isosurface of the concentration in dense particle, with contour level C = 0.5. (c-d) Isosurfaces of the non-dimensional temperature (relative to average), with contour levels T-<T> = -0.15 (blue) and T-<T> = 0.15 (red). (e) Spectral heterogeneity map (SHM) of the chemical density anomalies, dlnρ_c. (f) SHM of the thermal density anomalies, dlnρ_T. SHMs are plotted with both a color scale and contour levels (red curves, interval is 0.2). h is the non-dimensional altitude. (g) Profile of the horizontally average concentration in dense particle. (h) Profile of the RMS of the chemical density anomalies dlnρ_c. (i) Profile of the horizontally average non-dimensional temperature. (j) Profile of the RMS of the thermal density anomalies dlnρ_T.

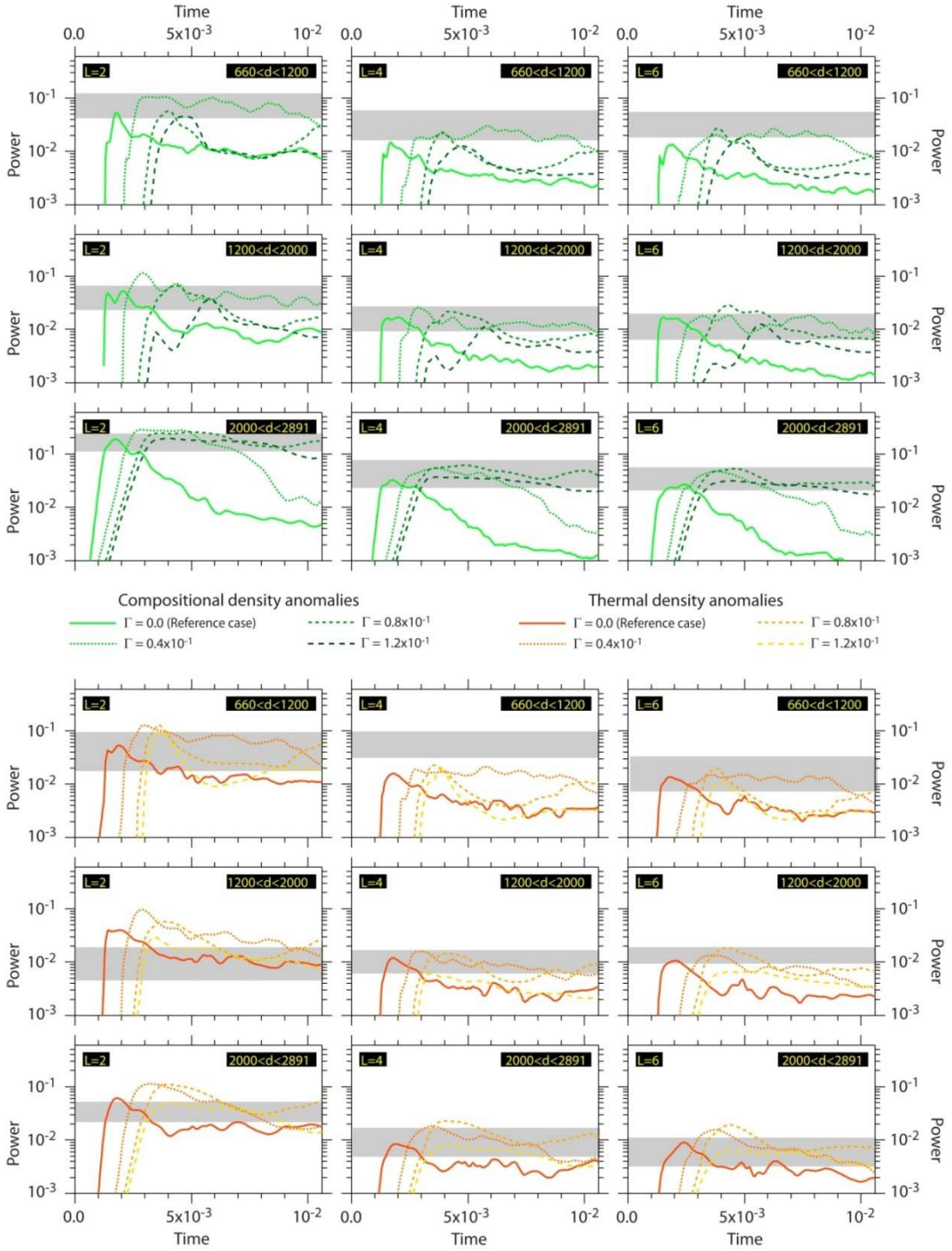

Figure 6. Same as Figure 2, but for various values of the Clapeyron slope at z = 660 km, Γ_{660}.

4. Influence of compositional parameters

4.1 Buoyancy ratio

We varied the buoyancy ratio in the range 0.1-0.5, which according to the scalings in Table 1 is equivalent to density contrasts between 41.3 and 206.3 kg m^{-3}. As expected, we observed major

changes in the flow pattern and mixing efficiency depending on *B*. For buoyancy ratio less than 0.22, we observe patterns similar to the reference case. The dense layer is unstable, and t_{onset} increases with *B* (Fig. 7a). After the onset of instability, large thermo-chemical plumes develop and remain active for short interval of time ($\delta t \sim 10^{-3}$). Dense and regular materials quickly mix (Fig. 7d), and consequently, the power spectra of chemical density anomalies do not fit those from probabilistic tomography in the long term (Figure 9).

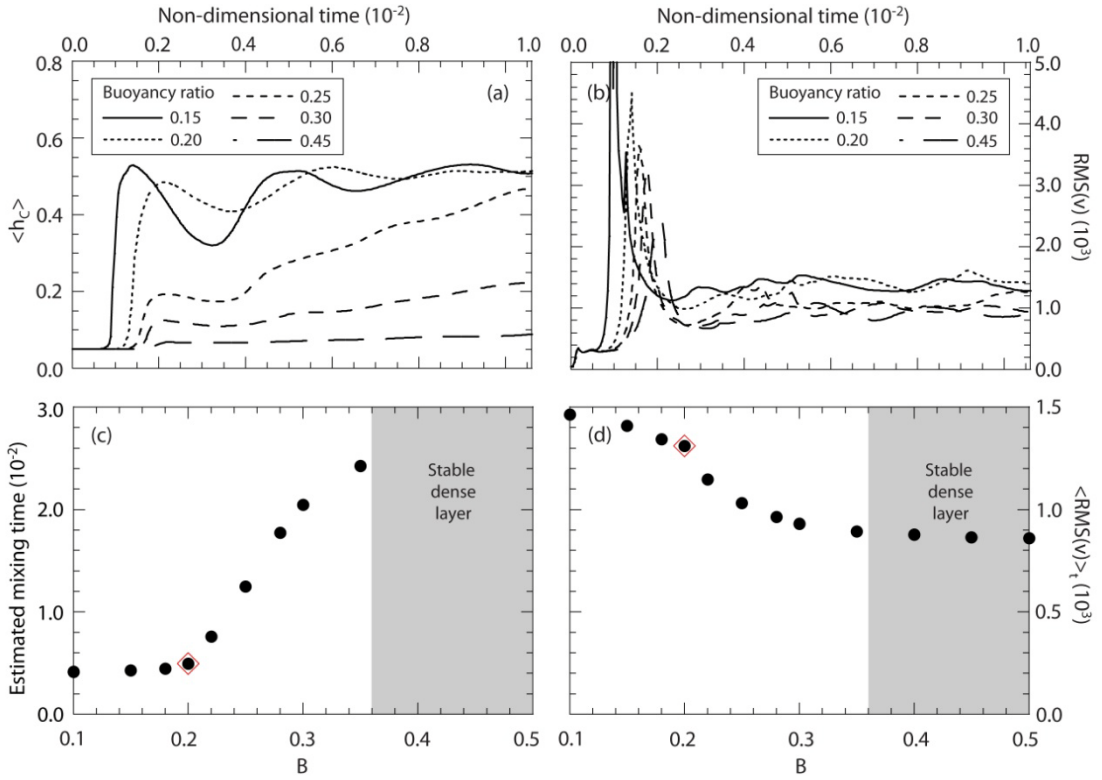

Figure 7. Same as Figure 1, but for various values of the buoyancy ratio, *B*.

For buoyancy ratio between 0.25 and 0.35, on the contrary, the dense layer does not participate actively to convection. Rather, thermal plumes that rise from its top induce some thermal erosion that entrains dense material upwards. Thermal plumes are smaller and more numerous than in the reference case, and they are interconnected by hot ridges (Fig. 8, plots c and d). As expected, the efficiency of thermal erosion decreases with increasing *B* (Fig. 7c; see also the evolution $<h_C>$ for $B = 0.25$ and $B = 0.30$ in Fig. 7a). Because it is mainly controlled by convection in the layer of regular material, $<RMS(v)>_t$ velocity does not vary much with *B* (Fig. 7d). At large time, thermal erosion results in holes in the layer of dense material (Fig. 8, plots a and b). This induces strong chemical density anomalies up to large ($k = 4$) wave number at the bottom of the system ($z \geq 0.85$) (Fig. 8e). As a result, the power spectra of density anomalies in this layer (Fig. 9, 3rd row) fit well those from probabilistic tomography. On the contrary, because most of the dense material remains in the lowermost part of the

system, power spectra in the intermediate and upper layers strongly disagree with probabilistic tomography at any time of the run.

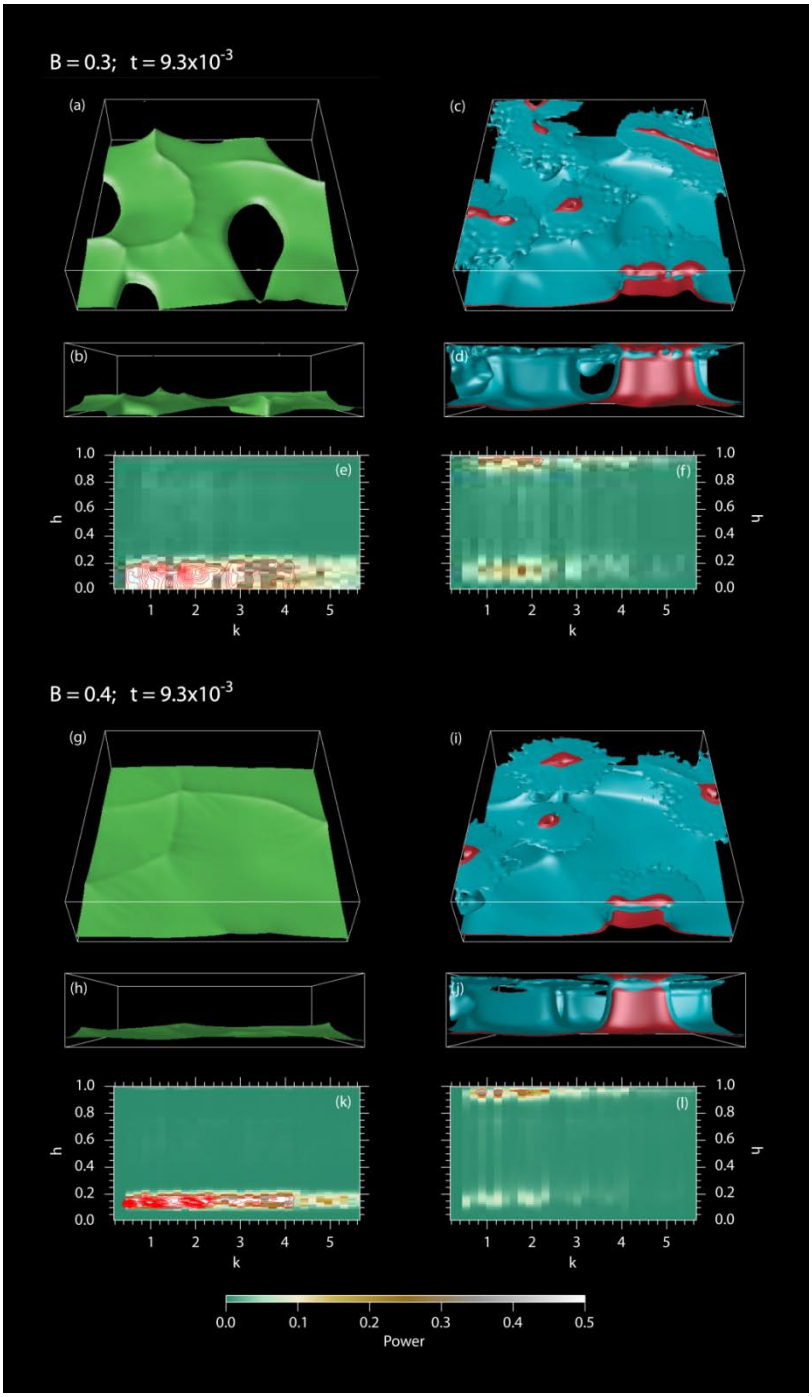

Figure 8. (a-f) Snapshot of the case B = 0.3 at t = 9.3×10^{-3} (3.9 Gyr). Other parameters are as in the reference case (Ra_S = 10^8, H_c = 25, X = 10%, and Γ_{660} = 0). (a-b) Isosurface of the concentration in dense particle, with contour level C = 0.5. (c-d) Isosurfaces of the non-dimensional temperature (relative to average), with contour levels T-<T> = -0.05 (blue) and T-<T> = 0.05 (red). (e) Spectral heterogeneity map (SHM) of the chemical density anomalies, dlnρ_c. (f) SHM of the thermal density anomalies, dlnρ_T. SHMs are plotted with both a color scale and contour levels (red curves, interval is 0.2). h is the non-dimensional altitude. (g-l) Snapshot of the case B = 0.4 at t = 9.3×10^{-3} (3.9 Gyr). Other parameters are as in the reference case (Ra_S = 10^8, H_c = 25, X = 10%, and Γ_{660} = 0). Plots description is similar to that for plots (a-f). In plots i and j, contour levels for temperature isosurfaces are T-<T> = -0.05 (blue) and T-<T> = 0.05 (red).

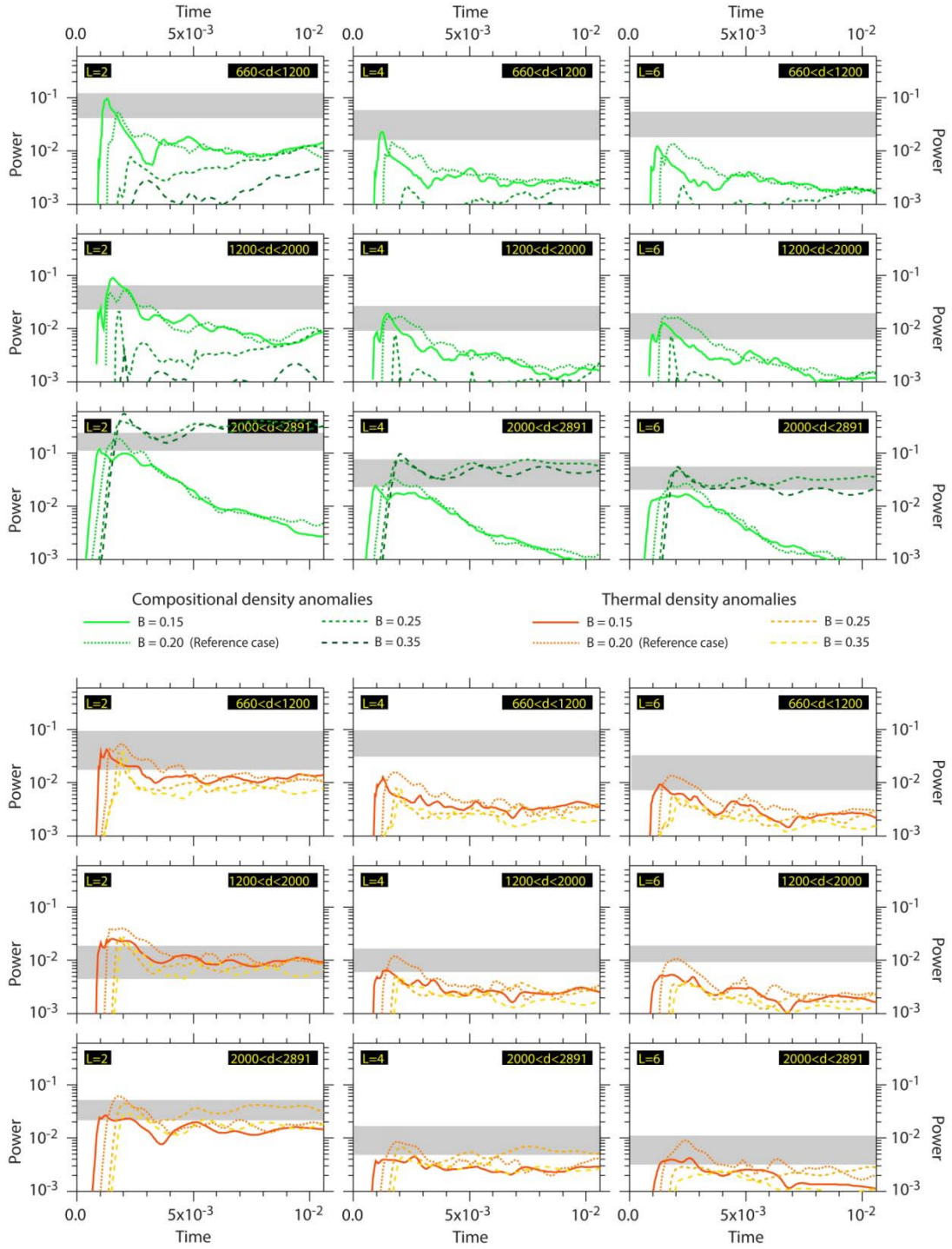

Figure 9. Same as Figure 2, but for various values of the buoyancy ratio, *B*.

Finally, for buoyancy ratio larger than 0.35, the layer of dense material remains stable during the entire run (Fig. 8, plots g and h). Thermal erosion is also present, but does not entrain enough dense material to create holes in the initial dense layer. The average altitude of dense material thus remains around 0.05 during the whole run (Fig. 7a), and strong chemical density anomalies localized at the top of the dense layer (Fig. 8k). Plots g and k in Fig. 8 indicate that the topography of the top of the dense layer is not negligible, around $\delta h = 0.1$. Topography is of course correlated with the hot ridges and the

base of thermal plumes. This pattern is very similar to that we observe by increasing the chemical density contrast (Deschamps and Tackley, *in press*) except that thermal plumes are larger, and that there is more topography at the top of the layer of dense material.

Clearly, the buoyancy ratio has a dominant role on the flow pattern and on the efficiency of mixing. Large (≥ 0.25) buoyancy ratios induce stable layering. Thermal erosion creates moderate topography, which, if buoyancy ratio is not too high, results in holes in the dense layer, but most of the chemical density anomalies are localized in the lowermost part of the system.

4.2 Fraction of dense material

Finally, we considered values of the volume fraction of dense material, *X*, between 5 and 30%. Figure 10 plots the non-dimensional time average of the mean altitude of dense material (Eq. 6) as a function of *B* and *X*. Clearly, the effect of *X* is of secondary order compared to that of *B*.

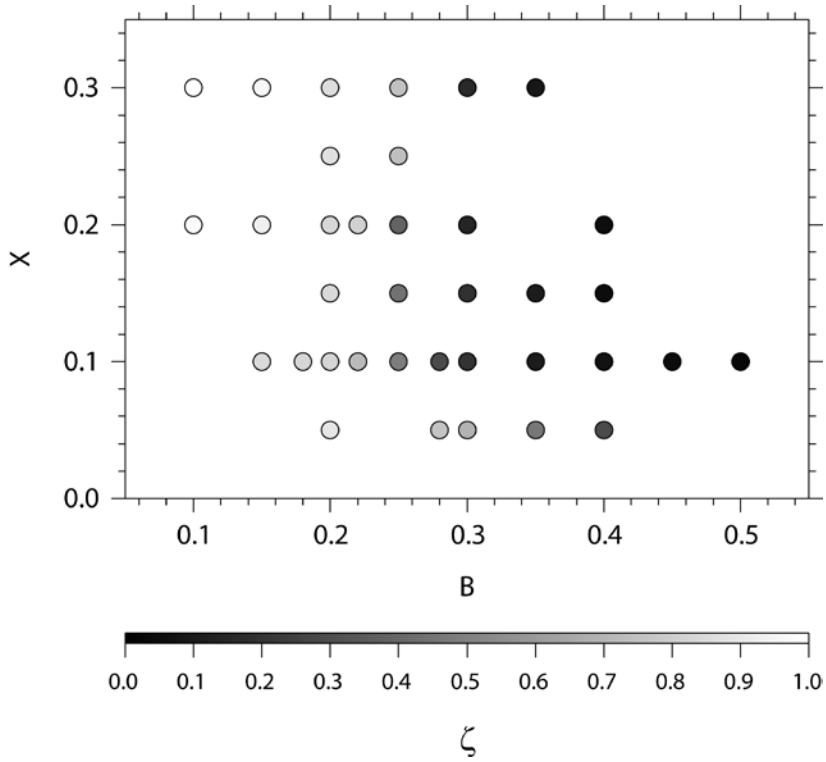

Figure 10. Non-dimensional time average of the average depth of dense material, ζ (Eq. 6), as a function of the Buoyancy ratio, *B*, and the fraction of dense material, *X*. The value of ζ is denoted by the gray-level scale.

It is reasonable to consider that the thickness of the dense layer (which increases with *X*) competes with the buoyancy ratio. The later increases the stability of the layer. On the contrary, the thicker the layer, the larger its Rayleigh number. Thus, there may exist a critical thickness (or equivalently, fraction of dense material), for which the dense layer switches from an active to passive (thermal erosion) mode of convection, and this thickness may increases with *B*. This competition, however, is

visible only for values of B around 0.25 (Fig. 10). For $X \leq 0.2$, the dense layer does not participate to convection. Mixing results from thermal erosion (dense material is entrained upwards by thermal plumes), and its efficiency decreases with increasing X. On the contrary, for $X \geq 0.25$, the dense layer is unstable and participates to convection. For smaller (≤ 0.2) values of B, the dense layer is getting unstable for all the values of X we considered, and the efficiency of mixing varies very few with X. For larger (≥ 0.3) values of B, the density contrast is strong enough to prevent instability of the dense layer. In the case $B = 0.3$ and $X = 0.3$, for instance, the layer of dense material remains present during the entire run (unlike the case $B = 0.3$ and $X = 0.1$, Fig. 8, plots a and b, thermal erosion is not efficient enough to create some holes). Additional experiments (not plotted in Fig. 10) for $B = 0.3$ and $B = 0.4$ show that the layer is still stable for $X = 50\%$.

Clearly, the stability, and thus the efficiency of mixing, mainly depends on the buoyancy ratio, and the fraction of dense material is not a controlling parameter. This conclusion is in good agreement with the analogical experiments of Jaupart et al. (2007).

5. Mantle convection: important ingredients

Based on the extensive search in the model space of thermo-chemical we conducted (Deschamps and Tackley, *in press*; this paper) we identify five ingredients needed to create and maintain strong thermo-chemical anomalies in the lower mantle. (1) A reasonable buoyancy ratio, between 0.15 and 0.25 (corresponding to chemical density contrasts in the range 60-100 kg/m^3) (this paper). Larger density contrasts induce stable layering for long period of time, rather than the strong topography required by seismic observations. (2) A moderate, typically in the range 0.1-10, chemical viscosity contrast (companion paper). Small chemical viscosity contrasts induce rapid mixing, whereas large chemical viscosity contrasts lead to stable layering. (3) A large, 10^4 or more, thermal viscosity contrast (companion paper). Temperarure-dependent viscosity creates and maintains pools of dense material with large topography at the bottom of the mantle. (4) A 660-km viscosity contrast around 30 (companion paper). (5) And a Clapeyron slope of the 660-km transition around –3.0 to –1.5 MPa/K (this paper). These two last ingredients help to maintain dense material in the lower mantle. Interestingly, they strongly inhibit the rise of thermo-chemical plumes above 660 km, but still allow the penetration of downwellings in the lower mantle. In addition to these five ingredients, it is important to note that reducing the Rayleigh number by a factor 3 compared to its assumed value (which is not unreasonable given the uncertainties in upper mantle viscosity, thermal expansion and thermal diffusivity) also contribute to maintain compositional anomalies in the lower mantle during a long period of time.

To test whether a combination of these ingredients can explain the observed tomography, we conducted an additional experiment with the following properties: $B = 0.2$, $R\mu_c = 0.5$, $R\mu_T = 10^6$,

$R\mu_{660}$ = 30, and Γ_{660} = -6.68×10^{-2} (-2.5 MPa/K). Figure 11 shows a snapshot of this experiment by the end of the run (t = 10^{-2}, corresponding to a dimensional time of 4.2 Gy). Large pools of dense material rise from the bottom of the system up to the 660-km transition (Fig. 11, plots a and b). They induce

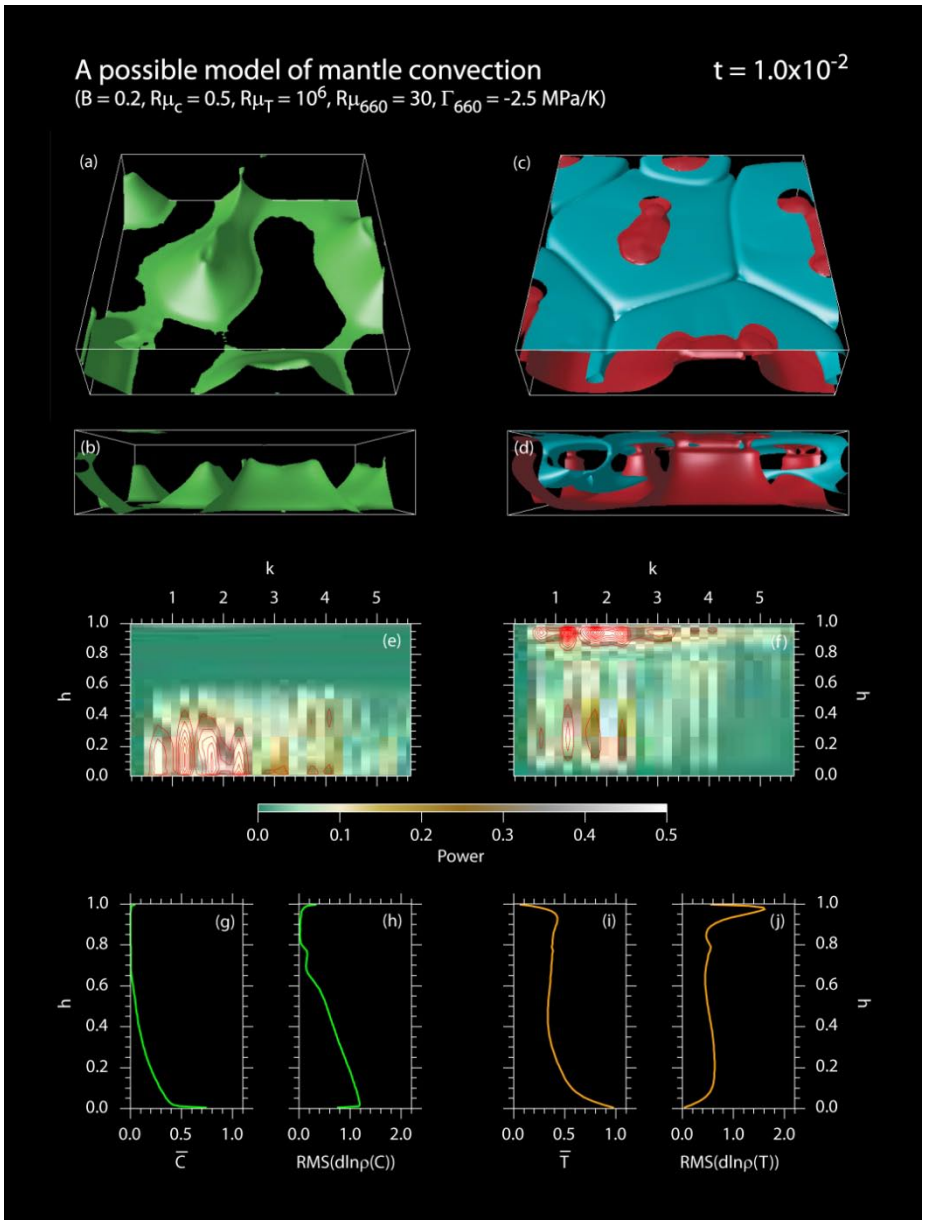

Figure 11. Snapshot at time t = 1.0×10^{-2} (4.2 Gyr) of a model that combines important ingredients for mantle convection: B = 0.2, $R\mu_c$ = 0.5, $R\mu_T$ = 10^6, $R\mu_{660}$ = 30, and Γ_{660} = -2.5 MPa/K (i.e., a non-dimensional value of -6.68×10^{-2}). Other parameters are as in the reference case: Ra_S = 10^8, H_c = 25, and X = 10%. Plots description is similar to that in Figure 5. In plots c and d, contour levels for temperature isosurfaces are T-<T> = -0.225 (blue) and T-<T> = 0.15 (red).

strong chemical density anomalies with wave number up to k = 2.5 (Fig. 11e) and increasing amplitude with depth (Fig. 11h). Due to the value of the Clapeyron slope of the 660-km transition, very small amount of dense material penetrates in the upper mantle. Large hot plumes also rise from the bottom of the mantle, but the combined actions of the 660-km viscosity contrast and endothermic

phase transition considerably thin them as they enter the upper mantle (Fig. 11, plots c and d). Note that unlike cases that account for the phase transition only (Fig. 5), plumes are not stopped but only thinned (Fig. 11d; see also the temperature profile, Fig. 11i, which do not show a sharp increase around 660 km-depth). A possible explanation is that the plume temperature reduces their viscosity, which in turn increases their buoyancy enough to balance the negative buoyancy due to the phase transition. Downwellings, by contrast, are able to penetrate more easily in the lower mantle. The thinned plumes and the downwellings induce strong thermal density anomalies in a layer that extends from the surface down to $z \sim 0.1$ (~300 km-depth) (Fig. 11, plots f and j). Interestingly, these thermo-chemical structures are long lived. Extending the calculations up to time $t = 0.0212$ (9.0 Gyr), we observe that they are still present. Furthermore, the power spectrum of density anomalies predicted by this model is in excellent agreement with that from probabilistic tomography, except in the layer 660-1200 km (open circles in Figure 12). A possible explanation for this disagreement is that the anomalies

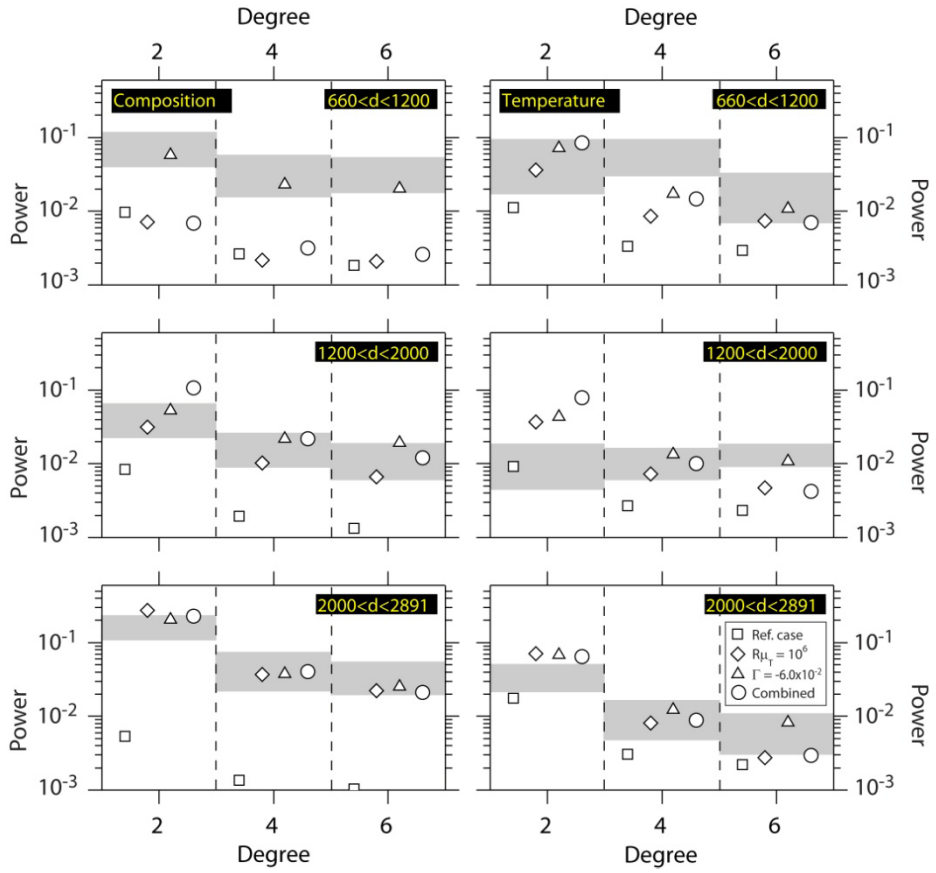

Figure 12. Power spectra of chemical (left column) and thermal (right column) density anomalies by the end of the run and for various cases. Anomalies are averaged within three layers ($660 \leq d \leq 1200$ km, $1200 \leq d \leq 2000$ km, and $2000 \leq d \leq 2891$ km), and we considered three spherical harmonics ($L = 2$, $L = 4$, and $L = 6$). Power spectra are further averaged in time in the period range 0.85×10^{-2} - 1.06×10^{-2} (3.5-4.5 Gyr). Gray bands indicate the power spectrum predicted by RT246g within twice its standard deviation. The squares are for the reference case, the diamonds for the case $R\mu_T = 10^6$, the triangles for the $\Gamma_{660} = -2.3$ MPa/K (i.e., a non-dimensional value of -6.0×10^{-2}), and the circles for the combined case discussed in section 5 ($B = 0.2$, $R\mu_c = 0.5$, $R\mu_T = 10^6$, $R\mu_{660} = 30$, and $\Gamma_{660} = -2.5$ MPa/K).

observed by probabilistic tomography in this layer are related to accumulation of slabs around the 660-km boundary. Because we assumed two types of particles only (regular material and dense material concentrated in an initial layer), our treatment of the chemical field does not account for the effects of downwellings on the distribution of chemical density anomalies. To achieve this, a more complex modeling including a third type of particle and the generation of MORB and harzburgite materials from an initial mantle reservoir and their recycling in the deep mantle, is needed. It is however interesting to note that the thermal density anomalies fit well those from probabilistic tomography (right row in Fig. 12), which might be the thermal signature of slabs. Alternatively, anomalies in this layer may be due to dense material that remains trapped below the phase transition, as one would expect for a Clapeyron slope around -2.3 MPa/K (-6.0×10^{-2}) and a viscosity that is not temperature-dependent (Fig. 5b, and top row in Fig. 6).

6. Concluding remarks

Our search for successful dynamic models of Earth's mantle was essentially based on comparison between models of thermo-chemical convection and a tomographic model that include estimates of density distribution, which play a crucial role in resolving the trade-off between temperature and composition. To give more support to our findings, it is important to compare the five ingredients we identified with other available geophysical constraints. (1) First, one may estimate possible values of buoyancy ratio assuming that the density excess at the bottom of the mantle is related to the presence of iron-rich post-perovskite. Assuming that the average mantle composition is pyrolitic (Si/Mg ~ 0.8 and Fe/Mg ~ 0.11), and using available data for post-perovskite (Tsuchiya et al., 2004) and an appropriate equation of state modeling (Deschamps and Trampert, 2004), we find that a 2.0-2.5 % excess in the volume fraction of iron in the lowermost mantle (Trampert et al., 2004) may result in a chemical density contrast between 80 and 96 kg m^3. Compared to the thermal density contrast, $\Delta\rho_S$ = 412.5 kg m^3 (Table 1), this lead to a buoyancy ratio between 0.19 and 0.22. (2) To date, very few data concerning the viscosity of post-perovskite and the iron end-members of mantle minerals are available, and it is difficult to make reasonable estimates of the compositional viscosity contrast. (3) The viscosity of mantle aggregate is clearly temperature-dependent, and this dependence is well explained by an Arrhenius type of law. Taking a mantle adiabat and a superadiabatic temperature difference equal to T_{as} = 1200 C and ΔT = 2500 K, respectively, a thermal viscosity contrast in the range 10^5-10^7 would correspond to a thermal activation energy between 220 and 310 kJ/mol. These values are consistent with mineral physics data for the activation energies of perovskite and magnesio-wüstite (Yamazaki and Karato, 2001). (4) Estimates of the 660-km viscosity jump from various

geophysical observations are also available (e.g., Hager and Richards, 1989; Nakada and Lambeck, 1989; Forte and Mitrovica, 1996), and our preferred range of values for this viscosity contrast (10-30) is consistent with the observed values. (5) Finally, the transformation of ringwoodite into perovskite and magnesio-wüstite is endothermic, with Clapeyron slope between –3.0 and –2.0 MPa K^{-1} (Bina and Helffrich, 1994). Note that the transformation of garnet may modify the effective Clapeyron slope at z = 660 km (see discussion below). Overall, the ingredients we identified are in very good agreement with available independent geophysical data.

Case	T_{UM} (K) [b]	Φ_{surf} (mW/m^2) [c]	RMS(V_{surf}) (cm/y)
Reference case	970	77.5	3.1
$Ra_S = 3.0\times10^7$	1080	66.7	1.4
$Ra_S = 3.0\times10^8$	760	74.1	4.9
Γ_{660} = 0.76 MPa/K [d]	960	76.4	3.3
Γ_{660} = 1.53 MPa/K	950	74.9	2.3
Γ_{660} = 3.06 MPa/K	650	33.8	1.4
B = 0.15	950	82.0	3.4
B = 0.25	930	71.0	2.4
B = 0.40	840	55.1	2.0
Combined case [e]	1230	45.8	0.6

Table 2. Predicted upper mantle temperature, surface heat flow, and RMS of surface velocity for selected cases[a]

[a] Average values over the last Gyr of the run. Possible values for the Earth upper mantle temperature are in the range 1200-1400 K. Surface heat flow strongly varies with location. The compilation of Pollack et al. (1993) proposes a global value around 87 mW/m^2, with oceanic and continental values around 101 mW/m^2 and 65 mW/m^2, respectively.

[b] The upper mantle potential temperature is averaged in the layer $200 \le d \le 660$ km ($0.07 \le z \le 0.228$), and scaled with a super-adiabatic temperature difference ΔT_S = 2500 K and a surface temperature T_{surf} = 300 K. The real temperature can be estimated by assuming that the adiabatic gradient in this layer is 0.4 K/km, i.e, by adding an adiabatic contribution of about 100 K.

[c] Surface heat flow includes a contribution from the adiabatic gradient of temperature. In the reference state we used (Tackley 1996, 1998b), the adiabatic gradient below the surface gradient is about 0.8 K/km. Taking k_S = 3.0 W/m/K, the adiabatic contribution to the surface heat flow is thus 2.4 mW/m^2.

[d] Non-dimensional Clapeyron slopes are -0.2×10^{-1}, -0.4×10^{-1}, and -0.8×10^{-1}, respectively.

[e] Combined case properties are $Ra_S = 10^8$, B = 0.2, X = 10%, $R\mu_c$ = 0.5, $R\mu_{660}$ = 30, $R\mu_z$ = 10, $R\mu_T = 10^6$, and Γ_{660} = -2.5 MPa/K (i.e., a non-dimensional value of -6.68×10^{-1}).

Our models also predict surface heat flow, Φ_{surf}, average temperature of the upper mantle ($200 \le d \le 660$ km), T_{UM}, and surface velocity, V_{surf}, that we can compare with values observed for the Earth. Table 2 lists the time-average (over the last Gyr for of the run) of these parameters for selected models of thermo-chemical convection. Heat flow values may be compared against that of the compilation of Pollack et al. (1993). One must however keep in mind that the observed surface heat flow is likely

overestimating the heat flow at the top of the mantle. The reason is that the measured surface heat flow includes a contribution related to crustal heat production, which is difficult to estimate. In cratonic regions, this contribution may be large and the mantle heat flux could be as low as 15 to 20 mW/m^2 (Jaupart and Mareschal, 2007). Classical value for the average temperature the upper mantle is in the range 1200-1400 K. Both Φ_{surf} and T_{UM} decrease with increasing buoyancy ratio and increasing absolute value of the Clapeyron slope. This decrease is more pronounced for $\Gamma_{660} \leq$ -1.5 MPa/K (-4.0×10^{-2}), and for Γ_{660} = -3.0 MPa/K (-8.0×10^{-2}) the calculated Φ_{surf} and T_{UM} are difficult to reconcile with the observed surface heat flow and the upper mantle adiabat. For the combined case, the predicted upper mantle temperature is comparable to that expected for the Earth's upper mantle, but the predicted heat flux is low (45.8 mW/m^2) compared to the global average heat flow (87 mW/m^2, Pollack et al., 1993). Again, this disagreement may be partly explained by the fact that the observed surface heat flow is not corrected from the crustal heat production and is thus higher than the actual heat flow coming out of the mantle. Except for the combined case, the models listed in Table 2 do not include lateral variations of viscosity, and thus the horizontal velocity is fully poloidal. For the Earth, the ratio between toroidal and poloidal velocities is around 0.4-0.6 (Lithgow-Bertelloni et al., 1993; Becker, 2006), and the average surface poloidal velocity is typically in the range 2-6 cm/yr. In our models, the surface velocity decreases with both the buoyancy ratio and the amplitude of the Clapeyron slope, but remains close to the typical value for the Earth. Unsurprisingly, V_{surf} increases with the Rayleigh number. Note that for Ra_S around 3.0×10^7 and less, V_{surf} is too small compared to the observed values for the Earth. Due to the large value of the thermal viscosity ratio, which increases the rigidity of the fluid close the surface, the surface velocity predicted by the combined case is small, less than 1 cm/yr. Note that the presence of additional ingredients prevent the combined case to fit in the conductive-lid regime observed for strongly temperature-dependent viscosity fluid (e.g., Davaille and Jaupart, 1993; Moresi and Solomatov, 1995). The disagreement between the surface velocity predicted by the combined case and the observed one may be fixed by imposing an appropriate rheology at the top of the fluid to model that would properly models the lithosphere (Tackley, 1998b).

The role of the phase transition at d = 660 km is of particular importance. Clearly, downwellings can penetrate below this transition. In agreement with purely thermal convection models (Tackley et al., 1993, 1994), we observe that avalanches occur at any time, but not necessarily at the same location. This is consistent with tomographic images, which show that slabs can either sink into the deep mantle or stack around 1000 km depth (van der Hilst et al., 1997; Fukao et al., 2001). By contrast, the large hot plumes that rise from the bottom thermal boundary layer are strongly inhibited as they cross the 660-km phase transition and, if temperature-dependent viscosity is not accounted for, they even stopped below it. Upward mass transfer is strongly inhibited, and most of the dense material remains trapped in the lower mantle. Interestingly, this observation gives support to the existence of a buried reservoir enriched in dense material in the lower mantle. The existence of two reservoirs in the

mantle (a pyrolitic reservoir and a reservoir enriched in dense material) is often advocated to explain geochemical differences observed between OIB and MORB materials (e.g., Zindler and Hart, 1986; Hofmann, 1997). Possible origins for the reservoir enriched in dense material include a subducted early crust (Boyet and Carlson, 2006), and the formation and crystallization of a magma ocean at the bottom of the mantle (Labrosse et al., 2007).

The 660-km phase transition was modeled with a single Clapeyron slope imposed around d = 660 km. The real Earth is however thermodynamically more complex, with various minerals transforming at different depths and with different Clapeyron slopes. Garnets, for instance, transform at greater depth than Ringwoodite, around 710 km (e.g., Stixrude, 1997). It is thus an oversimplification to model the 660-km phase chemical change with a single endothermic phase transition. Accounting for the full phase diagram in this depth-range may have strong implications in the flow pattern and in the distribution of density anomalies. More generally, multiphase models of mantle convection may have important consequences for mantle dynamics and heat transfer (Nakagawa and Tackley, 2005a). In addition, the post-perovskite phase transition at the bottom of the system, which is not included in our model, may have some specific signatures. It has been pointed out, for instance, that the distributions of dense material and post-perovskite are anti-correlated (Nakagawa and Tackley, 2005b, 2006), and that the spectra of chemical anomalies are strongly influenced by the topography of the post-perovskite phase transition (Nakagawa and Tackley, 2006).

Other limitations of our approach and models were discussed in our companion paper. They include the lack of sources and sinks of dense material, which may slightly bias our results. Accounting for sources and sinks of dense material may for instance allow the creation and recycling of MORB material. More importantly, spherical geometry modifies the stability of top and bottom thermal boundary layers, and may strongly affect the flow pattern and the stability a basal layer of dense material. In particular, sphericity increases the stability of the bottom thermal boundary layer, and the ingredients that stabilize the layer of dense material (large compositional viscosity and density contrasts) are likely to have stronger effects.

References

Bina, C.R., and G. Helffrich, 1994. Phase transitions Clapeyron slopes and transition zone seismic discontinuity tomography. J. Geophys. Res. 99, 15853-15860.

Becker T.W., 2006. On the effect of temperature and strain-rate dependent viscosity on global mantle flow, net rotation, and plate driving forces. Geophys. J. Int. 167, 943-957.

Boyet, M., and R.W. Carlson 2006. ^{142}Nd evidence for early (>4.53 Ga) global differentiation of the silicate Earth. Science 309, 576-581.

Chevrot, S., J.-P. Montagner, and R. Snieder, 1998. The spectrum of tomographic Earth models. Geophys. J. Int. 133, 783–788.

Christensen, U.R., and D.A. Yuen, 1985. Layered convection induced by phase transitions. J. Geophys. Res. 90, 10291-10300.

Coltice, N., 2005. The role of convective mixing in degassing the Earth's mantle. Earth Planet. Sci. Lett. 234, 15-25.

Davaille, 1999. Simultaneous generation of hotspots and superswells by convection in a heterogeneous planetary mantle. Nature 402, 756-760.

Davaille, A., and C. Jaupart, 1993. Transient high-Rayleigh number thermal convection with large viscosity variations. J. Fluid Mech. 253, 141-166.

Deschamps, F., and J. Trampert, 2003. Mantle tomography and its relation to temperature and composition. Phys. Earth Planet. Inter. 140, 277-291.

Deschamps, F., and J. Trampert, 2004. Towards a lower mantle reference temperature and composition. Earth Planet. Sci. Lett. 222, 161-175.

Deschamps, F., J. Trampert, and P.J. Tackley, 2007. Thermo-chemical structure of the lower mantle: seismological evidence and consequences for geodynamics, in D.A. Yuen et al. (Ed.), Superplumes: Beyond Plate Tectonics, Springer, pp .293-320.

Deschamps, F., and P.J. Tackley. Exploring the model space of thermo-chemical convection I – Principles and influence of the rheological parameters. Phys. Earth Planet. Inter., in press.

Forte, A.M., and J.X. Mitrovica, 1996. New inferences of mantle viscosity from joint inversion of long-wavelength mantle convection and post-glacial rebound data. Geophys. Res. Lett. 23, 1147-1050.

Fukao, Y., S. Widiyantoro, and M. Obayashi, 2001. Stagnant slabs in the upper and lower mantle transition region. *Rev. Geophys.* 39, 291-323.

Hager, B.H., and M.A. Richards, 1989. Long-wavelength variations in Earth's geoid: physical models and dynamical implications. Phil. Trans. Roy. Soc. London A 328, 309-327.

Hofmann, A.W., 1997. Mantle geochemistry: the message from oceanic volcanism. Nature 385, 219-229.

Ishii, M., and J. Tromp, 1999. Normal-mode and free-air gravity constraints on lateral variations in velocity and density of Earth's mantle. Science 285, 1231-1236.

Jaupart, C., P. Molnar, and E. Cottrell, 2007. Instability of a chemically dense layer heated from below and overlain by a deep less viscous fluid. J. Fluid Mech. 572, 433-469.

Jaupart, C., and J.-C. Mareschal, 2007. Heat flow and thermal structure of the lithosphere. In: G. Schubert et al. (Eds.), Treatise on Geophysics Volume 3: Crust and Lithosphere Dynamics, 218-251.

Karato, S.-I., and B.B. Karki, 2001. Origin of lateral variation of seismic wave velocity and density in the deep mantle. J. Geophys. Res. 106, 21771-21783.

Katsura, T., and E. Ito, 1989. The system Mg_2-SiO_4-Fe_2-SiO_4 at high pressures and temperatures: precises determination of stabilities of olivine, modified spinel, and spinel. J. Geophys. Res. 94, 15663-15670.

Labrosse, S., J.W. Hernlund, and N. Coltice, 2007. A crystallizing dense magma ocean et the base of the Earth's mantle. Nature 450, 866-869.

Lithgow-Bertelloni, C., M.A. Richards, Y. Ricard, R.J. O'Connell, and D.J. Engebretson, 1993. Toroidal-poloidal partitioning of plate motion since 120 Ma. Geophys. Res. Lett. 20, 375-378.

Machetel P., and P. Weber, 1991. Intermittent layered convection in a model mantle with an endothermic phase change at 670 km. Nature 350, 55-57.

Moresi, L.-N., and V.S. Solomatov, 1995. Numerical investigation of 2D convection with extremely large viscosity variations. Phys. Fluids 7, 2154-2162.

Nakada M., and K. Lambeck, 1989. Late Pleistocene and Holocene sea-level change in the Australian region and mantle rheology. Geophys. J. Int. 96, 497-517.

Nakagawa, T., and P.J. Tackley, 2005a. Deep mantle heat flow and thermal evolution of Earth's core in thermo-chemical multiphase models of mantle convection. Geochem. Geophys. Geosys. 6, doi:10.1029/2005GC000967.

Nakagawa, T., and P.J. Tackley, 2005b. The interaction between the post-perovskite phase change and a thermo-chemical boundary layer near the core-mantle boundary. Earth Planet. Sci. Lett. 238, 204-216.

Nakagawa, T., and P.J. Tackley, 2006. Three-dimensional structures and dynamics in the deep mantle: Effects of post-perovskite phase change and deep mantle layering. Geophys. Res. Lett. 33, doi:10.1029/2006GL025719.

McNamara, A.K., and S. Zhong, 2004. Thermochemical structures within a spherical mantle. J. Geophys. Res. 109, doi: 10.1029/2003JB002847.

McNamara, A.K., and S. Zhong, 2005. Degree-one mantle convection: dependence on internal heating and temperature-dependent rheology. Geophys. Res. Lett. 32, doi: 10.1029/2004GL021082.

Pollack, H.N., S.J. Hurter, and J.R. Johnson, 1993. Heat flow from the earth interior: analysis of global data set. Rev. Geophys. 31, 267-280.

Saltzer, R.L., R.D. van der Hilst, and H. Kárason, 2001. Comparing P and S wave heterogeneity in the mantle. Geophys. Res. Lett. 28, 1335-1338.

Solheim, L.P., and W.R. Peltier, 1994. Phase boundary deflection at 660-km depth and episodically layered isochemical convection in the mantle. J. Geophys. Res. 99, 15861-15875.

Sotin, S., and S. Labrosse, 1999. Three-dimensional thermal convection in an iso-viscous, infinite Prandtl number fluid heated from within and from below: applications to the transfer of heat through planetary mantles. Phys. Earth Planet. Inter. 112, 171-190.

Stixrude, L., 1997. Structure and sharpness of phase transitions and mantle discontinuities. J. Geophys. Res. 102, 14835-14852.

Tackley, P.J., 1996. On the ability of phase transitions and viscosity layering to induce long wavelength heterogeneity in the mantle. Geophys. Res. Lett. 23, 1985-1988.

Tackley, P.J., 1998a. Three-dimensional simulations of mantle convection with a thermo-chemical CMB boundary layer: D"? In: M. Gurnis et al. (Eds.), The Core-Mantle Boundary Region, Geodynamical Ser. 28, 231-253.

Tackley, P.J., 1998b. Self-consistent generation of tectonic plates in three-dimensional mantle convection. Earth Planet. Sci. Lett. 157, 9-22.

Tackley, P.J., 2002. Strong heterogeneity caused by deep mantle layering. Geochem. Geophys. Geosys. 3, doi: 10.1029/2001GC000167.

Tackley, P.J., and S.D. King, 2003. Testing the tracer ratio method for modeling active compositional fields in mantle convection simulations. Geochem. Geophys. Geosys. 4, doi: 10.1029/2001GC000214.

Tackley, P.J., D.J. Stevenson, G.A. Glatzmaier, and G. Schubert, 1993. Effect of an endothermic phase transition at 670 km in a spherical model of convection in the Earth's mantle. Nature 361, 699-704.

Tackley, P.J., D.J. Stevenson, G.A. Glatzmaier, and G. Schubert, 1994. Effects of multiple phase transitions in three-dimensional spherical model of convection in the Earth's mantle. J. Geophys. Res. 99, 15877-15901.

Trampert, J., F. Deschamps, J.S. Resovsky, and D.A. Yuen, 2004. Probabilistic tomography maps significant chemical heterogeneities in the lower mantle. Science 306, 853-856.

Travis, B., and P. Olson, 1994. Convection with internal sources and turbulence in the Earth's mantle. Geophys. J. Int. 118, 1-19.

Tsuchiya, T., J. Tsuchiya, K. Umemoto, and R.M. Wentzcovitch, 2004. Phase transition in $MgSiO_3$ perovskite in the lower mantle. Earth Planet. Sci. Lett. 224, 241-248.

van der Hilst, R.D., S. Widiyantoro, and E.R. Engdahl, 1997. Evidence for deep mantle circulation from seismic tomography. Nature 386, 578-584.

Weinstein, S.A., 1992. Induced compositional layering in a convective fluid layer by an endothermic phase transition. Earth Planet. Sci. Lett. 113, 23-39.

Yamazaki, D., and S.-I. Karato, 2001. Some mineral physics constraints on the rheology and geothermal structure of Earth's lower mantle. Amer. Mineral. 86, 385-391.

Yuen, D.A., D.M. Reuteler, S. Balachandar, V. Steinbach, A.V. Malevsky, and J.J. Smedsmo, 1994. Various influences on three-dimensional mantle convection with phase transition. Phys. Earth Planet. Inter. 86, 185-203.

Zindler, S., and S. Hart, 1986. Chemical geodynamics. Ann. Rev. Earth Planet. Sci. 14, 493-571.

Conclusion

Vers une géophysique probabiliste

Tous ces instants se perdront dans le temps comme des larmes dans la pluie

(Ridley Scott, Blade Runner)

Ce qu'il faut (entre autre) retenir de ce mémoire

Au cours de notre voyage entre Moho et la base du manteau, j'ai tenté de montrer comment intégrer certaines observables géophysiques, et tout particulièrement l'information sismologique, aux modèles géodynamiques. Autour du Moho, sous le centre-est des États-Unis, des déformations actuelles et passées d'origines géodynamiques différentes ont créé des fabriques, qui sont aujourd'hui distribuées en trois couches superposées. Ces fabriques sont responsables de l'anisotropie sismique observée dans cette région. Il est ensuite clairement apparu, en analysant les anomalies de vitesse des ondes de volumes et de la densité, que le manteau n'est pas chimiquement homogène. La détermination de la structure thermochimique nécessite de contraindre les variations de densité, si possible indépendamment des variations de vitesse sismique, ainsi qu'une modélisation appropriée de l'équation d'état. Autre point crucial, la prise en compte des diverses sources d'incertitudes qui permet de restreindre le nombre de modèles possibles, tout en gardant une certaine marge de sécurité. Deux régions ont particulièrement retenu notre attention. La lithosphère continentale archéenne, bien visible sur les modèles tomographiques, est sans doute appauvrie en éléments denses, ce qui lui vaut sa stabilité à long terme. À la base du manteau, les anomalies de vitesse de cisaillement résultent très probablement d'anomalies thermiques et chimiques à grande échelle. La nature et l'origine des ces variations chimiques restent à préciser. Disons simplement qu'une variation de la fraction volumique de fer semble être un excellent candidat, et qu'une hypothèse séduisante concernant l'origine de ces anomalies est l'interaction entre la convection du manteau et des réservoirs issus d'une différentiation partielle dans la jeunesse de la Terre.

Une hypothèse

Pour clore ce tableau, j'aimerais proposer une hypothèse, sans doute un peu prématurée, mais qui d'une certaine façon permet de créer un lien entre les anomalies thermochimiques localisées à la base et au sommet du manteau. La lithosphère archéenne est le résultat d'une forte activité volcanique et plutonique il-y-a environ 3 milliard d'années. Cette activité est certainement liée au fait que le manteau était plus chaud à cette époque, mais elle pourrait avoir été amplifiée par le démarrage de la convection thermochimique. Les modèles de convection thermochimiques explorés dans ce mémoire (Chapitre 4), montrent que la déstabilisation de la couche de matériau dense est immédiatement suivie par la formation de panaches thermochimiques (ou, si l'influence de la transition de phase à 660 km est importante, simplement thermiques) de grande taille. L'arrivée de ces panaches sous la surface génère localement de fortes élévations de la température (avec une RMS de l'ordre de 500 K) qui, dans le cas de la Terre archéenne, pourraient avoir contribué à l'augmentation du taux de fusion partielle, et donc à l'extraction des éléments denses et de l'eau de la lithosphère. Par la suite, l'activité des panaches continue, mais plus modestement, avec des variations de température sous la surface réduites de moitié. Selon cette hypothèse, et si une petite fraction au moins du matériau dense a pu franchir la discontinuité des 660 km, la croûte archéenne devrait être enrichie en éléments denses (notamment Fe, Al, et Ca), point sur lequel il ne semble pour le moment pas y avoir de consensus (Rudnick et Fountain, 1995).

Vers une géophysique probabiliste

Au début du 20ième siècle, les physiciens entamèrent une révolution dans leur compréhension du monde microscopique, en passant de la description déterministe de la mécanique classique, à celle probabiliste de la mécanique quantique. La position d'un électron autour de son noyau atomique à un instant donné, par exemple, n'est plus décrite par trois nombres, mais par une densité de probabilité (sa fonction d'onde) qui, comme son nom l'indique, donne la probabilité de trouver l'électron en chaque point de l'espace. Peut-être les Sciences de la Terre doivent-elles à leur tour évoluer vers une formulation probabiliste des phénomènes qu'elles étudient.

Précisons un peu les choses afin d'éviter les confusions. La mécanique quantique dit que la nature même des lois qui régissent la dynamique d'une particule (ou d'un système de particules) est probabiliste. Dans le cas des Sciences de la Terre, la nature probabiliste provient plutôt de ce que l'on traite d'un objet complexe, où de nombreux phénomènes entrent en jeu et interagissent. De ce point de vue, on se rapproche plus de la physique

statistique qui déduit des quantités moyennes à l'échelle macroscopique à partir de propriétés locales microscopiques. Lorsque l'on considère une observable géophysique ou géochimique, il faut garder à l'esprit qu'elle est passée au travers d'un filtre hautement non-linéaire et dispersif, la Terre. La répartition et la disponibilité des observables, leurs incertitudes aussi, augmentent, parfois beaucoup, le pouvoir dispersif de ce filtre. Résultat, lorsqu'on déroule ce filtre à l'envers, on n'obtient pas à proprement parler de solution unique, mais un ensemble de solutions expliquant plus ou moins bien les observables. Nous avons brièvement vu, en introduction, les difficultés que peuvent rencontrer les problèmes inverses pour trouver la solution la mieux adaptée aux observables disponibles, et la subjectivité des solutions finalement retenues. D'où l'idée, pour un problème donné, d'explorer l'espace des modèles à l'aide d'une méthode de Monte-Carlo (donc, une méthode directe) en calculant la densité de probabilité (basée sur l'accord entre les observables modélisées et les observables réelles) en chaque point de cet espace. Une cartographie appropriée de l'espace des modèles permet *de facto* de localiser le maximum (absolu) de la densité de probabilité, en évitant d'éventuels maximum locaux. Dans les problèmes inverses, en revanche, la prescription de régularisation et d'information a priori pousse souvent la solution vers un maximum local de la densité de probabilité (Figure C.1).

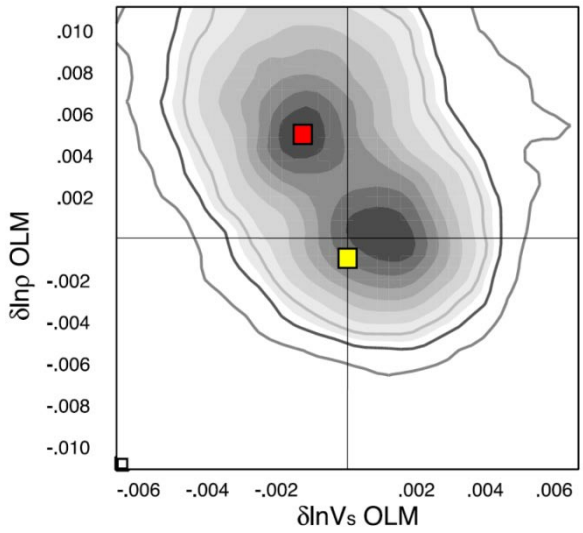

Figure C.1 – Densité de probabilité pour le sommet du manteau inférieur (670-1200 km) représentée en fonction de l'anomalie de densité et de l'anomalie de vitesse de cisaillement (Resovsky et Trampert, 2003). Le maximum de probabilité est indiqué en rouge. Une étude similaire, mais basée sur une inversion de données (Ishii et Tromp, 1999) localise la solution (en jaune) près d'un maximum de probabilité secondaire.

Bien sûr, l'idée d'un traitement probabiliste (on parle aussi d'approche Bayesienne) des problèmes rencontrés en Sciences de la Terre n'est pas nouvelle, et la théorie en est bien développée (p.e., Tarantola, 1987; Mosegaard et Tarantola, 1995; Sambridge et Mosegaard, 2002). Avec l'augmentation de la puissance de calcul, elle a même récemment

connu un certain essor. Cette approche reste cependant marginale, surtout lorsqu'il s'agit d'établir des fonctions de densité de probabilité. Le champ d'application est pourtant vaste, potentiellement tous les problèmes qui impliquent, à des degrés divers, des observables géophysiques, géochimiques ou géologiques. La plupart des perspectives évoquées à la fin de chacun des chapitres de ce mémoire en fait partie.

Une exploration exhaustive de l'espace des modèles peut cependant se révéler très coûteuse en temps de calcul. Pour un problème donné, la taille de l'espace des modèles est bien sûr contrôlée par le nombre de dimensions de cet espace, chaque paramètre que l'on souhaite résoudre comptant pour une dimension. Avec 10 processeurs, chacun capable de tester 1000 modèles par seconde, l'exploration systématique d'un espace modèle à N dimensions prendra, si l'on échantillonne chaque dimension avec 10 valeurs, 10^{N-4} secondes. Tant que le nombre de paramètres est petit, de l'ordre de 10, les méthodes de Monte-Carlo classiques parviennent à échantillonner convenablement l'espace des modèles dans un temps raisonnable (une dizaine de jour selon l'estimation précédente). Cela permet déjà d'aborder un grand nombre de problèmes, par exemple la détermination un profil de vitesse sismique dans le manteau supérieur. Pour des problèmes plus complexes (notamment en tomographie sismique) le nombre de paramètres augmente rapidement, et il est illusoire de vouloir utiliser une méthode de Monte-Carlo classique. Il faudra plutôt faire appel à des méthodes 'intelligentes', c'est-à-dire capables de converger vers la solution la plus probable sans échantillonner l'espace des modèles de façon systématique. Citons notamment :

- Les algorithmes génétiques (p.e., PIKAIA, Charbonneau et Knapp, 1995), qui sont inspirés de la théorie darwinienne de l'évolution des espèces. Chaque nouvelle génération de modèles est construite à partir des meilleurs individus de la génération précédente et de quelques (le taux est fixé par l'opérateur) modèles mutants.
- La méthode Metropolis (p.e., Mosegaard et Tarantola, 1995), également très populaire en Sciences de la Terre, et qui s'apparente à une marche au hasard (ou promenade de l'ivrogne), à ceci près le choix de la position n+1 n'est pas complètement aléatoire, mais dépend du rapport entre la valeur de la fonction de coût pour les modèles n et n+1 (il reste à l'ivrogne quelques facultés qui lui permettent de reconnaître plus ou moins bien le chemin vers son domicile).
- L'algorithme de voisinage (Sambridge, 1999a, 1999b), utilisé avec succès par la tomographie probabiliste (Resovsky et Trampert, 2003; Trampert et al., 2004), et dont l'avantage, par rapport aux méthodes précédentes, est de cartographier l'ensemble de l'espace des modèles, ce qui permet de définir entre autre des fonctions de densité de probabilité 1D ou 2D. La Figure C.2 représente la première étape de cette méthode, c'est-à-dire la détermination d'une cartographie approximative de la densité de

probabilité en échantillonnant l'espace des modèles avec une fréquence d'échantillonnage dépendant de la fonction de coût.

- Les réseaux neuronaux, enfin, méthode très prometteuse (p.e., van der Baan et Jutten, 2000; Meier et al. 2007), qui consiste à représenter une fonction non-linéaire de plusieurs variables en combinant plusieurs fonctions mathématiques simples (p.e., la tangente hyperbolique, ou la gaussienne) et des paramètres adaptatifs (les matrices pondérées et les biais).

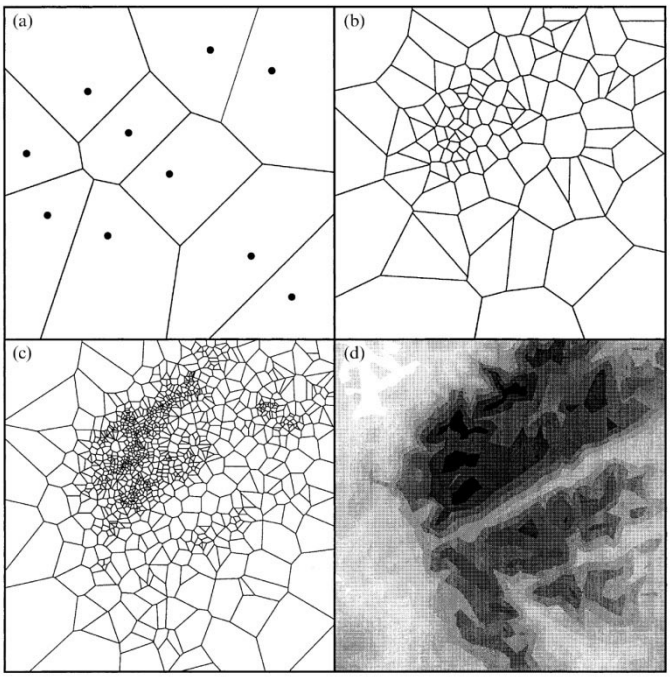

Figure C.2 – Détermination de la densité de probabilité approximative par l'algorithme de voisinage (Sambridge, 1999a). L'espace modèle est d'abord échantillonné par dix points et leur cellules de Voronoi (a), puis divisé en cellules plus petites (b et c) avec une densité plus élevée dans les portions de l'espace où la densité de probabilité est plus forte. La densité de probabilité à la fin du processus est représentée en (d).

Ces méthodes se différencient par leur capacité à converger vers la solution la plus probable et/ou, à échantillonner l'espace modèle. Dans le cas des algorithmes génétiques, par exemple, la convergence vers la solution la plus probable n'est pas garantie. Tout dépend de la topologie de l'espace modèle (le nombre et la localisation de minimums locaux de la fonction de coût), et des choix du taux de mutation et du nombre d'individus retenus pour construire la génération suivante. Metropolis converge mieux (l'espace modèle est bien échantillonné), mais elle fourni difficilement des fonctions de densité de probabilité 1D ou 2D. De ce point de vue l'algorithme de voisinage offre pour le moment la meilleure option, et permet de résoudre des problèmes relativement complexes, notamment en sismologie.

La théorie, les méthodes et les moyens numériques pour une géophysique probabiliste – mais pas aléatoire ! – sont déjà en place. Dans un futur proche, les méthodes

numériques vont sans doute s'affiner, et la puissance de calcul augmenter de nouveau. Reste à appliquer plus massivement et plus systématiquement ces méthodes probabilistes aux problèmes et questions posés par les Sciences de la Terre.

Post-scriptum (où l'auteur referme ce mémoire par une épanadiplose)

Dans le film d'Henri Verneuil, la cohabitation entre Jean Gabin et Alain Delon est parfois difficile, chacun des deux personnages ayant une personnalité bien trempée, et la modération de Maurice Biraud (un troisième larron) n'est pas de trop pour maintenir l'attelage sur les rails. Le casse se déroule sans accroc majeur jusqu'au moment où l'inexpérience d'Alain Delon fait capoter l'affaire. Le butin se retrouve en fin de compte dispersé au fond de la piscine d'un grand hôtel. L'étude de la Terre et de ses propriétés comporte de nombreux pièges, indéterminations, et autres fausses pistes. Souhaitons que géophysiciens, géochimistes et géologues saurons éviter ces pièges et parviendront à proposer, dans un futur proche, un modèle de Terre globalement cohérent.

Bibliographie

Charbonneau, P., et B. Knapp, 1995. A user's guide to PIKAIA 1.0, NCAR Technical Note 418+IA, National Center for Atmospherical Researches, Boulder.

Ishii, M., et J. Tromp, 1999. Normal-mode and free-air gravity constraints on lateral variations in velocity and density of Earth's mantle, *Science*, **285**, 1231-1236.

Mosegaard, K., et A. Tarantola, 1995. Monte Carlo sampling to inverse problems, *J. Geophys. Res.*, **100**, 12431-12447.

Resovsky, J.S., et J. Trampert, 2003. Using probabilistic seismic tomography to test mantle velocity-density relationships, *Earth Planet. Sci. Lett.*, **215**, 121-134.

Sambridge, M., 1999a. Geophysical inversion with a neighbourhood algorithm – I. Searching a parameter space, *Geophys. J. Int.*, **138**, 479-494.

Sambridge, M., 1999b. Geophysical inversion with a neighbourhood algorithm – II. Appraising the ensemble, *Geophys. J. Int.*, **138**, 479-494.

Sambridge, M., et K. Mosegaard, 2002. Monte Carlo methods in geophysical inverse problem, *Rev. Geophys.*, **40**, doi: 10.1029/2000RG000089.

Tarantola, A., 1987. Inverse problem theory, Elsevier, Amsterdam.

Trampert, J., F. Deschamps, J. Resovsky, et D.A. Yuen, 2004. Probabilistic tomography maps chemical heterogenities throughout the mantle, *Science*, **306**, 853-856.

Rudnick, R.L., et D.M. Fountain, 1995. Nature and composition of the continental crust: a lower crust perspective, *Rev. Geophys.*, **33**, 267-309.

van der Baan, M., et C. Jutten, 2000. Neural networks in geophysical applications, *Geophysics*, **65**, 1032-1047.